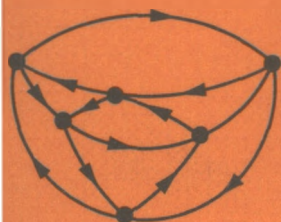


Lectures presented  
at the  
International Course  
on Nuclear Theory,  
Trieste, 13 January - 12 March 1971  
organized by the  
International Centre  
for Theoretical Physics,  
Trieste



# THE STRUCTURE OF NUCLEI



INTERNATIONAL ATOMIC ENERGY AGENCY, VIENNA, 1972



## THE STRUCTURE OF NUCLEI



INTERNATIONAL CENTRE FOR THEORETICAL PHYSICS, TRIESTE

# THE STRUCTURE OF NUCLEI

LECTURES PRESENTED AT THE  
INTERNATIONAL COURSE ON NUCLEAR THEORY  
AT TRIESTE FROM 13 JANUARY TO 12 MARCH 1971  
ORGANIZED BY THE  
INTERNATIONAL CENTRE FOR THEORETICAL PHYSICS, TRIESTE

INTERNATIONAL ATOMIC ENERGY AGENCY  
VIENNA, 1972

INTERNATIONAL CENTRE FOR THEORETICAL PHYSICS, TRIESTE  
IAEA, VIENNA, 1972  
STI/PUB/305

Printed by the IAEA in Austria  
June 1972

## FOREWORD

The International Centre for Theoretical Physics has maintained an interdisciplinary character in its research and training program as far as different branches of theoretical physics are concerned. In pursuance of this aim the Centre has organized extended research courses with a comprehensive and synoptic coverage in varying disciplines. The first of these - on plasma physics - was held in 1964; the second, in 1965, was concerned with the physics of particles; the third, in 1966, covered nuclear theory; the fourth, in 1967, dealt with condensed matter; the fifth, in 1969, was a course on nuclear structure; the sixth, in 1970, concerned imperfect crystalline solids. The proceedings of all these courses were published by the International Atomic Energy Agency. The present volume records the proceedings of the seventh course, held from 13 January to 12 March 1971, which dealt with the study of nuclear structure. A grant from the Swedish International Development Authority, which made it possible to increase the participation of physicists from Africa, India and Pakistan, is gratefully acknowledged.

The program of lectures was organized by Professors L. Fonda (Trieste, Italy) and G. Ripka (Saclay, France).

Abdus Salam



# CONTENTS

## PART I: NUCLEAR REACTIONS

### 1. Heavy-ion reactions

Nuclear spectroscopy with direct reactions induced by heavy ions (IAEA-SMR-8/3) .....	3
W. von Oertzen	
Nuclear spectroscopy in the 1f-2p shell with heavy-ion reactions (IAEA-SMR-8/26) .....	43
M.-C. Lemaire	

### 2. Low-energy nuclear reactions

Spin-orbit interaction in the inelastic nucleon scattering (IAEA-SMR-8/8) .....	75
J. Raynal	
A unified theory of nuclear reactions and bound structures and cluster representations (IAEA-SMR-8/25) .....	117
K. Wildermuth	
Optical potential for deuteron scattering (IAEA-SMR-8/20) .....	145
M. Bauer	
Direct methods in scattering theory (IAEA-SMR-8/41) .....	149
B.N. Zakhariev	
Rearrangement collisions (IAEA-SMR-8/9) .....	163
B.N. Zakhariev Yu.I. Fenin and V.L. Shmonin	
On Kapur-Peierls theory (IAEA-SMR-8/11) .....	171
M.A. Nagarajan	

### 3. High-energy nuclear reactions

Scattering of high-energy particles on light nuclei (IAEA-SMR-8/17) .....	185
R. Guardiola	
High-energy scattering of hadrons from nuclei (IAEA-SMR-8/27) ....	195
J. Gillespie	
High-energy scattering of electrons from nuclei (IAEA-SMR-8/31) ...	217
C. Ciofi degli Atti	

## PART II: NUCLEAR STRUCTURE

### 1. Microscopic theory of effective interactions

Theory of effective interactions (IAEA-SMR-8/7) .....	257
M. W. Kirson	
Hartree-Fock theory of finite nuclei in the local density approximation (IAEA-SMR-8/29) .....	287
J. Németh	

### 2. Shell-model configuration mixing

Microscopic description of the 2p-1f shell nuclei (IAEA-SMR-8/43) ...	309
A. Rimini	
Number-conserving quasi-particle calculations (IAEA-SMR-8/13) ....	319
T. Weber	
Ground-state properties of light nuclei as deduced from variational calculations (IAEA-SMR-8/23) .....	329
S. Boffi	

### 3. Theory of collective motion and fission

Anharmonicity and the particle-vibration coupling (IAEA-SMR-8/30) .....	339
L. Šips	
Quasi-particle vibration coupling (IAEA-SMR-8/10) .....	357
W. Rybarska	
Nuclear fission (IAEA-SMR-8/21) .....	373
K. Dietrich	
Quadrupole coupling constant for large deformations (IAEA-SMR-8/14) .....	401
M. Zielinska-Pfabé, Z. Bochnacki, S. Gabrakov	

### 4. Short-range correlations

Jastrow correlations - diagrammatic expansions (IAEA-SMR-8/24) .....	413
G. Ripka	
Variational determination of the effective interaction in nuclei (IAEA-SMR-8/22) .....	439
M. E. Grypeos	

## PART III: SLOWING-DOWN AND IMPLANTATION OF IONS IN SOLIDS

Ion implantation and channelling (IAEA-SMR-8/51) .....	457
J. A. Davies	
Static magnetic interaction and nuclear magnetic moments (IAEA-SMR-8/47) .....	565
S. Ogaza	
List of directors, lecturers and participants .....	589

## PART I: NUCLEAR REACTIONS

### 1. Heavy-ion reactions



# NUCLEAR SPECTROSCOPY WITH DIRECT REACTIONS INDUCED BY HEAVY IONS

W. VON OERTZEN  
Max-Planck-Institut für Kernphysik,  
Heidelberg,  
Federal Republic of Germany

## Abstract

NUCLEAR SPECTROSCOPY WITH DIRECT REACTIONS INDUCED BY HEAVY IONS.

1. Introduction; 2. One-nucleon transfer reactions; 3. Multi-nucleon transfer reactions; 4. Nuclear-structure effects in the elastic scattering of nuclei on nuclei.

## 1. INTRODUCTION

The study of the direct interactions of complex nuclei with nuclei was started more than ten years ago. The development of this field of nuclear physics was rather slow, because of both experimental and theoretical problems. In recent years, more efforts have been devoted to this field. The main motivations which were put forward for the use of heavy ions as particularly interesting probes for the study of nuclear properties may be listed as follows:

(1) The large mass of the projectile introduces large angular momenta and high recoil velocities to the residual nuclei. The small value of the ratio (nucleon mass/nuclear mass) can be used to introduce specific approximations in the analysis.

(2) The high charge of the projectile makes the Coulomb interaction the dominating feature at lower energies. Effects observed below or at the Coulomb barrier can be treated quantitatively; for large values of the Coulomb parameter semi-classical models can be used.

(3) Transfer reactions involving many nucleons are possible, and it is expected to obtain information on states with many-particle excitations.

(4) The strong absorption of the projectile in the target nucleus for small impact parameters (strong absorption of the lower partial waves) gives to the direct reactions the character of surface reactions.

However, the theoretical complications in the quantitative interpretation of direct reactions above the Coulomb barrier is still one of the main obstacles in the application of the heavy-ion-induced direct reaction to quantitative studies of nuclear structure. In the three sections, three subjects will be discussed for which a satisfactory analysis of the data can be given or the information can be extracted qualitatively with a high degree of confidence.

## 2. ONE-NUCLEON TRANSFER REACTIONS

One-nucleon transfer reactions induced by light ions have been used extensively as a spectroscopic tool. The methods of analysis are well developed for these reactions and it is possible to extract rather reliable spectroscopic information from the experiments. The use of the heavy-ion reaction for the study of single-particle properties can be motivated by the following aspects: (a) transfer reactions below the Coulomb barrier can be subjected to rigorous quantitative analysis [1 - 3] (mostly restricted to ground-state transitions); (b) at energies well above the Coulomb barrier the single-nucleon transfer reaction is also only sensitive to the nuclear surface, because of the strong absorption of the scattering waves. The calculated cross-sections therefore become independent of the nuclear interiors, i.e. much more independent of the choice of the scattering

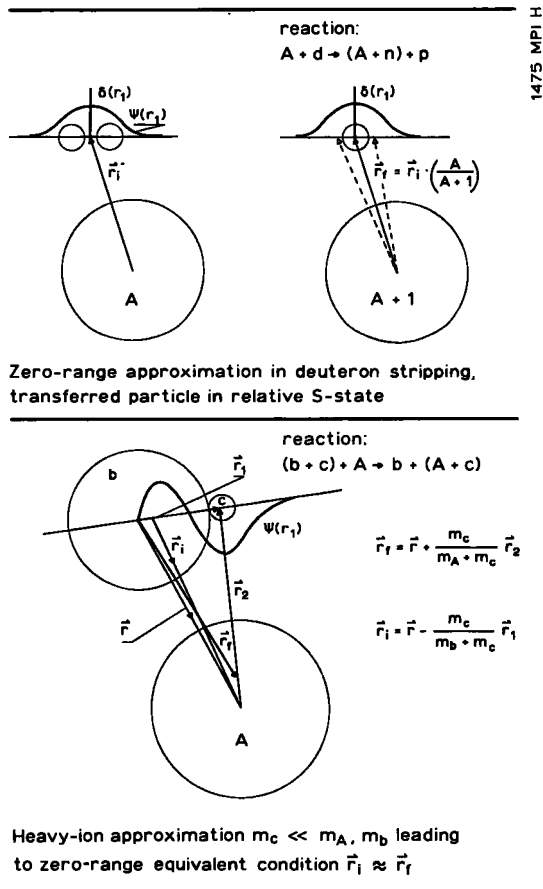


FIG. 1. Co-ordinates and mass relations in one-nucleon transfer reactions with light projectiles and with heavy ions.

potential parameters than in reactions with light ions. The absolute cross-sections, as a rule, are difficult to reproduce quantitatively, whereas the relative spectroscopic information for different nuclear levels is obtained rather accurately. Furthermore, the analysis of the single-nucleon transfer reaction gives insight into the problems of the multi-nucleon transfers reaction.

The analysis of the sub-Coulomb transfer reactions on the basis of the DWBA has been extensively discussed by Buttle and Goldfarb [2, 3]. Their method of calculating the transition amplitude will be sketched in the following. Under certain conditions, the same approach can then be used for reactions above the Coulomb barrier.

For a reaction  $A(a, b)B$  with  $a = (b+c)$ ,  $c$  being a nucleon, the DWBA transition amplitude reads

$$T_{if} = \int d\vec{r}_f d\vec{r}_i \chi^{(-)}(\vec{k}_f, \vec{r}_f) \psi_{\ell_2 j_2}(\vec{r}_2) V(\vec{r}_2) \psi_{\ell_1 j_1}(\vec{r}_1) \chi^{(+)}(\vec{k}_i, \vec{r}_i)$$

Here  $\chi(\vec{k}_j, \vec{r}_j)$  are the scattering wave-functions in the initial and final channels (pure Coulomb wave-functions for energies up to  $2/3$  of the Coulomb barrier). The interaction  $V(r_2)$ , in the representation chosen here, is the potential which binds the transferred particle in the final nucleus, and  $\psi_{\ell j}(\vec{r}_1)$  are the bound-state wave-functions of the transferred particle in the initial and final nuclei.

The six-dimensional integral can be reduced to a three-dimensional integral by using approximations which are specific to the properties of heavy ions. A complete integration of the integral has been done by Yoshida [4]. The first approximation is to neglect terms of the order (nucleon mass/nuclear mass) in the co-ordinates of the scattering wave-functions (see Fig.1). The neglect of these terms (together with the second approximation) makes it possible to separate the integration over the variables  $\vec{r}_1$  (or  $\vec{r}_2$ ) and  $\vec{r}$ , the latter variable being the argument common to both scattering wave-functions. The second approximation rests on the fact that only the tails of the bound-state wave-functions are involved in the reaction, because of the large distances between the two nuclei at energies below the Coulomb barrier. For energies above the Coulomb barrier the same approximations may be used. The bound-state wave-functions are approximated by equivalent spherical Hankel functions (for bound states of charged particles reasonable descriptions by Hankel functions can be obtained using an effective binding energy [2]).

$$\psi_{\ell_1 j_1}(\vec{r}_1) = N_1 h_{\ell_1}^{(1)}(i\alpha_1 r_1) Y_{\ell_1}^{m_1}(\theta_1)$$

where  $N_1$  is the normalization constant and  $\alpha = \sqrt{2m_c E_B} h^{-2}$ .

The DWBA-cross-section becomes, under these conditions,

$$\frac{d\sigma}{d\Omega} \sim S_{\ell_1 j_1} S_{\ell_2 j_2} |A_{\ell_1} \cdot N_2|^2 \sum_{\ell m} (j_1 \frac{1}{2} \ell 0 | j_2 \frac{1}{2})^2 |T_{\ell m}(\theta)|^2$$

With

$$T_{\ell m}(\theta) = \int d\vec{r} \chi^{(-)}(\vec{k}_f, \vec{r}) h_{\ell}^{(1)}(i\alpha_2 \vec{r}) Y_{\ell}^m(\vec{r}) \chi^{(+)}(k_i, \vec{r})$$

This integral is equivalent to those integrals obtained in the zero-range approximation for light ions where the nucleons in the projectile are in an S-state. This fact is illustrated in Fig.1, where the co-ordinates used in the formulas are defined.

The normalization factor  $A_{\ell_1}$  is an integral over the variable  $r_1$  and can be expressed analytically (for  $\alpha_1 \approx \alpha_2$ )

$$A_{\ell_1} = (-)^{\ell_1} \frac{\hbar^2}{2m_c} N_1 \frac{\alpha_2^{\ell_1}}{\alpha_1^{\ell_1+1}}$$

Two facts, which give a certain distinction to transfer reactions induced by light ions, have to be noted. The absolute cross-section depends on the product of two unknown spectroscopic factors  $S_{\ell_1 j_1}$  and  $S_{\ell_2 j_2}$  for the two nuclei involved. In reactions with light ions the factor for the light projectile is usually assumed to be unity. The absolute cross-section further depends on the normalization constants  $N_i$  of the single-particle wave-functions in the outer region of the nuclei. This circumstance is due to the restriction of the interaction region to the very surface of the

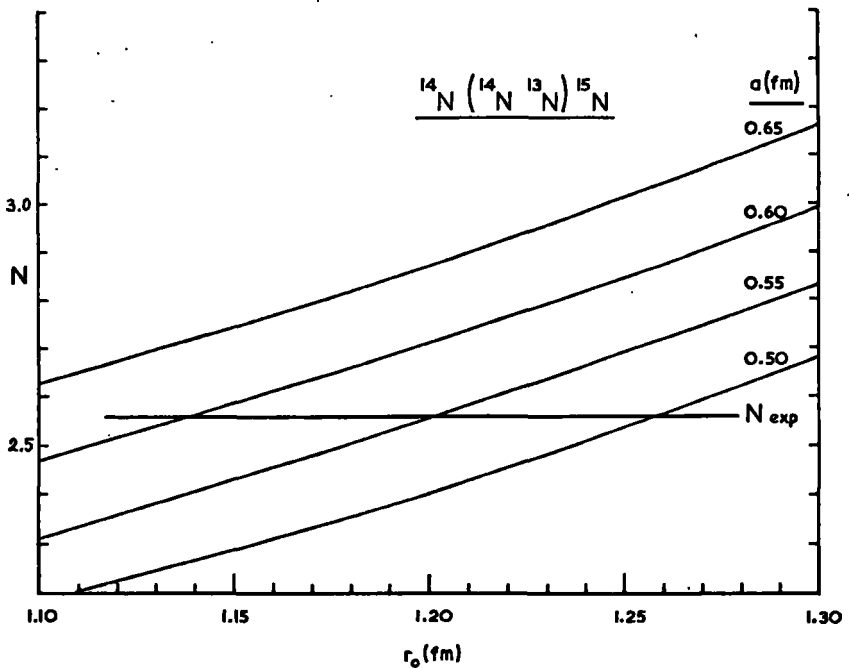


FIG. 2. Normalization of the neutron bound-state wave-functions in their dependence on shell-model parameters (Ref. [5]).

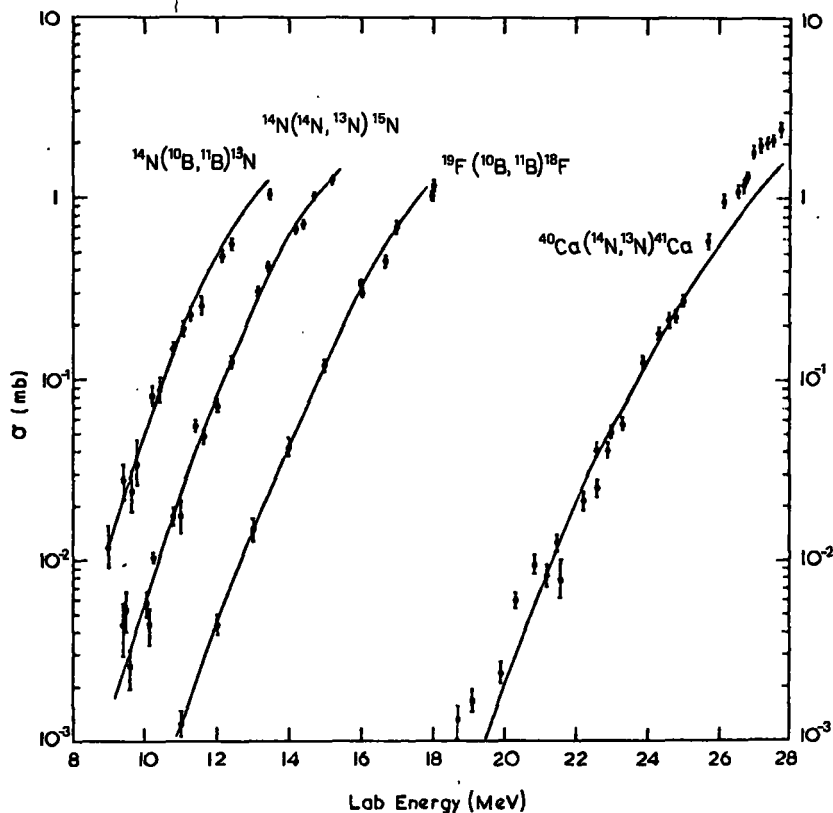


FIG. 3. Excitation functions of neutron transfer reactions and their comparison with DWBA calculations (Ref.[5]).

nuclei. In reactions with light ions the integration in the transition matrix element gives contributions from all parts of the nucleus because the scattering wave-functions still have appreciable amplitudes in the interior of the nuclei.

The sub-Coulomb transfer reaction, as well as the heavy-ion transfer reaction dominated by strong absorption, are only sensitive to the tails of the wave-functions and therefore indirectly sensitive to the choice of the shell-model potential used to calculate the single-particle wave-function and their asymptotic normalization. As an example, Fig.2 (Ref.[5]) shows the normalization constant  $N$  in its dependence on the parameters of the Woods-Saxon well for nitrogen. The parameters  $r_0$  and  $a$  are defined in the usual way. Assuming that the spectroscopic factors are well known from other sources, for example Ref.[6], the experimental quantity obtained in the analysis of the data can be defined to be the normalization constant  $N$ . Using this approach a determination of the shell-model-potential parameters can be obtained as has been done, for example, with the sub-Coulomb (d, p)-reaction on lead [7].

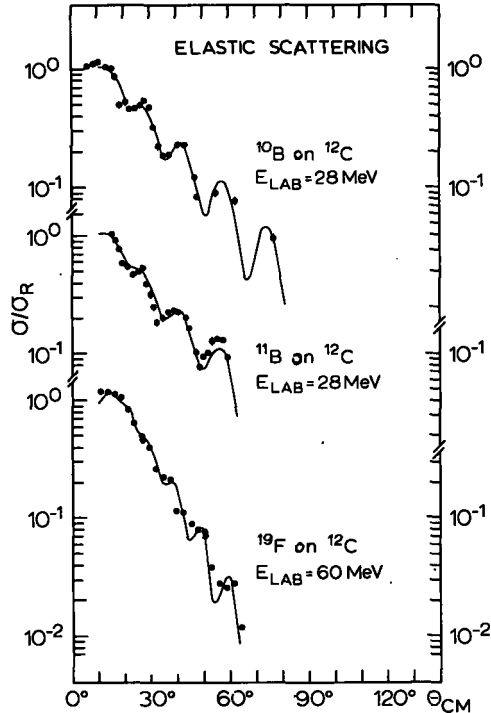


FIG. 4. Elastic scattering of  $^{10}\text{B}$ ,  $^{11}\text{B}$  and  $^{19}\text{F}$  on  $^{12}\text{C}$  at small angles. Optical-model calculations with the parameters given in Fig. 21; they are the same in all three cases.

Figure 3 gives an impression of the quality of the fits obtained to excitation functions of neutron transfer reactions. Here the shell-model parameters of the single-particle wave-functions were adjusted for fixed values of the spectroscopic factors.

For the description of the one-nucleon transfer reactions above the Coulomb barrier the same formulas as discussed for the sub-Coulomb region can be applied if there are no contributions from small internuclear distances. This is guaranteed if the wave-functions of relative motion are generated by strongly absorbing optical potentials which give negligible contributions from small internuclear distances and small partial waves. Figure 4 shows that a good description of elastic scattering is obtained with these potentials. The use of strongly absorbing potentials is important for two reasons. First, the optical-model wave-functions are always poorly determined for small internuclear distances. The optical model is only able to calculate correctly the asymptotic phases if no further information is available. The second reason comes from the derivation of the transition amplitude as discussed above.

Further, it has been pointed out by Dar [8] that the DWBA is not expected to be valid for strongly absorbed partial waves. The elastic scattering of heavy ions is mainly determined by the relatively weakly absorbed partial waves, at least in the forward hemisphere (see also

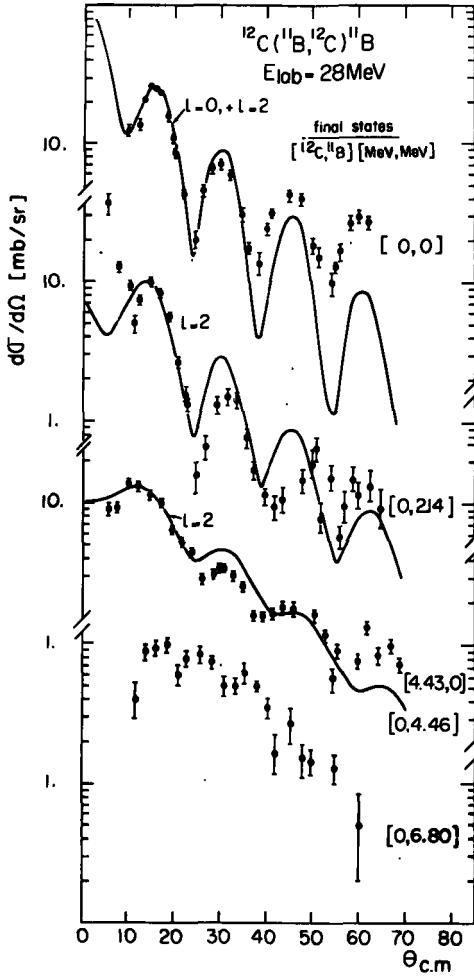


FIG. 5. DWBA-calculations for the reaction  $^{12}\text{C}(^{11}\text{B}, ^{12}\text{C})^{11}\text{B}$  leading to excited states of  $^{11}\text{B}$  and  $^{12}\text{C}$  (Ref. [9]).

section 3), and the same partial waves determine the features of the transfer reactions if the reaction is localized in angular momentum space. To achieve localization of the reaction, it is required that the partial waves at the surface,  $L_i$  and  $L_f$  for the initial and final channels, respectively, be matched by the angular momentum transfer  $\ell$  given by selection rules contained in the vector coupling coefficients:

$$|L_i - L_f| = \ell$$

This well known angular momentum matching condition can be put into the form  $R_{\text{int}}|k_i - k_f| = \ell$ . Here  $R_{\text{int}}$  is the interaction radius defined by the values of  $L_i$  and  $L_f$  for which the reflection coefficient in the elastic

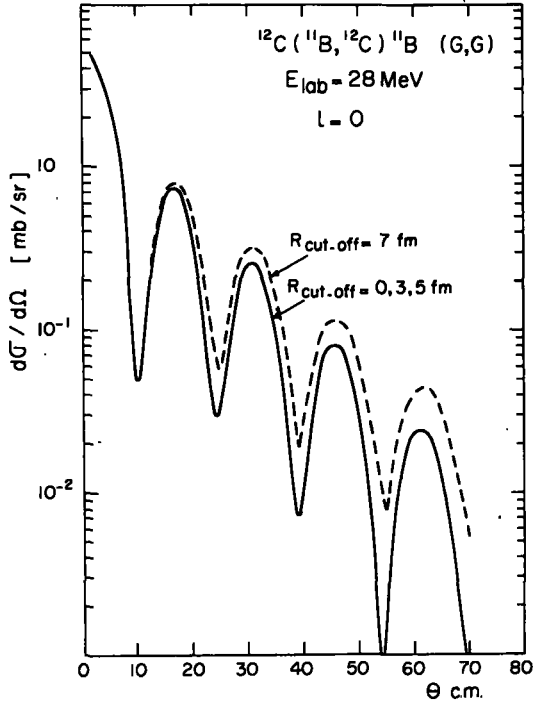


FIG. 6. Dependence of the calculated cross-section on the lower cut-off radius (Ref.[9]).

TABLE I. SPECTROSCOPIC FACTORS FROM THE ANALYSIS OF THE REACTION  $^{12}\text{C}(^{11}\text{B}, ^{12}\text{C})^{11}\text{B}$

Energy (MeV) of final states		Angular momentum transfer	Relative spectroscopic factors	
$^{12}\text{C}$	$^{11}\text{B}$		this experiment	Ref.[6]
0	0	0 and 2	1	1
0	2.14	2	0.27	0.263
4.43	0	2	0.1	0.19

scattering is  $|\eta_i| = 0.5$ , and  $L_i = k_i \cdot R_{\text{int}}$ . If the angular momentum matching condition is fulfilled within the limit of approximately one to two units of angular momenta, the reaction usually shows pronounced diffraction oscillations in the angular distributions (for small Coulomb parameter).

Figure 5 shows angular distributions of the proton transfer  $^{12}\text{C}(^{11}\text{B}, ^{12}\text{C})^{11}\text{B}$  (from Ref.[9]). The diffraction pattern shows that the reaction is well localized in angular momentum space. The use of strongly

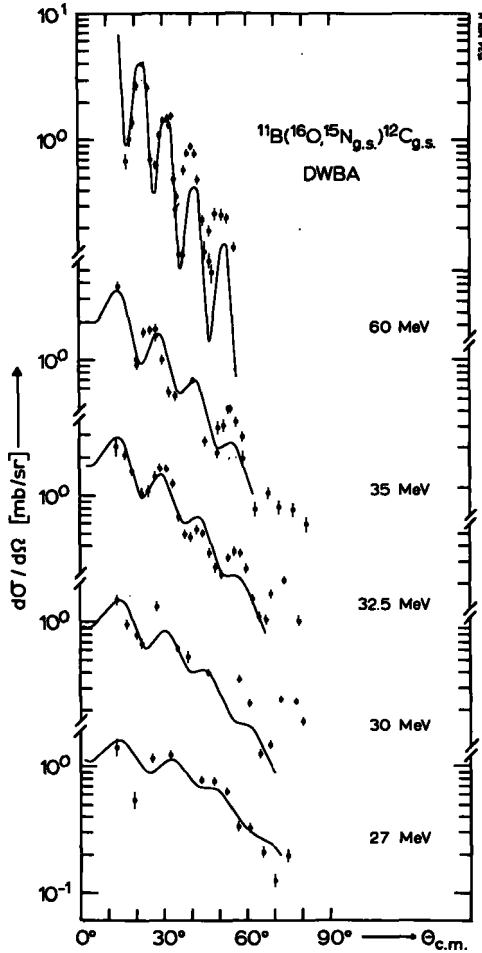


FIG. 7. Angular distributions of the proton transfer  $^{11}\text{B}(^{16}\text{O}, ^{15}\text{N})^{12}\text{C}$  at several energies and their comparison with DWBA-calculations (Ref. [20]).

absorbing optical potentials also ascertains that the reaction is localized in configuration space. In Fig.6 the dependence on the lower limit of integration in the transition amplitude is shown for the calculated cross-sections. A lower cut-off radius of 7 fm changes the cross-section in the maximum at  $18^\circ$  by only 10%. A distance of 7 fm between the two nuclei corresponds to a nuclear radius parameter  $r_0 = 1.55$  fm. At this radius, the single-particle wave-function has already good asymptotic behaviour. For the determination of relative spectroscopic factors the accurate description of the wave-function in this region is not important.

The relative spectroscopic factors corresponding to the calculations shown in Fig.5 are given in Table I.

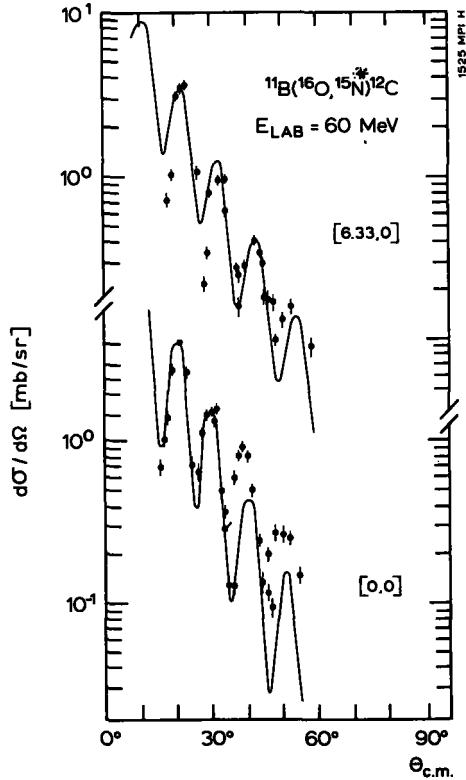


FIG. 8. Angular distributions of the proton transfer  $^{11}\text{B}(^{16}\text{O}, ^{15}\text{N})^{12}\text{C}$  at several energies and their comparison with DWBA-calculations (Ref.[20]).

As another example the proton transfer reaction  $^{11}\text{B}(^{16}\text{O}, ^{15}\text{N})^{12}\text{C}$  which has been studied at several energies is shown in Figs 7 and 8 (Ref.[10]). Strong transitions are observed for the single-particle states, the ground state and the 6.33 MeV state in  $^{15}\text{N}$ . The first transition is a pure  $\ell = 2$  transition, the  $p_{3/2}$  hole state at 6.33 MeV is populated by  $\ell = 0$  and  $\ell = 2$ . The angular distributions clearly show that the reaction is strongly localized, at the higher energy (Fig.7) where the Coulomb parameter is small, very strong diffraction structures are observed. At the lower energies, irregularities arise in the angular regions shown, because of the interference with the four nucleon transfer  $^{11}\text{B}(^{16}\text{O}, ^{12}\text{C})^{15}\text{N}$ . The structures around  $60^\circ$  to  $90^\circ$  at 27 MeV until 32.5 MeV are not produced by the proton transfer alone.

The relative normalization of the calculations shown, to the experiment, is the same for the five energies, within 15%, which is in the limits of the experimental errors for the absolute cross-sections. The relative spectroscopic factors for the two transitions shown in Fig.8 are (ground state)/(6.33 MeV state) = 2./3.9. This value is again in excellent agreement with expectations from shell-model calculations and other determinations.

Instead of giving more examples on the extraction of relative spectroscopic factors from heavy ion reactions, it is more apropos to discuss the effects which arise from the neglect of the terms of the order (nucleon mass/nuclear mass) in the co-ordinates of the transition amplitude (recoil effects). These effects will be particularly important for transfer reactions at high energies and for multi-nucleon transfer reactions discussed in the next section. For the illustration of these recoil effects it is useful to follow the approach of Greider [11].

The distorted waves are approximated for this purpose by a phase and amplitude function:

$$\chi^{(-)}(\vec{k}_f, \vec{r}_f) = B_f(\vec{k}_f, \vec{r}_f) \exp \left[ i \vec{k}_f \cdot \left( \frac{m_A}{m_B} \vec{r} + \frac{m_c}{m_B} \vec{r}_1 \right) \right]$$

$$\chi^{(+)}(\vec{k}_i, \vec{r}_i) = B_i(\vec{k}_i, \vec{r}_i) \exp \left[ i \vec{k}_i \cdot \left( \vec{r} - \frac{m_c}{m_a} \vec{r}_1 \right) \right]$$

The amplitudes  $B_j$  are slowly varying functions, which modulate the plane waves  $\exp(i\vec{k}_j \cdot \vec{r}_j)$ . For the transition amplitude one obtains

$$T_{if} \sim \int B_f^*(\vec{k}_f, \vec{r}) B_i(\vec{k}_i, \vec{r}) e^{i\vec{q} \cdot \vec{r}} \int d\vec{r}_1 e^{i\vec{p} \cdot \vec{r}_1} G(\vec{r}_1) d\vec{r}$$

with  $\vec{q} = \vec{k}_i - (m_A/m_B)\vec{k}_f$  and  $\vec{p} = -(\vec{k}_i/A_i + \vec{k}_f/A_f)$ ; the mass ratios are defined as  $A_i = m_a/m_c$  and  $A_f = m_B/m_c$ . The two momenta  $\vec{q}$  and  $\vec{p}$  give two sources of angular momentum transfer in the reaction. The first is related to the distance vector  $\vec{r}$  between the two colliding nuclear cores and is determined by the change in the wave numbers due to Q-values and changes in mass. It is the well known difference of the angular momenta in the grazing collisions. The second momentum is connected with the radius vector  $\vec{r}_1$ , the co-ordinate of the transferred particle, and gives an additional angular momentum transfer only for reactions in which the transferred particle comes from the surface of the projectile (this angular momentum transfer does not occur in (d, p) reactions, see Fig.1). The momentum  $\vec{p}$  is the difference in linear momentum per transferred particle between the incoming particle  $\vec{k}_i/A_i$  and the linear momentum per transferred particle of the final nucleus which recoils into the opposite direction  $-\vec{k}_f/A_f$ . The angular momentum connected with  $\vec{p}$  and  $\vec{r}_1$  can be estimated by assuming that the transferred particle is transferred on the interconnection line between the two nuclear cores. Then we obtain  $\vec{r} \parallel \vec{r}_1$  and  $|\vec{r}_1|$  is approximately  $|\vec{r}|/2$ . With  $A_i \cong A_f$  we obtain

$$L_p \cong (L_i + L_f)/2A_i$$

i.e. the angular momentum transfer  $L_p$  is given roughly by the angular momentum per nucleon (or per transferred particle) in the grazing collision averaged over the initial and final channels.

The angular momentum  $L_p$  is zero for the trivial case,  $m_c = 0$  (inelastic scattering) and is very small for transferred particles originating from states with very small values of  $\vec{r}_1$  like ( ${}^3\text{He}$ ,  ${}^4\text{He}$ ) or ( ${}^6\text{Li}$ , d).

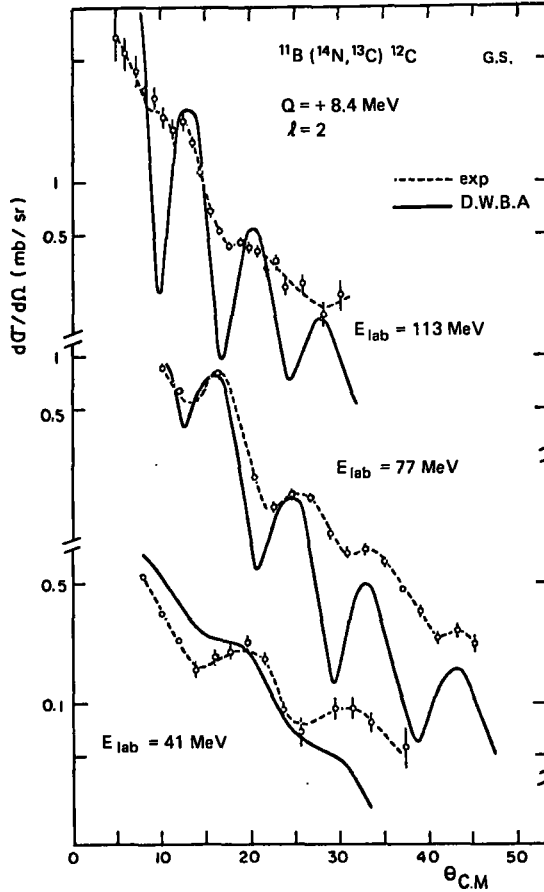


FIG. 9. Damping of the structure in the angular distributions of the reaction  $^{11}\text{B}(^{14}\text{N}, ^{13}\text{C})^{12}\text{C}$  with increasing energy. The curves represent DWBA-calculations with neglect of recoil terms (Ref.[13]).

The two angular momenta  $L_q$  and  $L_p$  are perpendicular to the reaction plane defined by  $\vec{r}$  and  $\vec{k}_j$ . The value of  $L_p$  will be appreciable at high energies in heavy-ion reactions where the angular momenta of grazing collision attain values of 30 to 50 units of  $\hbar$ . This fact can lead to a preferential population of single-particle states with orbital quantum numbers equal to  $L_p$ , as for example observed in high energy  $^{11}\text{B}$  induced reactions [12]. The presence of the angular momentum  $L_p$  can further lead to an increased mismatch in angular momentum space and thus lead to a damping of structures in angular distributions. This effect is shown for the reaction  $^{11}\text{B}(^{14}\text{N}, ^{13}\text{C})^{12}\text{C}$  in Fig.9 (Ref.[13]). The diffraction structure observed in the angular distributions at lower energies for the ground-state transition disappears at higher energies.

In heavy-ion-induced transfer reactions,  $L_p$  can be the more important source of angular momentum transfer; especially, at smaller scattering angles where the kinematical momentum transfer is small,  $L_p$  attains its maximum value and can give rise to strong populations of high-spin states.

### 3. MULTI-NUCLEON TRANSFER REACTIONS

In a reaction in which several nucleons are transferred from one nucleus to the other, the structure of the initial and final state has equal influence on the reaction process. This fact is, of course, true for any transfer reaction. However, for a multi-nucleon transfer reaction it is desirable that, at least, one of the states involved in the transition has a simple structure in order to extract information without too much complication. One can therefore try to deduce some general rules which help in the interpretation of the data. Following Rotter [14] the structural factors of the reaction will be discussed.

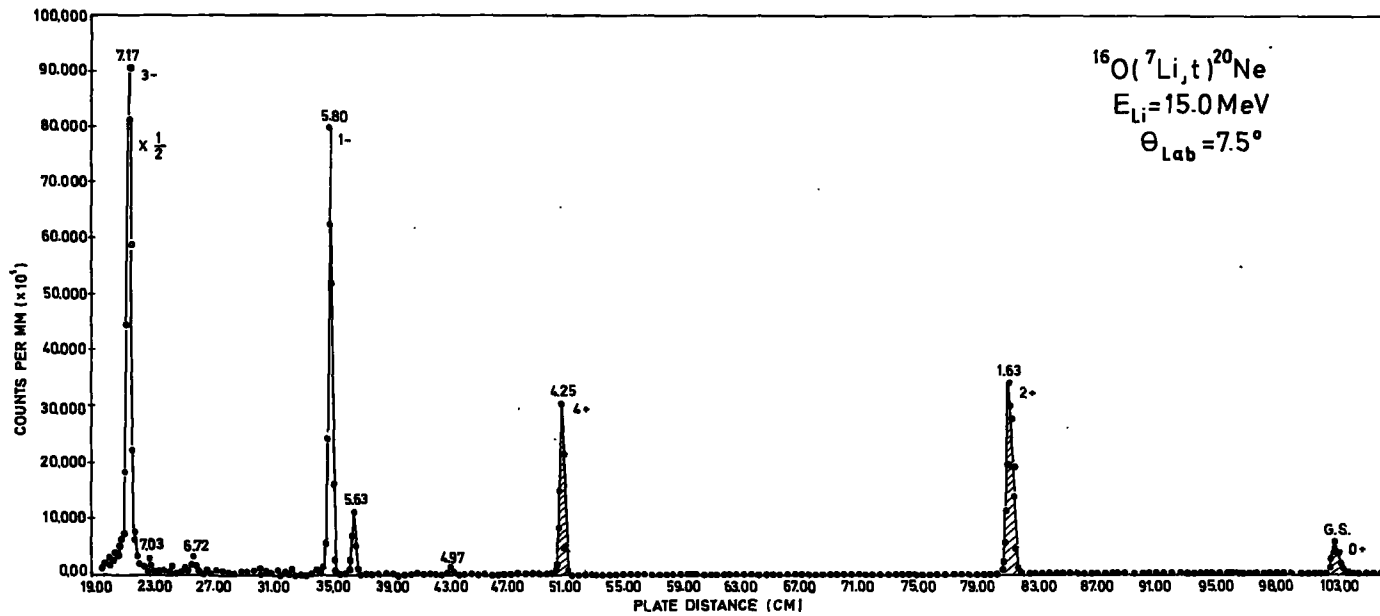
In a reaction  $A + B \rightarrow (A - k) + (B + k)$ , the transfer of  $k$  particles is adequately classified by the intermediate states of the  $k$  particles, with quantum numbers which are compatible with the quantum numbers of the initial and final states. The cross-section of the multi-nucleon transfer reaction can be written in terms of a structural part  $A_{NL}^{N'L'}$  and a dynamical part  $B_{NL}^{N'L'}$

$$\sigma(\theta) \sim \sum_{NLN'L'} \left( A_{NL}^{N'L'} B_{NL}^{N'L'} \right)^2$$

The sum is taken over all possible intermediate states of the  $k$  particles. The structural part consists of the overlap of the wave-function  $\phi_A$  of the nucleus  $A$  with the wave-function of the nucleus  $(A-K)$  and the  $k$  particles  $\phi_{A-k} \phi_k \psi_{NLM}$  and corresponding for the system  $(B+k)$ ,  $\phi_{B+k}$  and  $\phi_B \phi_k \psi_{N'L'M'}$ . The wave-function  $\psi_{NLM}$  describes the relative motion in the CM-system of the combined systems. Generally, the structural overlap can not be split into parts which depend independently on the initial and final system. The overlap can be factored in the following way to illustrate the appearance of the symmetry properties of the intermediate states ( $A_{NL}^{N'L'}$  corresponds in a certain way to the product of spectroscopic factors in one-nucleon transfer reactions):

$$A_{NL}^{N'L'} \sim \langle \chi_A | \chi_{A-k} \chi_k \rangle \langle \chi_{B+k} | \chi_B \chi_k \rangle \\ \times K_i(n\ell, NL, L_k) K_f(n\ell, N'L', L'_k)$$

The first two integrals are overlaps of the shell-model wave-functions with the  $k$  particles being in a state specified by inner quantum numbers  $(n, \ell)$  with definite values of spin, isospin and symmetry ( $S_k, T_k$  and  $[f_k]$ ). These two integrals represent the fractional parentage coefficients. The other two factors  $K_i$  and  $K_f$  give the probability of the formation of the



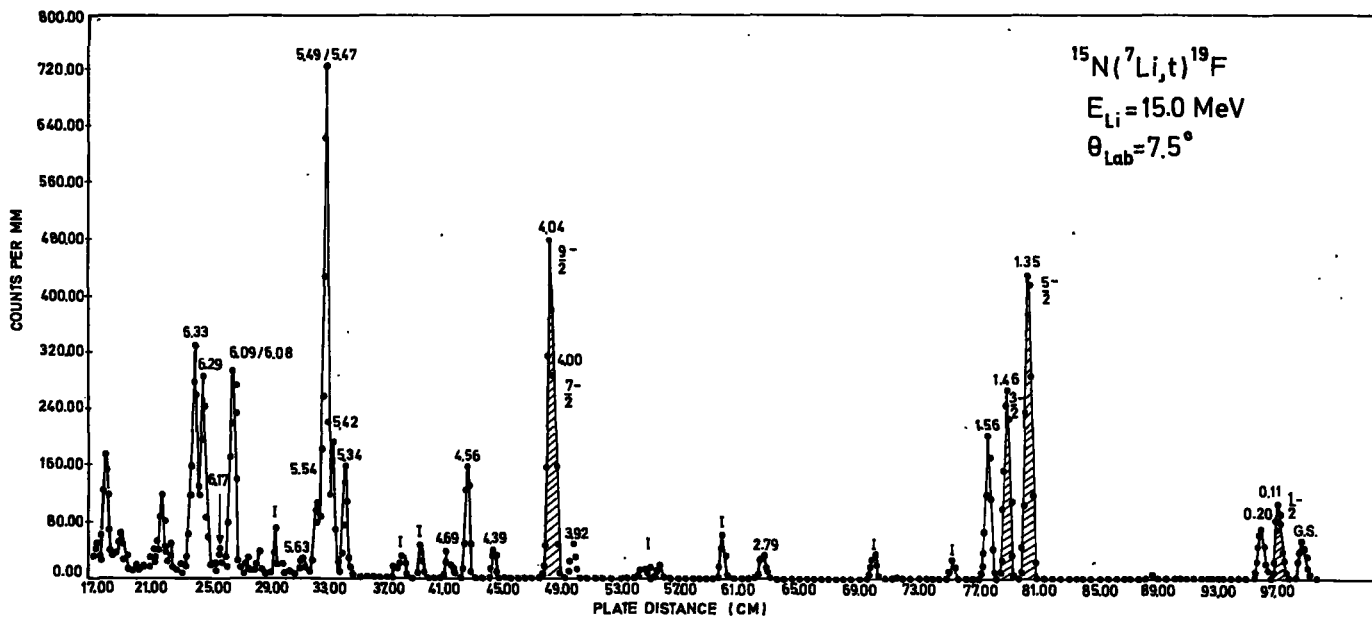


FIG. 10. Spectra of the four-nucleon transfer reactions ( $^7\text{Li}, t$ ) on  $^{16}\text{O}$  and  $^{15}\text{N}$  (from Ref. [15]).

state of the  $k$  nucleons with the given inner quantum numbers: overlap of the  $k$  separated particles with the wave-function of these particles in the intermediate state specified above

$$K(n\ell NL, L_k) = \int \chi_k^* (\phi_k \psi_{NLM})_{n\ell} d\tau$$

The fractional parentage coefficients contain the nuclear-structure information and primarily determine the strength of a transition. However, also the factors  $K_i$  and  $K_f$  have substantial influence on the value of the cross-section. From a discussion of these factors [14] important predictions related to features of experimental spectra can be derived.

(a) The values of  $K_i$  and  $K_f$ , when summed over all intermediate states, involving a change of internal quantum numbers  $(n, l)$  in the transition are as a rule much smaller (factor 10 to 100) than those which involve no change. Therefore, one can expect that for strong transitions always  $(n, l) = (n', l')$ . This fact immediately reduces the number of possible values of  $N, L$  and  $N', L'$ .

(b) If the Young scheme of the particles is changed during the transfer process, the cross-section is either zero or very small. This corresponds to a Young-tableau selection rule.

(c) The cross-section is maximum if the angular-momentum quantum numbers of the transferred nucleons are identical in the initial and final state ( $L'_k = L_k$ ). The cross-section is maximum if  $L_k$  and  $L'_k$  have maximum values.

(d) Transitions with pronounced structures in the angular distributions as a rule will be the result of only very few amplitudes in the sum for the differential cross-section. These transitions then correspond to transfer reactions where the internal quantum numbers and the Young scheme have not changed during the transfer, and both states have unique and simple structure (only one  $L_k$  and  $[f_k]$ , for example).

A few experimental examples will be given below which either prove these rules through known structure of the states involved, or examples which give qualitative structural information by application of these rules.

The absolute cross-section depends also on the radial form factor of the transferred nucleons, so the relation between reduced width and absolute intensity of a transition can not be put into a rule.

The choice of the projectile for a specific transfer reaction involves also the choice of the outgoing particle and can thus have considerable influence on the information obtainable from the experiment. In the reactions induced by  ${}^6\text{Li}$  and  ${}^7\text{Li}$ , the outgoing particles are very light particles ( $p, d, t, {}^3\text{He}, {}^4\text{He}$ ) which often have large cross-sections for compound-nucleus emission. The use of heavier ions as projectiles often gives more confidence to a direct discussion of experimental spectra, especially for the weaker transitions because the reactions have negligible contributions from compound nuclear processes.

In the following discussion a few examples of three-nucleon and four-nucleon transfer reactions are given. The four-nucleon transfer has been studied with very high resolution by Middleton et al. [15] with the ( ${}^7\text{Li}, t$ ) and the ( ${}^6\text{Li}, d$ ) reactions. In the  ${}^{16}\text{O}({}^7\text{Li}, t){}^{20}\text{Ne}$  reaction, the ground-state four-particle-zero-hole ( $4p-0h$ ) band of  ${}^{20}\text{Ne}$  is selectively populated

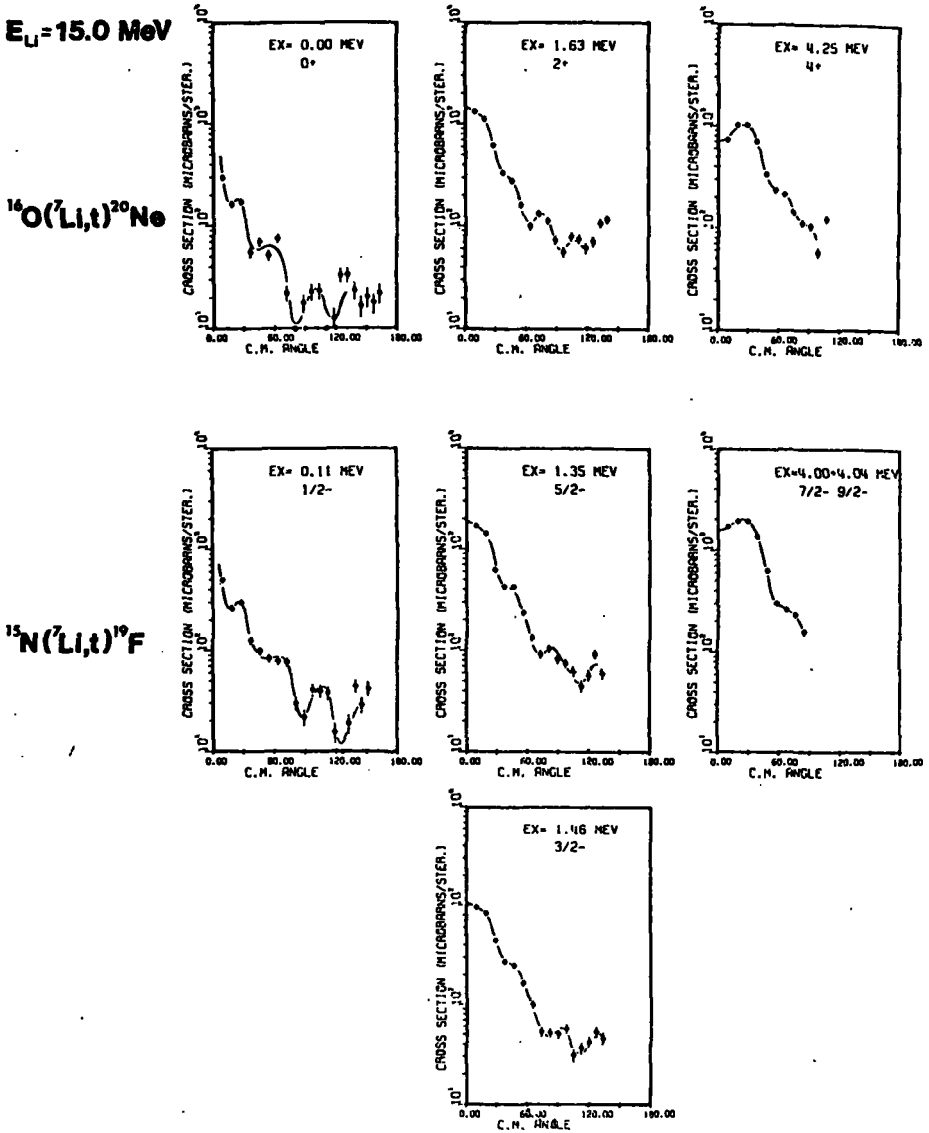


FIG. 11. Angular distributions of the four-nucleon transfer reactions ( $^7\text{Li}, t$ ) on  $^{16}\text{O}$  and  $^{15}\text{N}$  (from Ref. [15]).

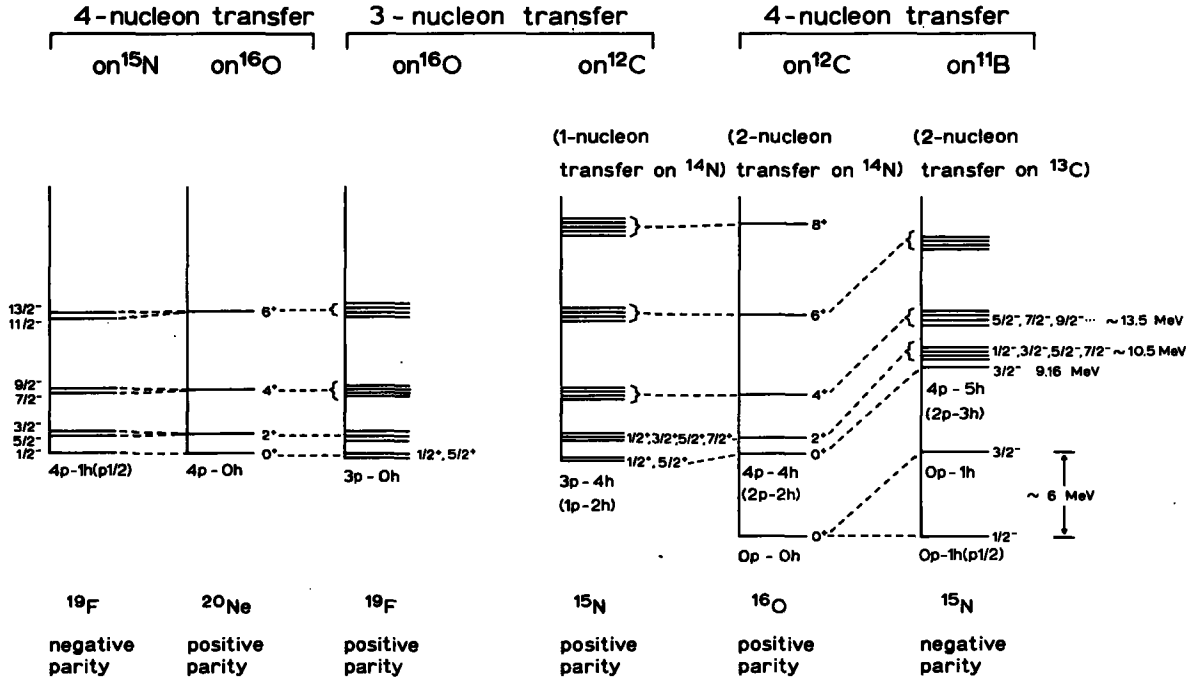


FIG. 12. Correspondence between (n-particle, n-hole) states in  $^{20}\text{Ne}$ ,  $^{19}\text{F}$ ,  $^{16}\text{O}$  and  $^{15}\text{N}$ . The relevant transfer reactions are indicated on top of the figure.

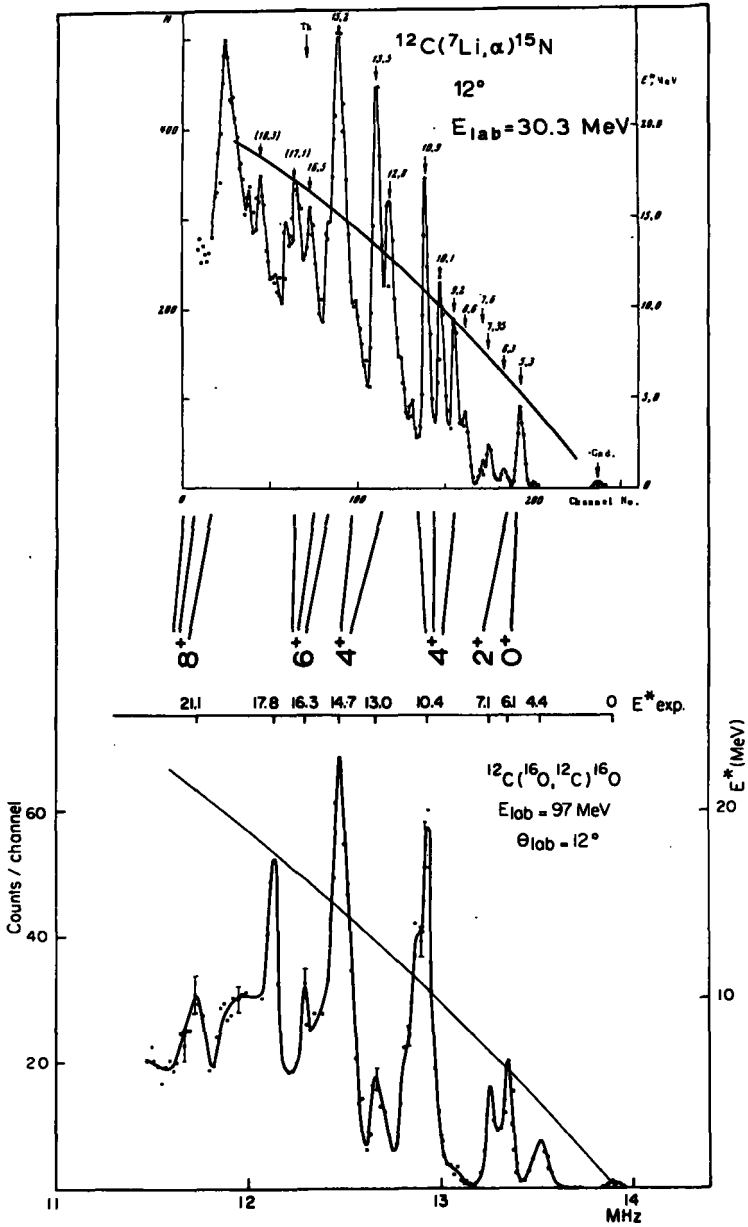


FIG. 13. Comparison of the four-nucleon and three-nucleon transfer reactions on  $^{12}\text{C}$  (Refs [19, 23]).

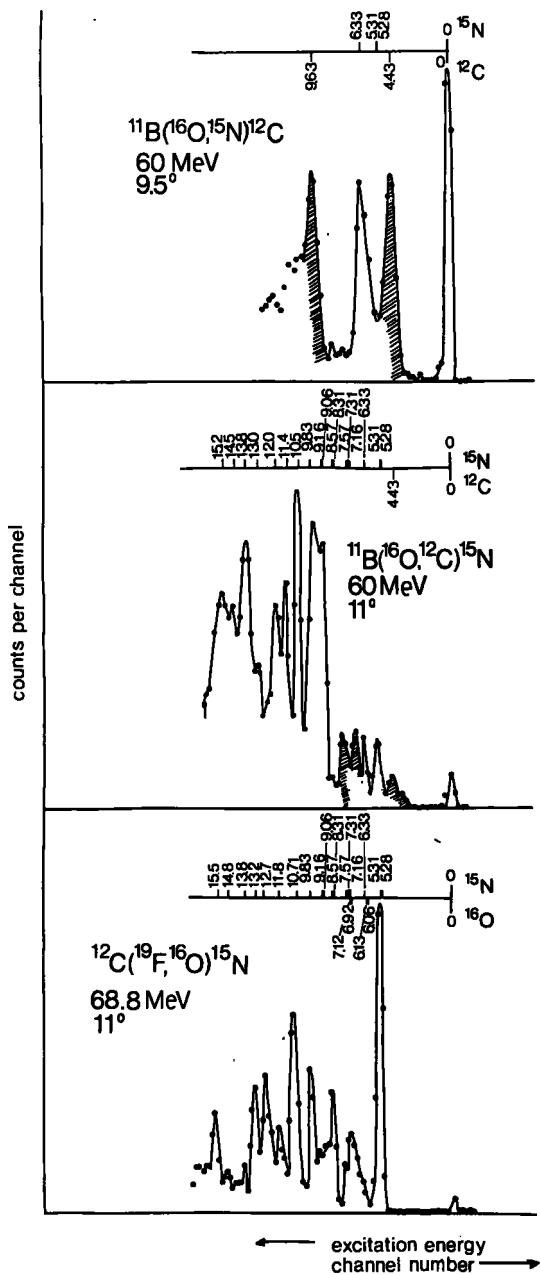


FIG. 14. Population of states of  $^{15}\text{N}$  in one-, three- and four-nucleon transfer reactions.

(Fig.10). The corresponding four-nucleon reaction on  $^{15}\text{N}$  populates many states in  $^{19}\text{F}$  (Fig.10). It is, however, possible to select from the experiment the states which correspond to the coupling of the  $p_{1/2}$  hole ( $^{15}\text{N}$  ground state) to the rotational band in  $^{20}\text{Ne}$ . Because of the identical structure of the wave function of the last four nucleons the angular distributions of corresponding transitions have the same shape (Fig.11). The correspondence of the states in  $^{20}\text{Ne}$  and  $^{19}\text{F}$  is shown in Fig.12 and has been drawn assuming weak coupling of holes and particles to the rotational band in  $^{20}\text{Ne}$  (and  $^{16}\text{O}$ ).

This example clearly illustrates the mechanism of the four-nucleon transfer reaction ( $^7\text{Li}$ , t). In strong transitions the four nucleons are transferred into one shell preserving the initial configuration which they had in the projectile (the hole in the target nucleus  $^{15}\text{N}$  is not filled in the reaction).

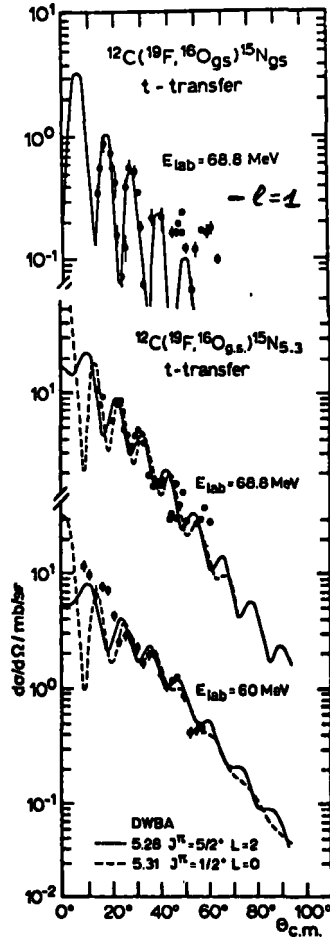
The four-nucleon transfer reaction on  $^{12}\text{C}$  has been extensively studied with many projectiles [16 - 19]. It is well established that the rotational band in  $^{16}\text{O}$  (starting at 6.06 MeV,  $0^+$ ) has large 4p-4h components. Using this knowledge, one can try to discuss the structure of  $^{15}\text{N}$  in terms of holes weakly (or less weakly) coupled to states in  $^{16}\text{O}$ . The correspondence of states emerging from this suggestion (weak coupling) is also shown in Fig.12.

Negative-parity states are obtained by removal of  $p_{1/2}$  particles (if possible) and  $p_{3/2}$  particles. The positive-parity states are obtained if one particle is removed from the s-d shell. This classification of states also gives suggestions in which reactions these states should be populated, as indicated on top of Fig.12.

As a test of these suggestions, the relevant transfer reactions can be studied. Figure 13 shows a comparison of a four-nucleon transfer reaction [23] ( $^{16}\text{O}$ ,  $^{12}\text{C}$ ) and a three-nucleon transfer reaction ( $^7\text{Li}$ ,  $\alpha$ ) (Ref.[19]) on  $^{12}\text{C}$ . The spacing of the strongly excited levels indeed seems to be rather similar in both reactions and may be taken as an indication that the states populated in  $^{15}\text{N}$  are indeed the positive parity states as suggested in Fig.12. The states can mix with states of simpler 1p-2h structure and experiments with higher resolution are necessary to test the weak coupling assumption. The ground-state rotational band of  $^{20}\text{Ne}$  being very similar to the rotational band of  $^{16}\text{O}$ , the correspondence between states in  $^{19}\text{F}$  and  $^{15}\text{N}$  should be rather close. Indeed, in the reaction  $^{12}\text{C}(^{19}\text{F}, ^{16}\text{O})^{15}\text{N}$  an extremely strong transition to the states at 5.3 MeV in  $^{15}\text{N}$  is observed (Fig.14) from Ref.[20]). The angular distributions of this reaction are shown in Fig.15 and give a nice example for the application of the rules for multi-nucleon transfer reactions mentioned before. The transitions are very strong if the angular momenta  $L_k$  and  $L'_k$  are the same in the initial and final channel. The transition to the two states at 5.3 MeV ( $1/2^+$  and  $5/2^+$ ) has the unusually high cross-section of 10 mb at forward angles, suggesting that indeed the initial and final state have identical structure. This result, as well as the correspondence to the rotational band in  $^{16}\text{O}$  (and  $^{20}\text{Ne}$  for  $^{19}\text{F}$ ) is strongly supported by the wave-functions obtained by Zuker et al. [21] for the states in  $^{15}\text{N}$  and  $^{16}\text{O}$ . Table II gives the wave-functions of the first states ( $0^+$  and  $2^+$ ) of the  $^{16}\text{O}$  rotational band of the states at 5.3 MeV in  $^{15}\text{N}$ . The removal of  $d_{5/2}$  or  $s_{1/2}$  particle from the states of  $^{16}\text{O}$  leads to configurations which are listed for the  $^{15}\text{N}$  states. The ground-state transition in the reaction

TABLE II. WAVE-FUNCTIONS OF  $^{16}\text{O}$  AND  $^{15}\text{N}$  (Ref. [21]).

$^{16}\text{O}$ 6.06 MeV	$0^+$	$-0.62 s^4 + 0.39 d^2 (01) s^2 (01) - 0.4 d^2 (10) s^2 (10)$ $(+0.34 p^4)$
$^{15}\text{N}$ 5.30 MeV	$1/2^+$	$+0.54 s^3 - 0.48 d^2 (01) s + 0.3 d^2 (10) s$ $(-0.54 sp^2 (01))$
$^{16}\text{O}$ 6.92 MeV	$2^+$	$-0.43 ds^3 + 0.37 d^2 (21) p^2 (01)$ $+0.39 dsp^2 (01) + 0.47 d^3 (5/21/21) s + 0.34 d^4 (202)$
$^{15}\text{N}$ 5.28	$5/2^+$	$+0.77 dp^2 (01) - 0.48 d^3 (5/21/21)$

FIG. 15. Angular distributions of the three-nucleon transfer reaction  $^{12}\text{C}(^{19}\text{F}, ^{16}\text{O})^{15}\text{N}$ .

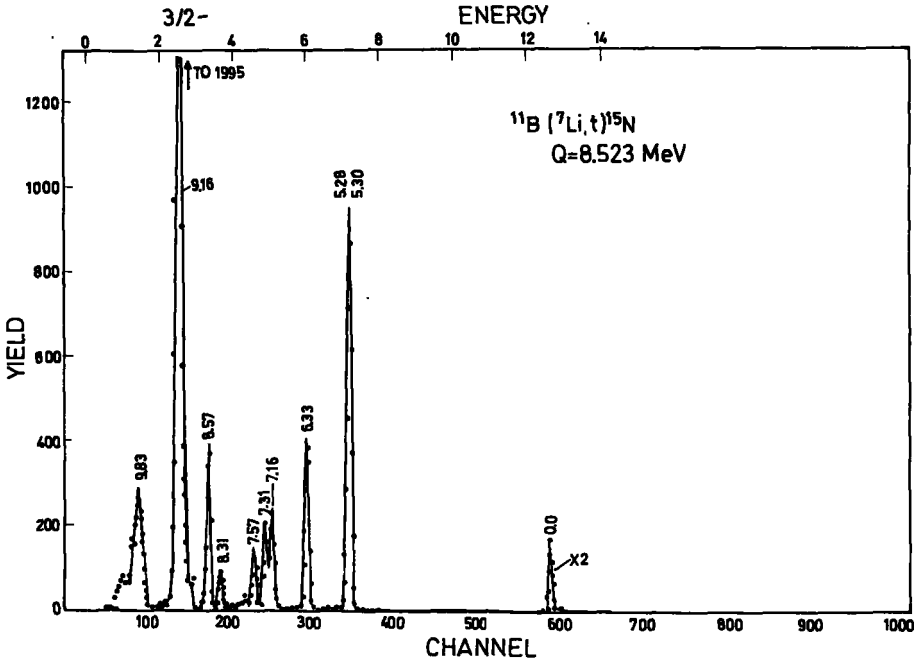


FIG. 16. Population of the  $3/2^-$  state at 9.16 MeV in  $^{15}\text{N}$  in the four-nucleon transfer ( $^7\text{Li}, t$ ) (Ref.[22]).

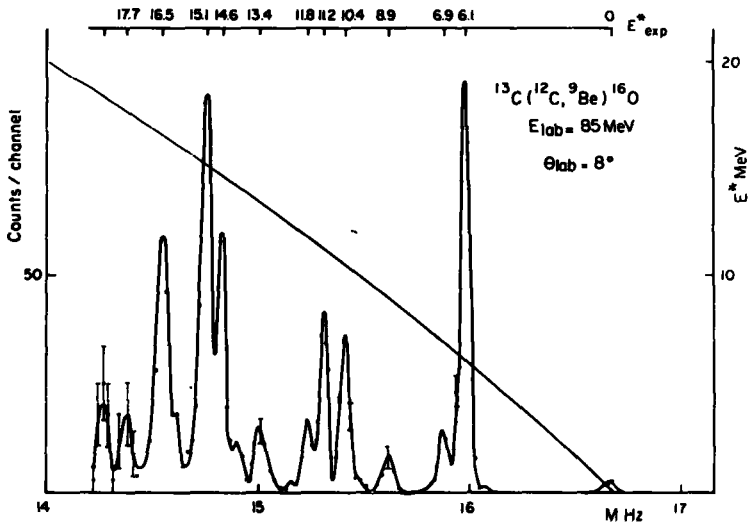


FIG. 17. Population of states of  $^{16}\text{O}$  in the three-nucleon transfer reaction ( $^{12}\text{C}, ^9\text{Be}$ ) (Ref.[23]).

$^{12}\text{C}(^{19}\text{F}, ^{16}\text{O})^{15}\text{N}$  shown in Fig.15 shows also pronounced structure in the angular distribution suggesting that the three nucleons are transferred in one amplitude from the s-d shell to the p-shell with a corresponding small cross-section.

For the population of the negative-parity states in  $^{15}\text{N}$  one sees in Fig.14 that the four-nucleon reaction  $^{11}\text{B}(^{16}\text{O}, ^{12}\text{C})^{15}\text{N}$  gives strong transitions only for excitation energies larger than 9 MeV. This observation is in very good agreement with the suggestion of Fig.12 for the structure of the negative-parity states in  $^{15}\text{N}$ . The  $(^7\text{Li}, t)$  reaction [22] indeed gives a very strong transition to the  $3/2^-$  level at 9.16 MeV as well (Fig.16). Thus this state will be the first of the states which correspond to the  $^{16}\text{O}$  rotational band with a  $p_{3/2}$  hole coupled.

In many transfer reactions information is precluded because of the complex structure of the projectile or target nucleus. As an example of a three-nucleon transfer reaction in which the structure of the target nucleus plays an important role, the reaction  $^{13}\text{C}(^{12}\text{C}, ^9\text{Be})^{16}\text{O}$  (Ref.[23]) can be quoted. This reaction can be used to excite 3p-3h states in  $^{16}\text{O}$ . However, the  $^{13}\text{C}$  ground state has no pure configuration. The three-nucleon transfer reaction therefore populates not only states with 3p-3h structure but also those with 2p-2h and 1p-1h components (Fig.17). The reaction is not very selective because of the structure of the target nucleus and a still perceptible cross-section for the transitions with complex final structure.

Using the  $^{10}\text{B}$  nucleus as projectile for four-nucleon transfer, the structure of the complex initial state is again reflected in spectra with small selectivity [24]. Figure 18 shows the spectrum of the  $^{12}\text{C}(^{10}\text{B}, ^6\text{Li})^{16}\text{O}$  reaction. The  $2^-$  state at 8.88 MeV can only be excited by four nucleons in the  $[3, 1]$ -symmetry, because this state has predominant 1p-1h structure. The cross-section for this transition being comparable with the

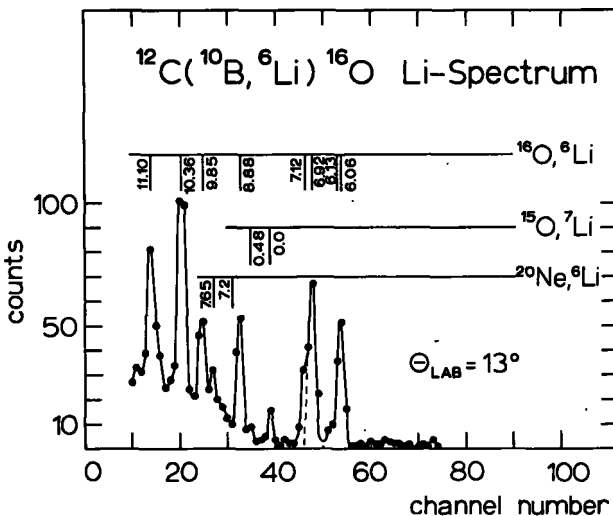


FIG. 18. Population of states in  $^{16}\text{O}$  in the four-nucleon transfer reaction  $(^{10}\text{B}, ^6\text{Li})$  (Ref.[24]).

transitions leading to the states of the rotational band in  $^{16}\text{O}$  (which is populated by four nucleons in the [4]-symmetry) one can immediately conclude that the  $^{10}\text{B}$  nucleus must contain large components with the [3,1]-symmetry simultaneously with components of the [4]-symmetry. This statement is confirmed by shell-model calculations [25].

The examples discussed in this section show that the multi-nucleon transfer reactions yield interesting information on nuclear structure even in the present stage of development of our theoretical knowledge.

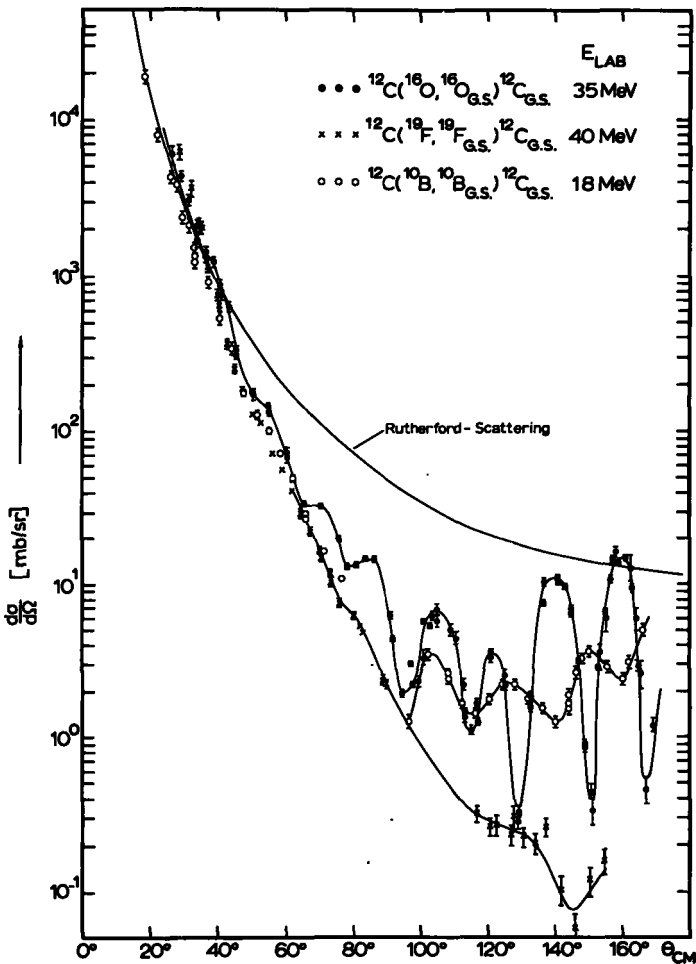


FIG. 19. Comparison of the elastic scattering of  $^{10}\text{B}$ ,  $^{16}\text{O}$ ,  $^{19}\text{F}$  on  $^{12}\text{C}$ .

#### 4. NUCLEAR-STRUCTURE EFFECTS IN THE ELASTIC SCATTERING OF NUCLEI ON NUCLEI

Elastic scattering of nuclei on nuclei enables us to study special effects connected with the shell structure of nuclei. In the scattering process, the two colliding nuclei can exchange a certain number of nucleons, the probability of the exchange being related to the structure of the nuclei. As a result of these rearrangement processes, the elastic scattering of heavy ions in many cases consists not just of potential scattering (the two nuclei retain their identity microscopically) but of other events which add coherently to the final channel. For a reasonable discussion of the rearrangement processes, it is necessary to have good knowledge of the pure potential scattering.

For the study of potential scattering it is necessary either to find systems in which contributions from re-arrangements are negligible, or to restrict the analysis of the data to angular regions in which the interference with other processes is small.

As an example for the differences which can occur in the scattering of heavy ions, Fig.19 shows the elastic scattering of  $^{10}\text{B}$ ,  $^{16}\text{O}$  and  $^{19}\text{F}$  on  $^{12}\text{C}$  at comparable energies above the Coulomb barrier [26]. The angular distributions of the three cases are very similar at small angles.

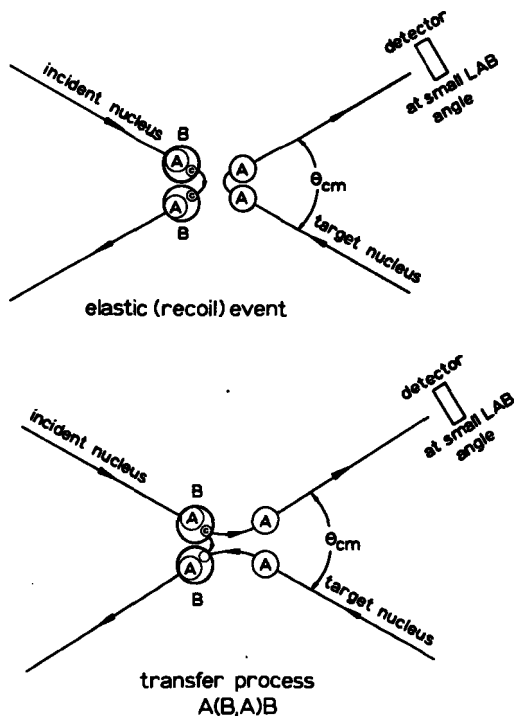


FIG. 20. Kinematic relation between elastic scattering and elastic transfer.

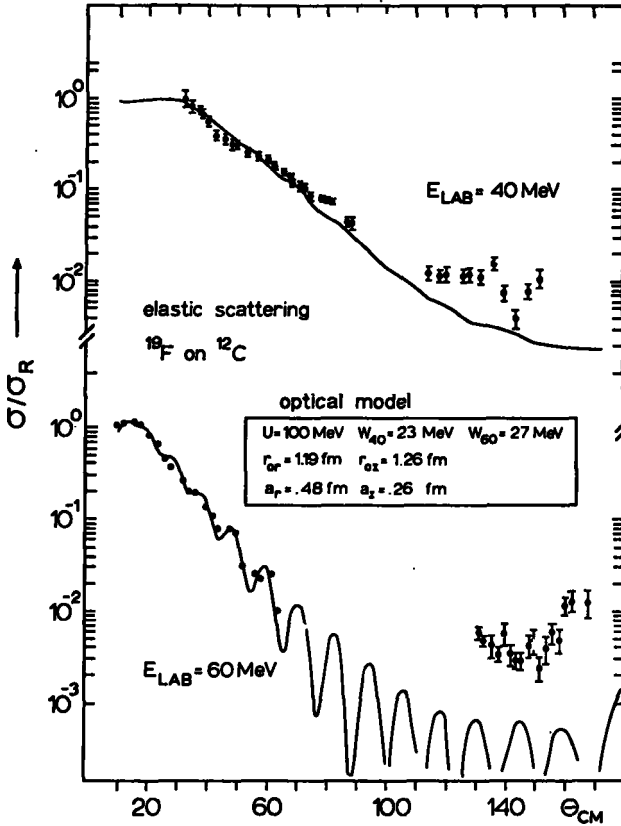


FIG. 21. Elastic scattering of  $^{19}\text{F}$  on  $^{12}\text{C}$  with optical-model calculations (Ref.[27]).

At angles larger than  $90^\circ$ , however, differences are observed because of the exchange of nucleons between the two colliding nuclei. The elastic-exchange process leads to the same final channel but with a maximum at backward angles in elastic scattering for energies above the Coulomb barrier. The kinematical relation between the potential scattering and the elastic transfer is illustrated in Fig.20. The recoil events can be due to potential scattering (target nuclei) or, for systems in which elastic transfer of the difference  $c$  occurs, more probably, due to the rest of the incoming particle after the transfer process. For the scattering of  $^{19}\text{F}$  on  $^{12}\text{C}$  the exchange of seven nucleons becomes rather improbable and a very small cross-section at large angles results. This system can be used to study the properties of potential scattering. The Coulomb interaction is still strong at 60 MeV and only slight oscillations are observed at smaller angles as shown in Fig.21 from Ref.[27].

The strong absorption in the scattering process is reflected in the potential parameters given in the figure and gives rise to the pronounced decrease of the cross-section below the Rutherford scattering cross-section. The small cross-section observed experimentally at large

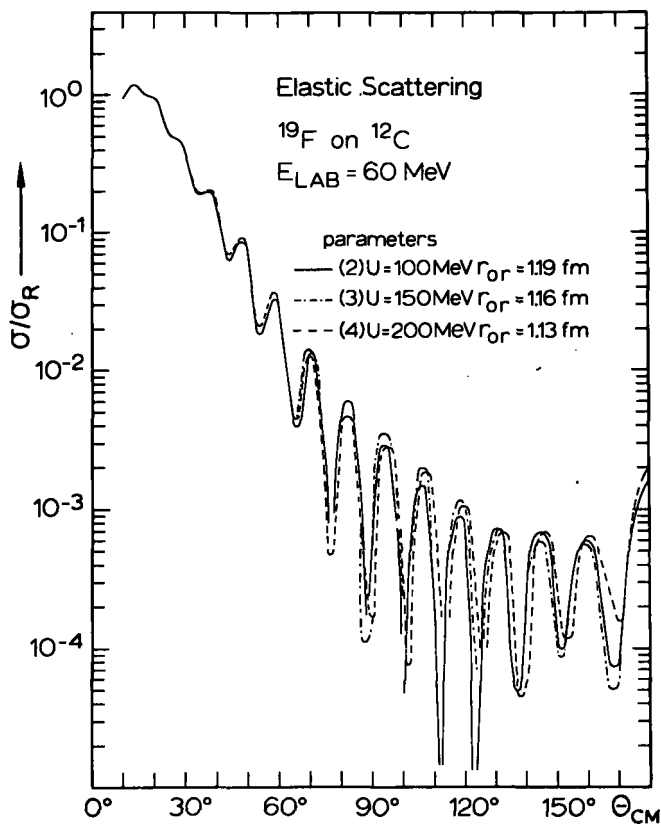


FIG. 22. Ambiguities in the real part of the strongly absorbing complex Woods-Saxon potential (Ref.[27]).

angles exceeds slightly the value predicted by the optical model calculation and can be due to contributions from compound nucleus decay and from seven-nucleon transfer. Using the strongly absorbing optical potential for the description of the elastic scattering of heavy ions (see also section 2) a very consistent description of many scattering systems has been obtained [27] using the parameter set given in Fig.21. As a consequence of strong absorption the parametrization of the complex potential by Woods-Saxon form factors becomes redundant,  $f(r) = V_0 (1 + \exp((r-R)/a))^{-1}$ , because only the surface of the potential enters into the calculation (and into the scattering process). This fact is illustrated for the real potential in Fig.22 where different calculations which yield the same differential cross-sections are given. The three cases correspond to the same potential surface [27].

For the description of adiabatic re-arrangement processes occurring in collisions at energies in the vicinity of the Coulomb barrier the system can be adequately described by adiabatic wave-functions [28] (also molecular wave-functions or method of perturbed stationary states). There are several reasons for the use of this method. The atomic nuclei

are successfully described by the shell model. Therefore in systems of appropriate structure (nuclei not far from closed shells) the nucleons outside the closed shells can be treated as valence nucleons and can be arranged into molecular orbitals. The collision time of the two nuclei at the Coulomb barrier is comparable to or usually shorter than the typical re-arrangement time of the outer nucleons. Furthermore, the mass of the valence particles is small compared to the mass of the cores.

In the method of adiabatic functions the total wave-function is separated into a part depending on the distance of the inert cores alone (co-ordinate  $\vec{R}$ ) and another part describing the motion of the valence particles and depending on  $\vec{R}$ . Both parts of the total wave-function are antisymmetrized (A) independently:

$$\Psi^t(\vec{R}, \vec{r}_j) \sim A \sum_i \chi^i(\vec{R}) A \Psi^i(\vec{R}, \vec{r}_j)$$

This description suggests that the motion of the cores is slow relative to the motion of the valence nucleons and that the wave-functions of the valence nucleons arrange themselves adiabatically for every distance  $\vec{R}$ . The energies of the molecular states described by the wave functions add adiabatically to the potential to which the two cores are submitted. In the adiabatic approximation the scattering of nuclei on nuclei reduces to a central-field problem with symmetry restrictions on the adiabatic potential. The potential-energy curves of the whole system could be obtained in a most complete way by two-centre shell-model theory [29], or in a corresponding Hartree-Fock calculation.

In the following an approach will be given, in which the core-core potential is taken to be the empirically determined complex potential and the adiabatic energies of the molecular states are obtained by using the method of linear combination of nuclear shell-model orbitals [28], LCNO, corresponding to the LCAO approach in atomic physics [30]. The number of nucleons which have to be separated out into molecular orbitals can be chosen corresponding to the incident energy and the spacing between the orbitals in the nucleus. A brief discussion of systems with one valence particle is given below.

In the method of LCNO, the adiabatic wave function is obtained by a linear combination

$$\Psi^{AJp}(\vec{R}, \vec{r}_j) = \frac{1}{N(\vec{R})} \left( C_1 \phi_{\ell_1 j_1 m_1}(\vec{r}_{Ac}) + C_2 \phi_{\ell_2 j_2 m_2}(\vec{r}_{A'c}) \right)$$

Here  $\phi(\vec{r})$  are single-particle wave-functions for particle c with core A or A'.

In the following, only cases with identical cores will be discussed [28]. These cases give  $|C_1| = |C_2| = 1/\sqrt{2}$ . The molecular orbits are classified corresponding to their behaviour relative to the interchange of the cores as even (g) or odd (u) for  $C_2 > 0$  or  $C_2 < 0$ , respectively (this correspondence depends on  $\ell$ !). Furthermore, because of the axial symmetry of the system, the molecular states have to be classified corresponding to the projections of angular momenta on the molecular axis:  $\Lambda$  for orbital angular momentum, J for total spin of the valence particle.

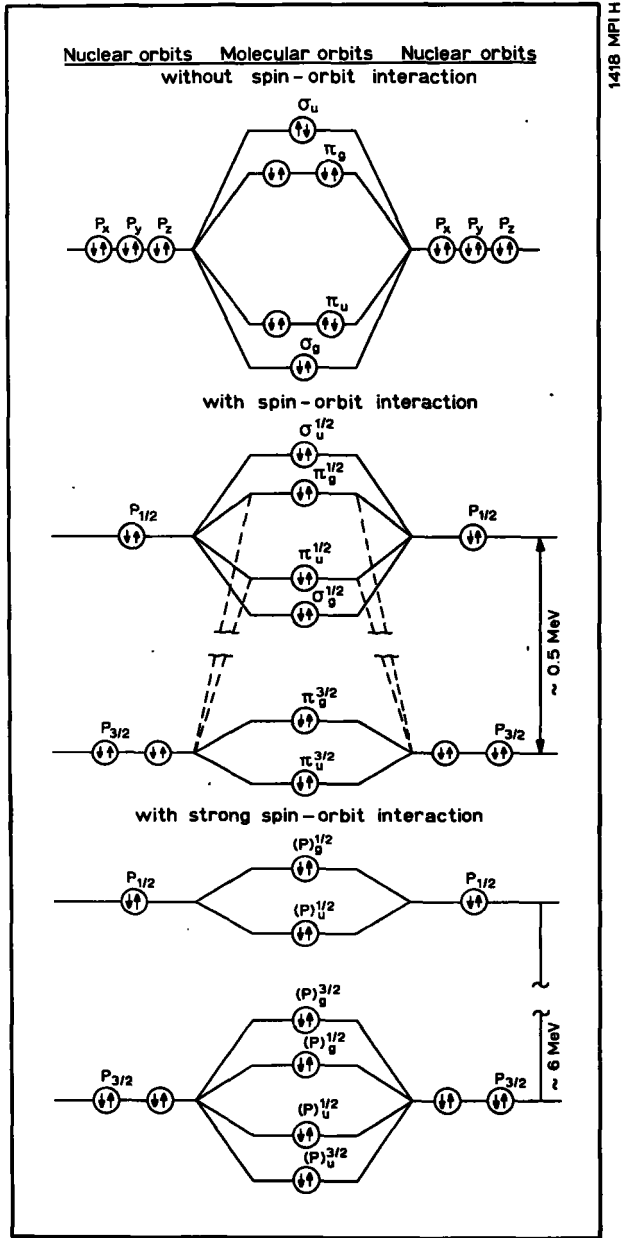


FIG. 23. Classification of molecular orbitals in the p-shell.

Using this method for the construction of the wave-function, all the valence particles can be filled into orbitals taking into account the Pauli principle. For the assembly of all valence particles then the same classification as for single orbitals has to be used. A schematic representation of the classification of the orbitals and their splitting (energy of the molecular states) is given in Fig.23 for  $p_{1/2}$  and  $p_{3/2}$  nucleons.

The molecular wave function is a function of the internuclear distance through the normalization  $N(\vec{R}) : N(\vec{R}) = \sqrt{1 + S(\vec{R})}$  with

$$S^{AJ}(\vec{R}) = \int \phi_{\ell_1 j_1 m_1}^*(\vec{r}_{AC}) \phi_{\ell_2 j_2 m_2}(\vec{r}_{A'C}) d\vec{r}_{AC}$$

being the overlap integral between the two separated orbitals. The energy of the molecular orbitals becomes

$$W^{AJP}(\vec{R}) = \frac{H_{AA} \pm H_{AA'}^{AJ}(\vec{R})}{1 \pm S^{AJ}(\vec{R})}$$

with

$$H_{if}^{AJ} = \int \phi_{\ell_i j_i m_i}^*(\vec{r}_{ic}) H \phi_{\ell_f j_f m_f}(\vec{r}_{fc}) d\vec{r}_{ic}$$

$$H = -\frac{\hbar^2}{2m_c} \nabla^2 + V^A(r_{AC}) + V^{A'}(r_{A'C})$$

Molecular orbitals can only be constructed from separated orbitals with the same symmetry behaviour with respect to the molecular axis (otherwise  $S^{AJ} \equiv 0$ ). This fact implies that the orientations of the overlapping orbitals are always the same and  $m_i = m_f = \Lambda$ . The evaluation of the energy as a function of the core-core distance  $\vec{R}$  for large distances can be made analytically [28]. One obtains a Yukawa form factor for the interaction energy induced by the exchange of the particle:

$$J^{AJ}(\vec{R}) \sim C(\Lambda, J) \sum_L (L 0 \ell_2 0 | \ell_1 0) \left\{ \begin{matrix} \ell_1 & j_1 & j_C \\ j_2 & \ell_2 & L \end{matrix} \right\} \frac{E_B (SN)^2}{\alpha^3} \frac{e^{-\alpha R}}{\alpha R} P_L(\theta)$$

The decay constant  $\alpha$  is related to the effective binding energy  $E_B$  and the reduced mass of the exchanged particle  $m_c$  by

$$\alpha = \sqrt{2 m_c E_B} \hbar^{-2}$$

The overlap integral  $S^{AJ}(\vec{R})$  becomes (for large  $\vec{R}$ )

$$S^{AJ}(\vec{R}) = J^{AJ}(\vec{R})/E_B$$

For the asymptotic region the correction due to  $S(\vec{R})$  is rather negligible. For smaller internuclear distances the overlap integrals and the energies have to be calculated numerically as discussed for example by Pruess

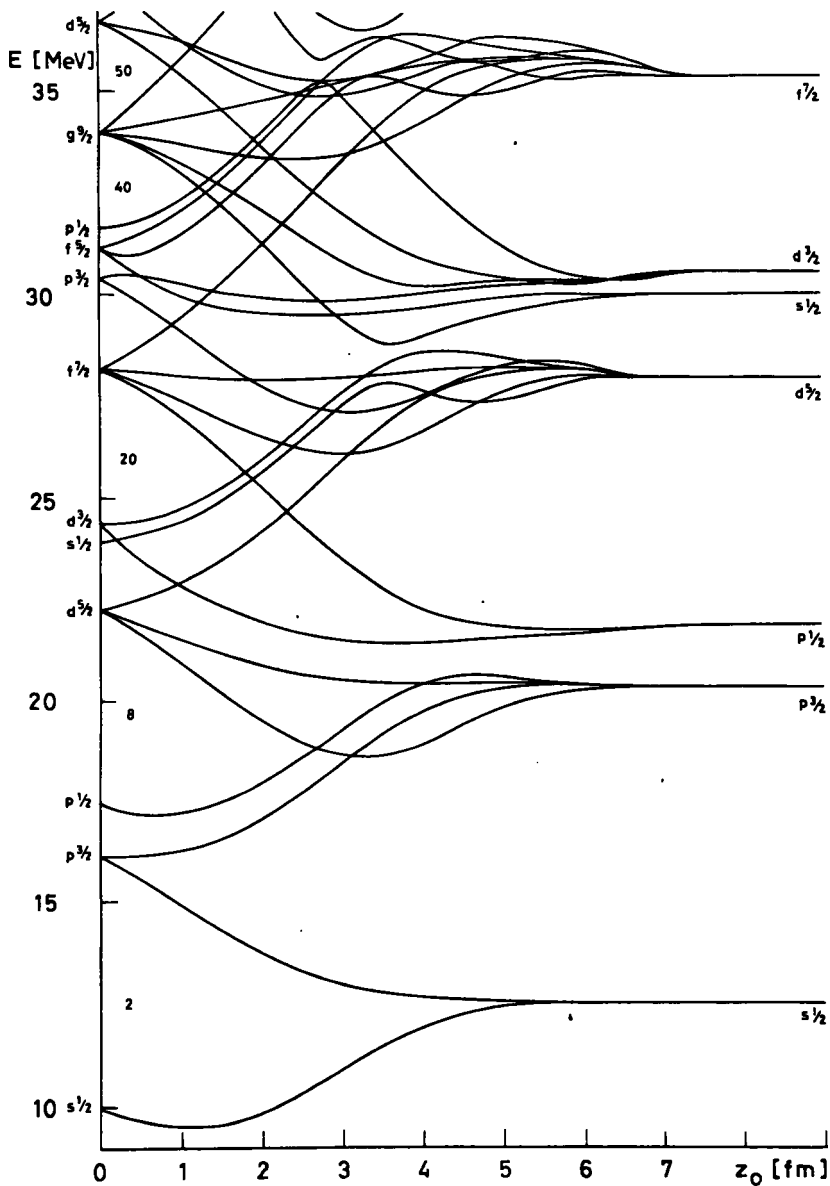


FIG. 24. Energies of molecular orbitals as functions of internuclear distance (Ref.[29]).

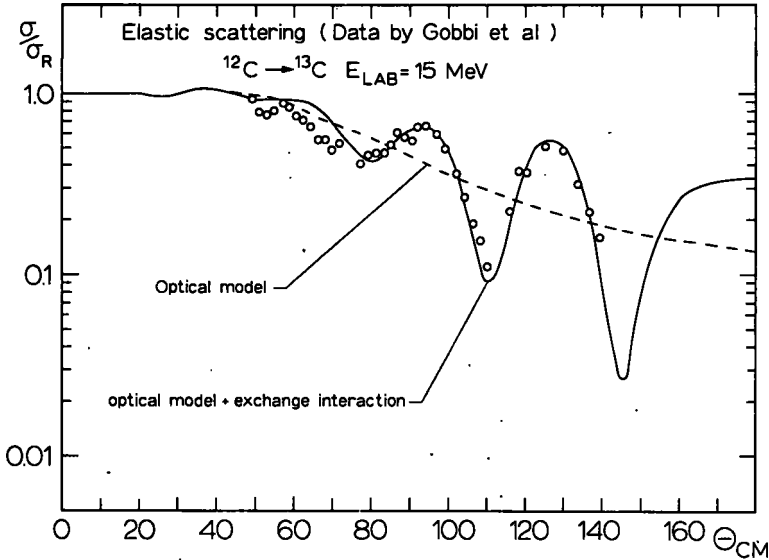


FIG. 25. Elastic scattering of  $^{12}\text{C}$  on  $^{13}\text{C}$  at low energy. The full line represents the calculation with the inclusion of the neutron transfer (Ref.[28]).

and Greiner [29]. Figure 24 gives an example of the dependence of the energy of the molecular orbitals on the internuclear distance (from Ref.[29b]). For many cases the asymptotic values will be sufficiently well determined by using the methods of atomic physics [31].

For the description of the scattering processes it is useful to apply the two-state approximation. As the two basis states of the systems, the  $g$ (even) and  $u$ (odd) states of the molecular system are taken which are obtained from a linear combination consisting of the ground states of the nuclei involved. As a result for each set of orbital quantum numbers  $\Lambda$  and  $J$  two equations are obtained [32] which are decoupled due to the orthogonality of the basis states

$$\left\{ \nabla_{\mathbf{R}}^2 + k^2 - V_{AA'}(\vec{\mathbf{R}}) \pm J^{\Lambda J}(\mathbf{R}) \right\} \chi_{\mathbf{P}}^{\Lambda J}(\vec{\mathbf{R}}) = 0, \quad \mathbf{P} = g, u$$

Depending on the  $g$  and  $u$  properties of the molecular states and on the properties of the total wave-function, the scattering wave-functions  $\chi_{\mathbf{P}}^{\Lambda J}(\mathbf{R})$  will contain only even or odd partial waves respectively. Thus the even and odd partial waves will be connected in the scattering process with different adiabatic potentials.

For the simplest case, for cores with spin zero and with one particle in the molecular orbits ( $^{12}\text{C} \rightarrow ^{13}\text{C}$  scattering), the total wave-function is even under the interchange of the cores (the total wave-function always reflects the symmetry properties of the core structure):

$$\Psi^t(\vec{\mathbf{R}}, \vec{\mathbf{r}}_j) = \Psi^t(-\vec{\mathbf{R}}, \vec{\mathbf{r}}_j), \quad \text{for } J_A = 0$$

$$\Psi^t = \chi_{\ell_{\text{even}}}^g(\vec{\mathbf{R}}) \Psi_g^{\Lambda J}(\vec{\mathbf{R}}, \vec{\mathbf{r}}_j) + \chi_{\ell_{\text{odd}}}^u(\vec{\mathbf{R}}) \Psi_u^{\Lambda J}(\vec{\mathbf{R}}, \vec{\mathbf{r}}_j)$$

and the total scattering amplitude becomes

$$f_{J_A=0}^t(\theta) = \frac{1}{2ik} \left\{ \sum_{\ell \text{ even}} (2\ell+1) a_{\ell}^g P_{\ell}(\theta) + \sum_{\ell \text{ odd}} (2\ell+1) a_{\ell}^u P_{\ell}(\theta) \right\}$$

As an example, in Fig.25 the scattering of  $^{12}\text{C}$  on  $^{13}\text{C}$  is shown [33]. In the calculation shown in the figure the classification corresponding to  $\Lambda$  and  $J$  has not yet been taken into account. Therefore the strength of the splitting of the  $g$  and  $u$  states is not given quantitatively from this calculation (in Ref.[28] the strength  $SN$  is further by a factor 10 too small, because of an error in the program). The strength  $\bar{SN}$  in formula  $J^{\Lambda J}(\vec{R})$  is adjusted until a fit is obtained to the data. For the core-core interaction  $V_{AA}(\vec{R})$ , the optical-model potential as discussed before has been used.

The sign of the splitting of the  $g$  and  $u$  state is determined uniquely by the experiment as illustrated in Fig.26. The sign of the splitting is strongly connected to the quantum numbers of the separated orbitals.

The structure of the angular distributions as shown in Figs 25 and 26 can also be influenced in the phase by the symmetry properties of the total wave-function. For systems with a core spin of  $1/2$  the total wave-function has to be odd under the interchange of the cores:

$$\Psi^t(\vec{R}, \vec{r}_j) = -\Psi^t(-\vec{R}, \vec{r}_j) \quad \text{for } J_A = 1/2$$

The total wave-function which is correctly antisymmetrized becomes

$$\begin{aligned} \Psi^t(\vec{R}, \vec{r}_j) = & \Phi^{s=1}(1/2, 1/2) \left\{ \chi_{\ell \text{ odd}}^g(\vec{R}) \Psi_g^{\Lambda J}(\vec{R}, \vec{r}_j) + \chi_{\ell \text{ even}}^u(\vec{R}) \Psi_u^{\Lambda J}(\vec{R}, \vec{r}_j) \right\} \\ & + \Phi^{s=0}(1/2, 1/2) \left\{ \chi_{\ell \text{ even}}^g(\vec{R}) \Psi_g^{\Lambda J}(\vec{R}, \vec{r}_j) + \chi_{\ell \text{ odd}}^u(\vec{R}) \Psi_u^{\Lambda J}(\vec{R}, \vec{r}_j) \right\} \end{aligned}$$

Here  $\Phi^s(1/2, 1/2)$  represents the spin wave-function of the cores. In the total scattering amplitude, the role of the even and odd partial waves is interchanged relative to the  $g$  and  $u$  adiabatic states (with weights which correspond to the Clebsch-Gordan coefficients):

$$\begin{aligned} f_{J_A=1/2}^t(\theta) = & \frac{1}{2ik} \left\{ \frac{3}{4} \sum_{\ell \text{ odd}} (2\ell+1) a_{\ell}^g P_{\ell}(\theta) + \frac{1}{4} \sum_{\ell \text{ odd}} (2\ell+1) a_{\ell}^u P_{\ell}(\theta) \right. \\ & \left. + \frac{3}{4} \sum_{\ell \text{ even}} (2\ell+1) a_{\ell}^u P_{\ell}(\theta) + \frac{1}{4} \sum_{\ell \text{ even}} (2\ell+1) a_{\ell}^g P_{\ell}(\theta) \right\} \end{aligned}$$

As an illustration of this case, Fig.27 shows the elastic scattering of  $^{14}\text{N}$  on  $^{12}\text{C}$  and  $^{13}\text{C}$  at the same CM energy [34]. The energy is very near to the Coulomb barrier. In the first case the core is  $^{12}\text{C}$  with spin zero, and the molecular orbits are filled with two different particles - a

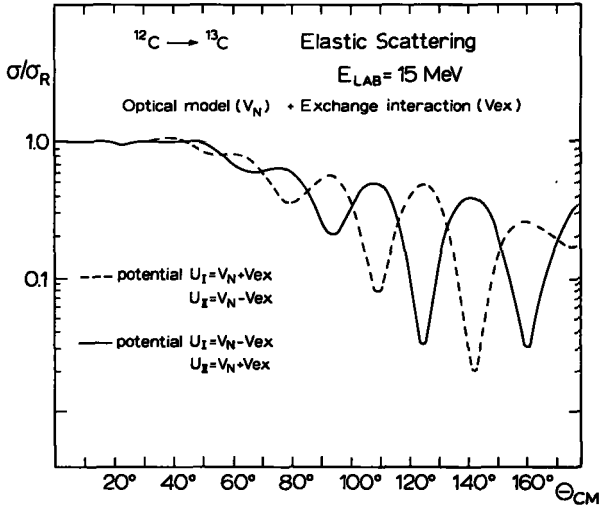


FIG. 26. Influence of the sign of the splitting of the molecular states  $g$  and  $u$  on the structure in the angular distributions (Ref.[28]).

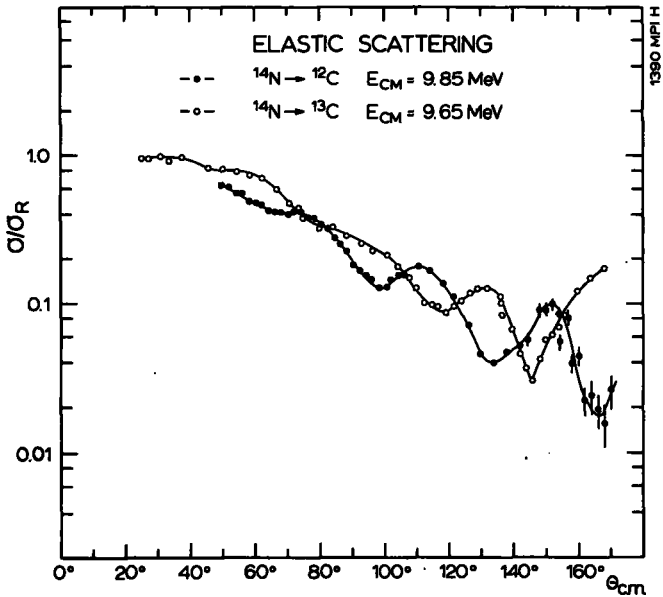


FIG. 27. Elastic scattering of  $^{14}\text{N}$  on  $^{12}\text{C}$  and  $^{13}\text{C}$ , illustrating the effect of the core spin (Ref.[34]).

proton and a neutron. In the second case, we define as a core the  $^{13}\text{C}$  nucleus which is possible as long as the energy in the collision is not too high. The core has spin  $1/2$  and the molecular orbits are filled with one proton. The two angular distributions are out of phase as is predicted by the theory.

These two examples show that the adiabatic approach gives a good description of the effects observed in the elastic scattering of nuclei on nuclei. It is expected that the experimental determination of the adiabatic potential energy curves (energies of molecular states as function of inter-nuclear distance) and their comparison with theory will yield interesting information on nuclear structure.

As a last point, the semi-classical aspects of the re-arrangement processes in the elastic scattering will be discussed. In the two-state system consisting of two nuclei A and  $(A' + c)$ , in a scattering event, the initial condition is

$$\Psi^t(T=0, \vec{R}, r_j) = \phi_{\ell_{1j1}}(\vec{r}_{AC}) = \phi_A$$

For a given distance R of the two identical cores A and A', the system is in a state which corresponds to linear combination of the two basis states as discussed above. The system is split into two states which are odd or even with respect to the interchange of the cores, and their time dependence for a given distance is given by their energy:

$$\Psi(T) = \left\{ \psi^g \exp(iJ(R)T/\hbar) + \psi^u \exp(-iJ(R)T/\hbar) \right\}$$

Because of the relations

$$\psi^g = \frac{1}{\sqrt{2}} (\phi_A + \phi_{A'}), \quad \psi^u = \frac{1}{\sqrt{2}} (\phi_A - \phi_{A'})$$

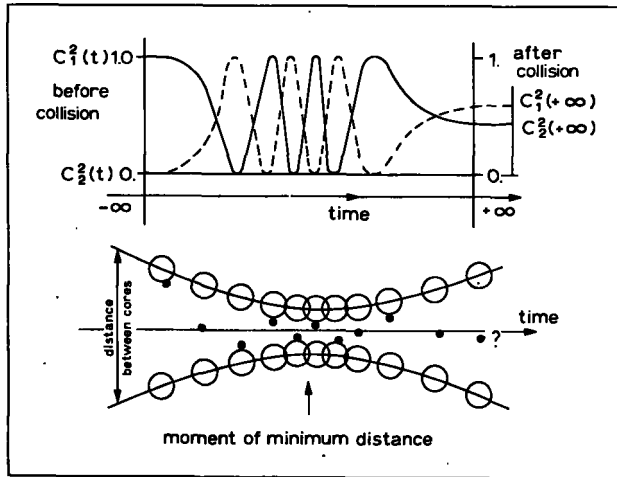


FIG. 28. Idealized picture of a multiple exchange of a particle between two identical cores moving on scattering orbits.

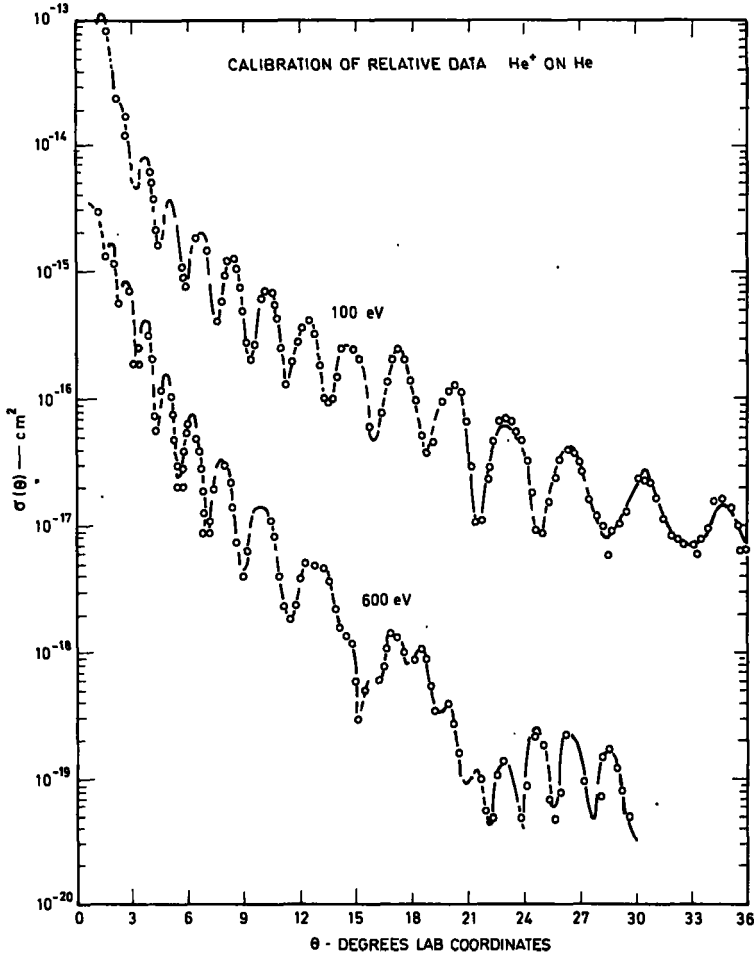


FIG. 29. Elastic scattering of  $\text{He}^+$  on neutral He at small angles illustrating the effect of the multiple exchange of an electron (Ref. [35]).

we obtain

$$\Psi(T) = \phi_A \cos\left(J(R) \frac{T}{\hbar}\right) + \phi_{A'} i \sin\left(J(R) \frac{T}{\hbar}\right) = C_1(T) \phi_A + i C_2(T) \phi_{A'}$$

The system is flipping from state  $\phi_A$  to state  $\phi_{A'}$  with a frequency  $J(R)/\hbar$ . The larger the splitting between the  $g$  and  $u$  state, the higher is the frequency with which the particles outside the cores are exchanged. This is the well known "resonance effect" which leads to the molecular binding in atomic physics.

In the scattering process one can imagine that the frequency of the exchange changes adiabatically as the two cores move on Rutherford-orbits as suggested in Fig. 28. The system starts with probabilities 0

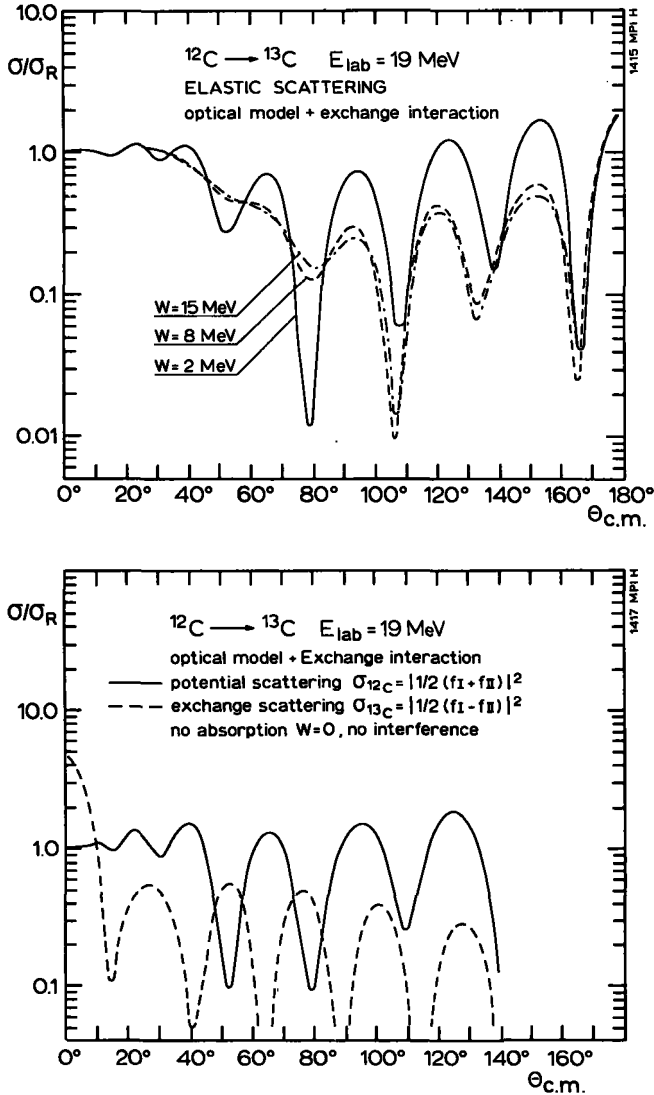


FIG. 30. Elastic scattering of  $^{12}\text{C}$  on  $^{13}\text{C}$  under different conditions of absorption (upper part). Potential scattering and exchange calculated separately without interference and without absorption (lower part). These curves allow recognition of the multiple exchange of the neutron.

and 1 for the attachment of the particles to the cores. During the collision the distance diminishes as the particles pass each other and the frequency of exchange goes through a maximum at the minimum distance. Finally, certain probabilities  $C_1^2(T \rightarrow \infty)$  and  $C_2^2(T \rightarrow \infty)$  are observed at asymptotic distances. These probabilities can be calculated using the integral

$$A = \int_{-\infty}^{+\infty} J \cdot (R(T)) \, dT$$

This is the total action on the system along the scattering path. Changing the energy or the scattering angle (and thus the minimum distance in the scattering orbit) the probabilities  $C_1^2(+\infty)$  and  $C_2^2(+\infty)$  change their value from 0 to 1 or vice versa. This classical behaviour of the differential cross-section as a function of energy or scattering angle has been observed in atomic systems. Figure 29 shows as an illustration the scattering of  $\text{He}^+$  ions on neutral He-gas [35]. The intensity of  $\text{He}^+$  ions as function of scattering angle clearly shows the features predicted by the classical picture. The irregularities at larger angles are due to interference effects, which come from the indistinguishability of the identical cores.

In nuclear physics these interference effects are the dominating features observed in the angular distributions. To obtain the intensities which can be submitted to classical interpretation, the interference has to be separated out [28]. Figure 30 illustrates the situation in the  $^{12}\text{C}$  on  $^{13}\text{C}$  scattering. The upper half of the figure shows that the structures in the angular distributions are strongly damped by the presence of the imaginary potential. Therefore, in the lower part of the figure calculations with no absorption are shown. The two cross-sections corresponding to  $|C_1|^2$  and  $|C_2|^2$  as they emerge from a quantum-mechanical calculation are shown separately (no interference). The oscillations can, in this case, be submitted to the classical interpretation. The figure tells us that the neutron is exchanged four times in the collision leading to a scattering with  $90^\circ$  deflection. This effect is precluded in the real experimental data by the presence of the strong absorption. The multiple exchange of the neutron is damped because of the imaginary part of the scattering potential.

The possibility of a multiple exchange in the collision process shows that the adiabatic condition is indeed satisfactorily fulfilled in the case discussed above and will be fulfilled in many other cases. The classifications of molecular states which are determined by projections on the adiabatic molecular symmetry axis are expected to be relevant for many systems in which nucleons are exchanged between two identical cores.

#### ACKNOWLEDGEMENTS

The author is very much indebted to his colleagues in Orsay and Heidelberg for supplying him with recent data and many comments. Special thanks for discussions are due to Drs M. Liu, J.C. Roynette, U.C. Schlotthauer-Voos and D. Walter.

#### REFERENCES

- [1] BREIT, G., POLAK, J.A., TORCHIA, D.A., *Phys. Rev.* 161 (1967) 993 and references quoted therein.
- [2] BUTTLE, P.J.A., GOLDFARB, L.J., *Nucl. Phys.* 78 (1966) 409; *Nucl. Phys.* A115 (1968) 461.

- [3] GOLDFARB, L.J.B., STEED, J.W., Nucl. Phys. A116 (1968) 321.
- [4] KAMMURI, T., YOSHIDA, H., Nucl. Phys. A129 (1969) 625.
- [5] GOLDFARB, L.J.B., in Nuclear Reactions Induced by Heavy Ions (Proc. Conf. Heidelberg, 1969) North Holland (1970) 115.
- [6] COHEN, S., KURATH, D., Nucl. Phys. A101 (1967) 1.
- [7] DOST, M., HERING, W.R., SMITH, W.R., Nucl. Phys. A93 (1967) 357.
- [8] DAR, A., reprint (1969).
- [9] VON OERTZEN, W., GUTBROD, H.H., VOOS, U.C., BOCK, R., Nucl. Phys. A133 (1969) 101.
- [10] BOCK, R., GROSSE-SCHULTE, M., VON OERTZEN, W., Physics Letts 22 (1966) 456;  
SCHLOTTHAUER-VOOS, U.C., Thesis, Heidelberg; Nuclear Phys. A180 (1972) 385.
- [11] DODD, L.R., GREIDER, K.R., Phys. Rev. 121 (1969) 443; GREIDER, K.R., loc. cit. Ref.[5] 217.
- [12] POTH, J.E., OVERLEY, J.C., BROMLEY, D.A., Phys. Rev. 164 (1967) 1295.
- [13] LIU, M., Thesis, IPN, Orsay (1969), Nucl. Phys. A165 (1971) 118.
- [14] ROTTER, I., Nucl. Phys. A135 (1969) 378.
- [15] MIDDLETON, loc. cit. Ref.[5] 263.
- [16] VON OERTZEN, W., BOHLEN, H.G., GUTBROD, H.H., HILDENBRAND, K.D., VOOS, U.C.,  
BOCK, R., loc. cit. Ref.[5] 156.
- [17] BETHGE, K., *ibid.* 277.
- [18] JACMART, J.C., LIU, M., ROYNETTE, J.C., CAVERZASIO, C., POUGHEON, F., STEPHAN, C.,  
RIOU, M., VON OERTZEN, W., *ibid.* 128.
- [19] OGLOBLIN, A.A., *ibid.* 231.
- [20] SCHLOTTHAUER-VOOS, U.C., Thesis, MPI für Kernphysik, Heidelberg (1970).
- [21] ZUKER, A.P., BUCK, B., McGRORY, J.B., Phys. Rev. Letts 21 (1968) 39.
- [22] McGRATH, R.L., Phys. Rev. 145 (1966) 802.
- [23] ROYNETTE, J.C., Nucl. Phys. A157 (1970) 297.
- [24] HILDENBRAND, K.D., GUTBROD, H.H., VON OERTZEN, W., BOCK, R., Nucl. Phys. A157 (1970) 297.
- [25] YOSHIDA, H., private communication.
- [26] VON OERTZEN, W., GUTBROD, H.H., MÜLLER, M., VOOS, U.C., BOCK, R., Physics Letts 26B  
(1968) 291.
- [27] VOOS, U.C., VON OERTZEN, W., BOCK, R., Nucl. Phys. A135 (1969) 207.
- [28] VON OERTZEN, W., Nucl. Phys. A148 (1970) 529 and to be published.
- [29] PRUESS, K., GREINER, W., Physics Letts 33B (1970) 197; MOSEL, U., GSI Seminar, Darmstadt (1970).
- [30] BALLHAUSEN, C.J., GRAY, H.B., Molecular Orbital Theory, Benjamin Inc., New York (1964).
- [31] KOTANI, M., OHNO, K., KAYMA, K., Encyclopedia of Phys. 37/2 (FLÜGGE, S., Ed.) 2.
- [32] WU, T.Y., OHMURA, T., Quantum Theory of Scattering, Prentice Hall (1962).
- [33] GOBBI, A., MATTER, U., PERRENOUD, J.L., MARMIER, P., Nucl. Phys. A112 (1968) 537.
- [34] VON OERTZEN, W., BOHLEN, H.G., GEBAUER, B., HABIB, E.E., MARQUARDT, N., Physics  
Letts 34B (1971) 51.
- [35] LORENTS, D.C., ABERTH, K., Phys. Rev. 139A (1965) 1017.

# NUCLEAR SPECTROSCOPY IN THE 1f-2p SHELL WITH HEAVY-ION REACTIONS

M.-C. LEMAIRE

Département de physique nucléaire,  
Centre d'études nucléaires de Saclay,  
France

## Abstract

NUCLEAR SPECTROSCOPY IN THE 1f-2p SHELL WITH HEAVY-ION REACTIONS.

1. Existence of four-nucleon correlations; 2. Experimental techniques; 3. Reaction mechanism;
4. Nuclear spectroscopy with heavy-ion experiments; 5. Summary.

Direct transfer reactions induced by light projectiles have long been established as a powerful tool in nuclear-spectroscopy studies. In particular, one-nucleon transfer reactions such as (d, p) or ( $^3\text{He}$ , d) have been commonly used to investigate single-particle states in nuclei. In a similar way, information about pairing correlations in vibrational nuclei has been collected from two-like-particle transfer reactions such as (t, p) and (p, t). More recently, important information about four-nucleon correlations has been provided by alpha transfer experiments which have become possible with the advent of heavy ions or Li beams. To emphasize the role played by the alpha transfer reactions, we shall give here a brief review of the work which has pointed out the existence of four-nucleon correlations. First, we shall briefly review some of the theoretical calculations suggesting four-nucleon correlations and then discuss the experimental evidence.

## 1. EXISTENCE OF FOUR-NUCLEON CORRELATIONS

### 1.1. Calculations for even-even $N = Z$ nuclei

It is well known that for doubly closed shell nuclei such as  $^{16}\text{O}$  and  $^{40}\text{Ca}$ , low-lying deformed states co-exist with spherical ones. Let us consider the  $^{16}\text{O}$  nucleus which has 8 protons and 8 neutrons. In a simple shell-model picture, the 1s and 1p shells are filled and the 2s-1d shell is empty. The ground state corresponds to a 0p-0h configuration. The description of the first excited states requires particle-hole configurations of higher order (1p-1h, 2p-2h, 3p-3h, 4p-4h...). From Fig. 1 it can be seen that all these configurations lie in the same energy region [1].

As far as the low-lying positive-parity states of  $^{16}\text{O}$  are concerned, the most striking evidence relating to the structure of these states is given by the alpha elastic-scattering excitation function for  $^{12}\text{C}$ , due to Carter et al. [2]. They have shown that the set of strongly excited states  $0^+(6.06 \text{ MeV})$ ,  $2^+(6.92 \text{ MeV})$ ,  $4^+(10.36 \text{ MeV})$  and  $6^+(16.2 \text{ MeV})$  can be approximately fitted by the  $J(J+1)$  energy law typical of the rotational spectrum of a deformed nucleus. The collective nature of these states is

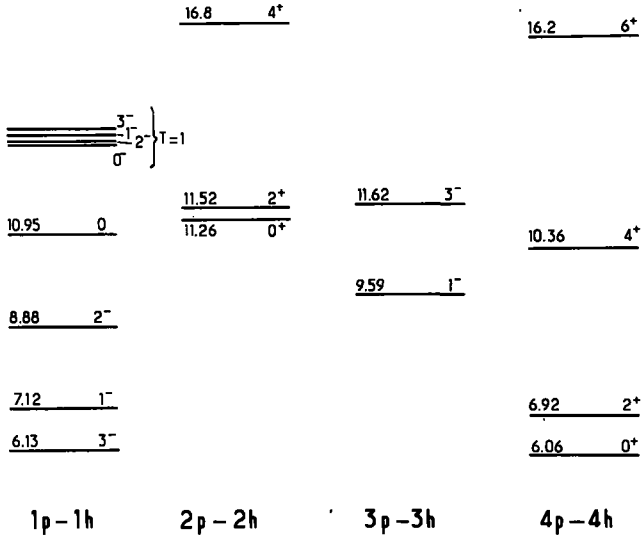


FIG. 1. Particle-hole configurations in  $^{16}\text{O}$ . The energy levels are taken from Refs [1, 4, 6].

further supported by the large  $B(E2)$  reduced transition probabilities between these levels:

$$B(E2; 2^+_{6.92 \text{ MeV}} \rightarrow 0^+_{6.06 \text{ MeV}}) = 40 e^2 \text{fm}^4$$

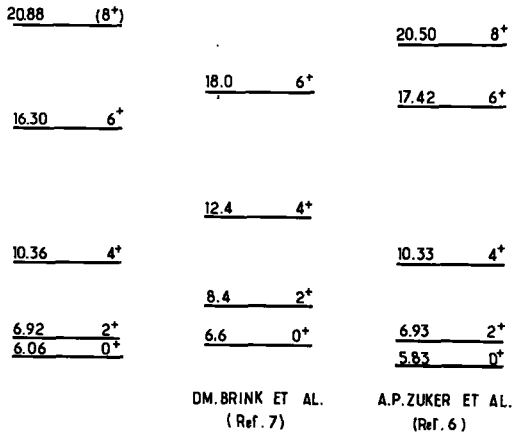
$$B(E2; 4^+_{10.36 \text{ MeV}} \rightarrow 2^+_{6.92 \text{ MeV}}) = 117 e^2 \text{fm}^4$$

Important theoretical work has been performed to explain the existence of such deformed states in doubly closed shell nuclei.

#### 1.1.1. Calculations with deformed orbits

The first attempt to explain the low-lying positive parity states of  $^{16}\text{O}$  was made by Morinaga [3], and Brown and Green [4] who assumed that the nucleus was deformed. If one looks at the Nilsson diagram in the  $^{16}\text{O}$  region it can be seen that for large prolate deformation ( $\beta \approx 0.3$ ) it costs relatively little energy to lift two or four particles from the 1p shell to the 2s-1d shell.

This suggests that the low-lying positive-parity states of  $^{16}\text{O}$  can be described in terms of 2p-2h and 4p-4h excitations. Hartree-Fock calculations performed by Bassichis and Ripka [5], in the framework of the deformed-orbital method, have shown that the 4p-4h states of  $^{16}\text{O}$  can be lower than the 2p-2h ones. These results strongly suggested that the  $^{16}\text{O}$  rotational band based on the first  $0^+$  excited state is well described by configurations with four particles in the  $k=1/2^+$  Nilsson orbital number 6 and with four holes in the  $k=1/2^-$  orbital number 4. With such a deformation, the energy lost by exciting the particles is partly compensated by the large spatial-symmetry energy of the four excited particles. These four nucleons with a high permutation symmetry in their spatial wave-functions look like an alpha-particle.



## EXPERIMENT

## THEORY

FIG. 2. Comparison of experimental and theoretical energies of the first rotational band levels. The 16.30 MeV and 20.88 MeV excitation energy levels reported in the experimental spectrum have been seen in the  $^{12}\text{C}(^6\text{Li}, d)^{16}\text{O}$  reaction (Ref. [7]). The comparison with the microscopic calculations of Zuker et al. [6] strongly suggests that the state at 20.88 MeV is the  $J^\pi = 8^+$  member of the 4p-4h rotational band.

## 1.1.2. "Exact" shell-model calculations

Shell-model calculations have been performed in the  $^{16}\text{O}$  region by Zuker, Buck and McGrory [6]. They assume a  $^{12}\text{C}$  inert core and four particles moving in the  $1p_{1/2}$ ,  $2s_{1/2}$  and  $1d_{5/2}$  orbitals. By diagonalizing the residual interaction between all the two-neutron and two-proton configurations which can be constructed with the four particles in these three sub-shells, they obtain all the observed states of  $^{16}\text{O}$  up to 13 MeV. The wave-functions of these states confirm the many-particle-many-hole description mentioned above. In addition, they calculate the mixing of the p-h configurations of different order. Such calculations show clearly that the  $^{16}\text{O}$  rotational band based on the  $0^+$  first excited state is strongly dominated by 4p-4h components (Fig. 2). These shell-model calculations are only well suited for nuclei in the neighbourhood of closed shells, where the configuration space which must be taken into account is not too large.

## 1.1.3. The alpha-cluster model

The alpha clustering of the four nucleons in the 4p-4h deformed states of  $^{16}\text{O}$  is pointed out by the calculations of Brink, Friedrich, Weinguny and Wong [7] who use the alpha-particle model. These authors describe the  $^{16}\text{O}$  nucleus by means of four alpha-particles. For the ground state, they consider a tetrahedron configuration and minimize the energy to get the equilibrium shape. They found that, when the distance between two alpha-particles goes to zero, the wave-function becomes that of a closed shell. The description of the deformed states requires mixing of rhombic and square configurations. It can be seen from Fig. 2 that the energy

spectrum obtained by angular momentum projection of such a configuration shows a rather good agreement with the 6 MeV first rotational band of  $^{16}\text{O}$ . The most striking feature of these calculations is that the head of the rotational band is given at 6.6 MeV without any fitting. Moreover, Hartree-Fock calculations including projection procedure performed by Bouten [8] confirm that the  $0^+$  (6.05 MeV) level is the band-head of a  $K=0$  rotational band. With the use of a Brink effective interaction, the alpha-particle configurations appear to be a good description of nuclei up to  $^{24}\text{Mg}$ .

#### 1.1.4. The stretch scheme

Another description of nuclear rotations for medium-weight nuclei is provided by the stretch model of Danos and Gillet [9].

This model is based on the  $j$ - $j$  coupling of the nucleons. Let us consider the simplest case of two protons in a shell of angular momentum  $j$  and two neutrons in a shell of angular momentum  $k$  and vice-versa. The stretched wave-function is constructed in the following way: each proton-neutron pair is coupled to maximum angular momentum  $c = j+k$ . The two stretched pairs are then coupled to the angular-momentum  $I$ -spin of the four-nucleon state. They form a "quartet". It is for  $I=0$  that the overlap between the wave-functions of the two aligned pairs is maximum; this gives then the lowest state. The rotational excitations of the nuclei are obtained by coupling the two stretched pairs of the quartet to angular momentum  $I$  different from zero. The maximum overlap between a quarter configuration and an alpha-particle wave-function is obtained when the protons and the neutrons are in the same orbit  $j=k$  and for  $I_{\text{max}} = 4j - 2$ . It is the high spatial symmetry of the quartet wave-function which gives a large intrinsic binding energy for these configurations.

In this quartet scheme, the  $0^+$  4p-4h state is described by means of a quartet of particles and a quartet of holes coupled together. Diagonalizations of several residual interactions in this model have shown that the  $0^+$  state can be very low [10].

### 1.2. Calculations for $N > Z$ -nuclei

The quartet scheme has also been extended to single-open-shell nuclei [10]. Let us consider the nickel isotopes. The structure of the nickel isotopes has recently been the subject of many investigations. Calculations of these nuclei [11] based on an inert  $^{56}\text{Ni}$  core have been very successful in reproducing the low-lying energy spectra. In contrast, such a description is incompatible with the strong E2-transitions observed between low-lying energy levels in these isotopes. Furthermore, there is clear evidence [12] from stripping and pick-up experiments that even the lowest levels in the Ni isotopes involve core excitation. Calculations of Wong, Davis [13] and Jaffrin [10] suggest that 4p-4h configurations lie low in the  $^{56}\text{Ni}$  energy spectrum. Thus, 4p-2h configurations will be important in the structure of the low-lying positive-parity states of  $^{58}\text{Ni}$ . Because of the high symmetry of the two-proton-two-neutron quartet configuration, the stretch model suggests that in  $^{58}\text{Ni}$  the configurations involving a quartet and two  $1f_{7/2}$  proton holes is competitive with the lowest excited two-neutron configurations. Each two-proton two-neutron quartet configuration constructed in the  $2p_{3/2}$ ,  $1f_{5/2}$  and  $2p_{1/2}$  sub-shells gives rise to a multiplet

of positive-parity states. Each multiplet of states having mainly the same configurations forms a "quasi-rotational band" [14].

### 1.3. Experimental investigation of four-nucleon correlations

In light nuclei, the alpha structure of the deformed states suggests that these levels should be strongly excited by alpha transfer experiments. The ( ${}^6\text{Li}$ , d) and ( ${}^7\text{Li}$ , t) four-nucleon transfer reactions have been used to a great extent [15]. As is shown in Von Oertzen's contribution [16], the ground-state 4-particle-0-hole band of  ${}^{20}\text{Ne}$  is selectively populated by the  ${}^{16}\text{O}({}^7\text{Li}, t){}^{20}\text{Ne}$  reaction. A strong excitation of the 4p-4h rotational band of  ${}^{16}\text{O}$  is also obtained by means of ( ${}^7\text{Li}$ , t), ( ${}^6\text{Li}$ , d) and ( ${}^{16}\text{O}$ ,  ${}^{12}\text{C}$ ) four-nucleon-transfer reactions performed on a  ${}^{12}\text{C}$  target [15, 17, 18]. The most prominent peaks in the  ${}^{12}\text{C}({}^6\text{Li}, d){}^{16}\text{O}$  energy spectra obtained by Bassani et al. [17] correspond to levels of the (4p-4h) rotational band  $k=0$ : 6.91 MeV  $2^+$ , 10.35 MeV  $4^+$ , 16.36 MeV  $6^+$  and 20.88 MeV  $8^+$ . In this experiment, the cross-section of the  $0^+$  state at 6.06 MeV, the band-head level, appears to be small. A comparison of the excitation energies of the  ${}^{16}\text{O}$  states strongly populated by the  ${}^{12}\text{C}({}^6\text{Li}, d)$  reaction with the results of the microscopic calculations of Zuker et al. [6] is also given in Fig. 2. It suggests that the states at 16.30 MeV and 20.88 MeV excitation energies are probably the  $J=6^+$  and  $8^+$  members of the first rotational band.

Although alpha transfer reactions were quite successful in 1p and 2s-1d shell nuclei by means of the ( ${}^6\text{Li}$ , d) and ( ${}^7\text{Li}$ , t) reactions, it was found that the cross-sections of these reactions for targets heavier than  $A=40$  were too small to be measured. In medium-weight nuclei, the alpha transfer experiments have first been performed successfully by means of the ( ${}^{16}\text{O}$ ,  ${}^{12}\text{C}$ ) reaction. We present here a survey of several ( ${}^{16}\text{O}$ ,  ${}^{12}\text{C}$ ) reactions studied with calcium, titanium, iron and nickel isotopes as targets. In a few cases, we are able to collect simultaneously the spectra corresponding to the ( ${}^{16}\text{O}$ ,  ${}^{14}\text{C}$ ) and ( ${}^{16}\text{O}$ ,  ${}^{12}\text{C}$ ) reactions. The ( ${}^{16}\text{O}$ ,  ${}^{14}\text{C}$ ) two-proton transfer reaction should give the same kind of spectroscopic information about the proton pairing correlation as the ( ${}^3\text{He}$ , n) reaction; experimentally, the ( ${}^{16}\text{O}$ ,  ${}^{14}\text{C}$ ) reaction has definite advantages over ( ${}^3\text{He}$ , n). The ( ${}^{16}\text{O}$ ,  ${}^{14}\text{C}$ ) results obtained for some Ca and Ti target isotopes will be discussed later.

## 2. EXPERIMENTAL TECHNIQUES

The experiments were performed with the  ${}^{16}\text{O}$  beam of Saclay's F. N. Tandem by Faivre, Faraggi, Gastebois, Harvey, Lemaire, Loiseaux, Mermaz, and Papineau. The incident-energy range was from 42 to 56 MeV. In these experiments, the main difficulty was heavy-fragment identification. The telescope used to detect the reaction products was made of two ORTEC surface-barrier detectors, a thin one giving the energy loss  $\Delta E$  and a thicker one in which the particles are stopped. A two-dimensional analysis of the  $\Delta E$  versus  $\Delta E + E$  signals gave straight lines for carbon, nitrogen and oxygen in the energy range from 15 to 50 MeV. These results are in good agreement with the range-energy loss given by the Northcliff tables. A simple identification function is obtained with the

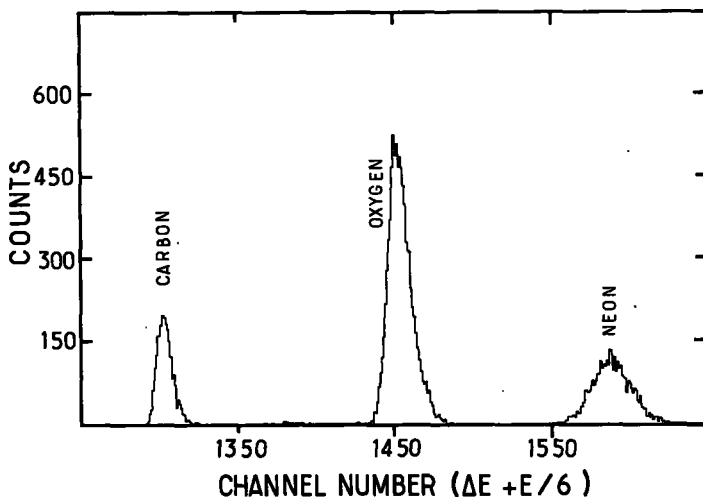


FIG. 3. Identification spectrum obtained by bombarding the  $^{12}\text{C}$  target with 48 MeV  $^{16}\text{O}$  beam.

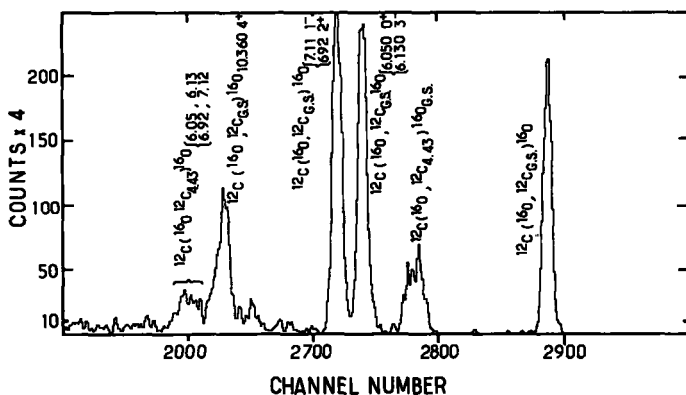


FIG. 4.  $^{12}\text{C}(^{16}\text{O}, ^{12}\text{C})^{16}\text{O}$  reaction energy spectrum.

relationship  $I(Z) = \Delta E(Z) + E(Z)/\alpha$  where  $\alpha$  depends essentially on the thickness of the first detector (for example,  $\alpha = 6$  for  $\Delta E \approx 13\mu\text{m}$ ). An identification spectrum is shown in Fig. 3. It was obtained by bombarding a  $^{12}\text{C}$  target with the  $^{16}\text{O}$  beam at 48-MeV incident energy. Good separation between different Z-nuclei was achieved. The energy spectrum corresponding to the  $^{12}\text{C}$  identification peak is shown Fig. 4. The overall experimental resolution was about 450 keV due to kinematic broadening; the angular aperture of the telescope in the reaction plane was around  $1/3$  degree in the reaction plane. The first level corresponds to the  $^{12}\text{C}$  detected and the  $^{16}\text{O}$  recoil nucleus both in their ground state, the second peak is due to the detection of the  $^{12}\text{C}$  nucleus in its first  $2^+$  excited state

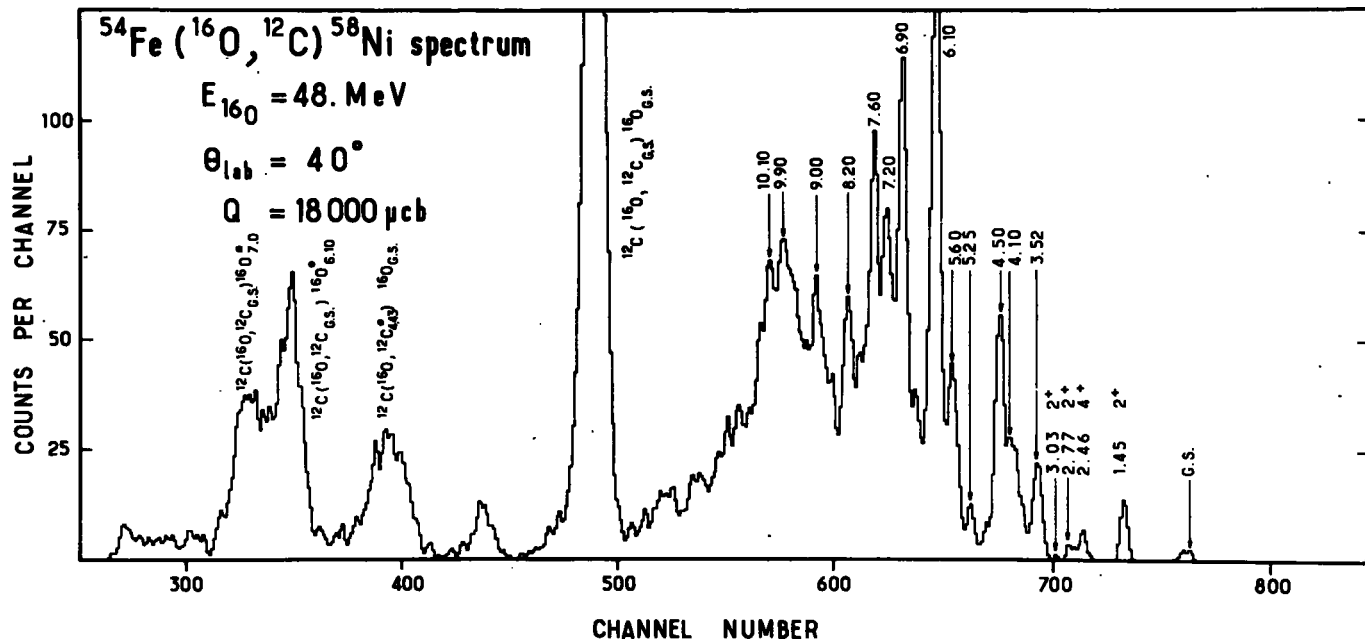


FIG. 5.  $^{54}\text{Fe} (^{16}\text{O}, ^{12}\text{C}) ^{58}\text{Ni}$  energy spectrum.

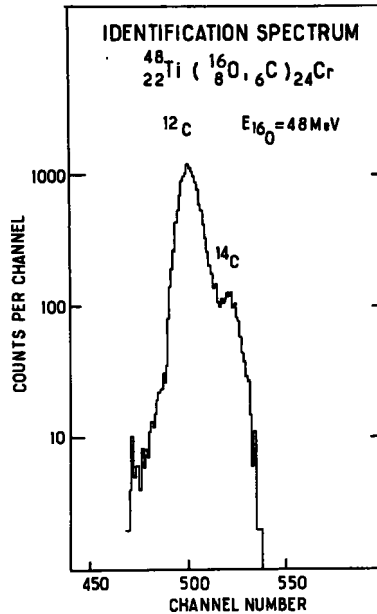


FIG. 6. Detail of the identification spectrum corresponding to the various carbon channels.

at 4.43 MeV. Experimentally, we are not able to resolve the doublet containing the 6.06 MeV  $0^+$  and 6.13 MeV  $3^-$  states, and the doublet containing the 7.11 MeV  $1^-$  and 6.92 MeV  $2^+$  states in  ${}^{16}\text{O}$ . We note the weak intensity of the excitation of both  ${}^{12}\text{C}$  and  ${}^{16}\text{O}$ . Generally, the  $Q$ -values of the  $({}^{16}\text{O}, {}^{12}\text{C})$  reactions are close to zero; this results from the similar binding energies of the  $\alpha$ -particle in the  ${}^{16}\text{O}$  projectile and in the residual nuclei. In contrast to this, the  $({}^{16}\text{O}, {}^{13,14}\text{C})$  and  $({}^{16}\text{O}, {}^{14,15}\text{N})$  reactions have negative  $Q$ -values varying from few MeV to more than 10 MeV.

Most of our experiments were performed in the vicinity of the  ${}^{16}\text{O}$  Coulomb barrier and just a few MeV above the barrier for  ${}^{12}\text{C}$ . Thus only reactions with  $Q$  values a few MeV negative are competitive with  $({}^{16}\text{O}, {}^{12}\text{C})$  reaction. For these reasons, in our experiments performed between 48 to 56 MeV incident energy on  ${}^{54,56}\text{Fe}$  and  ${}^{58,60}\text{Ni}$  targets, only the  ${}^{12}\text{C}$  channel can be observed, and a separation of the heavy ions based on the nuclear charge  $Z$  is sufficient. Figure 5 shows a  ${}^{54}\text{Fe}({}^{16}\text{O}, {}^{12}\text{C}){}^{58}\text{Ni}$  energy spectrum. The experimental resolution is about 250 keV. The cut-off in the energy spectrum above ten MeV excitation is due to the Coulomb barrier of the  ${}^{12}\text{C}$  channel. On the left-hand side of the spectrum, the strongly excited peaks come from the  $({}^{16}\text{O}, {}^{12}\text{C})$  reaction on the  ${}^{12}\text{C}$  target backing. In contrast to this fact, at 48 MeV incident energy and for  ${}^{44,48}\text{Ca}$  and  ${}^{48,50}\text{Ti}$  targets the detection of  ${}^{13}\text{C}$ ,  ${}^{14}\text{C}$  and  ${}^{14,15}\text{N}$  becomes possible. Figure 6 shows that there is a considerable separation between  ${}^{12}\text{C}$  and  ${}^{14}\text{C}$ . The spectra of the reactions  ${}^{50}\text{Ti}({}^{16}\text{O}, {}^{12}\text{C}){}^{54}\text{Cr}$  and  ${}^{50}\text{Ti}({}^{16}\text{O}, {}^{14}\text{C}){}^{52}\text{Cr}$  are presented in Fig. 7. In the spectrum of the

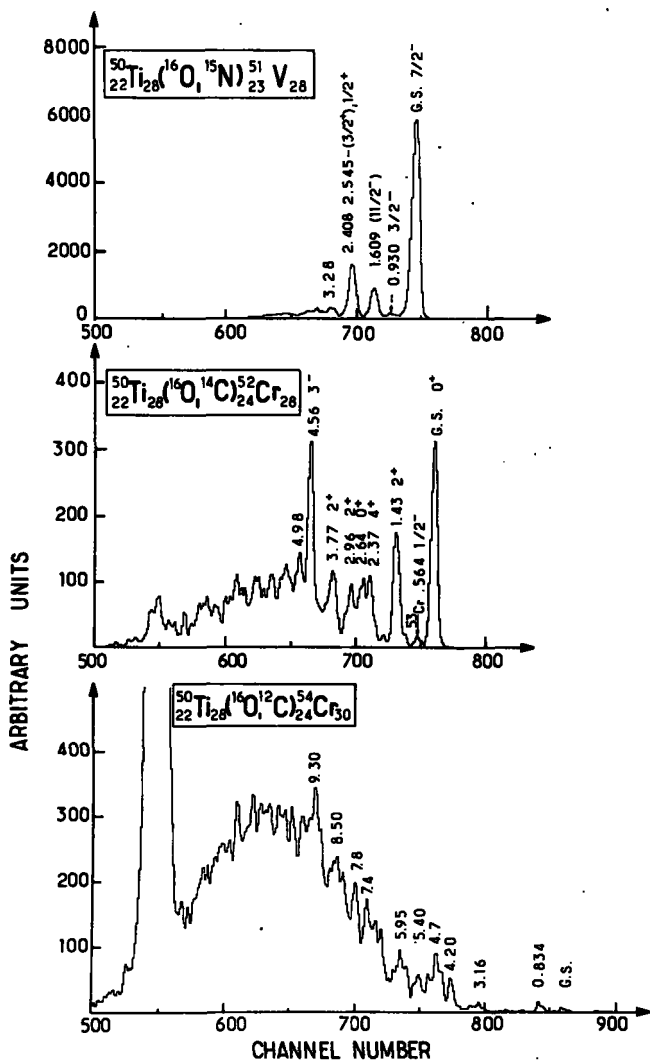


FIG. 7. ( $^{16}\text{O}, ^{15}\text{N}$ ), ( $^{16}\text{O}, ^{12,14}\text{C}$ ) energy spectra obtained at  $40^\circ$  laboratory system by bombarding a  $^{50}\text{Ti}$  target with a 48-MeV  $^{16}\text{O}$  beam.

( $^{16}\text{O}$ ,  $^{14}\text{C}$ ) reaction, we can see that the ( $^{16}\text{O}$ ,  $^{13}\text{C}$ ) reaction appears only as a tiny contamination. The energy spectrum related to the nitrogen identification peak clearly shows that only  $^{15}\text{N}$  is observed.

### 3. REACTION MECHANISM

#### 3.1. Elastic scattering

Information important for the understanding of the transfer-reaction mechanism is given by elastic-scattering data. Thus, we have measured the  $^{16}\text{O}$  elastic scattering on  $^{54}\text{Fe}$  at two incident energies 48 MeV and 52 MeV. The corresponding angular distributions are shown in Fig. 8. They deviate from pure Coulomb scattering, respectively, at  $50^\circ$  centre-of-mass and  $45^\circ$  centre-of-mass; the exponential decrease which follows is characteristic of strong absorption.

In the case of strong absorption Blair's sharp cut-off model predicts that the angle  $\theta$ , where the cross-section ratio between elastic scattering and Coulomb scattering is 0.25, corresponds to the "grazing" angle where the minimal distance of approach  $D$  is equal to the sum  $R_1 + R_2$  of the nuclear radii,

This hypothesis leads to the following relationship

$$D = \frac{Z_1 Z_2 e^2}{2E_{\text{centre-of-mass}}} \left( 1 + \frac{1}{\sin \frac{\theta}{2}} \right) = r_0 (A_1^{1/3} + A_2^{1/3})$$

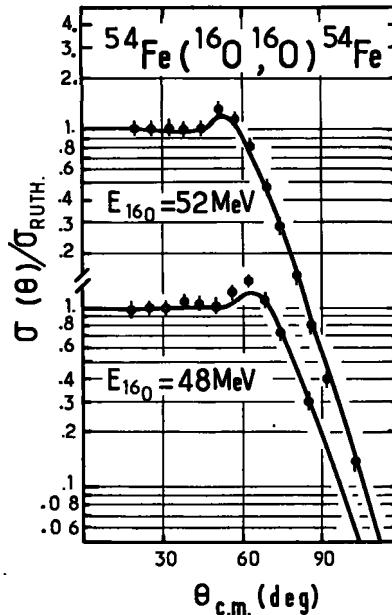
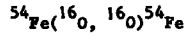


FIG. 8.  $^{54}\text{Fe}(^{16}\text{O}, ^{16}\text{O})^{54}\text{Fe}$  elastic-scattering angular distributions.



${}^{16}\text{O}$	Incident Energy	$r_0 = r_i = r_c$ (F)	$V_0$ (MeV)	$a_0$ (F)	$W_i$ (MeV)	$a_i$ (F)	$\chi_m^2$
	48. MeV	1.44	5.47	.450	3.53	.450	1.10
		1.25	20.34	.650	6.05	.650	.85
		1.25	20.34	.656	6.05	.628	.83
	52. MeV	1.44	5.18	.450	4.97	.450	.88
		1.25	16.14	.650	13.02	.650	1.30
		1.25	16.14	.708	17.56	.553	0.50

$$V(r) = V_0(1 + \exp[(r - R_0)/a_0])^{-1} + i W_i(1 + \exp[(r - R_i)/a_i])^{-1} + V_{\text{coul.}}(R_c, r)$$

$$R_{i,o,c} = r_{i,o,c}(A_1^{1/3} + A_2^{1/3})$$

FIG. 9. Optical-model parameters for the  ${}^{54}\text{Fe}({}^{16}\text{O}, {}^{16}\text{O}){}^{54}\text{Fe}$  elastic scattering.

Knowing  $\theta$ , we can then extract  $r_0$ . In our experiments, we have in this way obtained the value  $r_0 = 1.55$  fm which is typical for heavy-ion scattering. For the incident energies considered, the total kinetic energy available in the centre-of-mass system is then just a few MeV above the Coulomb-barrier energy calculated with this radius.

The fits shown have been obtained from an optical-model analysis using Raynal's Saclay code Magali. Wood-Saxon form factors were used for the real and imaginary part of the potential. The interaction radius was taken to be the sum of the radii of the two scattered nuclei. The different families of parameters are given in Fig. 9. They present the common features encountered in heavy-ion analyses, i.e. small depth for both real and imaginary parts of the potential.

### 3.2. Selectivity of transfer reactions

It is well-known that one-particle-transfer reactions occurring through direct processes strongly excite states in the residual nucleus which are well described by the coupling of a one-nucleon wave-function to the target ground-state wave-function. Using this feature, important information on the reaction mechanism can be obtained by studying the selectivity of the reactions induced by heavy ions which lead to well-known state configurations.

In Fig. 10 we compare the results obtained for one-proton transfer reactions ( ${}^{16}\text{O}, {}^{15}\text{N}$ ) and ( ${}^3\text{He}, d$ ) leading to the same residual nuclei. For ( ${}^3\text{He}, d$ ) reactions we list the single-particle strength deduced from DWBA analyses of angular distributions. In the case of the ( ${}^{16}\text{O}, {}^{15}\text{N}$ ) reaction,



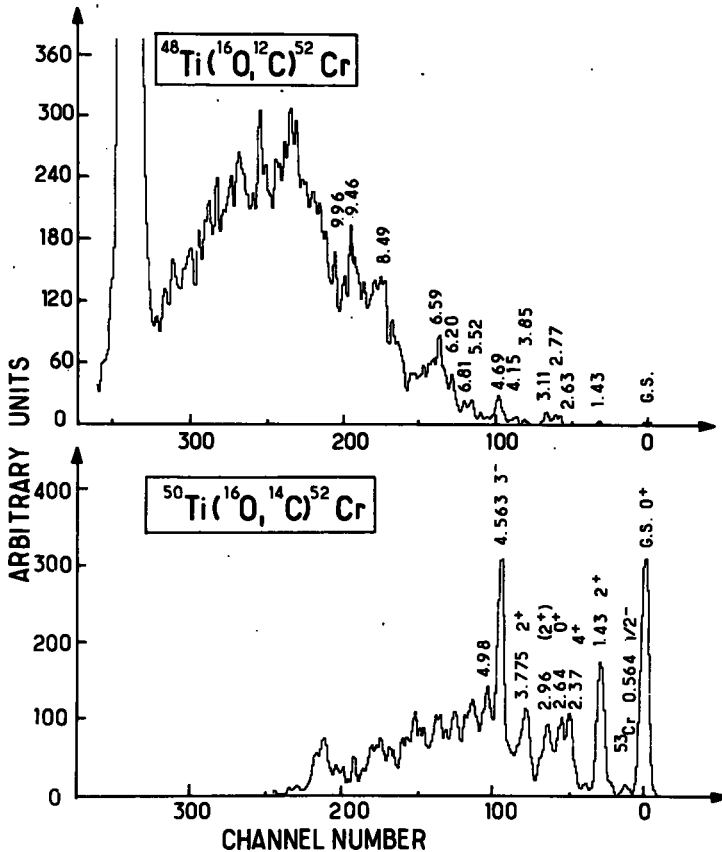


FIG. 11. Comparison between  $^{48}\text{Ti}(^{16}\text{O}, ^{12}\text{C})^{52}\text{Cr}$  and  $^{50}\text{Ti}(^{16}\text{O}, ^{14}\text{C})^{52}\text{Cr}$  energy spectra obtained at  $40^\circ$  laboratory system and 48 MeV incident beam energy.

we give for each spectrum the relative intensities of the levels observed at  $40^\circ$ ; this corresponds to the grazing angle where the  $(^{16}\text{O}, ^{15}\text{N})$  cross-section reaches its maximum value. The general picture is that the  $(^{16}\text{O}, ^{15}\text{N})$  reactions excite fewer levels than  $(^3\text{He}, \text{d})$  reactions [19]. In heavy-ion experiments, the Coulomb-barrier energy limits the observable excitation energy, additionally the experimental resolution does not allow as many levels to be distinguished as the  $(^3\text{He}, \text{d})$  reactions do. However, the observed levels in  $(^{16}\text{O}, ^{15}\text{N})$  reactions are those which have the largest single-particle strength. This result supports the idea that in the vicinity of the Coulomb barrier the  $(^{16}\text{O}, ^{15}\text{N})$  reaction takes place through a direct process.

Figure 11 gives a comparison of the  $(^{16}\text{O}, ^{12}\text{C})$  and  $(^{16}\text{O}, ^{14}\text{C})$  spectra leading to the same residual nuclei  $^{52}\text{Cr}$ . As is expected in a direct process, strong differences are observed between the selectivity of the two- and four-nucleon transfer reactions. The first levels strongly excited by the two-proton-transfer reactions have very weak intensities in  $(^{16}\text{O}, ^{12}\text{C})$  reaction.

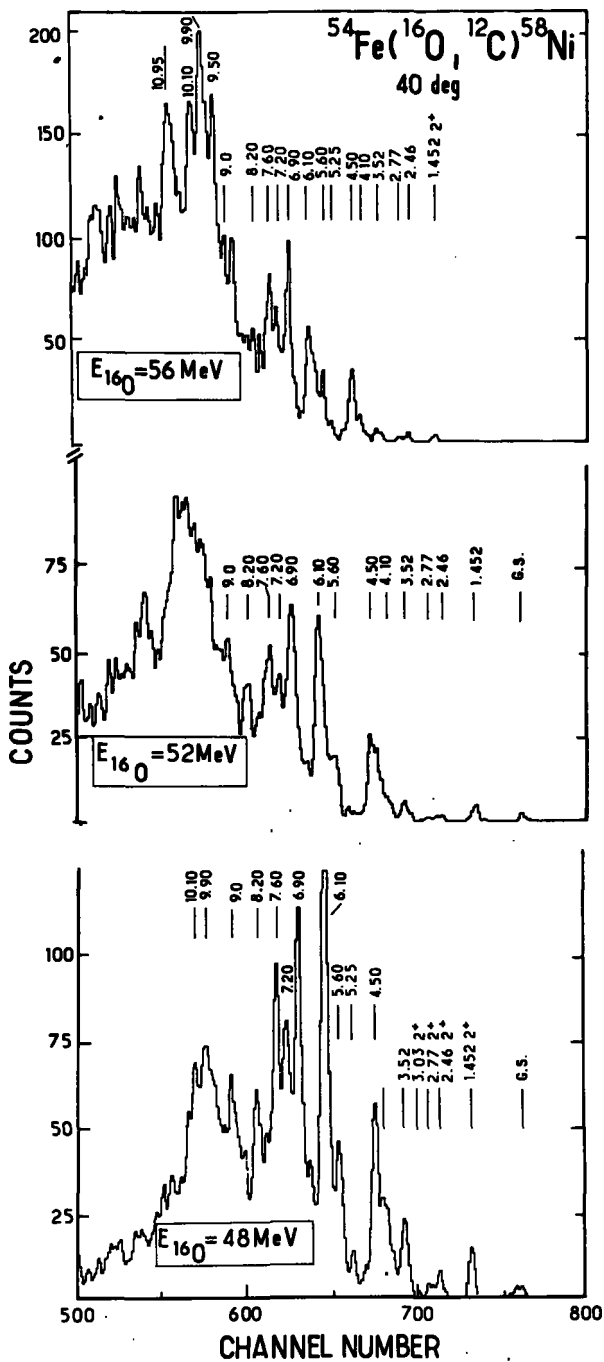


FIG. 12. Three spectra of the  $^{54}\text{Fe}(^{16}\text{O}, ^{12}\text{C})^{58}\text{Ni}$  reaction measured at  $40^\circ$  laboratory system for the following incident energies: 48, 52 and 56 MeV.

Finally, let us recall the  $^{54}\text{Fe} (^{16}\text{O}, ^{12}\text{C})^{58}\text{Ni}$  energy spectrum (Fig. 5). The first few levels, well known to be vibrational states, are weakly excited by the  $\alpha$ -transfer reaction. In contrast to this, strong peaks appear between 4 and 10 MeV of excitation energy. Although more than 80 levels have been seen in this region by means of  $(p, p'\gamma)$  experiments, the  $(^{16}\text{O}, ^{12}\text{C})$  reaction appears to be very selective for a small number of them. The widths of the strongly excited peaks are the same as those of the well separated levels. Thus, most of them should correspond to the excitation of a single level.

Some of the peaks observed might result from the emission of a  $^{12}\text{C}$  excited nucleus, in the 4.43 MeV  $2^+$  state. In fact, no systematic 4.4 MeV interval can be observed between the strongest peaks. A better proof would be obtained by comparing the  $(^{16}\text{O}, ^{12}\text{C})$  and the  $(^{20}\text{Ne}, ^{16}\text{O})$  spectra for the same residual nuclei. Such an experiment is planned at Saclay as soon as the cyclotron is able to deliver a  $^{20}\text{Ne}$  beam.

### 3.3. Energy dependence of the spectra

The  $^{54}\text{Fe} (^{16}\text{O}, ^{12}\text{C})^{58}\text{Ni}$  reaction has been performed at 42, 48, 52 and 56 MeV incident energies. At 42 MeV, the cross-section was too small to be measured. Great similarity is observed in the three other spectra (Fig. 12). There appears to be some background under the peaks at the highest energy of excitation, the intensity of which increases as the incident

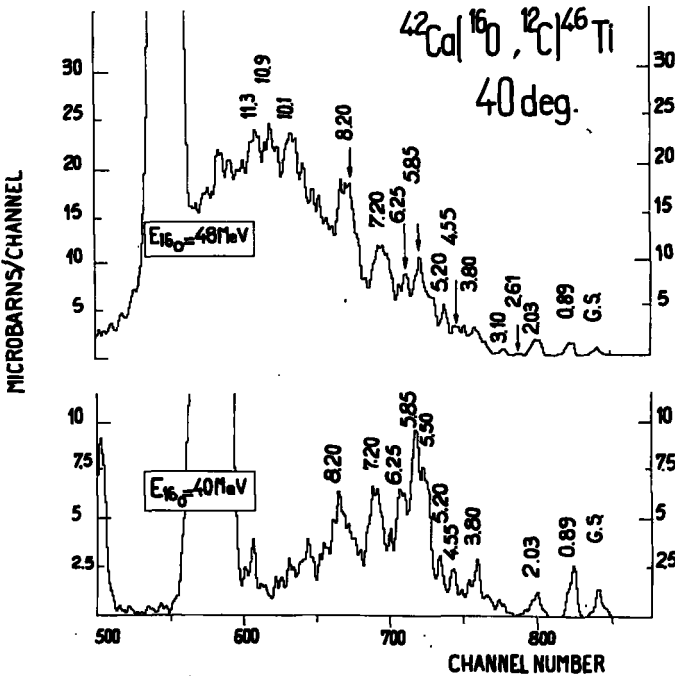


FIG. 13. The  $^{42}\text{Ca} (^{16}\text{O}, ^{12}\text{C})^{46}\text{Ti}$  energy spectra obtained at  $40^\circ$  laboratory system for two different incident energies (40 and 48 MeV).

energy becomes higher. The nature of this background remains an open problem. It may come from the break-up of the  $^{16}\text{O}$  into a  $^{12}\text{C} + \alpha$  in the target field or from a kind of compound-nucleus process resulting in the emission of  $^{12}\text{C}$ . The break-up process is expected to be low because of the 7.2 MeV alpha-binding energy in  $^{16}\text{O}$  compared with 1.47 MeV in  $^6\text{Li}$  and 2.46 MeV in  $^7\text{Li}$ . For the  $^{54}\text{Fe} (^{16}\text{O}, ^{12}\text{C})^{58}\text{Ni}$  energy spectrum obtained at 48-MeV incident energy, the upper kinematic energy limit of the break-up is under the 6.1 MeV excitation energy peak. However, looking back to the  $^{12}\text{C} (^{16}\text{O}, ^{12}\text{C})^{16}\text{O}$  energy spectrum, the upper limit of the break-up process lies below the doublet  $1^-$  7.14 MeV and  $2^+$  6.92 MeV and in fact there is no background at all. At Berkeley, Québert et al. [20] have studied the  $^6\text{Li}$ ,  $^{12}\text{C}$ ,  $^{16}\text{O}$  break-up on gold target; they do not observe any break-up for  $^{16}\text{O}$ . Moreover, we have observed that the intensity of the background varies from one nucleus to another. For example, the energy spectrum of the  $^{40}\text{Ca} (^{16}\text{O}, ^{12}\text{C})^{44}\text{Ti}$  does not show any background. In contrast to this, the energy spectra of the  $^{42}\text{Ca} (^{16}\text{O}, ^{12}\text{C})^{46}\text{Ti}$  reaction (Fig. 13) obtained at 40 and 48 MeV show that the strongly excited levels in  $^{46}\text{Ti}$  observed in the 40 MeV spectrum have almost disappeared in the 48 MeV spectrum. For the different cases studied we have calculated the ratio between the distance of closest approach  $D$  of the nuclei and the interaction radius  $R$  (Table I).

TABLE I. RATIO BETWEEN  $D$  AND  $R$ 

$E_{^{16}\text{O}}$ (MeV) targets	40	48	52	56
$^{42}\text{Ca}$	1.11	0.94		
$^{54}\text{Fe}$		1.11	1.02	0.95

An important background is observed whenever the two nuclei interpenetrate each other. Thus, it is possible that a kind of compound-nucleus process occurs when  $D/R < 1$ . To avoid this effect, we have chosen the incident energy so as to have the total centre-of-mass kinetic energy available in the entrance channel close to the Coulomb barrier energy:  $B_C = 1.44 (Z_1 Z_2)/(R_1 + R_2)$ .

### 3.4. Angular distributions

The angular distributions of one and two proton transfer reactions on the  $^{50}\text{Ti}$  target are simultaneously measured using a 48 MeV  $^{16}\text{O}$  beam. On Fig. 14 are plotted the  $^{50}\text{Ti} (^{16}\text{O}, ^{15}\text{N})^{51}\text{V}$  angular distributions. Each of them has a maximum at  $50^\circ$  centre-of-mass which corresponds to the grazing angle in the elastic scattering  $^{50}\text{Ti} (^{16}\text{O}, ^{16}\text{O})^{50}\text{Ti}$ . The shape of the angular distributions can be well described by a tunnelling process with nuclear absorption. At small angles where the impact parameters are large, the increase of the cross-sections may be described by the proton tunnelling process. We assume that nucleon transfer occurs when the

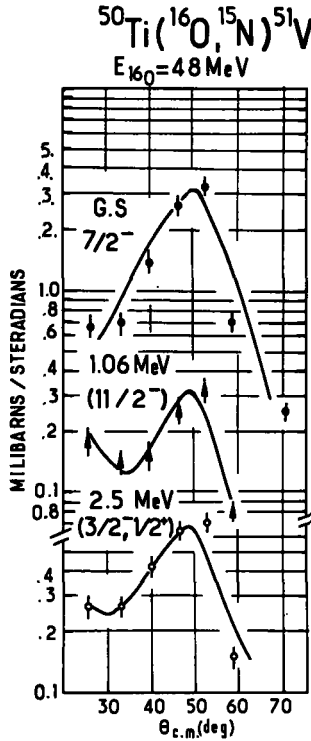


FIG. 14.  $^{50}\text{Ti}(^{16}\text{O}, ^{15}\text{N})^{51}\text{V}$  angular distributions.

projectile and the target are at their closest distance. For larger angles, the impact parameter is smaller than  $R_1 + R_2$  and then the decrease of the cross-section reflects the influence of nuclear absorption. Nevertheless, at  $25^\circ$  centre-of-mass the experimental points seem to be too high to be explained by a simple tunnelling process.

The  $^{50}\text{Ti}(^{16}\text{O}, ^{14}\text{C})^{52}\text{Cr}$  two-proton-transfer angular distributions are shown in Fig. 15. All exhibit the same exponential decrease of the cross-sections for backward angles. Similar shapes are obtained for the  $^{54}\text{Fe}(^{16}\text{O}, ^{12}\text{C})^{58}\text{Ni}$  angular distributions measured with a 52 MeV  $^{16}\text{O}$  beam (Fig. 16). At 80 and 120 degrees laboratory angle, the cross-section of the  $^{54}\text{Fe}(^{16}\text{O}, ^{12}\text{C})^{58}\text{Ni}$  reaction is too small to be measured. The exponential decrease observed for the angular distribution is described by the Dodd and Greider [21] DWBA stripping model for heavy ions. Using a sharp cut-off model to generate the so-called elastic distorted wave-functions for the entrance and the exit channel, including finite-range interaction for the transferred cluster and taking into account the recoil terms, these authors give the following approximate expression for the cross-section:

$$\frac{d\sigma}{d\Omega} \rightarrow q^{-3} \exp\left(-p^2 \frac{a^2}{6}\right)$$

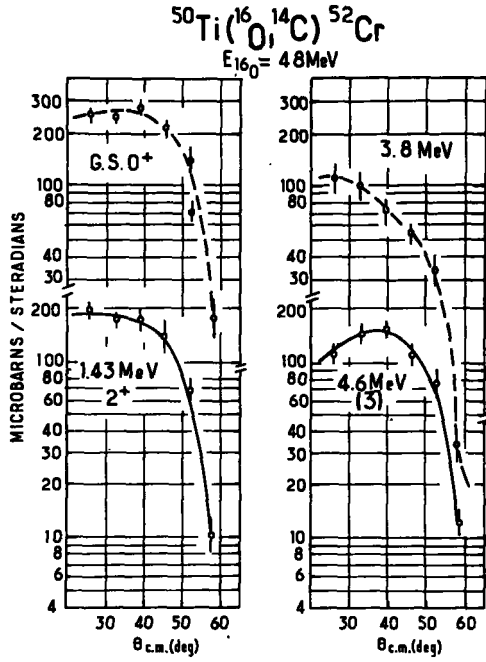


FIG. 15. Angular distributions of the most strongly excited states of  $^{52}\text{Cr}$  seen in the  $(^{16}\text{O}, ^{14}\text{C})$  two-proton transfer reaction.

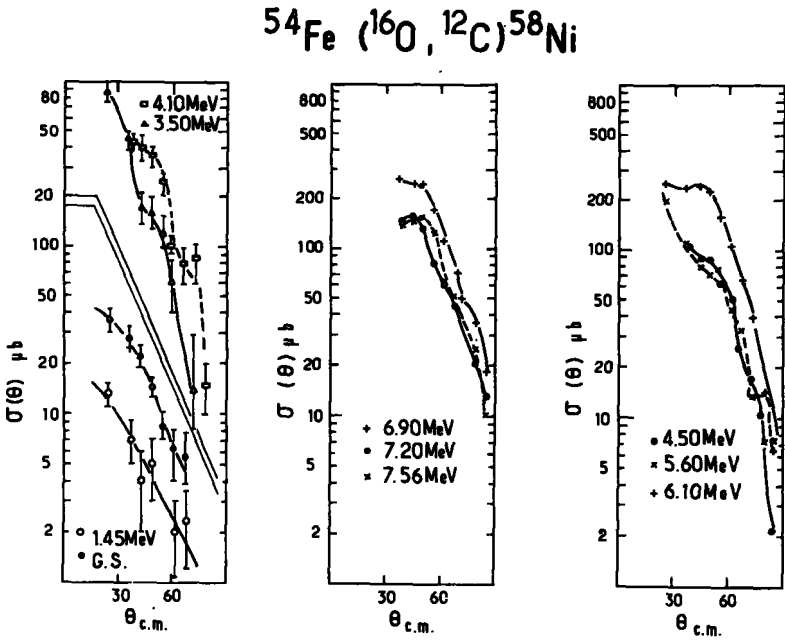


FIG. 16. The  $^{54}\text{Fe} (^{16}\text{O}, ^{12}\text{C}) ^{58}\text{Ni}$  angular distributions.

where  $p$  is the target recoil parameter,  $a$  the range of the bound state wave-functions of the transferred cluster and  $q$  the transferred momentum. This model predicts well an exponential decrease of the cross-section for increasing transferred momenta. A more elaborate distorted-wave analysis is now in progress at Saclay [22]. The shape of the angular distributions does not allow spins to be assigned. All the nuclear spectroscopy is included in the comparison of the relative intensities.

#### 4. NUCLEAR SPECTROSCOPY WITH HEAVY-ION EXPERIMENTS

This section is essentially devoted to the experimental investigation of four-nucleon correlations in medium-weight nuclei by means of alpha transfer experiments. But, first of all, a short summary is given on the experimental results obtained with the ( $^{16}\text{O}, ^{14}\text{C}$ ) two-proton-transfer reaction.

##### 4.1. Two-proton-transfer reactions

As was mentioned previously, the ( $^{16}\text{O}, ^{14}\text{C}$ ) reaction is a very easy technique for obtaining two-proton transfer. Thus we have studied the  $^{44,48}\text{Ca} (^{16}\text{O}, ^{14}\text{C})$ ,  $^{46,50}\text{Ti}$  and  $^{50,52}\text{Ti} (^{16}\text{O}, ^{14}\text{C})$ ,  $^{52,54}\text{Cr}$  reactions at 48 MeV incident energy.

The simultaneous collection of the  $\alpha$ - and two-proton-transfer data on Ca and Ti isotopes is very interesting: the comparison of the states excited on the same residual nuclei by  $\alpha$ - or two-proton transfer exhibits distinct differences. A typical example was given previously with the  $^{48}\text{Ti} (^{16}\text{O}, ^{12}\text{C})$   $^{52}\text{Cr}$  and  $^{50}\text{Ti} (^{16}\text{O}, ^{14}\text{C})$   $^{52}\text{Cr}$  spectra (Fig. 11). The dominant two-nucleon or dominant four-nucleon configurations are easy to identify and discriminate without ambiguity. Again, all the spectroscopic information is contained in the cross-section intensities. Figure 17 summarizes the two-proton-transfer results obtained for  $^{48,50}\text{Ti}$  and  $^{52,54}\text{Cr}$  residual nuclei. The intensities of the two-proton transitions are stronger in the

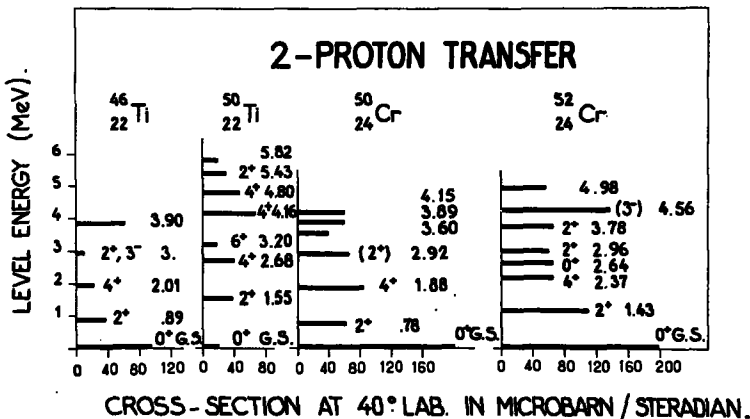
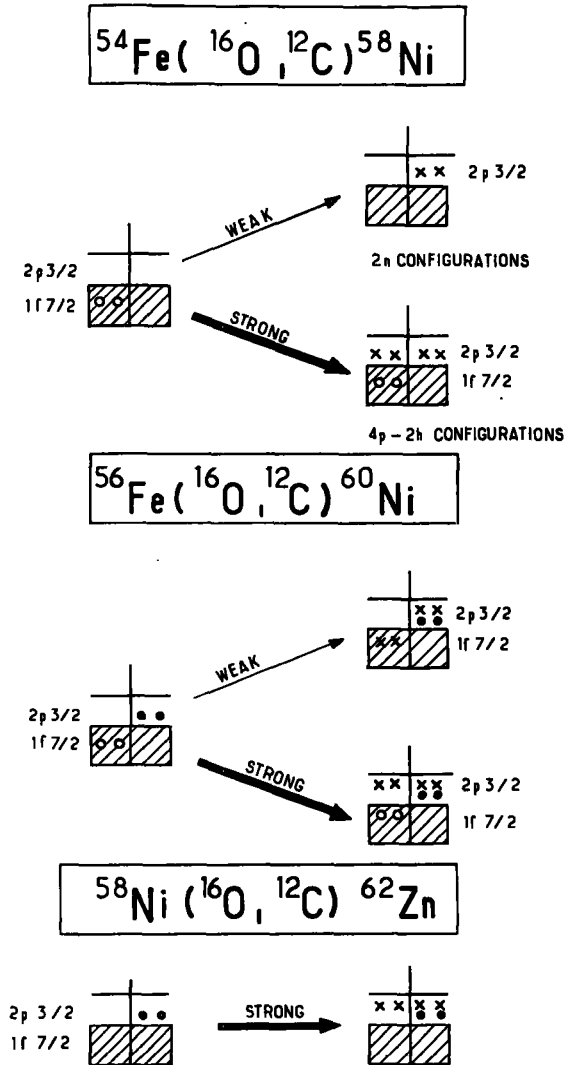


FIG. 17. A summary of the ( $^{16}\text{O}, ^{14}\text{C}$ ) two-proton-transfer experiments.

TABLE II. B(E2) TRANSITION PROBABILITIES

Residual nuclei	$^{46}_{22}\text{Ti}$	$^{50}_{22}\text{Ti}$	$^{50}_{24}\text{Cr}$	$^{54}_{24}\text{Cr}$
B(E2, $2^+_1 \rightarrow 0^+_1$ G.S.) ( $e^2 \cdot \text{fm}^4$ )	$700 \mp 140$	$320 \mp 80$	$1200 \mp 80$	$670 \mp 70$

FIG. 18. Schematic description of the  $\alpha$ -transfer experiments by means of the shell-model picture ( $\bullet$  one proton hole,  $\circ$  one target particle,  $\times$  one transferred particle).

Cr than in the Ti isotopes. The  $^{50}\text{Ti}$  isotope exhibits a singular behaviour with a very weak excitation of its ground state. The states populated by the  $(^{16}\text{O}, ^{14}\text{C})$  reaction are those excited by  $(\alpha, \alpha')$  inelastic scattering. These results show the importance of vibrational states in the two-proton configurations. For the residual nuclei obtained by  $(^{16}\text{O}, ^{14}\text{C})$  reactions, the  $B(E2)$  transition probabilities are given in Table II.

These  $B(E2)^\dagger$  values show that the smallest  $B(E2)$  value observed corresponds to the smallest two-proton transition intensity.

#### 4.2. Experimental evidence for four-nucleon correlations in Ni, Zn, Ti and Cr isotopes

The  $(^{16}\text{O}, ^{12}\text{C})\alpha$  transfer reaction has been performed on several isotopes of calcium, titanium, iron and nickel. The  $^{54}\text{Fe} (^{16}\text{O}, ^{12}\text{C}) ^{58}\text{Ni}$  angular distributions being structureless and having similar shapes for all the  $^{58}\text{Ni}$  excited states, we can obtain relevant data with only a few angle measurements. To avoid the contamination of the  $^{12}\text{C}$  spectra by the  $^{12}\text{C} (^{16}\text{O}, ^{12}\text{C}) ^{16}\text{O}$  reaction from the target backing we have generally chosen angles between  $35^\circ$  and  $50^\circ$  in the laboratory system. The two incident energies 48 and 40 MeV respectively used for Fe, Ni and Ca, Ti targets, correspond to a total kinetic energy available in the centre-of-mass system equal to the Coulomb barrier. The states strongly excited by means of the  $(^{16}\text{O}, ^{12}\text{C})$  reaction are discussed here in terms of quartet states, i.e. two protons and two neutrons in a highly symmetric configuration.

The first reaction studied was  $^{54}\text{Fe} (^{16}\text{O}, ^{12}\text{C}) ^{58}\text{Ni}$  [23]. In a single-shell-model picture, the  $^{54}\text{Fe}$  ground state is described by two proton holes in the  $1f_{7/2}$  shell (Fig.18). The first levels of  $^{58}\text{Ni}$  have essentially two-neutron configurations. The excitation of these states by the  $(^{16}\text{O}, ^{12}\text{C})$  reaction is expected to be weak since it requires the breaking of the quartet corresponding to the  $\alpha$  transferred. In contrast to this, the excitation of  $4p-2h$  states in  $^{58}\text{Ni}$  can be reached leaving the four nucleons highly correlated in the  $2p_{3/2}$  shell, for example. Thus in  $\alpha$ -transfer experiments these transitions are expected to be strong. The lowest part of Fig.19 shows the  $^{58}\text{Ni}$  energy spectrum from the  $^{54}\text{Fe} (^{16}\text{O}, ^{12}\text{C}) ^{58}\text{Ni}$  reaction. The first levels of  $^{58}\text{Ni}$  which are vibrational states are weakly excited; the strong peaks appear between 4 and 10 MeV excitation energy.

Then, it seems interesting to study the behaviour of these states in neighbouring residual nuclei, with different numbers of protons and neutrons. Figure 19 shows the comparison between the energy spectra of the  $^{54}, ^{56}\text{Fe} (^{16}\text{O}, ^{12}\text{C}) ^{58}, ^{60}\text{Ni}$  and  $^{58}\text{Ni} (^{16}\text{O}, ^{12}\text{C}) ^{62}\text{Zn}$  reactions. The similarity between the  $^{58}\text{Ni}$  and  $^{60}\text{Ni}$  spectra indicates that the addition of two neutrons to  $^{54}\text{Fe}$  plays a little role only.

A phenomenological estimate of the energy of the lowest quartet state  $^{60}\text{Ni}$  can be made by considering binding energies according to the following relation:

$${}^{60}\text{Ni}_{(Q-2h)} = ({}^{62}\text{Zn} - {}^{58}\text{Ni}) - ({}^{58}\text{Ni} - {}^{56}\text{Fe}) + 8\chi + 2\Delta\epsilon_c$$

$$\begin{array}{c|c} \text{XX} & \text{XX} \\ \text{XX} & \text{XX} \\ \hline \text{OO} & \end{array} = \left( \begin{array}{c|c} \text{XX} & \text{XX} \\ \text{XX} & \text{XX} \\ \hline & \end{array} - \begin{array}{c|c} & \\ & \text{XX} \\ \hline & \end{array} \right) - \left( \begin{array}{c|c} & \text{XX} \\ & \text{XX} \\ \hline & \end{array} - \begin{array}{c|c} & \\ \text{OO} & \text{XX} \\ \hline & \end{array} \right)$$

Z            N

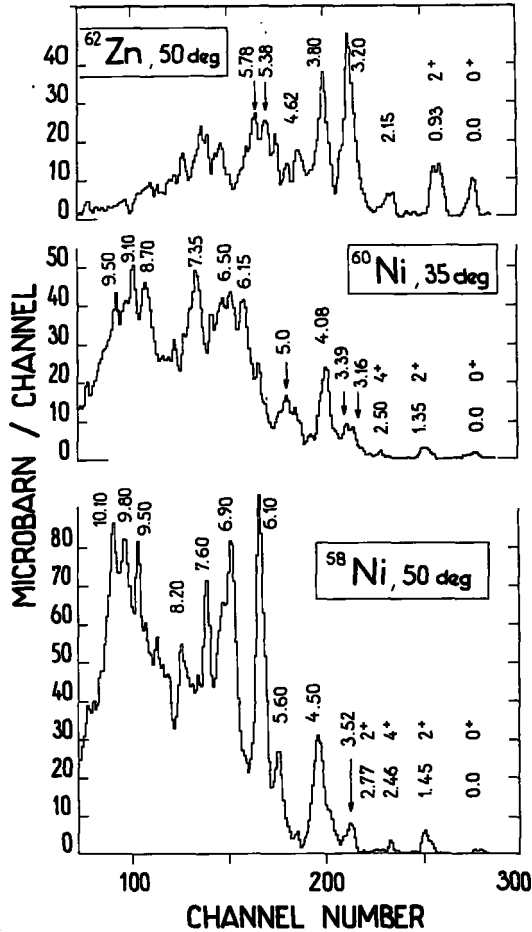


FIG. 19. Three energy spectra corresponding to the reactions  $^{54, 56}\text{Fe}(^{16}\text{O}, ^{12}\text{C})^{58, 60}\text{Ni}$  and  $^{60}\text{Ni}(^{16}\text{O}, ^{12}\text{C})^{62}\text{Zn}$  studied at 48 MeV incident energy.

where  $\chi$  is the average particle-hole repulsive interaction energy and  $\Delta\epsilon_c$  is the attractive Coulomb particle-hole interaction. With the reasonable estimates:  $\chi \approx 0.5$  to 1 MeV and  $\Delta\epsilon_c \sim 0.5$  MeV [23], the first quartet state in  $^{60}\text{Ni}$  might appear between 2 and 6 MeV excitation energy. Relatively strongly excited groups are observed in  $^{60}\text{Ni}$  above 3 MeV excitation energy.

On the other hand, the  $^{62}\text{Zn}$  energy spectrum shows a different behaviour: the ground state and the  $2^+$  first excited state are strongly populated by the  $(^{16}\text{O}, ^{12}\text{C})$  reaction.  $^{58}_{28}\text{Ni}_{30}$  differs from  $^{56}_{28}\text{Fe}_{30}$  by the filling of the two  $1f_{7/2}$  proton holes. Starting from a  $^{58}\text{Ni}$  target the transfer of the four nucleons in the  $2p_{3/2}$  shell can give directly a relatively strong excitation of the first levels of  $^{62}\text{Zn}$  (Fig. 18).

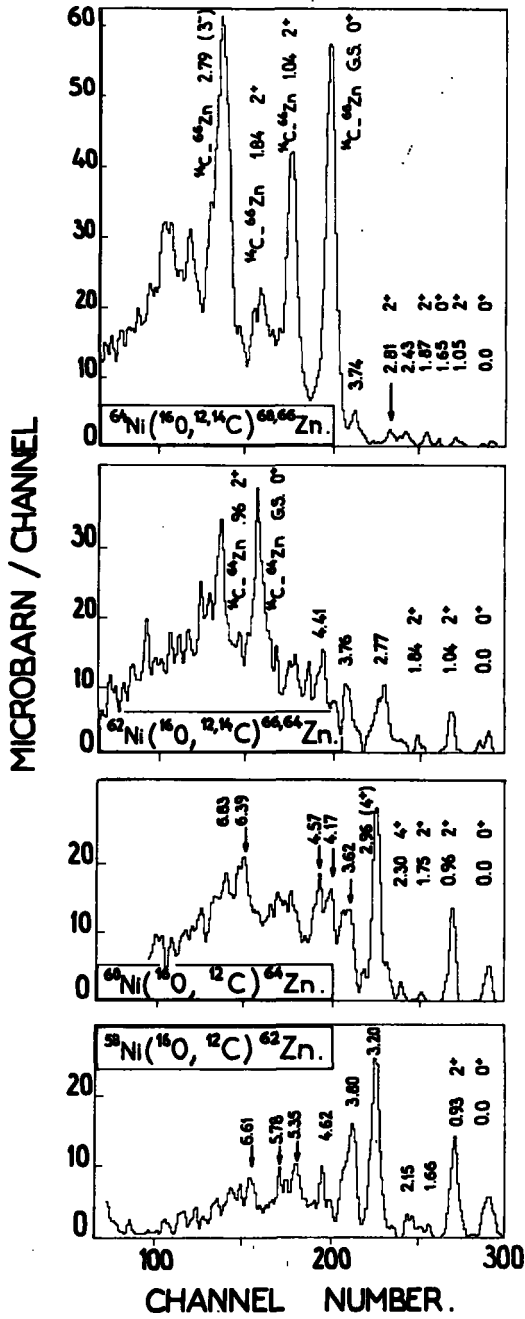


FIG. 20. Systematic of the Ni( $^{16}\text{O}$ ,  $^{12}\text{C}$ ) Zn reactions performed at 48 MeV incident energy.

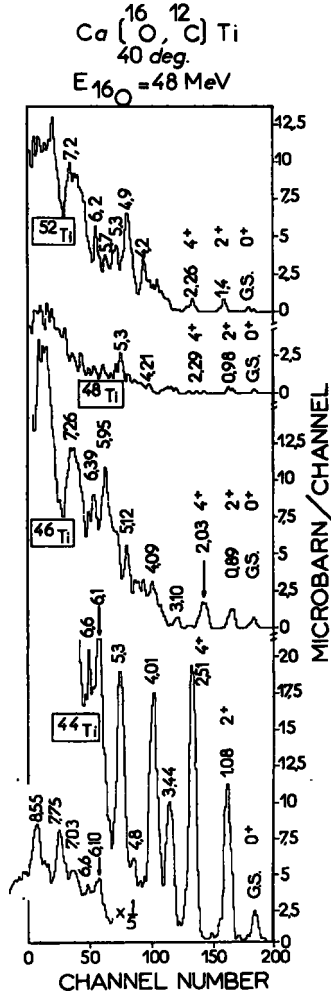


FIG. 21. Survey of the  $Ca(^{16}O, ^{12}C)Ti$  reactions studied at 48 MeV incident energy. These spectra are obtained at  $40^\circ$  laboratory system.

We have studied the behaviour of the main peaks when the number of neutrons is increasing. The four stable even isotopes of nickel were chosen for this purpose. The energy spectra of the reactions  $^{58, 60, 62, 64}Ni(^{16}O, ^{12}C)^{62, 64, 66, 68}Zn$  are shown in Fig. 20. The data were taken at 48 MeV incident energy, and  $40^\circ$  degrees in the laboratory system. The most striking features of these spectra are the following:

The ground state and the first  $2^+$  excited states are strongly populated in  $^{62}Zn$  and  $^{64}Zn$ , weakly populated in  $^{66}Zn$  and very weakly populated in  $^{68}Zn$ . This feature supports the idea that the  $0^+$  and  $2^+$  states of  $^{62}Zn$  and  $^{64}Zn$  are mainly excited by the transfer of the four nucleons in the  $2p_{3/2}$  shell. This is easy to achieve when the targets have only a few nucleons in

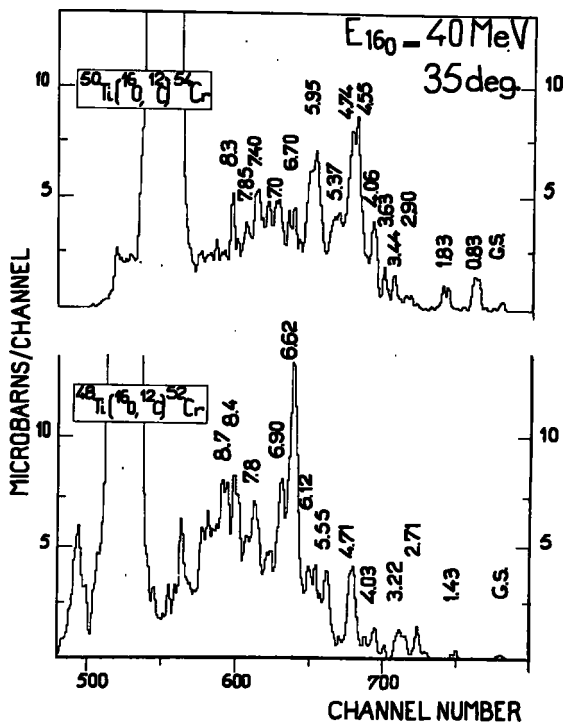


FIG. 22. The  $^{48}\text{Ti}$ ,  $^{50}\text{Ti}$  ( $^{16}\text{O}$ ,  $^{12}\text{C}$ )  $^{52}\text{Cr}$ ,  $^{54}\text{Cr}$  energy spectra measured at 40 MeV incident energy.

the  $2p_{3/2}$  shell. One observes a neutron blocking effect, in the excitation of the first levels, which corresponds to filling in neutrons of the  $2p_{3/2}$  shell.

In  $^{62}\text{Zn}$ , a clean quartet structure is observed up to 6 MeV excitation energy. It is tempting to try to correlate this structure with the one observed previously in  $^{60}\text{Ni}$  between 4 and 10 MeV excitation energy. In the other Zn isotopes, the quartet structure is gradually washed out as the neutron shell is filled.

The strongest peaks observed in the  $^{62,64}\text{Ni}$  ( $^{16}\text{O}$ ,  $^{12}\text{C}$ )  $^{66,68}\text{Zn}$  energy spectra correspond to  $^{62,64}\text{Ni}$  ( $^{16}\text{O}$ ,  $^{14}\text{C}$ )  $^{64,66}\text{Zn}$  two proton transfer reactions.

A natural extension of these experiments is the study of the blocking effect due to the gradual filling of the neutron shells in the even Ca-isotopes.

The energy spectra of the Ca ( $^{16}\text{O}$ ,  $^{12}\text{C}$ ) Ti reactions are shown in Fig. 21. They are obtained at 48 MeV incident energy and at  $40^\circ$  in the laboratory system. The alpha transfer on the doubly closed shell nucleus  $^{40}\text{Ca}_{20}$  strongly and selectively excites several states of the  $^{44}\text{Ti}$  residual nucleus. A drastic decrease of the cross-sections is observed between the first excited levels of  $^{44}\text{Ti}$  and those of  $^{46}\text{Ti}$ . From  $^{46}\text{Ti}$  to  $^{48}\text{Ti}$ , the levels below 4 MeV excitation energy are very weakly excited. The general behaviour in titanium isotopes is very similar to that previously observed in the zinc isotopes.

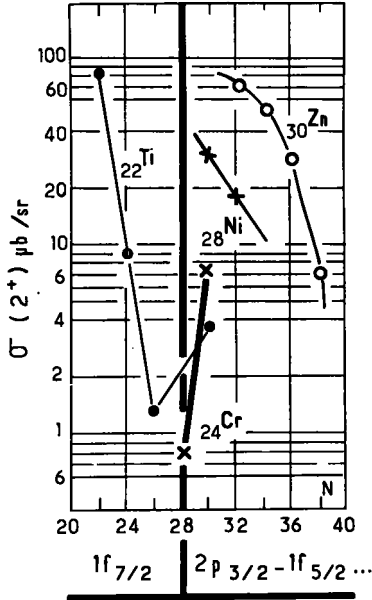


FIG. 23. The first- $2^+$ -excited-state absolute cross-sections for various residual nuclei obtained by  $(^{16}\text{O}, ^{12}\text{C})$  transfer reactions. The spectra were taken at  $40^\circ$  laboratory system and 48 MeV  $^{16}\text{O}$  incident energy respectively on Ca, Ti, Fe and Ni isotopes. There is a large discontinuity in the cross-sections at the neutron-shell closure  $N=28$ .

In a similar way, the  $^{48,50}\text{Ti}(^{16}\text{O}, ^{12}\text{C})^{52,54}\text{Cr}$  reactions studied at 48 MeV incident energy show a weak population of the first excited levels. This shows clearly that the target neutron pair excess results in a decrease of the cross-section to the first levels (neutron blocking effect). In contrast to this, strong excitation of the  $^{46}\text{Ti}$ ,  $^{50}\text{Ti}$  and  $^{52}\text{Cr}$  states below 5 MeV is observed by means of the  $(^{16}\text{O}, ^{14}\text{C})$  two-proton-transfer reaction. These results indicate that the wave-functions of the first levels of  $^{46}\text{Ti}$  and  $^{52}\text{Cr}$  have weak quartet components.

At 48 MeV  $^{16}\text{O}$  incident energy, titanium and chromium states above 6 MeV excitation energy are obscured by a large background (this is not the case for  $^{44}\text{Ti}$ ). From Fig. 22 it can be seen that at 40 MeV  $^{16}\text{O}$  incident energy there is a strong and selective excitation of the states above 4 MeV excitation for the  $^{48,50}\text{Ti}(^{16}\text{O}, ^{12}\text{C})^{52,54}\text{Cr}$  reactions.

The behaviour of the cross-sections of the  $(^{16}\text{O}, ^{12}\text{C})$  transfer reaction leading to the first  $2^+$  excited states of all the residual nuclei studied are presented in Fig. 23. The neutron blocking effect within each set of isotopes is clearly seen, together with the rather sharp discontinuity at  $N=28$ . The  $0^+$  ground state cross-sections display the same features.

#### 4.3. Comparison of experimental data with theoretical $^{58}\text{Ni}$ , $^{60}\text{Ni}$ and $^{62}\text{Zn}$ energy spectra calculated in the stretch scheme

A calculation of  $^{58}\text{Ni}$ ,  $^{60}\text{Ni}$  and  $^{62}\text{Zn}$  energy levels has been performed by Jaffrin using the stretch scheme of Danos and Gillet [9]. The details

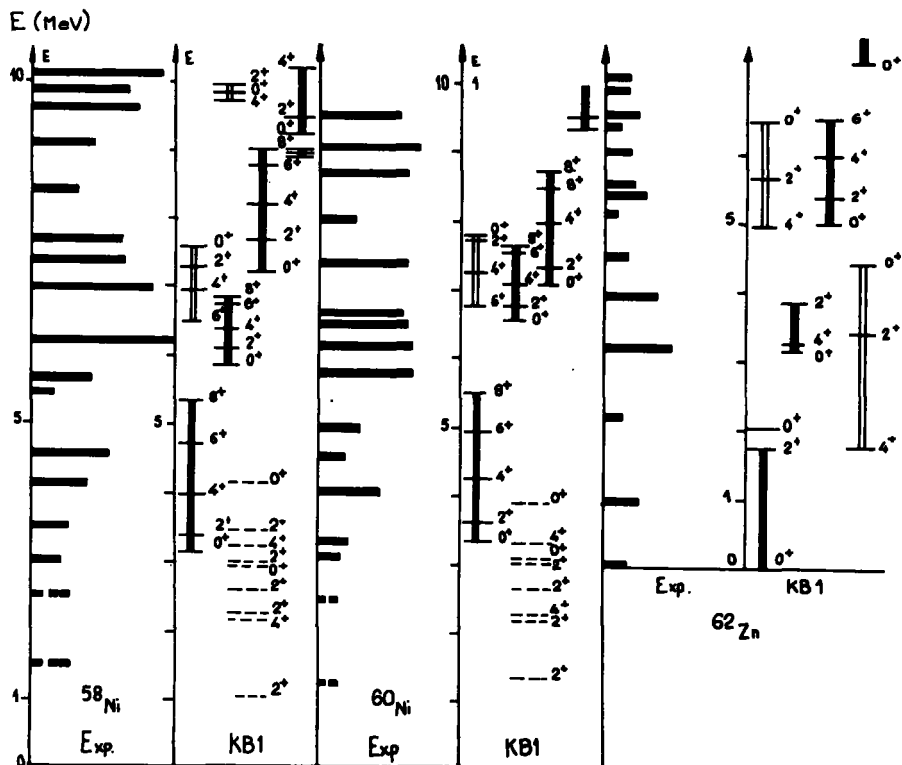


FIG. 24. Comparison between the experimental spectra of the  $^{54,56}\text{Fe}(^{16}\text{O}, ^{12}\text{C})^{58,60}\text{Ni}$  and  $^{58}\text{Ni}(^{16}\text{O}, ^{12}\text{C})^{62}\text{Zn}$  reactions and the  $^{58,60}\text{Ni}$  and theoretical energies calculated in the stretched scheme.

of calculations will be published in the de-Shalit Memorial Book of Annals of Physics [24]. Here only the principal points are presented. Let us consider, for example, the  $4p-2h$  state of  $^{58}\text{Ni}$  described by two protons in a shell of angular momentum  $j$ , two neutrons in the shell of angular momentum  $k$  and two proton holes in the shell of angular momentum  $\bar{j}$ . The stretch wave-function has to satisfy the following rules: i) maximum proton-neutron overlap; ii) minimum alignment between the angular momentum of particles and holes. The wave-function which satisfies these properties can be expressed in terms of a Slater determinant corresponding to an oblate shape:

$$\psi = \text{Det}[\phi^P(j, j) \phi^P(j, -j) \phi^N(k, -k) \phi^N(k, -k) \phi^{\bar{P}}(\bar{j}, 1/2) \phi^{\bar{P}}(\bar{j}, -1/2)]$$

and another with a prolate shape:

$$\psi' = \text{Det}[\phi^P(j, 1/2) \phi^P(j, -1/2) \phi^N(k, 1/2) \phi^N(k, -1/2) \phi^{\bar{P}}(j, \bar{j}) \phi^{\bar{P}}(\bar{j}, -\bar{j})]$$

In  $^{58}\text{Ni}$ , Jaffrin has shown, using a phenomenological force (which has a Gaussian radial dependence, spin and isospin admixture parameters

determined from 1qp and 2qp calculations in the Ni-region) that the prolate shape is more strongly bound than the oblate one.

In the nickel region, the calculations have been performed with all the prolate 4p-2h configurations constructed with  $j$  and  $k$  for any of the  $2p_{3/2}$ ,  $1f_{5/2}$  and  $2p_{1/2}$  orbits and  $\bar{j}$  restricted to the  $1f_{7/2}$  orbit. The  $\psi$ -wave-functions do not have a good angular momentum. Thus it was necessary to project each configuration on the space of angular momentum  $I$  before diagonalizing the residual interaction.

The results of the calculations are presented in Fig. 24. The dashed lines correspond to two-neutron configurations and the solid lines indicate 4p-2h states; they are grouped into "quasi-rotational bands". A "band" is a group of levels in which the wave-functions are dominated by the same configuration. In each band the states have the spin sequence  $0^+$ ,  $2^+$ ,  $4^+$  but their energies do not satisfy the  $J(J+1)$  law because of the relatively small intrinsic angular momentum  $j$  and the small number of nucleons involved in each configuration.

Similar calculations were performed for  $^{60}\text{Ni}$  and  $^{62}\text{Zn}$ . In  $^{60}\text{Ni}$  the two extra neutrons were regarded as "spectators". For  $^{62}\text{Zn}$ , the wave-function was constructed with two protons and four neutrons aligned. In  $^{58}\text{Ni}$  and  $^{60}\text{Ni}$  the 4p-2h states are competitive in energy with two neutron configurations. In the case of  $^{62}\text{Zn}$ , the ground state and first excited states could be the first members of the "band" dominated by the following configuration  $(2p_{3/2})^{2p} - (2p_{3/2})^{4n}$ . At this stage it would be difficult to identify the other states as definite members of the "bands".

## 5. SUMMARY

Alpha transfer experiments on medium-mass nuclei with the ( $^{16}\text{O}$ ,  $^{12}\text{C}$ ) reaction provide a powerful tool for investigating four-nucleon correlations in these nuclei. In a similar way, the ( $^{16}\text{O}$ ,  $^{14}\text{C}$ ) reactions provide a spectroscopic tool for studying two-proton correlations in nuclei. This reaction is in many respects more convenient to perform than the ( $^3\text{He}$ , n) reaction.

Although more investigations into the reaction mechanism are required to explain the heavy-ion experiments, the selectivity of the reactions studied, the energy independence of this selectivity and the angular distributions show that these reactions proceed via a direct process in the vicinity of the Coulomb barrier.

The most striking features of the ( $^{16}\text{O}$ ,  $^{12}\text{C}$ ) spectra between  $^{40}\text{Ca}$  and  $^{64}\text{Ni}$  can be summarized as follows:

In the close vicinity of  $N = Z$ -doubly-closed-shell nuclei, such as  $^{40}\text{Ca}$  and  $^{56}\text{Ni}$ , alpha transfer is allowed for the first ground-state band.

For all other targets with a neutron excess, the cross-sections of the excited states below 4 MeV are weak. Moreover, the intensity of the cross-sections of these states decreases as the number of neutrons of the target increases. This clearly establishes the excess-neutron pair-blocking effect.

The complete pattern observed in  $^{52,54}\text{Cr}$  and  $^{58,60}\text{Ni}$  residual nuclei is shifted by about 4 MeV when the  $1f_{7/2}$  shell is filled with both protons and neutrons.

The very different selectivity of the  $\alpha$ - and two-proton transfer reactions leading to the same residual nuclei  $^{46}_{22}\text{Ti}_{24}$  and  $^{52}_{24}\text{Cr}_{28}$  gives us a good discrimination between two- and four-nucleon configuration states.

### ACKNOWLEDGEMENTS

The author wishes to thank Dr. G. Ripka for valuable discussions and Dr. M. C. Mermaz for his fruitful collaboration in all phases of this work. For helpful collaboration and many comments sincere thanks are also due to Dr. H. Faraggi and my colleagues J. C. Faivre, J. Gastebois, B. G. Harvey, J. M. Loiseaux and A. Papineau. I am also very grateful to Dr. V. Gillet and A. Jaffrin for their guidance and continued interest in this work.

### REFERENCES

- [1] GREEN, A.M., Rep. Progr. Physics 28 (1965) 113 and Ref.[4].
- [2] CARTER, E.B., MITCHELL, G.E., DAVIS, R.H., Phys. Rev. 133 (1964) B 1421.
- [3] MORINAGA, H., Phys. Rev. 101 (1956) 254.
- [4] BROWN, G.E., GREEN, A.M., Nucl. Phys. 75 (1966) 40, Nucl. Phys. 85 (1966) 87.
- [5] BASSICHIS, W.H., RIPKA, G., Physics Letts 15 (1965) 320.
- [6] ZUKER, A.P., BUCK, B., McGRORY, J.B., Phys. Rev. Letts 21 (1968) 39.
- [7] BRINK, D.M., FIEDRICH, H., WEINGUNY, A., WONG, C.W., Physics Letts 33B (1970) 143 and private communication.
- [8] BOUTEN, M., (private communication).
- [9] DANOS, M., GILLET, V., Phys. Rev. 161 (1967) 1034.
- [10] JAFFRIN, A., "Proceedings of the International Conference on Properties of Nuclear States", Montreal (1969) 338, 340.
- [11] AUERBACH, N., Phys. Rev. 163 (1967) 1203.  
COHEN, S., LAWSON, R.D., MacFARLANE, M.M., PANDYA, S.P., SOGA, M., Phys. Rev. 160 (1967) 903.
- [12] HIEBERT, J.C., NEWMAN, E., BASSEL, R.H., Physics Letts 15 (1965) 160.
- [13] WONG, S.S.M., DAVIS, W.G., Physics Letts 77 (1968) 77.
- [14] JAFFRIN, A., Physics Letts 32B (1970) 448.
- [15] Nuclear reactions induced by heavy ions (Heidelberg International Conference, 1969) OGLOBIN, A.A., 231, MIDDLETON, R., 263, BETHGE, K., 277, COTTON, E., 289.
- [16] VON OERTZEN, W., these Proceedings.
- [17] BASSANI, G., SAUNIER, N., TRAORE, B.M., PAPPALARDO, G., Physics Letts (to be published).
- [18] ROYNETTE, J.C., Nucl. Phys. A155 (1970) 548.
- [19] Nuclear Data Sheets, Section B vol.4 (1970), Section B vol.3 (1970).
- [20] QUEBERT, J., (private communication).
- [21] DODD, L.R., GREIDER, K.R., Phys. Rev. Letts 14 (1965) 959.
- [22] GRAUD, B., BONCHE, P., in Nuclear Physics Problems, (Proc. 2nd Symp. 12-19 June 1970, Novosibirsk) (to be published).
- [23] FAIVRE, J.C., FARAGGI, H., GASTEBOIS, J., HARVEY, B.G., LEMAIRE, M.C., LOISEAUX, J.M., MERMAZ, M.C., PAPINEAU, A., Phys. Rev. Letts 24 (1970) 1188.
- [24] FARAGGI, H., JAFFRIN, A., LEMAIRE, M.C., MERMAZ, M.C., FAIVRE, J.C., GASTEBOIS, J., HARVEY, B.G., LOISEAUX, J.M., PAPINEAU, A., de-SHALIT Memorial Book, Annals of Physics (to be published).



## **PART I: NUCLEAR REACTIONS**

### **2. Low-energy nuclear reactions**



# SPIN-ORBIT INTERACTION IN INELASTIC NUCLEON SCATTERING

J. RAYNAL

Service de physique théorique,  
Centre d'études nucléaires, Saclay,  
Gif-sur-Yvette, France

## Abstract

SPIN-ORBIT INTERACTION IN INELASTIC NUCLEON SCATTERING.

1. Introduction; 1.1. Polarization measurements; 1.2. Inelastic scattering; 1.3. Macroscopic models; 1.4. Microscopic models; 2. Macroscopic description; 2.1. The rotational model; 2.2. Deformed  $\vec{L} \cdot \vec{S}$  coupling; 2.3. E.C.I.S.; 2.4. Results; 3. Microscopic description; 3.1. The helicity formalism; 3.2. Application to nuclear reactions; 3.3. Two-body spin-orbit interaction; 3.4. Shell effects; 3.5. Results; 4. Conclusion.

## 1. INTRODUCTION

$\vec{L} \cdot \vec{S}$  coupling was introduced into the optical model in order to describe the polarization phenomena in the elastic scattering of particles with spin. Its need was obvious even when no precise polarization measurement had yet been performed. At first one used an  $\vec{L} \cdot \vec{S}$  potential of which the form factor was deduced from the central one as shown by the formulae obtained when the small components are eliminated from Dirac's equation. The strength of this potential was obtained phenomenologically; it is of opposite sign and far larger than the one obtained from Dirac's equation.

### 1.1. Polarization measurements

We have only in mind some particular polarization measurements, the ones for which it was decided, at the Symposium of Madison [1] to use the words of "analysing-power" measurement or "efficiency tensor". The word polarization has a general meaning and the particular one of describing the outgoing particle. The effects of the polarization of the ingoing particle on the cross-section are these "analysing powers" (of the polarization of the ingoing particle). In spite of the Madison convention, we shall use for "efficiency tensors" the name of "asymmetries" which was used in the publication of almost all the experimental results.

Let us consider only spin-1/2 particles. In the earliest experiments, a beam polarized by a first reaction is sent on a target. The polarization  $p$  is transverse. The cross-section of a second reaction is given by

$$\frac{d\sigma(\theta, \varphi)}{d\Omega} = \left[ \frac{d\sigma(\theta, \varphi)}{d\Omega} \right]_{n,p} (1 + pA(\theta) \cos \varphi)$$

where  $\varphi$  is the angle between the reaction plane and the plane orthogonal to the polarization. The "asymmetry" measurement

$$A(\theta) = \frac{1}{p} \frac{\frac{d\sigma(\theta, 0)}{d\Omega} - \frac{d\sigma(\theta, \pi)}{d\Omega}}{\frac{d\sigma(\theta, 0)}{d\Omega} + \frac{d\sigma(\theta, \pi)}{d\Omega}}$$

needs the use of two detectors, symmetric with respect to the direction of the beam. Geometrical errors are important limitations of the precision of these experiments.

These geometrical errors were eliminated when polarized beams became available. The particles are polarized before acceleration [2-4] upward or downward. The absolute value of the polarization of the beam and its intensity are independent of the sign of the polarization (anyway, these quantities are monitored by a known reaction during the experiment). If  $[\frac{d\sigma(\theta)}{d\Omega}]_+$  is the cross-section given by a detector in the plane orthogonal to the polarization, while the polarization is positive and  $[\frac{d\sigma(\theta)}{d\Omega}]_-$  is the cross-section given by the same detector when the polarization is negative, we obtain

$$A(\theta) = \frac{1}{P} \frac{\left[ \frac{d\sigma(\theta)}{d\Omega} \right]_+ - \left[ \frac{d\sigma(\theta)}{d\Omega} \right]_-}{\left[ \frac{d\sigma(\theta)}{d\Omega} \right]_+ + \left[ \frac{d\sigma(\theta)}{d\Omega} \right]_-}$$

The sign of the polarization is changed several times a second and  $p$  can be greater than 80%. By this method the asymmetries can be measured with the precision usual for cross-section measurements.

For elastic scattering, the polarization measurements with polarized beams have shown that the  $\vec{L} \cdot \vec{S}$  potential must be used with a radius and a diffuseness smaller than the ones of the central potential.

## 1.2. Inelastic scattering

The outgoing particles go through two junctions, one thin and the other sufficiently thick to stop it; the detector, which consists in these two junctions, identifies the particle as a proton and measures its energy. A spectrum is obtained for each sign of the polarization; their comparison gives at the same time the polarization of the elastic scattering and the analysing power of each reaction which can be seen.

One of the earliest experiments of this kind was performed with the cyclotron of Saclay at the end of 1965 on  $^{54}\text{Fe}$  at 18.6 MeV [5]. This energy was chosen because the cross-section was already measured with precision [6]. Large values were obtained for the first  $2^+$  at 1.41 MeV (see Fig. 4). A second  $2^+$  has similar angular distribution but smaller values, chiefly forwards. Results for  $^{56}\text{Fe}$  are intermediate.

Measurements done with targets ranging from Ti to Sn were classified by the experimentalists into two groups:

- (a) "large asymmetries" which are the first  $2^+$  of  $^{54}\text{Fe}$ ,  $^{52}\text{Cr}$ ,  $^{50}\text{Ti}$ ,  $^{92}\text{Mo}$ ,  $^{90}\text{Zr}$  and  $^{88}\text{Sr}$ ;
- (b) "small asymmetries" as the second  $2^+$  of  $^{54}\text{Fe}$  and  $^{52}\text{Cr}$  and the first  $2^+$  of  $^{58}\text{Ni}$ ,  $^{60}\text{Ni}$ ,  $^{62}\text{Ni}$ ,  $^{64}\text{Ni}$ . In this group there are also  $^{56}\text{Fe}$ ,  $^{92}\text{Zr}$ ,  $^{94}\text{Mo}$  of which the values are somewhat larger.

Note that the nuclei of which the first  $2^+$  shows a large asymmetry have 28 or 50 neutrons and an open shell of protons. Small asymmetries are obtained for nuclei with an open shell of neutrons. The division into

two groups was essentially due to the difficulties encountered when trying to explain the experimental results of the first group [7, 8].

There are also some difficulties to explain the  $3^-$  and  $4^+$  results, but less than for the  $2^+$ . Generally, they are some details of the form. Some other targets have also been used and have shown their own problems: for example, targets of the s-d shell with  $^{20}\text{Ne}$ ,  $^{22}\text{Ne}$ ,  $^{24}\text{Mg}$ ,  $^{26}\text{Mg}$ ,  $^{28}\text{Si}$  etc. [7].

Thus we have experimental results related to the nuclear structure of the target and of which the mechanism must be understood.

### 1.3. Macroscopic models

The optical model obtained for elastic scattering is also used to study the reactions in coupled-channel [9] or DWBA calculations. The  $\bar{L}, \bar{S}$  potential is used to describe the ingoing and the outgoing waves.

In the rotational model, a deformed optical model describes all the states of the target; in the earliest calculations, only the central potential was deformed, the imaginary and  $\bar{L}, \bar{S}$  potentials were included only into the diagonal couplings. Later on, the imaginary potential was also deformed in order to obtain better fits for the inelastic cross-sections. When precise polarization measurements became available for these reactions, the deformation of  $\bar{L}, \bar{S}$  coupling seemed necessary. At first, the simple expression of the optical model was used, in its Hermitian form. The results were frustrating for the large asymmetries. This method is not valid because [10]:

- (a) The obtained expression is not a vector;
- (b) from the macroscopic point of view, the analogy with the elimination of small components of Dirac's equation does not remain;
- (c) from the microscopic point of view, it is very different from a nucleon-nucleon  $\bar{L}, \bar{S}$  interaction.

Sherif and Blair [11,12] proposed to maintain the analogy with Dirac's equation. The expression they must use is more complicated than the preceding one. Nevertheless, a sufficiently simple form can be obtained, which can be used in coupled-channel calculations and allows some discussion of the results. The good fits obtained in DWBA [11-14] are found also in coupled-channel calculations and generalized to some cases out of the scope of DWBA as the  $0^-$ -  $2^+$ -  $4^+$  excitations of the s-d shell. These improvements are chiefly forwards, in an angular region which decreases when the incident energy and the mass of the target increase. They are coherent effects. In the other angular regions, it was never very difficult to obtain a fit.

In these calculations, the  $\bar{L}, \bar{S}$  potential must be often more deformed than the central one. If this multiplying factor were always the same, it could be considered to be a phenomenological result. But this factor which is 1.5 in almost all the calculations of Blair and Sherif, must be increased up to 2.5 or 3 for  $^{90}\text{Zr}$  and decreased to 0 for the second  $2^+$  of  $^{54}\text{Fe}$ . Thus, we found an effect which is strongly dependent upon the structure of the target.

### 1.4. Microscopic models

The reaction can be studied with a more detailed description of the initial and the final states of the target and a nucleon-nucleon interaction.

With a zero-range nucleon-nucleon interaction or no antisymmetrization of the incident nucleon with those of the target, the description of the reaction is very similar to the macroscopic models. Coupled channels can be used. With antisymmetrization, the computations are heavier and we shall use only DWBA.

The helicity-formalism [15] gives a form somewhat easy to handle for the nucleon-nucleon  $\vec{L} \cdot \vec{S}$  interaction [16]. As the  $\vec{L} \cdot \vec{S}$  interaction is known to have a smaller range than the central interaction [17, 18], the zero-range limit can be used. In this limit, the  $\vec{L} \cdot \vec{S}$  interaction acts only for a relative angular momentum of the two nucleons  $l=1$ ; as  $S$  is necessarily 1,  $T$  must be 1, too. So, this interaction is twice stronger between two protons than between a proton and a neutron. Furthermore, it is strongly dependent upon the quantum numbers of the nucleons of the target. When all the terms without macroscopic equivalents are neglected in the expression obtained at the zero-range limit, and when the remaining part is made Hermitian, an expression very similar to the one of the macroscopic description is obtained. This approximation is macroscopic as long as the excitation of the target can be described as a coherent sum of many particle-hole excitations; it is also a high-energy approximation as long as the values of the quantum numbers of the bound nucleons can be neglected compared to the ones of the free nucleon.

In these conditions, one can understand why the deformation of the  $\vec{L} \cdot \vec{S}$  potential used by Blair and Sherif must be increased or not, according to the structure of the excited state and also why the experimental results are more difficult to fit at low energy than at high energy. Good fits are more usual at 150 MeV than at 20 MeV.

From now on, we shall consider only diffusion of spin-1/2 particles. Formulae are not always valid for larger spins.

## 2. MACROSCOPIC DESCRIPTION

By macroscopic description, we mean a description of the target nucleus in which the individual orbits of nucleons do not matter. The target is known by a mass density  $\rho(\vec{r})$ . With a zero-range nucleon-nucleon interaction, a potential  $V(\vec{r})$  which is proportional to it is obtained. With a finite-range interaction and without antisymmetrization, a potential is obtained by a convolution with  $\rho(\vec{r})$ ; its form is quite the same.

The macroscopic models [9] are the rotational and the vibrational models. We shall take the rotational model as an example; we shall remember briefly how a coupled-channel calculation occurs for this model and then show how to introduce the deformed  $\vec{L} \cdot \vec{S}$  coupling and discuss its effects.

### 2.1. The rotational model

The interaction between the particle and the target is some potential  $V(\vec{r}, \hat{r}')$  where  $\hat{r}'$  is the intrinsic axis of the nucleus. This potential is parametrized by quadrupole and hexadecupole deformations  $\beta_2$  and  $\beta_4$ , using a radius  $R(\theta)$

$$R(\theta) = R_0(1 + \beta_2 Y_2^0(\theta) + \beta_4 Y_4^0(\theta)) \quad (1)$$

where  $\theta$  is the angle between  $\vec{r}$  and  $\vec{r}'$ . This radius is used instead of  $R_0$  in the usual expressions of the optical model. The potential can be expanded into multipoles:

$$V(\vec{r}, \hat{r}') = 4\pi \sum_{\lambda} V_{\lambda}(r) Y_{\lambda}^{\mu}(\hat{r}) Y_{\lambda}^{\mu*}(\hat{r}') \quad (2)$$

There are only even values of  $\lambda$ . A state of the target, member of a rotational spectrum starting with a  $0^+$ , is described by [19]

$$|\psi_{I,M}\rangle = \sqrt{\frac{2I+1}{8\pi^2}} R_{M0}^{(I)*}(\Omega) \chi(r')$$

where  $\chi(r')$  is the intrinsic wave-function. The nuclear part of the problem is eliminated by

$$\begin{aligned} \langle \psi_{I_f, M_f} | V(\vec{r}, \hat{r}') | \psi_{I_i, M_i} \rangle &= \sqrt{4\pi} \sum_{\lambda} V_{\lambda}(r) Y_{\lambda}^{\mu}(\hat{r}) \\ &\times (-)^{M_i} \sqrt{(2I_i+1)(2I_f+1)(2\lambda+1)} \begin{pmatrix} I_i & I_f & \lambda \\ 0 & 0 & 0 \end{pmatrix} \begin{pmatrix} I_f & I_i & \lambda \\ M_f & -M_i & \mu \end{pmatrix} \end{aligned} \quad (3)$$

The potential between an ingoing wave  $|\psi_{I_i M_i}\rangle | \ell_i j_i m_i \rangle$  coupled to  $J, M$  and an outgoing wave  $|\psi_{I_f M_f}\rangle | \ell_f j_f m_f \rangle$  also coupled to  $J$  and  $M$ , is

$$\begin{aligned} \sum_{\lambda} V_{\lambda}(r) (-)^{J+\lambda-\frac{1}{2}} (2\lambda+1) \sqrt{(2I_i+1)(2I_f+1)(2j_f+1)(2j_i+1)} \\ \times \begin{pmatrix} I_i & I_f & \lambda \\ 0 & 0 & 0 \end{pmatrix} \begin{pmatrix} j_f & \lambda & j_i \\ -\frac{1}{2} & 0 & \frac{1}{2} \end{pmatrix} \begin{Bmatrix} I_i & I_f & \lambda \\ j_f & j_i & J \end{Bmatrix} \end{aligned} \quad (4)$$

This expression has a part which depends only upon the target and a part which depends only upon the nucleon, the two of them related by a 6j-coefficient. When  $I_i$  is 0, this coupling is only:

$$(-)^{j_f+I_f+\frac{1}{2}} V_{I_f}(r) \sqrt{(2I_f+1)(2j_f+1)} \begin{pmatrix} j_f & I_f & j_i \\ -\frac{1}{2} & 0 & \frac{1}{2} \end{pmatrix} \quad (5)$$

For a  $0^+ \rightarrow 2^+$  excitation and for an ingoing wave of given  $\ell_i, j_i$ , the total spin  $J$  of the system is  $j_i$  and its parity  $\pi = (-)^{\ell_i}$ . For a sufficiently large  $J$  and a given  $\pi$  there are five outgoing waves  $\ell_f, j_f$ ;  $j_f$  ranges from  $j_i - 2$  to  $j_i + 2$  and  $\ell_f$  is the value  $j_f \pm \frac{1}{2}$  of parity  $\pi$  (see Table I). A set of six coupled equations is obtained; it is

$$y_i'' + \sum_j V_{ij} y_j = E_i y_i \quad (6)$$

TABLE I. QUANTUM NUMBERS AND GEOMETRY FOR A  $0^+ \rightarrow 2^+$  REACTION

$j_i$	$j_f$	$\ell_f$	$\gamma_i$	$\gamma_f$	$\gamma_i + \gamma_f$	$\gamma_i - \gamma_f$	$6 - (\gamma_i - \gamma_f)(\gamma_i - \gamma_f + 1)$	$G_{j_i j_f}^2$	
$\ell + 1/2$	$\ell + 5/2$	$\ell + 2$	$\ell$	$\ell + 2$	$2\ell + 2$	$-2$	$4$	$-\sqrt{\frac{3(\ell+1)(\ell+2)(\ell+3)}{(2\ell+3)(2\ell+5)}}$	$-\sqrt{\frac{3\ell}{4}}$
"	$\ell + 3/2$	"	"	$-\ell - 3$	$-3$	$2\ell + 3$	$-4\ell^2 - 14\ell - 6$	$\sqrt{\frac{6(\ell+1)(\ell+2)}{(2\ell+1)(2\ell+3)(2\ell+5)}}$	$\sqrt{\frac{3}{4\ell}}$
"	$\ell + 1/2$	$\ell$	"	$\ell$	$2\ell$	$0$	$6$	$\sqrt{\frac{2\ell(\ell+1)(\ell+2)}{(2\ell+1)(2\ell+3)}}$	$\sqrt{\frac{\ell}{2}}$
"	$\ell - 1/2$	"	"	$-\ell - 1$	$-1$	$2\ell + 1$	$-4\ell^2 - 6\ell + 4$	$-\sqrt{\frac{6\ell(\ell+1)}{(2\ell-1)(2\ell+1)(2\ell+3)}}$	$-\sqrt{\frac{3}{4\ell}}$
"	$\ell - 3/2$	$\ell - 2$	"	$\ell - 2$	$2\ell - 2$	$2$	$0$	$-\sqrt{\frac{3\ell(\ell+1)(\ell-1)}{(2\ell+1)(2\ell-1)}}$	$-\sqrt{\frac{3\ell}{4}}$
$\ell - 1/2$	$\ell + 3/2$	$\ell + 2$	$-\ell - 1$	$-\ell - 3$	$-2\ell - 4$	$2$	$0$	$-\sqrt{\frac{3\ell(\ell+1)(\ell+2)}{(2\ell+1)(2\ell-1)}}$	$-\sqrt{\frac{3\ell}{4}}$
"	$\ell + 1/2$	$\ell$	"	$\ell$	$-1$	$-2\ell - 1$	$-4\ell^2 - 2\ell + 6$	$\sqrt{\frac{6\ell(\ell+1)}{(2\ell-1)(2\ell+1)(2\ell+3)}}$	$\sqrt{\frac{3}{4\ell}}$
"	$\ell - 1/2$	"	"	$-\ell - 1$	$-2\ell - 2$	$0$	$6$	$\sqrt{\frac{2\ell(\ell-1)(\ell+1)}{(2\ell-1)(2\ell+1)}}$	$\sqrt{\frac{\ell}{2}}$
"	$\ell - 3/2$	$\ell - 2$	"	$\ell - 2$	$-3$	$-2\ell + 1$	$-4\ell^2 + 6\ell + 4$	$-\sqrt{\frac{6\ell(\ell-1)}{(2\ell-3)(2\ell-1)(2\ell+1)}}$	$-\sqrt{\frac{3}{4\ell}}$
"	$\ell - 5/2$	"	"	$-\ell + 1$	$-2\ell$	$-2$	$4$	$-\sqrt{\frac{3\ell(\ell-1)(\ell-2)}{(2\ell-1)(2\ell-3)}}$	$-\sqrt{\frac{3\ell}{4}}$

where

$$V_{ij} = \sum_{\lambda} \tilde{G}_{ij}^{-\lambda} V_{\lambda}(r) \quad (7)$$

Let us denote the ingoing partial wave by the index  $i = 0$  and the outgoing ones by  $i = 1$  to 5. The interaction  $V_{00}$  includes only the multipole  $\lambda = 0$ , which is an optical potential. The  $V_{0i}$  and  $V_{i0}$  for  $i \neq 0$  include only  $\lambda = 2$ . The  $V_{ij}$  for  $i \neq 0$  and  $j \neq 0$  include the optical potential and the multipoles  $\lambda = 2$  and  $\lambda = 4$  (it is the mean difference with the vibrational model in which  $V_{ij}$  is usually diagonal); the optical model is diagonal, the multipole  $\lambda = 2$  is there only when the difference between the  $j_f$  is not greater than 2 and the multipole  $\lambda = 4$  is always there. The set (6) must be solved numerically in order to find the solution of which  $y_0$  is a plane wave plus an outgoing wave and the  $y_i$  are pure outgoing waves at large distances. The coefficients of the outgoing waves are used to compute reaction amplitudes, cross-sections and asymmetries.

This set of equations can be solved to the first order for the multipoles  $V_{\lambda}(r)$ . This approximation is called DWBA and uses the coupling (7) only between the  $0^+$  and the  $2^+$  states. The geometrical coefficient  $\tilde{G}_{ij}^{-\lambda}$  is almost the one which will be called  $G_{ij}^2$  in the helicity formalism and of which the values are given in Table I.

## 2.2. Deformed $\vec{L} \cdot \vec{S}$ coupling

The optical model includes a spin-orbit potential

$$\frac{1}{r} \frac{d}{dr} \{V(r)\} (\vec{L} \cdot \vec{\sigma}) \quad (8)$$

where  $V(r)$  is a potential of which the form factor is similar to the one of the real potential. For a state of a given parity and angular momentum, the operator  $(\vec{L} \cdot \vec{\sigma})$  has the eigenvalue which we shall denote by  $\gamma$ :

$$\text{if } j = \ell + \frac{1}{2} \quad \gamma = \ell$$

$$\text{if } j = \ell - \frac{1}{2} \quad \gamma = -\ell - 1$$

### 2.2.a. Incomplete Thomas term

If the potential (8) is not isotropic but has some angular dependence which can be described by expression (2), it can be expanded into multipoles

$$4\pi \sum_{\lambda} \frac{1}{r} \frac{d}{dr} \{V_{\lambda}(r)\} Y_{\lambda}^{\mu}(\hat{r}) Y_{\lambda}^{\mu*}(\hat{r}')$$

Some versions of this operation [20] were tried, without noticeable results. The elimination of the nuclear part of the problem leads to the same result as Eq.(3). In the following step,  $(\vec{L} \cdot \vec{\sigma})$  obtains its eigenvalue  $\gamma_i$  and the total result is not Hermitian.

To avoid this difficulty, one can use the well-known recipe which is to write it as follows:

$$\frac{1}{2} \left[ \frac{1}{r} \frac{d}{dr} \{V(\vec{r})\} (\vec{L} \cdot \vec{\sigma}) + (\vec{L} \cdot \vec{\sigma}) \frac{1}{r} \frac{d}{dr} \{V(\vec{r})\} \right]$$

Then, the coupling becomes

$$\tilde{G}_{if}^{\lambda} \frac{1}{r} \frac{d}{dr} \{V_{\lambda}(r)\} \frac{\gamma_i + \gamma_f}{2} \quad (9)$$

This term has been largely used. It is often called Oak-Ridge term. It is included in Tamura's and Hill's codes.

### 2.2. b. Full Thomas term

It is the term used by Blair and Sherif in DWBA computations:

$$\nabla \{V(\vec{r})\} \times \frac{\nabla}{i} \cdot \vec{\sigma} \quad (10)$$

Substituting the gradient by its expression:

$$\nabla = \frac{\vec{r}}{r} \frac{d}{dr} - i \frac{1}{r^2} \vec{r} \times \vec{L} \quad (11)$$

expression (8) is obtained when  $V(\vec{r})$  is isotropic. By elementary manipulations, the term (10) can be changed into a form similar to (9), i.e. the geometry of a central interaction can be factorized. To show that, let us consider a single multipole of  $V(\vec{r})$  and use the formula:

$$(\vec{\sigma} \cdot \vec{A}) \cdot (\vec{\sigma} \cdot \vec{B}) = (\vec{A} \cdot \vec{B}) + i(\vec{\sigma} \cdot \vec{A} \times \vec{B})$$

so that we obtain

$$\nabla \{V_{\lambda}(r) Y_{\lambda}^{\mu}(\hat{r})\} \times \frac{\nabla}{i} \cdot \vec{\sigma} = - (\vec{\sigma} \cdot \nabla \{V_{\lambda}(r) Y_{\lambda}^{\mu}(\hat{r})\}) (\vec{\sigma} \cdot \nabla) + \nabla \{V_{\lambda}(r) Y_{\lambda}^{\mu}(r)\} \cdot \nabla$$

Again with the same formula and expression (11) for the gradient, we get:

$$(\vec{\sigma} \cdot \nabla) = \frac{(\vec{\sigma} \cdot \vec{r})}{r} \frac{1}{dr} - i \frac{1}{r^2} \vec{\sigma} \cdot (\vec{r} \times \vec{L}) = \frac{(\vec{\sigma} \cdot \vec{r})}{r} \left\{ \frac{d}{dr} - \frac{1}{r} (\vec{L} \cdot \vec{\sigma}) \right\}$$

As  $(\vec{L} \cdot \vec{\sigma})$  anticommutes with  $(\vec{\sigma} \cdot \vec{r})$  and  $(\vec{\sigma} \cdot \vec{r})^2 = r^2$ , we have

$$\begin{aligned} \vec{\nabla} \{V_{\lambda}(r) Y_{\lambda}^{\mu}(\hat{r})\} \times \frac{\vec{\nabla}}{i} \cdot \vec{\sigma} &= - \left( \frac{d}{dr} + \frac{1}{r} \vec{L} \cdot \vec{\sigma} \right) \{V_{\lambda}(r) Y_{\lambda}^{\mu}(\hat{r})\} \left( \frac{d}{dr} - \frac{1}{r} \vec{L} \cdot \vec{\sigma} \right) \\ &+ \frac{d}{dr} \left\{ V_{\lambda}(r) Y_{\lambda}^{\mu}(\hat{r}) \right\} \frac{d}{dr} - \frac{V_{\lambda}(r)}{r^2} [\vec{r} \times \vec{L} \{Y_{\lambda}^{\mu}(\hat{r})\}] \cdot \frac{1}{r^2} [\vec{r} \times \vec{L}] \end{aligned}$$

The terms with two derivatives cancel. In the last term, the first  $\vec{L}$  acts only on the spherical harmonic; it can be simplified to

$$\vec{r} \times \vec{L} \{Y_{\lambda}^{\mu}(\hat{r})\} \cdot \vec{r} \times \vec{L} = r^2 \vec{L} \{Y_{\lambda}^{\mu}(\hat{r})\} \cdot \vec{L}$$

There remains

$$\begin{aligned} \nabla \{V_{\lambda}(r) Y_{\lambda}^{\mu}(\hat{r})\} \times \frac{\nabla}{i} \cdot \vec{\sigma} &= \frac{1}{r} \frac{d}{dr} \{V_{\lambda}(r)\} Y_{\lambda}^{\mu}(\hat{r}) (\vec{L} \cdot \vec{\sigma}) - \frac{V_{\lambda}(r)}{r} (\vec{L} \{Y_{\lambda}^{\mu}(\hat{r})\} \cdot \vec{\sigma}) \frac{d}{dr} \\ &+ \frac{V_{\lambda}(r)}{r^2} (\vec{L} \{Y_{\lambda}^{\mu}(\hat{r})\} \cdot \vec{\sigma}) \cdot (\vec{L} \cdot \vec{\sigma}) - \frac{V_{\lambda}(r)}{r^2} (\vec{L} \{Y_{\lambda}^{\mu}(\hat{r})\} \cdot \vec{L}) \end{aligned}$$

In the first of these four terms,  $(\vec{L} \cdot \vec{\sigma})$ , being on the right-hand side obtains its eigenvalue  $\gamma_i$ . In the second term, acting only on the spherical harmonic, it gets the same value as if it were acting on the whole, minus  $\gamma_i$ ; to act on the whole means to act on the left, hence the value  $\gamma_f - \gamma_i$ . In the third term, these operators can be replaced by  $(\gamma_f - \gamma_i)\gamma_i$ . In the last term, the angular momentum operators are equivalent to the scalar product  $\vec{\lambda} \cdot \vec{\ell}_i$  which is easily evaluated with  $\vec{\ell}_f = \vec{\ell}_i + \vec{\lambda}$ . As a matter of fact, the relation

$$2\vec{\lambda} \cdot \vec{\ell}_i = \vec{\ell}_f^2 - \vec{\lambda}^2 - \vec{\ell}_i^2$$

corresponds term by term to

$$2\vec{L} \{Y_{\lambda}^{\mu}(\hat{r})\} \cdot \vec{L} = \vec{L}^2 Y_{\lambda}^{\mu}(\hat{r}) - \vec{L}^2 \{Y_{\lambda}^{\mu}(\hat{r})\} - Y_{\lambda}^{\mu}(\hat{r}) \vec{L}^2$$

Furthermore, as

$$\vec{L}^2 = (\vec{L} \cdot \vec{\sigma})^2 + (\vec{L} \cdot \vec{\sigma})$$

we have  $\vec{L}^2 = \gamma(\gamma+1)$ . Gathering all these results, we obtain

$$\begin{aligned} \nabla \{V_{\lambda}(r) Y_{\lambda}^{\mu}(\hat{r})\} \times \frac{\nabla}{i} \cdot \vec{\sigma} &= Y_{\lambda}^{\mu}(\hat{r}) \left[ \frac{1}{r} \frac{d}{dr} \{V_{\lambda}(r)\} \gamma_i + \frac{V_{\lambda}(r)}{r} (\gamma_i - \gamma_f) \frac{d}{dr} \right. \\ &\left. + \frac{V_{\lambda}(r)}{2r^2} \{\lambda(\lambda+1) - (\gamma_f - \gamma_i)(\gamma_f - \gamma_i + 1)\} \right] \end{aligned}$$

In almost all the computations, the wave-function is multiplied by  $r$ . Taking this fact into account,  $2(\gamma_f - \gamma_i)$  must be added into the parenthesis of the last term because the preceding one includes  $d/dr$ . Therefore, for this interaction we have obtained an expression which can be easily compared with expression (9) and is given by

$$\tilde{G}_{if}^{\lambda} \left\{ \frac{1}{r} \frac{d}{dr} \{V_{\lambda}(r)\} \gamma_i + \frac{V_{\lambda}(r)}{r} (\gamma_i - \gamma_f) \frac{d}{dr} + \frac{V_{\lambda}(r)}{2r^2} [\lambda(\lambda+1) - (\gamma_f - \gamma_i)(\gamma_f - \gamma_i \pm 1)] \right\} \quad (12)$$

with  $+1$  or  $-1$  when the radial wave function is not or is multiplied by  $r$ .

2.2.c. Comparison of the two deformed  $\vec{L} \cdot \vec{S}$  potentials

Table I gives the quantum numbers of the equations coupled for a  $0^+ \rightarrow 2^+$  reaction. One can note at first sight a large difference in the behaviour of potentials (9) and (12). When angular momenta are large, term (9) is predominant for  $j_i - l_i = j_f - l_f$  and increases linearly with  $\ell$ . On the contrary, the potential (12) is predominant when  $j_i - l_i \neq j_f - l_f$  and increases quadratically with  $\ell$ . However one must take into account the geometrical coefficient

$$G_{if}^\lambda = (-)^{j_i+1/2} \sqrt{(2j_i+1)(2j_f+1)} \begin{pmatrix} j_f & \lambda & j_i \\ -\frac{1}{2} & 0 & \frac{1}{2} \end{pmatrix}$$

given in the last but one column. This coefficient is larger when  $j_i - l_i = j_f - l_f$ . The asymptotic values are given in the last column.

For large values of  $\ell$  and with respect to the deformed central potential for  $j_i - l_i = j_f - l_f$  as a unit:

- the deformed central potential is of the order  $1/\ell$  when  $j_i - l_i \neq j_f - l_f$ ;
- the deformed  $\vec{L} \cdot \vec{S}$  potential (9) is of the order  $\ell$  when  $j_i - l_i = j_f - l_f$  and  $1/\ell$  in the other case;
- the deformed  $\vec{L} \cdot \vec{S}$  potential (12) is of the order  $\ell$  when  $j_i - l_i \neq j_f - l_f$  and remain constant in the other case.

The behaviour of expression (12) is a vector behaviour: the difference  $\gamma_i - \gamma_f$  is also found to be the ratio of the geometries for a transfer of spin and a scalar interaction:

$$\left\{ \begin{array}{ccc} \ell_i & \ell_f & J \\ \frac{1}{2} & \frac{1}{2} & 1 \\ j_i & j_f & J \end{array} \right\} = \frac{\gamma_i - \gamma_f}{\sqrt{3J(J+1)}} \left\{ \begin{array}{ccc} \ell_i & \ell_f & J \\ \frac{1}{2} & \frac{1}{2} & 0 \\ j_i & j_f & J \end{array} \right\}$$

However, the transfer of spin does not increase linearly with the angular momentum as the expression (12) does.

The consequences of these two deformed  $\vec{L} \cdot \vec{S}$  potentials on the reaction amplitudes will be very different, chiefly in the angular region where coherence effects can occur, that is forwards. In the first approximation these potentials act on the polarization and not on the cross-section.

In the diagonal potentials the derivative term disappears in expression (12). It remains:

$$\tilde{G}_{if}^\lambda \left[ \frac{1}{r} \frac{d}{dr} \{V_\lambda(r)\} \gamma_i + \frac{V_\lambda(r)}{2r^2} \lambda(\lambda+1) \right] \quad (13)$$

The difference between the two deformed  $\vec{L} \cdot \vec{S}$  potentials is only a constant term which vanishes when  $\lambda = 0$  (the two of them give back the  $\vec{L} \cdot \vec{S}$  potential of the optical model).

### 2.3. E. C. I. S.

The full Thomas term has been introduced into a coupled-channel code which uses the sequential iteration method [21]. The derivative term would be quite a difficulty for the usual coupled-channel codes as the most efficient numerical methods are valid only because there is no first derivative in the set of Eqs (6). Our method is to write the set of equations as follows:

$$y_0'' + (V_{00} - E_0)y_0 = - \sum_{j \neq 0} V_{0j} y_j \quad (14)$$

$$y_i'' + (V_{ii} - E_i)y_i = - \sum_{j \neq i} V_{ij} y_j \quad i \neq 0 \quad (15)$$

Equation (14) holds for the ground state and Eqs (15) for the excited states. One must find a solution which has only outgoing waves for Eqs (15). The starting point of the iterative process is  $y_i^{(0)}$ , normalized solution of Eq. (14) without second number for  $i=0$  and  $y_i^{(0)}=0$  for  $i \neq 0$ . The current equations of the iteration are

$$y_0^{(n)''} + (V_{00} - E)y_0^{(n)} = - \sum_{j \neq 0} V_{0j} y_j^{(n)}$$

$$y_i^{(n)''} + (V_{ii} - E + Q)y_i^{(n)} = - \sum_{j < i} V_{ij} y_j^{(n)} - \sum_{j > i} V_{ij} y_j^{(n-1)} - V_{0i} y_0^{(n-1)}$$

This method is a "sequential iteration" because, for any order  $n$  of iteration, the wave-functions are obtained for increasing values of index  $i$  and are used for the wave-functions of greater value of  $i$ , the value  $i=0$  being the last one. We call this method E. C. I. S.: "équations couplées en itérations séquentielles".

In the first step, one has to obtain the solutions of the equations without second member which are normalized to a plane wave plus an outgoing wave, as

$$\xi_i(r) \xrightarrow{r \rightarrow \infty} F_i + C_i^{(0)} (G_i + iF_i)$$

where  $F_i$  and  $G_i$  are the regular and irregular Coulomb functions for equation  $i$ . The starting point being  $y_0^{(0)} = \xi_0$  and  $y_i^{(0)} = 0$ , the first equation is:

$$y_1^{(1)''} + (V_{11} - E + Q)y_1^{(1)} = - V_{01} y_0^{(0)}$$

A numerical solution is  $\eta_1$ . The sought solution is

$$y_1^{(1)} = \eta_1 + \alpha \xi_1 \xrightarrow{r \rightarrow \infty} C_1^{(1)} (G_1 + iF_1)$$

The value of  $\alpha$  is the Wronskian of the solution  $\eta_1$  with  $G_1 + iF_1$  and  $C_1^{(1)}$  is the sum of  $\alpha C_1^{(0)}$  with the Wronskian of  $\eta_1$  and  $F_1$ . Then, the same method must be used to solve the equation

$$y_2^{(1)''} + (V_{22} - E + Q)y_2^{(1)} = -V_{02}y_0^{(0)} - V_{12}y_1^{(1)}$$

The end of the first iteration is the solution of

$$y_0^{(1)''} + (V_{00} - E)y_0^{(1)} = - \sum_{i \neq 0} V_{0i} y_i^{(1)}$$

but now we must add  $(1 + \alpha)\xi_0$  to the numerical solution  $\eta_0$  ( $\alpha$  being obtained in the same way as above), in order that

$$y_0^{(1)} = \eta_0 + (1 + \alpha)\xi_0 \xrightarrow{r \rightarrow \infty} F_0 + C_0^{(1)} (G_0 + iF_0)$$

The first iteration is then finished. One can now proceed to the second iteration. If the differences  $C_i^{(1)} - C_i^{(2)}$  are not small enough the iterations are followed until the differences  $C_i^{(n-1)} - C_i^{(n)}$  can be neglected for any value of  $i$ .

The convergence is faster if the energy is increased. It can be accelerated by Padé approximants. The convergence is easier when the total angular momentum increases. As the convergence test needs, at least, two iterations, one can limit them to one as soon as two of them are sufficient for the last value of the angular momentum.

The advantages of this method are:

(a) An important reduction of computation time. The time needed increases as the square of the number of equations instead of its cube. It needs more storage in the computer but this disadvantage can be limited if large steps of integration are used. For 20 MeV protons, our methods allow steps of 0.4 fermis without spoiling the results.

(b) A very convenient comparison with DWBA. One can consider results with one, two, three iterations. Furthermore, the first iteration leads to already good results for a double excitation, which cannot be studied by DWBA.

(c) It is specially fitted for the integro-differential coupled equations which are obtained with non-local potentials or a finite-range interaction with antisymmetrization.

However, for usual coupled equations, it is advantageous only when the number of equations for the ground state is small with respect to the total number of equations.

To use the full Thomas term, we only had to add the derivative term to the second member. The first derivatives of the wave-functions are obtained by a seven-point numerical derivation.

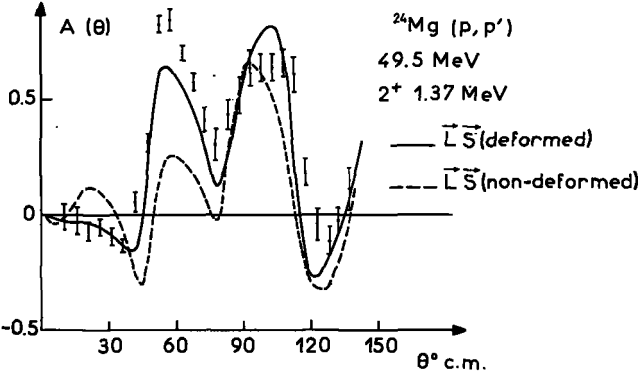


FIG.1. Coupled-channel calculations for  $^{24}\text{Mg}(p, p')$  (rot. model).

The deformed  $\vec{L} \cdot \vec{S}$  potential (12) has been parametrized as follows:

$$\begin{aligned} \tilde{G}_{if}^{\lambda} \left\{ (z_1 + z_3 \gamma_i + z_4 \gamma_f) \frac{1}{r} \frac{d}{dr} \{V_{\lambda}\} + z_6 (\gamma_i - \gamma_f) \frac{V_{\lambda}}{r} \frac{d}{dr} + \frac{V_{\lambda}}{2r^2} z_5 \right. \\ \left. \times [z_2 \lambda(\lambda+1) - (\gamma_f - \gamma_i)(\gamma_f - \gamma_i - 1)] \right\} \end{aligned} \quad (16)$$

The full Thomas term is obtained, by putting

$$z_1 = z_4 = 0 \quad z_2 = z_3 = z_5 = z_6 = 1$$

The coupling (9), is obtained by setting

$$z_1 = z_2 = z_5 = z_6 = 0 \quad z_3 = z_4 = \frac{1}{2}$$

In the rotational model, the interaction can be increased by

$$z_1 = z_4 = 0 \quad z_2 = 1 \quad z_3 = z_5 = z_6 = \lambda \quad (17)$$

which has about the same effect as the multiplication of the deformation of the  $\vec{L} \cdot \vec{S}$  potential by  $\lambda$ .

#### 2.4. Results

The first coupled-channel calculation was performed for the inelastic scattering of 49.5 MeV protons on the first  $2^+$  of  $^{24}\text{Mg}$ . These experimental results were studied with the potential (9) by Rush and Ganguly [22]. Using the DWBA parameters of these authors, Sherif [12] obtained a much better fit. With their coupled channels parameters, the solid curve of Fig. 1 is obtained. Both in coupled channels and in DWBA, the deformation of  $\vec{L} \cdot \vec{S}$  potential must be 1.5 to 2 times greater than the one of central potential in order to fit the data. We used the rotational model with  $\beta = 0.49$ .

## 2.4. a. The large asymmetries

Let us consider a parameter  $\lambda$ , the ratio of the deformation of the spin-orbit potential to that of the central potential (it is the parameter of Eq. (17)). If we assume that the deformation of the spin-orbit potential depends upon nuclear structure, the nuclear structure is parametrized by  $\lambda$ . Figure 2 shows that this parameter is about one for a nucleus with a closed shell for protons and an open shell for neutrons as  $^{62}\text{Ni}$ . However, for a nucleus with an open shell for protons as  $^{90}\text{Zr}$  (Fig. 3) or the first  $2^+$  of  $^{54}\text{Fe}$  (Fig. 4),  $\lambda$  must be of the order of 2.5 to 3. Figure 5 is the cross-section of the first  $2^+$  of  $^{54}\text{Fe}$ . For the neighbouring nuclei, with an open shell of protons and only two external neutrons, the experimental results are similar, but the amplitudes of asymmetries are smaller. So, the experimental results for  $^{92}\text{Zr}$  or  $^{56}\text{Fe}$  are fitted with the same potentials and  $\lambda = 1.5$ . On the contrary, for the second  $2^+$  of  $^{54}\text{Fe}$ ,  $\lambda$  is smaller than one (Fig. 6). The spin-orbit effects are smaller because its wave function is orthogonal to the one of the first  $2^+$ , which increases them. All these computations use the vibrational model with  $\beta = 0.1$  for  $^{90}\text{Zr}$ , 1.4 and 1.3 for the two  $2^+$  of  $^{54}\text{Fe}$ .

Figures 4 and 6 are obtained with the potential a of Table II. Figures 7 and 8 show results for the potential b given by the same authors [7]. These results are clearly worse and show the importance of the optical model.

The curves of Figs 2 to 8 could have been obtained in DWBA. However, they are more conclusive as they show that there is no special effect due to coupled channels. For  $^{62}\text{Ni}$ , the incomplete Thomas term gives exactly the same result if its deformation is multiplied by 2. For the first  $2^+$  of  $^{54}\text{Fe}$ , with the potential a and  $\lambda$  multiplied by 2, there are some differences on the first bump of the asymmetry.

In this region of intermediate mass and for this energy, from the three parts of the interaction (12), the first one is equivalent to the interaction (9), the second one doubles the effects of the first and the last one

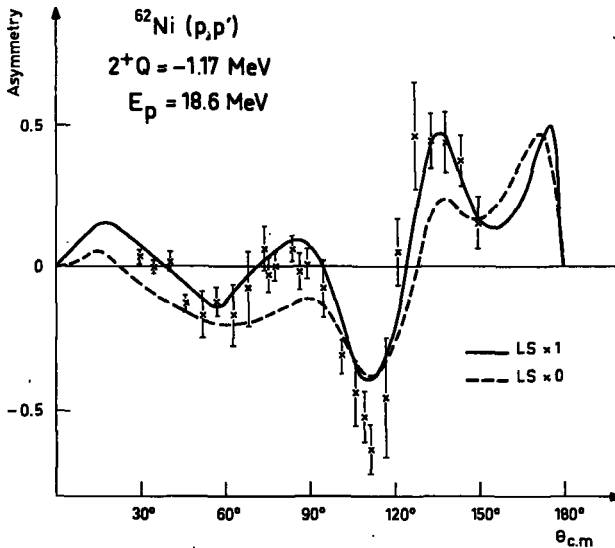


FIG. 2. Asymmetry for  $^{62}\text{Ni}(p, p')$  (vib. model).

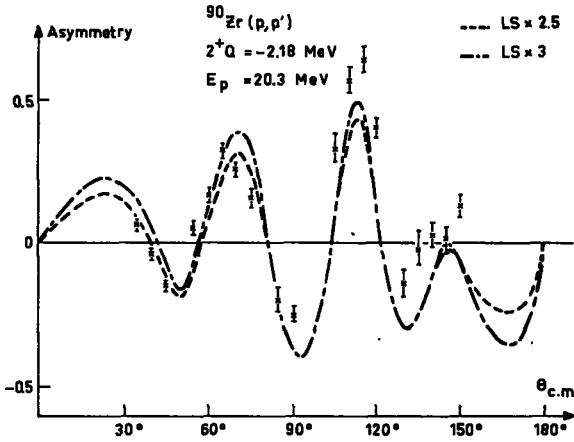
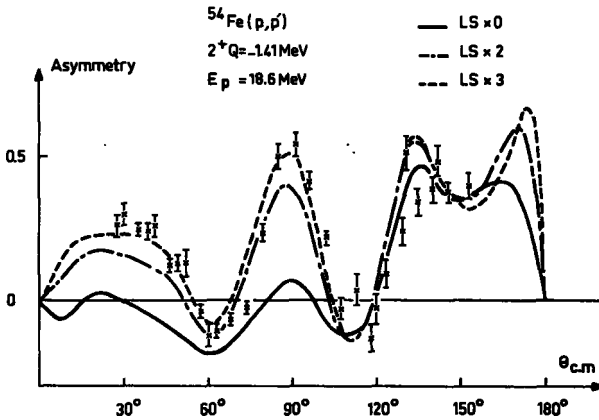
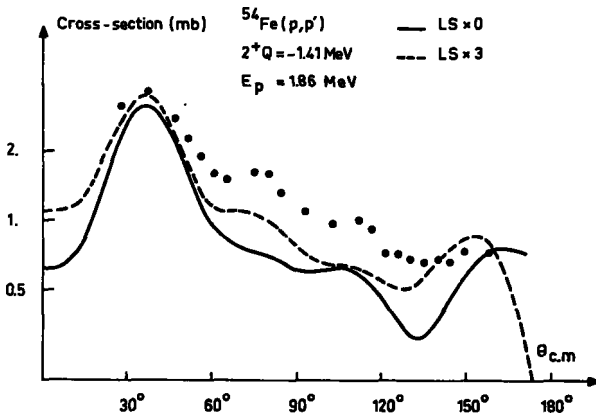
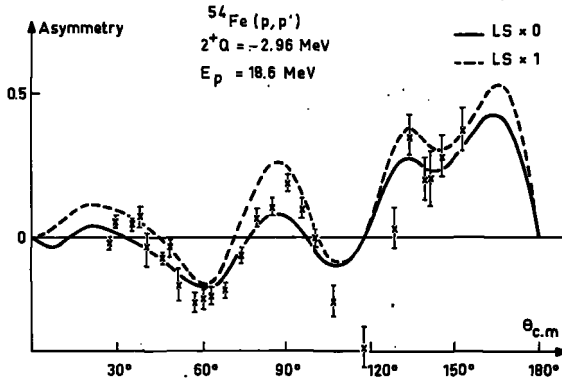
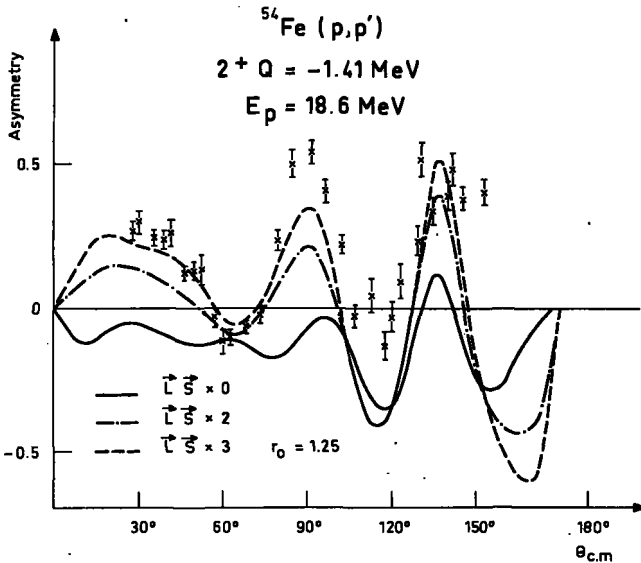
FIG. 3. Asymmetry for  $^{90}\text{Zr}(p,p')$  (vib. model).FIG. 4. Asymmetry for first  $2^+$  of  $^{54}\text{Fe}$  with potential a (vib. model).FIG. 5. Cross-section of first  $2^+$  of  $^{54}\text{Fe}$  with potential a (vib. model).

TABLE II. OPTICAL-MODEL PARAMETERS

	$r_c$	$V$	$r$	$a$	$W_V$	$r_V$	$a_V$	$W_D$	$r_D$	$a_D$	$V_{LS}$	$r_{LS}$	$a_{LS}$
$^{90}\text{Zr}$	1.25	48.2	1.238	0.618	0	0	0	8.05	1.288	0.638	5.75	1.07	0.526
$^{62}\text{Ni}$	1.10	62.07	1.100	0.75	0	0	0	9.00	1.300	0.55	7.14	0.98	0.55
$^{54}\text{Fe}$ a)	1.00	61.44	1.100	0.75	0	0	0	9.80	1.300	0.55	5.94	1.04	0.55
b)	1.25	50.5	1.25	0.65	0	0	0	11.6	1.25	0.47	5.2	1.16	0.47
$^{24}\text{Mg}$	1.1	46.1	1.09	0.67	5.52	1.4	0.35	4.11	1.40	0.35	6.47	0.96	0.58
$^{22}\text{Ne}$		57.0	1.05	0.75	0	0	0	6.3	1.33	0.55	3.95	0.88	0.31
$^{20}\text{Ne}$		59.0	1.01	0.75	0	0	0	6.5	1.26	0.55	3.97	0.90	0.33

FIG. 6. Asymmetry for second  $2^+$  of  $^{54}\text{Fe}$  with potential a (vib. model).FIG. 7. Asymmetry for first  $2^+$  of  $^{54}\text{Fe}$  with potential b (vib. model).

does not contribute.  $^{24}\text{Mg}$  at 49.5 MeV is different: all the parts are needed for a good fit and only the complete interaction (12) leads to an agreement.

#### 2.4.b. The s-d shell

The first calculations, presented in Ref. [10] and continued by Miss Lombard, concerned the experiments performed at Saclay on some nuclei of the s-d shell, with 20.3 MeV protons. These nuclei have quite large deformations and coupled channels are needed. The drawback of large deformations is the difficulty which one encounters in obtaining good optical-model parameters from elastic scattering. These parameters must be modified when used for the rotational model. So, when the fit is slightly better

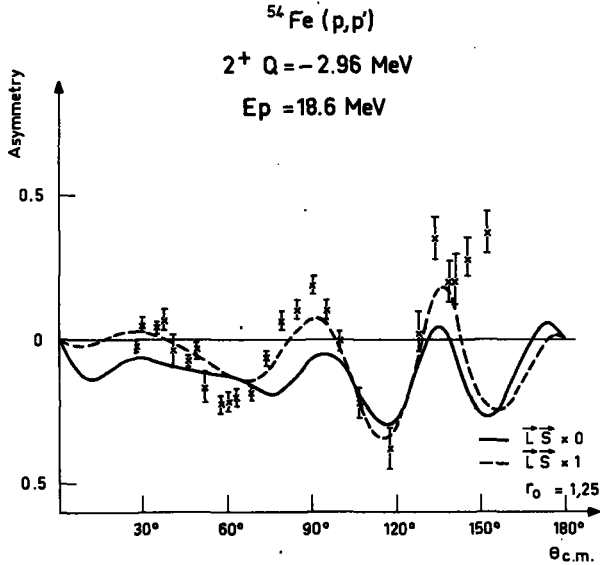


FIG. 8. Asymmetry for second  $2^+$  of  $^{54}\text{Fe}$  with potential b (vib. model).

with a negative deformation or an asymmetric one, we cannot take these conclusions about the form of the target as very sure. Nevertheless, fits obtained for  $^{26}\text{Mg}$  or  $^{28}\text{Si}$  are very good [23].

Up to now, results obtained by de Swinarsky for his experimental results  $0^+ - 2^+ - 4^+$  on  $^{20}\text{Ne}$  and  $^{22}\text{Ne}$  at 24.5 MeV are the best [24]. The data on  $^{20}\text{Ne}$  were already analysed without the full Thomas term. The cross-sections are fitted with well defined values of  $\beta_2$  and  $\beta_4$ , but the asymmetries do not agree, as shown in Fig. 9. With a spin-orbit deformation twice greater than the central one (which seems to be a general rule in the s-d shell), the asymmetries are reproduced and the calculations confirm the  $\beta_2$  and  $\beta_4$  already obtained. Data for  $^{22}\text{Ne}$  were analysed directly with interaction (12) and a good fit was obtained for cross-sections and asymmetries (Fig. 10). The results of a large  $\beta_4$  for  $^{20}\text{Ne}$  and a small one for  $^{22}\text{Ne}$  are in agreement with theoretical predictions.

### 3. MICROSCOPIC DESCRIPTION

The microscopic description takes into account each nucleon of the target. A more precise nuclear model than for the macroscopic description and a two-body interaction between the projectile and a nucleon of the target are needed. The interaction behaves as a one-body operator for the target and can be expanded into multipoles. With a complete set of creation and annihilation operators  $a_{jm}^\dagger$  and  $a_{j'm}$ , the reduced matrix elements

$$Z_{jj'}^I = \frac{1}{\sqrt{2J+1}} \langle I_i \| A_{jj'}^\dagger; j_m \| I_i \rangle \quad (18)$$

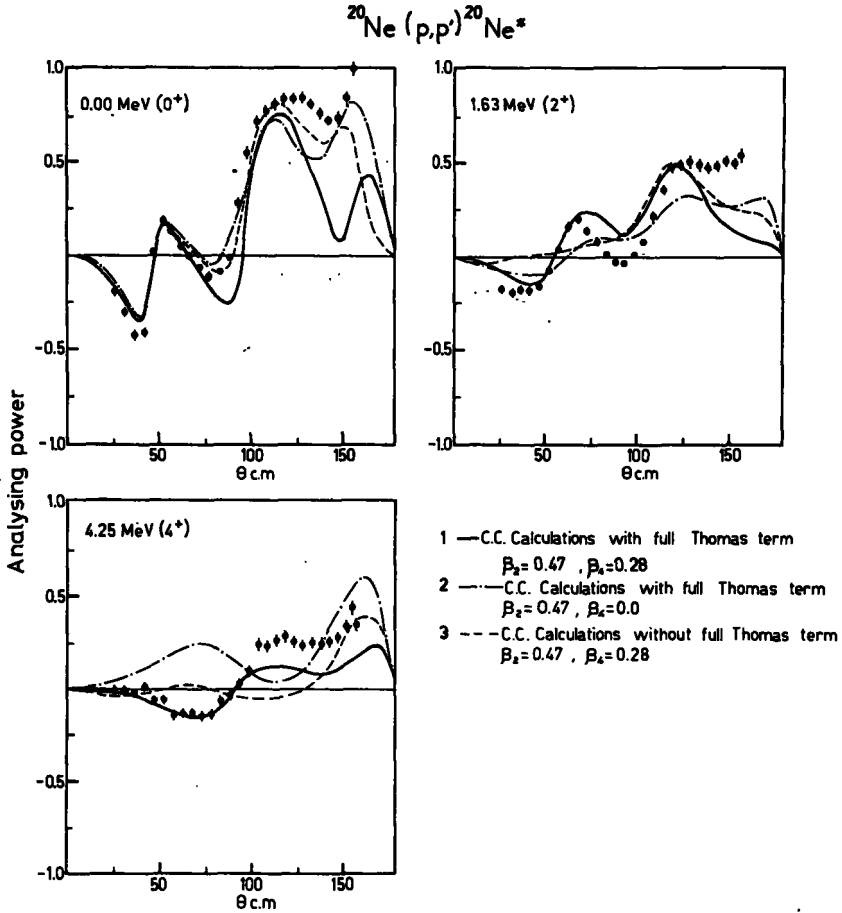


FIG. 9. Elastic polarization and asymmetries for  $^{20}\text{Ne}$  (rot. model).

where

$$A_{jj'; JM}^\dagger = \sum_{m, m'} (-)^{j-m} \langle j' j m' - m | JM \rangle a_{j' m'}^\dagger a_{j m}$$

are the only elements of nuclear description which matter for the reaction. How to obtain the amplitudes  $Z_{jj'}^J$  will vary with the nuclear model (quasi-particles, recoupling of particles or holes outside closed shells, etc.). For each model, there is an expression of the  $Z_{jj'}^J$  with the parameters of this model.

When the state  $|I_i\rangle$  is a core,  $A_{jj'; JM}^\dagger$  is a creation operator of a particle-hole state on this core. Therefore, the particle-hole excitations are very important: the description of any reaction is reduced to them. However, the notion of particle-hole excitation used here is more general

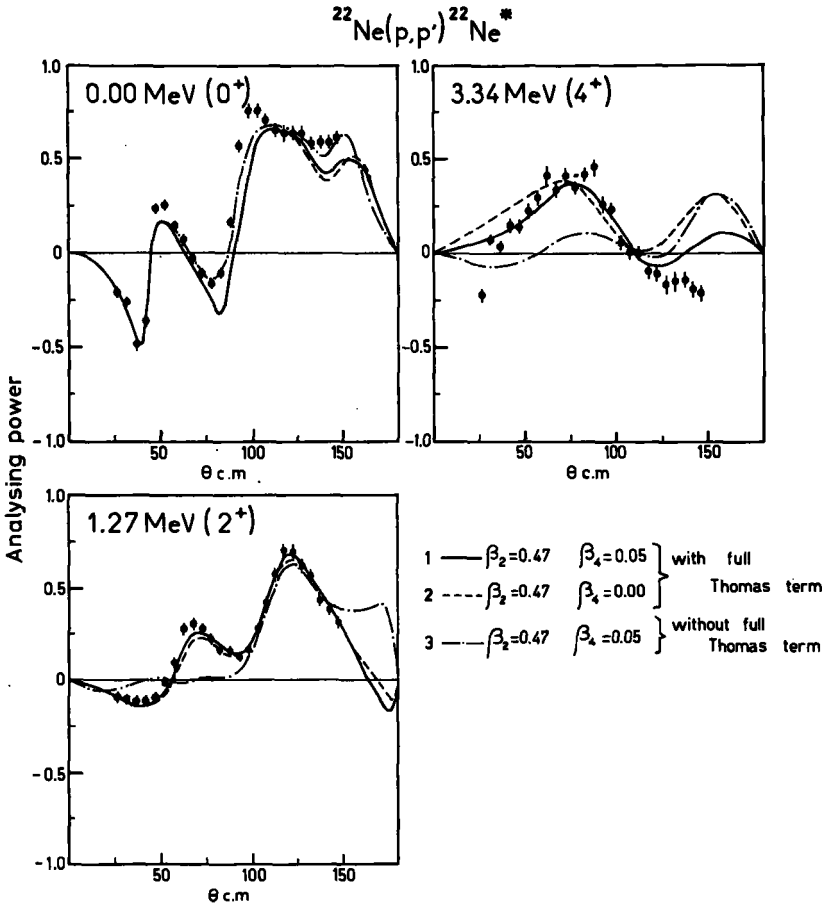


FIG. 10. Elastic polarization and asymmetries for  $^{22}\text{Ne}$  (rot. model).

than the one of nuclear spectroscopy: it is more formal and includes chiefly geometrical informations about the coupling. For example, let us consider a target described by two identical particles in a shell  $j$ , coupled to initial spin  $I_i$  or final spin  $I_f$ . The particle-hole excitations to be used are quite special since the particle and the hole are in the same shell:

$$Z_{jj}^J = 2 (-)^{1+J+I_i} \sqrt{(2I_f+1)(2I_i+1)} \begin{Bmatrix} I_f & J & I_i \\ j & j & j \end{Bmatrix}$$

Especially, when  $I_i$  is zero,  $Z_{jj}^J = 2/\sqrt{2j+1}$ .

For the microscopic description of reactions, we shall only consider DWBA-calculations (the only one we can present here). The computation

of the matrix elements of the interaction is the same as for nuclear spectroscopy, except that two wave-functions are in the continuum, known numerically and with large quantum number. Therefore, the use of relative coordinates is more difficult than the use of multipole expansions. A realistic interaction cannot be expanded into multipoles, and we must use some effective force with zero or finite range. A finite-range interaction is a function of the distance between the two nucleons with a form factor which can be the sum of several Yukawa form factors. One can separate  $V_p$ , interaction of the incoming proton with a proton of the target, from  $V_n$ , the one with a neutron; both interactions include a scalar, a  $(\vec{\sigma}_1 \cdot \vec{\sigma}_2)$ , a spin-orbit and a tensor part [25].

The use of these interactions is simplified in the helicity formalism for multipole expansions [15]. First, this formalism will be presented; almost all the geometry can be expressed in terms of the eigenvalues of the  $(\vec{l} \cdot \vec{\sigma})$  operator on the single-particle wave-functions. The generalized notion of particle-hole excitation is needed.

### 3.1. The helicity formalism

The helicity formalism which we use here is very different from the helicity formalism of Jacob and Wick [26, 27], although there are many similarities. The Jacob-and-Wick formalism applies to the scattering matrix and is the projection of the spin of the particle on its momentum. The helicity formalism for the multipole expansion of an interaction needs the choice of some point origin in the space, around which a multipole expansion can be performed; the spins are projected on the position vectors of the particles with respect to the chosen origin. For a reaction, both helicity formalisms can be used at the same time.

In these two formalisms the more complicated problems are simplified, but the simplest ones are complicated. For example, for the Jacob-and-Wick formalism, there is no important difference in the scattering matrix, when it is spin-dependent or when it is not. In the two formalisms one can define a scattering matrix or an interaction which depends upon angles between some helicity states, which are sums of rotation-matrix elements multiplied by scattering-matrix elements for a given total spin or by a multipole of the interaction. Parity invariance leads to the same requirements in the two cases; time reversal is not exactly the same. In each formalism, the number of elements is greater than the number of independent ones; but they are related by very simple equalities or changes of sign. Here also, we shall only consider spin  $\frac{1}{2}$ -particles.

#### 3.1. a. Description of a bound state

The multipole expansion in the helicity formalism starts with a somewhat peculiar description of the state of a particle with spin. In the usual description

$$|l j m\rangle = f_{lj}(r) \sum_{\mu, \sigma} \langle l \frac{1}{2} \mu \sigma | j m \rangle Y_l^\mu(\theta, \varphi) |\sigma\rangle$$

the spherical harmonic can be replaced by a rotation-matrix element and the spin  $|\sigma\rangle$  can be projected on the direction  $\vec{r}$ . Then

$$\begin{aligned} Y_{\ell}^{\mu}(\theta, \varphi) &\rightarrow \sqrt{\frac{2\ell+1}{4\pi}} R_{\mu,0}^{(\ell)*}(\varphi, \theta, \psi) \\ |\sigma\rangle &\rightarrow \sum_{\lambda} R_{\sigma,\lambda}^{(1/2)*}(\varphi, \theta, \psi) |\lambda\rangle \end{aligned} \quad (19)$$

The angle  $\psi$  is related to some origin around  $\vec{r}$  as a reference frame. This angle is arbitrary and can be introduced into the wave-function if the function is divided by  $\sqrt{2\pi}$  to maintain its normalization. The product of the two rotation-matrix elements can be reduced and the wave-function becomes:

$$|\ell jm\rangle = \left(\frac{2\ell+1}{8\pi^2}\right)^{1/2} f_{\ell j}(r) \sum_{\lambda} \langle \ell \frac{1}{2} 0 \lambda | j \lambda \rangle R_{m,\lambda}^{(j)*}(\varphi, \theta, \psi) |\lambda\rangle$$

The Clebsch-Gordon coefficient which remains must be replaced by its explicit value. The final result is

$$|\ell jm\rangle = \frac{1}{4\pi} (2j+1)^{1/2} f_{\ell j}(r) \sum_{\lambda} \epsilon_{\lambda} R_{m,\lambda}^{(j)*}(\varphi, \theta, \psi) |\lambda\rangle \quad (20)$$

with

$$\epsilon_{-1/2} = 1 \quad \epsilon_{1/2} = (-)^{\ell+j-1/2} \quad (21)$$

All references to the orbital quantum number  $\ell$  have disappeared from the description of the wave function, but there is, now, a parity  $\epsilon_{1/2}$ . For a given value of  $j$  and  $\epsilon_{1/2}$ , there is only one possible value of  $\ell$ . Such a description has been used by Bohr and Mottelson [28] for the computation of the matrix elements of a zero-range interaction.

It should be noted that there are now two radial functions which are equal within the sign. A state described by a single radial function (a pure helicity state) has no direct physical significance. This is because it would be the superposition of an odd- and an even-parity state and wave-functions of different angular momentum cannot have the same behaviour around the origin.

### 3.1.b. Two-body interaction

Any nucleon-nucleon interaction is a  $4 \times 4$  matrix on the helicity basis. Each of these matrix elements can be expanded into multipoles. The following form can be used:

$$\begin{aligned} V(1,2) &= \sum_{J, \lambda_1, \lambda_2, \lambda'_1, \lambda'_2} (2J+1) |\lambda'_1\rangle |\lambda'_2\rangle V_{\lambda'_1 \lambda'_2, \lambda_1 \lambda_2} \langle \lambda_1 | \langle \lambda_2 | (-)^{\lambda_1 - \lambda'_1} \\ &\times R_{\lambda'_1 - \lambda'_2, \lambda_1 - \lambda_2}^{(J)}(\psi_1, \theta, \psi_2) \end{aligned} \quad (22)$$

where  $\psi_1$  and  $\psi_2$  are arbitrary angles around  $\vec{r}_1$  and  $\vec{r}_2$  and  $\theta$  the angle between these two directions. This description is symmetrical with respect to co-ordinates 1 and 2. If  $\varphi_1, \theta_1, \psi_1$  describes a co-ordinate system with its z-axis along  $r_1$  and  $\varphi_2, \theta_2, \psi_2$  another one with its z-axis along  $r_2$  in an arbitrary reference frame,

$$(-)^{\lambda_1 - \lambda_i} R_{\lambda_1 - \lambda_1, \lambda_2 - \lambda_2}^{(J)}(\psi_1, \theta, \psi_2) = \sum_{\mu} (-)^{\mu} R_{\mu, \lambda_1 - \lambda_i}^{(J)}(\varphi_1, \theta_1, \psi_1) \times R_{-\mu, \lambda_2 - \lambda_2}^{(J)}(\varphi_2, \theta_2, \psi_2) \quad (23)$$

The scalar-product form comes from the independence of the total expression with respect to the reference frame and the second magnetic quantum number of the rotation-matrix elements, from the invariance with respect to the choice of the azimuthal origin around  $\vec{r}_1$  and  $\vec{r}_2$ .

Parity invariance leads to the same conditions as in the Jacob-and-Wick formalism because  $\vec{r}$  and  $\vec{p}$  behave in the same way. Therefore:

$$V_{\lambda_1 \lambda_2, \lambda_1 \lambda_2}^J(1, 2) = V_{-\lambda_1 - \lambda_2, -\lambda_1 - \lambda_2}^J(1, 2)$$

When studying time-reversal invariance, something must be known about the multipoles  $V^J$ . For a scalar interaction, they can only be functions of  $r_1$  and  $r_2$ ; for an  $\vec{L} \cdot \vec{S}$  interaction they can have derivative terms and antisymmetric expressions of the quantum numbers. If  $\eta$  is the parity of the multipole, time reversal invariance leads to

$$V_{\lambda_1 \lambda_2, \lambda_1 \lambda_2}^J = \eta V_{-\lambda_1 - \lambda_2, -\lambda_1 - \lambda_2}^J$$

Note that there is no change of sign of the helicity in the corresponding relation of the Jacob-and-Wick formalism.

For a given values of  $J$ , the matrix  $V_{\lambda_1 \lambda_2, \lambda_1 \lambda_2}^J$  can be written on the basis of Kronecker products of  $2 \times 2$  matrices. There are two even matrices:

$$\begin{vmatrix} 1 & 0 \\ 0 & 1 \end{vmatrix} \quad \begin{vmatrix} 0 & 1 \\ 1 & 0 \end{vmatrix} \quad (24)$$

and two odd ones

$$\begin{vmatrix} -1 & 0 \\ 0 & 1 \end{vmatrix} \quad \begin{vmatrix} 0 & -1 \\ 1 & 0 \end{vmatrix} \quad (25)$$

If parity conservation applies, the two-body interaction can be separated into an even part

$$a^J(1, 2) \begin{vmatrix} 1 & 0 \\ 0 & 1 \end{vmatrix} \otimes \begin{vmatrix} 1 & 0 \\ 0 & 1 \end{vmatrix} + b^J(1, 2) \begin{vmatrix} 1 & 0 \\ 0 & 1 \end{vmatrix} \otimes \begin{vmatrix} 0 & 1 \\ 1 & 0 \end{vmatrix} + b'^J(2, 1) \begin{vmatrix} 0 & 1 \\ 1 & 0 \end{vmatrix} \otimes \begin{vmatrix} 1 & 0 \\ 0 & 1 \end{vmatrix} + c^J(1, 2) \begin{vmatrix} 0 & 1 \\ 1 & 0 \end{vmatrix} \otimes \begin{vmatrix} 0 & 1 \\ 1 & 0 \end{vmatrix} \quad (26)$$

and an odd part

$$\begin{aligned}
 d^J(1,2) \begin{vmatrix} -1 & 0 \\ 0 & 1 \end{vmatrix} \otimes \begin{vmatrix} -1 & 0 \\ 0 & 1 \end{vmatrix} + e^J(1,2) \begin{vmatrix} -1 & 0 \\ 0 & 1 \end{vmatrix} \otimes \begin{vmatrix} 0 & -1 \\ 1 & 0 \end{vmatrix} \\
 + e'^J(2,1) \begin{vmatrix} 0 & -1 \\ 1 & 0 \end{vmatrix} \otimes \begin{vmatrix} -1 & 0 \\ 0 & 1 \end{vmatrix} + f^J(1,2) \begin{vmatrix} 0 & -1 \\ 1 & 0 \end{vmatrix} \otimes \begin{vmatrix} 0 & -1 \\ 1 & 0 \end{vmatrix}
 \end{aligned} \quad (27)$$

For two identical particles  $a, c, d, f$ , are invariant when variables 1 and 2 are permuted,  $b^J(1,2) = b'^J(2,1)$  and  $e^J(1,2) = e'^J(2,1)$ . Time-reversal invariance requires that  $a, c, d, e, f$  are expressed in terms of time-invariant operators and  $b$  must change sign.

When the usual multipole expansion of the form factor of the interaction is given by

$$V(|r_1 - r_2|) = \sum_L (2L+1) V_L(r_1, r_2) P_L(\cos \theta)$$

we get

- (a) for an interaction which does not depend upon the spins:

$$\begin{aligned}
 a^J &= V_J(r_1, r_2) \\
 b^J &= c^J = d^J = e^J = f^J = 0
 \end{aligned}$$

- (b) for an interaction  $(\vec{\sigma}_1 \cdot \vec{\sigma}_2)$ :

$$\begin{aligned}
 a^J &= b^J = 0 \\
 c^J &= -V_J(r_1, r_2) \\
 d^J &= \frac{1}{2J+1} \{JV_{J-1}(r_1, r_2) + (J+1)V_{J+1}(r_1, r_2)\} \\
 e^J &= \frac{\sqrt{J(J+1)}}{2J+1} \{V_{J-1}(r_1, r_2) - V_{J+1}(r_1, r_2)\} \\
 f^J &= \frac{1}{2J+1} \{(J+1)V_{J-1}(r_1, r_2) + JV_{J+1}(r_1, r_2)\}
 \end{aligned}$$

(c) for a tensor interaction,  $a^J = b^J = 0$  and the other ones are given in Ref. [15]. Therefore, there is no fundamental difference between a tensor and a  $(\vec{\sigma}_1 \cdot \vec{\sigma}_2)$  interaction,

- (d) the  $\vec{L} \cdot \vec{S}$  interaction will be discussed in more detail.

Between given helicity states, the  $\vec{\sigma}_1 \cdot \vec{\sigma}_2$  or the tensor operators are functions of the angle between  $r_1$  and  $r_2$ ; this angular dependence is combined with that of the usual expansion to get the above expressions.

## 3.1.c. Matrix elements between bound states

The non-antisymmetrized particle-hole matrix element

$$\begin{aligned}
 f_{j_1' j_2' j_1 j_2}^J &= \langle (j_1' j_1^{-1}) JM | V(1, 2) | (j_2 j_2^{-1}) JM \rangle_{n.a} = \sum_{m_1 m_2 m_1' m_2'} (-)^{j_1 - m_1 + j_2 - m_2} \\
 &\times \langle j_1' j_1 m_1' - m_1 | JM \rangle \langle j_2 j_2 m_2 - m_2 | JM \rangle \langle j_1' m_1' | \langle j_2 m_2 | \\
 &\times V(1, 2) | j_2 m_2 \rangle | j_1 m_1 \rangle
 \end{aligned} \quad (28)$$

is the basic element of the computation of an antisymmetrized matrix element in particle-hole:

$$\begin{aligned}
 \langle (j_1' j_1^{-1}) J | V(1, 2) | (j_2 j_2^{-1}) J \rangle &= f_{j_1' j_2' j_1 j_2}^J - \sum_{J'} (-)^{j_1 + j_2 + J + J'} (2J' + 1) \\
 &\times \left\{ \begin{array}{ccc} j_1 & j_1 & J \\ j_2 & j_2 & J' \end{array} \right\} f_{j_1' j_2' j_1 j_2}^{J'}
 \end{aligned} \quad (29)$$

as well as particle-particle coupling:

$$\begin{aligned}
 \langle (j_1' j_2') J | V(1, 2) | (j_1 j_2) J \rangle &= \sum_{J'} (-)^{J + j_1 + j_2} (2J' + 1) \left\{ \begin{array}{ccc} j_1 & j_2 & J \\ j_2' & j_1' & J' \end{array} \right\} f_{j_1' j_2' j_1 j_2}^{J'} \\
 - \sum_{J'} (2J' + 1) \left\{ \begin{array}{ccc} j_1 & j_2 & J \\ j_1' & j_2' & J' \end{array} \right\} f_{j_1' j_2' j_1 j_2}^{J'}
 \end{aligned} \quad (30)$$

The geometrical coefficients of these two formulae do not depend upon the spins of the particles but only on the total angular momenta. The helicity formalism can only simplify the computation of the  $f^J$ .

Let us introduce into definition (28) the description (20) for the states and (22) for the interaction. Taking into account relation (23), we get a product of three rotation-matrix elements of argument  $(\varphi_1, \theta_1, \psi_1)$  and three other ones of argument  $(\varphi_2, \theta_2, \psi_2)$ . After integration over the angles we obtain:

$$\begin{aligned}
 f_{j_1' j_2' j_1 j_2}^J &= \frac{1}{4} \sum_{\lambda_1 \lambda_2 \lambda_1' \lambda_2'} (-)^{j_1 - \lambda_1 + j_2 - \lambda_2} \epsilon_{\lambda_1} \epsilon_{\lambda_1'} \epsilon_{\lambda_2} \epsilon_{\lambda_2'} \sqrt{(2j_1 + 1)(2j_1' + 1)(2j_2 + 1)(2j_2' + 1)} \\
 &\times \left( \begin{array}{ccc} j_1' & J & j_1 \\ \lambda_1' & \lambda_1 - \lambda_1' & -\lambda_1 \end{array} \right) \left( \begin{array}{ccc} j_2' & J & j_2 \\ \lambda_2' & \lambda_2 - \lambda_2' & -\lambda_2 \end{array} \right) \iint V_{\lambda_1' \lambda_1, \lambda_2 \lambda_2'}^J(r_1, r_2) \\
 &\times f_{j_1'}(r_1) f_{j_2'}(r_2) f_{j_1}(r_1) f_{j_2}(r_2) r_1^2 r_2^2 dr_1 dr_2
 \end{aligned} \quad (31)$$

Let us perform the integration over  $r_1$  and the summation on  $\lambda_1$  and  $\lambda_1'$ , in order to define form-factors for the nucleon 2:

$$F_{j_1 j_1}^J(2) = \frac{1}{2} \sum_{\lambda_1 \lambda_1'} (-)^{j_1 - \lambda_1} \epsilon_{\lambda_1} \epsilon_{\lambda_1'} \sqrt{(2j_1+1)(2j_1'+1)} \begin{pmatrix} j_1' & J & j_1 \\ \lambda_1' & \lambda_1 - \lambda_1' & -\lambda_1 \end{pmatrix} \times \int V_{\lambda_1 \lambda_2, \lambda_1' \lambda_2'}^J(r_1, r_2) f_{j_1'}(r_1) f_{j_1}(r_1) r_1^2 dr_1 \quad (32)$$

This one-body form factor can be written by using the elementary matrices (24) and (25):

$$F_{j_1 j_1}^J(2) = A_{j_1 j_1}^J(2) \begin{vmatrix} 1 & 0 \\ 0 & 1 \end{vmatrix} + B_{j_1 j_1}^J(2) \begin{vmatrix} 0 & 1 \\ 1 & 0 \end{vmatrix} + C_{j_1 j_1}^J(2) \begin{vmatrix} -1 & 0 \\ 0 & 1 \end{vmatrix} + D_{j_1 j_1}^J(2) \begin{vmatrix} 0 & -1 \\ 1 & 0 \end{vmatrix} \quad (33)$$

With expressions (26) and (27) of the most general interaction, we can see that only  $a^J$  and  $b^J$  matter for  $A^J$ ,  $b^J$  and  $c^J$  for  $B^J$ ,  $d^J$  and  $e^J$  for  $C^J$ ,  $e^J$  and  $f^J$  for  $D^J$ . Each contribution is the sum of two terms with opposite helicities. With the parity  $\eta$  of the matrix, this sum in equation (32) leads to

$$\frac{1}{2} (-)^{j_1 - \lambda_1} \left[ 1 + \eta (-)^{\ell_1 + \ell_1' + J} \right] \epsilon_{\lambda_1} \epsilon_{\lambda_1'} \sqrt{(2j_1+1)(2j_1'+1)} \begin{pmatrix} j_1' & J & j_1 \\ \lambda_1' & \lambda_1 - \lambda_1' & -\lambda_1 \end{pmatrix} \quad (34)$$

The matrix element is a natural parity one if  $\ell_1 + \ell_1' + J$  is even, an "unnatural parity" one if  $\ell_1 + \ell_1' + J$  is odd. The even part (26) of the interaction contributes only to natural-parity matrix elements and the odd part (27) for the unnatural-parity ones. The choice  $\lambda_1' = -1/2$  eliminates  $\epsilon_{\lambda_1}$  from expression (34). When the matrix for the particle 1 is diagonal in the helicity space, this geometrical coefficient becomes

$$G_{j_1 j_1}^J = (-)^{j_1 + 1/2} \sqrt{(2j_1+1)(2j_1'+1)} \begin{pmatrix} j_1' & J & j_1 \\ -\frac{1}{2} & 0 & \frac{1}{2} \end{pmatrix} \quad (35)$$

instead of

$$G_{j_1 j_1}^J = (-)^{j_1 - 1/2} \sqrt{(2j_1+1)(2j_1'+1)(2\ell_1+1)(2\ell_1'+1)} \begin{pmatrix} \ell_1 & \ell_1' & J \\ 0 & 0 & 0 \end{pmatrix} \begin{Bmatrix} \ell_1 & \ell_1' & J \\ j_1' & j_1 & \frac{1}{2} \end{Bmatrix}$$

in the usual formalism. This coefficient is given by the simplified formula which holds for 3-j coefficients of which the magnetic quantum numbers are zeros:

$$G_{j_1 j_1}^J = (-)^{\text{In}\left\{\frac{J+j'-j+2}{2}\right\}} \frac{g(j+j'+J+1)}{g(J+j-j')g(J+j'-j)g(j+j'-J)} \quad (36)$$

where

$$g(n) = \frac{(n!)^{1/2}}{n!!} = \begin{cases} \left[ \frac{2 \times 4 \times \dots \times (n-1)}{3 \times 5 \times \dots \times n} \right]^{1/2} & \text{when } n \text{ is odd} \\ \left[ \frac{2 \times 4 \times \dots \times n}{3 \times 5 \times \dots \times (n-1)} \right]^{1/2} & \text{when } n \text{ is even.} \end{cases}$$

and  $\text{In}\{p\}$  is the integer part of  $p$ . For integer values of  $j$  and  $j'$ , formula (36)

$$\text{is } (-)^{j+1} \begin{pmatrix} j' & J & j \\ 0 & 0 & 0 \end{pmatrix}.$$

When the matrix is non diagonal in the helicity space of particle 1, the geometry is:

$$(-)^{j_1+1} \frac{1}{\sqrt{(2j_1+1)(2j_1'+1)}} \begin{pmatrix} j_1' & J & j_1 \\ -\frac{1}{2} & 1 & -\frac{1}{2} \end{pmatrix} = \alpha_{j_1 j_1}^J G_{j_1 j_1}^J$$

Recurrence relations between Clebsh-Gordon coefficients gives:

$$\alpha_{j_1 j_1}^J = (-1)^{j_1+j_1-1/2} \frac{(j_1 + \frac{1}{2}) + (-)^{j_1+j_1+J} (j_1' + \frac{1}{2})}{\sqrt{J(J+1)}}$$

which can be expressed with the eigenvalues of  $\vec{L} \cdot \vec{\sigma}$  as follows:

$$\begin{aligned} \alpha_{j_1 j_1}^J &= \frac{\gamma_1 - \gamma_1'}{\sqrt{J(J+1)}} && \text{for a natural parity matrix element} \\ &= \frac{\gamma_1 + \gamma_1' + 2}{\sqrt{J(J+1)}} && \text{for an unnatural parity one} \end{aligned}$$

Using these notations, we get two form factors for a natural-parity matrix element:

$$\begin{aligned} A_{j_1 j_1}^J(2) &= G_{j_1 j_1}^J \int \left[ a^J(1,2) + \alpha_{j_1 j_1}^J b^J(2,1) \right] f_{j_1}(r_1) f_{j_1}(r_1) r_1^2 dr_1 \\ B_{j_1 j_1}^J(2) &= G_{j_1 j_1}^J \int \left[ b^J(1,2) + \alpha_{j_1 j_1}^J c^J(1,2) \right] f_{j_1}(r_1) f_{j_1}(r_1) r_1^2 dr_1 \end{aligned} \quad (37)$$

For an unnatural parity one, we get  $C_{j_1 j_1}^J(2)$  and  $D_{j_1 j_1}^J(2)$ , with  $d, e, f$ , instead of  $a, b, c$ . The unusual choice of matrices (24) and (25) was done

in order to get similar formulae for all the form factors. Bringing back the form factors (33) into the matrix element (31), we get:

$$f_{j_1 j_2 j_1 j_2}^J = (-)^{j_2 - j_1} G_{j_2 j_2}^J \int \left[ A_{j_1 j_1}^J(2) + \alpha_{j_2 j_2}^J B_{j_1 j_1}^J(2) \right] f_{j_2}(r_2) f_{j_2}(r_2) r_2^2 dr_2 \quad (38)$$

for the natural-parity case. For the unnatural-parity case, A and B must be replaced by C and D.

The nucleon-nucleon interaction is often written in the isotopic spin formalism:

$$V = V_0 + V_\sigma(\vec{\sigma}_1 \cdot \vec{\sigma}_2) + (V_\tau + V_{\sigma\tau}(\vec{\sigma}_1 \cdot \vec{\sigma}_2))(\vec{\tau}_1 \cdot \vec{\tau}_2) \quad (39)$$

There is a proton-proton interaction,  $T = 1$ :

$$V_p = (V_0 + V_\tau) + (V_\sigma + V_{\sigma\tau})(\vec{\sigma}_1 \cdot \vec{\sigma}_2)$$

and a proton-neutron interaction, half-sum of  $T = 1$  and  $T = 0$ :

$$V_n = (V_0 - V_\tau) + (V_\sigma - V_{\sigma\tau})(\vec{\sigma}_1 \cdot \vec{\sigma}_2)$$

In the exchange term, the helicity formalism takes into account the permutation of space and spin co-ordinates. Permutation of isotopic-spin co-ordinates must be done:

$$V_p^{\text{ech}} = V_p \qquad V_n^{\text{ech}} = V_p - V_n$$

### 3. 2. Application to nuclear reactions

The application of the helicity formalism to DWBA is almost the same as to bound states: two wave-functions are in the continuum. We shall first consider the simplest case: the inelastic scattering of a nucleon on a spin-zero target with a residual nucleus which can be described by a single particle-hole state.

The expansion of the distorted wave is usually written as [29]

$$X_{\vec{\sigma}}^{(+)}(\vec{k}, \vec{r}) = \frac{4\pi}{kr} \sum_{jm\mu\mu'\sigma} i^\ell X_{\ell j}(kr) \langle \ell 1/2 \mu \sigma | jm \rangle \langle \ell 1/2 \mu' \sigma' | jm \rangle \\ \times Y_{\ell}^{\mu*}(\theta_k, \varphi_k) Y_{\ell}^{\mu'}(\theta_r, \varphi_r) | \sigma' \rangle \quad (40)$$

where  $\sigma$  is the spin projection of the incoming plane wave on an arbitrary axis and  $\sigma'$  is the projection at the point  $\vec{r}$  on the same axis. If we choose this arbitrary axis along  $\vec{k}$ , we introduce the Jacob-and-Wick helicity  $\lambda$

instead of  $\sigma$ . Then, transformation (19) can be performed for  $|\sigma'\rangle$ , introducing the helicities  $|\lambda'\rangle$ . The wave-function (40) is now given by

$$X_{\lambda}^{(+)}(\vec{k}, \vec{r}) = \frac{1}{2k\sqrt{2\pi}} \sum_{j, \lambda'} (2j+1) X_{\lambda\lambda'}^j(kr) R_{\lambda, \lambda'}^{(j)*}(\varphi_f, \theta_f, \psi_f) |\lambda'\rangle \quad (41)$$

where

$$X_{\lambda\lambda'}^j = \frac{j^{j-1/2}}{r} \left[ X_{\ell=j-1/2, j}(kr) + i(-)^{\lambda-\lambda'} X_{\ell=j+1/2, j}(kr) \right] \quad (42)$$

With the same transformation, the outgoing wave is given by

$$X_{\lambda}^{(-)*}(\vec{k}, \vec{r}) = \frac{1}{2k\sqrt{2\pi}} \sum_{j, \lambda'} (2j+1) \tilde{X}_{\lambda\lambda'}^j(kr) R_{\lambda, \lambda'}^{(j)*}(\varphi_f, \theta_f, \psi_f) |\lambda'\rangle \quad (43)$$

where  $\tilde{X}_{\lambda\lambda'}^j$  is  $X_{\lambda\lambda'}^j$  with  $-i$  instead of  $i$ .

The reaction is described by the helicity amplitudes

$$f_{\sigma_f \mu_f; \sigma_i}(\vec{k}_i, \vec{k}_f) = -\frac{m}{2\pi\hbar^2} \left(\frac{v_f}{v_i}\right)^{1/2} \langle X_{\sigma_f}^{(-)}(\vec{k}_f, \vec{r}) \psi_{\mu_f}^{I_f} | v | X_{\sigma_i}^{(+)}(\vec{k}_i, \vec{r}) \psi^{I_i} \rangle \quad (44)$$

for an incoming nucleon in the direction  $\vec{k}_i$  with the helicity  $\sigma_i$  and an outgoing nucleon in the direction  $\vec{k}_f$  with the helicity  $\sigma_f$ . The nucleus initially in a state  $\psi^{I_i}$  is left in a final state  $\psi_{\mu_f}^{I_f}$  (with helicity  $\mu_f$ ) described by a particle  $j_p$  and a hole  $j_h$ ;  $m$  is the reduced mass of the nucleon,  $v_i$  and  $v_f$  its velocity in the initial and the final state. The normalization has been chosen in such a way that:

$$\frac{d\sigma}{d\Omega}(\vec{k}_i, \vec{k}_f) = \frac{1}{2} \sum_{\sigma_i \sigma_f \mu_f} |f_{\sigma_f \mu_f; \sigma_i}(\vec{k}_i, \vec{k}_f)|^2$$

The asymmetry is related to the non-diagonal elements of the  $2 \times 2$  matrix:

$$F_{\sigma_i, \sigma_i'} = \left[ 2 \frac{d\sigma}{d\Omega}(\vec{k}_i, \vec{k}_f) \right]^{-1} \sum_{\sigma_f, \mu_f} f_{\sigma_f \mu_f; \sigma_i}(\vec{k}_i, \vec{k}_f) f_{\sigma_f, \mu_f; \sigma_i'}^*(\vec{k}_i, \vec{k}_f)$$

The amplitude (44) is easily calculated if the axis of quantization is along  $\vec{k}_f$ ,  $\varphi$  being zero and  $\theta$  the angle between  $\vec{k}_i$  and  $\vec{k}_f$ . The only difference between free waves and bound ones is a factor  $(1/k)\sqrt{(2j+1)/2\pi}$ . The rotation-matrix element of equation (41) becomes:

$$\sum_{\mu} R_{\lambda\mu}^{(j)*}(\vec{k}_i, \vec{k}_f) R_{\mu\lambda}^{(j)*}(\vec{k}_f, \vec{r})$$

and all that is needed in order to use formula (28) is to couple  $j_i$  and  $j_f$  to  $I_f$ . The result is:

$$f_{\sigma_f \mu_f; \sigma_i}(\theta) = -\frac{m}{\hbar^2} \left( \frac{v_f}{v_i} \right)^{1/2} \frac{1}{k_f k_i} \sum_{j_i j_f m_i} (-)^{j_i - \sigma_i} \sqrt{(2j_i + 1)(2j_f + 1)(2I_f + 1)} \\ \times \begin{pmatrix} j_i & j_f & I_f \\ m_i & -\sigma_f & \mu_f \end{pmatrix} r_{m_i \sigma_i}^{(j_i)}(\theta) f_{j_p(j_f \sigma_f), j_h(j_i \sigma_i)}^{I_f} \quad (45)$$

If a normal-parity state has been excited, integration over the particle-hole variable gives the two one-body form factors  $A_{j_p j_h}^J(2)$  and  $B_{j_p j_h}^J(2)$  for  $J = I_f$ . The second integration becomes:

$$f_{j_p(j_f \sigma_f), j_h(j_i \sigma_i)}^{I_f} = (-)^{j_f - j_i} \frac{1}{2} G_{j_i j_f}^J \int \left\{ A_{j_p j_h}^J(2) \left[ \tilde{X}_{\sigma_f - 1/2}^{j_f} X_{\sigma_i - 1/2}^{j_i} - \eta (-)^{j_f + j_i + J} \right. \right. \\ \times \left. \tilde{X}_{\sigma_f 1/2}^{j_f} X_{\sigma_i 1/2}^{j_i} \right] - \frac{(j_i + \frac{1}{2}) + (-)^{j_i + j_f + J} (j_f + \frac{1}{2})}{\sqrt{J(J+1)}} B_{j_p j_h}^J(2) \\ \left. \times \left[ \tilde{X}_{\sigma_f 1/2}^{j_f} X_{\sigma_i - 1/2}^{j_i} - \eta (-)^{j_i + j_f + I_f} \tilde{X}_{\sigma_f - 1/2}^{j_f} X_{\sigma_i 1/2}^{j_i} \right] \right\} r_2^2 dr_2 \quad (46)$$

with  $\eta = 1$ . For an unnatural parity excitation, A and B must be replaced by C and D and  $\eta = -1$ . Changing the signs of  $\sigma_i$  and  $\sigma_f$ , the matrix element (46) is multiplied by  $-\eta (-)^{j_i + j_f + I_f}$  and the parity relations are fulfilled for the helicity amplitudes (45). The amplitudes are only needed for  $\sigma_f = \frac{1}{2}$ . Going back to the usual wave-functions and with the notations

$$F_{\pm, \pm} = \int F(2) \tilde{X}_{\ell_f = j_f \pm 1/2, j_f}(r) X_{\ell_i = j_i \pm 1/2, j_i}(r) dr \quad (47)$$

where the first sign is related to the outgoing wave and the second to the incoming one, the following expressions are obtained: for a natural-parity transition

$$f_{j_p(j_f 1/2), j_h(j_i \pm 1/2)}^{I_f} = i^{j_i - j_f + 1} G_{j_i j_f}^J \left\{ \left( A + \frac{\gamma_i - \gamma_f}{\sqrt{J(J+1)}} B \right)_{+, -} \mp \left( A + \frac{\gamma_i - \gamma_f}{\sqrt{J(J+1)}} B \right)_{-, +} \right\} \quad (48)$$

when  $j_i + j_f + J$  is even and

$$f_{j_p(j_f 1/2), j_h(j_i \pm 1/2)}^{I_f} = i^{j_i - j_f} G_{j_i j_f}^J \left\{ \left( A - \frac{\gamma_i - \gamma_f}{\sqrt{J(J+1)}} B \right)_{-, -} \mp \left( A - \frac{\gamma_i - \gamma_f}{\sqrt{J(J+1)}} B \right)_{+, +} \right\} \quad (49)$$

when  $j_i + j_f + J$  is odd. The  $\pm$  sign refers to the sign of  $\sigma_i$ . For an unnatural parity transition A and B must be replaced by C and D,  $\gamma_i - \gamma_f$  by  $\gamma_i + \gamma_f + 2$  and the parity condition on  $j_i + j_f + J$  inverted.

Antisymmetrization is obtained with

$$f_{j_p(j_f \sigma_f), j_h(j_i \sigma_i)}^J - \sum_{J'} (-)^{J'+I_f+j_h+j_i} (2J'+1) \begin{Bmatrix} j_i & j_p & J' \\ j_h & j_f & J \end{Bmatrix} f_{j_p(j_f \sigma_f), (j_i \sigma_f) j_h}^{J'}$$

instead of  $f^J$  in Eq. (45). The same calculation is needed with the initial distorted wave instead of the hole function, for all the  $J'$  values consistent with the entering angular momenta. For a given  $J'$ , the matrix elements are natural parity ones or not according to the angular momentum of the incoming particle. It is more difficult to foresee the effect of a given interaction.

In a more complete description of the nucleus, the components (18) of the excitation must be summed. Expressions (48) and (49) are indication of the geometry needed in a coupled-channel calculation.

### 3.3. Two-body spin-orbit interaction

The relative spin-orbit interaction is

$$V(|\vec{r}_1 - \vec{r}_2|) \left[ (\vec{r}_1 - \vec{r}_2) \times \frac{\vec{V}_1 - \vec{V}_2}{i} \cdot (\vec{\sigma}_1 + \vec{\sigma}_2) \right] = \left[ \vec{L}_1 + \vec{L}_2 + i(\vec{r}_1 \times \vec{r}_2) \right. \\ \left. \times \left( \frac{1}{r_2} \frac{d}{dr_2} - \frac{1}{r_1} \frac{d}{dr_1} \right) + \frac{1}{r_2^2} \vec{r}_1 \times (\vec{r}_2 \times \vec{L}_2) + \frac{1}{r_1^2} \vec{r}_2 \times (\vec{r}_1 \times \vec{L}_1) \right] \cdot (\vec{\sigma}_1 + \vec{\sigma}_2) \quad (50)$$

This expression is simple in relative co-ordinates. The multipole expansion is much more complicated, as indicated by formula (50). When looking how to replace a soft-core  $\vec{L} \cdot \vec{S}$  potential [18] by the sum of two Yukawa form-factors, the ranges are 0.55 and 0.325 fermis, the depth 156 and -4400 for  $V_p$ , 116 and -2200 MeV for  $V_n$ . This potential is negative at small distances and positive at large ones. These small ranges allow the use of a zero range limit. However, if the form-factor is a  $\delta$  function, the matrix elements vanish. Thus, the zero range limit corresponds to a  $\delta''$  form-factor.

#### 3.3.a. Finite range

The multipoles for the helicity formalism are listed in Appendix B of reference 10. They are used in the code DWBA 70 [25].

There are five one-body form-factors for a natural parity excitation. In the code notation, they are

$$F_{Ls}(r) = A(r) + B(r) \frac{(\gamma_i - \gamma_f)}{\sqrt{J(J+1)}} + A_1(r) \frac{(\gamma_i - \gamma_f)^2}{J(J+1)} + A_2(r) \frac{(\gamma_i - \gamma_f)(\gamma_i + \gamma_f + 2)}{J(J+1)} \\ + B_2(r)(\gamma_i + \gamma_f + 2) + \left\{ A_3(r) + B_3(r) \frac{\gamma_i - \gamma_f}{\sqrt{J(J+1)}} \right\} \frac{d}{dr} \quad (51)$$

For an unnatural-parity excitation, there are only three of them

$$F_{LS}(r) = C(r) + D(r) \frac{\gamma_1 + \gamma_f + 2}{\sqrt{J(J+1)}} + C_1(r) \frac{(\gamma_1 + \gamma_f + 2)^2}{J(J+1)} \quad (52)$$

Each of these one-body form-factors depends on the multipoles of  $V(|r_1 - r_2|)$  in such a complicated way that no relation between them can be seen.

For a natural parity excitation, the interaction (51) includes a derivative term as the collective interaction (12) did. In the limit of large angular momentum  $l$ , the microscopic interaction (51) exhibits the same structure as the collective interaction.

In an interaction  $V_0 + V_\sigma(\vec{\sigma}_1 \cdot \vec{\sigma}_2)$ ,  $V_0$  leads to an A type form-factor and  $V_\sigma$  to a B type one. Taking into account the geometry (36), the complete interaction is:

$$\begin{aligned} A(r) + B(r) + F_{LS}(r) & \quad \text{when} \quad j_i - l_i = j_f - l_f \\ \frac{1}{l} A(r) + B(r) + l F_{LS}(r) & \quad \text{when} \quad j_i - l_i \neq j_f - l_f \end{aligned}$$

For an unnatural-parity state, the interaction (52) does not include derivative terms. In contrast to the natural-parity case, the interaction is stronger when  $j_i - l_i = j_f - l_f$ . Including an interaction  $V_\sigma(\vec{\sigma}_1 \cdot \vec{\sigma}_2)$  which gives C and D type form-factors, the total interaction is:

$$\begin{aligned} \frac{1}{l} C(r) + D(r) + l F_{LS}(r) & \quad \text{if} \quad j_i - l_i = j_f - l_f \\ C(r) + D(r) + F_{LS}(r) & \quad \text{if} \quad j_i - l_i \neq j_f - l_f \end{aligned}$$

The antisymmetrization effects are more complex than for a central interaction. It is not possible to discuss the complete expression for a finite range.

### 3.3.b. Expansion for small ranges

The zero range limit of the helicity multipoles is obtained when all the  $V_J(r_1, r_2)$  are replaced by  $\delta(r_1 - r_2)/r_1^2$ . For an interaction  $\{V_0 + V_1 \vec{\sigma}_1 \cdot \vec{\sigma}_2\} \delta(\vec{r}_1 - \vec{r}_2)$ , one gets:

$$\begin{aligned} (-)^{j_i - j_f} G_{\frac{1}{2} \frac{1}{2}}^J G_{\frac{1}{2} \frac{1}{2}}^J \left\{ V_0 - \frac{(\gamma_1 - \gamma_1')(\gamma_2 - \gamma_2')}{J(J+1)} V_1 \right\} & \quad \text{natural parity} \\ (-)^{j_i - j_f} G_{\frac{1}{2} \frac{1}{2}}^J G_{\frac{1}{2} \frac{1}{2}}^J V_1 \left\{ 1 + \frac{(\gamma_1 + \gamma_1' + 2)(\gamma_2 + \gamma_2' + 2)}{J(J+1)} \right\} & \quad \text{unnatural parity} \end{aligned} \quad (53)$$

The exchange term includes sums of products of a  $6j$  coefficient and  $(-)^{j_i - j_f} G_{\frac{1}{2} \frac{1}{2}}^J G_{\frac{1}{2} \frac{1}{2}}^J$ . This geometry can be reduced to the one of formulae (53). If the interaction is defined by its intensity for each set of values (S, T),

only the components  $S = 0$ ,  $T = 1$  and  $S = 1$ ,  $T = 0$  remain when direct and exchange terms have been summed.

Using this approximation, the multipoles of a tensor or an  $\vec{L} \cdot \vec{S}$  interaction disappear. An expansion of the interaction with respect to its range must be performed:

$$V(r) = \sum_{n=0}^{\infty} C_n \delta^{(2n)}(r) \quad (54)$$

To define the coefficients  $C_n$ , let us consider the Fourier transform of  $V(r)$

$$W(q) = \int e^{iqr} V(r) dr = \sum_{n=0}^{\infty} C_n \int e^{iqr} \delta^{(2n)}(r) dr = \sum_{n=0}^{\infty} (-)^n C_n q^{2n}$$

Thus, the  $C_n$  are the coefficients of the expansion into powers of  $q^2$  of the Fourier transform of  $V(r)$ . They are also related to the moments of  $V(r)$ , which are integrals of  $V(r)r^{2n}$ . Integrating by parts, the interaction (54) is changed into

$$\frac{\delta(r_1 - r_2)}{r_1^2} \sum_{n=0}^{\infty} C_n \Delta_1^n$$

where  $\Delta_1$  acts on all functions of  $r_1$  in the radial integral. In peculiar, for  $n = 1$ ,  $V_J$  must be replaced by

$$\frac{\delta(r_1 - r_2)}{r_1} \left[ \frac{d^2}{dr_1^2} r_1 - \frac{J(J+1)}{r_1} \right] f_{j_1}(r_1) f_{j_1}(r_1)$$

with the notations of Eq. (31).

An interaction of range  $\mu$  and intensity  $V$  corresponds to a zero-range interaction of intensity  $V\mu^3$ . When the zero-range interaction does not exist, the related zero-range limit interaction has an intensity  $V\mu^5$ . The proton-proton  $\vec{L} \cdot \vec{S}$  interaction has a zero-range limit of  $-8$  MeV, including the part of range  $0.325$  fm corresponding to  $-16$  MeV and the  $0.55$  one corresponding to  $8$  MeV.

For the zero-range tensor interaction [15], the term  $n = 1$  also vanishes. The limit is obtained with  $n = 2$ .

### 3.3.c. Zero-range limit $\vec{L} \cdot \vec{S}$ interaction

This approximation can be applied to the one-body form-factors of the  $\vec{L} \cdot \vec{S}$  interaction. Let us consider a particle-hole excitation with radial functions  $f_p(r)$  and  $f_h(r)$ . Setting

$$V_J(r) = G_{ph}^J f_p(r) f_h(r)$$

we obtain

$$\begin{aligned} & \left[ J(J+1)(\alpha_1^2 + \alpha_2^2 - 2) - 1 \right] \frac{V_J}{r^2} + \left[ 1 - (-)^{\ell_p + \ell_h + J} \alpha_1 \alpha_2 \right] \left[ -(\gamma_i + \gamma_f + 1) \frac{V_J(r)}{r^2} \right. \\ & \left. + (\gamma_p + \gamma_h - \gamma_i - \gamma_f) \frac{1}{r} \frac{d}{dr} \{V_J(r)\} \right] + \left[ 1 + (-)^{\ell_p + \ell_h + J} \right] \\ & \times \left[ (\gamma_i + \gamma_p + 1) \frac{V_J(r)}{r^2} + (\gamma_h - \gamma_p - \gamma_i + \gamma_f) \left( \frac{V_J(r)}{r} \frac{d}{dr} + \frac{1}{r} f_p(r) \frac{d}{dr} \{f_h(r)\} \right) \right] \quad (55) \end{aligned}$$

with  $\alpha_1 = \alpha_{ph}^J$  and  $\alpha_2 = \alpha_{if}^J$ .

This formula includes natural-parity as well as unnatural-parity excitations. The expression  $[1 + (-)^{\ell_p + \ell_h + J}]$  is a 2 for natural parity and vanishes for unnatural parity. Thus, there is a derivative term only for natural parity excitation.

The interaction (55) is invariant under antisymmetrization. Direct and exchange terms add for  $T=1$  and cancel each other for  $T=0$ . This result was a priori evident: the  $\vec{L} \cdot \vec{S}$  interaction exists only for  $S=1$  and the relative angular momentum is conserved. The zero-range limit selects the smaller relative angular momentum which is 1. In the isospin formalism,  $\ell=1$ ,  $S=1$  involves  $T=1$ . So, the depths are -16 for  $V_p$  (twice the direct term) and -8 for  $V_n$ .

When the excited state is a collective one, there are many nucleons which take part in the excitation and it seems that the terms with  $\gamma_p$  or  $\gamma_h$  must cancel each other and, also,  $\frac{1}{r} f_p(r) \frac{d}{dr} \{f_h(r)\}$ . The interaction (55) becomes

$$[(\gamma_i - \gamma_f)(\gamma_i - \gamma_f + 1) - 2J(J+1)] \frac{V_J(r)}{r^2} - (\gamma_i + \gamma_f) \frac{1}{r} \frac{d}{dr} \{V_J(r)\} + 2(\gamma_f - \gamma_i) \frac{V_J(r)}{r} \frac{d}{dr}$$

This expression is not Hermitian. Its Hermitian part is:

$$[(\gamma_i - \gamma_f)(\gamma_i - \gamma_f + 1) - 2J(J+1)] \frac{V_J(r)}{r^2} - 2\gamma_i \frac{1}{r} \frac{d}{dr} \{V_J(r)\} + 2(\gamma_f - \gamma_i) \frac{V_J(r)}{r} \frac{d}{dr} \quad (56)$$

It is expression (12) multiplied by -2, within a factor 2 before  $J(J+1)$ .

Note that expression (56) is obtained by using  $\frac{1}{2r} \frac{d}{dr} \{V_J(r)\}$  as an approximation for  $\frac{1}{r} f_p(r) \frac{d}{dr} \{f_h(r)\}$  and the factor 2 before  $J(J+1)$  disappears if  $\alpha_1^2$  is replaced by 1. The same expression is obtained at the high energy limit, when  $\gamma_p$  and  $\gamma_h$  are small with respect to  $\gamma_i$  and  $\gamma_f$ . For an unnatural parity excitation, the same approximation leads to:

$$[(\gamma_i + \gamma_f + 2)(\gamma_i + \gamma_f + 1) - 2J(J+1)] \frac{V_J(r)}{r^2} - (\gamma_i + \gamma_f) \frac{1}{r} \frac{d}{dr} \{V_J(r)\}$$

In the peculiar case  $J=0$  and natural parity, summation over all the nucleons must lead to the optical model. Interaction (55) becomes:

$$2\gamma_p \frac{V_0(r)}{r^2} + 2(\gamma_p - \gamma_i) \frac{1}{r} \frac{d}{dr} \{V_0(r)\}$$

The factors  $\gamma_p$  disappear after summation on two complete shells ( $\ell, j = \ell + 1/2$ ) and ( $\ell, j = \ell - 1/2$ ) with the same radial functions. For a mirror nucleus, the  $\vec{L} \cdot \vec{S}$  interaction with a depth of  $-16$  MeV is equivalent to  $12$  MeV multiplied by the nuclear density, that is  $9$  MeV if  $r_0 = 1.1$  or  $7$  MeV if  $r_0 = 1.2$ .

Keeping  $V\mu^5$  constant, the matrix elements increase very quickly when  $\mu$  decreases. Although they are still smaller than their zero-range limit for a Yukawa form-factor with range  $\mu = 0.5$ , the results of a DWBA calculation for an inelastic scattering is almost the same as with interaction (51). Thus, the use of this limit is fully justified.

### 3.4. Shell effects

In all the expressions obtained, the eigenvalues of  $(\vec{L} \cdot \vec{\sigma})$  have a primary importance. There are two limiting cases:

- (1) recoupling in a single shell:  $\gamma_p = \gamma_h = \gamma$
- (2) a nucleon  $\ell, j = \ell + 1/2$  is excited into  $\ell, j = \ell - 1/2$ :  $\gamma_p - \gamma_h = 2\ell + 1$

Amongst the other possible excitations, the one with  $j_p - \ell_p = j_h - \ell_h$  is quite similar to the first case and the one with  $j_p - \ell_p \neq j_h - \ell_h$ , to the second case. Let us consider only a natural parity excitation and the zero-range

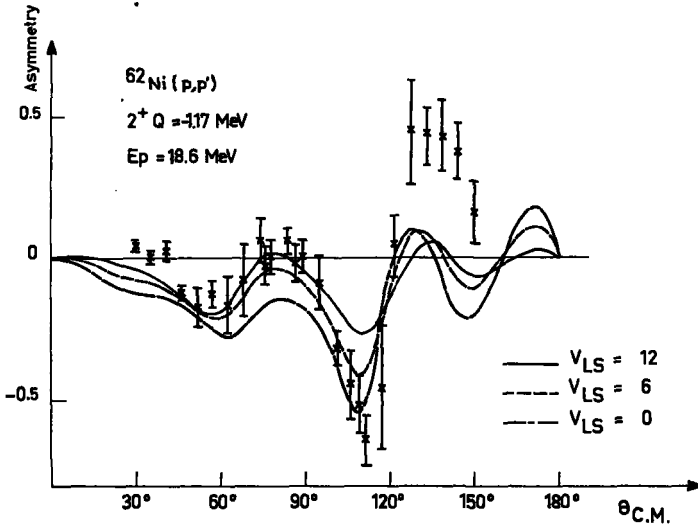


FIG.11. Asymmetry for  $^{62}\text{Ni}$  in the microscopic model. The mixed curve is obtained with  $V_{LS} = 0$ , the dashed one with  $V_{LS} = 6$  and the full one with  $V_{LS} = 12$  MeV, where  $V_{LS}$  is twice the direct term.

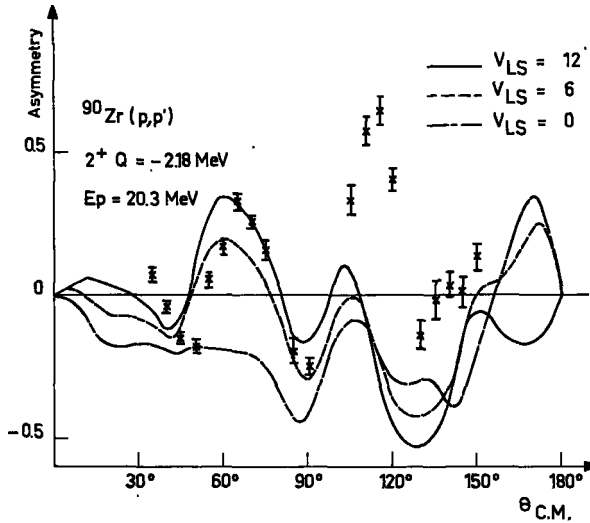


FIG.12. Asymmetry for  $^{90}\text{Zr}$ . Same notations as for Fig. 11.

limit. In the first case, there is no contribution coming from a  $(\vec{\sigma}_1 \cdot \vec{\sigma}_2)$  or a tensor interaction. The  $\vec{L} \cdot \vec{S}$  interaction is

$$[(\gamma_i - \gamma_f)(\gamma_i - \gamma_f + 1) - 2J(J+1) + 2\gamma] \frac{V_J(r)}{r^2} + 2(\gamma_f - \gamma_i) \frac{V_J(r)}{r} \frac{d}{dr} + (2\gamma - 2\gamma_i) \frac{1}{r} \frac{d}{dr} [V_J(r)]$$

It is almost the macroscopic interaction. In the second case, the geometrical coefficient of  $V_J(r)$  is smaller and the  $(\vec{\sigma}_1 \cdot \vec{\sigma}_2)$  interaction is more important since it is multiplied by  $(2l+1)(\gamma_i - \gamma_f)/J(J+1)$ . The effects of the  $\vec{L} \cdot \vec{S}$  interaction is steeped in those of the other parts of the interaction.

### 3.5. Results

The target is described by the wave function obtained by Gillet et al. [30] for nuclei with a closed shell. The open shell is described by quasi-particle excitations and the closed shell by particle-hole excitations. Schaeffer [31] has shown that, when the proton components are multiplied by some factor in order to fit the  $B(E2)$ , and the neutron component by another factor such that proton and neutron deformations are the same, the cross-section of inelastic scattering is reproduced by a DWBA calculation including antisymmetrization. But asymmetries are not fitted.

#### 3.5. a. Closed-shell effects

The zero-range limit of the  $\vec{L} \cdot \vec{S}$  interaction was used in the first calculations [32]. Figure 11 shows results obtained for  $^{62}\text{Ni}$ , in the same conditions as for Schaeffer calculations. The three curves are no spin-orbit, -6 MeV and -12 MeV respectively. The fit is definitely better at forward angles, including  $\vec{L} \cdot \vec{S}$  interaction, but the discrepancy remains at backward angles. Around  $100^\circ$ , the agreement is worse.

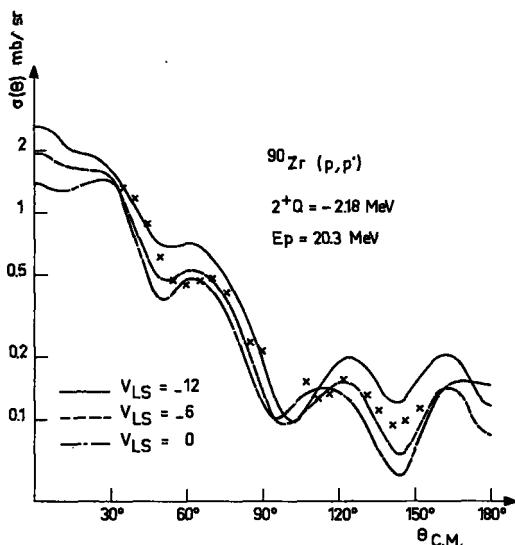


FIG.13. Cross-section for  $^{90}\text{Zr}$ . Same notations as for Fig.11.

Figure 12 shows results for  $^{90}\text{Zr}$  in the same conditions. An  $\vec{L} \cdot \vec{S}$  interaction of -12 MeV gives a good amplitude for the asymmetry around  $70^\circ$  but no agreement is obtained above  $90^\circ$ . The oscillations of the calculated curve are slightly at smaller angles than the experimental ones, and the first bump is weakened. Effects on cross-section (Fig. 13) are greater than for  $^{62}\text{Ni}$ , but quite similar to the ones in the macroscopic model.

For  $^{62}\text{Ni}$ , the amplitudes of proton configurations were multiplied by 2. The main contribution is  $(2p_{1/2}, f_{7/2}^{-1})$ . The neutron configurations are numerous and emerge from the shells  $2p_{3/2}$ ,  $2p_{1/2}$ ,  $f_{5/2}$  and  $g_{9/2}$ . For  $^{90}\text{Zr}$  the main proton configuration is a recoupling in  $g_{9/2}$ ; the neutron amplitudes were multiplied by 2.75 and the most important configuration is  $(2d_{5/2} - g_{9/2}^{-1})$ . Results are not very sensitive to the neutron-proton ratio. However, a calculation with protons only leads to a cross-section which depends drastically upon the  $\vec{L} \cdot \vec{S}$  interaction and an asymmetry which does not agree with the experiment.

As shown on Fig. 14, differences between finite range and zero-range limit for the  $\vec{L} \cdot \vec{S}$  interaction are small.

### 3.5. b. The two $2^+$ states of $^{54}\text{Fe}$

The first two  $2^+$  states of  $^{54}\text{Fe}$  are described mainly by a recoupling in  $f_{7/2}$  shell and  $(2p_{3/2} - f_{7/2}^{-1})$  for protons,  $(2p_{3/2} - f_{7/2}^{-1})$  for neutrons. The first  $2^+$  is mainly the recoupling in the  $f_{7/2}$  shell and the second one, the excitation of a proton into the  $f_{7/2}$  shell.

Figures 15 and 16 show the asymmetries and cross-sections obtained without  $\vec{L} \cdot \vec{S}$  interaction, with a zero-range one of intensity -16 MeV and a finite-range one. The agreement is worse than for  $^{90}\text{Zr}$  because the maximum of the asymmetry is found at  $80^\circ$  instead of  $90^\circ$ . Backward values are too small. Fit is better without antisymmetrization. Almost always the asymmetry is more negative at backward angles when one takes into account

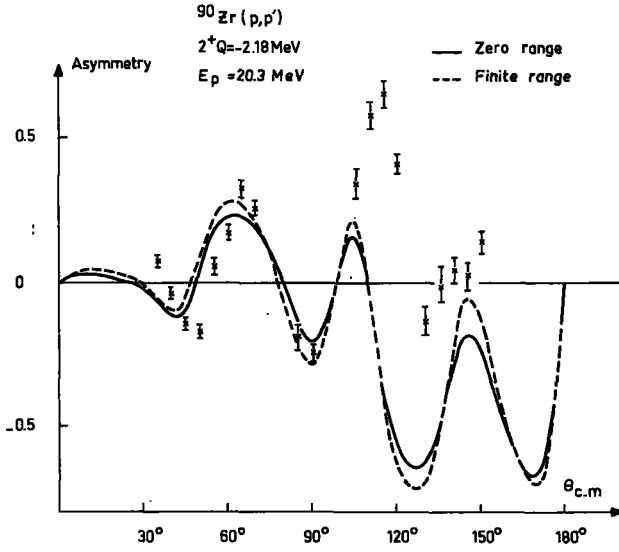


FIG.14. Comparison of the finite-range force described in the text with its zero-range limit for the asymmetry of  $^{90}\text{Zr}$ .

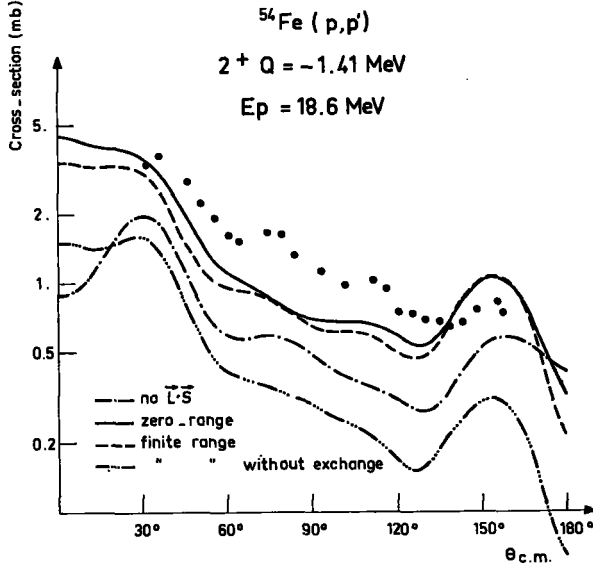
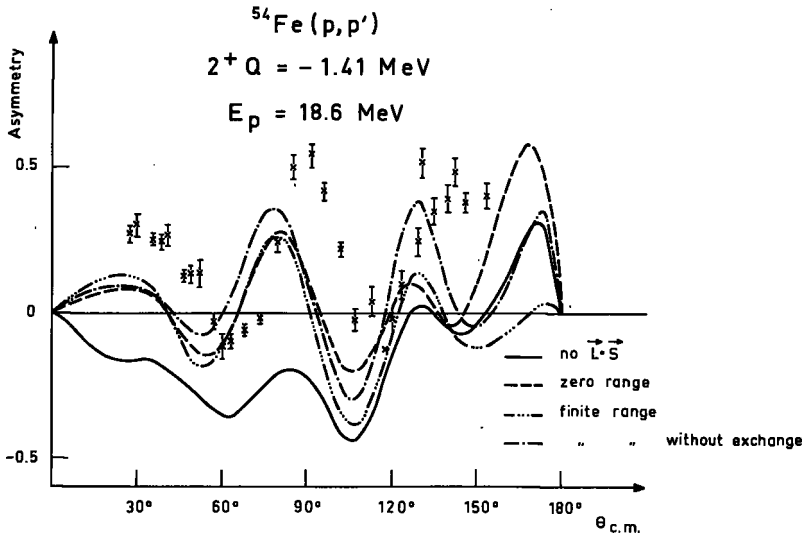
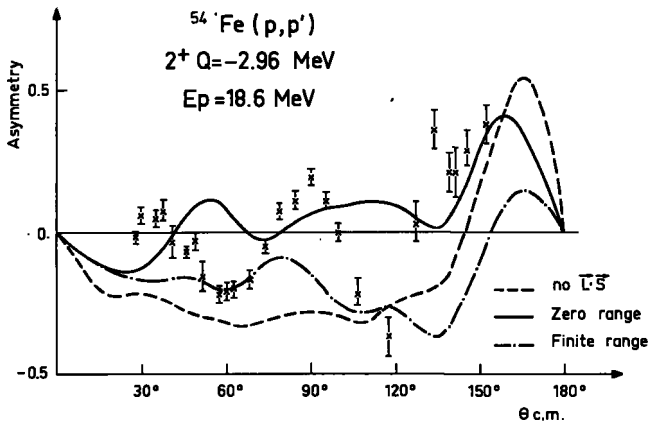


FIG.15. Cross-section for first  $2^+$  of  $^{54}\text{Fe}$  in the microscopic model.

FIG.16. Asymmetry for first  $2^+$  of  $^{54}\text{Fe}$  in the microscopic model.FIG.17. Asymmetry for second  $2^+$  of  $^{54}\text{Fe}$  in the microscopic model.

antisymmetrization than without. The Serber force used here can be inappropriate when an  $\vec{L} \cdot \vec{S}$  interaction is added. As shown in Fig. 17, the effects of  $\vec{L} \cdot \vec{S}$  interaction are not so clear for the second  $2^+$  state. These curves are obtained with the potential a. Results with potential b are worse: for example, the second  $2^+$  is affected more by the  $\vec{L} \cdot \vec{S}$  interaction than the first one, but the oscillations are opposite to the experimental ones. The angle of the maximum for the first  $2^+$  changes slightly with the potential.

The bad fit can come from the description of neutrons by only one important configuration. Figure 18 shows results obtained without antisymmetrization when the first  $2^+$  state is described by a recoupling in the  $f_{7/2}$

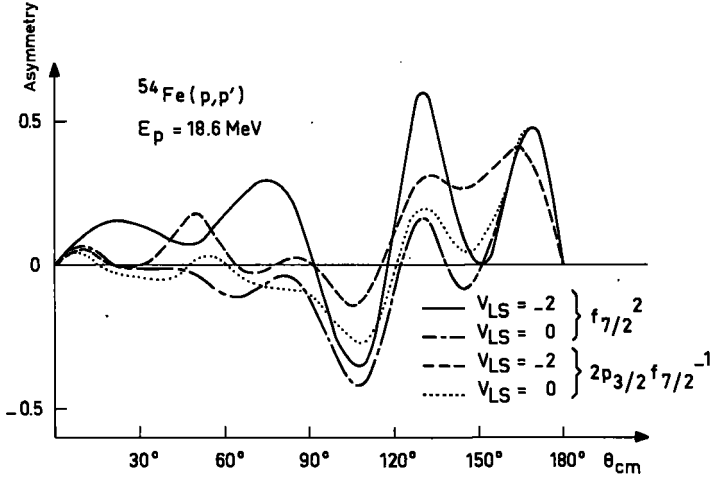


FIG.18. Results for  $^{54}\text{Fe}(p,p')$  obtained with a single configuration.

shell and the second one by  $2p_{3/2} - f_{7/2}^{-1}$ ; the central interaction is  $-10[1 - (\vec{\sigma}_1 - \vec{\sigma}_2)]$  with a Yukawa form-factor of range 1.4 fm. The curves are obtained without and with one fourth of the  $\vec{L} \cdot \vec{S}$  interaction in order to simulate the effects of other configurations by the relative enhancement of the central interaction. There is a large effect on the first  $2^+$  state with a maximum of asymmetry at  $75^\circ$  instead of the experimental  $90^\circ$ .

The two  $2^+$  states of  $^{54}\text{Fe}$  can be interpreted as mixing of these two configurations for protons and many configurations for neutrons, our description being too poor for neutrons. The asymmetry is dominated by the re-coupling in  $f_{7/2}$  shell. This configuration is the main one for the first  $2^+$  state and is weak for the second one, but its effects are clearly seen. If the computations of Fig.18 are completed with antisymmetrization, asymmetries become negative.

### 3.5.c. Use of cut-off

Fits with the macroscopic model are far better than those of the microscopic model. In the macroscopic model, form-factors are placed at the surface of the nucleus, while in the microscopic model they are pushed more inside. With a finite-range interaction there is almost no difference between the use of harmonic-oscillator wave-functions or solutions in a Saxon potential for the bound states. The microscopic description is insufficient (for example, for  $B(E2)$ ). This description seems to neglect certain components and a better description should give form-factors more at the surface.

Furthermore, a local potential is used for the unbound functions, but antisymmetrization corresponds to a non-local effect for the transition. A non-local potential is known to reduce the wave-function inside the nucleus.

For these two reasons, we have multiplied bound functions or free waves by a damping factor. Sometimes, a better fit is obtained at backward angles but we did not find a systematic effect. Although the use of a cut-off is fully justified, it does not seem to be the solution.

### 3.5.d. Unnatural parity states

Only one case has been studied up to now: the excitation of the  $0^+$  state in  $^{14}\text{N}$  of which the ground state is  $1^+$ . For unnatural-parity states, the tensor interaction is important as was shown with the cross-section of this inelastic scattering [33]. With an  $\vec{L} \cdot \vec{S}$  interaction, the oscillations of the asymmetry are, at least,  $20^\circ$  in advance compared to the experimental ones [34].

## 4. CONCLUSION

When the asymmetry of the inelastic scattering is taken into account, the microscopic model yields information on the structure of the excited state. A nucleon-nucleon  $\vec{L} \cdot \vec{S}$  interaction must be included. Studies on nuclei with a closed shell show that, for a natural-parity state, there are not only simple excitations of the open shell, but also polarization of the closed shell. Equal excitations of neutron and proton shells seem to be a good assumption. Large asymmetries are related to a simple excitation of the proton shell with many components for the neutron shell.

Besides a microscopic description which is perhaps not valid, a nucleon-nucleon interaction is necessary for these calculations. As is usual, we used a Serber force of range 1.4 fermi which leads to good fits for the inelastic cross-section. This force is only  $T=1$ ,  $S=0$  and  $T=0$ ,  $S=1$ . From the studies of the nucleon-nucleon interaction, we derived an  $\vec{L} \cdot \vec{S}$  interaction with so small a range that it is almost only  $T=1$ ,  $S=1$ . This force is similar to a  $T=1$ ,  $S=1$  central interaction with a very small range. The Hamada-and-Johnson  $T=1$ ,  $S=1$  central force has the same strength as the  $\vec{L} \cdot \vec{S}$  interaction for the range  $\mu/2$ , but with a change of sign and is much smaller for the range  $\mu/3$ . There is no complete justification for the interaction which was used.

By comparison of microscopic calculations with and without spin-orbit coupling, some parameter  $\lambda$  can be defined, which ranges from 0 (no effect) to 3 ( $^{90}\text{Zr}$ ) and characterizes the nuclear structure. For example,  $\lambda=3$  corresponds to a recoupling of two protons in a shell and a collective neutron structure. A macroscopic calculation with  $\beta_{LS} = \lambda\beta_c$  gives good fits.

## REFERENCES

- [1] Polarization Phenomena in Nuclear Reactions (Proc. 3rd Int. Symp., Madison 1970) (BARSHALL, H.H., HAEBERLI, W.), The University of Wisconsin Press Madison (1971).
- [2] BEURTEY, R., Thesis Report CEA 2366.
- [3] Proceedings of the International Symposium on Polarization Phenomena of Nucleons (HUBER, P., MEYER, K.F.), Birkhäuser Verlag Basel und Stuttgart (1961).
- [4] Proceedings of the 2nd International Symposium on Polarization Phenomena of Nucleons (HUBER, P., SCHOPPER, H.), Birkhäuser Verlag Basel und Stuttgart (1966).
- [5] GARIN, A. et al., Physics Letts 21 (1966) 73.
- [6] ECCLES, S.F. et al., Phys. Rev. 141 (1966) 1067.
- [7] GLASSHAUSER, C. et al., Phys. Rev. 164 (1967) 1437.
- [8] GLASSHAUSER, C. et al., Phys. Rev. 181 (1969) 1217.
- [9] TAMURA, T., Ann. Rev. Nucl. Sci. 19 (1969) 99.
- [10] RAYNAL, J., Symposium sur les Mécanismes de Réactions Nucléaires et phénomènes de Polarisation - Université, Laval, Québec (1969).

- [11] SHERIF, H., BLAIR, J.S., *Physics Letts* 26B (1968) 489.
- [12] SHERIF, H., Spin-dependent effects in proton inelastic scattering, Thesis University of Washington (1968).
- [13] SHERIF, H., de SWINIARSKI, R., *Physics Letts* 28B (1968) 96.
- [14] SHERIF, H., *Nucl. Phys. A* 131 (1969) 532.
- [15] RAYNAL, J., *Nucl. Phys. A* 97 (1967) 572.
- [16] There are some errors in formulae of the Appendix of Ref.[15] for the  $\vec{L} \cdot \vec{S}$  interaction. Correct formulae can be found in Ref. [10].
- [17] HAMADA, T., JOHNSON, I.D., *Nucl. Phys.* 34 (1962) 382.
- [18] BRESSEL, C.N. et al., *Nucl. Phys. A* 124 (1969) 624.
- [19] We always use notations of Appendix C of *A Messiah - Mécanique quantique*, Dunod, Paris (1960).
- [20] GLASSHAUSER, C., THIRION, J., *Adv. Nucl. Physics*, Plenum Press, New York (1969).
- [21] RAYNAL, J., *Equations couplées et DWBA*, Aussois (1968), Report LYCEN N. 6804.
- [22] RUSH, A.A., GANGULY, N.K., *Nucl. Phys. A* 117 (1968) 101.
- [23] LOMBARD, R.M. et al., *J. Physique* 31 (1970) C2-90.
- [24] de SWINIARSKI, R., BACHER, A.D., RESMINI, F.G., PLATTNER, G.R., HENDRIE, D.I., RAYNAL, J. (to be published).
- [25] SCHAEFFER, R., RAYNAL, J., DWBA 70 (unpublished).
- [26] JACOB, M., WICK, G.C., *Ann. Phys.* 7 (1959) 404.
- [27] JACOB, M., *Théorie Formelle des Collisions et Etats Propres d'Hélicité*, Thesis Paris (1961).
- [28] BOHR, A., MOTTELSON, B., *Nuclear Structure*, Benjamin, New-York (1969).
- [29] SATCHLER, G.R., *Nucl. Phys.* 37 (1965) 879.
- [30] GILLET, V. et al., *Phys. Rev.* 178 (1969) 1695.
- [31] SCHAEFFER, R., *Un Modèle Microscopique pour la Diffusion Inélastique à Basse et Moyenne Energie*, Thesis (Orsay 1969), Report CEA R 4000.
- [32] RAYNAL, J., *J. Physique* 31 (1970) C2-92.
- [33] CRAWLEY, G.M. et al., *Physics Letts* 32B (1970) 92.
- [34] ESCUDIE, J.L., TARRATS, A., RAYNAL, J., Ref.[4], p. 705.

#### NOTE ADDED IN PROOF

Since the lecture given at Trieste, a difference of a factor 4 has been pointed out between my own notation of two-body spin-orbit interaction and the Hamada and Johnson one. Consequently, I overestimated this interaction by a factor four. After correction the two-body spin-orbit interaction is much smaller than the optical-model one and not slightly stronger.

In fact, the value used here seemed quite too large, but the Hamada and Johnson value, after correction, seems to be too small.

# A UNIFIED THEORY OF NUCLEAR REACTIONS AND BOUND STRUCTURES AND CLUSTER REPRESENTATIONS\*

K. WILDERMUTH

Institute for Theoretical Physics,  
University of Tübingen,  
Federal Republic of Germany

## Abstract

A UNIFIED THEORY OF NUCLEAR REACTIONS AND BOUND STRUCTURES AND CLUSTER REPRESENTATIONS.

1. Introduction; 2. Special examples; 3. Generalization of theory and influence of Pauli principle; 4. Combination of shell-model- and other bound-state calculations with cluster reaction calculations. Semi-quantitative considerations; 5. Discussion of some general properties of the unified theory of nuclei; 6. Conclusions.

## 1. INTRODUCTION.

As a starting point for a quantum-mechanical description of a many-particle system one can use the time-dependent Schrödinger equation for the many particle wave-function  $\Psi$

$$H\Psi = \frac{\hbar}{i} \frac{\partial}{\partial t} \Psi \quad (1)$$

where

$$H = \sum_{i=1}^A \frac{p_i^2}{2M} + \sum_{i>k=1}^A V(i, k) - T_{cm} \quad (2)$$

is the Hamiltonian of the system where the kinetic energy of the centre of mass  $T_{cm}$  is subtracted.

Usually, one tries to solve Eq.(1) by expanding  $\Psi$  into a complete orthogonal set of eigenfunctions belonging to a certain Hamiltonian  $H_0$ . In nuclear physics, very often products of single-particle shell-model wave-functions are used. However, in this way, it is practically impossible to treat nuclear reactions of complex nuclei as, e.g. the scattering of deuterons or  $\alpha$ -particles on other nuclei. This is because the expansion of the pertinent scattering wave functions having the correct boundary conditions into a fixed set of single-particle shell-model wave-functions becomes very complicated. Therefore, one has to look for a method which allows from the beginning the boundary conditions which belong to the considered reaction process to be

---

\* These lecture notes were rewritten by D. Clement, University of Tübingen, Federal Republic of Germany.

introduced into the ansatz for  $\Psi$ . This can be done in a basically very simple way by formulating the Schrödinger equation (1) as a projection equation<sup>1</sup>:

$$\langle \delta\Psi | H - \frac{\hbar}{i} \frac{\partial}{\partial t} | \Psi \rangle = 0 \quad (3)$$

As usual, the Dirac brackets indicate that one has to integrate and to sum over the whole range of space- and spin-isospin co-ordinates, respectively. If  $\delta\Psi$  describes a completely arbitrary variation of  $\Psi$  at a given instant  $t$  in the function space which belongs to the above co-ordinates then Eq.(3) means that

$$\left( H - \frac{\hbar}{i} \frac{\partial}{\partial t} \right) \Psi$$

must be orthogonal to any arbitrary function in this function space. This will evidently be the case only if  $\Psi$  obeys the Schrödinger equation (1). Therefore Eq.(3) is just another formulation of Eq.(1) if  $\delta\Psi$  describes a completely arbitrary variation of  $\Psi$ . However, as we shall see later on, Eq.(3) allows us to introduce from the beginning the correct boundary conditions into the wave-function  $\Psi$ .

If we make for  $\Psi$  the ansatz

$$\Psi = \psi \exp \left[ \frac{i}{\hbar} Et \right] \quad (4)$$

and insert it into Eq.(3) we obtain the reformulated stationary Schrödinger equation

$$\langle \delta\psi | H - E | \psi \rangle = 0 \quad (5)$$

In the same way as for the usual time-dependent Schrödinger equation any time-dependent solution of Eq.(3) can be represented as a linear superposition of stationary solutions of Eq.(5). Therefore, in our further considerations we shall stick to the more simple Eq.(5).

We shall now briefly discuss some general properties of the solutions of Eq.(5) which we shall need at a later stage.

Let us make for  $\psi$  the ansatz

$$\psi = \sum_r a_r \varphi_r + \int a_k \varphi_k dk \equiv \sum_k a_k \varphi_k \quad (6)$$

where  $a_r$  and  $a_k$  are discrete and continuous linear variational parameters<sup>2</sup>.

<sup>1</sup> Why we prefer to call Eq.(3) a projection equation and not a variational equation will be discussed later.

<sup>2</sup> How one chooses the functions  $\varphi_r$  and  $\varphi_k$  for a given problem will be discussed in section 2 by means of some special examples.

By inserting this ansatz into Eq. (5) we obtain a coupled set of integral equations of the form

$$\langle \varphi_{k'} | H - E | \sum_k a_k \varphi_k \rangle = 0$$

-----

(7)

where  $k'$  can assume discrete and continuous values. The set of Eqs (7) follows from the fact that the variation  $\delta\psi$  is obtained by any arbitrary variation of the discrete and continuous linear amplitudes  $a_k$

$$\delta\psi = \sum_k \delta a_k \varphi_k$$
(8)

If the  $\varphi_k$  form a complete set of functions of the co-ordinates of the many-particle system considered then the eigensolutions of the coupled Eqs (7) are equal to the time-independent solutions of Eq. (1). We wish to emphasize that the functions  $\varphi_k$  need not be orthogonal to each other but only linearly independent.

When all degeneracies are removed then the eigensolutions of Eqs (7) are mutually orthogonal. This will be the case even if we restrict the number of variational parameters in the ansatz (6). To prove these orthogonality relations we consider the two normalized solutions  $\psi_n$  and  $\psi_{n'}$ :

$$\psi_n = \sum_k a_k^n \varphi_k$$
(9a)

$$\psi_{n'} = \sum_k a_k^{n'} \varphi_k$$
(9b)

which belong to the sets of equations

$$\langle \varphi_k | H - E_n | \psi_n \rangle = 0$$

-----

(10a)

$$\langle \varphi_k | H - E_{n'} | \psi_{n'} \rangle = 0$$

-----

(10b)

After multiplying all Eqs (10a) by  $(a_k^n)^*$  and (10b) by  $(a_k^{n'})^*$  we obtain by summing or integrating all equations over  $k$ :

$$\langle \psi_n | H - E_n | \psi_n \rangle = 0$$
(11a)

$$\langle \psi_{n'} | H - E_{n'} | \psi_{n'} \rangle = 0$$
(11b)

When we subtract the complex conjugate of Eq.(11b) from Eq.(11a) then due to the hermiticity of H we get

$$\langle \psi_{n'} | \psi_n \rangle = \delta(n, n') \quad (12)$$

$$\langle \psi_n | H | \psi_{n'} \rangle = \langle \psi_{n'} | H | \psi_n \rangle = E_n \delta(n, n') \quad (13)$$

where the symbol  $\delta(n, n')$  means the Kronecker symbol  $\delta_{nn'}$  in the case of discrete  $n$  and the Dirac  $\delta$ -function  $\delta(n-n')$  for continuous values of  $n$ .

Equations (12) and (13) show that even if we restrict the number of linear variational parameters to some finite value, i. e. we only work in a sub-space of the Hilbert space, then we have the result, that 1) any two solutions  $\psi_n$  and  $\psi_{n'}$  are orthonormalized, and that 2) in this sub-space the Hamiltonian H can be represented by a real diagonal matrix. This corresponds completely to the behaviour of the usual Schrödinger equation.

In a practical calculation one has to restrict the number of the linear variational parameters, i. e. the number of trial functions  $\varphi_k$  in the ansatz (6) for the wave function  $\psi$ . It is quite reasonable to neglect in expression (6) all those terms  $\varphi_k$  which can be expected to have a very small amplitude  $a_k$  in the final stationary solution of Eq.(5). An indication for this is the following. Suppose, in a first approximation, that there is a given set of functions  $\varphi_k$  which have energy expectation values  $\langle \varphi_k | H | \varphi_k \rangle$  near to the considered energy value  $E$  of the system. Then it can be shown that any function  $\varphi_\nu$  for which

$$\left| \frac{\langle \varphi_k | H | \varphi_\nu \rangle}{E - \langle \varphi_\nu | H | \varphi_\nu \rangle} \right| \ll 1 \quad (14)$$

will have a relatively small amplitude  $a_\nu$ . In other words, a function  $\varphi_\nu$  which has a small overlap  $\langle \varphi_k | H | \varphi_\nu \rangle$  and whose expectation value of the energy  $\langle \varphi_\nu | H | \varphi_\nu \rangle$  lies far away from the energy  $E$  of the system, will give only a small contribution to the wave function  $\psi$ . For a more detailed discussion of condition (14) we refer to Ref. [1].

In the following parts of this paper, we shall first consider some special examples which will show how the correct boundary conditions are introduced into the ansatz for the wave-function  $\psi$  of a given reaction process or bound state problem. By virtue of these examples we shall discuss also how one can approximately solve Eq.(5) and the coupled Eqs (7), respectively.

After this we shall discuss how one can make use of Eq.(5) in order to investigate the general features of a unified theory of nuclear reactions and bound structures. By this we shall see how one can formulate such a unified theory.

## 2. SPECIAL EXAMPLES

### a) Scattering of neutrons on $\alpha$ -particles

The Hamiltonian for the  $n$ - $\alpha$ -system is of the form

$$H = - \frac{\hbar^2}{2M} \left[ \sum_{i=1}^5 \nabla_i^2 - \frac{1}{5} \left( \sum_{i=1}^5 \nabla_i \right)^2 \right] + \sum_{i>k=1}^5 V(i, k) \quad (15)$$

The first part in expression (15) contains the kinetic energy of the five nucleons in the centre of mass system. The potentials  $V(i, k)$  are supposed to be 2-nucleon-potentials chosen in such a way that they describe approximately the low-energy two-nucleon scattering data as well as the two-nucleon bound-state data. A simple potential of that kind is, for example,

$$V(i, k) = -V_0 \exp\left[-\kappa (\vec{r}_i - \vec{r}_k)^2\right] \cdot \left\{w + m P_{ik}^r + b P_{ik}^o - h \cdot P_{ik}^r\right\} \quad (16)$$

where  $V_0 = 72.98 \text{ MeV}; \quad \kappa = 0.46 \times 10^{-26} \text{ cm}^{-2}$   
 $w = m = 0.41; \quad b = h = 0.09$

and  $w, m, b, h$  as usually stand for the amplitudes of the Wigner, Majorana, Bartlett and Heisenberg forces.

Additional terms describing spin-orbit, tensor and Coulomb interactions have to be added. In general, these terms do not substantially influence our fundamental considerations. Therefore, these terms will not be taken into account explicitly, but we shall mention when their influence plays an important role.

Now, the  $\alpha$ -particle has a very tightly bound structure. Therefore, any configuration  $\varphi_{\text{exc}}$  of the  $n$ - $\alpha$ -system where the  $\alpha$ -particle is in an internally excited state has a large energy distance from the low-energy  $n$ - $\alpha$ -scattering configuration. Furthermore, the overlap  $\langle \varphi_{\text{exc}} | H | \varphi_{n-\alpha} \rangle$  is relatively small, too. Therefore, having in mind formula (14), for low  $n$ - $\alpha$ -scattering energies ( $E \ll 20 \text{ MeV}$ ), we can approximately neglect configurations of the above kind in the pertinent wave-function  $\psi$ . In other words, we neglect distortion effects on the  $\alpha$ -particle (except those due to the Pauli principle). Therefore the following ansatz for  $\psi$  seems to be justified:

$$\psi = \mathcal{A} \left\{ \varphi(\alpha) \cdot \chi(\vec{r}_5 - \vec{R}_\alpha) \cdot f(t_i, s_i) \right\} \quad (17)$$

Here and in the following  $\mathcal{A}$  means the antisymmetrizer. The function  $\varphi(\alpha)$  describes the internal spatial structure of the  $\alpha$ -cluster. We assume the following simple form of a product of Gaussians

$$\varphi(\alpha) = \varphi(\vec{r}_1, \dots, \vec{r}_4) = \exp\left[-\frac{\beta}{2} \sum_{i=1}^4 (\vec{r}_i - \vec{R}_\alpha)^2\right] \quad (18)$$

$$\vec{R}_\alpha = \frac{1}{4} (\vec{r}_1 + \vec{r}_2 + \vec{r}_3 + \vec{r}_4); \quad \beta = 0.5 \times 10^{26} \text{ cm}^{-2}$$

The parameter  $\beta$  was chosen in such a way that  $\varphi(\alpha)$  yields the experimental mean-square-radius of the  $\alpha$ -particle.

The function

$$f(t_i, s_i) = (\alpha_s(1) \alpha_\tau(1)) (\beta_s(2) \alpha_\tau(2)) (\alpha_s(3) \beta_\tau(3)) \times (\beta_s(4) \beta_\tau(4)) (\alpha_s(5) \beta_\tau(5)) \quad (19)$$

describes the spin- and isospin configuration. The  $\alpha_s$ ,  $\beta_s$ ,  $\alpha_\tau$ ,  $\beta_\tau$  are the well known Pauli spin- and isospin functions, respectively. Their product is written in such a way that  $f(t_i, s_i)$  is an eigenfunction of the third component of spin and isospin:

$$S_Z = \sum_{i=1}^5 S_{Zi}; \quad T_3 = \sum_{i=1}^5 \tau_{3i} \quad (20)$$

with quantum numbers  $S_Z = \frac{1}{2}$ ;  $T_3 = -\frac{1}{2}$ . Moreover, after antisymmetrization  $\psi$  should be an eigenfunction of the total spin  $\vec{S}^2$  and isospin  $\vec{T}^2$

$$\vec{S}^2 = \left( \sum_{i=1}^5 S_{Xi} \right)^2 + \left( \sum_{i=1}^5 S_{Yi} \right)^2 + \left( \sum_{i=1}^5 S_{Zi} \right)^2 \quad (21)$$

$$\vec{T}^2 = \left( \sum_{i=1}^5 \tau_{1i} \right)^2 + \left( \sum_{i=1}^5 \tau_{2i} \right)^2 + \left( \sum_{i=1}^5 \tau_{3i} \right)^2 \quad (22)$$

The required quantum numbers are  $S = 1/2$  and  $T = 1/2$ . That this comes out by using the product (19) is due to the fact that the function  $\varphi(\alpha)$  is a completely symmetric function of all four spatial co-ordinates.

The function  $\chi(\vec{r}_5 - \vec{R}_\alpha)$  describes the relative motion between the neutron and the  $\alpha$ -particle and represents the continuous variational amplitudes which are varied arbitrarily. In order to make this point clear in more detail we write down the wave function  $\psi$  as

$$\psi = \int \mathcal{A} \left\{ \varphi(\vec{r}_1, \vec{R}_\alpha) \cdot \chi(\vec{R}') \delta(\vec{R} - \vec{R}') f(t_i, s_i) \right\} d\vec{R}' \quad (23)$$

$$\vec{R} = \vec{r}_5 - \vec{R}_\alpha$$

Obviously, integrating over the parameter co-ordinate  $\vec{R}'$  one regains the wave function in the form (17). We want to point out that the antisymmetrizer  $\mathcal{A}$  acts merely on the (physical) nucleon co-ordinates, i. e.  $\vec{r}_1, \vec{r}_2, \dots, \vec{r}_5$  (and by this also on the relative vector  $\vec{R}$ ), but not on the parameter co-ordinates, i. e. here  $\vec{R}'$ .

The wave-function  $\psi$ , as it is written in expression (23), represents a continuous linear superposition of trial functions of the form

$$\mathcal{A} \left\{ \varphi(\vec{r}_1, \vec{R}_\alpha) \delta(\vec{R} - \vec{R}') f(t_i, s_i) \right\} \quad (24)$$

which describe the  $n - \alpha$  clusters having a relative distance  $\vec{R}'$ . The continuous amplitude of each of these trial functions which has to be varied arbitrarily at every point  $\vec{R}'$  is now given by the factor  $\chi(\vec{R}')$ . Therefore we have

$$\delta\psi = \int \delta\chi(\vec{R}') \mathcal{A} \left\{ \varphi(\vec{r}_1, \vec{R}'_\alpha) f(t_1, s_1) \delta(\vec{R} - \vec{R}') \right\} d\vec{R}' \quad (25)$$

We see from this that the ansatz (17) or (23) for the wave-function  $\psi$  corresponds to the term  $\int a_k \varphi_k dk$  in Eq. (6).

Going now into more details on antisymmetrization we first note that after inserting Eq. (17) or (23) into Eq. (7) we must antisymmetrize on one side of the expression only, i. e. either  $\delta\psi$  or  $\psi$ . Namely, because of the hermiticity of  $\mathcal{A}$  and the symmetry of H with respect to all nucleon coordinates we can put both  $\mathcal{A}$  on one side. Having done this we can use the property  $\mathcal{A}^2 = A! \mathcal{A}$ . This reduces the amount of calculations quite considerably. Normally it is more practical if one antisymmetrizes the wave function  $\psi$  standing on the right side. In low-energy problems the wave function  $\psi$  often has a simple structure. This results in many exchange terms due to antisymmetrization being either equal to each other or not contributing to Eq. (7), at all; i. e. in our example, because of the symmetry of the ansatz (17) and the fact that in the potentials  $V(i, k)$  in Eq. (16) the spin exchange (Bartlett) force and the charge-exchange (Heisenberg) force appear with exactly the same factors but opposite signs, the contributions of these forces cancel each other. Furthermore, the Wigner force having no exchange character, as well as the space exchange (Majorana) force do not change the spin and isospin configuration. Therefore, only those terms of the antisymmetrized wave-function  $\psi$  contribute which have the same spin and isospin configuration as  $\delta\psi$ . By this the number of terms in the wave function  $\psi$  which contribute in our special example to Eq. (7) is reduced to only two terms, the 'direct' term

$$\psi_D = \exp \left[ -\frac{\beta}{2} \sum_{i=1}^4 (\vec{r}_i - \vec{R}'_\alpha)^2 \right] \times \chi(\vec{r}_5 - \vec{R}'_\alpha^D) \times f(t_1, s_1) \quad (26)$$

$$\vec{R}'_\alpha^D = \frac{1}{4} (\vec{r}_1 + \vec{r}_2 + \vec{r}_3 + \vec{r}_4)$$

and the so-called 'one-particle-exchange term'

$$\psi_1 = - \exp \left[ -\frac{\beta}{2} \sum_{\substack{i=1 \\ i \neq 3}}^5 (\vec{r}_i - \vec{R}'_\alpha^1)^2 \right] \times \chi(\vec{r}_3 - \vec{R}'_\alpha^1) \times f(t_1, s_1) \quad (27)$$

$$\vec{R}'_\alpha^1 = \frac{1}{4} (\vec{r}_1 + \vec{r}_2 + \vec{r}_4 + \vec{r}_5)$$

The minus sign in front of the right-hand side of Eq. (27) appears because this term represents a one-particle (odd) permutation of the original ('direct') order of nucleons.

The calculations are simplified further because again due to the symmetrical structure of the wave function many terms in the sum

$$\sum_{i > k=1}^5 V(i, k)$$

turn out to be equal to each other or cancel each other. For further discussions of this point we refer to [1].

For practical calculations it is usually not necessary to decompose the wave function  $\psi$  as it was done in Eq.(23)<sup>3</sup>. This means that in Eq.(7) we can write  $\delta\psi$  which needs not be antisymmetrized any more as

$$\delta\psi = \delta\chi(\vec{R}) \varphi(\alpha) f(t_1, s_1) \quad (28)$$

If in Eq.(7) we carry out all summations over spin and isospin co-ordinates as was pointed out above<sup>4</sup> and all integrations over the space co-ordinates except that over the relative co-ordinate  $\vec{R} = \vec{r}_5 - \vec{R}_\alpha$  and if we set the factor by which the arbitrary variation  $\delta\chi(\vec{R})$  is multiplied equal to zero we obtain a definitive equation for  $\chi(\vec{R})$  which is, in fact, an integro-differential equation of the following form:

$$\left\{ -\frac{\hbar^2}{2M_{\text{red}}} \Delta_{\vec{R}} + V(\vec{R}) \right\} \chi(\vec{R}) + \int K(\vec{R}, \vec{R}') \chi(\vec{R}') d\vec{R}' = E_k \cdot \chi(\vec{R}) \quad (29)$$

$$\frac{1}{M_{\text{red}}} = \frac{1}{4M} + \frac{1}{M} = \frac{5}{4M}$$

In case of scattering processes,  $E_k$  is the relative kinetic energy of the two fragments, here the  $\alpha$ -particle and the neutron, for  $|\vec{R}| \rightarrow \infty$ . The potential  $V(\vec{R})$  which describes the effective local  $n$ - $\alpha$ -interaction stems essentially from the direct term (26) in  $\psi$ . The effective non-local  $n$ - $\alpha$ -potential which is expressed by the kernel  $K(\vec{R}, \vec{R}')$  stems essentially from the exchange terms in  $\psi$  (here  $\psi_1$  of Eq.(27)) and from the exchange forces (here Majorana forces). It should be mentioned that  $K(\vec{R}, \vec{R}')$  depends explicitly on the total energy  $E$ . Because of the hermiticity of the Hamiltonian (15), the direct potential  $V(\vec{R})$  turns out to be real whereas  $K(\vec{R}, \vec{R}')$  will be Hermitian which means that

$$K(\vec{R}, \vec{R}') = K^*(\vec{R}', \vec{R}) \quad (30)$$

Furthermore, because of the rotational invariance of the Hamiltonian (15) and the neglect of spin-orbit as well as tensor forces (by this, no spin-orbit effects are taken into account), the direct potential  $V(\vec{R})$  is, in fact, a

<sup>3</sup> The main advantage of such a decomposition will be evident, especially if one deals with basic investigations, as e.g. the general behaviour of rotational states.

<sup>4</sup> Because of the normalization of  $f(t_1, s_1)$  in expression (19) the summation over spin and isospin co-ordinates yields a factor of 1.

function of  $R = |\vec{R}|$  only, and the kernel  $K(\vec{R}, \vec{R}')$  depends on  $R = |\vec{R}|$ ,  $R' = |\vec{R}'|$  as well as  $(RR')$ . Therefore one can expand  $K(\vec{R}, \vec{R}')$  in the following way:

$$\begin{aligned} K(\vec{R}, \vec{R}') &= \sum_{\ell} \bar{K}_{\ell}(R, R') Y_{\ell, 0}(\cos \gamma) \\ &= \sum_{\ell} \bar{K}_{\ell}(R, R') \left[ \sum_{m=-\ell}^{\ell} Y_{\ell m}^{*}(\vartheta, \varphi) Y_{\ell m}(\vartheta', \varphi') \right] \end{aligned} \quad (31)$$

where  $\gamma$  stands for the angle between  $\vec{R}$  and  $\vec{R}'$ , whereas  $(\vartheta, \varphi)$  and  $(\vartheta', \varphi')$  denote the directions of  $\vec{R}$  and  $\vec{R}'$ , respectively, in spherical co-ordinates. If we consider scattering processes which are rotationally symmetric around the z-axis, and expand also  $\chi(\vec{R})$  into spherical harmonics we obtain

$$\chi(\vec{R}) = \sum_{\ell} \frac{u_{\ell}(R)}{R} Y_{\ell, 0}(\vartheta, \varphi) \quad (32)$$

After inserting Eqs (31) and (32) into Eq.(29) and using the orthogonality relations for the spherical harmonics we are left with the following set of (uncoupled) integro-differential equations for the radial functions  $u_{\ell}(R)$ :

$$\begin{aligned} \left[ -\frac{\hbar^2}{2M_{\text{red}}} \cdot \left( \frac{d^2}{dR^2} - \frac{\ell(\ell+1)}{R^2} \right) + V(R) \right] u_{\ell}(R) \\ + \int K_{\ell}(R, R') u_{\ell}(R') dR' = E_{\ell} u_{\ell}(R) \quad \ell = 0, 1, 2, \dots \end{aligned} \quad (33)$$

where we have substituted  $K_{\ell}(R, R') = R \cdot \bar{K}_{\ell}(R, R') \cdot R'$ .

The fact that we obtain a separate integrodifferential equation for each partial wave with angular momentum  $\ell \hbar$  is a consequence of the rotational invariance of the Hamiltonian (15) and expresses the conservation of angular momentum. Thereby, we derived a non-local Hermitian potential  $K_{\ell}(R, R')$  which depends explicitly on the quantum number  $\ell$  and the energy  $E$ . Already in this rather simple example the analytic expressions for the direct and non-local potentials are rather complicated. The direct potential  $V(R)$ , for example, is of the form

$$V(R) = -V_0(4w-m) \left( 1 + \frac{3\kappa}{4\beta} \right)^{-3/2} \exp \left[ -\frac{\kappa}{1 + \frac{3\kappa}{4\beta}} R^2 \right] \quad (34)$$

For the non-local part  $K_{\ell}(R, R')$  which is much more complicated we refer to Ref. [2].

In principle, equations of the form (29) or (33) are able to describe bound states - if the potentials  $V(i, k)$  are sufficiently attractive - as well as elastic-scattering states. For bound states besides the boundary condition, which states that  $u_{\ell}(R)$  must tend to zero for  $R \rightarrow 0$ , we have to require that  $u_{\ell}(R)$  tend to zero for  $R \rightarrow \infty$ , too. This leads to an eigenvalue equation for

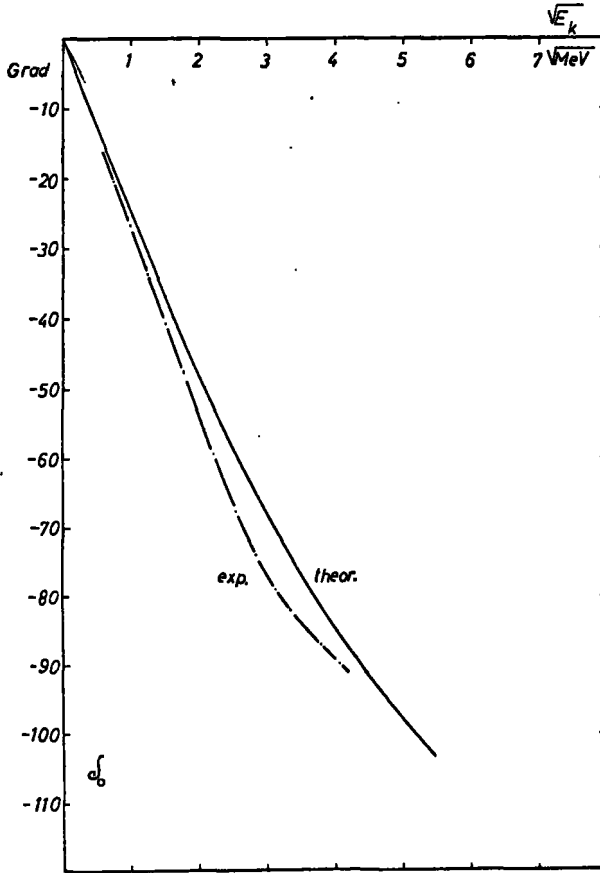


FIG. 1. *s*-wave phase shift of elastic *n*- $\alpha$ -scattering. Experimental curve: [3], theoretical curve see, e.g. Ref. [4].

the bound-state energies  $E_k$ . For scattering states,  $E_k$  is given, and one has the boundary condition that for  $R \rightarrow \infty$  there are incoming and outgoing waves. This is completely analogous to the boundary conditions of the simple one-particle Schrödinger equation.

In Fig. 1 both the experimental and the calculated phase shifts for the *S*-wave elastic scattering of neutrons on  $\alpha$ -particles are plotted<sup>5</sup>.

Going up to scattering energies of 15 to 20 MeV  $E_{cm}$  it becomes now energetically possible for the  $\alpha$ -cluster to be broken up. Therefore, according to our considerations in section 1, one has to take into account, at least, the next energetically favoured cluster configuration which is, in fact, a deuteron-triton configuration where the deuteron cluster is contained in a triplet state. That this can be expected is due to the fact that the two-nucleon forces between a proton and a neutron are more attractive in the

<sup>5</sup> As to the derivation of the phase shift from the asymptotic behaviour of  $u_\rho(R)$ , see e.g. Ref. [15].

case of a  $^3S$ - than in the case of a  $^1S$ -configuration. Furthermore, owing to the same argument, in the case of an  $L = 0$  relative motion between  $d$  and  $t$ , the parallel alignment of the two spins of the clusters is energetically more favourable than the antiparallel one. Summarizing, we can say that we can expect the lowest-lying  $n$ - $\alpha$ -configuration to be followed energetically by a  $t$ - $d$ -configuration having a total spin  $S = 3/2$  and a relative orbital angular momentum  $L = 0$ .

As an extension of the  $n$ - $\alpha$ -scattering as considered above we are now going to discuss briefly the coupling between the  $n$ - $\alpha$ -channel and the  $t$ - $d$ -configuration just mentioned. Rotational invariance of the Hamiltonian and its invariance under space reflection lead to conservation of total angular momentum  $J$  and parity  $\pi$ , respectively. This means, in our example, that only the  $n$ - $\alpha$ -configuration with  $J = 3^+/2$  (relative orbital momentum  $L = 2$ , neutron spin antiparallel) can be coupled with the  $t$ - $d$ -configuration having also the quantum numbers  $J = 3^+/2$  (with  $L = 0$  and  $S = 3/2$ ). In this case, a proper ansatz for the wave-function should comprise the partial waves of the configurations which are coupled with each other. In contrast to the choice. in Eq.(17) we now choose

$$\psi = \mathcal{A} \left\{ \varphi(\alpha) \chi_I(R_I) \left[ \sqrt{\frac{1}{5}} \cdot Y_{21}(\vartheta_I, \varphi_I) \alpha_s(5) + \sqrt{\frac{4}{5}} \cdot Y_{22}(\vartheta_I, \varphi_I) \beta_s(5) \right] \right. \\ \times (\alpha_s(1)\alpha_\tau(1))(\beta_s(2)\alpha_\tau(2))(\alpha_s(3)\beta_\tau(3))(\beta_s(4)\beta_\tau(4))\beta_\tau(5) \\ \left. + \varphi(t)\varphi(d)\chi_{II}(R_{II})Y_{0,0}(\vartheta_{II}, \varphi_{II}) \right. \\ \left. \times (\alpha_s(1)\alpha_\tau(1))(\beta_s(2)\beta_\tau(2))(\alpha_s(3)\beta_\tau(3))(\alpha_s(4)\alpha_\tau(4))(\alpha_s(5)\beta_\tau(5)) \right\} \quad (35)$$

where subscript I refers to the relative vector  $\vec{R}_I = \vec{r}_s - \vec{R}_\alpha$ , and subscript II refers to the vector  $\vec{R}_{II} = \vec{R}_d - \vec{R}_t$ . The functions  $\chi_I(R_I)$  and  $\chi_{II}(R_{II})$  are the radial functions of the relative motion of the  $n$ - $\alpha$ -clusters and the  $t$ - $d$ -clusters, respectively. The expression in square brackets in relation (35) denotes a state with the quantum numbers  $J = 3/2$ ,  $J_Z = 3/2$  and  $L = 2$ ,  $S = 1/2$ . In analogy to the previous case, the products of spin and isospin spinors lead, after antisymmetrization, to channel spin and isospin quantum numbers  $S = 1/2$  and  $T = 1/2$  in the  $n$ - $\alpha$ -channel, and  $S = 3/2$ ,  $T = 1/2$  in the  $d$ - $t$ -channel.

This time both radial functions  $\chi_I(R_I)$  and  $\chi_{II}(R_{II})$  have to be varied arbitrarily. We insert Eq.(35) into Eq.(5), carry out all summations over the spin and isospin co-ordinates as well as integrations over the space co-ordinates - except  $R_I$  and  $R_{II}$  - and set all factors equal to zero by which the arbitrary variations  $\delta\chi_I(R_I)$  and  $\delta\chi_{II}(R_{II})$  are multiplied. Then we obtain a set of two coupled integro-differential equations<sup>6</sup> for  $u_I(R_I) = \chi_I(R_I)/R_I$  and  $u_{II}(R_{II}) = \chi_{II}(R_{II})/R_{II}$ :

<sup>6</sup> Note that to obtain these equations it is necessary that in expression (35) the functions  $\varphi(\alpha)$ ,  $\varphi(t)$  and  $\varphi(d)$  contain factors normalizing these internal functions together with their spin-isospin parts after antisymmetrization to 1.

$$\begin{aligned}
& \left[ -\frac{\hbar^2}{2M_{\text{red}}^I} \left( \frac{d^2}{dR_I^2} - \frac{6}{R_I^2} \right) + V_I(R_I) \right] u_I(R_I) + \int K_I(R_I, R_I') u_I(R_I') dR_I' \\
& \quad + \int K_{I,II}(R_I, R_{II}') u_{II}(R_{II}') dR_{II}' = E_{\text{cm}}^I u_I(R_I) \\
& \left[ -\frac{\hbar^2}{2M_{\text{red}}^{II}} \frac{d^2}{dR_{II}^2} + V_{II}(R_{II}) \right] u_{II}(R_{II}) + \int K_{II}(R_{II}, R_{II}') u_{II}(R_{II}') dR_{II}' \\
& \quad + \int K_{II,I}(R_{II}, R_I') u_I(R_I') dR_I' = E_{\text{cm}}^{II} u_{II}(R_{II})
\end{aligned} \tag{36}$$

In addition to Eq.(33), kernels  $K_{I,II}$  and  $K_{II,I}$  are contained now in Eq.(36). These kernels will describe transitions from channel I ( $n-\alpha$ -configuration) to channel II ( $d-t$ -configuration) and vice versa. Because of the hermiticity of the original Hamiltonian, also  $K_{I,II}$  and  $K_{II,I}$  obey a hermiticity relation

$$K_{I,II}(R_I, R_{II}') = K_{II,I}^*(R_{II}', R_I) \tag{37}$$

We mention here that, to obtain non-vanishing transition kernels  $K_{I,II}$  and  $K_{II,I}$  in our example, one must include two-nucleon-tensor forces [5] in the Hamiltonian (15).

By means of Eq.(36) it is easy to show that the following equation holds (if  $R_I$  and  $R_{II}$  tend to infinity):

$$\begin{aligned}
& \frac{i\hbar}{2M_{\text{red}}^I} \left[ u_I(R_I) \frac{d}{dR_I} u_I^*(R_I) - u_I^*(R_I) \frac{d}{dR_I} u_I(R_I) \right] \\
& \quad + \frac{i\hbar}{2M_{\text{red}}^{II}} \left[ u_{II}(R_{II}) \frac{d}{dR_{II}} u_{II}^*(R_{II}) - u_{II}^*(R_{II}) \frac{d}{dR_{II}} u_{II}(R_{II}) \right] = 0
\end{aligned} \tag{38}$$

This is simply a consequence of the reality of the local potentials and the hermiticity as well as the finite-range property of the kernels. The physical interpretation of Eq.(38) is just the conservation of current in the asymptotic region ( $R_I, R_{II} \rightarrow \infty$ ). Equation (38) states that for any time interval  $\Delta t$  the number of incoming particles in the  $n-\alpha$ -entrance-channel is equal to the sum of outgoing particles in the  $n-\alpha$ -exit-channel and the  $d-t$ -channel. In a region where the clusters penetrate each other strongly, it is meaningless to speak of currents made of  $n-\alpha$ -clusters or  $d-t$ -clusters, respectively. This is because here the Pauli principle destroys any resemblance of the clusters to the corresponding free particles. The considerable influence of the Pauli principle on our considerations will be dealt with again later on.

Equation (36) allows us to describe quite different problems such as reactions or bound states simply by choosing the appropriate boundary conditions as:

- 1) Elastic scattering of neutrons on  $\alpha$ -particles together with transitions to the  $t-d$ -channel. Here one has incoming and outgoing waves in the  $n-\alpha$ -channel and only outgoing waves in the  $d-t$ -channel.

- 2) Triton-deuteron elastic scattering together with transitions to the  $n$ - $\alpha$ -channel. In this case, there are incoming and outgoing waves in the  $t$ - $d$ -channel and only outgoing waves in the  $n$ - $\alpha$ -channel.
- 3) Bound states (if present) having a  $t$ - $d$ - and an  $\alpha$ - $n$ -cluster structure have to fulfil the conditions that for  $R_I, R_{II} \rightarrow \infty$  the corresponding relative-motion functions tend to zero.

Figure 2 shows the results of calculations made by Hackenbroich and Heiss [5]. They investigated the influence of the  $3^+/2$ - $d$ - $t$ -structure on  $p$ - $\alpha$ -scattering (which is, in fact, the mirror reaction of the  $\alpha$ - $n$ -scattering process) in a region between 15- and 25-MeV centre-of-mass scattering energy. The resonance behaviour of the  $p$ - $\alpha$ -cross-section at about 17 MeV is due to a resonance state having essentially a  $d$ - $^3\text{He}$ -cluster structure.

If one looks only for the influence of the  $t$ - $d$ -channel on the elastic  $n$ - $\alpha$ -channel one can simplify the calculations considerably, bearing in mind that the 17-MeV state is deeply embedded in the Coulomb barrier. Therefore, to a large extent, it can be treated as a bound state. Its coupling to the  $n$ - $\alpha$ -channel is relatively weak. These arguments give rise to the following idea. First, we determine the  $3/2$ -state separately using a bound-state variational (e.g. Ritz's) procedure. Adding this state afterwards with an (energy-dependent) linear variational amplitude  $a(E)$  to the pure  $n$ - $\alpha$ -channel wave function we obtain the following ansatz:

$$\psi = \mathcal{A} \left\{ \varphi(\alpha)\chi_I(R_I) \Phi(I) + a(E) \varphi(t)\varphi(d) F(R_{II}) \Phi(II) \right\} \quad (39)$$

The functions  $\Phi(I)$  and  $\Phi(II)$  denote the spin-isospin as well as the orbital momentum parts of the corresponding cluster structures. They look exactly

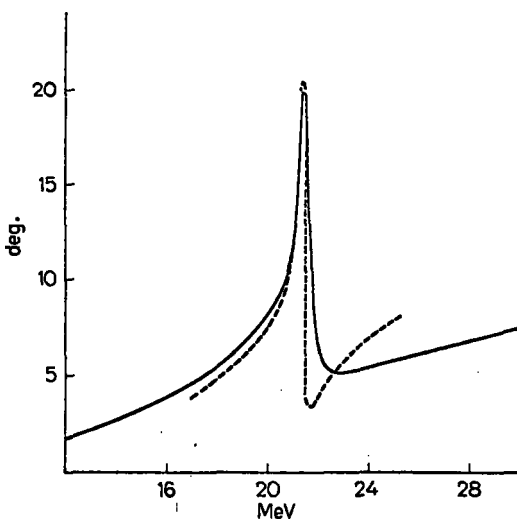


FIG. 2.  $\frac{3^+}{2}$ - $^4\text{He}$ - $p$ -scattering phase shift versus  $E_{\text{cm}}$ . Theoretical curve (solid line): [5], experimental data (dashed line): [6]. Experimental curve is shifted to calculated threshold energy.

as those in Eq. (35). The function  $F(R_{II})$  now stands for a given function which is part of the result of the preceding bound-state calculation. Inserting Eq. (39) into Eq. (5) we obtain two equations, one linear integro-differential equation arising from the arbitrary variation of  $\chi_I(R_I) = u_I(R_I)/R_I$  and one linear integral equation arising from the variation of the amplitude  $a(E)$ . Thus we obtain

$$\left[ -\frac{\hbar^2}{2M_{red}^I} \left( \frac{d^2}{dR_I^2} - \frac{6}{R_I^2} \right) + V_I(R_I) \right] u_I(R_I) + \int K_I(R_I, R_I') u(R_I') dR_I' + \int K_{I,II}(R_I, R_{II}') F(R_{II}') R_{II}' dR_{II}' = E_{cm}^I u_I(R_I) \quad (40)$$

$$a(E) \sum_{t_i, s_i} \int \varphi^*(t) \varphi^*(d) F^*(R_{II}) \Phi^*(II) (H-E) \varphi(t) \varphi(d) \Phi(II) F(R_{II}) dR_{II} + \int F^*(R_{II}) R_{II} K_{II,I}(R_{II}, R_I') u_I(R_I') dR_{II}' = 0$$

### b) Elastic scattering of deuterons on $\alpha$ -particles ( $L=0$ )

The simplified approach as it was described just above can be used in describing such effects as, e. g. distortion and polarization in reactions. As an example, we shall briefly discuss the inclusion of distortion effects in the calculation of s-wave elastic d- $\alpha$ -scattering as it was done by Jacobs et al. [7].

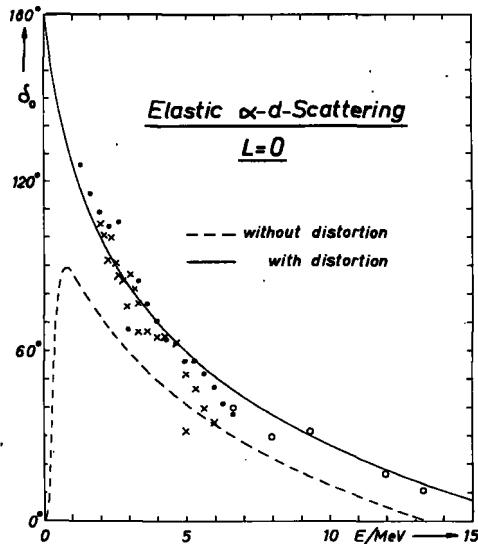


FIG. 3. s-wave phase shift of elastic  $\alpha$ -d-scattering versus  $E_{cm}$ . Theoretical curves: [7], experimental data: [8] (full dots), [9] (open circles), [10] (crosses).

In a first approximation, one could think of writing down such a simple ansatz similarly to that in Eq. (17) for the  $n$ - $\alpha$ -scattering, containing now one given internal cluster wave-function for each one of the two clusters  $\alpha$  and  $d$ , the parameters of which are chosen such as for the corresponding free particles, whereas the relative-motion function is considered to be varied arbitrarily. It turns out, however, that the  $s$ -wave phase shift obtained in this way differs quite appreciably from the experimental data (see the broken line in Fig. 3). Moreover, one knows from calculations in the  ${}^6\text{Li}$  compound system that an ansatz containing these 'free-particle parameters' is not able to describe a bound state of the  $\alpha$ - $d$ -system (with the boundary condition that  $u_\ell(R)$  tends to zero for  $R \rightarrow \infty$ ). Obviously, this simple trial wave-function is not flexible enough to describe the  $\alpha$ - $d$ -system adequately.

Because of the attractive character of nuclear forces two clusters approaching one another could be expected to tend to increase their overlap. This effect will mainly lead to a distortion of the deuteron inside the region of interaction. Although, because of the Pauli principle, the situation certainly is more complex, this simple picture is a guide for how one might construct a better trial wave-function. The distortion may be taken into account explicitly by adding some bound-state cluster functions to the scattering channel each one of them coupled by a free variable linear amplitude. The deuteron cluster in these functions may be expanded or contracted. Thus we write the ansatz

$$\psi = \mathcal{A} \left\{ \varphi(\alpha)\varphi^0(d)\chi(R) + \sum_{i=1, \dots} a_i(E)\varphi(\alpha)\varphi^i(d)F^i(R) \right\} \quad (41)$$

For simplicity, we think the spin-isospin functions in expression (41) to be included in the internal cluster functions. Since we consider purely elastic  $s$ -wave scattering, no orbital angular part appears in the ansatz (41). As in the example above the given internal wave-functions as well as the given relative motion functions  $F^i(R)$  are described by superpositions of functions of the Gaussian type (this has the advantage that all integrations leading to the coupled equations can be carried out analytically).

After inserting Eq. (41) into Eq. (5) we obtain a coupled set of equations comprising one linear integro-differential equation and several linear integral equations of the same kind as discussed just above (Eq. 40).

The result of the calculations was that, by adding a certain bound structure which contains a considerably contracted deuteron cluster compared to the free deuteron, the phase shift obtained agrees quite well with the experimental data (see solid line in Fig. 3). Moreover, taking into account more bound structures differing from one another in the size of the deuteron cluster the result was almost the same curve in all cases as long as the abovementioned contracted deuteron-cluster wave-function was present. The variational amplitudes of the additional terms turned out to be very small. This stability of the result shows an intrinsic consistency of our approach which is free of data fitting.

### 3. GENERALIZATION OF THEORY AND INFLUENCE OF PAULI PRINCIPLE

It will be clear by now in which way one can extend and refine these calculations in order to describe any kind of nuclear reactions and bound

states, namely, by introducing more and more channel wave-functions whose relative-motion functions are free variational functions, as well as bound-state wave-functions coupled by linear variational amplitudes. The most general ansatz for a trial function comprising linear variational functions and variational amplitudes will be of the form [4]

$$\begin{aligned} \psi = \mathcal{A} \left\{ \sum_i \varphi(A_i)\varphi(B_i)\chi(\vec{R}_i) + \sum_j \varphi(A_j)\varphi(B_j)\varphi(C_j)\chi(\vec{R}_j^1, \vec{R}_j^2) \right. \\ \left. + \sum_k \varphi(A_k)\varphi(B_k)\varphi(C_k)\varphi(D_k)\chi(\vec{R}_k^1, \vec{R}_k^2, \vec{R}_k^3) + \dots + \sum_l a_l F_l \right\} \end{aligned} \quad (42)$$

The spin and isospin functions are thought to be included in the internal cluster functions  $\varphi$ . The cluster terms containing relative-motion functions  $\chi(\vec{R}_j^1, \vec{R}_j^2)$ ,  $\chi(\vec{R}_k^1, \vec{R}_k^2, \vec{R}_k^3)$  etc., are responsible for three-, four-, etc. particle decays. The given functions  $F_l$  describe bound structures which vanish for large relative distances. For the sake of simplicity, we shall confine ourselves, for the present, to reactions where three or more particle decays do not occur. Therefore, the terms which would describe decays into three and more particles can be included in the sum of the bound structures. To obtain the corresponding set of linear integro-differential as well as linear integral equations Eq. (42) is again inserted into our fundamental Eq. (5). The coupled set of equations which is a generalization of Eqs (29), (33), (36) and (40) is of the form

$$\begin{aligned} \sum_i \langle \varphi(A_m)\varphi(B_m)\delta(\vec{R}_m - \vec{R}_m^i) | H-E | \mathcal{A} \left\{ \varphi(A_i)\varphi(B_i)\chi(\vec{R}_i) \right\} \rangle \\ + \sum_l a_l \langle \varphi(A_m)\varphi(B_m)\delta(\vec{R}_m - \vec{R}_m^i) | H-E | \mathcal{A} F_l \rangle = 0 \end{aligned} \quad (43)$$

$$\sum_i \langle F_m | H-E | \mathcal{A} \left\{ \varphi(A_i)\varphi(B_i)\chi(\vec{R}_i) \right\} \rangle + \sum_l a_l \langle F_m | H-E | \mathcal{A} F_l \rangle = 0$$

$m = 1, 2, \dots$

Because of the rotational, translational and reflectional invariance of the Hamiltonian (15) and since the cluster wave-functions are constructed so as to depend on the relative co-ordinates between the clusters, the wave-function  $\psi$  can be split into wave-functions of given total momentum, total angular momentum and parity.

If we restrict the number of variational functions and amplitudes in Eq. (42) (as we did in the examples of section 2) we project, by our variational procedure, a certain sub-space in which our coupled equations are defined out of the complete Hilbert space. This is the reason why Eqs (3) and (5) are called projection equations. As was pointed out in section 1 neither the general structure of the set of coupled equations nor the general properties of the corresponding solutions depend on the size of this sub-space.

We want to emphasize three essential points which have already been discussed in section 1 and 2:

- 1) Although normally the different cluster trial functions are not orthogonal to each other the solutions  $\psi_m$  to Eq.(5) form an orthonormalized basis of this sub-space. This behaviour of our linear variational procedure is most valuable because by this an orthonormalized set of solutions is generated which have the correct boundaries appropriate to the considered problem. Of course, all degeneracies are supposed to be removed so that the solutions  $\psi_m$  have well defined total angular momentum, parity etc.
- 2) On the basis of these solutions  $\psi_m$ , the Hamiltonian H can be represented as a real diagonal matrix in such a sub-space.
- 3) The law of current conservation in the asymptotic region or, in other words, the unitarity of the S-matrix is always exactly fulfilled in such a sub-space.

These properties of the solutions of the coupled equations belonging to a sub-space of the Hilbert space allow general features of the unified theory as discussed here to be studied, even by means of simple examples.

Up to now we have not yet discussed the question of how the saturation character of nuclear forces which is essentially due to their short-range repulsive core ( $r_0 \sim 0.4 \times 10^{-13}$  cm) will influence our considerations.

If, in contrast to the forces of Eq.(16), we use more realistic nuclear forces containing a repulsive core, then certain two-nucleon correlations must be introduced into the trial functions by multiplying the different cluster terms in the wave-function  $\psi$  by suitably chosen short-range correlations known as Jastrow factors<sup>7</sup> which prevent any two nucleons from approaching each other too closely. As an example, they can be of the form

$$\phi_{\text{corr}} = \prod_{\text{all pairs}} f(|\vec{r}_i - \vec{r}_j|) \quad (44)$$

with

$$f(|\vec{r}_i - \vec{r}_k|) = 1 - e^{-\beta_{ik} (|\vec{r}_i - \vec{r}_k|)^{n_{ik}}} \quad \beta_{ik} \sim 0.4 \times 10^{+13} \text{ cm}^{-1}$$

For  $r_{ik} = |\vec{r}_i - \vec{r}_k| \rightarrow 0$  also  $f(r_{ik})$  tends to zero with a power  $(r_{ik})^{n_{ik}}$ , whereas for  $r_{ik} \rightarrow \infty$  the functions  $f(r_{ik})$  tend to unity very rapidly. To refine the calculations one can introduce additional variational terms in  $\psi$  with different correlation functions  $f(r_{ik})$ , differing, e. g. in their width parameter  $\beta_{ik}$  or their power  $n_{ik}$ , all of them added to  $\psi$  with linear variational amplitudes as it should be. Even if for all (i, k) we assume that  $n_{ik}$  equals two, by which we obtain analytically integrable Gaussians, these correlation factors seriously complicate the calculations of the integrals leading to the coupled equation as well as the final numerical work in solving these equations. However, they neither influence the general structure of the coupled set of equations nor the general properties of their solutions. Therefore, they do not cause a fundamental change in our considerations. This is why in our further considerations we shall not explicitly take the short-range correlations into account.

<sup>7</sup> See Ripka's contribution to these Proceedings.

As the next step, we shall discuss the influence of the Pauli principle on our unified nuclear theory. It will turn out to be a most fundamental point. We mainly want to stress two aspects. The first is that the Pauli principle resolves the contradictions between the different single-particle and collective models used in nuclear physics. Secondly, it also considerably reduces the number of terms in a clustering ansatz to be taken into account in practical calculations. The common reason for both effects lies in the fact that the differences between wave-functions describing, before antisymmetrization, quite different nuclear correlations are substantially reduced by the antisymmetrization procedure. Sometimes these differences even vanish.

To understand this, let us consider, as a simple example, an ensemble of a large number of fermions being contained in a square well potential, without any mutual interaction. Take for this, say, the electrons of a conductor. In the ground state all single-particle states which have momenta lying inside the Fermi sphere (see Fig. 4A) are filled. If this system as a whole is now given a small velocity  $\Delta\vec{V}$ , the Fermi sphere is shifted so that its centre is no longer at the origin (see Fig. 4B). The change relative to the situation of Fig. 4A is a collective excitation in which each fermion receives a small change in momentum  $m\Delta\vec{V}$ . Now let us instead start with the Fermi sphere at the origin (as in Fig. 4A) and impart various large amounts of momentum to a few of the fermions (all those in states in region 1 of Fig. 4C) at the left of the sphere so as to excite them into states just to the right of the sphere (filling the states in regions 3 of Fig. 4C). Because of the indistinguishability of the fermions, corresponding to the antisymmetrization of the wave-function, the situation in Fig. 4C is completely equivalent to that in Fig. 4B. This shows how under antisymmetrization a large excitation imparted to a few fermions can be equivalent to a collective excitation of all the fermions as a whole.

Another example is that of a collective dipole oscillation of fermions against each other. That this can be exactly equivalent to a one-particle excitation if antisymmetrization of the wave-functions is carried out was shown by Brink [11].

A third example is the  ${}^6\text{Li}$  ground state. One can show that, in this case, the shell-model representation, the  $\alpha$ -d-cluster representation and the t- ${}^3\text{He}$ -cluster representation after antisymmetrization, give the same wave-function if in all three cases one uses oscillator wave-functions with the same frequency for the internal wave-functions and for the relative-motion functions [1].

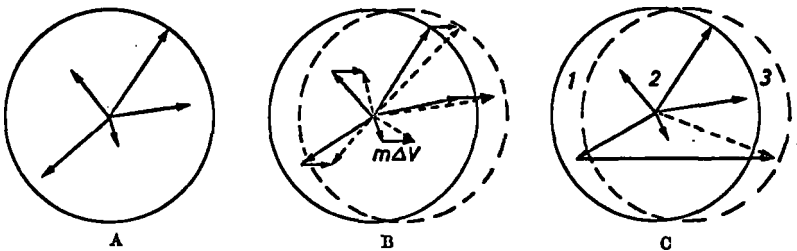


FIG. 4. Equivalence under antisymmetrization. A: ground state, B: collective excitation, C: single-particle excitation.

As an explanation of this effect, we note that many terms appearing in the non-antisymmetrized wave-function will vanish after antisymmetrization. By this procedure, the differences between different nuclear correlations (which are expressed by different cluster representations) are reduced. If, e.g. two nucleons are in the same single-particle state then through antisymmetrization the corresponding terms of the wave-function are cancelled completely. For explicit calculations concerning this point see the references given above.

The influence of the Pauli principle is especially effective if the clusters penetrate each other strongly. Very often this has the consequence that any resemblance of the clusters with the corresponding free particles is completely destroyed. On the other side, as soon as the mutual penetration of the clusters decreases, the influence of the Pauli principle decreases, too. That is why clusters in the nuclear surface region behave approximately like the corresponding free particles.

In practice, for the wave-function  $\psi$  in Eq. (41), this influence of the Pauli principle means that many terms in the expansion (41), especially the different bound structures  $F_{\ell}$ , overlap to a larger extent after antisymmetrization. This is most valuable for practical calculations since it quite appreciably reduces the number of terms to be taken into account for ensuring enough flexibility of the wave-function; in addition, it allows the combination of calculations which have been carried out in the framework of different nuclear models. In section 4, we shall discuss the combination of shell-model and cluster reaction calculations as an example for this statement.

#### 4. COMBINATION OF SHELL-MODEL AND OTHER BOUND-STATE CALCULATIONS WITH CLUSTER REACTION CALCULATIONS. SEMIQUANTITATIVE CONSIDERATIONS

The practical calculations can be simplified considerably first by using the fact that, because of the weakness of the Coulomb force as compared to the nuclear forces, one can, to a very good approximation, neglect all polarization effects as soon as the reaction products are separated (which is not true for atomic and molecular reactions, of course). This fact was first used systematically for nuclear reaction calculations by Hackenbroich [12]. Secondly, owing to the influence of the Pauli principle just discussed, one can couple in a very simple way cluster wave-functions with shell-model and also other bound-state wave-functions which are especially suited for describing the interior of a nucleus. We shall discuss these simplifications by means of  $\alpha$ - $^{16}\text{O}$  scattering. To simplify notation we neglect Coulomb interaction. We consider elastic s-wave scattering and neglect any other reaction processes, such as inelastic-scattering processes. We split the wave-function  $\psi$  into two parts:

$$\psi = \psi_{\text{inside}} + \psi_{\text{outside}}$$

with

$$\begin{aligned} \psi_{\text{inside}} &= \mathcal{A} \left\{ \sum_{\ell} a_{\ell} F_{\ell} \right\} \\ \psi_{\text{outside}} &= \mathcal{A} \left\{ f(R) \varphi(^{16}\text{O}) \varphi(\alpha) \frac{\sin KR}{R} + b f(R) \varphi(^{16}\text{O}) \varphi(\alpha) \frac{\cos KR}{R} \right\} \end{aligned} \quad (45)$$

where  $K$  denotes the wave number of the  $\alpha$ - $^{16}\text{O}$  relative motion in the asymptotic region;  $b$  is a variational parameter. Its magnitude determines the elastic-scattering phase shift. The function  $f(R)$  is a cut-off function, for example, of the form  $f(R) = 1 - \exp[-R^n/R_0^n]$  which cuts off the  $\alpha$ - $^{16}\text{O}$ -channel wave-function near the nuclear surface ( $R \sim R_0$ ) and approaches unity for  $R \rightarrow \infty$ . For  $\psi_{\text{inside}}$  which describes the interior of the compound nucleus ( $^{20}\text{Ne}$ ) one can use the most convenient representation. For heavier nuclei the most convenient representation is very often a superposition of shell-model wave-functions with linear variational parameters as factors. To improve the flexibility of  $\psi_{\text{inside}}$ , it is sometimes useful to add cluster terms which are only appreciably different from zero at the nuclear surface and which can describe energetically favoured cluster structures in the nuclear surface. The terms  $F_i$ , with factors  $a_i$  being linear variational parameters, in expression (45) have then to be chosen so as to describe such a mixture of shell-model wave-functions and bound-cluster wave-functions.

For the determination of the variational amplitudes in the Hulthén-Kohn ansatz (45) one again uses Eq. (5). By doing this, we automatically obtain a coupling between  $\psi_{\text{inside}}$  and the elastic-channel terms:

$$\langle f(R)\varphi(^{16}\text{O})\varphi(\alpha) \frac{\sin KR}{R} | H - E | \psi_{\text{inside}} \rangle \quad (46)$$

If one constructs  $\psi_{\text{inside}}$  in such a way that it describes the compound nucleus state in a sphere of a relatively large radius  $R_0$  which is at the same time the cut-off radius of the elastic-channel function, then one has essentially to consider only the coupling of the elastic-channel terms with the nucleons inside the surface region of  $\psi_{\text{inside}}$ . This means, for example, that in such coupling terms one only has to carry out the antisymmetrization with the nucleons in the nuclear surface. Sometimes even this can be neglected. Such simplifications could be very important in calculating heavy-ion reactions which otherwise might not be feasible. Another advantage of the above separation into an inside and an outside region of the nucleus is that the overlap between different terms in the trial function is strongly reduced and this reduces both computer memory and computing time.

If one has to take into consideration, in addition to the elastic channel, other reaction channels — as, e.g. in case of  $n$ - $\alpha$ -scattering the  $d$ - $t$ -channel — then one has to add outgoing waves with the correct asymptotic behaviour belonging to the different open channels. These waves also contain linear variational amplitudes as factors and they are also cut off near the nuclear surface.

Since in the method sketched above the trial function  $\psi$  now contains an inhomogeneous term the solutions of the projection equation (5) do not automatically fulfil the law of current conservation. However, there are methods (e.g. Kato's condition) that show how one can correct this point afterwards such that one ends up with a unitary  $S$ -matrix, too<sup>8</sup>. From this discussion we see that it is necessary to choose the term in the trial function  $\psi$  in such a way that, in particular, the variational calculation gives a good description of the transition region near the nuclear surface. Especially here in the

<sup>8</sup> See, e.g. the book of Wu and Ohmura [15] p. 76.

transition region, the Pauli principle plays an important role because — as we have pointed out before — it smooths out the differences between different structures as e. g. between  $\psi_{\text{inside}}$  and  $\psi_{\text{outside}}$ .

To test the convergence of the method the  $n$ - $\alpha$ -scattering and the  $\alpha$ - $\alpha$ -scattering have been calculated. Even with a relatively small number of variational terms in  $\psi$  one obtains for different choices of the trial functions in  $\psi_{\text{inside}}$  and for different cut-off functions in  $\psi_{\text{outside}}$  practically the same result [13,14]. On the other hand, these results also fit the corresponding resonating group calculations where the relative-motion functions of the clusters are used as variational functions which are varied arbitrarily as discussed in section 2.

The method sketched here can be considered to be a quantitative formulation of the R-matrix theory where one splits the wave function in an (unknown) inside and an outside region.

The amount of numerical work increases exponentially with the increasing number of nucleons even if the simplifications discussed above are used. Therefore, it is important to apply semi-quantitative considerations by using the physical ideas which we can gain from the general structure of our theory. In this respect, it is especially important to obtain some insight into the influence of the Pauli principle without carrying out the antisymmetrization of the wave functions explicitly.

To see how this works we shall discuss a specific example. We discuss the electric quadrupole transition probability  $T_E(2)$  of the first excited  $2^+$  state of  $^{20}\text{Ne}$  to its  $0^+$  ground state and its connection to the energy distance  $\Delta E(2^+ \rightarrow 0^+)$  of these two levels. Because of the very rigid structure of the  $\alpha$ -cluster and the doubly closed shell cluster  $^{16}\text{O}$  one can consider these two states, to a good approximation, to be the lowest states of a rotational band where the  $\alpha$ -cluster rotates around the  $^{16}\text{O}$ -cluster. This rotation takes place essentially in the surface of the  $^{16}\text{O}$ -cluster because, owing to the closed shell structures of the  $\alpha$ - and the  $^{16}\text{O}$ -clusters they do not penetrate each other to a large extent. This has the consequence that for the calculation of the rotational energy of the  $2^+$ - $^{20}\text{Ne}$ -state (energy distance  $\Delta E(2^+ \rightarrow 0^+)$  to the  $0^+$  ground state) one can neglect the antisymmetrization between the  $\alpha$ - and the  $^{16}\text{O}$ -cluster approximately. This is even more the case for the electric quadrupole transition probability  $T_E(2)$  because the corresponding transition operator is a long-range operator. Under these circumstances, a very simple relation between  $\Delta E(2^+ \rightarrow 0^+)$  and  $T_E(2)$  exists. One can easily check that this relation is of the form<sup>9</sup>.

$$T_E(2) = \frac{3}{100} \left( \frac{e}{M_{\text{nucl.}}} \right)^2 \frac{(\Delta E)^3}{c^5 \cdot \hbar^2} \quad (47)$$

For the derivation of this formula it was assumed that

$$\left\langle \frac{1}{R^2} \right\rangle = \frac{1}{\langle R^2 \rangle} \quad (48)$$

This will be approximately true if the centre of the  $\alpha$ -cluster has a relatively constant distance from the centre of the  $^{16}\text{O}$ -cluster. Because of the Pauli

<sup>9</sup> Because of the spherical structure of  $^{16}\text{O}$  and the  $\alpha$ -cluster one can consider the masses and the charges of the clusters to be concentrated at their centres of mass.

principle which, as has just been mentioned, prevents the two clusters from penetrating each other to a large extent, this is approximately true.

If in expression (47) we insert the experimental energy distance  $\Delta E(2^+ \rightarrow 0^+)$  we obtain  $T_E(2) = 1.6 \times 10^{12} \text{ s}^{-1}$  which has to be compared to the experimental  $T_E(2)$ -value  $(1.6 \pm 0.7) 10^{12} \text{ s}^{-1}$ . Evidently, the theoretical value for  $T_E(2)$  lies within the limits of the experimental errors.

Similar semiquantitative considerations can be applied to numerous other cases, see e. g. Refs [14, 16].

## 5. DISCUSSION OF SOME GENERAL PROPERTIES OF THE UNIFIED THEORY OF NUCLEI

Up to now, we have been discussing how, in the framework of the unified nuclear theory presented here a general basis for carrying out nuclear-structure and reaction calculations can be obtained. But we have not yet discussed problems of a more general character as, e. g., in which way the general description of resonances, the optical-model description, the direct-reaction descriptions, the description of collective states, etc. are contained in this unified theory.

Since we have to restrict ourselves, we shall only consider elastic resonance scattering in the vicinity of an isolated level in greater detail (single-level resonance formula). We shall further assume that only the elastic channel is open. After wards we shall briefly discuss how these considerations can be extended to a derivation of other resonance formulas, the optical model etc. in the framework of this theory.

The fundamental equation for our investigation is again Eq.(5). We split the wave-function  $\psi$  into two parts:

$$\psi = \psi_D + \psi_C \quad (49)$$

with

$$\psi_D = \mathcal{A} \left\{ \varphi(A) \varphi(B) \chi(\vec{R}_{AB}) \right\}$$

and

$$\psi_C = \mathcal{A} \left\{ \sum_l a_l F_l \right\}$$

We do not need the other terms appearing in ansatz (42) for  $\psi$ , since we assume that only the elastic channel is open. With ansatz (49) we obtain the following coupled equations from Eq.(5):

$$\langle \delta\psi_D | H - E | \psi_D \rangle + \langle \delta\psi_D | H - E | \psi_C \rangle = 0 \quad (50a)$$

$$\langle \delta\psi_C | H - E | \psi_D \rangle + \langle \delta\psi_C | H - E | \psi_C \rangle = 0 \quad (50b)$$

where  $\delta\psi_C$  is an arbitrary variation in the sub-space of the bound structures  $F_l$ , and  $\delta\psi_D$  an arbitrary variation in the sub-space of the elastic-channel functions. We mention that the two sub-spaces are normally not orthogonal

to each other. The fact that the bound structures  $F_l$  can introduce resonance structures into the scattering wave functions can be seen from a derivation of the Breit-Wigner resonance formula. To do this, in Eq.(50a) we introduce the resolvent  $G_C$  belonging to Eq.(50b). This resolvent is defined by the equation

$$\langle \delta\psi_C | H - E | G_C = \langle \delta\psi_C | \quad (51)$$

and can be represented by means of the solutions of the homogeneous equation

$$\langle \delta\psi_C | H - E | \psi_C \rangle = 0 \quad (52)$$

If we denote by  $E_C^n$  the discrete energy eigenvalues of Eq.(52) we can write

$$G_C = \sum_n \frac{|\psi_C^n\rangle \langle \psi_C^n|}{E_C^n - E} \quad (53)$$

For Eq.(53) to be a solution of Eq.(51), the  $\psi_C^n$  must be orthonormalized, i.e.

$$\langle \psi_C^{n*} | \psi_C^n \rangle = \delta_{nn'} \quad (54)$$

If we further bear in mind that  $\langle \delta\psi_C |$  can be represented as

$$\langle \delta\psi_C | = \sum_n \delta a_n^* \langle \psi_C^n | \quad (55)$$

we immediately see that ansatz (53) for the resolvent  $G_C$  with the orthonormalization (54) is a solution of Eq.(51). By introducing  $G_C$  in Eq.(50b) we obtain for  $|\psi_C\rangle$ :

$$|\psi_C\rangle = -G_C | H - E | \psi_D \rangle = - \sum_n \frac{|\psi_C^n\rangle \langle \psi_C^n | H - E | \psi_D \rangle}{E_C^n - E} \quad (56)$$

Substituting this in Eq.(50a) provides the following reduced equation for the open channel part  $\psi_D$  of the wave-function:

$$\langle \delta\psi_D | H - E | \psi_D \rangle = \sum_n \frac{\langle \delta\psi_D | H - E | \psi_C^n \rangle \langle \psi_C^n | H - E | \psi_D \rangle}{E_C^n - E} \quad (57)$$

We have thus derived an effective non-local but Hermitian optical potential for  $\psi_D$  which depends on the resonance structures  $\psi_C^n$  and is further an explicit function of the energy  $E$ . Because of the singularities in the denominators  $E_C^n - E$  this potential gives rise to more or less narrow resonances.

For the derivation of the single-level resonance formula for elastic scattering around  $E_C^1$  we write expression (57) in the following form:

$$\langle \delta\psi_D | H'(\mathbf{E}) - E | \psi_D \rangle = \frac{\langle \delta\psi_D | H - E | \psi_C^1 \rangle \langle \psi_C^1 | H - E | \psi_D \rangle}{E_C^1 - E} \quad (58a)$$

with

$$H'(\mathbf{E}) = H - \sum_{n \neq 1} \frac{|H - E | \psi_C^n \rangle \langle \psi_C^n | H - E |}{E_C^n - E} \quad (58b)$$

Equation (58a) can be solved formally by means of the resolvent  $G_D^{1+}(\mathbf{E})$  for  $H'$  in the sub-space of the open (elastic) channel with outgoing-wave boundary conditions. In the same way as  $G_C$ ,  $G_D^{1+}(\mathbf{E})$  is defined by the equation

$$\langle \delta\psi_D | H' - E | G_D^{1+}(\mathbf{E}) = \langle \delta\psi_D | \quad (59)$$

and can be represented by the solutions of the homogeneous equation

$$\langle \delta\psi_D | H'(\mathbf{E}) - E_D^\beta | \psi_D^\beta(\mathbf{E}) \rangle = 0 \quad (60)$$

$E_D^\beta$  denotes the energy eigenvalues of Eq. (60) in contrast to the fixed total energy  $E$  of the reaction process.  $E_D^\beta$  and  $\psi_D^\beta(\mathbf{E})$  are functions of  $E$ .

If the  $\psi_D^\beta(\mathbf{E})$  with discrete and continuous eigenvalues  $E_D^\beta$  are orthonormalized

$$\langle \psi_D^{\beta'} | \psi_D^\beta \rangle = \delta(\beta, \beta') \quad (61)$$

then the spectral representation of  $G_D^{1+}(\mathbf{E})$  becomes

$$G_D^{1+}(\mathbf{E}) = \sum_{\beta} \frac{|\psi_D^\beta(\mathbf{E}) \rangle \langle \psi_D^\beta(\mathbf{E}) |}{E_D^\beta - E - i\epsilon} \quad (62)$$

The term  $(-i\epsilon)$  guarantees that the coupling between the bound state  $\psi_C^1$  and the elastic channel produces only an outgoing wave.

We need  $G_D^{1+}(\mathbf{E})$  in an energy region where the energy spectrum of the  $E_D^\beta(\mathbf{E})$ , in contrast to the  $E_C^1$ , is continuous, i.e. where the channel in  $G_D^{1+}(\mathbf{E})$  (elastic channel) is open. In this energy region,  $G_D^{1+}(\mathbf{E})$  is non-Hermitian due to the continuous  $E_D^\beta$  and the term  $(-i\epsilon)$  in the denominator.

With the resolvent  $G_D^{1+}(\mathbf{E})$ , we obtain from Eq. (58a):

$$|\psi_D \rangle = |\psi_D^{1+}(\mathbf{E}) \rangle + \frac{G_D^{1+}(\mathbf{E}) | H - E | \psi_C^1 \rangle \langle \psi_C^1 | H - E | \psi_D \rangle}{E_C^1 - E - i\epsilon} \quad (63)$$

$|\psi_D^{i+}(\mathbf{E})\rangle$  is a purely elastic scattering solution of the homogeneous Eq. (60) with  $E_D^\beta = E$  and it is matched to the incoming wave of the bombarding particles.

Equation (63) can be solved immediately and one obtains

$$|\psi_D\rangle = |\psi_D^{i+}(\mathbf{E})\rangle + G_D^{i+}(\mathbf{E}) |H-E|\psi_C^1\rangle \frac{\langle\psi_C^1|H-E|\psi_D^{i+}(\mathbf{E})\rangle}{E_C^1 - E - \langle\psi_C^1|H-E|G_D^{i+}(\mathbf{E})|H-E|\psi_C^1\rangle} \quad (64)$$

Before we derive from the asymptotic behaviour of Eq. (64) the single level Breit-Wigner formula for elastic scattering we have to add some remarks about the validity of the solution (64) of Eq. (5).

At a first glance it looks as if the ansatz (49) for  $\psi$  does no more allow to represent the exact solution of our problem because this ansatz already selects a subspace of the complete Hilbert space for our A-particle system. But this is not the case if one demands that the  $F_l$  in  $\psi_C$  form a complete set of wave functions in a finite volume which is larger than the volume of the compound nucleus. Because of the completeness of the  $F_l$  they can together with  $\psi_D$  therefore describe the exact wave-function inside and in the surface region of the finite volume just mentioned. Therefore by the ansatz (49) for  $\psi$  the exact wave function of our system can be described in the whole space as long as no other but the elastic channel is open. Thus Eq. (64) represents an exact solution with the correct boundary conditions of the Hamiltonian which governs our many particle systems<sup>10</sup>.

We shall now derive the single-level Breit-Wigner formula. For this purpose, we consider a resonance state of given total spin  $J$  and parity, expand the elastic-scattering wave and  $G_D^{i+}(\mathbf{E})$  into waves of given  $J$  and parity and select the wave which has the same spin and parity as the resonance state. Furthermore, by using the integral identity

$$\frac{1}{E_D^\beta - E - i\epsilon} = P \frac{1}{E_D^\beta - E} + i\pi\delta(E_D^\beta - E) \quad (65)$$

we can split the non-Hermitian operator  $G_{D,j}^{i+}$  into a Hermitian and an anti-Hermitian part and obtain

$$\begin{aligned} G_{D,j}^{i+}(\mathbf{E}) &= \sum_{\beta}^{\infty} P \frac{1}{E_D^\beta - E} |\psi_{D,j}^\beta(\mathbf{E})\rangle \langle\psi_{D,j}^\beta(\mathbf{E})| + i\pi |\psi_{D,j}^{i+}(\mathbf{E})\rangle \langle\psi_{D,j}^{i+}(\mathbf{E})| \\ &= G_{D,j}^{i+P}(\mathbf{E}) + i\pi \tilde{G}_{D,j}^{i+}(\mathbf{E}) \end{aligned} \quad (66)$$

where  $G_{D,j}^{i+P}(\mathbf{E})$  is the principal value of the resolvent  $G_{D,j}^{i+}(\mathbf{E})$ .

<sup>10</sup> The difficulty which is due to the fact that some of the  $F_l$  in  $\psi_C$  are not linearly independent of  $\psi_D$  is not discussed here, for the sake of brevity. It can be avoided easily by means of a projection method without changing any essential result (see Ref. [4]).

Using relation (66) we obtain from the asymptotic behaviour of Eq. (64) for the phase factor  $A_j$  which multiplies the outgoing partial wave of total spin  $j^{11}$ :

$$A_j = \left\{ e^{2i\delta_j^*(E)} + \frac{i \Gamma_j(E) e^{2i\delta_j^*(E)}}{E_C^1 - E - \Delta_j(E) - \frac{1}{2} i \Gamma_j(E)} \right\} \quad (67a)$$

$$= e^{2i\delta_j^*(E)} \left\{ \frac{E_C^1 - E - \Delta_j(E) + \frac{1}{2} i \Gamma_j(E)}{E_C^1 - E - \Delta_j(E) - \frac{1}{2} i \Gamma_j(E)} \right\}$$

with

$$\Delta_j(E) = \langle \psi_C^1 | H - E | G_{D,j}^{1P}(E) | H - E | \psi_C^1 \rangle \quad (67b)$$

$$\Gamma_j(E) = 2\pi |\langle \psi_C^1 | H - E | \psi_{D,j}^{1+}(E) \rangle|^2$$

where  $\exp(2i\delta_j^*(E))$  is the phase factor of the outgoing asymptotic wave  $\psi_{D,j}^{out}(E)_{\text{asympt}}$  without resonance scattering, i. e. that phase factor which near the resonance considered belongs to the potential or background scattering. Relation (67a) is exact and valid for any scattering energy provided that only the elastic-scattering channel is open, i. e. also for scattering energies far away from any resonance. Equation (67a) looks already like the single-level Breit-Wigner resonance formula where only the elastic channel is open. The only but essential difference to this formula is that  $\Delta_j(E)$  and  $\Gamma_j(E)$  are energy-dependent. To get rid of this difference we have to make an approximation. We have to use here, for the first time, the fact that we want to consider an isolated resonance level. For an isolated resonance level all other resonance levels lie energetically so far away that  $\delta_j^*(E)$  and  $\Gamma_j(E)$  are approximately energy-independent over the energy width of a sharp resonance level. Furthermore, near sharp resonances  $\Delta_j(E)$  can be expanded in a Taylor series around the resonance energy and cut off after the linear term. With this we obtain the following Breit-Wigner resonance formula from expression (67):

$$A_j \approx e^{2i\delta_j^*(E)} \left( 1 + \frac{i \Gamma_{j\text{res}}}{E_{\text{res}} - E - \frac{1}{2} i \Gamma_{j\text{res}}} \right) \quad (68a)$$

$$= e^{2i\delta_j^*(E)} \frac{(E_{\text{res}} - E) + \frac{1}{2} i \Gamma_{j\text{res}}}{(E_{\text{res}} - E) - \frac{1}{2} i \Gamma_{j\text{res}}}$$

with

$$\Gamma_{j\text{res}} = \frac{\Gamma_j(E)}{1 + \partial \Delta_j(E) / \partial E} \Big|_{E=E_{\text{res}}} \quad (68b)$$

<sup>11</sup> The relation between the scattering amplitude  $J_j$  and  $A_j$  is given by  $J_j = \frac{1}{2i} (A_j - 1)$ .

$E_{\text{res}}$  is defined by the energy  $E$  for which the real part of the denominator in expression (67a) becomes zero, i. e. by the equation

$$E_C^1 - E - \Delta_j(E) = 0 \quad (68c)$$

The energy shift  $\Delta_j(E)$  which is due to the coupling of the compound nucleus state  $\psi_C^1$  with the elastic channel and which corrects  $E_C^1$  can be quite large. This is the case if  $\psi_C^1$  does not describe the compound-nucleus state very exactly. Also the "correct" energy width  $\Gamma_{j \text{ res}}$  can be quite different from  $\Gamma_j(E)$ . This is, for example, the case if the extension of  $\psi_C^1$  is much larger than the volume of the compound nucleus because then  $\partial \Delta_j(E) / \partial E$  becomes negative and of the order of one. We state this here without proof. Analogously, we can derive the Breit-Wigner-many-level formula, the optical-model approximation, the different direct-reaction approximations, etc. The guiding idea for all these derivations is always that one splits, in analogy to the case dealt with above, the wave function  $\psi$  into different parts  $\psi_i$  in such a way that this splitting, and the non-orthogonal sub-spaces of the Hilbert space which are defined by the  $\delta\psi_i$ , are especially suited for a theoretical derivation of the different phenomenological nuclear models. For the derivation of the optical model, for example, one splits  $\psi$  into two parts  $\psi_1$  and  $\psi_2$ , where  $\delta\psi_1$  defines the elastic-channel subspace, and  $\delta\psi_2$  the rest of the Hilbert space which contains, e. g. all inelastic channels and all open reaction channels. For a more detailed discussion of these problems the reader is referred to Ref. [4].

## 6. CONCLUSIONS

In the preceding sections, we have discussed a method which opens a way to a unified nuclear theory which covers, in principle, all nuclear phenomena, i. e. nuclear-structure problems as well as all kinds of reactions, e. g. fission, etc. The central part of our considerations was the reformulation of the many-particle Schrödinger equation in the form of Eqs (3) and (5), respectively, i. e. as a projection (or variational) equation. The most striking advantage of this is the fact that one does not have to stick to any special kind of representation, as e. g. the shell-model representation, but that one is free to choose, for any given problem, the most suitable representation or even mixture of representations which will, in particular, allow the introduction of the correct boundary conditions from the very beginning. This is a similar situation to that which we know from analytical mechanics. There, the Lagrangian variational principle also has the advantage of allowing the most convenient co-ordinates appropriate to a description of the mechanical problem considered to be introduced from the start. It was shown that as long as we deal with linear homogeneous variational functions the solutions of Eq. (5) automatically form an orthonormalized set of functions. Thus we can say that by the ansatz for the variational procedure we automatically choose the most convenient basis system appropriate for the description of the system under consideration.

Particularly useful for such a unified description of all nuclear phenomena are the cluster representations because they allow even complicated many-particle correlations with a relatively small number of parameters and functions to be described.

In many cases it will be convenient to combine the cluster representations with other kinds of representations, say e.g. the shell-model representation. This is made possible by the strong influence of the Pauli principle which can very often reduce the difference between different nuclear wave-functions drastically. By this procedure, e.g. the contradictions between different nuclear models are resolved. Together with the formulation of the Schrödinger equation as projection equation, the Pauli principle makes it possible to couple all different kinds of nuclear-model wave-functions with each other as was discussed in sections 4 and 5.

Finally, we want to emphasize that the derivation of a unified theory of bound states and reactions with the help of the projection method discussed here is certainly not restricted to low-energy nuclear physics. It can be applied, in a very similar way, to the construction of a reaction theory for atomic physics and solid-state physics. Very probably, such considerations might also be helpful to describe reactions in high-energy physics. The properties of the reactions in high-energy physics should resemble in many respects (e.g. the correlations) the properties of the reactions in low-energy nuclear physics because in both cases the main interactions are of short-range character.

#### REFERENCES

- [1] WILDERMUTH, K., McCLURE, W., Springer Tracts in Modern Physics, 41 Springer, Berlin/Vienna (1966).
- [2] WURSTER, E.-J., BMwF Forschungsbericht K 67-69 (1967).
- [3] HOOP, B., Jr., BARSHALL, H.H., Nucl.Phys. 83 (1966) 65.
- [4] BENÖHR, H.C., WILDERMUTH, K., Nucl.Phys. A 128 (1969) 1.
- [5] HEISS, P., HACKENBROICH, H.H., Z.Physik 235 (1970) 422.
- [6] WEITKAMP, W.G., HAEBERLI, W., Nucl.Phys. 83 (1966) 46.
- [7] JACOBS, H., WILDERMUTH, K., WURSTER, E.-J., Phys.Letts 29B (1969) 455.
- [8] McINTYRE, L.C., HAEBERLI, W., Nucl.Phys. A 91 (1967) 382.
- [9] DARRIULAT, P. et al., Nucl.Phys. A 94 (1967) 653.
- [10] MANI, G.S., TARRATS, A., Nucl.Phys. A 107 (1968) 624.
- [11] BRINK, D.M., Nucl.Phys. 4 (1957) 215.
- [12] HACKENBROICH, H.H., BMwF Forschungsbericht K 67-93 (1967).
- [13] WILDERMUTH, K., in Clustering Phenomena in Nuclei, (Proc.Int.Conf.Bochum, 1969, IAEA, Vienna (1969) 3.
- [14] FEDERSEL, H. et al., Phys.Letts 33B (1970) 140.
- [15] WU, T.Y., OHMURA, T., Quantum Theory of Scattering, Prentice Hall, London (1962).
- [16] RISSER, J., WILDERMUTH, K., in Clustering Phenomena in Nuclei (Proc.Int.Conf.Bochum, 1969) IAEA, Vienna (1969) 305.

For further references see Refs [1] and [14] and the references given there.

# OPTICAL POTENTIAL FOR DEUTERON SCATTERING \*

M. BAUER

Instituto de Física

Universidad Nacional Autónoma de México,

México

## Abstract

### OPTICAL POTENTIAL FOR DEUTERON SCATTERING.

In the paper the optical potential for the scattering of composite nuclear projectiles is discussed.

The optical-model description of elastic scattering is one of the simplest and most successful phenomenological models of nuclear reactions. It works exceedingly well for single-nucleon scattering and also in the case of composite projectiles [1]. The phenomenological approach produces, however, a number of definitely distinct sets of optical-potential parameters that give equally good fits to the data. This is immediately understandable from the fact that in elastic scattering only the asymptotic part of the wave function (phase shifts) intervenes [1]. But once one starts using these optical potentials in DWBA-calculations of other nuclear reactions (inelastic scattering, particle transfers, etc.), where knowledge of the complete wave function is necessary, the ambiguity must be resolved as different potentials will give rise to different wave functions in the internal region.

In fact, the qualitative aspects of the phenomenological optical potentials (real, imaginary and spin-orbit terms, radial dependence, energy dependence, etc.) have been justified from a theoretical point of view [2, 3]. However, calculations using "realistic" two-body forces and Hartree-Fock theory (it is reasonable to think that there is a connection between the optical potential and the self-consistent single-particle well in which the bound particles move) do not produce a unique answer [4]. Therefore, resolving the ambiguities is still an open problem.

In the case of composite projectiles, one has so far attempted to express the phenomenological optical potentials in terms of the corresponding single-nucleon ones. General expressions have been derived by several authors [5]. In a first approximation, the potential is given by the sum of the single-nucleon potentials folded over the matter distribution in the projectile. For deuterons, for example, we obtain

$$V_d^{\text{op}}(\vec{R}, E_d) = \int d^3r \left| \varphi_d(\vec{r}) \right|^2 \left\{ V_n^{\text{op}}(\vec{R} + \frac{1}{2}\vec{r}, E_n) + V_p^{\text{op}}(\vec{R} - \frac{1}{2}\vec{r}, E_p) \right\} \quad (1)$$

in self-explanatory notation. Obviously, such an expression does not contain the contribution of processes in which the projectile undergoes excitation

\* Work supported by the Comisión Nacional de Energía Nuclear de México.

or breaks up, but this should reflect more on the imaginary part than on the real part of the potential. Calculations of  $V_d^{OP}$  along these lines have reproduced well the shape but not the depth of the real part of the potential [6]. The values of the well depth obtained fall consistently half way between two of the phenomenological best-fit values. Estimates of additional terms give too small a contribution to resolve the ambiguity [7].

Now, in all calculations so far, the assumption  $E_n = E_p = (1/2) E_d$  has been made. A careful analysis [8] of the scattering process shows that this approximation is only justified for high bombarding energies ( $E_d \gg T_d$  where  $T_d$  is the internal kinetic energy of the deuteron), in which the scattering is in the forward direction. In fact, the single-nucleon energy (relative to the target nucleus) which is involved in the scattering of the deuteron through an angle  $\theta$ , depends on this angle through the relation

$$E_{n,p} = \frac{A+1}{A+2} E_d \frac{5-3 \cos \theta}{4} \quad (2)$$

where  $A$  is the mass number of the target. Therefore one gets (for large  $A$ )  $E_{n,p} \approx \frac{1}{2} E_d$  for  $\theta = 0^\circ$  but  $E_{n,p} \approx 2 E_d$  for  $\theta = 180^\circ$ . The use of relation (2), or of some average value  $\overline{E}_{n,p}$ , in expression (1) will produce a decrease in the values of  $\text{Re} V_d$  obtained so far. This is because, for the single-nucleon potential,

$$\text{Re} V_{n,p}(r_{n,p} = 0) = U_{n,p} - \alpha E_{n,p}, \quad \alpha > 0 \quad (3)$$

If we use  $E_{n,p} = \overline{E}(\theta) = (5/4) E_d$  instead of  $E_{n,p} = \frac{1}{2} E_d$ , the reduction in the value of  $\text{Re} V_d(R=0)$  is given by

$$\Delta \equiv \text{Re} V_d \Big|_{\frac{1}{2} E_d} - \text{Re} V_d \Big|_{\frac{5}{4} E_d} \approx \frac{3}{2} \alpha E_d$$

For the usually accepted value of  $\alpha \approx 0.3$  and a deuteron energy of  $E_d = 21.5$  MeV, we obtain  $\Delta = 9.4$  MeV, in good agreement with the  $\Delta = 10$  MeV of Johnson and Soper (Ref. [7], footnote 51). This change is sufficient to resolve the ambiguity in Perey and Satchler's work [6].

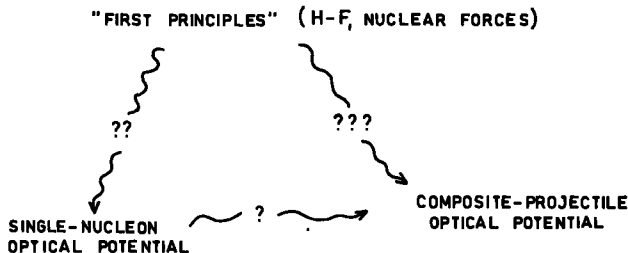


FIG. 1. State-of-the art in optical-model nuclear scattering.

It is felt that this angular dependence of the relation between energies should play an important role in establishing the connection between the optical potentials for heavier projectiles and the single-nucleon ones: especially in clarifying why one is obtaining, from the phenomenological analysis, rather shallow potentials, i. e. compared to the result of multiplying the single-nucleon potential by the number of particles in the projectile.

Finally, Fig. 1 below attempts to give an idea of the state of affairs in the problem of understanding the optical model of nuclear scattering.

## APPENDIX

We give here the corresponding relations to Eq. (2) for the case of  ${}^3\text{He}$ ,  $t$  and  $\alpha$ 's (in all cases s-wave internal relative motion is assumed):

$$\text{for } t \text{ and } {}^3\text{He} \quad E_{n,p} = \frac{A+1}{A+3} E_{(t, {}^3\text{He})} \frac{5-4 \cos \theta}{3} \quad (\text{A. 1})$$

$$\text{for } \alpha \quad E_{n,p} = \frac{A+1}{A+4} E_{\alpha} \frac{17-15 \cos \theta}{8} \quad (\text{A. 2})$$

We can see that the ranges of variation are appreciable. Combined with Eq. (3), they can give rise to important changes in the evaluation of the optical potentials.

## REFERENCES

- [1] HODGSON, P.E., *The Optical Model of Elastic Scattering*, Oxford University Press (1963);  
HODGSON, P.E., *Adv. in Phys.* 15 (1966) 329;  
BECCHETTI, F.D., GREENLESS, G.W., *Phys. Rev.* 182 (1969) 1190;  
WATSON, B.A., SINGH, R.P., SEGEL, R.E., *Phys. Rev.* 182 (1969) 977;  
HALBERT, E.C., *Nucl. Phys.* 50 (1964) 353;  
WEISSER, D.C. et al., *Phys. Rev.* C2 (1970) 544.
- [2] FESHBACH, H., *Ann. Rev. nucl. Sci.* 8 (1958) 49.
- [3] PEREY, F.G., BUCK, B., *Nucl. Phys.* 32 (1962) 353.
- [4] COZ, M. et al., *Ann. Phys. (NY)* 58 (1970) 504. I am grateful to Prof. F. Stancu for pointing out this paper. Earlier work like that of SLAMINA, D., McMANUS, H., *Nucl. Phys.* A116 (1968) 271 had seemed to settle the question; they used "effective" forces but an ad-hoc matter density, not one obtained self-consistently.
- [5] SAWADA, T., *Nucl. Phys.* 74 (1965) 289;  
JUNKIN, W.F., VILLARS, F., *Ann. Phys. (NY)* 45 (1967) 93;  
MUKHERJEE, S., *Nucl. Phys.* A118 (1968) 423;  
SUZUKI, T., *Progr. theor. Phys.* 42 (1969) 732.
- [6] WATANABE, S., *Nucl. Phys.* 8 (1958) 484;  
PEREY, F.G., SATCHLER, G.R., *Nucl. Phys.* A97 (1967) 515;  
ABUL MAGD, A.Y., EL NADI, M., *Progr. Theor. Phys. (Kyoto)* 35 (1966) 798.
- [7] TESTONI, J., GOMEZ, L.C., *Nucl. Phys.* 89 (1966) 288;  
JOHNSON, R.C., SOPER, P.J.R., *Phys. Rev.* C1 (1970) 976.
- [8] BLOCH, C., BAUER, M., *Phys. Letts* 33B (1970) 155.



# DIRECT METHODS IN SCATTERING THEORY

B. N. ZAKHARIEV

Laboratory for Theoretical Physics,  
JINR, Dubna,  
Union of Soviet Socialist Republics

## Abstract

### DIRECT METHODS IN SCATTERING THEORY

Introduction; 1. One particle in an external field  $V(r, \theta, \varphi)$ ; 2. Formulation of the three-body scattering problem; 3. Scattering without rearrangement of particles; 4. Reactions with rearrangement of particles; 5. Method of hyper-spherical harmonics in scattering problems; 6. Reactions of the type  $1+(23) \rightarrow 1+2+3$ ; 7. Variational bounds for scattering parameters; 8. Treatment of reactions of general type without separating asymptotic components in  $\Psi$ ; 9. Concluding remark (combination of different methods).

## INTRODUCTION

The most general and correct approach to the description of non-relativistic quantum mechanical scattering processes for many-body systems is realized by methods taking into account close multi-channel coupling. It is possible in this approach to minimize the number of phenomenological assumptions. Thus, for example, it is often only necessary to take fundamental two-body interactions in order to calculate the wave function of a system.

Considerable progress was achieved in this field of theory in recent years. Many different algorithms of treating the reactions of the most general type have been developed, e.g. rearrangement collisions and the reactions with more than two free particles in the initial or in the final state (see, for example, review article [1]).

The Schrödinger equation is, in the general case, a differential equation in partial derivatives in which the variables cannot be separated. And the present computers are most effective in solving equations with a single variable. So we use the direct methods of mathematical physics to reduce approximately the problem to the solution of a system of ordinary differential equations.

If we decompose the wave function  $\Psi$  into a complete set of known functions  $\Phi_\alpha$  and, as an approximation, take into account only a finite number of terms in this expansion:

$$\Psi \approx \Psi^N = \sum_{\alpha}^N F_{\alpha} \Phi_{\alpha} \quad (1)$$

then, according to Galerkin's principle, we obtain from the Schrödinger equation  $(H - E)\Psi = 0$  a system of equations

$$\langle \Phi_\alpha | (H - E) \sum_{\beta}^N F_\beta \Phi_\beta \rangle = 0 \quad (\alpha = 1, \dots, N) \quad (2)$$

for the unknown coefficients  $F_\beta$ .

Almost all methods of the so-called unified theory of nuclear reactions are a particular realization of this simple scheme.

Before proceeding to consider the methods by which the most complex general reactions can be treated, let us recall some simple information about the formalism of multichannel scattering.

One of the simplest examples of multi-channel scattering is the motion of a particle in a field  $V(\vec{r})$  without spherical symmetry.

### 1. ONE PARTICLE IN AN EXTERNAL FIELD $V(r, \theta, \varphi)$

Let  $V(\vec{r})$  have a finite range:  $V(r < r_0, \theta, \varphi) = 0$ .

We have to solve the wave equation ( $m = 1, h = 1$ ):

$$-\Delta \Psi(\vec{r}) + v(\vec{r}) \Psi(\vec{r}) = k^2 \Psi(\vec{r}) \quad (3)$$

with boundary conditions:

$$\Psi(r > r_0, \theta, \varphi) = \sum_{\ell m} N_\ell \left( \frac{1}{k^{1/2}} j_\ell(kr) + f_{\ell m} h^{(1)}(kr) \right) Y_{\ell m}(\theta, \varphi) \underset{r \rightarrow \infty}{\sim} e^{ikr} + f(\theta, \varphi) \frac{e^{ikr}}{r} \quad (4)$$

where  $f_{\ell m}$  are the partial scattering amplitudes, and  $N_\ell = [4\pi(2\ell+1)]^{1/2} i^\ell$ .

To reduce the problem to the solution of differential equations with a single variable, it is natural, according to Eq. (4), to choose as the basis functions  $\Phi_\alpha$  (Eq. (1)) spherical harmonics  $Y_{\ell m}(\theta, \varphi)$  divided by  $r$ :

$$\Psi(\vec{r}) = \sum_{\ell'm'} \frac{F_{\ell'm'}(r)}{r} Y_{\ell'm'}(\theta, \varphi) N_{\ell'} \quad (1a)$$

It is a good approximation to neglect in expression (1a) the terms with  $\ell \gg kr_0$ . So, for unknown coefficients  $F_{\ell m}$  we have a system of a finite number of ordinary differential equations (see Eq. (2)):

$$-\frac{d^2}{dr^2} F_{\ell m}(r) + \frac{\ell(\ell+1)}{r^2} F_{\ell m}(r) + \sum_{\ell'm'} V_{\ell m \ell' m'}(r) F_{\ell' m'}(r) = k^2 F_{\ell m}(r) \quad (2a)$$

where  $V_{\ell m \ell' m'}(r) = \int Y_{\ell m}^* V(\vec{r}) Y_{\ell' m'} d\Omega$  are the elements of the interaction matrix which realize the coupling of the equations in the system (2a)<sup>1</sup>.

<sup>1</sup> If  $V(\vec{r})$  has a spherical symmetry,  $V(\vec{r}) = V(r)$ , we have  $W_{\ell m \ell' m'} = \delta_{\ell \ell'} \delta_{m m'} V(r)$ , and the system (2a) becomes decoupled.

The scheme of numerical solution of Eq. (2a)

The interaction matrix  $\|V_{\ell m \ell' m'}(r)\|$  vanishes at  $r > r_0$  together with  $V(r)$  and Eqs (2a) become decoupled. According to Eq. (4)  $F_{\alpha}(r)$  must satisfy the following conditions:

$$F_{\ell m}(0) = 0; \quad F_{\ell m}(r > r_0) = \frac{r}{k^{1/2}} j_{\ell}(kr) + f_{\ell m} h_{\ell}^{(1)} \cdot r \quad (5)$$

Hence we must integrate the system (2a) numerically in the interval  $0 < r < r_0$ .

It is important to note that the boundary conditions (5) are given at both ends of this interval and the systems of ordinary differential equations could be solved by the computer directly only if all the conditions are formulated at the same point. Since, however, the system of  $N$  simple differential equations (2a) has only  $N$  linearly independent solutions with  $F_{\alpha}(0) = 0$ , and since the required solution of Eq. (2a) could be constructed as a linear combination of  $N$  such solutions, we can proceed in the following way:

The system (2a) is solved  $N$  times with  $N$  linearly independent auxiliary boundary conditions at  $r = 0$  (e. g.,  $F_{\alpha}^{(s)}(0) = 0$ ;  $((d/dr)F_{\alpha}^{(s)})_{r \rightarrow 0} \sim \delta_{s\alpha} r^{\ell}$ , where  $s = 1, 2, \dots, N$ ). Then a linear combination of these solutions is constructed:

$$F_{\alpha}(r) = \sum_s C_s F_{\alpha}^{(s)}(r) \quad (6)$$

which is a general solution of Eq. (2a) satisfying the conditions  $F_{\alpha}(0) = 0$ . Finally, we choose the coefficients  $C_s$  to satisfy the boundary conditions at  $r = r_0$  also:

$$\sum_s C_s F_{\alpha}^{(s)}(r_0) = \frac{r_0}{k^{1/2}} j_{\ell}(kr_0) + f_{\ell m} r_0 h_{\ell}^{(1)}(kr_0) \quad (7)$$

$$\sum_s C_s \left( \frac{d}{dr} F_{\alpha}^{(s)} \right)_{r=r_0} = \frac{1}{k^{1/2}} \left( \frac{d}{dr} r j_{\ell} \right)_{r=r_0} + f_{\ell m} \left( \frac{d}{dr} r h_{\ell}^{(1)} \right)_{r=r_0}$$

The second moment to be noted is that the coefficients  $\ell(\ell+1)/r^2$  increase infinitely for  $r \rightarrow 0$ , and computers can operate only with finite values. But for small values of  $r$ , Eq. (2a) can be approximately solved by use of the expansion of  $F_{\alpha}^{(s)}(r)$  in powers of  $r$ .

The constants  $F_{\alpha}^{(s)}(r_0)$  and  $((d/dr)F_{\alpha}^{(s)})_{r=r_0}$  in expressions (7) are known from the numerical integration of Eqs (2) (auxiliary solutions).

From the  $2N$  algebraic Eqs (7) we obtain  $2N$  unknown constants  $C_{\alpha}$  and

$$f_{\ell m}, \text{ which determine the wave function } \Psi = \sum_{s, \ell m} C_s F_{\ell m}^{(s)}(r) (1/r) Y_{\ell m}(\theta, \varphi) N_{\ell}$$

and the scattering cross-sections.

It is also useful to mention that the error of numerical integration of (2a) can be estimated by checking the violation of the conservation law:

$$\sum_{\alpha} \left( F_{\alpha}^{(s)} \frac{d}{dr} F_{\alpha}^{(s')} - F_{\alpha}^{(s')} \frac{d}{dr} F_{\alpha}^{(s)} \right) = \text{const.} \quad (8)$$

## 2. FORMULATION OF THE THREE-BODY SCATTERING PROBLEM

It is convenient to investigate the principal problems of scattering theory for many-particle systems in the particular case of the three-body system. The appearance of many important qualitative properties characteristic of complex systems begins from just this simplest system (addition of fourth, fifth, etc., particles does not introduce anything very new). Beginning from the three-particle systems, there appear the inelastic scattering (with excitation of sub-systems), reactions with rearrangement of particles, threshold effects, processes with more than two free particles in initial and final states, etc.

The Schrödinger equation for three particles (in c. m. s.) is given by

$$H\Psi(\vec{R}_1, \vec{r}_{jk}) \equiv \left( -\frac{\hbar^2}{2M_1} \Delta_{\vec{R}_1} - \frac{\hbar^2}{2\mu_{jk}} \Delta_{\vec{r}_{jk}} + V_{12} + V_{23} + V_{13} \right) \Psi = E\Psi \quad (i \neq j \neq k) \quad (9)$$

where  $\vec{R}$  and  $\vec{r}$  are Jacobi co-ordinates: the  $\vec{R}_1$ -vector, characterizing the relative position of  $i$ -th particle and the centre of mass of the pair (jk);  $\vec{r}_{jk} = \vec{r}_j - \vec{r}_k$ .

The boundary (asymptotic) conditions on  $\Psi$  can be formulated in terms of eigenfunctions of the asymptotic form of the Hamiltonian  $H$ . There are several such asymptotic Hamiltonians:

$$H_i = \lim_{R_i \rightarrow \infty} H = -\frac{\hbar^2}{2M_i} \Delta_{\vec{R}_i} + h_{jk} \quad (10)$$

according to the variety of ways of grouping the particles 1, 2, 3. This is one of the most important new properties of the three-body in comparison with the two-body system.

The Hamiltonian  $h_{jk}$  of relative internal motion of particles  $j$  and  $k$  has eigenfunctions  $\varphi_{\alpha}$  and eigenvalues  $\epsilon_{\alpha}$ :

$$h_{ij} \varphi_{\alpha}(\vec{r}_{ij}) = \epsilon_{\alpha} \varphi_{\alpha}(\vec{r}_{ij}) \quad (11)$$

According to Eqs (10) and (11), the solution of Eq.(9) has the following general form for  $R_i \rightarrow \infty$ :

$$\Psi(R_i \rightarrow \infty; r_{jk} < \infty) \sim \sum_{\alpha \ell m} \frac{F_{\alpha \ell m}(R_i)}{R_i} Y_{\ell m}(\Omega_{\vec{r}}) \varphi_{\alpha}(\vec{r}_{jk}) N_{\ell} \quad (12)$$

For a particular choice of potentials  $V_{ij}$  in Eq. (9) and energy values  $E$ , there can be several types of boundary conditions.

1) Let  $V_{ij}$  and  $E$  be chosen so that scattering is only possible in channels with a single grouping of particles. This situation is realized, for example, if one particle is scattered on a pair of other particles, which are coupled by an infinitely deep potential well. In this case, only such asymptotic states exist which differ from the entrance state by the excitation of the target pair. Only a single asymptotic Hamiltonian corresponds to the initial and final states in this case, as in the two-body problem. So we have:

$$\Psi(\vec{R}_1, \vec{r}_{jk}) \sim \begin{cases} \sum_{\alpha \ell m} \left[ \frac{\sin(k_\alpha R_1 - (\ell\pi/2))}{k_0^{1/2} R_1} \delta_{\alpha\alpha_0} \delta_{m0} + f_{\alpha\ell m} \frac{e^{i(k_\alpha R_1 - (\ell\pi/2))}}{R_1} \right] N_\ell \\ \quad \times Y_{\ell m}(\Omega_{R_1}) \varphi_\alpha(\vec{r}_{jk}) \text{ for } \begin{pmatrix} R_1 \rightarrow \infty \\ r_{jk} < \infty \end{pmatrix} \\ 0 \text{ for } R_1 < \infty, r_{jk} \rightarrow \infty \end{cases} \quad (13)$$

The summation in expression (13) is limited only by the states for which  $E - \epsilon_\alpha \geq 0$ , and  $\delta_{\alpha\alpha_0}$  corresponds to the condition that incoming waves are only in the entrance channels  $\alpha_0$ .

2) The boundary conditions will be more complex if rearrangement of particles is possible:

$$1 + (23) \Rightarrow \left\{ \begin{array}{l} 1 + (23) \text{ scattering without rearrangement.} \\ 2 + (13) \\ 3 + (12) \end{array} \right\} \text{ reactions with rearrangement.}$$

In this case, the asymptotic form of the wave function  $\Psi$  must describe all the possible final states, which correspond to several asymptotic Hamiltonians in different directions of configuration space ( $R_i \rightarrow \infty$ ,  $r_{jk}$  - finite;  $i \neq j \neq k = 1, 2, 3$ ):

$$\Psi \rightarrow \begin{cases} \sum_{\alpha \ell m} \left[ \frac{\sin(k_\alpha R_1 - (\ell\pi/2))}{k_0^{1/2} R_1} \delta_{\alpha\alpha_0} \delta_{m0} + f_{\alpha\ell m} \frac{e^{i(k_\alpha R_1 - (\ell\pi/2))}}{R_1} \right] Y_{\ell m}(\Omega_{R_1}) \varphi_\alpha(\vec{r}_{23}) N_\ell \\ \quad \text{for } R_1 \rightarrow \infty \\ \sum_{\beta \ell' m'} f_{\beta \ell' m'} \frac{e^{i(k_\beta R_2 - (\ell'\pi/2))}}{R_2} Y_{\ell' m'}(\Omega_{R_2}) \varphi_\beta(\vec{r}_{13}) N_{\ell'} \text{ for } R_2 \rightarrow \infty \\ \sum_{\gamma \ell'' m''} f_{\gamma \ell'' m''} \frac{e^{i(k_\gamma R_3 - (\ell''\pi/2))}}{R_3} Y_{\ell'' m''}(\Omega_{R_3}) \varphi_\gamma(\vec{r}_{12}) N_{\ell''} \text{ for } R_3 \rightarrow \infty \end{cases} \quad (14)$$

3) So far, we have considered only the reactions with two free fragments in initial and final states:  $A + B \rightarrow C + D$ .

Above the threshold of the division of the system into three parts there appears in the asymptotics of  $\Psi$  besides the two-fragment components (14) also the term which corresponds to the Hamiltonian  $H_0 = \lim H$  of free

motion of particles. It is convenient to write the boundary conditions for such states in new hyperspherical variables, [6]: the radius  $\rho_6 = \sqrt{R_i^2 + r_{jk}^2}$  and five angular variables (e.g. three Eulerian angles, characterizing the orientation of the triangle (123) in space, and two angles determining the form of this triangle):

The divergent wave in the disintegration channel has the following form in these variables:

$$\Psi \xrightarrow[\rho_6 \rightarrow \infty]{} f(\Omega_{\rho_6}) \frac{e^{ik_{\rho_6} \rho_6}}{\rho_6^{5/2}} ; \quad k_{\rho_6}^2 = k_r^2 + k_R^2 \quad (15)$$

### 3. SCATTERING WITHOUT REARRANGEMENT OF PARTICLES [2]

According to the form of asymptotic conditions for scattering without rearrangement of particles (jk) it is natural to take as a basis function in this case  $\Phi_{\alpha \ell m} = Y_{\ell m}(\Omega_{R_i}) \varphi_{\alpha}$ :

$$\Psi = \sum_{\alpha \ell m} \frac{F_{\alpha \ell m}(R_i)}{R_i} N_{\ell} Y_{\ell m}(\Omega_{R_i}) \varphi_{\alpha}(\vec{r}_{jk}) + \int \dots \quad (1b)$$

So the boundary conditions for  $\vec{r}_{jk}$  would be satisfied before the solution of the Schrödinger equation. The integral part of expansion (1b) is usually neglected (if  $h_{jk}$  has a continuous spectrum).

Equation (2) in this case has the form:

$$\left[ -\frac{\hbar^2}{2M_i} \frac{d^2}{dR_i^2} + \frac{\ell(\ell+1)}{2M_i R_i^2} - (E - \epsilon_{\alpha}) \right] F_{\alpha \ell m}(R_i) + \sum_{\alpha' \ell' m'} \langle \Phi_{\alpha \ell m} | V_{ij} + V_{ik} | \Phi_{\alpha' \ell' m'} \rangle \times F_{\alpha' \ell' m'}(R_i) = 0 \quad (2b)$$

The main difference between this system and that for the two-body system (2a) is in the fact that here the energy term  $(E - \epsilon_{\alpha})$  is not a constant for all the channels.

For the target states  $\alpha$ , whose excitation energy is less than the energy of the incident particle ( $E \geq \epsilon_{\alpha}$ ; open channels), the boundary condition for  $F_{\alpha \ell m}$  are:

$$F_{\alpha \ell m}(R_i) \xrightarrow[R_i \rightarrow \infty]{} \frac{1}{k_{\alpha}^{1/2}} \sin\left(k_{\alpha} R_i - \frac{\ell\pi}{2}\right) \delta_{\alpha\alpha_0} + f_{\alpha \ell m} e^{i(k_{\alpha} R_i - (\ell\pi/2))} ; \quad k_{\alpha}^2 = 2M_i (E - \epsilon_{\alpha}) \quad (16)$$

For closed channels ( $E < \epsilon_{\alpha}$ ) it is required that  $F_{\alpha}$  decreases exponentially with  $R_i$  (the  $i$ -th particle cannot leave the target with negative energy):

$$F_{\alpha \ell m} \xrightarrow[R_i \rightarrow \infty]{} A_{\ell m} e^{-\kappa_{\alpha} R_i} ; \quad \kappa_{\alpha}^2 = 2M_i (\epsilon_{\alpha} - E) \quad (17)$$

The scheme of numerical solution of Eq. (2b) is very similar to that for the system (2a). It is only necessary to take into account new boundary conditions (16) and (17) instead of (5).

#### 4. REACTIONS WITH REARRANGEMENT OF PARTICLES [3]

The method described above is not valid for re-arrangement collisions because the set of basic functions, corresponding to a single asymptotic Hamiltonian  $H$ , is too poor to satisfy the complex boundary conditions (14). In principle, the continuous spectrum of  $H_i$  is connected with the channels of different grouping of particles. But if the integral part of the expansion (1b) is taken into account, Eq. (2b) becomes a very complex system of integro-differential equations, and it is not clear how to formulate by means of the functions  $F_{\alpha\ell m}(R_i)$ , which depend on one variable, the boundary conditions for the channels described in terms of quite different variables.

It seems rather natural to try to expand  $\Psi$  by utilizing simultaneously the basic functions corresponding to all the asymptotic Hamiltonians:

$$\Psi = \sum_{\alpha\ell m} \frac{F_{\alpha\ell m}(R_1)}{R_1} \Phi_{\alpha\ell m}(\Omega_{R_1}; \vec{r}_{23}) + \sum_{\beta\ell'm'} \frac{F_{\beta\ell'm'}(R_2)}{R_2} \Phi_{\beta\ell'm'}(\Omega_{R_2}; \vec{r}_{31}) \\ + \sum_{\gamma\ell''m''} \frac{F_{\gamma\ell''m''}(R_3)}{R_3} \Phi_{\gamma\ell''m''}(\Omega_{R_3}; \vec{r}_{12}) + \int \dots \quad (1c)$$

But in this case we get the integro-differential equations for  $F_\alpha$ ,  $F_\beta$ ,  $F_\gamma$  even if we neglect the continuous part of expansion (1c) due to the non-orthogonality of the basic functions for channels with different grouping of particles. The difficulty of solving integro-differential equations is the main defect of this method. In addition, the question of the overcompleteness of the system of basic functions  $\overline{\Phi_{\alpha\ell m}}$ ,  $\overline{\Phi_{\beta\ell'm'}}$ ,  $\overline{\Phi_{\gamma\ell''m''}}$  is not sufficiently clear.

As mentioned above, the main cause of the special difficulty of reaction with rearrangement of particles consists in the presence of components with different grouping of particles in the asymptotic behaviour of  $\Psi$ . But we can utilize the fact that the asymptotic part of  $\Psi$  is the best known (there are only undetermined constants - partial reaction amplitudes). If we separate the asymptotic components in  $\Psi$  which prevent us from using the expansion (1b) (see Eq. (14)):

$$\Psi = \sum_{\beta\ell'm'} f_{\beta\ell'm'} \frac{e^{i(k_\beta R_2 - (\ell'\pi/2))}}{R_2} Y_{\ell'm'}(\Omega_{R_2}) \varphi_\beta(\vec{r}_{13}) S(R_2) N_{\ell'} \\ + \sum_{\gamma\ell''m''} f_{\gamma\ell''m''} \frac{e^{i(k_\gamma R_3 - (\ell''\pi/2))}}{R_3} Y_{\ell''m''}(\Omega_{R_3}) \varphi_\gamma(\vec{r}_{12}) S(R_3) N_{\ell''} + X(\vec{R}_1; \vec{r}_{23}) \quad (18)$$

the remaining part of  $\Psi$  can be expanded in the set of basic functions of a single asymptotic Hamiltonian  $H_1$ :

$$\chi = \sum_{\alpha \ell m} \frac{F_{\alpha \ell m}(R_1)}{R_1} Y_{\ell m}(\Omega_{R_1}) \varphi_{\alpha}(\vec{r}_{23}) N_{\ell} \quad (19)$$

The factors  $S(R)$  are introduced in the expansion (18) to remove the singularity of separated terms at  $R_{2(3)} = 0$  (they can be chosen in a form  $S(R) = 1 - \exp -\alpha R$ ). Inserting (19) in (18) we get an expression for  $\Psi$  which can be considered as an expansion of  $\Psi$  with coefficients  $f_{\beta \ell' m'}$ ,  $f_{\gamma \ell'' m''}$  and  $F_{\alpha \ell m}(R_1)$ :

$$\begin{aligned} \Psi = & \sum_{\alpha_1 \ell_1 m_1} \frac{F_{\alpha_1 m_1 \ell_1}(R_1)}{R_1} \Phi_{\alpha_1 \ell_1 m_1}(\Omega_{R_1}; \vec{r}_{23}) + \sum_{\beta \ell' m'} f_{\beta \ell' m'} \tilde{\Phi}(\vec{R}_2; r_{13}) \\ & + \sum_{\gamma \ell'' m''} f_{\gamma \ell'' m''} \tilde{\Phi}_{\gamma \ell'' m''}(\vec{R}_3; \vec{r}_{12}) \end{aligned} \quad (1d)$$

The Galerkin principle gives a system of differential and algebraic equations for the unknown coefficients:

$$\begin{aligned} & \left[ -\frac{\hbar^2}{2M_1} \frac{d^2}{dr^2} + \frac{\ell(\ell+1)}{2M_1 R_1^2} - (E - \epsilon_{\alpha}) \right] F_{\alpha \ell m}(R_1) \\ & + \sum_{\alpha_1 \ell_1 m_1} \langle \Phi_{\alpha, \ell, m} | V_{12} + V_{13} | \Phi_{\alpha_1, \ell_1, m_1} \rangle F_{\alpha_1 \ell_1 m_1}(R) \\ & = \sum_{\beta \ell' m'} f_{\beta \ell' m'} \langle \Phi_{\alpha \ell m}(\Omega_{R_1}; \vec{r}_{23}) | (E - H) \tilde{\Phi}_{\beta \ell' m'}(\vec{R}_2; \vec{r}_{13}) \rangle \\ & + \sum_{\gamma \ell'' m''} f_{\gamma \ell'' m''} \langle \Phi_{\alpha \ell m}(\Omega_{R_1}; \vec{r}_{23}) | (E - H) \tilde{\Phi}_{\gamma \ell'' m''}(\vec{R}_3; \vec{r}_{12}) \rangle \\ & \sum_{\beta_1 \ell'_1 m'_1} \langle \tilde{\Phi}_{\beta \ell' m'} | (H - E) \tilde{\Phi}_{\beta_1 \ell'_1 m'_1} \rangle f_{\beta_1 \ell'_1 m'_1} + \sum_{\gamma \ell'' m''} \langle \tilde{\Phi}_{\beta \ell' m'} | (H - E) \tilde{\Phi}_{\gamma \ell'' m''} \rangle f_{\gamma \ell'' m''} \\ & + \sum_{\alpha \ell m} \langle \tilde{\Phi}_{\beta \ell' m'} | (H - E) \frac{F_{\alpha, \ell_1 m_1}(R_1)}{R_1} \Phi_{\alpha_1 \ell_1 m_1} \rangle = 0 \\ & \sum_{\beta \ell' m'} \langle \tilde{\Phi}_{\gamma \ell'' m''} | (H - E) \tilde{\Phi}_{\beta \ell' m'} \rangle f_{\beta \ell' m'} + \sum_{\gamma \ell'_1 m'_1} \langle \tilde{\Phi}_{\gamma \ell'' m''} | (H - E) \tilde{\Phi}_{\gamma_1 \ell'_1 m'_1} \rangle f_{\gamma_1 \ell'_1 m'_1} \end{aligned}$$

$$+ \sum_{\alpha \ell m} \langle \tilde{\Phi}_{\gamma \ell^* m^*} | (H - E) \frac{F_{\alpha_1 \ell_1 m_1}(R_1)}{R_1} \Phi_{\alpha_1 \ell_1 m_1} \rangle = 0 \quad (2d)$$

The differential equations (2d) differ from Eqs (2b) only by terms on the right-hand side, which can be considered as "sources" providing the connection of direct channels with rearrangement channels.

The system (2d) can be solved in the following way. First, the general solution  $F(R_1)$  of the differential equations is constructed by using the fact that the sources depend linearly on unknown partial amplitudes<sup>2</sup>. This solution depends linearly on unknown amplitudes  $f$  and arbitrary constants  $C_i$  of the general solution of the homogeneous equation. We put this solution into the system of algebraic equations (2d) and add the algebraic equations which we obtain from the boundary conditions for  $F(R_1)$ . Thus we derive the system for the partial amplitudes  $f$  and constants  $C_i$  and obtain the wave function  $\Psi$  and the reaction amplitudes.

Recently, a description of the rearrangement collisions by a method without separation of asymptotic components in  $\Psi$  was proposed (see section 8).

## 5. METHOD OF HYPER-SPHERICAL HARMONICS IN SCATTERING PROBLEMS

For a system of identical particles, it is convenient to use the expansion of  $\Psi$  which has exactly the required symmetry properties with respect to particle permutation. But how shall we choose a single variable to reduce the problem to simple differential equations, thereby not violating the symmetry of  $\Psi$ ? It is possible if this single variable is an invariant of the particle permutation. In the two-body problem such an invariant is the absolute value of the vector  $\vec{\rho}_{12} = \vec{r}_1 - \vec{r}_2$ , and the spherical harmonics are chosen as basic functions.

For the three-body system the situation is more complex. Now we need two vectors to describe the system:  $\vec{R}_i$  and  $\vec{r}_{jk}$ . Neither  $|\vec{R}_i|$  nor  $|\vec{r}_{jk}|$  is the required invariant. But if we introduce the hyper-spherical co-ordinates (see sub-section 2.3), the absolute value of the vector  $\vec{\rho}_6 \equiv \{\vec{R}_i, \vec{r}_{jk}\}$  will be the invariant which we need. In analogy with the three-dimensional case we introduce the generalized spherical (hyper-spherical) functions  $Y_{\vec{K}}(\Omega_5)$ , where  $\vec{K}$  is a set of five quantum numbers. The unusual six-dimensional space and new quantum numbers should not confuse those who meet them for the first time. They are handled in the same way as the usual spherical functions.

When a function localized in a finite region (bound-state problems) is expanded in the set [4]

$$\Psi = \sum_{\vec{K}} F_{\vec{K}}(\rho_6) Y_{\vec{K}}(\Omega_5) \quad (1e)$$

<sup>2</sup> The general solution of the inhomogeneous equation  $\hat{L}F = \sum_i f_i M_i$  is:  $F = F^{(0)} + \sum_i f_i F_i$ , where  $F^{(0)}$  is a general solution of the homogeneous equation and  $F_i$  are partial solutions of the equations  $\hat{L}F_i = M_i$ .

the boundary conditions for  $F_{\vec{K}}$  are simple:  $F_{\vec{K}}(\rho_6) \xrightarrow{\rho_6 \rightarrow \infty} 0$ . The number of

$K$ -harmonics necessary for a satisfactory description of the function depends on the angular velocity of their variation (as in the case of  $Y_{\ell m}$ ).

It is therefore advisable to expand in the set of  $Y_{\vec{K}}(\Omega_5)$  in the scattering problems only that part of the wave function which has no two-fragment asymptotic components [5]:

$$\Psi = \sum_{\alpha \ell m} f_{\alpha \ell m} \tilde{\Phi}_{\alpha \ell m} + \sum_{\beta \ell' m'} f_{\beta \ell' m'} \tilde{\Phi}_{\beta \ell' m'} + \sum_{\gamma \ell'' m''} f_{\gamma \ell'' m''} \tilde{\Phi}_{\gamma \ell'' m''} + \sum_{\vec{K}} F_{\vec{K}}(\rho_6) Y_{\vec{K}}(\Omega_5) \quad (1f)$$

The solution of a proper system for coefficients  $f$  and  $F_{\vec{K}}(\rho_6)$  proceeds as in the case of Eq. (2d). The main difference is that it is required that  $F_{\vec{K}}(\rho_6)$  vanish for  $\rho_6 \rightarrow \infty$ .

## 6. REACTIONS OF THE TYPE $1 + (23) \rightarrow 1 + 2 + 3$

Let us now consider the reactions above the threshold of division of the system into three parts. Below this threshold, there is a discrete number of open channels, because the energy  $E$  is divided between the quantized inner motion of fragments and their relative motion. Above the threshold, the energy of the system is divided in a continuous way between three particles. It seems that in this case there is no possibility of avoiding the basic set with continuously varying quantum numbers for expansion of  $\Psi$ . But, as in the two-body problem, the continuous angular distribution of scattering products is described by means of a discrete set of spherical functions  $Y_{\ell m}$ , so the angular and energy distribution of three (and more) free particles can be described by a discrete set of hyper-spherical functions  $Y_{\vec{K}}$ . And for free motion of particles,  $\vec{K}$  are good quantum numbers. Therefore, there is no need to separate in  $\Psi$  the asymptotic components corresponding to the disintegration of the system. The expansion of  $\Psi$  coincides in this case with the expansion (1f). The equations for  $f$  and  $F_{\vec{K}}(\rho_6)$  are also the same. The difference is only in new boundary conditions for  $F_{\vec{K}}(\rho_6)$ . In accordance with relation (15) [6]:

$$F_{\vec{K}}(\rho_6) \xrightarrow{\rho_6 \rightarrow \infty} f_{\vec{K}} \frac{e^{ik\rho_6}}{\rho_6^{5/2}} \quad (20)$$

where  $f_{\vec{K}}$  are the partial amplitudes of disintegration.

## 7. VARIATIONAL BOUNDS FOR SCATTERING PARAMETERS

So far, the problem of estimating errors due to neglecting an infinite number of terms in expansion (1) is poorly investigated.

There is a well-known example in quantum mechanics when such errors can be controlled exactly. The calculations of eigenvalues of energy in the bound-state problem by means of variational methods give strict upper bounds for energy levels. This is widely used because in

many cases it allows definite conclusions to be made from the comparison of theoretical results with experiment, in spite of the fact that calculations may be very rough. If the theoretical value is below the experimentally measured energy level, it means quite certainly that the initial theoretical assumptions are wrong – more precise calculations would increase the discrepancy with experiment.

The situation for the scattering problem is much more complicated. This is because, in this case, the variational principle is no minimization problem, but only provides the condition  $\delta f = 0$  of the functional which gives the reaction amplitude.

Nevertheless, Hahn, O'Malley and Spruch [7], have shown that in multi-channel formalism it is possible to obtain the strict bounds for the reaction matrix  $K$  (for processes without rearrangement) below the threshold of division of the system into three parts. In the paper [8] the results of Spruch were applied to the reactions with the rearrangement of particles using the method of separation of asymptotic components in  $\Psi$ . Lkhagva [9] has proved the same theorem for the expansion of  $\Psi$  in a set of hyperharmonics. Recently, the theorem on upper bounds for the  $K$ -matrix was proved for reactions above the threshold of three-fragment reactions:  $A+B \rightarrow a+b+c$  [10].

#### 8. TREATMENT OF REACTIONS OF GENERAL TYPE WITHOUT SEPARATING ASYMPTOTIC COMPONENTS IN $\Psi$ [11]

The general expression for the reaction amplitude is

$$f_{\alpha} = \int \Phi_{\alpha} V_{\alpha} \Psi d\tau \quad (21)$$

where  $\Phi_{\alpha}$  is the wave function of free relative motion of fragments in the channel  $\alpha$ ,  $V_{\alpha}$  is the interaction neglected in  $\Phi_{\alpha}$ . It is evident from (21) that the non-zero contribution to  $f_{\alpha}$  is produced by the integrand in a localized region of configuration space, because the overlap of  $\Phi_{\alpha}$  and  $V_{\alpha}$  at large distances in configuration space tends to zero.

This fact makes it desirable to search for  $\Psi$  in the form of a linear combination of quadratically integrable functions ( $\Phi^{L_2} \in L_2$ ), since every function in a restricted region can be represented with any degree of accuracy by the basic functions in  $L_2$ . But here we meet a difficulty which seems to be insuperable at first sight. The Schrödinger equation in partial derivatives has an infinite number of linearly independent solutions if the boundary conditions are not fixed and the trial function

$$\Psi^N = \sum_1^N F_i \Phi_i^{L_2} \quad (1g)$$

with the coefficients  $F_i$  determined from the usual requirement (2) seems to be a linear combination of all these non-physical solutions to which the required solution gives a small contribution.

In the first section of this we used the fact that the ordinary differential equations have a finite complete set of linearly independent solutions. One

would think that for differential equations in partial derivatives, it is impossible to construct the proper solution from a finite number of auxiliary solutions. However, it is a remarkable property of the Schrödinger equation that in the class of non-increasing functions it has only as many linearly independent solutions as the number of open channels [11]. In some problems, this number is strictly finite; and in the general case, it often turns out that in a good approximation one can limit oneself to a finite number of open channels (e. g. neglect the higher orbital moments). Therefore, it is sufficient for us to find the necessary number of linearly independent solutions.

It will be convenient for the following to transform the wave equation and boundary conditions for the scattering problem, so that the inhomogeneity from asymptotic conditions is transferred into the equation. To do this, let us assume the following separation ( $\Phi_{0\alpha}$  is the incoming wave):

$$\Psi = \Phi_{0\alpha} + X_{\alpha} \quad (22)$$

Then the Schrödinger equation can be written in the form:

$$(H - E)X_{\alpha} = (E - H)\Phi_{0\alpha} \equiv J_{\alpha} \quad (23)$$

where  $J_{\alpha}$  is a known function (source).

Equation (23) can be solved by means of the standard Galerkin procedure, if we expand  $X_{\alpha}$ , using  $\Phi_{\alpha}^{\dagger}$  as the basic functions.

The wave function for the process under consideration could be constructed as a linear combination:

$$\Psi = \sum_{\alpha} a_{\alpha} (X_{\alpha} + \Phi_{0\alpha}) \quad (24)$$

where the summation goes over all open channels taken into account. The constants  $a_{\alpha}$  are determined by the values of amplitudes of incoming waves  $A_{\alpha}$ :

$$A_{\alpha} = \int \Phi_{\alpha}^{\dagger} V_{\alpha} \sum_{\beta} a_{\beta} (X_{\beta} + \Phi_{0\beta}) d\tau + S_{\alpha} \quad (25)$$

where  $\Phi_{\alpha}^{\dagger}$  is a free divergent wave in the partial channel  $\alpha$ .  $S_{\alpha}$  is the surface term due to the singularity of  $\Phi_{\alpha}^{\dagger}$  at  $R=0$  where  $R$  is the co-ordinate of the relative distance of fragment in channel  $\alpha$ . Thus we have the wave function (24), and can calculate the reaction amplitudes  $f_{\alpha}$  (21).

## 9. CONCLUDING REMARK (COMBINATION OF DIFFERENT METHODS)

If we take into account more and more terms in the expansion of  $\Psi$  in order to achieve a better approximation, we must solve a system with more and more equations. So that, at a definite moment, the additional accuracy due to new terms in the expansion of  $\Psi$  will be reduced by the growth of errors of numerical calculations of a larger number of equations.

There is, however, a trivial way of improving the results by using a combination of different methods.

Let  $\Psi^{(1)}$  denote the approximate wave function of a many-body system obtained by one method. It can be regarded as an exact solution  $\Psi$  with an error function  $\Delta\Psi^{(1)}$  :

$$\Psi^{(1)} = \Psi + \Delta\Psi^{(1)} \quad (26)$$

Let another method, for the same system, give an error  $\Delta\Psi^{(2)}$  of the same order as  $\Delta\Psi^{(1)}$  :

$$\Psi^{(2)} = \Psi + \Delta\Psi^{(2)} \quad (27)$$

If these results are averaged, we obtain a new wave function

$$\Psi^{(1,2,\dots)} = \Psi + \frac{1}{N} \sum_1^N \Delta\Psi^{(i)} \quad (28)$$

which, in general, is a better approximation because the errors in the different methods are independent (to some extent), and interference will lead to their mutual suppression.

## REFERENCES

- [1] ZHIGUNOV, V.P., ZAKHARIEV, B.N., Problems in the Physics of Elementary Particles and Nuclear Structure (in Russian) 2 (1971) 2.
- [2] FESHBACH, H., Ann. Phys. (N.Y.) 5 (1958) 357; 19 (1962) 287.
- [3] EFIMENKO, T.G., ZAKHARIEV, B.N., ZHIGUNOV, V.P., Ann. Phys. (N.Y.) 47 (1968) 275; AUSTERN, N., Phys. Rev. 188 (1969) 1595.
- [4] SIMONOV, Yu.A., Nucl. Phys. (in Russian) 3 (1966) 630. (Soviet Phys. J. nucl. Phys. 3 (1966) 461).
- [5] ZAKHARIEV, B.N., PUSTOVALOV, V.V., EFROS, V.D., Nucl. Phys. (in Russian) 8 (1968) 406. (Soviet Phys. J. nucl. Phys. 8 (1969) 234).
- [6] RUDGE, M.R.H., SEATON, M.J., Proc. Roy. Soc. (London) 283 (1965) 262. EFIMENKO, T.G., ZAKHARIEV, B.N., LKHAGVA, O., Preprint P4-4923, Dubna (1970).
- [7] HAHN, Y., O'MALLEY, T.E., SPRUCH, L., Phys. Rev. 134B, (1964) 397.
- [8] ZAKHARIEV, B.N., PERMJAKOV, V.P., FENIN, Y.I., Preprint P4-5332, Dubna (1970).
- [9] LKHAGVA, O., Preprint P4-5366, Dubna (1970).
- [10] ZAKHARIEV, B.N., LKHAGVA, O., NIJAZGULOV, S.A., FENIN, Yu.I., ICTP, Trieste, preprint IC/71/6 (submitted to Nuovo Cimento).
- [11] ZAKHARIEV, B.N., FENIN, Yu.I., SHMONIN, V.L., these Proceedings.



# REARRANGEMENT COLLISIONS

B.N. ZAKHARIEV, Yu.I. FENIN, V.L. SHMONIN  
 Joint Institute for Nuclear Research,  
 Dubna,  
 Union of Soviet Socialist Republics

## Abstract

### REARRANGEMENT COLLISIONS

1. Introduction; 2. The principle of limit absorption; 3. The principle of limit amplitude;  
 4. The basic equations; 5. Concluding remark.

## 1. INTRODUCTION

One of the basic problems of non-relativistic quantum scattering theory is the development of effective methods to solve the Schrödinger equation for different many-particle systems. This development has been hindered for a long time by the fact that there was no general theory of differential equations in partial derivatives which could serve as a foundation for constructing the algorithms of their approximate solution. True, there has been great progress in this field of mathematics in recent years closely connected with the successes of functional analysis and of the theory of generalized functions (distributions (see, e. g. Ref. [ 1])) Physicists still have to take full advantage of the potentialities of this new mathematical tool.

The solution of the Schrödinger equation for the many-body systems in problems of continuous spectra is much more complex than the description of bound states although the methods of the so-called unified theory of nuclear reactions are rather close to the procedure of mixing configurations widely used in the nuclear-structure investigations. The scattering problems require the creation of computer routines of an entirely different type and the experience accumulated in bound-state calculations (e. g. the technique of evaluating matrix elements, etc.) cannot be used there immediately. This is particularly the case in the treatment of multi-channel reactions of general type - rearrangement collisions and processes above the threshold of the division of the whole system into three parts [ 2]. So it would be highly desirable to approach the calculation techniques for the problems of continuous spectra to those of discrete spectra.

In this paper, a method is proposed in which the scattering wave function is constructed by utilizing the expansion in the set of the same basic functions as for the bound state problem (see section 4). This method has definite advantages over that developed earlier for the description of multi-channel processes of the most general type [ 3].

It is, however, advisable to consider first two principles concerning the solution of differential equations in partial derivatives in an unrestricted domain. This will clarify some interesting properties of the Schrödinger equation.

## 2. THE PRINCIPLE OF LIMIT ABSORPTION [ 4 ]

The Schrödinger equation transforms into an inhomogeneous equation if we separate in the wave function  $\Psi$  an incident wave  $\Phi_{0\alpha}$  in the partial channel  $\alpha$ :

$$\Psi = \Phi_{0\alpha} + X_{\alpha} \quad (1)$$

so that

$$(H-E)X_{\alpha} = (E-H)\Phi_{0\alpha} \equiv J_{\alpha} \quad (2)$$

where  $J_{\alpha}$  is a known function (source). If a small additional imaginary term  $+i\epsilon$  is introduced into Eq. (2),

$$(H-E \pm i\epsilon)X_{\alpha}^{(\epsilon)} = J_{\alpha} \quad (3)$$

then Eq. (3) has a unique solution in the space of quadratically integrable functions ( $X_{\alpha}^{(\epsilon)} \in L_2$ ). In the limit  $\epsilon \rightarrow 0$ , the function  $X_{\alpha}^{(\epsilon)} + \Phi_{0\alpha}$  becomes the required physical solution with divergent (convergent) waves.<sup>1</sup> This principle can be used for the approximate solution of scattering problems.

If we expand  $X_{\alpha}^{(\epsilon)}$  in the set of basic functions  $\{\varphi_i^{L_2}\}$  in  $L_2$ :

$$X_{\alpha}^{(\epsilon, N)} = \sum_i^N F_{\alpha i}^{(\epsilon, N)} \varphi_i^{L_2} \quad (4)$$

we obtain a system of coupled equations for the coefficients  $F_{\alpha i}^{(\epsilon, N)}$  according to the Galerkin principle (see Eq. (2. 5)):

$$\langle \varphi_j^{L_2} | (H-E \pm i\epsilon) \sum_i F_{\alpha i}^{(\epsilon, N)} \varphi_i^{L_2} \rangle = \langle \varphi_j^{L_2} | J_{\alpha} \rangle \quad (5)$$

It is necessary to mention that the passage to the limit  $\epsilon \rightarrow 0$  in expression (5) is not allowed if the number of terms taken into account in expansion (4) is finite ( $i < N$ ). For each  $N$  there exists the optimal value,  $\epsilon_N$  at which the approximate solution has minimal deviation from the required one.<sup>2</sup>

<sup>1</sup> This principle is not yet proved for the case of the Schrödinger equation but there is no serious doubt of it. The same is true for the principle of the limit absorption (see further).

<sup>2</sup> The value of  $\epsilon$  determines the distance ( $R_{\epsilon}$ ) at which the solution of Eq. (3) decreases so that it becomes negligible. And  $N$  must be large enough to describe the behaviour of  $X_{\alpha}^{(\epsilon)}$  inside the domain of configuration space with linear size  $\sim R_{\epsilon}$  rather well. If  $N$  is chosen so small that  $R_{\epsilon}$  is greater than the distance  $R_N$  at which the basic functions  $\varphi_i^{L_2}$  with  $i < N$  become negligible, this will have such an effect on  $X_{\alpha}^{(\epsilon)}$  as if an unphysical barrier were erected at  $\sim R_N$ . And it will lead to the appearance of undesirable waves in  $X_{\alpha}^{(\epsilon)}$  reflected from this barrier. On the other hand, the value of  $\epsilon$  is to be taken as small as possible in order to diminish the difference between  $X_{\alpha}^{(\epsilon)}$  and the required solution  $X_{\alpha}$ .

### 3. THE PRINCIPLE OF LIMIT AMPLITUDE

Let us transform Eq. (2) in another way and introduce a supplementary "time" dependence

$$\frac{d^2}{dt^2} \chi_\alpha(t) + H \chi_\alpha(t) = J_\alpha e^{\mp ikt}; \quad k^2 = 2ME \quad (6)$$

Solving Eq. (6) with the initial conditions:  $\chi_\alpha(0) = 0$ ;  $((d/dt)\chi_\alpha)_{t=0} = 0$ , we obtain for  $t \rightarrow \infty$ :

$$\lim_{t \rightarrow \infty} \chi_\alpha(t) = X_\alpha e^{\mp ikt} \quad (7)$$

where  $X_\alpha$  is the required solution of Eq. (2).

The function  $\chi_\alpha(t)$  is distinguished from zero in the bounded domain of configuration space for each fixed value of  $t$  because the wave  $\chi_\alpha(t)$ , created by the source  $J_\alpha \exp(\mp ikt)$  beginning from  $t = 0$ , cannot propagate infinitely far during the finite time interval. Therefore, we can construct the approximate solution of Eq. (6) in the form (expanding  $\chi_\alpha$  in the set of  $\varphi_i^{L_2}$ ):

$$\chi_\alpha(t) = \sum_i^N F_{\alpha i}(t) \varphi_i^{L_2} \quad (8)$$

For coefficients  $F_{\alpha i}(t)$ , according to the Galerkin principle, we have the system of ordinary differential equations which can easily be calculated by the computer:

$$\langle \varphi_j^{L_2} | \left( \frac{d^2}{dt^2} + H \right) \sum_i F_{\alpha i}(t) \varphi_i^{L_2} \rangle = \langle \varphi_j^{L_2} | J_\alpha e^{\mp ikt} \rangle \quad (9)$$

At sufficiently large  $t = t_0$  in the bounded region of configuration space where the reaction takes place, the oscillations of  $F_{\alpha i}(t)$  acquire a simple exponential dependence on  $t$ :  $F_{\alpha i}(t) = F_{\alpha i} \exp(\mp ikt)$ . Separating this "time" dependence we obtain according to (7) and (8) the required function  $X_\alpha$  (and  $\Psi$ ). As in the case of the principle of limit absorption, one must be careful in the choice of  $t_0$  and  $N$ . There is an optimal value  $t_0$  for each  $N$ .<sup>3</sup>

The principles of limit absorption and limit amplitude permit an approximation to the solution  $X_\alpha$  of the scattering problem from the class of  $L_2$  functions. Let us now consider a more effective way of obtaining such a solution.

<sup>3</sup> The value  $t_0$  should not exceed the time which is necessary for the wave  $\chi_\alpha(t)$  to reach the region where all the  $\varphi_i^{L_2}$  ( $i < N$ ) become negligible. This will lead to the appearance of reflected waves from the barrier which is effectively erected by the neglect of terms with  $i > N$  in expansion (8).

The value  $N$  must be chosen large enough to ensure a sufficiently good description of  $\chi_\alpha$  in the bounded region where the reaction takes place (where all the interactions are acting).

## 4. THE BASIC EQUATIONS

The following method is essentially based on the fact that the Schrödinger equation has exactly as many linearly independent solutions as the number of open channels for the given value of energy  $E$ . The required solution can be constructed as a linear combination of these solutions. As these auxiliary solutions, we shall take

$$X_{\alpha}^N = \sum_i^N F_{i\alpha}^N \varphi_i^{L_2}; \rightarrow \Psi_{\alpha} = X_{\alpha}^N + \Phi_{0\alpha} \quad (10)$$

and equations for coefficients  $F_{i\alpha}$  are:

$$\langle \varphi_k^{L_2} | (H-E) \sum_i^N F_{i\alpha}^N \varphi_i^{L_2} \rangle = \langle \varphi_k^{L_2} | J_{\alpha} \rangle \equiv j_{\alpha k}. \quad (11a)$$

Equation (11a) can be rewritten in the explicit form

$$\sum_i [(\epsilon_i - E) \delta_{ik} + W_{ki}] F_{\alpha i} = j_{\alpha k} \quad (11b)$$

where  $\epsilon_k$  are eigenvalues of the model Hamiltonian  $H_{\text{mod}}$ :

$$H_{\text{mod}} \varphi_k^{L_2} = \epsilon_k \varphi_k^{L_2}$$

and  $W_{ki} = \langle \varphi_k^{L_2} | \left( \sum_{l < j}^n V_{lj} - V_{\text{mod}} \right) \varphi_l^{L_2} \rangle$ . To solve the system (11b) one has

to calculate  $W_{ki}$  and inverse the matrix  $M = \left\| (\epsilon_i - E) \delta_{ki} + W_{ki} \right\|$ . This part of the problem is almost the same as in nuclear structure calculations. Then one multiplies the vector  $j_{\alpha}$  by the matrix  $M^{-1}$  and gets the coefficients  $F_{\alpha i}$ .

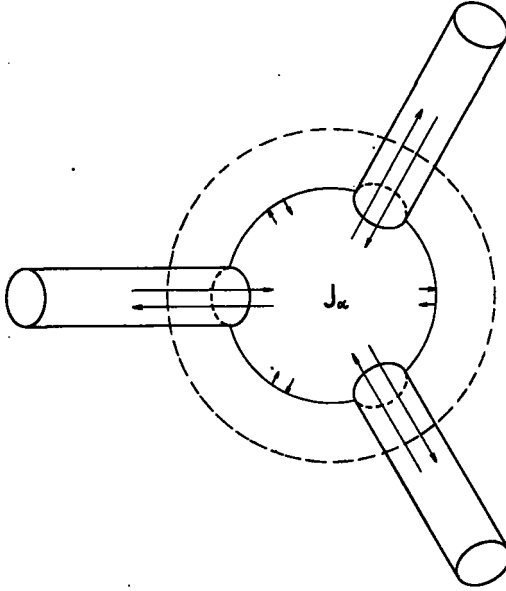
The wave function which we need has the form

$$\Psi = \sum_{\alpha} a_{\alpha} (X_{\alpha} + \Phi_{0\alpha}) \quad (12)$$

where the summation is over all the open channels. In a good approximation, it is sufficient to take into account in expression (12) only a finite number of terms giving a considerable contribution to  $\Psi$ . The constants  $a_k$  are defined by the amplitudes  $A_{\alpha}$  of incident partial waves

$$A_{\alpha} = \int \Phi_{\alpha}^{\dagger} V_{\alpha} \sum_{\beta} a_{\beta} (X_{\beta} + \Phi_{0\beta}) d\tau + S_{\alpha} \quad (13)$$

considering Eq. (13) as a system of algebraic equations for  $a_{\beta}$ .  $S_{\alpha}$  is the surface term due to the singularity of  $\Phi_{\alpha}^{\dagger}$  at  $R = 0$  where  $R$  is the co-ordinate of the relative distance of fragments in channel  $\alpha$ . The function  $\Phi_{\alpha}^{\dagger}$  in Eq. (13)

FIG. 1. Closed region around source  $J_\alpha$ .

is a divergent wave in the partial channel  $\alpha$ , and  $V_\alpha$  is the interaction which is neglected in  $\Phi_\alpha^+$ . The formula (13) can easily be checked. Substituting

$V_\alpha$  by  $H_{0\alpha} - E$  because of the requirement that  $\Psi = \sum_{\beta} a_{\beta} \Psi_{\beta}$  satisfies the

Schrödinger equation:  $(H_{0\alpha} + V_\alpha - E)\Psi = 0$ , and shifting the action of the operator  $(H_{0\alpha} - E)$  to the left using Green's theorem we get Eq. (13). The same formula is valid for reactions above the threshold of the system divided into three parts [5]. Thus, we obtain the wave function  $\Psi$  according to Eq. (12) and reaction amplitudes from the well-known general expression:

$$f_\alpha = \int \Phi_\alpha V_\alpha \Psi d\tau \quad (14)$$

where  $\Phi_\alpha$  is the wave function of free relative motion of fragments in channel  $\alpha$ .

It is useful to consider the physical sense of the auxiliary solutions  $X_\alpha^N$ . If we choose as basic functions  $\phi_i^2$ , the functions of independent motion of particles in an infinitely deep potential well, which is usually utilized in nuclear structure models ( $V_{\text{mod}}$ ), then the construction of the approximate solution  $X_\alpha^N$  in the form (10) as a linear combination of  $N$  functions  $\phi_i^2$  ( $i < N$ ), disappearing at large distances ( $\sim R_N$ ) in configuration space, is equivalent to introducing effective potential walls (see sections 2 and 3). The wave  $X_\alpha^N$  generated by the source  $J_\alpha$  (which corresponds to the incident wave  $\Phi_{0\alpha}$ ) moves in the closed region, represented schematically in Fig. 1.

The dashed line designates the effective potential barrier, and the tubes symbolize the different channels (e. g. elastic, inelastic scattering, re-arrangement of particles, etc.). Solution  $X_\alpha^N$  corresponds to the solution of Eq. (2) with boundary conditions - standing waves in all channels; divergent waves colliding with potential walls are completely reflected by them (arrows in Fig. 1). The situation is very similar to the eigenvalue problem, except that due to the inhomogeneity of the system (11a), its solution exists at any  $E$  above the threshold of elastic scattering.<sup>4</sup>

The linear combination (12) of such solutions  $\Psi_\alpha$  (with different  $\alpha$ ) permits one, by choosing the proper coefficients  $a_\alpha$ , to eliminate the convergent (incident) waves in those channels where they should not exist according to the boundary conditions of a given physical process.

The method described above can be slightly modified in order to use the hyperspherical harmonics  $Y_{\bar{K}}(\Omega_{3n-4})$  (generalized spherical harmonics) [6] as basic functions in expansion (10). Here  $\Omega_{3n-4}$  are  $3n-4$  angular variables,  $n$  is the number of particles in the system and  $\bar{K}$  is a set of  $3n-4$  quantum numbers. In this case, the coefficients  $F_{i\alpha}$  become the functions dependent on collective co-ordinate  $\rho$  (see Ref. [5]):

$$X_\alpha(\rho, \Omega_{3n-4}) = \frac{1}{\rho^{\frac{3n-4}{2}}} \sum_{\bar{K}} F_{\alpha\bar{K}}(\rho) Y_{\bar{K}}(\Omega_{3n-4}) \quad (15)$$

And instead of Eq. (11), we get a system of ordinary differential equations:

$$\left( -\frac{\hbar^2}{2M} \frac{d^2}{d\rho^2} + \frac{\hbar^2}{2M} \frac{L_K(L_K+1)}{\rho^2} - E \right) F_{\alpha\bar{K}}(\rho) + \sum_{\bar{K}'} W_{\bar{K}\bar{K}'} F_{\alpha\bar{K}'} = j_{\alpha\bar{K}'}(\rho) \quad (16)$$

where

$$L_K = K + \frac{3}{2}(n-2)$$

$$W_{\bar{K}\bar{K}'} = \int Y_{\bar{K}}^*(\Omega_{3n-4}) \left( \sum_{i < j}^n V_{ij} \right) Y_{\bar{K}'}(\Omega_{3n-4}) d\Omega_{3n-4}$$

and

$$j_{\alpha\bar{K}} = \int Y_{\bar{K}}^*(\Omega_{3n-4}) J_\alpha d\Omega_{3n-4}$$

with the boundary condition that  $F_{\alpha\bar{K}}$  does not increase at  $\rho \rightarrow \infty$ .

<sup>4</sup> For discrete values of  $E$ , corresponding to the eigenvalues of the homogeneous part of the system (11a), there is no solution of Eq. (11a). The solution near these points can be obtained by solving instead of (11a) the corresponding system of ordinary differential equations.

## 5. CONCLUDING REMARK

It is proposed in this article to describe reactions of general type (with rearrangement of particles and division of a system into three and more parts) in a different way than was done by the method of separation of asymptotics [3, 5]. According to the new procedure, it is not necessary to subtract from  $\Psi$  divergent waves with unknown amplitudes; this was equivalent to using a mixed basis and to introducing the truncation factors in order to correct the singular behaviour of trial functions. It seems that utilization only of completely orthonormalized basic functions  $\varphi_i^{1/2}$  in the proposed method will make the calculation procedure more stable with respect to the errors in the trial function.

## REFERENCES

- [1] BERESANSKY, Yu.M., Expansion in Eigenfunctions of Self-adjoint Operators, Transl. of Math. Monographs, 17 (1968).
- [2] ZHIGUNOV, V.P., ZAKHARIEV, B.N., Problems of the Physics Elementary Particles and Nuclear Structure (review article in Russian) 2 2 (1971).
- [3] EFIMENKO, T.G., ZAKHARIEV, B.N., ZHIGUNOV, V.P., Ann. Phys. (NY) 47 (1968) 275.
- [4] VEINBERG, B.R., Uspekhi Math. Nauk. 21 (1966) 115 (Russian); (Russian Math. Surveys 21 3 (1966) 115).
- [5] ZAHKARIEV, B.N., these Proceedings.
- [6] SIMONOV, Yu.A., Yadernaya Fizika 3 (1966) 630; (Soviet J. Nucl. Phys. 3 (1966) 461); BAZ, A.I., ZHUKOV, M.V., Yadernaya Fizika 11 (1970) 779; (Soviet J. Nucl. Phys. 11 (1971) 435).
- [7] ZAKHARIEV, B.N., PUSTOVALOV, V.V., EFROS, V.D., Yadernaya Fizika 8 (1968) 406; Soviet J. Nucl. Phys. 8 (1969) 234.



# ON KAPUR-PEIERLS THEORY

M. A. NAGARAJAN  
 University of Liège,  
 Sart-Tilman, Liège,  
 Belgium

## Abstract

ON KAPUR-PEIERLS THEORY.

1. Introduction; 2. Scattering of a particle by a spherical potential; 3. Many-channel calculations.

## 1. INTRODUCTION

In this short paper, we shall discuss the predictions of the Kapur-Peierls dispersion theory [1]. We shall consider simple systems to study the properties of Kapur-Peierls eigenstates and eigenfunctions. The work reported here has been done in collaboration with Lejeune [2]. For the sake of completeness, we shall also present some of the calculations of Gignoux [3] at the University of Grenoble.

For details of the formalism, we refer to the original paper of Kapur and Peierls [1] and the review by Brown [4]. This formalism has been applied to the study of resonant electron scattering by atoms and molecules by Herzenberg, Mandl and co-workers [5].

We shall be interested in the study of the energy dependence and radius dependence of the complex eigenvalues, as well as in the suitability of one-level approximation to the S-matrix in the analysis of isolated resonances. The relation between the Kapur-Peierls formalism and the pole expansion of the S-matrix by Humblet and Rosenfeld [6] has been studied by Minelli and Zardi [7].

## 2. SCATTERING OF A PARTICLE BY A SPHERICAL POTENTIAL

The first simple model we consider is that of the scattering of a particle by a spherical potential. The Kapur-Peierls eigenstates are solutions of the equation

$$\left[ \frac{d^2}{dr^2} - \frac{\ell(\ell+1)}{r^2} - \epsilon(r) + k_{\ell,n}^2(k, a_0) \right] U_{\ell,n}(r, k, a_0) = 0 \quad (2.1)$$

satisfying the boundary conditions

$$U_{\ell,n}(0, k, a_0) = 0, \quad \frac{\partial U_{\ell,n}}{\partial r} = L_{\ell}(k, a_0) U_{\ell,n} \text{ at } r = a_0 \quad (2.2)$$

$$L_{\ell}(k, a_0) = [ka_0 h_{\ell}^{(1)}(k, a_0)^{-1}] \frac{d}{da_0} [ka_0 h_{\ell}^{(1)}(k, a_0)]$$

where  $h_l^{(1)}(kr)$  is a spherical Hankel function of the first kind and order  $l$  and

$$\begin{aligned} k^2 &= 2mE/\hbar^2 \\ \psi(r) &= 2mV(r)/\hbar^2 \\ k_{l,n}^2 &= 2m \mathcal{E}_{l,n}/\hbar^2 \end{aligned} \quad (2.3)$$

In Eq. (2.3),  $E$  is the projectile energy,  $V(r)$  is the spherical potential and  $\mathcal{E}_{l,n}$  is the Kapur-Peierls eigenvalue.

In view of the boundary conditions, Eq. (2.2), we can show that the eigenvalues and eigenstates of Eq. (2.1) are energy-dependent and, in general, complex. They also depend upon the matching radius  $a_0$ . To be consistent with the assumption made by Kapur and Peierls, one should choose  $a_0$  such that for  $r > a_0$  the potential  $V(r)$  is very weak.

The trajectory of the eigenvalue  $k_{l,n}^2$  as a function of  $k$  is given by the equation [3]

$$\frac{\partial}{\partial k} k_{l,n}^2(k) = - \frac{U_{l,n}^2(k, a_0)}{a_0 \int_0^{a_0} dr U_{l,n}^2(r, k, a_0)} \frac{\partial}{\partial k} L_l(k, a_0) \quad (2.4)$$

Calculations for these trajectories have been made for a square-well potential [2] and for a Saxon-Woods potential [3]. In Fig. 1 the energy dependence of the eigenvalues for scattering by a Saxon-Woods potential are shown. The intersection of the line  $k^2 = \text{real part of } k_{l,n}^2$  with the trajectory defines the resonance energy.

We shall consider two cases where one could fit the exact cross-section by a one-level approximation. The  $S$ -matrix can be expressed in terms of the Kapur-Peierls eigenstates and eigenvalues in the form:

$$S_l = \frac{I_l(k, a_0)}{O_l(k, a_0)} + \frac{ik\hbar^2}{m} \sum_m \frac{U_{l,n}^2(k, a_0)}{(\mathcal{E}_{l,n}(k, a_0) - E) O_l(k, a_0)} \quad (2.5)$$

where

$$I_l(k, a_0) = ka_0 h_l^{(2)}(k, a_0)$$

and

$$O_l(k, a_0) = ka_0 h_l^{(2)}(k, a_0)$$

In Fig. 2, we show the comparison between the exact  $s$ -wave cross-section and a one-level approximation. The parameters of the square well are shown in the figure. The square well is slightly weaker than one needed to bind a particle. There exists a virtual state of a small positive energy which dominates the zero-energy cross-section. The corresponding state

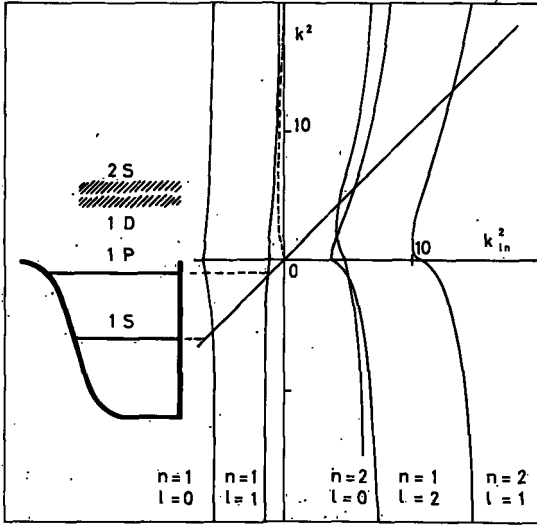


FIG. 1. Energy dependence of the real part of  $k_{l,n}^2$  as a function of  $k^2$ . The Saxon-Woods potential has a radius of 1; diffusiveness of 0.1 and a depth of 1200 in appropriate units. The figure is taken from Ref. [3].

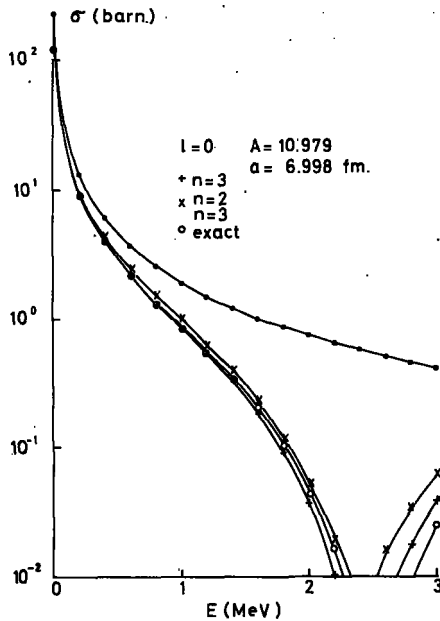


FIG. 2. s-wave scattering by a square well potential.

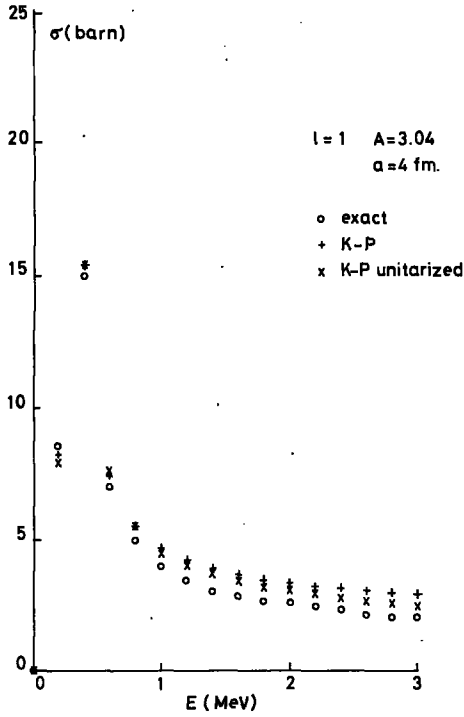


FIG. 3. p-wave scattering by a square well potential.

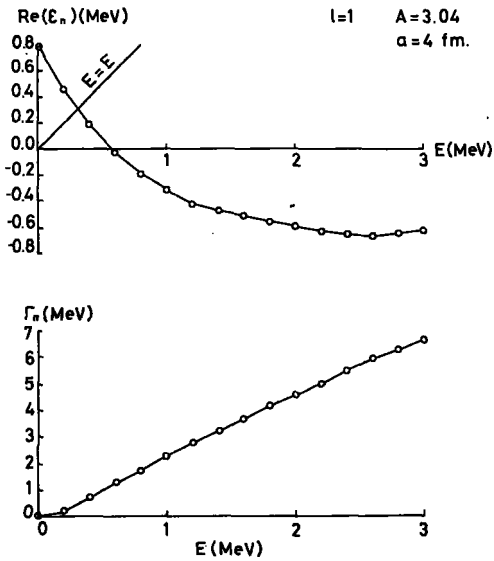


FIG. 4. Energy dependence of the resonant eigenstate in p-wave scattering.

in the Kapur-Peierls theory has an eigenvalue in the complex plane very close to zero energy. One can notice that the agreement is very good at very low energies and begins to become worse with increase in energy. We shall return to this point later.

In Fig. 3 we show a similar comparison for the case of p-wave scattering. The complex eigenvalue of the state included in the calculation of the S-matrix is  $(0.25 - (i/2) 0.50)$  MeV. The value quoted is at resonance. The eigenvalue is, however, energy-dependent. The energy dependence is shown in Fig. 4. The energy denominator appearing in the S-matrix is of the form  $(E_n - E - i\Gamma_n/2)$ . If

$$E_n = E_0 - \alpha E$$

$$\Gamma_n = \Gamma_0 + \beta E$$

the correct resonance eigenvalue is given by

$$(E_0 - (i/2)\Gamma_0)/(1 + \alpha + (i\beta)/2)$$

which gives us the value  $(0.29 - 0.152(i/2))$  MeV. The resonance occurs at an energy of 290 keV with a width of 152 keV. One also notices that the energy dependence of the real part  $E_n$  has a negative slope. This seems to be a characteristic feature of scattering resonances.

One more comment has to be made at this stage. A one-level approximation to the S-matrix in the framework of the Kapur-Peierls theory is non-unitary. It is this lack of unitarity that causes a discrepancy between the exact cross-section and the one-level cross-section as the energy is increased. An estimate of the lack of unitarity,  $1 - |S_{ll}|^2$ , shows that in the above two cases, it is less than one per cent in the s-wave case and less than about ten per cent in the p-wave case.

### 3. MANY-CHANNEL CALCULATIONS

The resonances which we have encountered in the previous section are single-particle resonances. One might feel that the one-level formula will be more suitable in the case of a "compound resonance". We shall therefore consider a soluble coupled square-well model which has been studied by Newton and Fonda [8], Weidenmüller [9] and others [10]. The model is the following: the exact scattering wave function satisfies the equation

$$\left[ \left( -\frac{\hbar^2}{2m} \frac{d^2}{dr^2} - E \right) \mathbb{1} + \mathbb{g} + \mathbb{V} \right] \psi_{\mathbb{E}}(r) = 0 \quad (3.1)$$

where  $\mathbb{1}$  is a unit matrix,  $\mathbb{g}$  is a diagonal matrix with

$$e_{ij} = e_i \delta_{ij} \quad (3.2)$$

where  $e_i$  is the threshold energy for the  $i$ -th channel and  $\underline{V}$  is a real symmetric square matrix. We assume that

$$V_{ij} = \text{constant} \quad (r \leq R) \quad (3.3)$$

$$V_{ij} = 0 \quad (r > R)$$

In Eq.(3.1)  $\underline{\Psi}_{\approx E}$  is a column matrix given by

$$\underline{\Psi}_{\approx E}(r) = \begin{pmatrix} \psi_E^{(1)}(r) \\ \psi_E^{(2)}(r) \\ \vdots \\ \psi_E^{(N)}(r) \end{pmatrix} \quad (3.4)$$

where  $\psi_E^{(i)}(r)$  are regular at the origin and satisfy the boundary conditions that

$$\psi_E^{(i)}(r) = (v_i)^{-1/2} [\exp(-ik_i r) \delta_{i1} - S_{i1} \exp(ik_i r)] \quad (3.5)$$

for  $r \geq R$  and where  $v_i$  is the velocity in the  $i$ -th channel.

The Kapur-Peierls eigenstates are solutions of the same Hamiltonian but satisfy the boundary conditions that

$$\frac{d\phi_n^{(i)}}{dr} = ik_i \phi_n^{(i)}(r) \text{ at } r = a_i \quad (3.6)$$

where  $k_i^2 = 2m(E - e_i)/\hbar^2$ , and  $a_i$  are the channel radii. One can show that the functions  $\phi_n^{(i)}$  satisfy the orthogonality relations

$$\sum_{i=1}^N \int_0^{a_i} dr \phi_n^{(i)}(r) \phi_m^{(i)}(r) = 0 \quad n \neq m \quad (3.7)$$

and we choose to normalize them such that

$$\sum_{i=1}^N \int_0^{a_i} dr \phi_n^{(i)2}(r) = 1 \quad (3.8)$$

The eigenvalues  $\mathcal{E}_n$  are complex and energy-dependent. If we write

$$\mathcal{E}_n = E_n - i\Gamma_n/2 \quad (3.9)$$

it can be shown that

$$\Gamma_n = \frac{\hbar^2}{m} \sum_{i=1}^M k_i |\phi_n^{(i)}(a_i)|^2 \left[ \sum_{i=1}^N \int_0^{a_i} dr |\phi_n^{(i)}(r)|^2 \right]^{-1} \quad (3.10)$$

where  $M$  is the number of open channels.

The S-matrix elements are given by the relation

$$S_{ii} = e^{-ik_1 a_1} \left( \delta_{i1} + i \sum_n \frac{\gamma_n^{(i)} \gamma_n^{(i)}}{\mathcal{E}_n - E} \right) e^{-ik_1 a_1} \quad (3.11)$$

where

$$\gamma_n^{(i)} = \left( \frac{\hbar^2 k_i}{m} \right)^{1/2} \phi_n^{(i)}(a_1) \quad (3.12)$$

We considered a model with one open channel and one closed channel. The potential matrix was of the form

$$\begin{aligned} \underline{V} &= \begin{pmatrix} -31 & -0.1 \\ -0.1 & -41 \end{pmatrix} \text{MeV for } r \leq 6 \text{ fm} \\ \underline{V} &= 0 \text{ for } r > 6 \text{ fm} \end{aligned}$$

The threshold energies were  $e_1 = 0$  and  $e_2 = 6$  MeV. The exact pole of the S-matrix occurs at an energy of  $(3.05 - (i/2)0.00388)$  MeV. When the two-channel radii  $a_1$  and  $a_2$  were both chosen equal to the range of the potentials, one of the Kapur-Peierls eigenvalues occurred at an energy  $(3.05 - (i/2)0.00542)$  MeV, which is very close to the exact pole energy. This eigenvalue is, however, energy-dependent. Once again, we obtain a linear dependence with negative slope. As in the previous section, if we renormalize the width due to the energy dependence, we obtain a width of 3.88 keV which agrees with the exact width. Next, we studied the dependence of the eigenvalue on the channel radii. It was found to be independent of the open channel radius. Its dependence on the closed channel radius is shown in Fig. 5. It is seen that for a closed-channel radius larger than 10 fermi,  $\Gamma_n$  becomes constant and equal to 3.88 keV. This effect is well known in R-matrix theory and corresponds to the fact that the main part of the closed channel wave function is confined in that region. The fact that the eigenvalue only depends on the closed-channel radius indicates that the resonant state corresponds to a state which was a bound state in the closed channel in the absence of coupling. Following up the argument about the renormalization of the width due to energy dependence of the eigenvalue, we anticipate that the energy dependence should be closely linked with the choice of the closed channel radius. This is shown in Fig. 6. It is seen that, for  $a_2$  larger than 10 fermi, the eigenvalue is independent of energy. It is thus seen that one has a very simple method of extracting the exact resonance energy from the Kapur-Peierls theory, particularly for narrow resonances. This is easy to understand from the projection operator formalism as shown below.

If we call the projection operators for the open and closed channels P and Q, one can show [11] that the resonance energy is an eigenvalue of the equation

$$(\mathcal{E}_n - QHQ - QHP \frac{1}{E^+ - PHP} PHQ) \phi_n = 0 \quad (3.13)$$

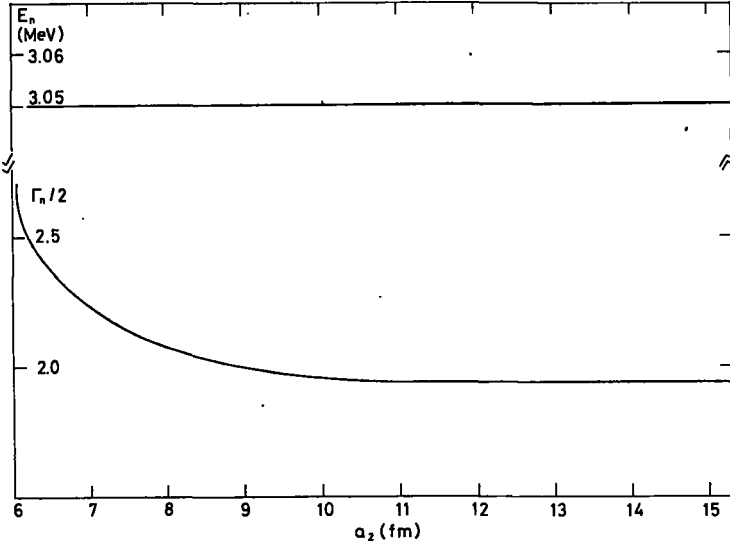


FIG. 5. Dependence of the Kapur-Peierls eigenvalue on the closed-channel radius.

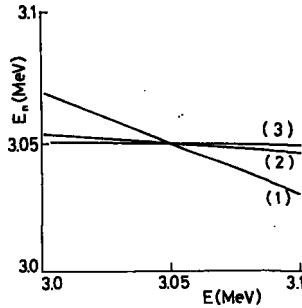


FIG. 6. Variation of the energy dependence of the eigenvalue with the closed-channel radius. 1 corresponds to a radius of 6 fermis, 2 to 8 fermis and 3 to 10 fermis.

The solution of the above equation is equivalent to solving the coupled equations (3.1) with purely outgoing boundary conditions and no incoming waves in any channel. This is exactly what is done in Kapur-Peierls theory and hence the predicted Kapur-Peierls eigenvalues are close to that of the exact pole energies in the case of narrow resonances.

The comparison between the exact cross-section and the one-level approximation is shown in Fig. 7. The full line curve is the exact cross-section and the dotted one is the one-level approximation. The one-level approximation overestimates the peak cross-section. The reason is the lack of unitarity of the corresponding S-matrix. If we examine the expression for the S-matrix, Eq. (3.11), we see that the partial width is given by

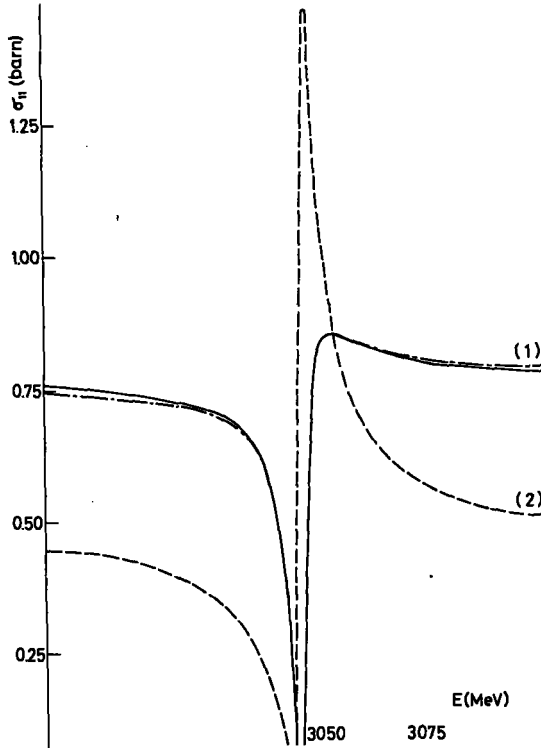


FIG. 7. Comparison of the non-unitarized and unitarized one-level approximations with the exact elastic scattering cross-section.

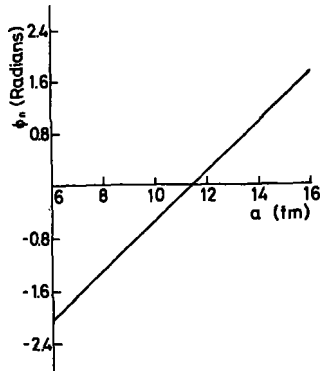


FIG. 8. Variation of  $\phi_n$ , the phase of the elastic width, with the open-channel radius.

$$\gamma_n^{(1)2} = \frac{\hbar^2 k_1}{m} \varphi_n^{(1)2} (a_1)$$

which is a complex quantity. For narrow resonances, the Kapur-Peierls eigenfunction has a large amplitude in the closed channel and a negligible amplitude in the open channel. One can thus write

$$\gamma_n^{(1)2} = \Gamma_n e^{-2i\phi_n} \quad (3.14)$$

The fact that the phase  $\phi_n$  is non-zero is what accounts for the lack of unitarity of the S-matrix. Using the above expression (Eq. (3.14)), one could unitarize the S-matrix and obtain

$$S_{el} = e^{-2i(ka + \phi_n)} \left[ 1 + i \frac{\Gamma_n}{E_n - E - i\Gamma_n/2} \right] \quad (3.15)$$

The cross-section with the unitarized one-level approximation is shown in Fig. 7 as a dot-dashed curve. The agreement with the exact cross-section is remarkable. We studied the dependence of the phase on the channel radii. It was found to be independent of the closed-channel radius and its dependence on the open-channel radius is shown in Fig. 8. This dependence indicated that there is a large contribution to the background from the elastic scattering channel. We looked again at the next nearest eigenstate, which was found to be at resonance at an energy of 4.68 MeV with a width of 6.83 MeV. This is associated with a very broad resonance in the open channel. We calculated the contribution of this state to the S-matrix. This gave rise to a phase which agreed very well with  $\phi_n$ . This feature is similar to the phenomenon discussed by McVoy [12] where there is a collision of poles of the S-matrix, the two poles belonging to different Riemann sheets. In the above case the two poles are necessary for the unitarity of the S-matrix.

Before concluding, we should comment about some calculations of Gignoux who has utilized the Kapur-Peierls formalism from a different point of view. One could start from the Lippmann-Schwinger equation

$$\Psi^{(+)} = \Phi + G^{(+)} V \Phi$$

where  $\Phi$  is the eigenstate of an unperturbed Hamiltonian,  $V$  is the residual interaction and  $G^{(+)}$  is the outgoing boundary condition Green's function. One could expand  $G^{(+)}$  as

$$G^{(+)} = \sum_n \frac{|n\rangle \langle n|}{E - \mathcal{E}_n}$$

where  $|n\rangle$  are Kapur-Peierls state vectors and  $\mathcal{E}_n$  their eigenvalues. A few-level approximation to the Green function leads to an expression for the S-matrix that differs from the Kapur-Peierls expression only in the

background. Comparing the results of Gignoux with ours, we could draw the following conclusions. In the case of reactions with isolated resonances, a unitarized S-matrix of the form of Eq. (3.15) seems very suitable whereas in the region of energies without resonances or with overlapping resonances, the method of Gignoux seems superior, and the convergence of the expansion for the Green function seems fairly rapid. In particular, one could calculate the optical potential [4] by using the Green function method.

#### ACKNOWLEDGEMENTS

The author is grateful to Dr. C. Gignoux for his permission to discuss some of his calculations.

#### REFERENCES

- [1] KAPUR, P. L., PEIERLS, R. E., Proc. Roy. Soc. (London) A166 (1938) 277.
- [2] LEJEUNE, A., NAGARAJAN, M. A., Nucl. Phys. A154 (1970) 602; Nucl. Phys. (to be published).
- [3] GIGNOUX, C., to appear in Journal de Physique.
- [4] BROWN, G. E., Rev. mod. Phys. 31 (1959) 893.
- [5] HERZENBERG, A., in Methods in Theoretical Physics (BOWCOCK; J. E., Ed.) North-Holland, Amsterdam (1968).
- [6] HUMBLLET, J., ROSENFELD, L., Nucl. Phys. 26 (1961) 529.
- [7] MINELLI, T. A., ZARDI, F., private communication.
- [8] FONDA, L., NEWTON, R. G., Ann. Phys. (N. Y.) 9 (1960) 416.
- [9] WEIDENMÜLLER, H. A., Ann. Phys. (N. Y.) 28 (1964) 60.
- [10] HAGLUND, M. E., ROBSON, D., Phys. Letts 14 (1965) 225;  
LEJEUNE, A., MAHAUX, C., Nucl. Phys. A145 (1970) 613.
- [11] FESHBACH, H., Ann. Phys. (N. Y.) 5 (1958) 357; see also  
FONDA, L., in Fundamentals in Nuclear Theory, IAEA, Vienna (1967) 793.
- [12] McVOY, K. W., in Fundamentals in Nuclear Theory, IAEA, Vienna (1967) 452.



**PART I: NUCLEAR REACTIONS**

**3. High-energy nuclear reactions**



# SCATTERING OF HIGH-ENERGY PARTICLES ON LIGHT NUCLEI

R. GUARDIOLA \*

International Centre for Theoretical Physics,  
Trieste, Italy

## Abstract

SCATTERING OF HIGH-ENERGY PARTICLES ON LIGHT NUCLEI.

The elastic and inelastic scattering of high-energy particles on light nuclei is studied by means of Glauber's multiple-scattering theory, in order to obtain information on the structure of the nuclear wave functions.

## 1. INTRODUCTION

The scattering amplitude of the "elastic" process

$$a + N_i \rightarrow a + N_f \quad (1)$$

is given, in the framework of Glauber's theory [1], by the formula

$$F_{if}(q) = \frac{ik}{2\pi} \int e^{i\vec{q}\vec{b}} d^2b \langle N_f | 1 - \prod_{\ell=1}^A \{1 - \Gamma_{\ell}(\vec{b} - \vec{s}_{\ell})\} | N_i \rangle \quad (2)$$

where  $|N_i\rangle$  and  $|N_f\rangle$  are the internal wave functions of the initial and final nuclear systems,  $\vec{b}$  is the impact parameter vector,  $\vec{s}_{\ell}$  is the projection of the nucleon co-ordinate  $\vec{r}_{\ell}$  on the plane perpendicular to the direction of the projectile (see Fig. 1) and the so-called "profile function"  $\Gamma(\vec{b})$  is the two-dimensional Fourier transform of the a-nucleon scattering amplitude

$$\Gamma(\vec{b}) = \frac{1}{2\pi ik} \int d^2q f(\vec{q}) e^{-i\vec{q}\vec{b}} \quad (3)$$

As is well known, expression (2) includes multiple-scattering contributions, with the restriction that the projectile cannot scatter twice on the same nucleon. The subindex  $\ell$  in the profile function takes into account the fact that the interaction of the external particle with the nucleons can be spin- and/or isospin-dependent. This fact is incorporated in actual calculations by putting in expression (3) the complete spin-isospin dependence of the amplitude and considering  $\Gamma(\vec{b})$  as an operator in spin-isospin space. However, when the operator form is used for  $\Gamma(\vec{b})$ , expression (2) is not, in general, valid, and it is necessary to introduce a time ordering of the individual interactions. To clarify this point, we shall consider a simple

\* On leave of absence from Departamento de Física Teórica, Facultad de Ciencias, Valencia, Spain.

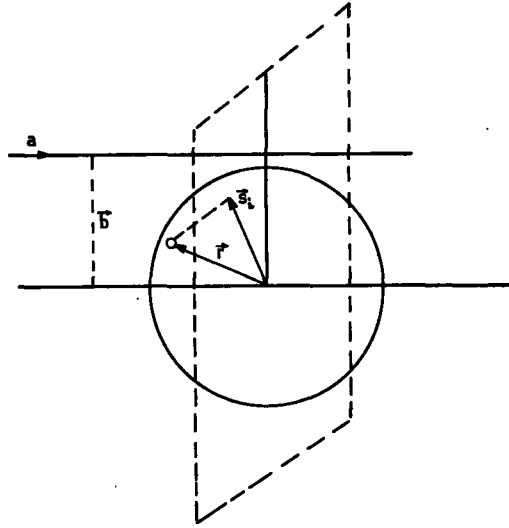


FIG. 1. Variables appearing in Eq.(2); the vector  $\vec{s}_1$  is in the plane perpendicular to the direction of the projectile  $a$ .

example, the  $\pi$ -nucleus interaction, and only the isospin structure of the amplitude will be considered, i. e.

$$f_{\pi N}(q) = f(q) + (\theta\tau) g(q) \quad (4)$$

This amplitude includes not only the elastic scattering of  $\pi^-$ ,  $\pi^0$  and  $\pi^+$ , but also inelastic processes like  $\pi^- p \rightarrow \pi^0 n$ , for instance. Now, if the incident particle is a  $\pi^-$ , it is no longer possible to consider the scattering of a  $\pi^0$  if that  $\pi^0$  has not already been produced. The time ordering of the events can very easily be introduced into the Glauber theory: as long as, in this theory, we consider only very small angles, the time ordering coincides with the ordering of the  $z$  co-ordinates of the nucleons (we are considering the  $z$ -axis in the direction of the incident particle) and in Eq. (2) we make the substitution

$$\prod_{i=1}^A (1 - \Gamma_i) \rightarrow \sum_{\text{permutations}} (1 - \Gamma_1)(1 - \Gamma_2) \dots (1 - \Gamma_A) \theta(z_2 - z_1) \dots \theta(z_A - z_{A-1}) \quad (5)$$

However, the dependence on the  $z$ 's of this expression makes its evaluation very lengthy, and in actual calculations one uses the approximate form

$$f_{\pi-N} \sim f(q) + \theta_3 \tau_3 \cdot g(q) \quad (6)$$

for expression (4) because, as long as the commutation relation  $[\Gamma_i, \Gamma_j] = 0$  is satisfied, the right-hand side of Eq. (5) is equal to the left-hand side.

This approximation is equivalent to discarding the inelastic intermediate states but takes into account the difference between the  $\pi^-p$  and  $\pi^-n$  scattering amplitudes.

In what follows we are going to work with scalar amplitudes and only corrections of the type of Eq. (6) will be included.

## 2. CALCULATION METHOD [2]

We are going to start with the simplest problem: elastic scattering on doubly closed shell nuclei, in particular  $^{12}\text{C}(1s_{1/2}^4, 1p_{3/2}^8)$  and  $^{16}\text{O}(1s_{1/2}^4, 1p_{3/2}^8, 1p_{1/2}^4)$ . The nuclear wave function is given by the Slater determinant

$$|N\rangle = \frac{1}{\sqrt{A!}} \det\{v_i(\vec{r}_j)\} \quad (7)$$

where the  $v_i$  are the normalized one-particle wave functions ( $i \equiv (n, \ell, j, j_3)$ ). It is possible to compute the complete multiple scattering series (2) using the simple rule

$$\langle N | \prod_{i=1} \{1 - \Gamma(\vec{b} - \vec{s}_i)\} | N \rangle = \det \langle v_i(\vec{r}) | 1 - \Gamma(\vec{b} - \vec{s}) | v_j(\vec{r}) \rangle \quad (8)$$

i. e. the problem is reduced to the evaluation of the matrix of the right-hand side of expression (8). These one-body matrix elements have very simple expressions when harmonic oscillator radial functions and Gaussian amplitudes are used. In the Appendix A we present the form of the matrix (8) for  $A = 16$ ; only the  $8 \times 8$  block matrix corresponding to proton (or neutron) states is written because, as long as the amplitude is isospin independent, all matrix elements between a proton and a neutron state are zero. If we had retained a part of the isospin dependence in the form given by Eq. (6) the two  $8 \times 8$  blocks of the matrix would have the same analytic form, but different numerical values.

The determinant (8) is only a function of  $\vec{b} \equiv (b, \varphi_b)$  and the dependence on  $\varphi_b$  of each matrix element is of the simple form

$$\langle (n\ell)jj_3 | \Gamma(b-s) | (n'\ell')j'_3 \rangle \sim \exp(i(j'_3 - j_3)\varphi_b) \quad (9)$$

and the dependence of the whole determinant on  $\varphi_b$  is going to be  $\exp(i(M' - M)\varphi_b)$ ,  $M'$  and  $M$  being the third component of the angular momentum of the final and initial states. (They are zero for the case presented here, that is, for doubly closed shells. However, the same method can be used for more general configurations with the difference that the wave functions will not be so simple as Eq. (7), but a linear combination of Slater determinants.) Then the integration on  $\varphi_b$  in Eq. (2) is very easily carried out using the relation

$$\int_0^{2\pi} e^{iqb \cos \varphi} e^{iM\varphi} d\varphi = 2\pi e^{i\frac{M\pi}{2}} J_M(qb) \quad (10)$$

Another feature of this matrix is that, since we have eliminated the spin dependence of the amplitude, it reduces to two  $4 \times 4$  blocks. Note, however, that the simplicity of the  $\varphi_b$  dependence and the reduction to two blocks arises from the choice of a particular quantization axis which is the direction of the incident particle (this must be taken into account when comparing our matrix with that of Bassel and Wilkin [2]: even if their matrix seems to be very different from ours, the matrix elements are related by simple linear combinations).

When the nuclear states have a non-zero angular momentum we have to compute the amplitudes  $F_{MM'}$ , square and sum on  $M'$  and average on  $M$ . However, when the interaction is spin-independent it can be shown [3] that the only amplitudes  $F_{MM'}$  different from zero are those which fulfil the relationship

$$(-1)^{M'-M} = P_i \cdot P_f \quad (11)$$

where  $P_i$  and  $P_f$  are the parities of the nuclear states.

### 3. HIGH-ENERGY SCATTERING ON $^{12}\text{C}$ AND $^{16}\text{O}$

At present the only high-energy experiments of elastic scattering are those of the Brookhaven group [4]. In Figs 2 and 3 we have plotted the differential cross-sections for these two nuclei and the prediction of the

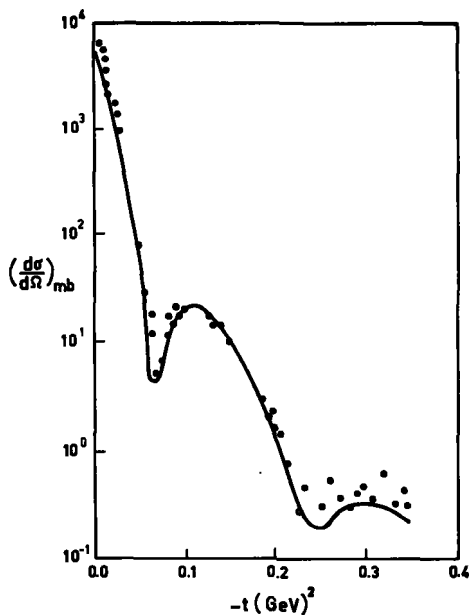


FIG. 2. Differential cross-section for the elastic scattering of 1 GeV protons on  $^{16}\text{O}$ . Data are from Ref. [4].

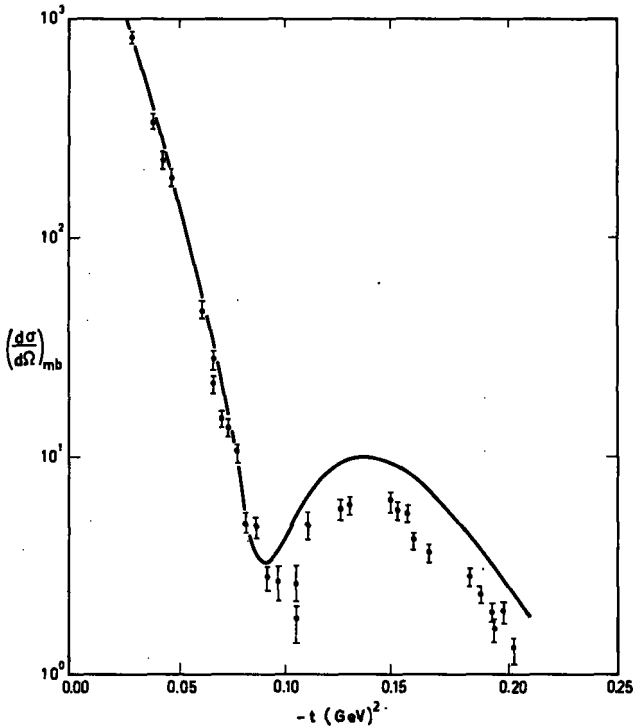


FIG. 3. Differential cross-section for the elastic scattering of 1 GeV protons on  $^{12}\text{C}$ . Data are from Ref. [4].

Glauber theory with simple shell model wave functions [5]. As we see, we have very good agreement between theory and experiment for the case of  $^{16}\text{O}$ , except for high momentum transfer where, however, the experimental data are not very reliable. On the contrary, in the case of  $^{12}\text{C}$  only the very-small-angle part of the angular distribution shows a good agreement with the calculation, and in the region of the first diffraction maximum the difference between theory and experiment amounts to 50%. A similar situation happens in  $\pi^{12}\text{C}$  and  $\pi^{16}\text{O}$  scattering at lower energies, as can be seen from the papers quoted in Ref. [6].

That we obtain good agreement with experiment for the case of  $^{16}\text{O}$  and not for  $^{12}\text{C}$  may be due to the fact that the former, being a magic nucleus, can be well described by the simple shell-model wave function and this is not the case for the latter (at this point it is interesting to remember the history of the high-energy proton and pion scattering on deuterons, where the small admixture of the D-wave solved a similar problem; see, for example, the lectures of Prof. Gillespie).

A first attempt towards the solution of this question has been presented in Ref. [7]: the wave function of  $^{12}\text{C}$  was written as the most general configuration mixing of the  $1p_{3/2}$  and  $1p_{1/2}$  shells, but still no sizable effects were produced. It is worth noting that with this wave function the nuclear density

$$\rho(r) = \frac{1}{A} \langle ^{12}\text{C} | \sum_{i=1}^A \delta(\vec{r}_i - \vec{r}) | ^{12}\text{C} \rangle \quad (12)$$

is the same as the one corresponding to the simple shell model. This puzzling situation has recently been solved by Lesniak and Lesniak [8] using for  $^{12}\text{C}$  the projected wave function of the deformed oscillator, although one might object to the many approximations they have used.

Another similar problem in the same energy range of the elastic processes which we have discussed before is met in the inelastic scattering  $\pi^{-12}\text{C} \rightarrow \pi^{-12}\text{C}^*(2^+)$ ,  $\pi^{-12}\text{C} \rightarrow \pi^{-12}\text{C}^*(3^-)$  and  $p^{12}\text{C} \rightarrow p^{12}\text{C}^*(2^+)$ . The first two cases have been studied in Ref. [3] with different wave functions for the final state, i. e. the simple shell-model configuration and the Tamm-Dancoff wave functions of Ref. [9]. The cross-section evaluated with the simple shell-model wave functions has very small values, roughly an order of magnitude smaller than the experimental measurements and a much better agreement is obtained with the Tamm-Dancoff wave functions (see Fig. 4). To analyse the origin of that enormous enhancement, we have plotted in Fig. 5 the contribution of the nuclear profile of the different components of the  $2^+$  wave function. We see that the curves corresponding to particles on the shells  $1p_{1/2}$ ,  $1f_{7/2}$ ,  $1d_{3/2}$  and  $1d_{5/2}$  have the same shape, so that if we mix shells with the same  $n$  we produce only enhancements of a multiplicative nature. This is not the case for the  $2p_{1/2}$  and  $2p_{3/2}$  shells;

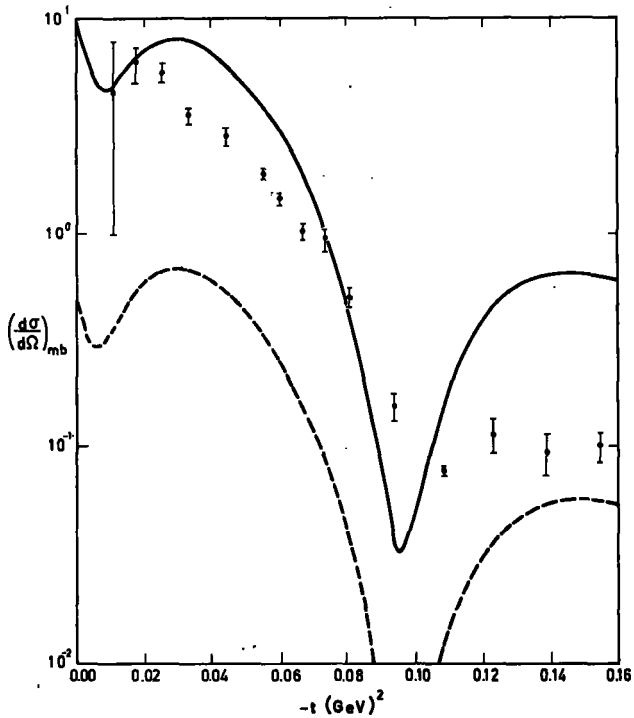


FIG. 4. Differential cross-section for the reaction  $\pi^{-}\text{C} \rightarrow \pi^{-}\text{C}^*(2^+)$  at 200 MeV. Dashed line: single shell model wave function  $(1p_{3/2})^{-1}(1p_{1/2})$ . Continuous line: Tamm-Dancoff wave function of Ref. [9]. Experimental data are from Ref. [10].

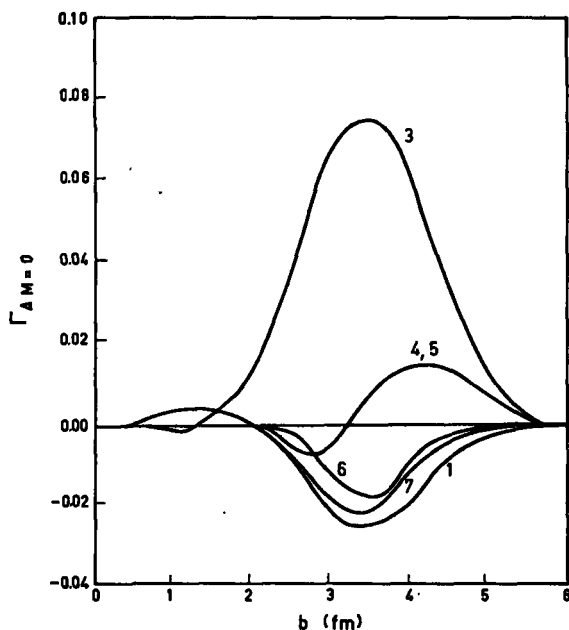


FIG. 5. Contribution to the real part of the profile for the process  $\pi^{12}\text{C} \rightarrow \pi^{12}\text{C}^*(2^+)$ ,  $J_3 = 0$  at a laboratory energy of 200 MeV with particle-hole wave functions for the final state:

- |                                |                                |
|--------------------------------|--------------------------------|
| 1. $(1p_{3/2})^{-1}(1p_{1/2})$ | 4. $(1p_{3/2})^{-1}(2p_{1/2})$ |
| 3. $(1p_{3/2})^{-1}(1f_{7/2})$ | 6. $(1s)^{-1}(1d_{3/2})$       |
| 5. $(1p_{3/2})^{-1}(2p_{3/2})$ |                                |
| 7. $(1s)^{-1}(1d_{5/2})$       |                                |

The contribution of  $(1p_{3/2})^{-1}(1f_{5/2})$  is negligible.

in fact, the presence of these shells changes the form of the angular distribution (in our case, because they tend to cancel each other, we do not observe essential changes in the angular distribution, and the calculations for simple shell-model and Tamm-Dancoff wave functions are almost parallel).

#### APPENDIX

#### THE ONE-PARTICLE MATRIX ELEMENTS

We are interested in the evaluation of the matrix elements

$$\langle (n\ell)jj_3 | \Gamma(\vec{b} - \vec{s}) | (n'\ell')j'j'_3 \rangle \quad (\text{A. 1})$$

and we consider the simple case of harmonic-oscillator radial functions and Gaussian amplitudes:

$$f(\mathbf{q}) = f(0) \exp\left(-\frac{1}{2} \beta^2 \mathbf{q}^2\right) \quad (\text{A. 2})$$

Then the profile function is given by

$$\Gamma(b) = \frac{\sigma}{4\pi} (1 - i\rho) \frac{1}{\beta^2} \exp(-b^2/2\beta^2) \quad (\text{A. 3})$$

(the optical theorem has been used to express  $f(0)$  in terms of the total cross-section, and  $\rho$  is the ratio of the real and imaginary parts of the forward amplitude).

The one-particle wave functions are constructed in the form

$$|(n\ell)jj_3\rangle = \sum C\left(\ell \frac{1}{2} j \mid m, j_3 - m\right) \psi_{n\ell m}(\vec{r}) \chi_{j_3 - m} \quad (\text{A. 4})$$

where the  $\psi_{n\ell m}$  are the usual harmonic oscillator wave functions. Since the  $z$ -co-ordinate plays a very special role in the Glauber theory, it is convenient to express  $\psi_{n\ell m}(\vec{r})$  as a product of the one-dimensional harmonic oscillator wave function  $\phi_{nz}(z)$  and the two-dimensional ones  $\phi_{n_s}^{(m_s)}(s, \varphi)$ . In particular, we obtain for the first shells

$$\begin{aligned} \psi_{100} &= \phi_0(z) \Phi_0^0(\vec{s}) \\ \psi_{110} &= \phi_1(z) \Phi_0^0(\vec{s}) \\ \psi_{11\pm 1} &= \phi_0(z) \Phi_1^{(\pm 1)}(\vec{s}) \end{aligned} \quad (\text{A. 5})$$

where

$$\begin{aligned} \phi_0(z) &= \left(\frac{\alpha}{\sqrt{\pi}}\right)^{\frac{1}{2}} \exp\left(-\frac{1}{2} \alpha^2 z^2\right) \\ \phi_1(z) &= \left(\frac{\alpha}{2\sqrt{\pi}}\right)^{\frac{1}{2}} 2\alpha z \exp\left(-\frac{1}{2} \alpha^2 z^2\right) \\ \Phi_0^0(\vec{s}) &= \frac{\alpha}{\sqrt{\pi}} \exp\left(-\frac{1}{2} \alpha^2 s^2\right) \\ \Phi_1^{(\pm 1)}(\vec{s}) &= \mp \frac{\alpha}{\sqrt{\pi}} \alpha s e^{i\varphi} \exp\left(-\frac{1}{2} \alpha^2 s^2\right) \end{aligned} \quad (\text{A. 6})$$

The  $z$ -integral needed to compute (A. 1) is simply carried out using the orthogonality of the  $\phi_{nz}(z)$ -functions; the integration over  $\varphi$  is easily evaluated by using formula (10) and we end up with integrals of the form

$$\int_0^\infty e^{-a^2 x^2} x^{m-1} I_n(bx) dx = \frac{b^n \cdot \Gamma\left(\frac{m+n}{2}\right)}{2^{n+1} a^{m+n} \Gamma(n+1)} e^{b^2/4a^2} \mathcal{G}\left(\frac{n-m}{2} + 1; n+1; \frac{-b^2}{4a^2}\right) \quad (\text{A. 7})$$

where  $\mathcal{F}(\alpha, \beta, x)$  is the confluent hypergeometric function which, given that in all cases of our interest  $\alpha$  is zero or a negative integer, degenerates into a polynomial in  $b^2/4a^2$ .

The matrix (A. 1) has then the following form:

$$\langle n'l|H_0|1-\Gamma(\bar{b}-\bar{a})|(n'l')|1\rangle =$$

	$ 1p_{1/2}, 1/2\rangle$	$ 1p_{3/2}, 3/2\rangle$	$ 1p_{3/2}, -1/2\rangle$	$ 1p_{1/2}, -1/2\rangle$	$ 1s_{1/2}, -1/2\rangle$	$ 1p_{3/2}, -3/2\rangle$	$ 1p_{3/2}, 1/2\rangle$	$ 1p_{1/2}, 1/2\rangle$
$\langle 1s_{1/2}, 1/2 $	$1 - \omega_1$	$\omega_2 e^{i\varphi}$	$-\sqrt{\frac{1}{3}} \omega_2 e^{-i\varphi}$	$\sqrt{\frac{2}{3}} \omega_2 e^{-i\varphi}$				
$\langle 1p_{3/2}, 3/2 $	$\omega_2 e^{-i\varphi}$	$1 - \omega_3$	$\sqrt{\frac{1}{3}} \omega_4 e^{-2i\varphi}$	$-\sqrt{\frac{2}{3}} \omega_4 e^{-2i\varphi}$				
$\langle 1p_{3/2}, -1/2 $	$-\sqrt{\frac{1}{3}} \omega_2 e^{i\varphi}$	$\sqrt{\frac{1}{3}} \omega_4 e^{2i\varphi}$	$1 - \frac{1}{3}(2\omega_1 + \omega_2)$	$-\frac{\sqrt{2}}{3}(\omega_1 - \omega_3)$				
$\langle 1p_{1/2}, -1/2 $	$\sqrt{\frac{2}{3}} \omega_2 e^{i\varphi}$	$-\sqrt{\frac{2}{3}} \omega_4 e^{2i\varphi}$	$-\frac{\sqrt{2}}{3}(\omega_1 - \omega_3)$	$1 - \frac{1}{3}(\omega_1 + 2\omega_2)$				
$\langle 1s_{1/2}, -1/2 $					$1 - \omega_1$	$-\omega_2 e^{-i\varphi}$	$\sqrt{\frac{1}{3}} \omega_2 e^{i\varphi}$	$\sqrt{\frac{2}{3}} \omega_2 e^{i\varphi}$
$\langle 1p_{3/2}, -3/2 $					$-\omega_2 e^{i\varphi}$	$1 - \omega_3$	$\sqrt{\frac{1}{3}} \omega_4 e^{2i\varphi}$	$\sqrt{\frac{2}{3}} \omega_4 e^{2i\varphi}$
$\langle 1p_{3/2}, 1/2 $					$\sqrt{\frac{1}{3}} \omega_2 e^{-i\varphi}$	$\sqrt{\frac{1}{3}} \omega_4 e^{-2i\varphi}$	$1 - \frac{1}{3}(2\omega_1 + \omega_2)$	$\frac{\sqrt{2}}{3}(\omega_1 - \omega_3)$
$\langle 1p_{1/2}, 1/2 $					$\sqrt{\frac{2}{3}} \omega_2 e^{-i\varphi}$	$\sqrt{\frac{2}{3}} \omega_4 e^{-2i\varphi}$	$\frac{\sqrt{2}}{3}(\omega_1 - \omega_3)$	$1 - \frac{1}{3}(\omega_1 + 2\omega_2)$

(A. 8)

where a particular ordering of rows and columns has been chosen to show the block structure. The functions  $\omega_1, \dots, \omega_4$  are given by

$$\begin{aligned} \omega_1 &= \frac{\sigma^1}{2\pi} \frac{\alpha^2}{1 + 2\alpha^2\beta^2} E \\ \omega_2 &= \frac{\sigma^1}{2\pi} \frac{\alpha^3}{(1 + 2\alpha^2\beta^2)^2} b \cdot E \\ \omega_3 &= \frac{\sigma^1}{2\pi} \frac{2\beta^2\alpha^4}{(1 + 2\alpha^2\beta^2)^2} \left\{ 1 + \frac{b^2}{2\beta^2(1 + 2\alpha^2\beta^2)} \right\} E \\ \omega_4 &= \frac{\sigma^1}{2\pi} \frac{\alpha^4}{(1 + 2\alpha^2\beta^2)^2} b^2 E \end{aligned} \quad (\text{A. 9})$$

where  $\sigma^1 = \sigma(1 - i\rho)$  and  $E = \exp(-\alpha^2 b^2 / (1 + 2\alpha^2\beta^2))$ .

The elastic scattering on  $^{16}\text{O}$  and  $^{12}\text{C}$  are given by the simple formula

$$F(q) = ik \int b db J_0(qb)(1 - \Gamma_A) \quad (\text{A. 10})$$

where  $\Gamma_A$  is given, for  $^{16}\text{O}$ , by the square of determinant (A. 8):

$$\Gamma_{16\text{O}} = [(1 - \omega_1)(1 - \omega_3 + \omega_4)\{(1 + \omega_1)(1 - \omega_3 - \omega_4) - 2\omega_2^2\}]^4 \quad (\text{A. 11})$$

and for  $^{12}\text{C}$  by the square of determinant (A. 8) suppressing the rows and columns labelled  $1p_{1/2}$  :

$$\Gamma_{^{12}\text{C}} = \left[ \frac{2}{3} ((1 - \omega_1)(1 - \omega_3) - \omega_2^2)(2 - \omega_1 - \omega_3 + \omega_4) - \frac{1}{3} (1 - \omega_1)(1 - \omega_3 + \omega_4)^2 \right]^4 \quad (\text{A. 12})$$

In such a form the calculations of Figs 2 and 3 involve only a very simple numerical integration over  $b$ .

## REFERENCES

- [1] GLAUBER, R.J., in Lectures in Theoretical Physics (BRITTIN, W.E. et al., Eds) 1, Interscience Publishers (1959).
- [2] This method was initially proposed by BASSEL, R.H., WILKIN, C., Phys. Rev. 174 (1968) 1179.
- [3] GUARDIOLA, R., Nuovo Cim. 3A (1971) 747.
- [4] PALEVSKY, H. et al., Phys. Rev. Letts 18 (1967) 1200;  
FRIEDES, J.L. et al., Nucl. Phys. A104 (1967) 294.
- [5] See Ref.[2] and the excellent review by CZYŻ, W., High-energy scattering from nuclei, to be published in Adv. nucl. Phys.
- [6] WILKIN, C., Nuovo Cim. Letts 4 (1970) 491.
- [7] GUARDIOLA, R., Nuovo Cim. Letts 4 (1970) 1005.
- [8] LESNIAK, H., LESNIAK, L., Nucl. Phys. B25 (1971) 525.
- [9] GILLET, V., VINH-MAU, V., Nucl. Phys. 54 (1964) 321.
- [10] BINON, F. et al., Nucl. Phys. B17 (1970) 168.

# HIGH-ENERGY SCATTERING OF HADRONS FROM NUCLEI

J. GILLESPIE

Department of Physics,  
Boston University, Boston,  
United States of America

## Abstract

### HIGH-ENERGY SCATTERING OF HADRONS FROM NUCLEI

1. Introduction; 2. Motivation; 3. New experiments; 4. Glauber's model; 5. Eikonal theory; 6. Multiple scattering; 7. Elastic and inelastic scattering; 8. Nuclear physics; 9. Two-particle amplitudes; 10. Predictions of the theory; 11. Comparison with experiment; 12. "Deuteronomy"; 13. The future.

## 1. INTRODUCTION

The study of high-energy scattering from nuclei has undergone extensive development in the last five years - on both theoretical and experimental fronts. The theoretical models evolve from the theory of Glauber; recent interest in the subject followed from the achievement of high-energy accelerator beams with energy resolutions typical of nuclear structure, and from the development of high-resolution neutron beams. The eikonal approximation, which underlies the theory, has recently been the subject of intensive investigation in all domains of scattering theory.

In this paper, we shall develop a strictly qualitative perspective of this field, its recent evolution, and its many interesting future prospects. A thorough exposition of the basic theory is to be found in Glauber's lectures at Boulder [1]; a compendium of recent theoretical and experimental developments are contained in the lectures of Glauber and others in the proceedings of the Rehovot [2] and Columbia [3] conferences on High Energy Physics and Nuclear Structure.

The recent development in this field has, in fact, been so extensive that even review articles have become somewhat encyclopedic and overwhelming. For this reason we shall highlight only those aspects which provide essential background and which we believe to be most relevant for future developments. For details, one may consult the comprehensive bibliography of Ref.[3].

## 2. MOTIVATION

It might at first seem surprising that hadron-nucleus scattering at GeV energies would be interesting for either nuclear physics or for elementary-particle physics since such energies are well beyond those characteristic of nuclear structure and well below those of greatest interest to current particle research. We list briefly some of the questions arising at this interface between the two fields which might be answered by such experiments. Some are obviously speculative.

## 2.1. Nuclear physics

- (1) Possible microscopic derivation of macroscopic models (e.g. the optical model).
- (2) Experiments complementing electron scattering at comparable energies and momentum transfers.
- (3) A supplementary tool for investigating correlations in nuclei, as well as concepts such as quasi-deuterons, impulse approximations, etc.
- (4) Detailed studies of the structure of light nuclei; in particular, a unique probe of the deuteron.

## 2.2. Particle physics

- (a) At present our knowledge of n-n and n-p scattering is obtained from the analysis of proton-deuteron scattering (neutron beam developments will soon change this situation).
- (b) The nucleus provides a dense target, thereby enhancing rare events.
- (c) The phenomenon of compositeness may be investigated - this is of relevance to concepts such as partons, quarks, etc.
- (d) Multiple-scattering theories are very sensitive to small effects such as the ratio of the real to the imaginary parts of high-energy hadron amplitudes which is important for testing dispersion relations and Regge theory.
- (e) Resonance-particle cross-sections (e.g.  $\sigma(\rho^0 n)$ ) may be determined - or bounded - by such experiments. Short life-times preclude direct measurements of these cross-sections, which are predicted by certain symmetry schemes. Thus the nucleus may be considered to provide a "beam of resonances".

## 3. NEW EXPERIMENTS

The great interest in this subject in recent years actually stems from two experimental developments:

- (1) high energy ( $E \approx \text{GeV}$ ) beams with nuclear resolutions ( $\Delta E \approx \text{MeV}$ ).
- (2) high-resolution neutron beams.

For many years, both CERN and Brookhaven have carried out extensive programs of very-high-energy ( $E \approx 20 \text{ GeV}$ ) scattering of pions and protons from nuclei such as  $^2\text{H}$ ,  $^4\text{He}$ ,  $^{12}\text{C}$ ,  $^{16}\text{O}$ , etc. with resolutions of the order of 50 MeV. (For references, consult the bibliography of Ref. [3].) Such resolutions obviously preclude distinguishing between elastic and inelastic final states. Beginning with the experiments of Palevsky et al. at Brookhaven [4], resolutions of several MeV were obtained. Thus these 'high-energy' experiments became genuinely 'nuclear' in that elastic events could be distinguished; with further refinement it will be possible eventually to identify some low-lying excited final states. Energy resolution, presently  $\Delta E/E \approx 10^{-3}$ , is expected to reach  $10^{-4}$  in the near future. Thus the structure of the nuclear targets becomes increasingly important for such high-energy experiments.

The advent of high-precision neutron beams is of special interest to the theorist. To date, our knowledge of n-p and n-n amplitudes has been obtained from p-d scattering analysed by Glauber's theory for the 'shadow term'. Neutron-beam experiments will provide us with n-p amplitudes, and thus we will have the shadow term  $[\sigma(pd) - \sigma(pp) - \sigma(np)]$ , determined experimentally - leaving to the theorists the explanation of any anomalous behaviour.

#### 4. GLAUBER'S MODEL

Leaving detailed derivation to later sections and previous expositions [1, 5], we summarize here the qualitative ingredients of the Glauber theory:

- (1) Scattering is limited to high energy and small angles, where amplitudes are well approximated by their eikonal form (see next section).
- (2) Multiple scattering of the projectile on the nucleons of the nucleus is included but re-scattering (of the projectile on the same nucleon) is excluded.
- (3) There is no longitudinal component of the momentum transfer.
- (4) Nucleus motion is 'frozen' during the passage of the projectile.
- (5) It is usually assumed (but, surprisingly, not always necessary) that between successive scatterings the projectile is freely propagating (see section 5 and Refs [6, 7]).
- (6) The projectile-nucleon amplitude is known (only the on-shell amplitude contributes).

Inelasticity in the form of nuclear excitation is included in the model, but not particle production.

For those more familiar with the language of field theory, the above model is equivalent to assuming that only a finite number of Feynman graphs contribute to the scattering, that only on-shell propagation is important, that re-scattering is excluded, and that two-particle unitarity is sufficient.

In general, relativistic effects other than kinematical ones are ignored. There do exist, however, relativistic eikonal formalisms [7]. These are particularly interesting in that they enable summation of important classes of diagrams.

#### 5. EIKONAL THEORY

The fundamental approximation underlying models related to Glauber's is the eikonal representation of the two-particle scattering amplitude. The characteristic feature of the eikonal representation is the "exponentiation of the dynamics". That is, the potential (in non-relativistic theories) or the diagrams representing the forces (in relativistic theory) enter the scattering amplitude only in the form  $\exp iX$ , where  $X$  is calculated from the interaction. The central role played by this feature is often obscured. As we shall see later, this form of the amplitude is responsible for the multiple-scattering series for particle-nucleus scattering.

We shall first remark on the classical origins of eikonal theory; then we will consider the more interesting method of directionally approximating the Green's function.

### 5.1. Wave-function approximation

Historically, the eikonal approximation arose from classical optics, where a light wave travelling through an optical medium acquires a phase depending on the index of refraction along its trajectory. The eikonal formalism takes, as a first approximation, the phase to be equal to that of the undeflected trajectory through the medium in the incident direction. For such plane waves, the wave function is given by

$$\begin{aligned}\Psi &= e^{iX} \\ X &= \vec{k} \cdot \vec{r} + \int^z [n(r') - 1] dz' \\ \vec{r}' &= (x, y, z')\end{aligned}\tag{5.1}$$

where  $n(r)$  is the index of refraction of the optical medium.

The analogous approximation for the Schrödinger equation

$$\left( \frac{1}{2m} \vec{\nabla}^2 + k^2 - V \right) \Psi = 0\tag{5.2}$$

consists of assuming a solution of the form

$$\Psi(\vec{r}) = e^{i\vec{k} \cdot \vec{r}} \phi(\vec{r})\tag{5.3}$$

for which  $V\phi$  is slowly varying in a Compton wavelength. The solution, assuming an undeflected trajectory (e.g. along the  $z$ -axis), is, for  $\vec{r} = (x, y, z)$ ;  $v = m^{-1}k$ ,

$$\begin{aligned}\phi(\vec{r}) &= e^{iX(\vec{r})} \\ X(\vec{r}) &= \frac{1}{\hbar v} \int_{-\infty}^z V(x, y, z') dz'\end{aligned}\tag{5.4}$$

Equivalent solutions may be obtained by approximating the Green's function [1]. This method, although less intuitive, is formally more useful, as we shall see below.

The amplitude for scattering from direction  $\vec{k}$  to  $\vec{k}'$ , with momentum transfer  $\vec{q} = \vec{k} - \vec{k}'$  is given by

$$f(\vec{q}) = - \frac{2m}{4\pi\hbar^2} \int d^3r e^{i\vec{k}' \cdot \vec{r}} V(r) \Psi_{\vec{k}}(\vec{r})\tag{5.5}$$

If we now limit ourselves to high-energy, small-angle (forward) scattering, we see from Fig.1 that, to a good approximation, the momentum transfer  $\vec{q}$  has no longitudinal component, i.e.  $\vec{q}$  is normal to both  $\vec{k}$  and  $\vec{k}'$ . If we insert the approximate  $\Psi$  of Eqs (5.3) and (5.4) into the amplitude (5.5), and decompose  $\vec{r}$  into components  $\vec{b}$  in the plane normal to  $\vec{k}$ , and  $z$  along  $\vec{k}$ , we obtain

$$f(q) = -\frac{1}{4\pi} \int d^2b e^{i\vec{q}\cdot\vec{b}} \int_{-\infty}^{\infty} dz V(b^2 + z^2) \exp \left[ \frac{i}{2k} \int_{-\infty}^z dz' V(b^2 + z'^2) \right] \quad (5.6)$$

We should emphasize that it is the physical assumption  $q_z \approx 0$  which reduces Eq.(5.6) to a two-dimensional Fourier transform ( $d^2b$ ) in which the  $z$ -integration may be completed to yield the eikonal structure:

$$f(q) = -\frac{ik}{2\pi} \int d^2b e^{i\vec{q}\cdot\vec{b}} [e^{2iX(b)} - 1] \quad (5.7)$$

$$X(b) = -\frac{1}{4k} \int V(b^2 + z'^2) dz'$$

As remarked above, the dynamics (here the potential  $V$ ) occurs only in the exponential phase function  $X$ .

## 5.2. Green's function approximation

The more formal and general approach to the eikonal approximation is via the "linearization" [1, 6] of the free Green's function

$$G^{-1}(k, p) = \frac{1}{2m} [k^2 - p^2 + i\epsilon] \quad (5.8)$$

appearing in the Schrödinger equation (5.2) or in the Lippman-Schwinger equation

$$T = V + VG T \quad (5.9)$$

The incident momentum is given by  $\vec{k}$ ;  $\vec{p}$  represents the intermediate momentum.

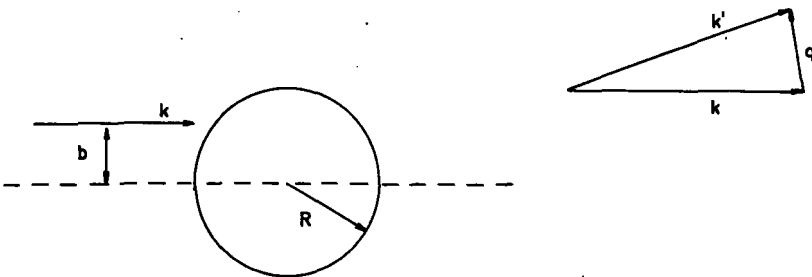


FIG. 1. Scattering for impact parameter  $b$ , momentum transfer  $\vec{q}$ .

If we reflect on the foregoing eikonal theory we realize that we are in essence selecting a preferred direction for the scattering. There is nothing sacred or unique about the forward direction we selected previously; any direction may be used. The ideal of an approximation scheme is to maximize the convergence rate - i.e. to maximize the relative importance of the leading terms. Both Glauber [1] and Sugar and Blankenbecler [6] have noted that symmetrizing the approximation in the initial and final directions improves the eikonal amplitude.

With this perspective, let us choose a vector  $\vec{k}_j$  having magnitude  $|\vec{k}_j| = |\vec{k}|$  and arbitrary direction  $\vec{k}_j$  and then expand  $\vec{p}$  about this direction:

$$\vec{p} = \vec{k}_j + (\vec{p} - \vec{k}_j) \quad (5.10)$$

This gives us for  $G$  a natural decomposition into a "linearized" term  $G_j$  and a perturbation term  $N_j$ :

$$\begin{aligned} G^{-1} &= \frac{1}{m} [k^2 - \vec{k}_j \cdot \vec{p} + i\epsilon] + \frac{1}{2m} (\vec{p} - \vec{k}_j)^2 \\ &\equiv G_j^{-1} + N_j \end{aligned} \quad (5.11)$$

The motivations for such a perturbation are threefold: (1) to maximize the importance of the lowest-order terms, (2) to obtain explicit and systematic corrections, and (3) to obtain closed-form expressions if possible.

The approximate, eikonal Green's function of Eq.(5.11) may be found explicitly [1, 6]; in configuration space it takes the form

$$G_i(\vec{r}, \vec{r}'; k) = \frac{im}{k} \delta^{(2)}(\vec{b} - \vec{b}') \theta(z - z') e^{ik(z-z')} \quad (5.12)$$

where we decompose the vectors into components in the plane  $\vec{b}$  and the  $z$ -direction of the incident beam. Moreover, unlike the solution for the full Green's function of Eq.(5.8), the linearized function gives us a closed form for the amplitude of Eq.(5.9):

$$T_i(k, \vec{q}) = \int d^3r e^{i\vec{q} \cdot \vec{r}} V(r) e^{iX_1(\vec{r})} \quad (5.13)$$

which we see to be precisely the eikonal amplitude of Eq.(5.6).

As we shall see in section 13, consideration of the correction term in Eq.(5.11) enables us to estimate and improve the simple eikonal amplitudes.

As a final observation, we note that, independently of the dynamics, the eikonal representation of the amplitude, Eq.(5.7) arises naturally at high energies out of the partial-wave representation of the scattering amplitude,

$$f(q) = \frac{1}{2ik} \sum_{\ell} (2\ell + 1) (e^{i\delta_{\ell}} - 1) P_{\ell}(\cos \theta) \quad (5.14)$$

Referring to Fig.1, we see that the maximum angular momentum for a given momentum  $k$  and scattering system of dimension  $R$  is  $\ell_{\max} \approx kR$ . Thus, in the high-energy limit, where  $\ell_{\max}$  will be very large, it is natural to go from the discrete summation over  $\ell$  to a continuous integration over the impact parameter  $b$  using the transformation

$$kb = \ell + 1/2 \quad (5.15)$$

The discrete phase shift  $\delta_\ell$  now becomes the continuous function  $X(b)$ . The amplitude is then

$$f(q) = -ik \int b db [e^{2iX(b)} - 1] P_{kb-1/2}(\cos \theta) \quad (5.16)$$

In the limit of large  $k$ , we obtain

$$f(q) = ik \int b db [e^{2iX(b)} - 1] J_0(2kb \sin \theta/2) \quad (5.17)$$

The same result may be obtained by carrying out the azimuthal integration of Eq.(5.7).

## 6. MULTIPLE SCATTERING

For a target such as a nucleus consisting of multiple scattering centres located at  $\vec{r}_1, \dots, \vec{r}_A$ , the interaction potential is given by

$$V(\vec{r}) = \sum_i V_i(\vec{r} - \vec{r}_i) \quad (6.1)$$

For this interaction, the eikonal formalism of section 5 gives us the composite eikonal phase function

$$X_A(\vec{b}; \vec{r}_1, \dots, \vec{r}_A) = \sum_{i=1}^A X_i(\vec{b} - \vec{r}_i) \quad (6.2)$$

In fact, this relation is usually postulated from analogy with the phase accumulated from a succession of independent scattering on passage through a sequence of diffractive media. It is interesting to note, however, that the additivity of the eikonal phase is more general than the distinct scattering model and, in fact, remains valid in some cases for overlapping interaction regions; Osborn[8] has investigated this feature in a variety of contexts.

Since the eikonal formalism (see Eq.(5.6)) effectively reduces the target to two dimensions (in the  $b$  plane), the  $\vec{r}_i$  appearing in Eq.(6.2) are in practice the  $b$ -plane projections of the nuclear co-ordinates.

We now illustrate that the eikonal additivity relation (6.2) is sufficient to give the multiple-scattering interpretation to the model. The eikonal

amplitude (5.7) is the two-dimensional Fourier transform of the "profile function"

$$\Gamma_i(\mathbf{b}) \equiv 1 - e^{2iX_i(\mathbf{b})} \tag{6.3}$$

Thus for the composite system the profile function is given by  $\Gamma_A(\vec{\mathbf{b}}; \vec{\mathbf{r}}_1, \dots, \vec{\mathbf{r}}_A)$ , where

$$\begin{aligned} \Gamma_A &= 1 - e^{2iX_A} \\ &= 1 - e^{2i \sum_j X_j} = 1 - \prod_j e^{2iX_j} \\ &= 1 - \prod_j [1 - \Gamma_j(\vec{\mathbf{b}} - \vec{\mathbf{r}}_j)] \end{aligned} \tag{6.4}$$

Expanding this product, we obtain

$$\Gamma_A = \sum_{j=1}^A \Gamma_j - \sum_{i < j} \Gamma_i \Gamma_j + \dots + \sum_{i..j..} \overbrace{\Gamma_i \dots \Gamma_j}^{A \text{ terms}} \dots \tag{6.5}$$

where  $\Sigma$  implies all summation indices are distinct. (We have obviously neglected the commutation properties of the  $\Gamma_i$  which would arise from the introduction of spin- and isospin-dependent amplitudes.)

The multiple-scattering interpretation of the series (5.5) is immediately evident: the first term corresponds to the coherent scattering from A distinct nucleons; the second from two successive scatterings, etc. The absence of repeated indices in any term corresponds to the absence of re-scattering in the model. Thus we see that the "exponentiation of the dynamics" characteristic of eikonal representations gives us directly the multiple scattering structure for the amplitude.

Finally, we construct the complete scattering amplitude from the profile function (6.4) and the initial and final state nuclear (target) wavefunctions:

$$\begin{aligned} T_{fi}(\vec{\mathbf{q}}) &= \int \dots \int d^2\mathbf{b} e^{i\vec{\mathbf{q}} \cdot \vec{\mathbf{b}}} d^3\mathbf{r}_1 \dots d^3\mathbf{r}_A \delta\left(\frac{1}{A} \sum_{j=1}^A \vec{\mathbf{r}}_j \Psi_i^*(\vec{\mathbf{r}}_1 \dots \vec{\mathbf{r}}_A)\right) \\ &\quad \times \Gamma_A(\vec{\mathbf{b}}; \vec{\mathbf{r}}_1 \dots \vec{\mathbf{r}}_A) \Psi_f(\vec{\mathbf{r}}_1 \dots \vec{\mathbf{r}}_A) \end{aligned} \tag{6.6}$$

We note here an important feature of the eikonal model. From Eq.(6.6) we note that the amplitude is composed of three parts: the nuclear physics contained in the wavefunctions  $\Psi$ , the elementary-particle physics contained in the profile function  $\Gamma$ , and the eikonal structure of that function. To the extent that the parameters of the nuclear and particle physics are independently determined, the theory is seen to be parameter-free. That

is, in its domain of validity the eikonal model follows directly from the Schrödinger or Lippman-Schwinger equations with no parameters introduced.

In our concluding section we shall see that this feature is lost as we go beyond the small-angle region.

## 7. ELASTIC AND INELASTIC SCATTERING

As noted in section I, the major development which led to the recent interest in multi-particle scattering was the achievement of nuclear resolutions at very high energies, enabling the experimenter to distinguish between elastic and inelastic events.

From the scattering amplitude (6.6), the differential cross-section is proportional to

$$\begin{aligned} \frac{d\sigma}{d\Omega} &\propto T^+ T \\ &\propto \langle i | \Gamma | f \rangle \langle f | \Gamma | i \rangle \end{aligned} \quad (7.1)$$

for particular initial and final states,  $|i\rangle$  and  $|f\rangle$ , respectively. When resolution is sufficient to determine that the scattering is elastic, i.e. the final state is the ground state  $|0\rangle$ , we have

$$\frac{d\sigma}{d\Omega}_{\text{elas}} \propto |\langle 0 | \Gamma | 0 \rangle|^2 \quad (7.2)$$

In contrast, for experiments with low resolution (e.g. those at 20 GeV with  $\Delta E \approx 50$  MeV), the final state of the target is undetermined and thus we sum over the possible final states,

$$\frac{d\sigma}{d\Omega} \propto \sum_f \langle 0 | \Gamma | f \rangle \langle f | \Gamma | 0 \rangle \quad (7.3)$$

When the resolution is such that a large part of the target's possible spectrum of final states is included in the sum over  $|f\rangle$ , it is appropriate to use closure,

$$\sum_f |f\rangle \langle f| = 1 \quad (7.4)$$

to approximate the summation:

$$\frac{d\sigma}{d\Omega} \propto \langle 0 | \Gamma^* \Gamma | 0 \rangle \quad (7.5)$$

The inelastic cross-section is obtained by subtracting the elastic term from the expression (7.5).

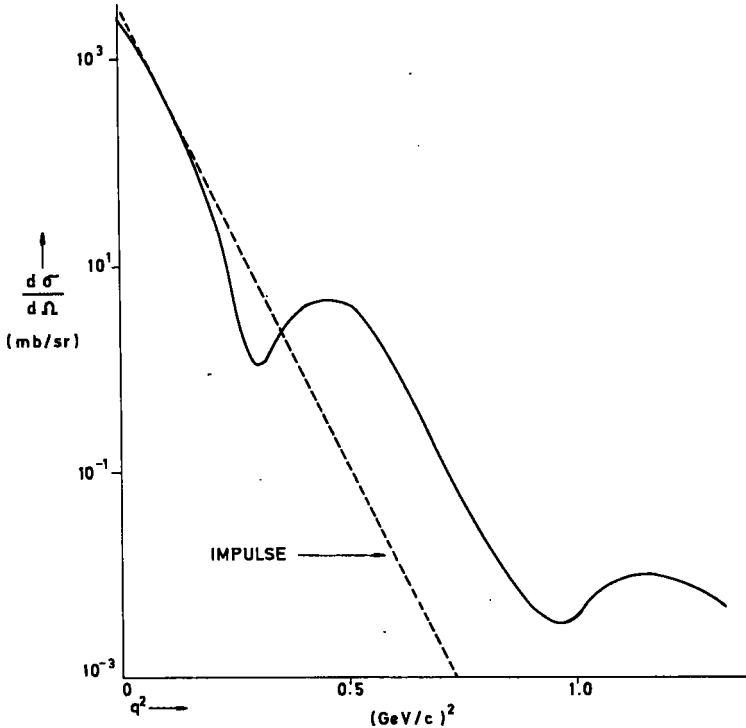


FIG. 2. Typical high-resolution cross-section (solid curve) and predictions of single-scattering (impulse) approximation (dashed curve) for  $p\text{-}^4\text{He}$  scattering.

The functions (7.3 and 7.4) are very different. For illustration we consider model curves for high-resolution (Fig.2) and low-resolution (Fig.3) experiments. For the low-resolution curve the elastic and inelastic contributions are shown. Actual data and calculations may be found in the proceedings of the Columbia Conference [3].

We shall be able to consider particular excited states in the sum of Eq.(7.3) as experimentalists further improve the resolution in the detection of the scattered projectile or residual nucleus.

## 8. NUCLEAR PHYSICS

The nuclear physics of the theory is contained in the wave-functions  $\Psi_i$  and  $\Psi_f$ . These may be analytical expressions with parameters fit to the particular target nucleus or may be numerical, obtained from shell-model calculations or derived from phenomenological potentials. The analytic forms have the obvious advantage of facilitating a study of the general structure of the resulting amplitudes.

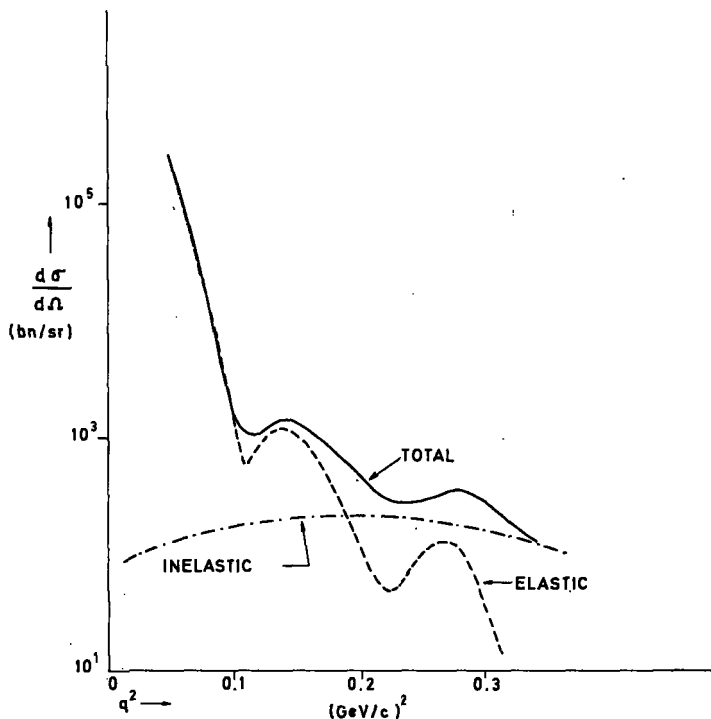


FIG. 3. Typical low-resolution cross-section, showing elastic and inelastic contributions for p - Pb scattering.

Typically, a very simple structure is assumed for the ground-state density, such as an uncorrelated harmonic-oscillator density:

$$\Psi^+ \Psi = \rho(r_1 \dots r_A) = \prod_{j=1}^A \rho_j(r_j)$$

$$\rho(r) = e^{-\alpha^2 r^2} \quad (8.1)$$

Correlations are introduced in such models in three forms:

1. Pauli correlations. This is merely the imposition of the Pauli principle on the states  $\phi_i$ :  $\Psi(\vec{r}_1 \dots \vec{r}_A) = \det |\phi_i(r_j)|$ .

2. Short-range correlations. These are usually expressed with a phenomenological correlation function  $g$ :

$$\Psi = \prod_{i < j} \phi_j [1 - g(r_{ij})] \quad (8.2)$$

Asymptotically,  $g \rightarrow 0$  for large  $r_{ij}$ ; for hard-core models,  $g = 1$  for  $r_{ij}$  smaller than the core radius.

3. Centre-of-mass correlation. This is merely the momentum-conserving delta function  $\delta(A^{-1} \sum_j \vec{r}_j)$  in the amplitude of Eq.(6.6). In general, this function causes serious technical difficulties for the calculations; it is often approximated by a distribution peaked at the zero of the argument.

One may, of course, escalate the sophistication of the nuclear structure. As both theory and experiments become more refined further nuclear properties may be introduced: deformations, hard cores, spin and isospin effects, particular excitations, Coulomb effects, etc. It is wise, however, to keep in perspective the elementary nature of the model which we have developed and the long sequence of approximations leading to it. The most impressive aspect of these models is that in their simplest form they fit so much so well.

The tough question is to decide if a correction introduced to improve a phenomenological fit is unique in the physics it represents. For example, both hard cores in nuclear densities and improvements in the eikonal phase function have been used to obtain equivalent improvement in the fit of Glauber-model calculations to experimental data.

It is important to distinguish the nuclear physics introduced via the  $\Psi$ 's from the details of the Glauber model itself, and its underlying eikonal approximation.

## 9. TWO-PARTICLE AMPLITUDES

The elementary particle physics enters the theory via the profile function  $\Gamma(b)$  of Eq.(6.3). The two-particle scattering amplitude  $f(q)$  and the profile function  $\Gamma(b)$  are mutual (2-dimensional) Fourier transforms:

$$f(\vec{q}) = \frac{ik}{2\pi} \int d^2b e^{i\vec{q}\cdot\vec{b}} [e^{2iX(\vec{b})} - 1]$$

$$\Gamma(\vec{b}) = e^{2iX(\vec{b})} - 1 = \frac{i}{2\pi k} \int d^2q e^{-i\vec{q}\cdot\vec{b}} f(\vec{q}) \quad (9.1)$$

Since our eikonal formalism involves only on-shell amplitudes, the  $f(q)$  are taken from the elastic-scattering experiments, e.g.  $\pi p$ ,  $pp$ , etc. In many calculations, spin and isospin details are approximated; often they are simply ignored.

The parametrization of the two-particle hadron amplitudes arises from two characteristic features of high-energy, small-angle scattering: the exponential fall-off of the forward diffraction peak, and the predominantly imaginary nature of the amplitude. These two properties, together with the optical theorem for the total cross-section,

$$\sigma_T = \frac{4\pi}{k} \text{Im} f(0) \quad (9.2)$$

lead naturally to the amplitude

$$f(q) = \frac{k\sigma_T}{4\pi} (i + \alpha) e^{-\alpha q^2} \quad (9.3)$$

where  $\alpha$  is the ratio of the real to the imaginary part of the amplitude (usually a few per cent at GeV energies).

The amplitude (9.3) may be viewed as a purely phenomenological fit to the data, or the functions  $\alpha$  and  $\sigma_T$  may express energy- and momentum-transfer behaviour explicitly predicted by Regge-pole theory or other models.

## 10. PREDICTIONS OF THE THEORY

Having now considered the scattering formalism, the nuclear model, and the particle physics, we can assemble the final amplitude from Eqs (6.4, 6). We again consider the model curves of Fig.2.

We wish to analyse the features common to all such cross-sections. We begin with Eq.(6.5), the multiple-scattering decomposition of the amplitude. In Fig.4 we plot the contribution of successive terms. Note that we plot the log of the contribution versus the scattering angle  $\theta$  (or, equivalently, the momentum transfer  $q$ ).

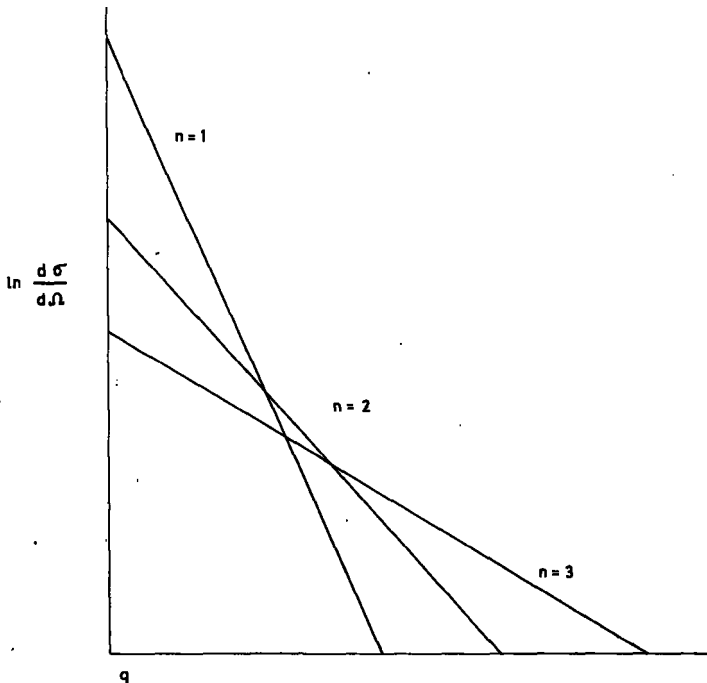


FIG. 4. Contributions of multiple-scattering terms to differential cross-section.

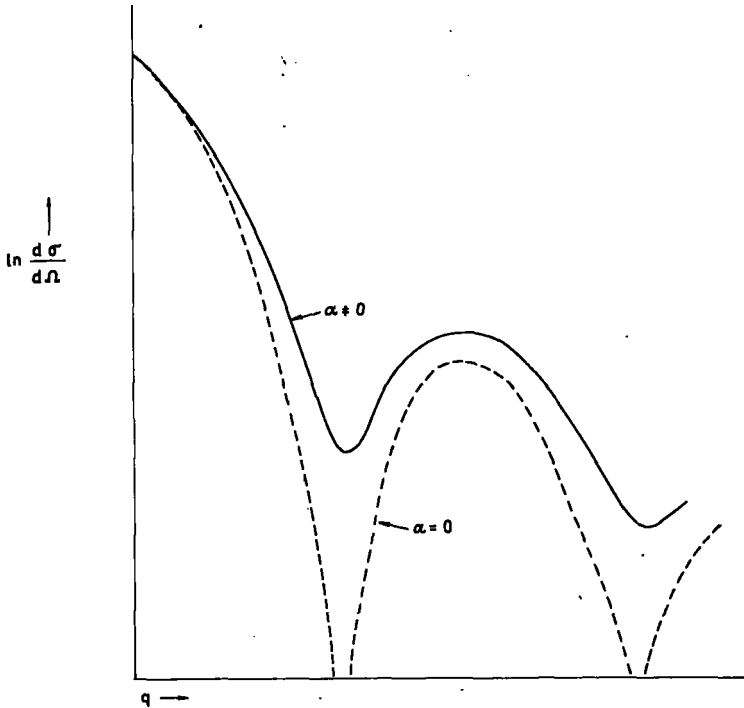


FIG. 5. Effect of  $\alpha \neq 0$  on minimum of diffraction pattern.

We note the following features:

1. Successive terms have decreasing amplitude in the forward direction but their fall-off with angle is progressively slower.
2. The terms contribute to the amplitude with alternating signs.

The summed amplitude for elastic scattering shows a characteristic diffraction as in Fig.5. For amplitudes [see Eq.(9.3)] that are purely imaginary, the alternating sign in successive terms give a polynomial with  $A$  zeros; for  $\alpha \neq 0$ , the zeros become merely minima as shown by the dashed curve in Fig.5.

Characteristic of such interference effects is a great sensitivity to perturbations. Since the unperturbed contributions completely cancel at these zeros, any derivation of the cross-section from zero at the minima is due to the perturbations. This property of effectively "amplifying" the effects of perturbations is the most interesting feature of the theory, apart from the generally successful prediction of the observed diffractive structure of measured cross-sections.

The location and depth of the minimum are extremely sensitive to effects such as nucleon correlations (see Eq.(8.2)) or the real components of the amplitudes. However, these effects are seldom unique in their

influence on the predicted cross-section. As we have mentioned previously, equivalent fits of the theory to experimental data have been obtained using modified eikonal phase functions as well as by modifications of the nuclear densities. To ascertain which of several possible perturbations is responsible for deviations from the simple model is usually difficult and frequently impossible. Ideally, such effects are corroborated by other experiments.

## 11. COMPARISON WITH EXPERIMENT

Rather than produce another compendium of experiments fit by eikonal models, we shall limit ourselves to drawing some generalizations from the range of experiments and calculations to date. Our interest is in assessing the success of the theory and in indicating the direction of future developments.

We again consider the cross-section curves for high- and low-resolution experiments in Figs 2 and 3, respectively.

Typically, the diffraction pattern features of high-resolution (elastic) scattering can be fit as far as the second minimum. (In judging the fit to experiment, one must keep in mind the logarithmic scale of the plots.) One observes that the low-resolution curves have significantly less structure than the elastic curves.

From such results we make two observations:

1. The more complex the structure of the predicted cross-section curves, the greater the physical information contained in a successful fit. In section 12 we shall see that the deuteron is an especially interesting illustration of this phenomena. As we noted, curves for low-resolution experiments are less complex and provide less critical tests of the theory or less precise determination of the parameters.

2. Many "successful" fits of theory to data extend beyond the range of energy and angle expected of the high-energy, small-angle eikonal theory [1]. For example, experiments fit by the theory [3] have ranged in energy from 20 GeV to less than 500 MeV, and in angle as far as  $40^\circ$ .

In planning future experiments it is important to determine which domains of energy and angle as well as which targets maximize the physics to be learned from the experiment. The general qualitative success is now well established, it is now appropriate to concentrate on the detailed fits.

An interesting question arises from the fits to date, which, as we have remarked, often succeed at larger momentum transfers than would be expected from simple estimates for the validity of the eikonal approximation. Is there some physics to be learned from the 'too successful' model, or, on the contrary, should we conclude that the ensemble of nuclear, particle and eikonal approximations, together with the uncertainty in the parameters provides an extremely flexible phenomenology? In section 13, we shall indicate some interesting possibilities for the former point of view.

To maintain our sense of perspective, we remark that the multiple-scattering model is by no means unique in fitting hadron-nucleus scattering. For heavy nuclei, equivalent results may be obtained from the optical model [3].

## 12. "DEUTERONOMY"

The deuteron, the simplest composite target, should provide the obvious first test of the theory. Surprisingly, it has been one of the most difficult - and interesting - applications in the history of the subject.

Since its inception, Glauber's model has been used to determine the 'shadow term' for proton-deuteron scattering. The expression arises from the intuitive notion that one nucleon partially eclipses the second as seen by the incident projectile. If we apply Eqs (6.5, 6) to the deuteron, we obtain

$$f_{pd}(\vec{q}) = f_{pn}(\vec{q})S(1/2\vec{q}) + f_{pp}(\vec{q})S(1/2\vec{q}) \\ + \frac{i}{2\pi k} \int d^2q' f_{pn}((1/2)\vec{q} + \vec{q}') f_{pp}((1/2)\vec{q} - \vec{q}') S(\vec{q}') \quad (12.1)$$

where  $S(\vec{q})$  is the deuteron form factor calculated from the wave-function  $\phi_d$ :

$$S(\vec{q}) = \int d^3r e^{i\vec{q}\cdot\vec{r}} |\phi_d(\vec{r})|^2 \quad (12.2)$$

In practice, the result (10.1) is used to determine the n-p amplitude (otherwise unobtainable without adequate neutron beams) from the directly measured p-p and p-d scattering. If we consider forward scattering ( $\vec{q}=0$ ) and use the optical theorem (Eq.(9.2)), we obtain the relation for the total cross-sections from Eq.(7.1):

$$\sigma_{pd} = \sigma_{pp} + \sigma_{pn} + \langle \text{"shadow"} \rangle \quad (12.3)$$

It is the angular or momentum transfer dependence of Eq.(12.1) that has caused considerable confusion and difficulty.

From Eq.(6.5) and from our remarks in section 10, we would expect a double diffraction peak with a single zero as shown by the dashed line of Fig.6. However, the experimental data, represented by the solid line, shows merely a shoulder with little structure. Although, as we shall see later, predictions for more complex systems such as  $^4\text{He}$ ,  $^{12}\text{C}$ , and  $^{16}\text{O}$  were quite successful, the theory seems to fail conspicuously for the simplest application, the deuteron.

A possible explanation follows from the observation that the successful applications,  $^4\text{He}$ ,  $^{12}\text{C}$ ,  $^{16}\text{O}$  all have spin 0; the deuteron has spin 1. Various authors [9] developed spin analyses of nucleon-deuteron and pion-deuteron scattering, incorporating the detailed spin dependence of the two-particle amplitudes. This is a substantial undertaking; for example, there are five nucleon-nucleon amplitudes, each usually determined by two complex parameters, not all of which are well known.

In brief, this impressive effort produced no compelling resolution of the problem of the missing minimum.

Returning to the data, we find that an important clue comes from the observation that pions as well as protons produced the same absence of a minimum, which suggests the possibility that the difficulty lies in the deuteron target and not in the two-particle amplitudes and their spin dependence.

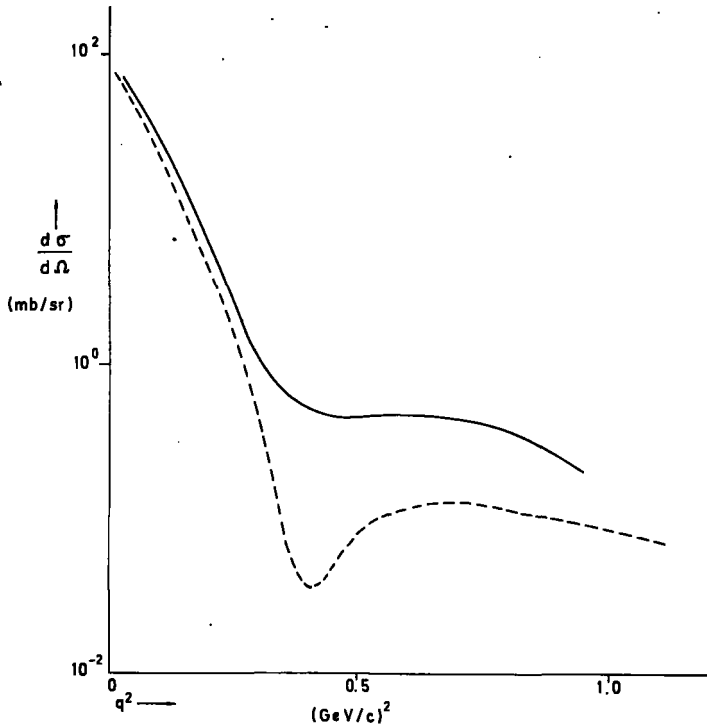


FIG. 6. Proton-deuteron cross-section (solid curve) and curve calculated without d-wave component (dashed curve).

Harrington [10] was the first to discover the simple resolution of the problem. The deuteron has a d-wave component, although its amplitude is only a few percent of the dominant s-wave component. We recall our remarks in section 10 where it was seen that the theory has the special feature of "amplifying" perturbations in those regions where the dominant amplitude cancels due to interference. The small d-wave component provides an excellent example of this effect.

In Fig.7 we see the form factors for the deuteron's s- and d-wave components, as well as their sum. It is this small d-wave effect, elsewhere unimportant, which produces the shoulder of the curve where one would expect a minimum or a zero.

A pessimist might at this point conclude that the formalism is not well tested by deuterons, and that we shall learn nothing of the deuteron from such analyses of experiments. Not so. Although the experiments just discussed yield too little structure in their angular dependence to be very informative, the deuteron spin may be exploited to recover the "lost" information by using polarized deuteron beams or targets.

Franco and Glauber [9] developed the formalism; experiments are now in the planning stages. For protons scattered from a polarized

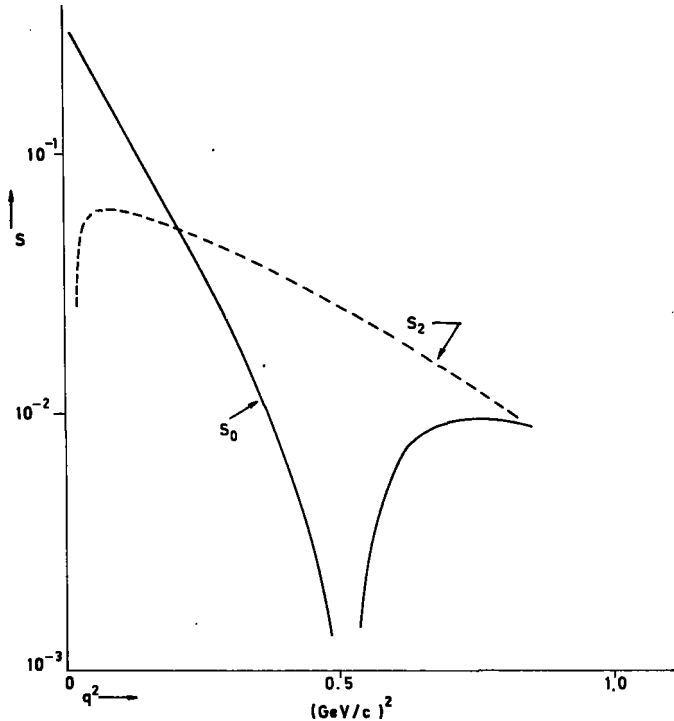


FIG. 7. Deuteron s- and d-wave form factors.

deuterium target, the predicted cross-section will have a structure depending on the direction of polarization. Of the obvious "physical" choices for the direction of polarization (incident momentum, momentum transfer, normal to the scattering plane), the second produces a differential cross-section with a particularly sharp dip [3, 9]. As alternative experiments [3] one may employ polarized deuteron beams on proton targets or measure the alignment of deuterons produced by scattering from unpolarized targets.

Thus the deuteron (with no small effort) becomes again an interesting target.

### 13. THE FUTURE

Being physicists rather than historians, it is now appropriate to ask what are the interesting remaining problems in the field.

The experimental future is clear. Improved resolution at the highest energies will provide increasingly rigorous challenge to the theory (or phenomenology). High-precision neutron beams as well as polarized targets and beams will significantly extend our knowledge of the nucleus with high-energy experiments.

For the theory, the future is interesting and complex. On the more technical level, there is the systematic inclusion in the models of details such as spin, isospin, Coulomb scattering, particle production, off-shell effects, nuclear deformations, three-body forces, etc. etc. To some extent, each of these effects has already been considered [3].

Of more fundamental interest is the validity of the model and its relation to other formalisms such as many-body theory and the optical model. Although these aspects of the problem have been studied to a limited extent [1, 3, 8], our understanding is very far from complete. We shall briefly consider a few topics under investigation, at present, and which seem most promising subjects for future development.

If we look at Fig.8 we see the angular range of an idealized experiment divided into three regions. In region I we see the forward diffraction peak. Since all reasonable theories predict such a peak - and fit it with one parameter (e.g. the nuclear radius), we learn little from this region. Likewise region III provides us with little that is new: at very high momentum transfers (large angles), the high-energy projectile tends to scatter from single nucleons, yielding merely the same information we obtain from two-particle scattering.

As we have seen, Glauber's eikonal theory leads us into the interesting region II where we learn most from a nuclear target. The first crucial question is how far into the region this theory is reliable and how its domain of validity might be extended.

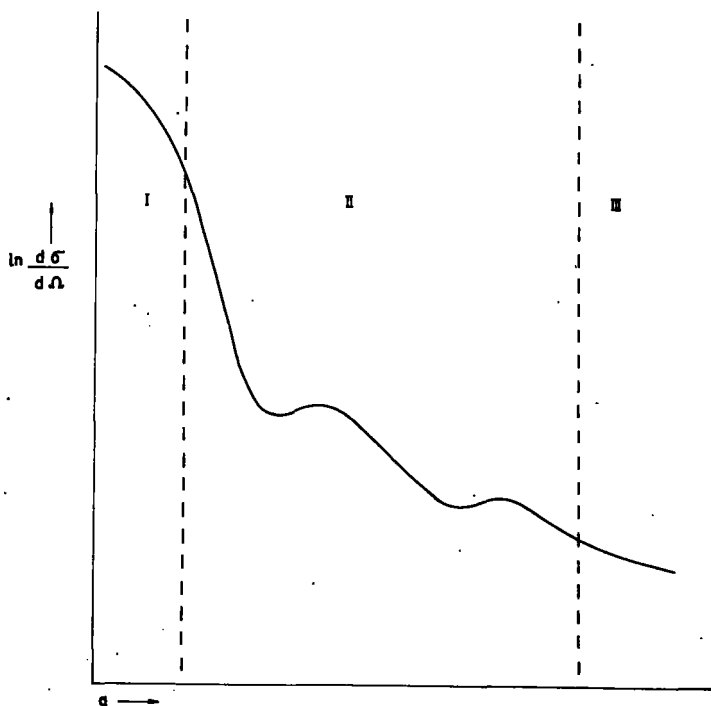


FIG. 8. Regions of hadron-nucleus scattering: I. Forward diffraction peak, II, multiple-scattering region, III, quasi-elastic region.

In fact, some answers to this question are already available. When we obtained the eikonal approximation by linearizing the Green's function in section 5, we neglected all but the lowest power of the intermediate momentum. We can continue the perturbation to higher orders to extend the angular range of our theory and to determine estimates of our errors. We shall comment briefly on the work of Sugar and Blankenbecler [6] who recently developed this method.

We saw in section 5 that the Green's function  $G$  may be separated into its directional approximation  $G_j$  and a perturbation  $N_j$ . Maximum accuracy and convergence is obtained by symmetrically approximating about the initial and final momenta  $\vec{k}_i$  and  $\vec{k}_j$ . We can then develop the symmetrized amplitude in the series

$$T = T_i + T_f G_f N_i G_i T_i + \dots \quad (13.1)$$

where for any  $\vec{k}_j$

$$T_j = V(1 - G_j V)^{-1} \quad (13.2)$$

Explicit calculation gives

$$\begin{aligned} T(\vec{q}) = & \int d^3r e^{i\vec{q}\cdot\vec{r}} V(r) e^{iX_i(\vec{r})} \\ & + \int d^3r e^{i\vec{q}\cdot\vec{r}} (e^{iX_f} - f) \left( -\frac{1}{2m} \nabla^2 \right) (e^{iX_i} - 1) + \dots \end{aligned} \quad (13.3)$$

where

$$X_j(\vec{r}) \equiv \int_0^\infty dt V(\vec{r} - m^{-1}\vec{k}_j t) \quad (13.4)$$

The first term of Eq.(13.3) as remarked in section 5, is just the original eikonal amplitude of Eq.(5.6) before the further approximation that  $q_z = 0$ . The second term turns out to be the expression obtained with quite different methods (stationary phase approximation to the Born series) by Saxon and Schiff [11] for wide-angle scattering. Ross [12] has recently investigated this term as a correction to the leading eikonal term.

Experiments at large momentum transfer obviously probe the details of the forces and the structure of the target more deeply. It is thus no surprise that in continuing beyond the leading eikonal term we lose two of the appealing features of the simple model (see section 11): the parameter-free nature of the multiple-scattering formalism, and the on-shell-only eikonal phase functions in which the potentials did not appear explicitly.

One might object at this point that the calculation of terms beyond the lowest-order (eikonal) expression involves no less effort than solving the complete many-body Lippman-Schwinger equation. The value of such a series is twofold. First it enables us to estimate the relative importance

of successive terms as a function of momentum transfer or angle. Second, from such bounds we gain insight into the mechanism of multiple scattering from a nuclear target. Again quoting typical results of Sugar and Blankenbecler, we find that for elastic scattering the leading terms of the amplitude have the following relative magnitudes:

$$1 : \frac{q^2 a}{k} : \left( \frac{q^2 a^2}{k} \right) \frac{V(\frac{1}{4} q^2)}{V(q^2) \Psi(q^2)} \quad (13.5)$$

where  $q$  is the momentum transfer,  $k$  the incident momentum,  $a$  the range of the potential  $V$ , and  $\Psi$  the bound-state wave function. Relation (13.6) is valid for potentials polynomially bounded in momentum space.

Clearly, such estimates are far from simple, depending on the relative fall-off (in momentum space) of the potential and of the bound-state wave-function. When both elastic and break-up reactions are considered, such bounds provide interesting insight into how different interactions favour multiple over single scattering for a given momentum transfer.

Obtaining such bounds is especially subtle for Gaussian potentials, which are obviously of great interest to nuclear physicists. Sugar [13] has recently obtained such bounds and found two interesting properties:

1. The Gaussian potential favours a maximally smooth scattering, i.e. for a fixed total momentum transfer, this potential favours terms corresponding to a large number of small scatterings on the nucleons of the target, adding up to the total transfer. (In contrast, some non-Gaussian interactions favour single (impulse) scattering from a single nucleon.)

2. The angular range of validity for the leading eikonal term, generally of order  $q^2 \approx a^{-2}$  is in the case of the Gaussian potential given by  $q^2 \lesssim a^{-1} k$ .

This latter result is most provocative since it may provide some insight into the often surprising success of simple models over a wide angular range. It suggests that for interactions typical of nuclear physics the angular range may be 'stretched' at high energies.

To date, the studies of the validity of the theory have raised as many questions as they have resolved. On the one hand, Ross [12] has found that for some potentials the eikonal approximation could produce order-of-magnitude errors at moderate angles; he subsequently developed corrections based on the method of Saxon and Schiff [11]. Calculations by Hüfner [14] have indicated that the eikonal approximation is least accurate at the minima, where, as we have remarked previously, the model is most interesting.

On the other hand, Osborn [8], Sugar [13], and Hüfner [14] have suggested aspects of multiple-scattering theory which may explain in part the exceptional success of simple models. The complexity of the process makes estimates rather subtle; for example, there are three characteristic lengths to be considered: interaction range, nuclear size, and correlation lengths. Furthermore, the eikonal phase by no means uniquely determines the underlying potential, as seen from Eq.(5.7). As we have seen above, some potentials produce exceptionally effective

eikonal amplitudes. Wallace [15] has recently made an extremely interesting and detailed analysis of the domain of validity of eikonal amplitudes.

It is also becoming evident that many of the features of the original Glauber model may be obtained without eikonal approximation. Osborn [8] has investigated the relationships between impulse approximation, unitarity, and eikonal formalism. The relation of the Glauber model to the Faddeev theory has not yet been fully explored.

The subject is rich with interesting problems.

#### REFERENCES

- [1] GLAUBER, R.J., in *Lectures In Theoretical Physics*, (BRITTIN, W.E. et al., Eds), Interscience, New York 1 (1959) 315.
- [2] GLAUBER, R.J., in *High Energy Physics and Nuclear Structure*, (ALEXANDER, G., Ed.), North-Holland, Amsterdam (1967) 311.
- [3] GLAUBER, R.J., in *High Energy Physics and Nuclear Structure*, (DEVONS, S., Ed.), Plenum Press, New York (1970) 207.
- [4] PALEVSKY, H., Ref. [2] 154; also *Phys. Rev. Letts* 18 (1967) 1200.
- [5] WILKIN, C., *Lecture Notes of the Summer School on Diffractive Processes*, McGill University, July (1969) (to be published).
- [6] SUGAR, R.L., BLANKENBECLER, R., *Phys. Rev.* 183 (1969) 1387.
- [7] ABARBANEL, H.D.I., ITZYKSON, C., *Phys. Rev. Letts* 22 (1969) 1334. SUGAR, R.L., BLANKENBECLER, R., *Phys. Rev.* D2 (1970) 3024.
- [8] OSBORN, T., *Annals Physics* 58 (1970) 417.
- [9] ALBERI, G., BERTOCCHI, L., *Physics Letts* 28B (1968) 186; FRANCO, V., GLAUBER, R.J., *Phys. Rev. Letts* 22 (1968) 370.
- [10] HARRINGTON, D.R., *Phys. Rev. Letts* 21 (1968) 1496; *Physics Letts* 29B (1969) 188.
- [11] SAXON, D.S., SCHIFF, L.L., *Nuovo Cim.* 6 (1957) 614.
- [12] ROSS, D.K., *Phys. Rev.* 173 (1968) 1695.
- [13] SUGAR, R., private communication.
- [14] HÜFNER, J., *Nucl. Phys.* B27 (1971) 260.
- [15] WALLACE, S.J., *Phys. Rev. Letts* 27 (1971) 622.

# HIGH-ENERGY SCATTERING OF ELECTRONS FROM NUCLEI

C. CIOFI DEGLI ATTI

Physics Laboratory,

Istituto Superiore di Sanità, Rome

and

Istituto Nazionale di Fisica Nucleare,

Sottosezione Sanità, Rome,

Italy

## Abstract

HIGH-ENERGY SCATTERING OF ELECTRONS FROM NUCLEI.

1. Introduction; 2. Fundamentals of electron scattering; 3. Elastic electron scattering and nuclear structure; 4. Quasi-elastic scattering and nuclear structure; 5. Summary and conclusions.

## 1. INTRODUCTION

The usefulness of electrons as probes of nuclear structure was first demonstrated in 1950 in the pioneering work by Lyman et al. [1], who observed, in elastic scattering by a nuclear target, the effects due to the finite sizes of the nucleus.

In the fifties, a considerable amount of work was done at Stanford University, where elastic electron-scattering experiments were systematically carried out on many nuclei (from proton up to uranium)[2]. The energy of the bombarding electrons in these experiments was sufficiently high ( $\sim(100 - 400)$  MeV) to allow the measurement of basic quantities such as the size of the charge distribution and its surface thickness, but it was still too low to reveal the details of the nuclear wave-function.

Recently, because of a rapid increase in experimental facilities, electron-scattering experiments became feasible at very high energies ( $\sim(500 - 1000)$  MeV) and with great accuracy, which allowed fine nuclear structure effects to be measured. At present, electron-scattering experiments are used to investigate in detail the wave-function of ground and excited states of nuclei, to measure nuclear separation energies, to produce baryon resonances in nuclei. The results of these experiments set a series of basic problems such as, for example, the origin of high-momentum components in the nuclear wave-function, the values of the separation energies of the deeply bound states, the width of baryon resonances in nuclear matter, and so on.

Because of the accuracy in producing and analysing high-energy electron beams, on the one hand, and because of the theoretically rather well-known nature of the electromagnetic interaction, on the other hand, high-energy electron scattering became one of the most powerful tools for studying nuclear structure.

In this paper the fundamentals of electron scattering will be briefly reviewed and the latest experimental results and theoretical interpretations presented, with particular emphasis on elastic and inelastic scattering in the continuum ("quasi-elastic" scattering).

## 2. FUNDAMENTALS OF ELECTRON SCATTERING

The formalism of electron-nucleus collisions is presented in detail in Refs [3,4]. In this paper only some basic concepts of the problem will be given.

### 2.1. Kinematics, energy spectra and angular distributions

The momenta and the energies of the electron before and after scattering will be denoted, respectively<sup>1</sup>, by

$$\vec{k}_1, \epsilon_1 \quad \text{and} \quad \vec{k}_2, \epsilon_2 \quad (1)$$

During the scattering the nucleus will be given a three-momentum ("momentum transfer")

$$\vec{q} = \vec{k}_1 - \vec{k}_2, \quad |\vec{q}| = (k_1^2 + k_2^2 - 2k_1 k_2 \cos \theta)^{1/2} \quad (2)$$

$\theta$  being the scattering angle, and an energy ("energy transfer")

$$\omega = \epsilon_1 - \epsilon_2 = k_1 - k_2 \quad (3)$$

There are, at present, two main classes of experiments with electrons: the non-coincidence experiments, when only the scattered electron is detected, and the coincidence experiments when, together with the scattered electron, some other reaction products are detected. The coincidence experiments, which are very difficult to carry out and therefore appeared feasible only in recent years, will be discussed in chapter 4. Now we start with the description of non-coincidence experiments, which is one of the richest sources of information on nuclear structure. In these experiments one usually measures the cross-section as a function of the energy transfer (the energy spectrum), keeping  $\epsilon_1$  constant, for example, and detecting for fixed  $\theta$  (or fixed  $q$ ) electrons with different  $\epsilon_2$ . The behaviour of the cross-section versus  $\omega$ , sketched in Fig. 1, shows (for more details, see Fig. 1 of Ref. [4]):

- (a) a peak at  $\omega \approx 0$ , corresponding to elastic scattering;
- (b) several peaks in a region of  $\omega$  less than the particle emission threshold, corresponding to the excitation of individual nuclear levels;
- (c) the giant resonance (GR) peak at  $\omega \sim 20$  MeV;
- (d) a broad peak located well above the GR ( $M$  is the nucleons mass)

$$\omega \approx \frac{q^2}{2M} + \langle B \rangle \quad (4)$$

<sup>1</sup> Since high-energy electrons are considered, we set  $m_e = 0$  so that  $\epsilon = |\vec{k}| = k$ .

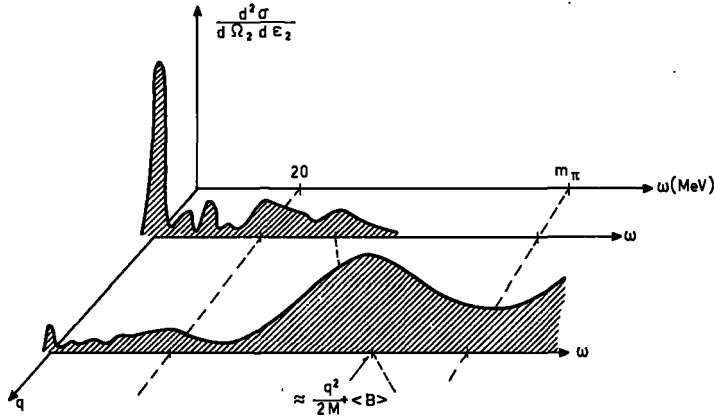


FIG. 1. Double differential cross-section ("energy spectrum") versus the energy transfer  $\omega$ , for different values of the three-momentum transfer  $q$ .

$\langle B \rangle$  being the average separation energy of the bound nucleons. This peak, called the "quasi-elastic (or quasi-free)" peak, is mainly due to a direct knock-out of single nucleons bound with momentum  $\vec{p}_i$  and emitted, after collision with the electron, with momentum  $\vec{k}_f = \vec{p} + \vec{q}$ . To have quasi-elastic (QE) scattering, the probability of collective excitation must be very low. This means that the interaction of the projectile with the target has to be localized in a region of space less than the nuclear sizes. In other words, one has QE scattering only when the momentum transfer is larger than the inverse of the nuclear radius; taking for the latter the value  $R \sim 3$  fm, we have

$$q \gtrsim (1 - 1.5) \text{ fm}^{-1} \quad (5)$$

(e) when  $\omega > m_\pi$  one has, finally, electroproduction of pions, and at higher  $\omega$ , production of nucleon resonances.

If the energy spectrum is measured at different values of  $q$ , and then the various peaks are integrated over  $\omega$ , one obtains the form factors of the different peaks appearing in the energy spectrum. With reference to the  $q$ -dependence of the cross-section, it should be noted that with increasing momentum transfer, the elastic cross-section strongly decreases and that at high momentum transfer the energy spectrum is dominated by the quasi-elastic peak.

## 2.2. Cross-section in Born approximation

The first Born approximation is widely used when scattering from light nuclei is considered, since the limits of its validity are fixed by the relation

$$Z \ll 137 \quad (6)$$

which is quite a good approximation up to  $Z \sim 10$ .

<sup>2</sup> If the nucleons were at rest and unbound, the position of the quasi-elastic peak should occur at  $q^2/2M$ .

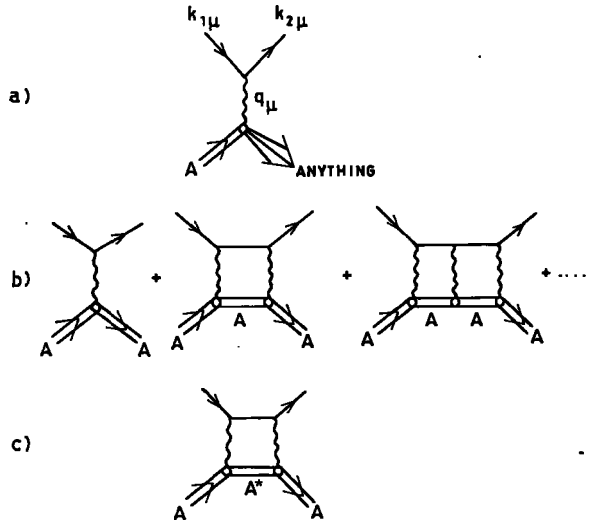


FIG. 2. Feynman graphs corresponding to a) the first Born approximation, b) the full Born series, and c) "dispersive effects".

In the first Born approximation the electron and nucleus are treated as two sources of currents which interact via the exchange of a virtual photon carrying a momentum equal to the 4-momentum momentum transferred to the nucleus:

$$q_\mu^2 = q^2 - \omega^2 = 4k_1 k_2 \sin^2 \frac{\theta}{2} \quad (7)$$

The process ("one-photon exchange") is described by the Feynman graph of Fig. 2a. The cross-section can be evaluated using electrodynamics. Plane waves for the electron are used, and in the nuclear current the wave function of the nucleus is taken to be a collection of non-relativistic nucleons having the same sizes as the free ones; this means that the mesonic degrees of freedom ("exchange currents") are neglected.

Within the above assumptions, the non-coincidence cross-section can be written in the following form [3], whatever the final state is:

$$\frac{d^2\sigma}{d\Omega_2 d\epsilon_2} = \frac{\sigma_M(\theta)}{1 + \frac{2k_1}{M_T} \sin^2 \frac{\theta}{2}} \left\{ \left( \frac{q_\mu}{q} \right)^4 R_L(q, \omega) + \left( \operatorname{tg}^2 \frac{\theta}{2} + \frac{1}{2} \frac{q_\mu^2}{q^2} \right) R_T(q, \omega) \right\} \quad (8)$$

where  $1 + \frac{2k_1}{M_T} \sin^2 \frac{\theta}{2}$  is the energy associated with the recoil of the target (with mass  $M_T$ ) and

$$\sigma_M(\theta) = \left( \frac{Ze^2}{2k_1} \right)^2 \frac{\cos^2 \frac{\theta}{2}}{\sin^4 \frac{\theta}{2}} \quad (9)$$

is the Mott cross-section describing the elastic scattering from a point nucleus. In Eq. (8), the two quantities  $R_L(q, \omega)$  and  $R_T(q, \omega)$ , which contain the information on nuclear structure, are called, respectively, the longitudinal and transverse form factors (or "response functions") since it can be shown [3, 4] that the former results from the interaction between the nuclear charge and the component of the electron current parallel to the vector  $\vec{q}$ , whereas the latter results from the interaction between the nuclear electric and magnetization currents and the components of the electron current perpendicular to the vector  $\vec{q}$ . The two form factors can be related to the Fourier transform of the charge (C) operator and to the electric (E) and magnetic (M) current operators

$$\begin{aligned} R_L(q, \omega) &= f_{\mathcal{N}}(q_\mu^2)^2 R^C(q, \omega) \\ R_T(q, \omega) &= f_{\mathcal{N}}(q_\mu^2)^2 [R^E(q, \omega) + R^M(q, \omega)] \end{aligned} \quad (10)$$

where  $f_{\mathcal{N}}(q_\mu^2)$  is the nucleon form factor<sup>3</sup>. The charge (or Coulomb) response function, which will be used in the following, is

$$R^C(q, \omega) = \frac{1}{2J_i + 1} \sum_{M_i M_f} |\langle \Psi_{J_f M_f} | \sum_{k=1}^A e_k \cdot e^{i\vec{q} \cdot \vec{r}_k} \delta(\vec{r} - \vec{r}_k) | \Psi_{J_i M_i} \rangle|^2 \delta(\omega + \epsilon_i - \epsilon_f) \quad (11)$$

with  $e_k = (1 + \tau_3)/2$  and  $\Psi$  denoting the nuclear state. The form of  $R^E$  and  $R^M$  is given in Ref. [3].

Performing a multipole expansion of the response functions (by expanding  $\exp(i\vec{q} \cdot \vec{r})$ ) and integrating over  $d\epsilon_2$ , we obtain the expression of the angular distributions [3, 4]

$$\begin{aligned} \frac{d\sigma}{d\Omega_2} &= \frac{\sigma_M(\theta)}{\left\{ 1 + \frac{2k_1}{M_T} \sin^2 \frac{\theta}{2} \right\}} f_{\mathcal{N}}(q_\mu^2)^2 \left\{ \left( \frac{q_\mu}{q} \right)^4 \sum_{J=0}^{\infty} \frac{|\langle J_f || \hat{M}_J^C(q) || J_i \rangle|^2}{2J_i + 1} \right. \\ &\quad \left. + \left( \frac{q_\mu^2}{2q^2} + tg^2 \frac{\theta}{2} \right) \sum_{J=1}^{\infty} \left[ \frac{|\langle J_f || \hat{T}_J^E(q) || J_i \rangle|^2}{2J_i + 1} + \frac{|\langle J_f || \hat{T}_J^M(q) || J_i \rangle|^2}{2J_i + 1} \right] \right\} \quad (12) \end{aligned}$$

where  $\langle || \rangle$  denotes a reduced matrix element and  $\hat{M}^C$ ,  $\hat{T}^E$ ,  $\hat{T}^M$  are the multipoles of the charge and current operators. Thus, by measuring the angular distributions, one maps out the Fourier transform of the nuclear charge and currents. The wider the range of momentum transfer explored, the finer are the details that can be studied.

Note that because the longitudinal component of the virtual photon field can carry zero angular momentum, the summation in the longitudinal term

<sup>3</sup> In Eq. (10) there are some other multiplicative factors resulting from relativistic corrections [3]. For the sake of simplicity, they will be omitted.

of Eq. (12) starts from  $J = 0$ . The transverse sum starts instead from  $J = 1$ , because it results from the transverse field of the virtual photon. The transverse matrix elements are thus identical, at  $q = \omega$  (which is the only possible momentum transferred by a photon of energy  $\omega$ ) to those appearing in photo-induced reactions. On the other hand, the longitudinal term has no equivalent in photon reactions and can induce  $(J = 0) \rightarrow (J = 0)$  transitions which are forbidden there.

### 2.3. Selection rules and contribution of longitudinal and transverse scattering

Selection rules on  $J_i$ ,  $J_f$  and  $J$  resulting from angular momentum and parity conservation and invariance of the theory under time reversal are summarized [3] in Table I.

From Table I it is easy to see that in elastic scattering ( $J_i = J_f$ ) all the transverse electric multipoles are forbidden by parity conservation ( $\Delta\tau = +$ ) and time reversal invariance ( $\Delta\tau = +$ ) while parity conservation forbids the odd Coulomb and the even magnetic multipoles.

Concerning the contribution of the various terms to the cross-section, the transverse multipoles dominate at  $\theta \approx 0^\circ$  and  $\approx 180^\circ$ , for at  $\theta \approx 0^\circ$

$$\left(\frac{q_\mu}{q}\right)^4 \ll \left(\frac{q_\mu^2}{2q^2} + \text{tg}^2 \frac{\theta}{2}\right) \quad (13)$$

as can easily be checked, while at  $180^\circ$

$$\sigma_M(\theta) \left(\frac{q_\mu}{q}\right)^4 \rightarrow 0 \quad \sigma_M(\theta) \left(\frac{q_\mu^2}{2q^2} + \text{tg}^2 \frac{\theta}{2}\right) \rightarrow \infty \quad (14)$$

At intermediate angles,  $30^\circ \lesssim \theta \lesssim 100^\circ$ , the Coulomb multipoles are always larger by about one order of magnitude than the transverse multipoles (the divergency in Eq. (14) is removed by taking into account the electron mass [4]).

TABLE I. SELECTION RULES ON  $J_i$ ,  $J_f$  AND  $J$

Conservation law Type of multipole	Angular momentum conservation	Parity conservation	Invariance under time reversal
Coulomb multipoles CJ	$ J_i - J_f  \leq J \leq J_i + J_f$	$(-1)^J$	$(-1)^{J_i - J_f + J}$
Electric transverse multipoles EJ	$ J_i - J_f  \leq J \leq J_i + J_f$	$(-1)^J$	$(-1)^{J_i - J_f + J + 1}$
Magnetic multipoles MJ	$ J_i - J_f  \leq J \leq J_i + J_f$	$(-1)^{J+1}$	$(-1)^{J_i - J_f + J + 1}$

#### 2.4. Corrections to the first Born approximation

Although very cumbersome from a numerical point of view, it is relatively easy to perform an exact calculation of the electron-nucleus cross-section [5]. "Exact" calculation means the summation of the whole Born series, as sketched in Fig. 2b, or, in other words, an exact treatment of the distortion of the electron waves by the static charge of the nucleus. It is clear that the heavier the nucleus, the larger will be the effect of the distortion. The exact calculation is accomplished by numerically solving the Dirac equation for the electron moving in the potential

$$V(r) = -4\pi Ze^2 \left\{ \frac{1}{r} \int_0^r \rho(r') r'^2 dr' + \int_r^\infty \rho(r') r' dr' \right\} \quad (15)$$

generated by the assumed charge  $\rho(r)$ .

The results of calculations [7] have shown that for light nuclei ( $Z \leq 10$ ) the effect of the electron distortion reduces practically only to filling in the zeros, which are always present in the cross-section  $d\sigma/d\Omega_2$  calculated in the first Born approximation. Thus, the information on the structure of

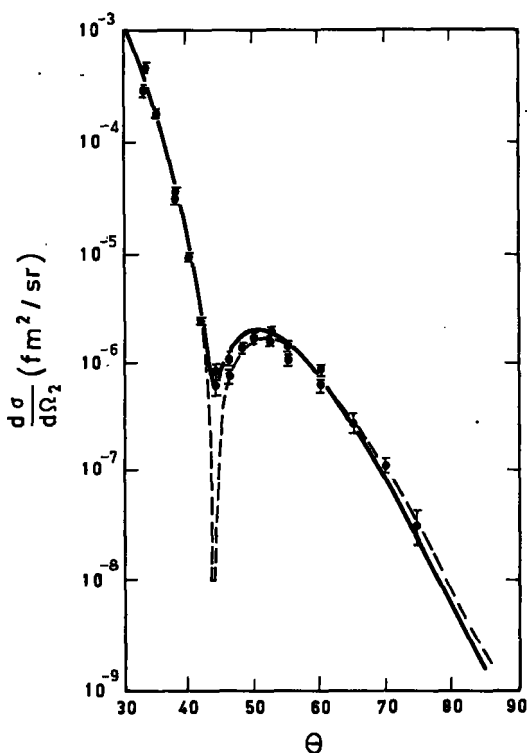


FIG. 3. Comparison of the exact calculation (continuous line) with Born approximation (dashed line) for  $^{16}\text{O}$ . The incident electron energy is 420 MeV (adapted from Ref. [7]).

light nuclei obtained by using the first Born approximation is quite reliable. For heavy nuclei, on the contrary, not only are the diffraction zeros filled in, but they are also shifted and, furthermore, the absolute value of the cross-section is affected. For this reason any nuclear structure information on heavy nuclei obtained by using the first Born approximation could be doubtful. In Fig. 3 the exact and Born approximation calculations for  $^{16}\text{O}$  are presented. The agreement for lighter nuclei is even better<sup>4</sup>.

In the Born series the intermediate nuclear state is always the initial state. However, there could be processes, as those shown in Fig. 2c, which correspond to the excitation of the nucleus to an excited state and its decay again to the ground state (we consider for simplicity elastic-scattering processes). Effects of this type ("dispersion effects") have been considered by several authors [8]. For the scope of this paper, it is enough to say that dispersion effects are extremely small (some per cent in the diffraction minima) and can be neglected without any trouble.

### 3. ELASTIC ELECTRON SCATTERING AND NUCLEAR STRUCTURE

#### 3.1. Introduction

Elastic electron scattering is defined by the following relations:

$$J_1 = J_f \quad k_1 = k_2 = k \quad q_\mu^2 = q^2 = 4k^2 \sin^2 \frac{\theta}{2}$$

Since, as shown in section 2.3, the only multipoles present in elastic scattering are  $C_0, C_2, \dots, M_1, M_3, \dots$ , we shall write Eq. (12) in the form

$$\frac{d\sigma}{d\Omega_2} = \frac{\sigma_M(\theta)}{\left\{1 + \frac{2k_1}{M_T} \sin^2 \frac{\theta}{2}\right\}} f_{\mathcal{M}}(q^2)^2 \left\{ |F_{C_0}(q^2)|^2 + |F_{C_2}(q^2)|^2 + \dots \right. \\ \left. + \left(\frac{1}{2} + \text{tg}^2 \frac{\theta}{2}\right) [ |F_{M_1}(q^2)|^2 + |F_{M_3}(q^2)|^2 + \dots ] \right\} \quad (16)$$

The various form factors appearing in Eq. (16) are proportional to given electric or magnetic moments and to the Fourier transform of their spatial

<sup>4</sup> A simple way of going beyond the first Born approximation is to use the high-energy approximation (see, for example, Ref. [3]), which says that the distortion by the Coulomb field can be taken care of by using an effective momentum transfer ( $R$  is the nuclear radius)

$$q_{\text{eff}} = q \left[ 1 + \frac{3}{2} \frac{Ze^2}{k_1 R} \right]$$

Away from the diffraction minima, this approximation gives results very similar to the exact calculation.

distribution. For example, the charge form factor  $F_{C0}(q)$  is proportional to the charge of the nucleus and to its spatial distribution. Due to the angular momentum conservation, it will be the only term present in the cross-section in scattering by nuclei with  $J = 0$ . The quadrupole form factor  $F_{C2}(q)$  is proportional to the spectroscopic quadrupole moment  $Q$  and thus it will be non-zero only for  $J \geq 1$ . The magnetic dipole moment form factor  $F_{M1}(q)$  is proportional to the nuclear magnetic moment  $\mu$  and it will be present only if  $J \geq \frac{1}{2}$ . The magnetic octupole moment form factor  $F_{M3}(q)$  is proportional to the nuclear octupole moment  $\Omega$  and will be present only for  $J \geq 3/2$ . And so on.

In the following, we shall be mainly interested in scattering from zero-spin nuclei. In this case the cross-section will be

$$\frac{d\sigma}{d\Omega_2} = \frac{\sigma_M(\theta)}{\left\{1 + \frac{2k_1}{M_T} \sin^2 \frac{\theta}{2}\right\}} f_{\mathcal{M}}(q^2)^2 |F_{\text{ch}}(q^2)|^2 \quad (17)$$

where

$$\begin{aligned} F_{\text{ch}}(q^2) &\equiv F_{C0}(q^2) = \frac{1}{Z} \langle \Psi_0(\vec{x}_1 \dots \vec{x}_A) | \sum_{k=1}^A e_k e^{i\vec{q} \cdot \vec{r}_k} | \Psi_0(\vec{x}_1 \dots \vec{x}_A) \rangle \\ &= \frac{1}{Z} \int j_0(qr) \langle 0 | \hat{\rho}(\vec{r}) | 0 \rangle d\vec{r} = 4\pi \int j_0(qr) \rho(r) r^2 dr \end{aligned} \quad (18)$$

We see that elastic electron scattering experiments are connected in a simple and direct way to the single-particle proton density in the nucleus  $\rho(r)$  ( $4\pi \int \rho r^2 dr = 1$ ).

The usefulness of elastic electron-scattering in testing nuclear structure strongly depends on the range of momentum transfer than can be explored. By expanding the charge form factor in powers of  $q$

$$F_{\text{ch}}(q^2) = 1 - \frac{1}{6} \langle r^2 \rangle q^2 + \dots \langle r^2 \rangle = 4\pi \int \rho r^4 dr \quad (19)$$

it can be seen that in scattering at low-momentum transfer ( $q \lesssim 0.5 \text{ fm}^{-1}$ ) the only parameter which matters is the nuclear mean square radius,  $\langle r^2 \rangle$ , which can be measured, however, in a model-independent way, that is, without any assumption about  $\rho(r)$ . It should be noted that elastic electron scattering at low-momentum transfer is a powerful tool for obtaining a model-independent determination of a series of characteristics of nuclei. For example, the scattering from a  $J = \frac{1}{2}$  or  $J = 1$  nucleus at  $180^\circ$  gives, at low  $q$ , a model-independent determination of the nuclear magnetic moment, since only M1-scattering is present. If higher multipoles are present, then even at low-momentum transfer they will interfere and their model-independent determination is impossible. However, the contribution from electric quadrupole and magnetic octupole scattering is very small at low-momentum transfer, becoming of the same order of the lower multipoles at higher ( $q \gtrsim 1 \text{ fm}^{-1}$ )

momentum transfer (see, for example, Figs 4 and 5 of Ref.[4]). For this reason, at low-momentum transfer the Coulomb scattering is predominantly charge scattering, while the magnetic scattering is mostly dipole. As the momentum transfer increases, the details of the spatial distribution of the various multipoles can be studied. In the last few years, the charge form factor of light nuclei has been experimentally studied up to very high momentum transfer ( $q \lesssim 4 \text{ fm}^{-1}$ ) [9-12]. In this way, experimental data on the high-momentum components of the single-particle wave function became available. This has stimulated a series of theoretical calculations, some of which will be discussed in the next sections.

### 3.2. Elastic electron scattering and single-particle (s. p.) wave functions

If the nucleus is described as a collection of particles moving in a common potential, then the s. p. density appearing in Eq.(18) is

$$\rho(r) = \frac{1}{Z} \sum_{\alpha} Z_{\alpha} |R_{\alpha}(r)|^2, \quad \sum_{\alpha} Z_{\alpha} = Z \quad (20)$$

where the summation extends over single-particle occupied states  $\alpha$ . We see that elastic electron scattering is a powerful tool for studying the radial part  $R_{\alpha}(r)$  of the s. p. wave functions. The latter can be generated either in a model-dependent way or as the solution of a Hartree-Fock (HF)-like calculation. The most common independent-particle model (IPM) is the well-known harmonic oscillator model (HO). This has proved very successful in explaining the experimental data for light nuclei ( $A < 40$ ) up to  $q \leq 2 \text{ fm}^{-1}$  [14]. However, the recently available data at high-momentum transfer show the dramatic failure of this model, as shown in Figs 4 and 5. A more realistic model is that of generating the s. p. wave functions in a finite well, for example, in square or Woods-Saxon wells. The effect of the finite well, as was first demonstrated in Ref.[15], is that of producing additional diffraction zeros in the form factor, in rough qualitative agreement with the experimental data. However, if a best-fit analysis is carried out, as in Figs 4 and 5, large discrepancies are found at high-momentum transfer. One can of course try to explain those discrepancies by inventing more sophisticated s. p. wells. However, a more interesting approach is to see if the discrepancies can be removed by taking into account higher-order effects in the nuclear wave function. Indeed, we know that the IPM is only a first approximation to the description of the nucleus, and it is reasonable to think that it does not give a good description of the high-momentum components. Several corrections to the IPM have been considered. Donnelly and Walker [15] have studied the effect of configuration mixing ("long-range correlations") which has been found to be very small. Elton and Webb [16] have analysed non-locality effects of the s. p. potential. They did not, however, give the results of the calculations for the high-momentum part of the form factors of light nuclei, so that it is not yet known how well their model works just in the most interesting region of momentum transfer. Systematic work (see next section) has been done in order to study the effect

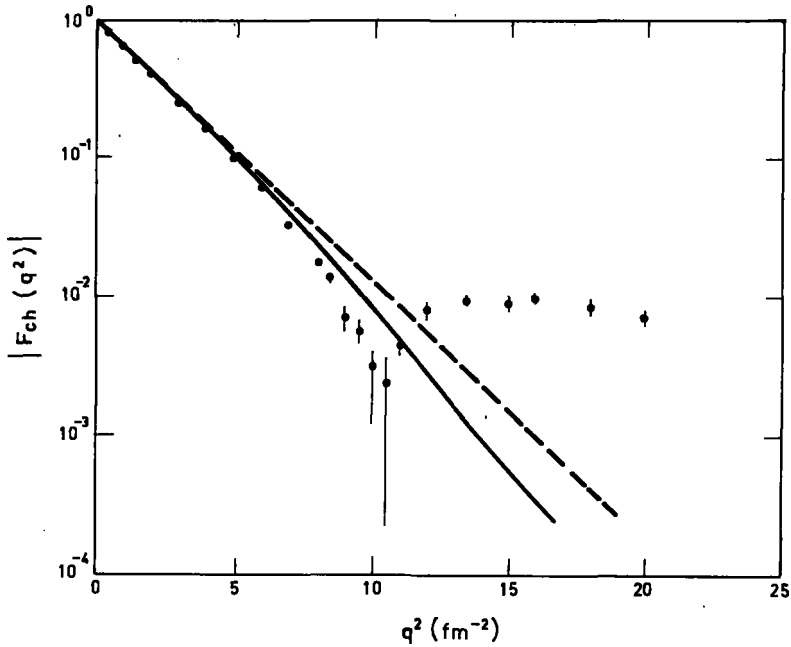


FIG. 4. Experimental charge form factor of  ${}^4\text{He}$  [10] compared with theoretical predictions by the independent-particle model generated in the harmonic oscillator (dashed line) and Woods-Saxon (continuous line) wells.

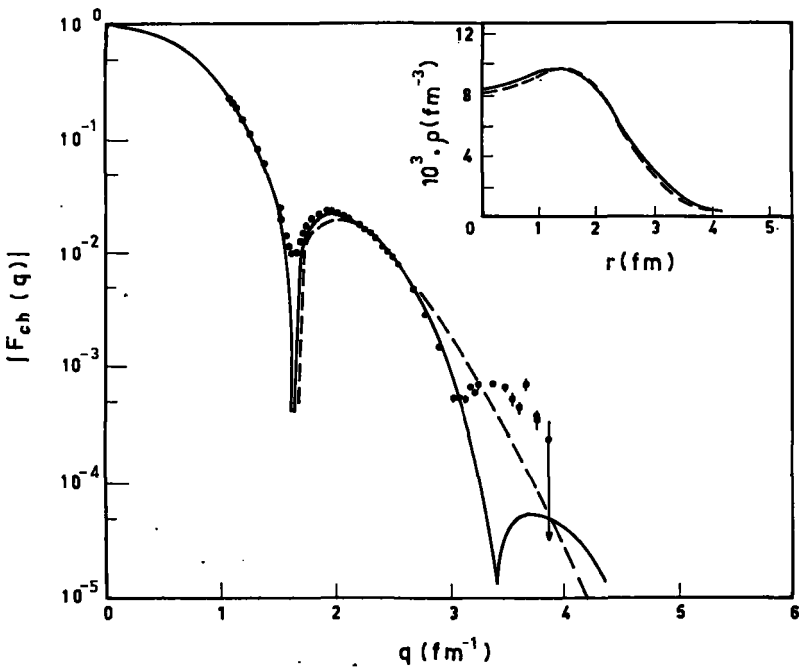


FIG. 5. The same as in Fig. 4 for  ${}^{16}\text{O}$ . (Experimental data from Ref. [12].) In the insert is shown the density calculated with the two models.

of short-range dynamic correlations [22-27]. As for the calculations performed with HF-like s.p. wave functions, the situation can be, very concisely, summarized as follows: the s.p. wave functions obtained from HF-like calculations are capable of giving a very good fit to the experimental data up to intermediate-momentum transfer, but at high-momentum transfers they do not seem to be very successful. Typical results are shown in Fig. 6.

### 3.3. Elastic electron scattering and Jastrow correlations

We have seen in the previous section that the high-momentum part of the charge form factors cannot be reproduced by reasonable phenomenological IPM and HF-like wave functions. Thus it is natural to look for such effects which influence the high-momentum components of the wave function. Effects of this kind are certainly those due to a strong repulsion at short internucleon separations ("short-range correlation" (SRC) effects). From what is known about the two-body potential one would expect SRC effects to be present in nuclei. However, there are many equivalent two-body potentials

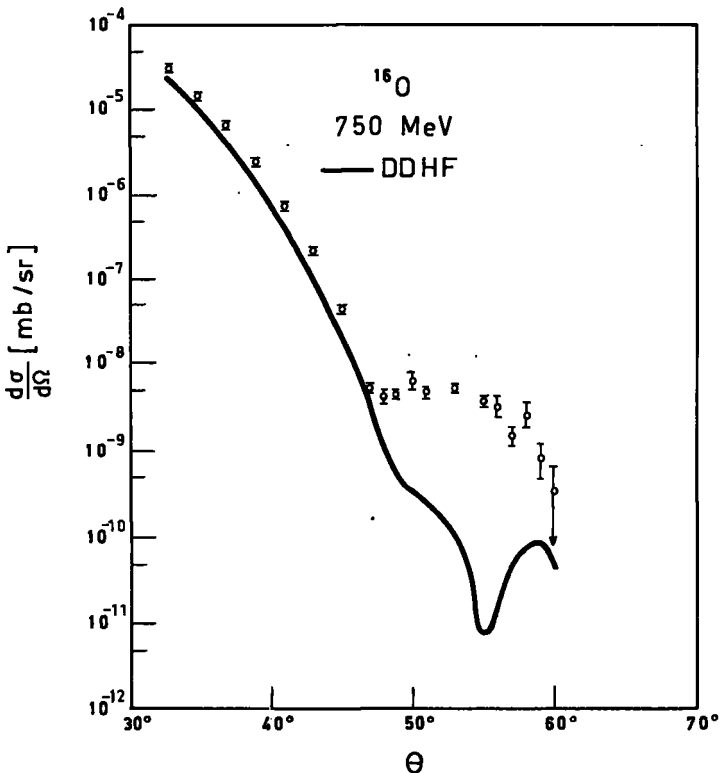


FIG. 6. Comparison with the 750 MeV data [12] of the  $^{16}\text{O}$  elastic cross-section calculated with wave functions resulting from density-dependent Hartree-Fock calculations [13] (private communication from J. Negele).

which differ just in the short-range behaviour, and, besides, the experimental study of the two-body relative wave function in nuclei is very difficult and, so far, very uncertain [17]. For these reasons, the real character of SRC is completely unknown. It is therefore interesting to analyse the effect of SRC on s. p. high-momentum components and to see if elastic electron scattering experiments can furnish some information on SRC. It is clear that such information (if any) will be indirect, since elastic scattering measures only the one-body density matrix; but still it will be useful.

A simple and straightforward way of studying SRC in electron scattering is to use the Jastrow wave function [18]

$$\Psi(x_1 \dots x_A) = N \Phi(x_1 \dots x_A) \prod_{i < j}^A f(r_{ij}) \quad N = \{ \langle \Phi | \prod_{i < j}^A f^2 | \Phi \rangle \}^{-1/2} \quad (21)$$

where  $\Phi$  is any uncorrelated wave function and  $f(r_{ij})$  is the Jastrow correlation function (JCF) which introduces SRC since it differs from one only for small internucleon separations. The JCF can be chosen at will providing that it heals ( $f \sim 1$ ) sufficiently rapidly. Once  $\Phi$  and  $f$  have been chosen, one has to calculate the form factor

$$F(q) = \frac{1}{Z} \frac{\langle \Phi | \sum_{k=1}^Z e^{i\vec{q} \cdot \vec{r}_k} \prod_{i < j} f(r_{ij})^2 | \Phi \rangle}{\langle \Phi | \prod_{i < j} f(r_{ij})^2 | \Phi \rangle} \quad (22)$$

which is a very difficult task, since one faces the evaluation of many-body matrix elements. One is forced to develop cluster expansions and then to calculate the leading terms. Therefore the prerequisites of a good cluster expansion are the following:

- (i) it must converge rapidly and must not contain terms which diverge with the increase of the mass of the nucleus;
- (ii) it should be "summable" as much as possible; that is, the various terms should contain the largest contribution from the correlation of a given type;
- (iii) every term of the expansion should possibly have a direct physical interpretation.

Several types of cluster expansions have been developed. An excellent review about their use in electron scattering is given in Ref. [20]. A cluster expansion satisfying the above conditions is the so-called factor cluster (or Van Kampen) expansion [20]. This is an expansion of the type

$$F(q^2) = F_0(q^2) + F_2(q^2) + F_3(q^2) + \dots \quad (23)$$

where the indices refer to the number of correlated orbitals which are present in a given term. The calculation of the term  $F_n(q)$  of Eq. (23) corresponds to the evaluation of  $n$ -body correlation effects. Calculations with Eq. (23) have been performed for  ${}^4\text{He}$  in Ref. [22] through two-body

terms, and in Ref. [23] exactly with all terms. The most frequently used cluster expansion is, however, the Iwamoto-Yamada [21] (IY) which, in the lowest order, yields for the form factor of a 1p shell nucleus with  $A = 2Z$

$$F(q^2) = \frac{1}{A} \left\{ \sum_{\alpha} \langle \alpha | e^{i\vec{q} \cdot \vec{r}_1} | \alpha \rangle + \sum_{\alpha\beta} \langle \chi_{\alpha\beta} | e^{i\vec{q} \cdot \vec{r}_1} | \chi_{\alpha\beta} \rangle - \sum_{\alpha\beta} \langle \chi_{\alpha\beta} | \chi_{\alpha\beta} \rangle \langle \alpha | e^{i\vec{q} \cdot \vec{r}_1} | \alpha \rangle \right. \\ \left. - 2 \sum_{\alpha\beta} \left[ \langle \phi_{\alpha\beta} | e^{i\vec{q} \cdot \vec{r}_1} | \chi_{\alpha\beta} \rangle - \langle \phi_{\alpha\beta} | \chi_{\alpha\beta} \rangle \langle \alpha | e^{i\vec{q} \cdot \vec{r}_1} | \alpha \rangle \right] \right\} \quad (24)$$

where

$$\chi_{\alpha\beta} \equiv \phi_{\alpha\beta} - f\phi_{\alpha\beta} \quad (25)$$

and  $\phi_{\alpha\beta}$  is the antisymmetrized two-particle uncorrelated wave function. Although the lowest order in the Iwamoto-Yamada expansion corresponds to only a part of the two-body correlations given by  $F_2$  of Eq. (23), it can be shown both formally [20] and numerically [22], that it gives similar results as the lowest order of Eq. (23), providing that correlations are short-range.

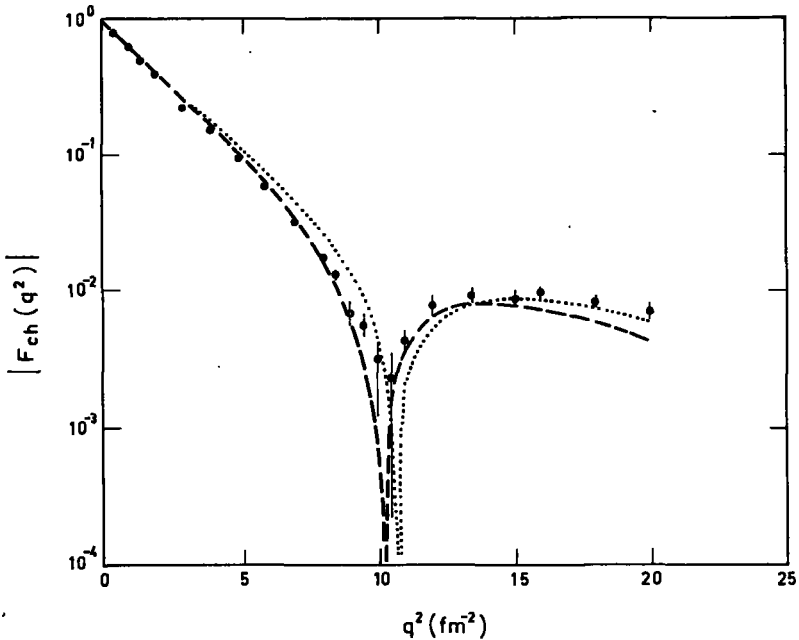


FIG. 7. Form factor of  ${}^4\text{He}$  calculated using harmonic oscillator orbitals plus Gaussian (dashed line) and oscillatory (dotted line) Jastrow correlation functions (JCF). The oscillator parameter is in both cases  $a = \hbar c / \sqrt{M\hbar\omega} = 1.21$  fm and the parameters of the two JCF's are  $b = 0.95$  fm and  $\bar{q} = 2.4$  fm $^{-1}$ , respectively.

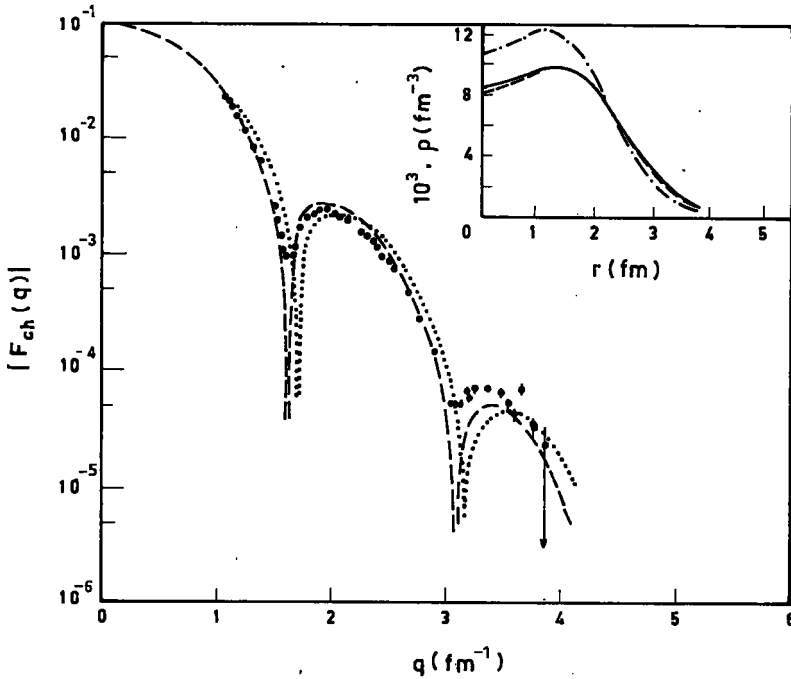


FIG. 8. The same as in Fig. 7 for  $^{16}\text{O}$  (oscillator parameter  $a = 1.64$  fm). In the insert the best uncorrelated density (continuous line from Fig. 5) is compared with the best correlated density (dashed line). The dot-dashed line was obtained without correlations using the same oscillator parameter as for the correlated density.

Another type of expansion has occasionally been used [19, 28, 57]. That consists of expanding the numerator and denominator of Eq. (22) using

$$i^2 = 1 - h \quad (26)$$

and retaining only

$$F(q^2) = \frac{1}{Z} \frac{\langle \Phi | \sum_k e^{i\vec{q} \cdot \vec{r}_k} \left( 1 - \sum_{i < j} h(r_{ij}) \right) | \Phi \rangle}{\langle \Phi | 1 - \sum_{i < j} h(r_{ij}) | \Phi \rangle} \quad (27)$$

It has been shown [20, 22] that Eq. (27) satisfies none of the conditions mentioned above. In particular, it contains divergent terms which contribute even for  $A > 4$ . Numerical calculations [22] for  $^4\text{He}$  and  $^{16}\text{O}$  using Eqs (23), (24) and (27), show that all give very similar form factors but the correlation parameter obtained using Eq. (27) differs by 20% from the values obtained using Eqs (23) and (24), which give very close results. For this reason the value of the parameters found by using Eq. (27) are not reliable.

Equation (24) has been fitted to the experimental data for  ${}^4\text{He}$  and  ${}^{16}\text{O}$  varying the correlation and IPM parameters. Two types of correlation function have been used:

$$\text{Gaussian} \quad f = \{1 - e^{-r^2/b^2}\}^{1/2} \quad (28)$$

$$\text{Oscillatory [28].} \quad f = \{1 - j_0(\bar{q}r)\}^{1/2} \quad (29)$$

The results of calculations are shown in Figs 7 and 8.<sup>5</sup> With reference to these results the following remarks should be made:

(i) The introduction of JCF accounts very well for the experimental data. It must be pointed out that the correlated and uncorrelated form factors strongly differ at  $q \gtrsim 3 \text{ fm}^{-1}$  while the corresponding densities are almost the same (see Figs 5 and 8). This is for the simple reason that even extremely small differences in the charge density can have very large effects in the region where the form factor is very small ( $10^{-4} - 10^{-5}$ ). Therefore, any conclusion on the effect of SRC based only on the calculation of the density (see, for example, Ref.[29]) can be doubtful.

(ii) Elastic electron scattering is rather insensitive to the form of the JCF. This was expected since only the one-body density matrix is measured.

(iii) The correlation parameters are independent of the mass number, which is quite satisfactory.

(iv) Although insensitive to the JCF, the experimental data are sensitive to the value of the "wound volume"  $\langle \chi\chi \rangle = \langle \phi(1-f)^2\phi \rangle$ . This is shown in Fig. 9 for  ${}^{16}\text{O}$  [26]. We have compared in Table II the values of the wound volume corresponding to the fits of Figs 7 and 8 with the values obtained in Brueckner theory by solving the Bethe-Goldstone equation [31]. The agreement between the two values should be noted.

Before drawing any general conclusion, two important problems should be investigated: the dependence of the results on the s.p. basis and the convergence of the expansion. As for the first problem, in Fig. 10 the results [24] for  ${}^{16}\text{O}$  obtained with HO and Woods-Saxon orbitals are shown. It is encouraging to see that in both cases the best fitting correlation parameter is the same.

The problem of convergence has been studied in detail for  ${}^4\text{He}$  in Ref.[23]. In Fig. 11, the results obtained with the Van Kampen expansion (Eq. (23)) are shown. The effect of many-body correlations increases, as expected, with the momentum transfer. It is, however, encouraging to see that good convergence in a wide region of momentum transfer is reached when three-body correlations are taken into account. Since it has been found that the correlation parameter is the same in  ${}^4\text{He}$  and  ${}^{16}\text{O}$  and since the terms of the expansion can be roughly classified in powers of  $\omega/\Omega$  ( $\omega$  is the total "correlation volume" and  $\Omega$  the total volume of the system), one expects the conclusions for  ${}^4\text{He}$  to be also valid for  ${}^{16}\text{O}$ .

<sup>5</sup> It should be remarked that the calculation with the oscillatory JCF is not exactly a best fit to the data but rather an attempt at selecting that value of  $\bar{q}$  giving, with the same HO constant, results similar to those of the Gaussian JCF (for which a best-fit analysis has been made). By using slightly different HO constants one can probably match the two curves of Figs 7 and 8. It is interesting to note that  $\bar{q}$  and  $b$  turned out to be connected through  $\bar{q} \approx \sqrt{6}/b$ , which follows from the relation between the Gaussian and the spherical Bessel functions [30]. In Ref.[28] it has been found that  $\bar{q} \approx 1.5 \text{ fm}^{-1}$ . In this connection it must be emphasized that there the not very reliable Eq.(27) has been used.

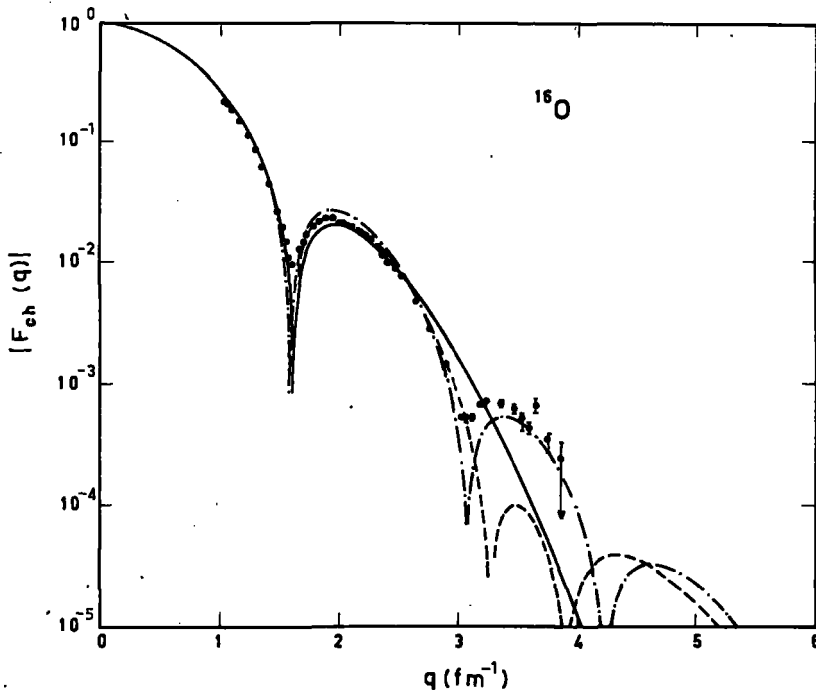


FIG. 9. Dependence of the form factor upon the value of the Jastrow wound volume  $\langle \phi_{\alpha\beta} (1-f)^2 \phi_{\alpha\beta} \rangle \equiv \langle \chi\chi \rangle$ . Continuous line: no correlations. Dot-dashed line:  $\langle \chi\chi \rangle \approx 0.009$ . Dashed line:  $\langle \chi\chi \rangle \approx 0.004$ . The r.m.s. radius is the same for the three cases (from Ref. [26]).

TABLE II. COMPARISON OF "WOUND VOLUME" VALUE OBTAINED FROM ELECTRON SCATTERING BY JASTROW METHOD AND VALUE OBTAINED FROM BRUECKNER THEORY USING A HARD-CORE POTENTIAL WITH CORE RADIUS  $r_c = 0.45$  fm

Method \ Nucleus	Electron scattering (Jastrow)	Brueckner theory
$^4\text{He}$	$\sim 0.022$	$\sim 0.024$
$^{16}\text{O}$	$\sim 0.009$	$\sim 0.011$

From the analysis of elastic electron scattering using Jastrow wave-functions we learned that:

- (i) the systematic deviations from the IPM can systematically be removed by Jastrow correlations;
- (ii) correlation effects seem to be independent of the mass number and of the single-particle orbitals;
- (iii) the charge form factors at high-momentum transfer are very sensitive to the value of the wound volume, whose best fitting value turned out to be very close to that predicted by Brueckner theory.

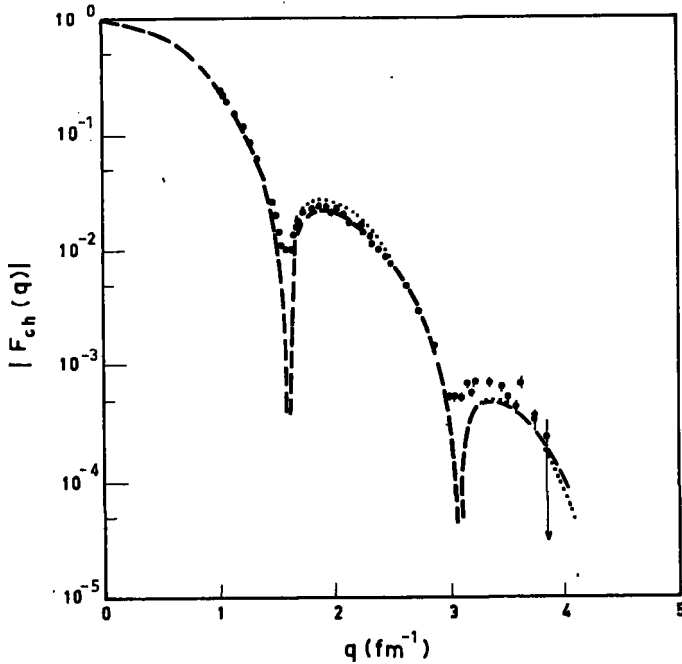


FIG. 10. Dependence of the Jastrow form factor upon the single-particle basis. Dashed line: Woods-Saxon orbitals. Dotted line: harmonic oscillator orbitals. The JCF is Gaussian and in both cases the correlation parameter is the same ( $b = 0.9$  fm). When the dotted line is not shown, it coincides with the dashed line (from Ref. [24].)

For the above reasons we think that elastic-electron-scattering experiments at high momentum transfers can help towards understanding the nature of SRC in nuclei.

A final comment on the interesting problem [32] of the formal comparison between Brueckner and Jastrow form factors. First of all, we note that Eq. (24) is usually written in the form

$$\begin{aligned}
 F(q^2) = \frac{1}{A} \left\{ \sum_{\alpha} \langle \alpha | e^{i\vec{q} \cdot \vec{r}_1} | \alpha \rangle + \sum_{\alpha\beta} \langle \phi_{\alpha\beta} | e^{i\vec{q} \cdot \vec{r}_1} (f^2 - 1) | \phi_{\alpha\beta} \rangle \right. \\
 \left. - \sum_{\alpha\beta} \langle \alpha | e^{i\vec{q} \cdot \vec{r}_1} | \alpha \rangle \langle \phi_{\alpha\beta} | (f^2 - 1) | \phi_{\alpha\beta} \rangle \right\} \quad (30)
 \end{aligned}$$

It is easy to see that Eqs (24) and (30) are identical, since  $f^2 - 1 = (f - 1)^2 + 2(f - 1)$ .<sup>6</sup> However, Eq. (24) is formally more convenient for a comparison

<sup>6</sup> Remember that Eqs (24) and (30) have been written down for the case of p-shell nuclei. In the general case one has to do the replacement  $\sum_{\alpha\beta} \rightarrow \sum_{\alpha\beta\gamma}$  in the third term of Eq.(30).

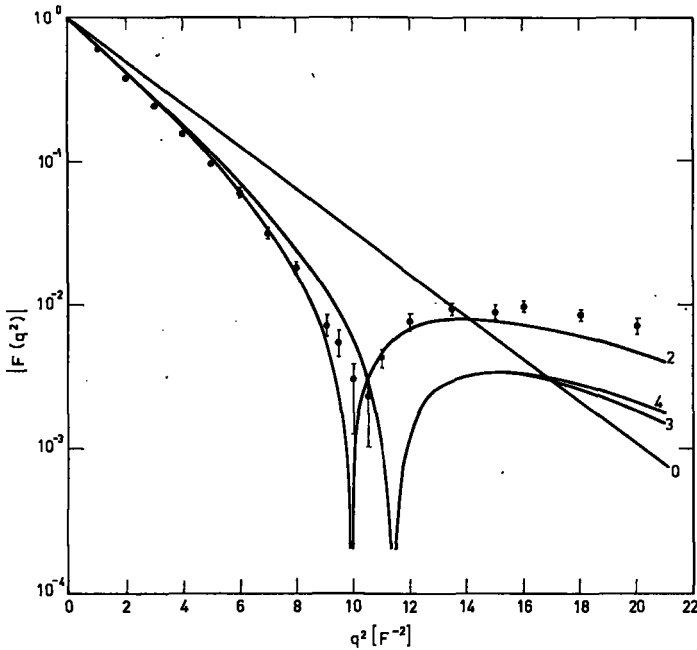


FIG.11. Convergence of the  ${}^4\text{He}$  form factor calculated with the Van Kampen expansion. Curve 0: no correlations. Curve 2: two-body correlations. Curve 3: three-body correlations. Curve 4: four-body correlations (exact calculation). The oscillator parameter is  $a=1.21$  fm and the Gaussian correlation parameter  $b=0.9$  fm. (From Ref.[23].)

with Brueckner theory because it shows that the Jastrow correlation contribution, like that of Brueckner contains one part proportional to the quantity  $\chi\chi$  and one part which is due to  $1p-1h$  excitations (we mean the term  $\langle \phi | e^{i\mathbf{q}\cdot\mathbf{r}_i} | \chi \rangle$  in Eq.(24) and the terms corresponding to the Goldstone graphs (a)-(d) in Fig. 2 of Ref.[31]). The  $1p-1h$  contribution in Brueckner theory is very important, at least in the calculation of radii and densities [31]. Therefore, one has to take it into account when the comparison with Jastrow method is carried out; it will be zero only if self-consistent orbitals are used, in which case, however, the uncorrelated form factors in Brueckner and Jastrow cases will be very different, and therefore one can compare only the total form factors but not the correlation corrections (2p-2h plus 1p-1h corrections in the Jastrow method and only 2p-2h corrections in the Brueckner method). A significant comparison between the two methods can only be made by referring to some specific Brueckner calculations.

The only calculation we know about is that performed in Ref.[31]. It is interesting and promising to see that the net effect of 2p-2h plus 1p-1h correlations on the radius of  ${}^4\text{He}$  is the same as in the Jastrow case. Namely, the (correct) value ( $\sim 1.41 \pm 0.05$  fm) of the mass radius obtained when 1p-1h and 2p-2h corrections are included, is  $\sim$  five per cent larger than the uncorrelated value (see last column of Tables in Ref.[31]). The same effect has been found in the Jastrow case for  ${}^4\text{He}$  and heavier nuclei [24].

## 4. QUASI-ELASTIC SCATTERING AND NUCLEAR STRUCTURE

### 4.1. Introduction

As was already mentioned in chapter I, for quasi-elastic (QE) scattering we mean a direct knock-out of the bound nucleons by the incident particle, occurring at high-energy and momentum transfers. QE scattering is one of the most attractive and direct ways of studying nuclear structure. In particular, if the emitted particle is detected in coincidence with the scattered one (both particles can be of any type), then unique information on momentum distribution and binding energy of bound nucleons and nucleon clusters can be obtained. (For a review of coincidence quasi-elastic scattering see Ref.[33].)

The energy transfer in QE scattering should be high enough in order to avoid the coupling of collective excitations (giant resonance) with the direct process<sup>7</sup>, and in order to produce nucleons with high kinetic energy, thus minimizing their absorption by the nuclear medium. However, it should not be too high, otherwise pion production becomes dominant. Typical values are

$$1.5 \text{ fm}^{-1} \lesssim q \lesssim 2.5 \text{ fm}^{-1} \quad 100 \text{ MeV} \lesssim \omega \lesssim 250 \text{ MeV}$$

How coincidence and non-coincidence QE scattering can be used to get information on nuclear structure will be the subject of this chapter. In the next section the elements of electron QE scattering will be worked out using the Born approximation. As we know, this is quite a good approximation provided the target nucleus is not too massive, in which case distortion of electron waves should be taken into account.

### 4.2. Kinematic and cross-section

Energy and momentum conservation when a nucleon (we consider it to be a proton) is ejected from the nucleus, reads

$$\begin{aligned} \vec{q} &= \vec{k}_p + \vec{K}_B \\ \omega - B_f &= T_p + T_B \end{aligned} \tag{31}$$

where  $\vec{K}_B$  is the recoil momentum of the final nucleus B,  $T_p$  and  $T_B$  are kinetic energies of the knocked-out proton and the residual nucleus and

$$B_f = E_{B_f}^* + M_B + M - M_A = E_{B_f}^* + \Delta M \tag{32}$$

is the energy ("separation energy") required to knock out the proton leaving the residual nucleus in the excited state  $E_{B_f}^*$ .

<sup>7</sup> Effects of this type have been considered in Ref.[56]. At  $\omega=22.6$  MeV, which is the position of the main peak of Giant Resonance, collective excitations are dominant.

If we suppose, for the sake of simplicity, that only Coulomb interaction is present (it is in fact the dominant contribution except in the backward direction), the cross-section will be (see Eqs (8) and (10))

$$\frac{d^2\sigma_f}{d\Omega_2 d\epsilon_2} = \sigma_M(\theta) \left(\frac{q\mu}{q}\right)^4 f_{\mathcal{R}}(q_\mu^2)^2 R^C(q, \omega) d\vec{k}_p \quad (33)$$

with  $R^C$  given by Eq. (11)

$$R^C(q, \omega) = \frac{1}{2J_f + 1} \sum_{M_i M_f} |g_{fi}(\vec{q}, \vec{k}_p)|^2 \delta(\omega - B_f - T_p - T_B) \quad (34)$$

Here, the "QE form factor" is

$$g_{fi}(\vec{q}, \vec{k}_p) = \langle \Psi_f(B) | \chi_{k_p}^{(-)} | \sum_{k=1}^A e_k e^{i\vec{q} \cdot \vec{r}_k} \delta(\vec{r} - \vec{r}_k) | \Psi_i(A) \rangle \quad (35)$$

where  $\Psi_f(B)$  and  $\Psi_i(A)$  are the wave-functions of nuclei A and B and  $\chi_{k_p}^{(-)}$  is proton continuum wave-function. If the latter is approximated by a plane wave

$$\chi_{k_p}^{(-)}(\vec{r}) \propto e^{-i\vec{k}_p \cdot \vec{r}} \quad (36)$$

we get

$$g_{fi}(\vec{K}_B) = \int e^{i\vec{K}_B \cdot \vec{r}} \langle \Psi_f(B) | \Psi_i(A) \rangle d\vec{r} \quad (37)$$

The important quantity entering Eq. (37) is the "overlap integral"

$$\langle \Psi_f(B) | \Psi_i(A) \rangle \quad (38)$$

which contains all the information on the structure of nuclei A and B. If we consider the final nucleus to be a hole state of the target, we obtain in the simplest version of the shell model (independent particles without any spin-orbit coupling)

$$\langle \Psi_f(B) | \Psi_i(A) \rangle = \varphi_{nlm}(\vec{r}) = y_{lm}(\theta\varphi) R_{nl}(r) \quad (39)$$

and the QE form factor becomes the momentum distribution of protons bound with momentum

$$\vec{p} = -\vec{K}_B \quad (40)$$

in the shell ( $n\ell$ )

$$g_{fi}(\vec{p}) = \int e^{-i\vec{p}\cdot\vec{r}} \varphi_{n\ell m}(\vec{r}) d\vec{r} \quad (41)$$

Performing the summation in Eq. (34) (we consider  $J_i = 0$ ) and expanding  $\exp(-i\vec{p}\cdot\vec{r})$  in partial waves, we obtain for the cross-section

$$\frac{d^2\sigma_{n\ell}}{d\Omega_2 d\epsilon_2} = \sigma_M(\theta) \left(\frac{q_\mu}{q}\right)^4 f(q_\mu^2)^2 \rho_{n\ell}(p) \delta(\omega - B_{n\ell} - T_p - T_B) d\vec{k}_p \quad (42)$$

where

$$\rho_{n\ell}(p) = N_{n\ell} |(\pi\sqrt{2})^{-1} \int j_\ell(pr) R_{n\ell}(r) r^2 dr|^2 \quad (43)$$

and  $N_{n\ell}$  is the number of protons in the shell.

We see that QE reactions depend on the momentum distribution of the knocked-out particle and, through the energy conservation  $\delta$ -function, on its separation energy  $B_{n\ell}$ . It is clear that a direct measurement of these quantities is possible only in a coincidence experiment. However, it is also important to study and to understand the real nature of the QE peak appearing in the non-coincidence energy spectrum, which will be done in the next section.

The approximations used to derive Eq. (42) have been made simply in order to introduce the problem. In fact, there is no need of them in actual calculations. First of all, one should introduce a more realistic description of the nucleus. This is usually done [34] by taking into account the residual interaction. The wave-function of the nucleus A can then be expanded in the form

$$\Psi_i(A) = \sum_f C_f^{(n\ell)} (0 \rightarrow E_{B_f}^*) \{\Psi_f(B) \varphi_{n\ell m}(\vec{r})\}_i \quad (44)$$

where  $C_f^{(n\ell)}$  (fractional parentage coefficient, f. p. c.) couples the ground state of A with excited states of B. Inserting Eq. (44) in the overlap integral (38), we get for the QE form factor (35)

$$g_{fi}(\vec{q}, \vec{k}_p) = \sum_f C_f^{(n\ell)} \{f, (\ell m)\}_i \int e^{i\vec{q}\cdot\vec{r}} \chi_{\vec{k}_p}^{(-)}(\vec{r}) \varphi_{n\ell m}(\vec{r}) d\vec{r} \quad (45)$$

where  $\{ \}_i$  is an algebraic factor coupling angular momenta.

As for the final state interaction, it has been shown [35] that at high energies ( $T_p \gtrsim 100$  MeV) the interaction of the proton with the nucleus B simply reduces to its absorption (the real part of the optical potential is

very small at such energies), i. e. to a reduction of the momentum distributions without significant changes of their form. Thus the plane-wave approximation can still be used in Eq. (42) provided a reduction factor is used to take proton absorption into account.

The transverse interaction can be taken into account without any difficulties. At high energies, a simple and accurate way to do that ("impulse approximation") is to factorize the electron-nucleus cross-section into the electron-proton free cross-section  $\sigma_p(\theta)$  (Rosenbluth cross-section) and the nuclear structure part. In doing that one neglects off-energy-shell effects which, however, are very small at high energies. Anyway, if one wants to avoid this minor approximation, one can directly calculate the electron-nucleus cross-section in Born approximation taking into account both longitudinal and transverse interactions [36].

With the refinements discussed, in impulse approximation, the cross-section will be

$$\frac{d^2\sigma_f^{(n\ell)}}{d\Omega_2 d\epsilon_2} = \sigma_p(\theta) \frac{k_1}{k_2} \theta_f^{(n\ell)} \left| \int e^{i\vec{q}\cdot\vec{r}} \chi_{\vec{k}_p}^{(-)}(\vec{r}) \varphi_{n\ell m}(\vec{r}) d\vec{r} \right|^2 \delta(\omega - B_{n\ell} - T_p - T_B) d\vec{k}_p \quad (46)$$

where  $\theta_f^{(n\ell)}$  is the "spectroscopic factor" defined by the square of the f. p. c. and the vector coupling coefficient. From Eq. (46) we see that QE scattering is no longer proportional to the momentum distribution of protons having momentum  $\vec{p} = \vec{k}_p - \vec{q}$ . However, since, as mentioned, the distortion can be factored out into a reduction factor, we can still claim that electron QE scattering is proportional to the true proton momentum distribution. The main approximation contained in Eq. (46), that is to consider the final nucleus simply as a hole state of the initial one, will be discussed later on.

#### 4.3. Non-coincidence quasi-elastic scattering

Here we have to consider that both proton and neutron emission can contribute to the process. Moreover, since the emitted particle is not detected, we must integrate Eq. (46) over  $\vec{k}_p$  and sum it over the final nuclear states; since  $\sum_f \theta_f^{(n\ell)} = 1$ , we have

$$\begin{aligned} \frac{d^2\sigma}{d\Omega_2 d\epsilon_2} &= \{\sigma_p(\theta) + \sigma_n(\theta)\} \left\{ 1 + \frac{2k_1}{M} \sin^2 \frac{\theta}{2} \right\} \sum_{(n\ell m)} \int \left| \int e^{i\vec{q}\cdot\vec{r}} \chi_{\vec{k}_p}^{(-)}(\vec{r}) \varphi_{n\ell m}(\vec{r}) d\vec{r} \right|^2 \\ &\times \delta(\omega - B_{n\ell} - T_p - T_B) d\vec{k}_p \end{aligned} \quad (47)$$

which becomes [37] in plane-wave approximation and neglecting the small quantity  $T_B$  (it is in practice not difficult to include the recoil),

$$\frac{d^2\sigma}{d\Omega_2 d\epsilon_2} = \{\sigma_p(\theta) + \sigma_n(\theta)\} \left\{ 1 + \frac{2k_1}{M} \sin^2 \frac{\theta}{2} \right\} \frac{2\pi M}{q} \sum_{(n\ell)} \int_{p_{\min}^{(n\ell)}}^{p_{\max}^{(n\ell)}} \rho_{n\ell}(p) p dp \quad (48)$$

$p_{\max}^{(n\ell)} = q + k_p^{(n\ell)}$   
 $p_{\min}^{(n\ell)} = |\vec{q} - k_p^{(n\ell)}|$

and

$$k_p^{(n\ell)} = \{2M(\omega - E_{n\ell})\}^{1/2} \quad (49)$$

Because of the integration over  $p$ , one expects the shape of the QE peak to be rather insensitive to the details of  $\rho_{n\ell}$ . This is in fact the case, as shown in Fig. 12, where the QE peak of  $^{12}\text{C}$  calculated [38] (with distorted wave) using two very different momentum distributions giving, however, similar nuclear radius, is compared with the experimental data [39]. From Fig. 12 we learn that the shape of the QE peak is not very sensitive to  $\rho_{n\ell}$  and that it can be satisfactorily reproduced by any IPM which gives the correct sizes of the nucleus. The qualitative effect of SRC on the shape of the QE peak of  $^{12}\text{C}$  has also been investigated [38]. The momentum distributions have been calculated with Jastrow wave function (see Fig. 13) and then have been used to calculate the QE cross-section (Fig. 14). The effect is very small, which is again due to the integration of  $\rho_{n\ell}$ . In fact, typical values in the experiment [39] are  $0 \text{ fm}^{-1} \lesssim p_{\min} \lesssim 1.5 \text{ fm}^{-1}$  and  $3.5 \text{ fm}^{-1} \lesssim p_{\max} \lesssim 7 \text{ fm}^{-1}$ . Thus, the region where correlation affects the momentum distributions is picked up by the integration, but the contribution of this region ( $\rho \sim 10^{-7} \text{ fm}^3$ ) to the integral is insignificant. We see that the information obtainable from the shape of the QE peak is very scarce. However, the area of the QE peak, which almost exhausts the inelastic spectrum at high  $q$ , might be a useful quantity since we need it when we want to compare with the experimental data the theoretical "sum rule", i. e. the inelastic

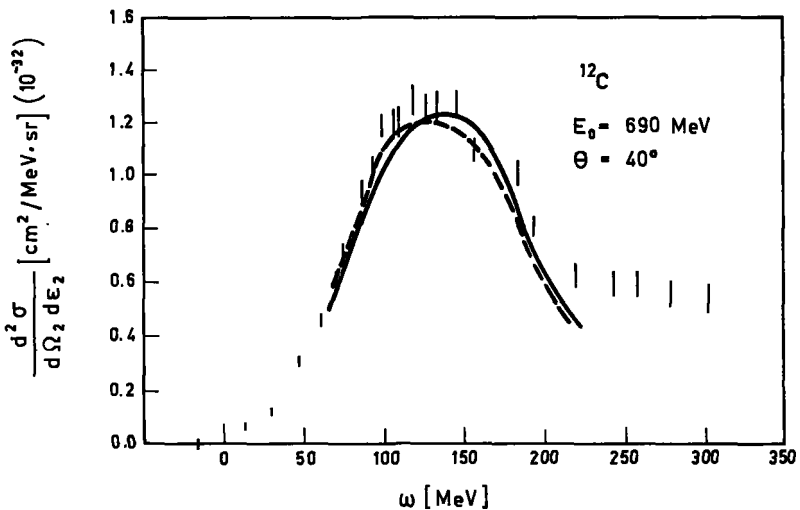


FIG. 12. Comparison between the experimental [39] quasi-elastic peak of  $^{12}\text{C}$  and the theoretical calculation based on the independent-particle model. Continuous line: oscillator parameters  $a_s = a_p = 1.64 \text{ fm}$ . Dashed line:  $a_s = 1.2 \text{ fm}$ ,  $a_p = 1.8 \text{ fm}$ . In this figure, as in Fig. 14,  $E_0$  is the incident electron energy ( $k_1$ ) and  $\theta$  the scattering angle. The value of the three-momentum transfer at the peak is  $q \sim 2.25 \text{ fm}^{-1}$ . (From Refs [27, 38].)

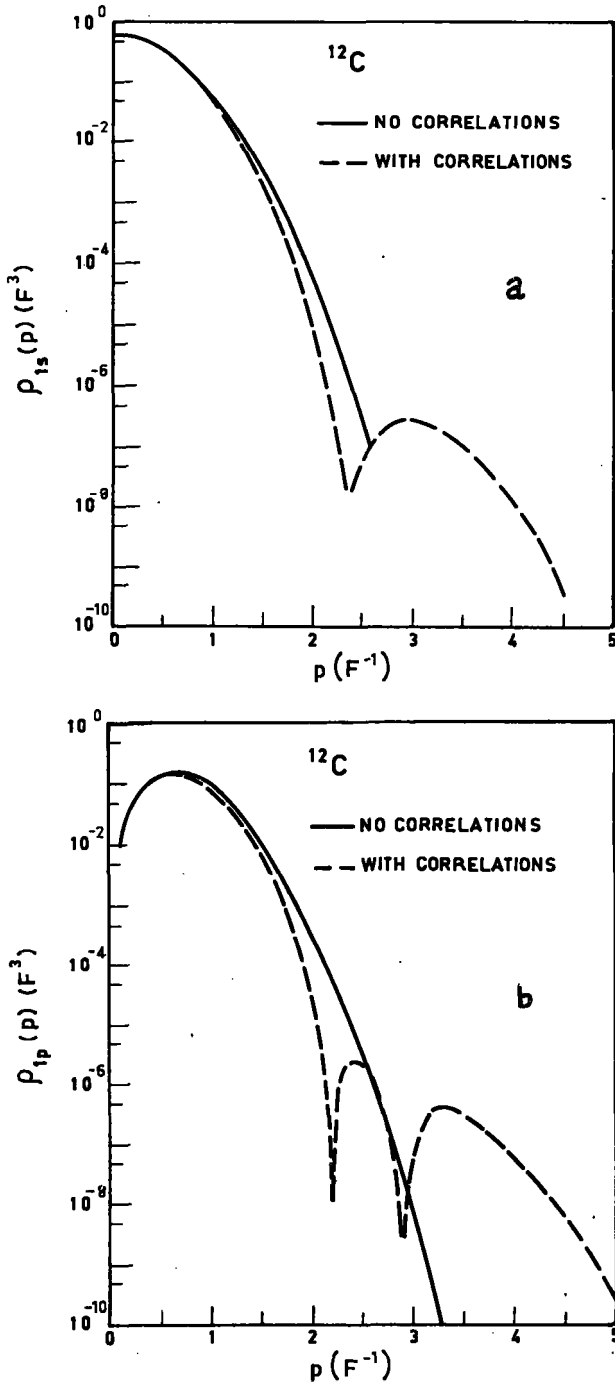


FIG.13. Effect of Jastrow correlations on the momentum distributions of  $^{12}\text{C}$ . Continuous line: no correlations. Dashed line: Jastrow correlations. (From Refs [27,38]. (a:  $\rho_{1s}$ , b:  $\rho_{1p}$ )

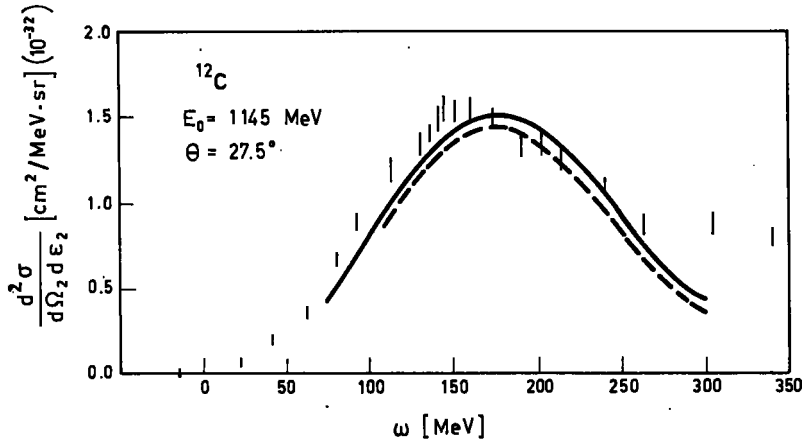


FIG. 14. Effect of Jastrow correlations on the quasi-elastic peak of  $^{12}\text{C}$  [39]. Continuous line: no correlations. Dashed line: Jastrow correlations. The value of the momentum transfer at the peak is  $q \sim 2.6 \text{ fm}^{-1}$ . (From Refs [27, 38].)

cross-section  $d^2\sigma/d\Omega_2 d\epsilon_2$  integrated over the energy transfer  $\omega$  at fixed  $q$  or  $\theta$  [3]. It can be shown [40] that at  $180^\circ$  and  $1 \lesssim q \lesssim 2 \text{ fm}^{-1}$  the sum rule ("transverse sum rule") is dominated by the term

$$\frac{q^2}{2M} (Z\mu_p^2 + N\mu_n^2) \quad (50)$$

where  $\mu$  is the magnetic momentum of the nucleon. Thus, by measuring the area of the QE peak (inelastic cross-section) versus  $q^2$  one could check the value of  $\mu$  for bound nucleons; preliminary experimental results [41] show that this value agrees with that of free nucleons.

The Coulomb (inelastic) sum rule gives [3]

$$\int \left\{ \frac{d^2\sigma}{d\Omega_2 d\epsilon_2} \cdot \frac{1}{\sigma_M (q_\mu/\bar{q})^4} \right\} d\omega \equiv R(q) = Z - Z^2 |F(q)|^2 + Z(Z-1) \times \int e^{i\vec{q} \cdot (\vec{r} - \vec{r}')} \rho(\vec{r}, \vec{r}') d\vec{r} d\vec{r}' \quad (51)$$

that is, a quantity directly proportional to the two-body correlation function  $\rho(\vec{r}\vec{r}')$ . Therefore, it would seem that one has a method for a direct study of SRC. Actual calculations [42] (see Fig. 15) show that the effect of SRC on the integrated cross-section is very small. The reason is clear from Eq. (51) (see also, in this connection, Fig. 14). At high  $q$ , where SRC are important, both  $F(q)$  and the Fourier transform of  $\rho(\vec{r}, \vec{r}')$  are much less than  $Z$ , so that, at high  $q$

$$R(q)/Z \rightarrow 1 \quad (52)$$

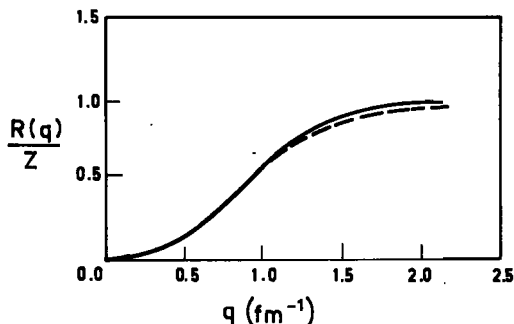


FIG. 15. Coulomb sum rule calculated with the independent-particle model (continuous line) and with short-range correlations included (dashed line). (Adapted from Ref. [42].)

It is now generally agreed that no information on SRC can be obtained from the Coulomb sum rule. Other applications of sum rules are discussed in Ref. [43].

#### 4.4. Coincidence quasi-elastic scattering

When the scattered electron is detected in coincidence with the emitted proton, one is able, by measuring  $\vec{q}$ ,  $\vec{k}_p$ ,  $\omega$  and  $T_p$  to determine  $B_f$  and  $\vec{K}_B$ . The advantages over the non-coincidence experiments are clear: neither the summation over the shells nor the integration over the recoil momentum occurs. Therefore, one can study the excitation spectrum of the residual nucleus and the momentum distributions  $\rho_{n\ell}(p)$ . Coincidence QE experiments for studying these quantities were first carried out and are currently performed [44] using protons as projectiles. The advantages of using protons are due to the high counting rate (cross-section) which is particularly important in coincidence experiments, while the drawbacks are some theoretical difficulties connected with the interaction of strongly interacting particles and the relevant absorption due to the presence of three distorted waves. This last fact sets serious limitations on the study of inner shells in heavy nuclei. The use of electrons as projectiles has therefore been proposed [35], since in this case none of the above troubles is present. Unfortunately, the low value of the electron-nucleon cross-section, resulting in rather poor counting rates, makes the coincidence experiments with electrons very difficult, since high-intensity beams and high-duty-cycle accelerators are required. Nevertheless, coincidence (e, e'p) experiments have been shown to be feasible [45, 46] and are now in progress in several laboratories [47-49].

The cross-section for an (e, e'p) reaction will be given in plane-wave approximation by Eq. (46):

$$\frac{d^4\sigma_f^{(n\ell)}}{d\Omega_2 d\epsilon_2 d\Omega_p d\epsilon_p} = Mk_p \left\{ 1 + \frac{2k_1}{M} \sin^2 \frac{\theta}{2} \right\} \sigma_p(\theta) \theta_f^{(n\ell)} \rho_{n\ell}(p) \delta(\omega - B_f^{(n\ell)} - T_p - T_B) \quad (53)$$

The character of the energy spectrum is determined by the spectroscopic factors  $\theta_f^{n\ell}$ . It will also depend, however, on the energy resolution of the apparatus, the better the resolution the clearer the structure of the spectrum.

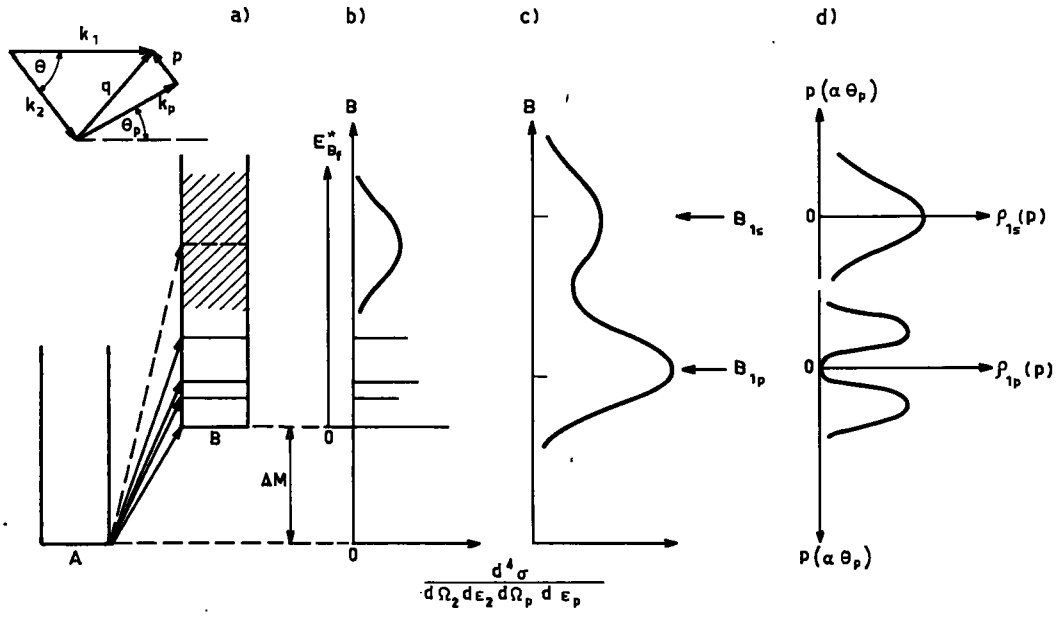


FIG.16. Sketch of the (e, e' p) reactions.

In Fig. 16 we drew a sketch of the  $(e, e'p)$  process for the case of 1p-shell nuclei. Figure 16a illustrates the transitions occurring from the ground state of nucleus A to the excited states of nucleus B. When nucleons are knocked out from less bound-shell (1p in our case) quasi-stationary states of normal parity are populated, whereas very short-lived highly excited states of anomaly parity are excited when knockout occurs in the deeply bound shell (1s shell). The decay width of such states was found to be about 10-15 MeV (see, for example, Ref. [33]). The possible effects of such very short-lived states on the reaction mechanism will be briefly discussed later on. Figure 16b shows the "theoretical" spectrum of the process, while in Fig. 16c is sketched the experimental spectrum, where the levels populated in the final state are spread out by the energy resolution. If this is very poor, then the position of the two resulting broad peaks yields the separation energies of the two shells ( $\ell=0, \ell=1$ ). Indeed, the separation energy of a given state of the initial nucleus can be defined as the weighted average of the separation energies of all states of the final nucleus, coupled to the given state of the initial one [50]. In a poor energy resolution experiment this averaging is automatically guaranteed.

The shape of the energy spectrum is already in itself good evidence of shell structure. However, more direct and stringent evidence can be obtained by measuring the momentum distributions  $\rho_{n\ell}(p)$ . This can be done, for example, by fixing  $q$  and  $K_p$  at the values corresponding to the two peaks and then varying the proton emission angle  $\theta_p$ . The expected results are shown in Fig. 16d.

It should be clear that according to Eq. (53), the form of the energy spectrum will depend on the values assumed by the momentum  $p$ , or, equivalently, by the bands of  $\rho_{n\ell}(p)$  picked up during the measurement of the energy spectrum. Indeed, if the energy spectrum is measured, say, varying  $k_0$  and keeping the other quantities fixed, there will be a variation of  $p$  (hence of  $\rho_{n\ell}(p)$ ) which strongly depends on  $k_p$ . The energy spectrum will, of course, depend on this variation, as illustrated in Fig. 17.

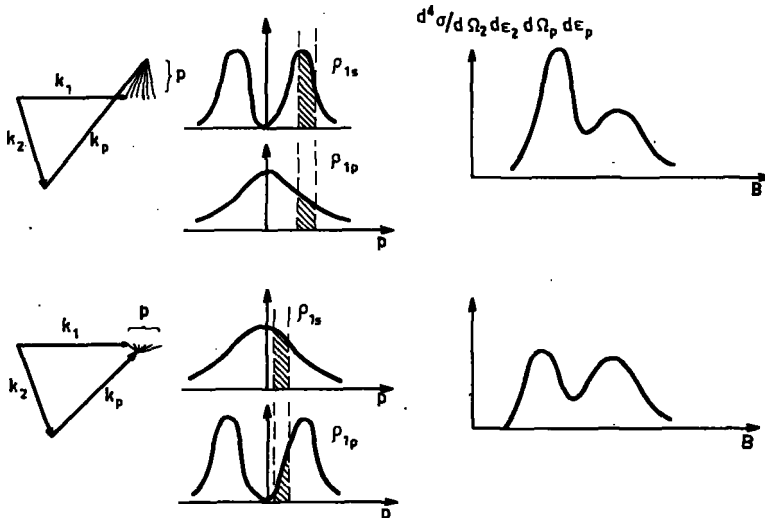


FIG. 17. Sketch of the effects of the kinematics on the shape of the energy spectrum of the  $(e, e'p)$  reaction.

First experiments on (e, e'p) reactions were carried out [45, 46] using incident electrons of  $\sim 600$  MeV and detecting in coincidence  $\sim 500$  MeV electrons and  $\sim 100$  - 200 MeV protons. Results for  $^{12}\text{C}$  are shown in Fig. 18 where  $k_1 \sim 500$  - 600 MeV,  $k_p \sim 2.3 \text{ fm}^{-1}$ ,  $\theta = 56^\circ$ ,  $q \sim 2.5 \text{ fm}^{-1}$ ,  $\omega \sim 150$  MeV. The poor energy resolution ( $\Delta E \sim \pm 6$  MeV) does not allow the contribution from the two shells to be separated out in the energy spectrum (Fig. 18a). The values of the B's agree, however, with the values found in (p, 2p) experiments performed with better resolution (see, for example, Ref. [44]). Furthermore, by looking at the shape of the angular distributions (Fig. 18b), there cannot be doubts that the energy spectrum is due to knock-out of  $\ell = 0$  and  $\ell = 1$  particles.

There have been several calculations [51 - 54] trying to reproduce these results. Most of them [51-53] were based on the impulse approximation (Eq. (53)), while in Ref. [54] the total (longitudinal plus transverse) electron-nucleus interaction was considered in Born approximation. The results in both cases are very similar. The interaction of the outgoing proton with the residual nucleus was taken care of [51-53] by means of the high-energy approximation (WKB), which allows the proton continuum wave function to be written in the form

$$\chi_{\vec{k}_p}(\vec{r}) = \exp \left\{ (i\vec{k}_p \cdot \vec{r}) + i \frac{E_p}{k_p} \int_{\vec{r}}^{\infty} V(t) dt \right\} \quad (54)$$

where  $V(r)$  is the complex optical model potential whose real part accounts for elastic scattering (distortion) and the imaginary part for compound nucleus processes (absorption). A direct partial-wave analysis of  $\chi_{\vec{k}_p}(\vec{r})$  has also been performed [54]:

$$\chi_{\vec{k}_p}(\vec{r}) = 4\pi \sum_{\lambda \nu} i^\lambda \mathcal{R}_\lambda(k_p, r) Y_\lambda^\nu *(\hat{k}_p) Y_\lambda^\nu(\hat{r}) \quad (55)$$

where  $\mathcal{R}_\lambda(k_p, r)$  is the continuum radial wave-function generated in the optical potential. Both Eqs (54) and (55) yield, however, very similar results. At  $T_p \sim 100$  MeV, the real part of the optical potential is very small [55], which results in a negligible distortion of the momentum distributions. As already mentioned, the only sizeable effect is an overall reduction which is larger for the inner shell, since in this case the path of the proton before escaping the nucleus is longer. The effect of the distortion in (e, e'p) reactions is shown in Fig. 19.

If the single-particle wave functions are generated in a local well reproducing the correct values of the separation energies ( $B_s \sim 36$  MeV,  $B_p \sim 16$  MeV), then a good fit to the data can only be obtained [51] if the 1s and the 1p wells are very different from each other. For example, assuming a square-well shape, the 1s well has  $\sim 70$  MeV depth and  $\sim 2$  fm radius and the 1p  $\sim 35$  MeV and  $\sim 4$  fm, respectively. If the harmonic oscillator is used, it turns out that  $a_s \sim 1.2$  fm and  $a_p \sim 1.8$  fm. These figures, although very indicative of the trend (state dependence of the potential well), cannot be taken too literally since they have at least a  $\sim 20$

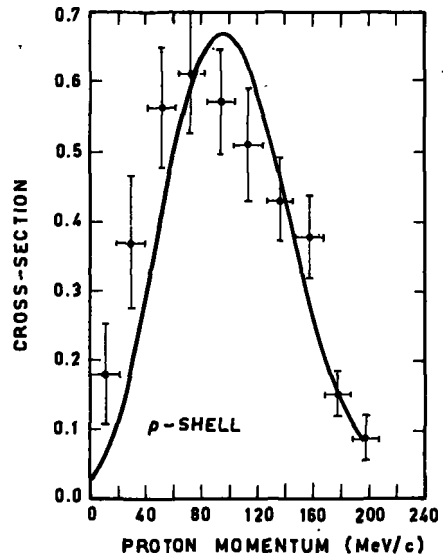
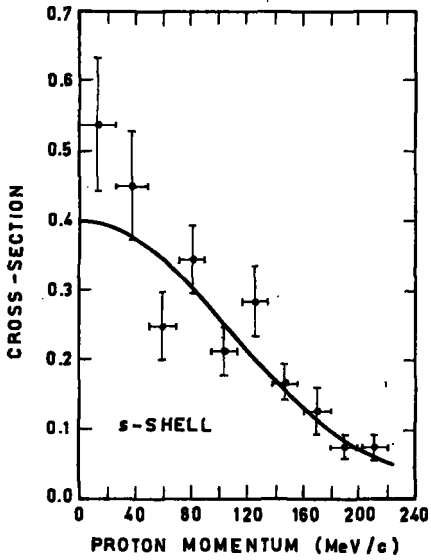
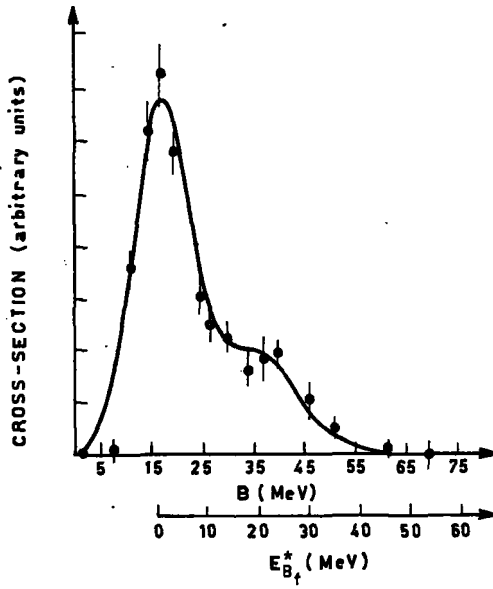


FIG.18. Energy spectrum (a) and angular distributions (b) of the  $^{12}\text{C}(e,e'p)^{11}\text{B}$  reaction. (Experimental data from Ref. [45].)

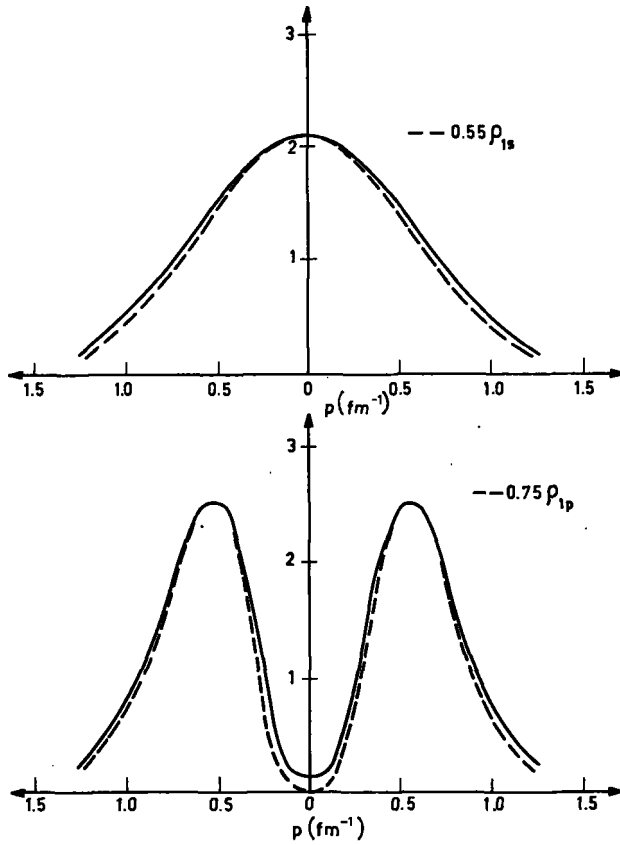


FIG. 19. Effect of the distortion on the momentum distributions of  $^{12}\text{C}$ . Dashed line: undistorted momentum distributions. Continuous line: distorted momentum distribution calculated using the WKB approximation and optical potential  $(Vr) = -(23+117) \exp(-0.41 r^2)$  MeV [51].

per cent variation due to the experimental errors. Typical fits are shown by the continuous line in Fig. 18. Here the energy spectrum has been calculated [51] by replacing the energy conservation  $\delta$ -function in Eq. (53) with a Gaussian  $\varphi_{\gamma_f, \Delta B}(B - B_f)$  defined by the relation

$$\int_0^{\infty} \delta(B - B_f) dB = \int_0^{\infty} \varphi_{\gamma_f, \Delta B}(B - B_f) dB \quad (56)$$

thus taking into account the natural width of the level  $\gamma_f$  and the experimental resolution  $\Delta B$  on the experimentally measured quantity ("missing energy")  $B = \omega - T_p$ . The nuclear model used is the same as in Ref. [34], that is an intermediate-coupling model calculated with residual interaction containing the well-known Rosenfeld mixture. The excitations of  $^{11}\text{B}$  predicted by the model for the knockout from 1p-shell are shown in Table III. It is clear the the poor experimental energy resolution does not allow the

TABLE III. SPECTROSCOPIC FACTORS  $\theta^{1p}$  FOR THE EXCITATION OF NORMAL-PARITY STATES OF  $^{11}\text{B}$  IN THE REACTION  $^{12}\text{C}(e, e'p)^{11}\text{B}$ . THE SPECTROSCOPIC FACTORS ARE NORMALIZED TO THE NUMBER OF PROTONS IN THE 1p-SHELL, i. e.  $\sum\theta^{1p} = 4$  (adapted from Ref. [4])

J, T	Residual nucleus $^{11}\text{B}$		$\theta_f^{(1p)}$
	$E_{\text{exp}}^*$ (MeV)	$E_{\text{th}}^*$ (MeV)	
$\frac{3}{2} \frac{1}{2}$	0	0	2.5
$\frac{1}{2} \frac{1}{2}$	6.81	6.9	0.78
$\frac{1}{2} \frac{1}{2}$	2.13	1.9	0.66

predicted transitions to be seen (a pure IPM gives almost the same spectrum), so that the correctness of the model remains to be checked in a good resolution experiment [56].

The good fit to the experimental data shown in Fig. 18 is only apparently satisfactory since the obtained parameter for the potential well (even with errors included) do not fit elastic electron scattering data [51]. This is illustrated in Fig. 20. Responsible for this situation is the deep s-well generating too high a central density. If parameters which fit the charge form factor are used, the fit to the (e, e'p) reaction is completely spoiled (see Fig. 21 and, for more details, Ref. [51]).

This apparent contradiction between two experiments which must be explained in a unified way might be ascribed to several reasons:

- (a) not enough accuracy in the quasi-elastic experimental data;
- (b) unrealistic wave-functions used in the calculation;
- (c) more complicated reaction mechanism.

As for the first point, it is clear that, the analysed experiments being the first, one should wait for other and better experimental data. However, recent high-energy ( $\sim 400$  MeV) (p, 2p) experiments performed with very good angular and energy resolution [44], fully confirm the state dependence effects found in the (e, e'p) reaction.

In order to check point b, calculations have been performed with different types of wave functions: IPM Woods-Saxon [54], parity-mixed orbitals [52], and projected Hartree-Fock wave-functions in a deformed basis [53]. No significant improvement with respect to Ref. [51] has been obtained. It remains to be seen if Hartree-Fock-like calculations performed with "realistic interaction" can give some improvement. One expects, however, the single-particle wave functions obtained from such a calculation to overlap strongly with those of the harmonic oscillator or the Woods-Saxon.

A different approach for the solution of this puzzle has been suggested in Ref. [51]. The quasi-elastic data should be fitted and then one has to look for some effects which should affect the charge form factor, leaving unaltered the fit to the quasi-elastic data. The effect of Jastrow correlations goes just in that direction, since it decreases the central density (see Fig. 8) leaving unchanged the momentum distributions in the region of small single-particle momentum measured in quasi-elastic processes (see Fig. 13).

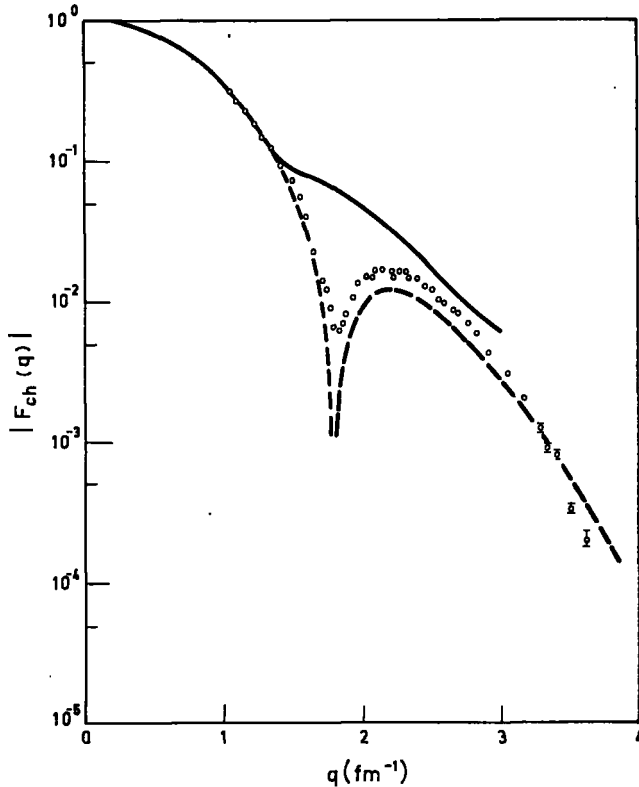


FIG. 20. Charge form factor of  $^{12}\text{C}$  (full line) calculated with parameters which fit the  $(e, e'p)$  reaction ( $a_s \sim 1.2$  fm,  $a_p \sim 1.8$  fm). The dashed line corresponds to the best IPM ( $a_s = a_p = 1.64$  fm). (Experimental data from Ref. [12].)

Indeed, an at least qualitative, coherent interpretation of both processes has been achieved [27, 57]. Before drawing any conclusion from this result, more and better experimental data are needed, in order to see how systematic is the trend of the state-dependence effect and to have more precise determination of the parameters of the wave-functions.

As for the reaction mechanism, it seems rather unlikely, because of the high energies both in the entrance and exist channels, that adding some non-direct or multi-step contributions, or treating distortion effects in a more sophisticated way, will change the character of the reaction<sup>8</sup>. There is, however, one side of the reaction mechanism that has been so far overlooked and which does deserve some attention [58-61]. We mean the complete neglect of the effects of the finite life-time of the deep hole state, created by knocking out the strongly bound protons. As a matter of fact, the time corresponding to a width of  $\sim 20$  MeV is almost the same as is

<sup>8</sup> Numerical results of Ref. [56] show that at energies of the outgoing proton higher than  $\sim 40$  MeV, resonant processes are negligible. As for the distortion, the mentioned  $(p, 2p)$  experiments [44] do not show, unlike the case when distortion is present, any filling in of the zero of the  $1p$  momentum distributions.

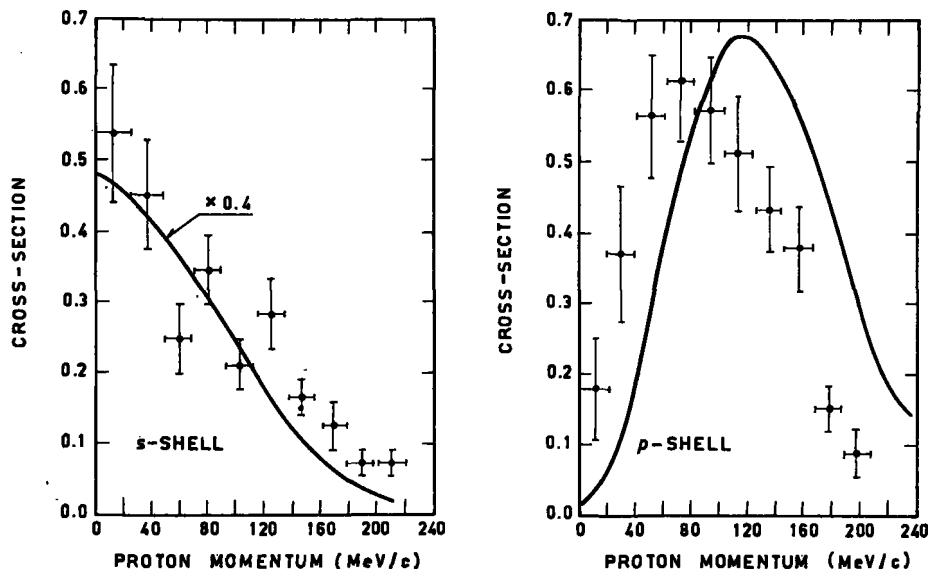


FIG. 21. Angular distribution of the  $^{12}\text{C}(e, e'p)^{11}\text{B}$  reaction calculated with parameters which fit the charge form factor shown in Fig. 20 (adapted from Ref. [51]).

needed for a 100 MeV proton to traverse an intermediate nucleus and it could happen that the proton is still inside the nucleus when it decays [58]. Thus one is faced with the difficult problem of calculating continuum wave functions of a decaying strong resonant state. There are no reasons to think that the finite life-time will not affect the angular distributions [59]. Therefore, before drawing final conclusions on the values of the nuclear model parameters, one has to estimate the effect of the width of the hole state on the momentum distributions. A first attempt has been presented in Refs [59, 60], where the overlap integral (Eq. 38) has been approximated by the solution of the Schrödinger equation for a hole moving in a complex potential, whose real part binds the hole in the shell-model potential and the complex part determines its "absorption", i. e. the decay width of the state. Although an approach of this kind is only an approximation of the real situation, it will still help to estimate the size of the effect. The dependence of the momentum distributions on the shape of the imaginary well has been investigated in Ref. [60]. The results for  $^{16}\text{O}$  show that for realistic shape, i. e. proportional to the density of the 1p particles<sup>9</sup>, negligible effects are obtained (~3%). On the other hand, extreme situations of absorption, either on the surface or in the centre, give a 10% decrease of the width of the 1s momentum distributions. If these results were a good approximation of the real situation, we should conclude that the difficulty in explaining in a unified way elastic and quasi-elastic scattering on  $^{12}\text{C}$  cannot be ascribed to

<sup>9</sup> Such a shape is called "realistic" because it is believed [33] that the decay of the highly excited state is due to the filling in of 1s-hole by a 1p-particle.

the effect of the finite life-time, since (see Fig. 21) they disagree more than 10% in the s shell and a strong disagreement is also present in the p-shell, where no problems of finite life-time exist. In heavier nuclei, however, the effect was found to be more sizeable, which casts a doubt on the validity and the meaning of the usual identification of the single-particle energies found in many-body calculations, with the separation energies measured in quasi-elastic experiments [58, 61]. It has already been pointed out that the separation energies are actually an averaging over several final states, so that their comparison with the solution of the Hartree-Fock equations is not very direct. If finite-life-time effects are going to modify the usual description of quasi-elastic processes, that comparison becomes even meaningless.

## 5. SUMMARY AND CONCLUSIONS

The most recent results on electron scattering at high energy and momentum transfers and the attempts to interpret them from the point of view of nuclear structure have been reviewed. From this analysis the usefulness of elastic scattering in checking different nuclear models (in particular, their predictions for the high-momentum components) and the possibilities offered by coincidence quasi-elastic scattering in directly measuring the proton separation energies and momentum distributions came out. If we consider the enormous quantity of information resulting from inelastic scattering to discrete levels [3, 4], we clearly see the potentiality of high-energy electron scattering in probing nuclear structure.

The theoretical attempts to interpret recent data on the form factors of light nuclei have already provided interesting results, namely some indications on short-range correlations and the failure of the available nuclear models to reproduce the high-momentum transfer region. Whether or not the successful Jastrow model will be confirmed by other experimental and theoretical facts or whether new Hartree-Fock wave-functions will be found which explain equally well the experimental data, useful information on the structure of nuclei will be obtained in any case.

The interpretation of the first experimental results on quasi-elastic ( $e, e'p$ ) reaction on  $^{12}\text{C}$  has also led to a remarkable result: the apparent contradiction in explaining coherently this experiment and elastic scattering. A possible solution to this puzzle has been given; its correctness will be checked by new and better experimental data. From the theoretical point of view, much work remains to be done in order to understand better the role played by the decay width of the deep hole state and the connection of its separation energy with the single-particle energies calculated theoretically.

## REFERENCES

- [1] LYMAN, E.M., HANSON, A.O., SCOTT, M.B., Phys. Rev. 179 (1950) 228.
- [2] HOFSTADTER, R., Ann. Rev. nucl. Sci. 7 (1957) 231.
- [3] de FOREST, T., WALECKA, J.D., Adv. Phys. 15 (1966) 1.
- [4] ÜBERALL, H., Springer Tracts in Modern Physics 49 (1969) 1.
- [5] YENNIE, D.R., RAVENHALL, D.G., WILSON, R.N., Phys. Rev. 95 (1954) 500.
- [6] SCHIFF, L., Phys. Rev. 103 (1956) 443.
- [7] EHRENBERG, H.F., HOFSTADTER, R. et al., Phys. Rev. 113 (1959) 666.

- [8] DRECHSEL, D., Invited talk at the Advanced Institute on Electron Scattering and Nuclear Structure, Cagliari (Italy), September 1970, to be published in the Proceedings (BOSCO, B., Ed.) Gordon and Breach and references therein; TOEPFER, C., DRECHSEL, D., Phys. Rev. Letts 24 (1970) 1131.
- [9] HEISENBERG, J., HOFSTADTER, R. et al., in *High-Energy Physics and Nuclear Structure (Proc. 3rd Int. Conf.)* (DEVONS, S., Ed.), Plenum Press (1970) 33.
- [10] FROSCH, R.F., MCCARTHY, J.S. et al., Phys. Rev. 160 (1967) 874.
- [11] LI, G., SICK, I., WHITNEY, R.R., YEARIAN, M.R., Nucl. Phys. A150 (1971) 631.
- [12] SICK, I., MCCARTHY, J.S., Nucl. Phys. A150 (1970) 631.
- [13] NEGELE, J.W., Phys. Rev. C1 (1970) 1260.
- [14] ELTON, L.R.B., "Nuclear Sizes" (Oxford University Press 1961).
- [15] DONNELLY, T.W., WALKER, G.E., Phys. Rev. Letts 22 (1969) 1121.
- [16] ELTON, L.R.B., WEBB, S.J., in *High-Energy Physics and Nuclear Structure (Proc. 3rd Int. Conf., DEVONS, S., Ed.)*, Plenum Press (1970) 67.
- [17] BROWN, G.E., Comments on Nuclear and Particle Physics 3 (1969) 48.
- [18] JASTROW, R.J., Phys. Rev. 98 (1955) 1479.
- [19] CZYŻ, W., LESNIAK, L., Physics Letts 25B (1967) 319.
- [20] CLARK, J.W., RISTIG, M.L., Nuovo Cim. 70 (1970) 313 and references therein.
- [21] IWAMOTO, F., YAMADA, M., Progr. theor. Phys. (Kyoto) 17 (1957) 543.
- [22] CIOFI DEGLI ATTI, C., GRYPEOS, M.E., Lettere al Nuovo Cim. 2 (1969) 587.
- [23] ROSCIOLI, G., Thesis, Rome University (to be published).
- [24] CIOFI DEGLI ATTI, C., KABACHNIK, N.M., Phys. Rev. C1 (1970) 809.
- [25] GERACE, W.J., SPARROW, D.A., Nucl. Phys. A145 (1970) 289.
- [26] CIOFI DEGLI ATTI, C., KABACHNIK, N.M., in *High-Energy Physics and Nuclear Structure (Proc. 3rd Int. Conf., DEVONS, S., Ed.)*, Plenum Press (1970) 74.
- [27] CIOFI DEGLI ATTI, C., to be published in the Proceedings of the Advanced Institute on Electron Scattering and Nuclear Structure, Cagliari (Italy) (BOSCO, B., Ed.), Gordon and Breach.
- [28] WEISE, G., HUBER, M.G., Nucl. Phys. A162 (1971) 330;  
TUAN, S.T., WRIGHT, L.E., HUBER, M.G., Phys. Rev. Letts 23 (1969) 174.
- [29] RIPKA, G., GILLESPIE, J., Phys. Rev. Letts 25 (1970) 1624.
- [30] KALLIO, A., Physics Letts 18 (1965) 51.
- [31] KALLIO, A., DAY, B.D., Nucl. Phys. A124 (1969) 177.
- [32] RIPKA, G., these Proceedings.
- [33] JACOB, G., MARIS, Th.A., Rev. mod. Phys. 38 (1966) 121.
- [34] BALASHOV, V.V., BOYARKINA, A.N., ROTTER, I., Nucl. Phys. 59 (1969) 417.
- [35] JACOB, G., MARIS, Th.A., Nucl. Phys. 31 (1962) 139, 152.
- [36] DEVANATHAN, V., Ann. Physics New York 43 (1967) 74.
- [37] SITENKO, A.G., GURIEV, V.N., Soviet Phys.-JETP 12 (1961) 1228.
- [38] CIOFI DEGLI ATTI, C., Lettere al Nuovo Cim. 1 (1971) 590.
- [39] DEMENTIY, S.V., AFANASIEV, N.Gh. et al., Sov. J. Nucl. Phys. 9 (1970) 142; 11 (1970) 10.
- [40] CZYŻ, W., Bull. Acad. Pol. Sci. 12 (1964) 649;  
CZYŻ, W., LESNIAK, L., MAŁECKI, A., Ann. Phys. New York 42 (1967) 119.
- [41] GOLBERG, J., ISABELLE, D.B., STOVALL, T., quoted by Isabelle, MIT 1967, Summer Study, 93.
- [42] McVOY, K.W., Van HOVE, L., Phys. Rev. 125 (1962) 1034.
- [43] CZYŻ, W., MIT 1967 Summer Study, 155.
- [44] JAMES, A.N. et al., Nucl. Phys. A133 (1969) 89.
- [45] AMALDI, U. et al., Phys. Rev. Letts 13 (1964) 341; Physics Letts 22 (1966) 593.
- [46] AMALDI, U. et al., Physics Letts 25B (1967) 24.
- [47] CAMPOS-VENUTI, G., CORTELLESSA, G. et al., private communications.
- [48] MOUGEY, J., JULIEN, J. et al., Saclay preprint (1969);  
MOUGEY, J., private communications.
- [49] HIRAMATSU, S., KAMAE, T. et al., INSJ preprint 122 (Tokyo), July 1970.
- [50] PINKSTON, W.T., SATCHLER, G.R., Nucl. Phys. 72 (1965) 641.
- [51] CIOFI DEGLI ATTI, C., Nucl. Phys. A106 (1968) 215.
- [52] BOFFI, S., PACATI, F.D., SAWICKI, J., Nuovo Cim. 57 (1968) 103.
- [53] BOFFI, S., BOUTEN, M., CIOFI DEGLI ATTI, C., SAWICKI, J., Nucl. Phys. A120 (1968) 135.
- [54] EPP, C.D., GRIFFY, T.A., Phys. Rev. C1 (1970) 1633.
- [55] BATTY, C.J., Nucl. Phys. 23 (1961) 562.
- [56] BALASHOV, V.V., KABACHNIK, N.M., MARKOV, V.I., Nucl. Phys. A129 (1970) 369.

- [57] CIOFI DEGLI ATTI, C., *Nuovo Cim.* 55B (1968) 570; *Nucl. Phys.* A129 (1969) 350. These works are based on the expansion (27) while in Ref.[27] the more correct expansion (24) has been used.
- [58] AMALDI, U., 38th Course of the International School of Physics "Enrico Fermi" (Academic Press, New York 1967) 284.
- [59] HERSCOVITZ, V.E., JACOB, G., MARIS, Th.A.J., *Nucl. Phys.* A109 (1968) 478.
- [60] HERSCOVITZ, V.E., *Nucl. Phys.* A161 (1971) 321.
- [61] AMALDI, U., talk given at the International School of Subnuclear Physics, "Elementary Processes at High Energy", Erice 1970 (to be published in the Proceedings of the School).

## PART II: NUCLEAR STRUCTURE

1. Microscopic theory of effective interactions



# THEORY OF EFFECTIVE INTERACTIONS

M. W. KIRSON

Department of Nuclear Physics,  
Weizmann Institute of Science,  
Rehovot, Israel

## Abstract

### THEORY OF EFFECTIVE INTERACTIONS.

The paper concentrates on the many-body perturbation theory approach to the theory of effective interactions. The emphasis is on the relative importance of various effects rather than on agreement with experiment.

The necessity for using effective operators in many-particle systems arises from the suppression of available degrees of freedom. When the number of degrees of freedom of a system becomes unmanageably large, it is necessary to abstract those which are most important for the process of interest, and to absorb the effect of those ignored in a "renormalization" of the operators acting on the system. Physics abounds with examples of this procedure. For example, mesonic degrees of freedom are suppressed in nuclear physics, leading to the appearance of inter-nucleon potentials and effective electromagnetic interactions (anomalous magnetic moments). Similarly, elementary treatments of electron motion in metals ignore the lattice degrees of freedom and compensate by the introduction of effective inertial parameters (effective mass). Even within the more obvious limitations, such as the exclusion of explicit mesons from non-relativistic nuclear systems, the number of particles whose degrees of freedom are retained is frequently too large to handle, and models must be constructed in which only a few degrees of freedom are excited. This evidently applies to the nuclear collective model, where collective coordinates are introduced at the expense of unknown parameters characterizing the effective interplay of these coordinates (mass and stiffness parameters); and to the nuclear shell model, where only a few particles are free to change their state, again at the cost of unknown parameters (effective interactions and moments). The task of microscopic nuclear theory is to determine the effective parameters, the range of applicability and the significant corrections of nuclear models in terms of the phenomenological nucleon properties and interactions obtained by ignoring mesonic degrees of freedom. At a yet more fundamental level, the aim is to construct these phenomenological parameters from the mutual interactions of the elementary particles, a program which is still in its infancy and will not be touched upon further here.

The shell model, with residual interactions, could be regarded as the first step in the construction of a microscopic theory. The prototype model operator is the effective interaction between a small number of active nucleons in a limited space of single-particle states. The dramatic success of the phenomenological shell model confirms the existence of two-body effective-interaction matrix elements which fit observed nuclear spectra [1]. Microscopic calculations must derive this effective interaction from

the observed nucleon-nucleon interaction [2], as abstracted from nucleon-nucleon scattering data and the bound-state properties of the two-nucleon system.

Among the various approaches to this fundamental problem are the following:

(i) Jastrow correlations [3] - This is a variational method, in which the many-particle wave-function is approximated by a shell-model wave-function multiplied by a factor which introduces two-body correlations. The correlation factor is determined by minimizing the expectation value of the Hamiltonian with this wave-function. Effective operators are defined by  $\langle \Psi | \mathcal{O} | \Psi \rangle = \langle \Phi | \mathcal{O}_{\text{eff}} | \Phi \rangle$ , where  $\Psi$  is the correlated and  $\Phi$  the uncorrelated wave-function. In practice, cluster expansions are used and truncated after a few terms. This method has the strengths and weaknesses of variational calculations, as well as some approximations of its own to make calculations tractable. Its connection with perturbation theory is a subject of current investigation.

(ii) Unitary operators [4] - Like the Jastrow method, this one modifies the wave-function, using  $\Psi = e^{iF} \Phi$ , with Hermitian  $F$  (though the hermiticity must be relaxed for hard-core potentials). Operators are modified by  $\mathcal{O} \rightarrow e^{-iF} \mathcal{O} e^{iF}$ . In practice,  $F$  is limited to two-body operators, variational methods are used, and the calculations (but not necessarily the results) are similar to the Jastrow ones.

(iii) Green's functions [5] - Perhaps the most powerful approach, it is very useful for obtaining very general formal results. Practical applications have been limited to a few selected areas of nuclear physics (random phase approximation, in particular) and once perturbation techniques are introduced, the method very closely resembles the pure perturbation theory approach to be detailed below.

This paper will concentrate on the many-body perturbation theory approach, which has the advantages that it is well understood, has, in principle, no ad-hoc elements, is formulated in pictorial and intuitively appealing form, and has been applied in very extensive calculations<sup>1</sup>. The basic formalism may be derived by time-independent methods (mainly Brandow [6]) or by time-dependent methods (Johnson and Baranger [7]), and has been frequently discussed in the literature, at other courses and in the earlier lectures of this course.

Many-body perturbation theory: A brief but clear derivation of the fundamental equation is obtained by following Löwdin [8]. The eigenvalues and eigenstates of a given Hamiltonian  $H = H_0 + V$  can be obtained by diagonalizing the (generally infinite) matrix of  $H$  in the basis defined by the complete set of eigenstates of  $H_0$ . The space spanned by these eigenstates may be split into two by dividing the eigenstates of  $H_0$  into two sets, labelled 1 and 2. Then the secular equation for  $H$  can be written

$$\begin{pmatrix} H_{11} & H_{12} \\ H_{21} & H_{22} \end{pmatrix} \begin{pmatrix} \Phi_1 \\ \Phi_2 \end{pmatrix} = E \begin{pmatrix} \Phi_1 \\ \Phi_2 \end{pmatrix}$$

<sup>1</sup> Many calculations have been performed of finite-nucleus reaction matrices and effective interactions. Since the emphasis in this paper is on the relative importance of various effects, rather than on agreement with experiment, almost all numerical results are quoted from the work of the lecturer and his collaborators. This should not be construed as implying special merit to these results, nor any disparagement of the work of others. Apologies are extended to all who feel that some particular efforts have been slighted or ignored. No denigration was intended.

in an obvious notation, where the  $H_{ij}$  are matrices and the  $\Phi_i$  columns. Writing this out in full,

$$H_{11} \Phi_1 + H_{12} \Phi_2 = E \Phi_1$$

$$H_{21} \Phi_1 + H_{22} \Phi_2 = E \Phi_2$$

The second equation is solved for  $\Phi_2$ , which is substituted into the first equation, to obtain

$$\Phi_2 = - (H_{22} - E)^{-1} H_{21} \Phi_1$$

$$[H_{11} - H_{12}(H_{22} - E)^{-1} H_{21} - E] \Phi_1 = 0$$

The result resembles an eigenvalue equation in the space 1 alone, where the eigenvalue is a true eigenvalue of  $H$  and the eigenstate is the projection onto space 1 of a true eigenstate of  $H$ . The effective Hamiltonian in the space 1 is  $\mathcal{H}^{(1)} = H_{11} - H_{12}(H_{22} - E)^{-1} H_{21}$ , which is explicitly dependent on the eigenvalue  $E$ , and contains in the second term the effect of the neglected degrees of freedom, those of space 2. It may be written  $\mathcal{H}^{(1)} = H_0 + \mathcal{V}(E)$ , where the effective interaction  $\mathcal{V}(E) = V - VQ(H_0 + QVQ - E)^{-1} QV$ , the projection operator  $Q$  projecting onto the space 2. It is easy to show that  $\mathcal{V}(E)$  satisfies the integral equation

$$\mathcal{V}(E) = V - V \frac{Q}{H_0 - E} \mathcal{V}(E)$$

using the fact that  $H_0$  and  $Q$  commute.

The above derivation has produced an effective Hamiltonian which, acting only in the space 1, produces correct eigenvalues and (projections of) correct eigenfunctions of  $H$ . It is thus precisely the kind of renormalized operator desired, involving implicitly the degrees of freedom (space 2) which have been suppressed. The energy-dependence of  $\mathcal{V}(E)$  is important. It has the consequence that the eigenvectors  $\Phi_1(E)$  and  $\Phi_1(E')$ , for  $E \neq E'$ , are not orthogonal — they are projections on space 1 of mutually orthogonal eigenvectors, but orthogonality is generally not preserved under projection. Consider the eigenvalue equation  $[H_0 + \mathcal{V}(E_0) - E] \Phi_1 = 0$ . If space 1 is  $n$ -dimensional, this equation has  $n$  real eigenvalues  $E(E_0)$  for every  $E_0$ , with  $n$  corresponding mutually orthogonal eigenvectors, since  $\mathcal{V}(E_0)$  is hermitian for fixed  $E_0$ . However, for an arbitrary  $E_0$ , none of these eigenvalues is likely to satisfy  $[H_0 + \mathcal{V}(E) - E] \Phi_1 = 0$ . The solutions of this equation are given by the intercepts of the line  $E = E_0$  with the multivalued function  $E(E_0)$ . Since the intercepts will generally fall at different values of  $E_0$ , the corresponding eigenvectors need not be orthogonal<sup>2</sup>.

The solution of the equation  $[H_0 + \mathcal{V}(E) - E] \Phi_1 = 0$ , with

$\mathcal{V}(E) = V - V \frac{Q}{H_0 - E} \mathcal{V}(E)$ , is equivalent to the solution of the Schrödinger equation. The iteration expansion is equivalent to the Brillouin-Wigner perturbation expansion, to which it reduces for a one-dimensional space 1.

<sup>2</sup> The function  $E(E_0)$  is called the bracketing function by Löwdin [8]. He shows that under certain general conditions  $E_0$  and  $E(E_0)$  bracket a solution of the secular equation  $[H_0 + \mathcal{V}(E) - E] \Phi_1 = 0$ .

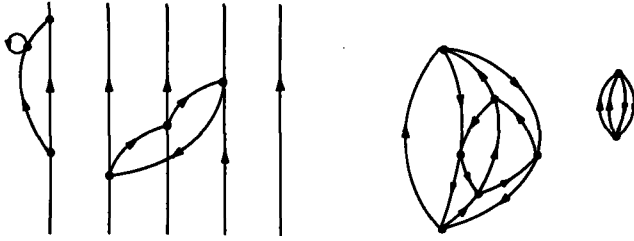


FIG. 1. An effective interaction diagram with five valence particles. The two disconnected portions on the right constitute "core parts".

Although the degrees of freedom of space 2 have been absorbed in the effective operator  $\mathcal{V}(E)$ , thus truncating the space in which the effective Hamiltonian acts, this has not yet produced the shell model — the inert core has not been explicitly achieved. This was done by Bloch and Horowitz [9], and rederived in the present formulation by Brandow [6], as follows.

The space 1 is defined in terms of the eigenstates of  $H_0$ . Choosing  $H_0$  to be the shell-model Hamiltonian  $H_0 = \sum_i (T_i + U_i)$ , where  $T$  is the kinetic energy operator and  $U$  the shell-model potential for an individual nucleon, define space 1 to be that space spanned by the set of shell-model states with a fully-occupied doubly-closed-shell core plus a number  $\nu$  of "valence" particles in a few valence orbits outside the core. Examples are:  $^{18}\text{O}$  — space 1 a closed  $^{16}\text{O}$  core plus two neutrons in the  $1s-0d$  shell;  $^{66}\text{Zn}$  — space 1 a closed  $^{56}\text{Ni}$  core plus two protons and eight neutrons in the  $1p-0f_{5/2}-0g_{9/2}$  shell; or  $^{116}\text{Sn}$  — space 1 a closed  $^{100}\text{Sn}$  core plus sixteen neutrons in the  $2s-1d-0g_{7/2}-0h_{11/2}$  shell<sup>3</sup>. A diagram representation is used for the perturbation expansion, with the vacuum being the closed core, and lines representing particles outside the core (upgoing lines) or holes in the core (downgoing lines). (Note that the formalism could also be applied to a space 1 of closed core plus  $\nu$  valence holes or closed core plus  $\nu_1$  valence particles and  $\nu_2$  valence holes.) The interaction  $V$  is denoted by a black dot, the single-particle potential  $U$  by a cross. The operator  $Q$  ensures that no intermediate state in the diagram will be in space 1, that is, will have only  $\nu$  valence particles. Every diagram has  $\nu$  valence lines entering the diagram from the bottom and leaving it at the top. Among the diagrams obtained are some in which sequences of interactions occur only in the core, with no connection to the valence lines (see Fig. 1). These "core parts" can be factorized, summed by a geometric series formula and added to the energy denominators, which have the form  $\sum \epsilon(\text{particles}) - \sum \epsilon(\text{holes}) + E_0 - E$ , where  $\epsilon$  are the shell-model single-particle energies and  $E_0$  is the shell-model energy  $\sum \epsilon$  of the core. After factorizing the core parts, the energy denominators become  $\sum \epsilon(\text{particles}) - \sum \epsilon(\text{holes}) - E_\nu$ , where  $E_\nu = E - \bar{E}_0$  and  $\bar{E}_0$  is the measured energy of the core, considered as a separate physical system (e.g.  $^{16}\text{O}$ ,  $^{56}\text{Ni}$  or  $^{100}\text{Sn}$  (!) in the examples above). This follows because the

<sup>3</sup> The definition of closed shells could be much less restrictive, and need not pay too much attention to real physical shell-breaking. The aim is simply to obtain a well-defined tractable space 1. For instance,  $^{116}\text{Sn}$  could have a closed  $^{114}\text{Sn}$  core plus two neutrons in the  $2s-1d_{3/2}-0h_{11/2}$  shell.

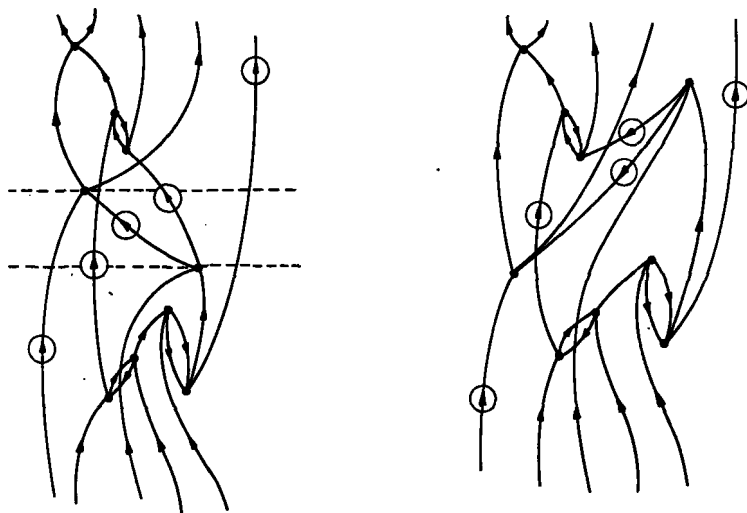


FIG. 2. Example of a five-valence-line folded diagram. On the left, the diagram before folding has an intermediate state of five valence particles (circled), which is forbidden. The diagram is folded on the dotted lines, and the diagram on the right is one of the possible results. (Others will differ in the relative order of interactions originally above and originally below the folds.) Note the downgoing valence lines.

sum of the core parts is just the Goldstone expansion for the energy shift  $\tilde{E}_0 - E_0$  of a non-degenerate system. At the same time, since some diagrams will have only core parts,  $\mathcal{V}(E) = \tilde{E}_0 - E_0 + \mathcal{V}_v(E_v)$  where  $\mathcal{V}_v(E_v)$  is the sum of diagrams with no core parts unlinked from the valence lines and with  $E_v$  energy denominators. The secular equation can then be written  $[H_{0(v)} + \mathcal{V}_v(E_v) - E_v] \Phi_1 = 0$ , where  $H_{0(v)}$  ignores the core, i. e.

$H_{0(v)} \Phi_1 = \sum_{i=1}^{\mu} \epsilon_i \Phi_i$ . This is the Bloch-Horowitz equation [9], which refers

to a limited number of valence particles in a few active orbitals outside an inert core. Except for the energy-dependence of  $\mathcal{V}_v(E_v)$ , this is a shell-model equation.

Brandow [6] proceeded to eliminate the energy-dependence of  $\mathcal{V}_v(E_v)$  by introducing a new kind of diagram, the "folded" diagram. These are obtained by drawing diagrams with intermediate states which violate the prohibition of  $Q$ , and then folding the diagram horizontally, as one would fold a long strip of paper, on the interaction immediately preceding and following the forbidden intermediate state (see Fig. 2). In the resulting folded diagram, the following rules hold: (i) the top interaction of the folded diagram must be the top interaction of the unfolded diagram; (ii) all relative orders of interactions on the two sides of the fold must be allowed, provided no  $Q$ -forbidden intermediate states arise; (iii) particle or hole lines which bend around the fold without interacting may be straightened out; (iv) any number of folds is permitted, but only one for each  $Q$ -forbidden intermediate state; (v) valence lines reversing direction because of the fold have the sign of their single-particle energy reversed

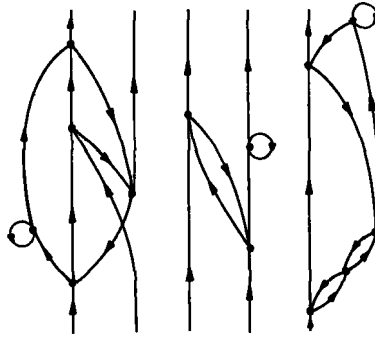


FIG. 3. A five-valence-line partially linked diagram. There are no core parts, but the valence lines fall into three independently interacting groups.

in energy denominators; (vi) each fold introduces a minus sign. (For detailed rules, see Brandow [6], *Revs. Mod. Phys.*) In addition to eliminating the energy-dependence of  $\mathcal{V}_v(E_v)$ , the folded diagrams also eliminate partially linked diagrams, where subsets of valence lines interact with one another and the core but not with the other subsets of valence lines, so that the diagram separates into independent parts (see Fig.3). Brandow calls the folded diagram expansion totally linked.

Folded diagrams arise in the time-dependent perturbation theory of Johnson and Baranger [8], where they are introduced to convert retarded effective interactions into instantaneous ones. They are also hidden in perturbation expansions of Green's functions [10]. That they are "real" diagrams and play a definite physical role can be demonstrated by the following simple examples<sup>4</sup>.

(i) Consider a simple two-particle system having only two eigenstates of  $H_0$ . The spaces 1 and 2 are one-dimensional, each containing one of the  $H_0$  eigenstates. The operator  $Q$  excludes the state 1 as an intermediate state. The Schrödinger equation is

$$\begin{pmatrix} V_{11} - E & V_{12} \\ V_{21} & V_{22} + e - E \end{pmatrix} \begin{pmatrix} \Phi_1 \\ \Phi_2 \end{pmatrix} = 0$$

with eigenvalues  $E_{1,2} = \frac{1}{2} [V_{11} + V_{22} + e \pm \sqrt{(V_{11} - V_{22} - e)^2 + 4|V_{12}|^2}]$ . In the limit of no coupling ( $V_{12} = 0$ ),  $E_1 = V_{11}$  and  $E_2 = V_{22} + e$ , and it is assumed that  $E_1 < E_2$ . To lowest order in the coupling,

$$E_1 = V_{11} - \frac{|V_{12}|^2}{V_{22} + e - V_{11}} + \dots = V_{11} - \frac{|V_{12}|^2}{V_{22} + e} - \frac{|V_{12}|^2 V_{11}}{(V_{22} + e)^2} \dots$$

The perturbation expansion contains the diagrams of Fig.4a, which contribute to the effective interaction an amount

$$V_{11} - \frac{V_{12} V_{21}}{e - E} + \frac{V_{12} V_{22} V_{21}}{(e - E)^2} \dots = V_{11} - \frac{|V_{12}|^2}{V_{22} + e - E}$$

<sup>4</sup> Both of these arguments arose in the course of discussions with Prof. L. Zamick.

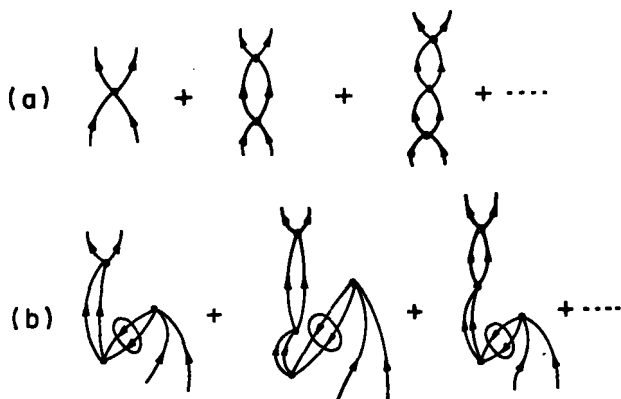


FIG. 4. Diagrams contributing to the effective interaction in a two-level, no-core model. (a) is the set of all non-folded diagrams, (b) a particular subset of once-folded diagrams.

The Bloch-Horowitz equation becomes  $E = V_{11} - |V_{12}|^2 (V_{22} + e - E)^{-1}$ , which is just the Schrödinger secular equation in another form. However, with energy-independent denominators ( $e - E \rightarrow e$ ), the sum of this diagram series is just  $E = V_{11} - |V_{12}|^2 (V_{22} + e)^{-1}$ , which is not even correct to lowest order in  $V_{12}$ . Including the once-folded diagrams of Fig. 4b, the sum of the perturbation series is increased by

$$- \frac{V_{12} V_{21} V_{11}}{e^2} + \frac{2V_{12} V_{22} V_{21} V_{11}}{e^3} - \frac{3V_{12} V_{22}^2 V_{21} V_{11}}{e^4} + \dots = - \frac{|V_{12}|^2 V_{11}}{(e + V_{22})^2}$$

which is the next term in the expansion of the correct result. More complicated once-folded diagrams produce higher powers of  $V_{12}$ , while twice-folded diagrams contribute terms of order zero, one and two in  $V_{11}$ . All folded diagrams are required to get the exact result.

(ii) If the single-particle potential  $U$  in  $H_0$  is changed by some constant amount  $C$  (a shift in the zero of single-particle energy), the single-particle wave-functions are unchanged, but every  $\epsilon$  becomes  $\epsilon' = \epsilon + C$ . In addition, there occur single-particle potential insertions  $C$  on every line in every diagram. For each intermediate state in a diagram, all possible  $C$ -insertions produce a multinomial geometric series which can be summed to all orders. The effect is simply to add  $C$  to each  $\epsilon'$  (hole) and to subtract  $C$  from each  $\epsilon'$  (particle), restoring the energy denominator to its old form, except for  $\epsilon'$  (ingoing valence) (see below), since  $C$ -insertions on ingoing valence lines produce  $Q$ -forbidden diagrams. This indicates that the folded diagrams can save the day. Indeed, the use of  $C$ -insertions on folded valence lines is just what is needed to restore all energy denominators to the form without  $C$ . This is clearly necessary — a shift in the zero of the arbitrary single-particle potential  $U$  should not affect the expansion.

After including folded diagrams, the perturbation expansion is completely linked and the energy denominators are of the form  $\sum \epsilon$  (upgoing) —  $\sum \epsilon$  (downgoing) —  $\sum \epsilon$  (ingoing valence). The expansion contains diagrams in which all but one of the valence lines are spectators, only the remaining valence line experiencing any interactions (see Fig. 5). The spectator

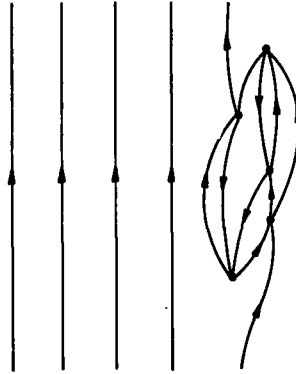


FIG. 5. A five-valence-line diagram belonging to the single-particle energy shift. Four of the valence lines are simply spectators.

lines do not enter the analytic expression at all, since they cancel out of all energy denominators and enter no interaction matrix elements. Thus the set of diagrams in which one particular valence line is the only one to interact define the effective interaction for a space 1 of the form "closed shells plus the specific valence line considered", a one-dimensional space in practice. The sum of this set of diagrams is just  $\tilde{E}_1 - \tilde{E}_0 - \epsilon$  (valence), where  $\tilde{E}_0$  is again the measured physical core energy and  $\tilde{E}_1$  is the measured physical energy of that state of the system core-plus-one-particle having the quantum numbers of the valence line considered. This is the experimental single-particle energy (not weighted with spectroscopic factors) relative to the core. The elimination of energy-dependent denominators is essential for this identification.

The final form of the fundamental equation is

$$\left( \sum [\tilde{E}_1 (\text{valence}) - \tilde{E}_0] + \mathcal{V}_v - E_v \right) \Phi_1 = 0$$

This looks just like a shell-model equation, except that  $\mathcal{V}_v$ , defined by the totally linked perturbation series, is not Hermitian. The effective Hamiltonian has real eigenvalues  $E_v$  but non-orthogonal eigenfunctions  $\Phi_1$ . It cannot be Hermitian, and the non-hermiticity must come from  $\mathcal{V}_v$ . In fact, it comes from the folded diagrams. In general, Hermitian conjugation of a diagram produces the inverted diagram, with the particle and hole lines not changing direction (see Fig. 6). The perturbation expansion defines a Hermitian operator if every diagram occurs together with its upside-down partner. Because of the "top-interaction" rule (i) for folded diagrams, there are no upside-down partners for folded diagrams. (Warning: There occur ordinary unfolded diagrams which look exactly like every folded diagram, except that the downgoing folded valence lines of the folded diagram are real downgoing hole lines in the non-folded diagram. Such non-folded diagrams do have upside-down partners.) Johnson and Baranger [7] show how to arrange that the energy-independent effective interaction be Hermitian, while Brandow [6] has demonstrated a transformation to a

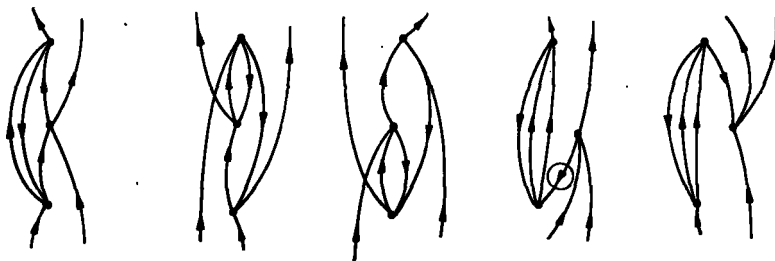


FIG. 6. Examples of Hermitian conjugation of diagrams. The first diagram is Hermitian; the next two are Hermitian conjugates of one another. The last two are Hermitian conjugates of one another if the circled line is a hole line. The folded diagram in which the circled line is a downgoing valence line has no Hermitian conjugate in the expansion.

Hermitian effective operator. Both of these methods lose the identification of the eigenfunction with the projection on space 1 of the true eigenfunction, but this is not so important, since perturbation expansions are available for the true eigenfunction and for matrix elements of any operator between true eigenfunctions. In practice, the non-hermiticity of  $\mathcal{V}_v$  is found to be small, in low orders, so numerical work has concentrated on the non-hermitian  $\mathcal{V}_v$ .

**Structure of the perturbation expansion:** The folded diagram perturbation expansion for the effective interaction has counterpart expansions for the true wave-function of the many-body system and for the matrix elements, between eigenfunctions of the total Hamiltonian  $H$ , of any operator [6, 7]. Provided antisymmetrized states  $\Phi$  are used (in practice, antisymmetrized matrix elements of  $V$  and factors  $\frac{1}{2}$  for equivalent pairs<sup>5</sup>), the Pauli principle is properly taken into account. This is generally achieved by deriving the diagram expansion in the notation of second quantization. However, the totally linked folded expansion contains many terms which appear explicitly to violate the Pauli principle. Since antisymmetrization has been properly handled, every such Pauli-violating diagram must have in the expansion a partner which is also Pauli-violating and which cancels it identically. Many of these compensating diagrams turn out to be unlinked or partially linked. They have thus already been taken into account in the partial summations leading to the totally linked form. The diagrams they compensate must thus be included in the evaluation of  $\mathcal{V}_v$  — the Pauli principle is respected only if all Pauli-violating terms are included in the totally linked expansion!

It should be noted that, even when  $V$  is at most a two-body operator,  $\mathcal{V}_v$  may contain effective three-, four- or many-body parts. As an effective operator in the valence space,  $\mathcal{V}_v$  contains parts which cannot be broken up into parts involving only two bodies in the valence space, as soon as the number of valence particles exceeds 2. Since it is known that the phenomenological shell model requires only two-body effective forces to fit spectra, it is to be expected that these many-body parts will either be small, or will somehow average out to appear like two-body interactions.

<sup>5</sup> Equivalent pairs are pairs of lines that start at the same interaction, end at the same interaction and go in the same direction [6].

That these many-body forces may be significant is indicated by fits to spectra which include them explicitly [11] and by the fact that the two-body matrix elements which fit spectra are generally not the same as those that fit relative binding energies. In the particular case of the calcium isotopes, Bertsch [12] has traced this difference to effective three-body forces arising from diagrams that compensate Pauli violations.

In principle, for sufficiently weak forces  $V$ , the totally linked folded expansion is sufficient to calculate  $\mathcal{V}_v$ . But the phenomenological nucleon-nucleon potentials obtained from scattering data are so strong that a simple perturbation approach is unlikely to converge. This problem is hopefully overcome by "Bruecknerizing" the expansion — all ladders of  $V$ 's on particle lines are summed<sup>6</sup> to produce Brueckner reaction matrices  $G = v - v(q/e)G$ , which are finite even for singular potentials  $v$ . The so-called Pauli operator  $q$  here restricts the intermediate two-body states to be particle states, and is not the same as the Bloch-Horowitz operator  $Q$ . Many methods are now available for computing  $G$ -matrix elements, some of which are surveyed in Baranger's excellent review [14].

Although it does take care of singular potentials  $v$ , the  $G$ -matrix introduces problems of its own. Those relevant to the present context are the following:

(i) "Up-ladders" — Since  $G$  sums ladders of  $v$ 's, the resulting  $G$ -matrix expansion should contain no ladders of  $G$ 's between particle lines. However, some of the approximate methods of treating the Pauli operator  $q$  in the evaluation of  $G$  are specifically designed to handle high-lying intermediate states. There has been some discussion of whether these methods do not leave out some of the contributions of the low-lying intermediate states to the ladder. This would make it necessary to include  $G$ -matrix ladders with low-lying intermediate states. Although this problem can be, and is, avoided by proper calculation of  $G$ , it appears that even the approximate methods do include the low-lying states satisfactorily [15], so that "up-ladders" of  $G$ -matrices should be omitted.

(ii) Off-energy-shell effects — The value of the  $G$ -matrix depends on the excitation energy of the system in the neighbouring intermediate state. Most  $G$ -matrices should thus be evaluated off the energy shell — at non-zero excitation energy. The factorization technique [6, 16, 18] used so extensively in eliminating unlinked and partially linked diagrams (generalized time ordering) is particularly valuable in that it allows many apparently off-energy-shell  $G$ -matrices to be evaluated on the energy shell. For example, all  $G$ -matrices between two hole lines can be put on the energy shell. Unfortunately, not all  $G$ -matrices can be treated in this way, and this feature should be taken into account. In addition, when folded diagrams are not introduced, so that the energy-dependence remains in the denominators, every  $G$ -matrix element is a function of the energy eigenvalue sought, which could severely complicate calculations. More recent methods of computing  $G$ , allowing for a dependence on the starting energy, make it possible to handle these complications, but they have been universally ignored in practice, so far. This is not as bad a procedure as it might appear to be — because of effect (iii) below, the distance off the energy shell is usually quite small.

<sup>6</sup> An excellent introduction to Brueckner theory is the review article by Day [13].

(iii) High-energy intermediate states - In evaluating perturbation theory diagrams, practical limitations of time, complexity and computer capacity require that only low-lying intermediate states be included in the calculation. This can be justified by noting that high-energy intermediate states can be reached only through the action of the very strong, short-ranged part of the nucleon-nucleon interaction. The range of this interaction is characterized by the hard-core radius  $c \sim 0.5$  fm. Since nucleons at normal nuclear densities have an average separation of the order of  $2r_0 \sim 2$  fm, the ratio of the "strong interaction volume" to the "occupation volume" of a nucleon is  $(c/r_0)^3 \sim 1/8$ . Relative to the strong short-range part of  $v$ , nuclei are low-density systems, and cluster methods are appropriate - since the close approach of two nucleons is of low probability, that of three is even less probable, and so on. The two-body cluster is taken into account exactly by the use of the G-matrix. The three- and four-body clusters have been computed in nuclear matter [17] and found to be much less important than G. It is thus expected that three- and more-body clusters should be negligible in computing effective interactions - insofar as the high-energy intermediate states are concerned. For low-lying states, where longer-range interactions of much less strength are active, the cluster approach is not appropriate, but simple perturbation theory, order by order in G, may well be satisfactory. Hence only low-lying intermediate states are included in the perturbation theory calculations.

(iv) Different q's - In calculating  $\mathcal{V}_v$ , the interaction between two valence particles alone is commonly taken to be G, the core remaining inert. However, in this case some of the intermediate states permitted by q are forbidden by the Bloch-Horowitz operator Q, namely states with only valence particles outside the core. Either q must be redefined, for this particular case only, to be consistent with Q, or the G-matrix must be corrected by the standard integral equation [16]  $G = G_a + G_a (q_a - q) e^{-1} G$ , where the subscript a means approximate. Once again, this requirement has been neglected in practice. Although the effect of this error has not been investigated numerically, it should be quite small, because the bulk of G comes from high-energy states, where the effects of Q and q are the same in this case.

(v) Single-particle potentials - The question of the choice of the "correct" single-particle potential has been discussed at great length [18, 19]. Many criteria, involving different types of self-consistency, have been suggested for the shell-model potential, all of them reducing in lowest order to Hartree-Fock. It should be noted that other single-particle potentials and energies can be defined, and need not be the same as, or even similar to, the shell-model potential. The off-energy-shell properties of the perturbation expansion complicate the choice of potential considerably, and are responsible for the present favoured definition - Hartree-Fock (with G replacing  $v$ ) for holes, no potential for particles. The second part of the definition follows from the small three-body correlations, and is thus most appropriate for the high-lying particle states. The particle states near the Fermi surface should feel some potential, perhaps Hartree-Fock averaged over off-energy-shell excitation. This definition leads to a finite-depth potential [20], in which the continuum wave-functions are determined completely by the bound-state wave-functions. In practice, harmonic-oscillator wave-functions are used for all the states

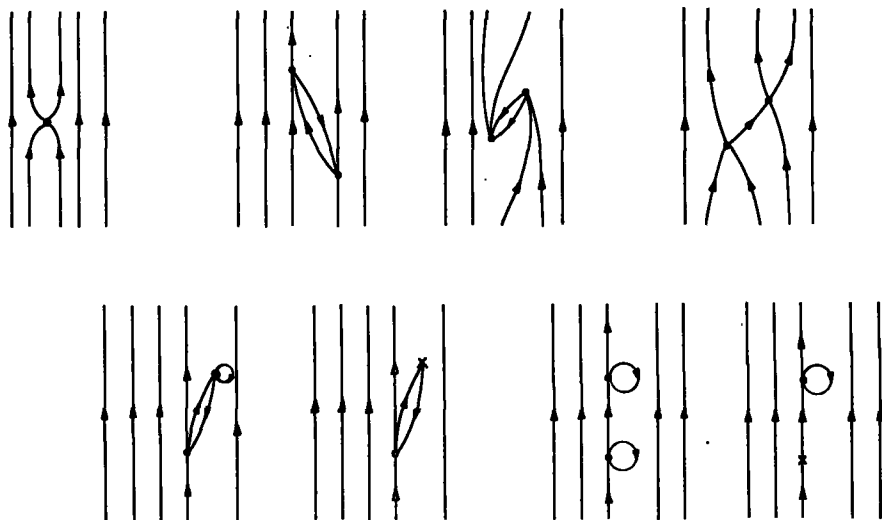


FIG. 7. First- and second-order contributions to the effective interaction for five valence particles outside a core. The first, the only first-order diagram, is a simple  $G$ -matrix. The next two are lowest-order core polarization and "deformed-state" contributions. The fourth diagram introduces three-body effective forces, while the last four give some self-consistency corrections — their sum vanishes (by pairs) for a self-consistent single-particle potential.

included in the folded diagram expansion, while continuum states are approximated by plane waves in some calculations of  $G$ . It should be observed that the single-particle wave-functions could be approximated, e.g. by harmonic oscillators, without approximating the single-particle energies. Even if the latter are taken as harmonic oscillator energies, as is frequently done, they need not have the same oscillator energy  $\hbar\omega$  as the single-particle wave-functions. This freedom has been little used in practice. It is important that this discussion does not affect the single-particle energies to be used in diagonalizing  $H_0 + \mathcal{V}_v$  — as shown above, these must be the experimental energies of the closed-shell-plus-one-nucleon nuclei, while the single-particle energies in the energy denominators should generally not be the experimental energies. The choice of single-particle potential by some self-consistency criterion implies that all single-particle potential insertions cancel all insertions of a particular kind in all diagrams. When the single-particle energies and wave-functions are chosen for convenience, some check should be made on how close they come to self-consistency and how much the lack of cancellation of insertions contributes to  $\mathcal{V}_v$ . This is usually not done.

**Identification of important renormalization effects:** The simplest approach is to apply the perturbation theory order by order in  $G$ . The lowest order term is just  $G$  itself. In second order, there are a number of terms (see Fig. 7), including core polarization, "deformed" states, three-body forces and self-consistency corrections. Since most effort to date has been concentrated on two-body effective forces, the three-body diagrams have not been investigated in detail. In the same way, deviations

TABLE I. LOWEST-ORDER CORE-POLARIZATION MATRIX ELEMENTS COMPARED WITH G-MATRIX ELEMENTS

All entries are in MeV. The matrix elements considered are

$$\begin{aligned} &\langle (0d_{5/2})^2 | G(J=0, T=1) | (0d_{5/2})^2 \rangle \text{ for } ^{18}\text{O} [27], \\ &\langle (0f_{7/2})^2 | G(J=0, T=1) | (0f_{7/2})^2 \rangle \text{ for } ^{42}\text{Ca} [22] \text{ and} \\ &\langle (1p_{3/2})^2 | G(J=0, T=1) | (0f_{5/2})^2 \rangle \text{ for } ^{58}\text{Ni} [22] \end{aligned}$$

	$^{18}\text{O}$	$^{42}\text{Ca}$	$^{58}\text{Ni}$
G	-1.236	-0.869	-0.56
Core polarization	-0.755	-0.938	-0.70

from self-consistency have generally been ignored. However, considerable attention has been paid to the other terms, which will now be taken one by one for further discussion.

(i) Core polarization — The importance of this effect was first indicated by Bertsch and confirmed by the pioneering calculation of Kuo and Brown [21]. The diagram describes an excitation of the inert core by interaction with a valence nucleon, the excitation then decaying by interaction with the second valence nucleon. In this way, the two valence nucleons "communicate" by way of the core, giving rise to an effective valence-nucleon interaction (through virtual excitation of the suppressed degrees of freedom of the core) which could well be of much longer range than the "bare" G-matrix interaction. The particular excitation of the core involved is a particle-hole excitation, corresponding to a density fluctuation, or vibration, of the core. The term "core polarization" will here be restricted to such vibrational excitations of the core. The importance of these excitations is well-known experimentally, from the occurrence of excited states in the spectrum of the closed-shell nucleus at surprisingly low (or surprisingly high) energies, with very large transition strengths. Well-known examples are the octupole vibrations ( $3^-, T=0$ ) and giant dipole states ( $1^-, T=1$ ). Thus it is perhaps not surprising that core polarization, even in lowest order in perturbation theory, gives rise to strong effects in the effective interaction. These effects have been observed throughout the periodic table [22]<sup>7</sup>, and include a dramatic lowering of the ground-state energy and an increase in the energy of high-spin excited states — both improving agreement with experiment (see Table I and Fig. 8).

However, the very identification of the physical mechanism (vibration of the core) responsible for core polarization raises questions about the validity of the calculation. It is well-known that the properties of vibrational excitations in closed-shell nuclei cannot be adequately explained by a simple particle-hole shell-model excitation. Both energies and transition strengths disagree greatly with experiment unless some residual interaction between the particle and the hole is introduced. This is done by diagonalizing the particle-hole interaction (TDA method) or by allowing for the presence of zero-point vibrations (ground-state correlations) in

<sup>7</sup> Kuo has collaborated with many workers in extensively applying the Kuo-Brown techniques, and many others have made similar calculations. An exhaustive list of references has not been given, but just a few representative examples.

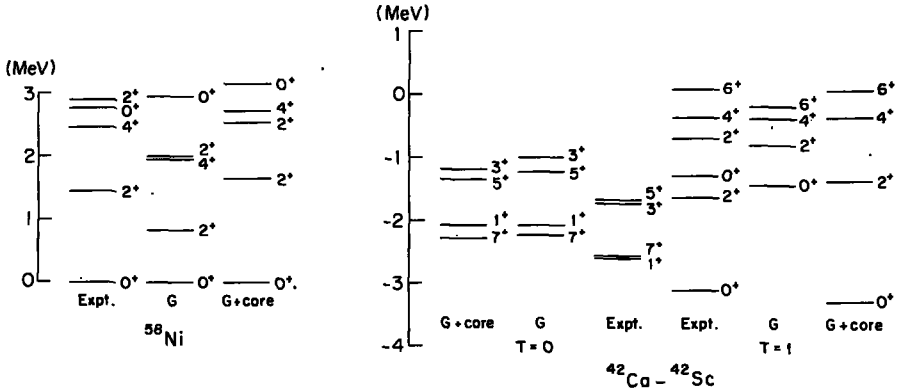


FIG. 8. Effect of lowest-order core polarization on nuclear spectra. For  $^{58}\text{Ni}$  the ground-state is set arbitrarily at zero MeV. For  $^{42}\text{Ca} - ^{42}\text{Sc}$ , the energy of the ground-state is significant. The effect of core polarization, compared to the simple G-matrix result, is dramatic for  $T=1$ , considerably less so for  $T=0$ . (See also Figs 16a and 16b.)

the core before diagonalizing (RPA method). Both of these improvements lead to better agreement between theory and experiment, but neither is taken into account in the simple second-order core polarization diagram. The correction of this defect requires the introduction of selected higher-order diagrams.

To maintain the identification of the effect under consideration as core polarization, it must consist of the excitation of a core vibration by a valence nucleon, followed by the "propagation" of the core vibration independently of the valence nucleons, followed finally by de-excitation of the core vibration by a different valence nucleon. (De-excitation by the same valence nucleon which excited it contributes to the single-particle energy of the nucleon and is already taken into account by the use of experimental single-particle energies.) The TDA and RPA modifications then involve a better treatment of the propagation of the vibration<sup>8</sup>.

If the propagating particle-hole pair are allowed to interact with one another any number of times, a sequence of diagrams of increasing order in G is generated (see Fig. 9), which can be summed by a geometric series formula. The effect is to replace the propagator  $[H_0(p-h)]^{-1}$  by  $[H_0(p-h) + V(p-h)]^{-1}$ , which is clearly equivalent to TDA. So core polarization can be treated in TDA by summing a suitable set of diagrams<sup>9</sup>. The results are predictable [23] — an enhancement of the core polarization effect in the effective interaction (see Table V and Figs 16(a) and 16(b)). It is very interesting to consider in this context the contribution to this effect of the different vibrations  $J^P T$  of the core (see Fig. 17). These do

<sup>8</sup> The numerical results quoted from this point on generally have the following features and approximations in common. The prototype system is  $^{16}\text{O} + \text{two particles}$ , i.e.  $^{18}\text{O}$  and  $^{18}\text{F}$ . Single-particle wavefunctions and energies are those of a harmonic oscillator with  $\hbar\omega = 14$  MeV. Hamada-Johnston G-matrix elements were very kindly supplied by Dr. T. T. S. Kuo. Only lowest-energy excitations are included, and all energy denominators are multiples of  $\hbar\omega$ . All G-matrices are on the energy shell and no self-consistency corrections are included.

<sup>9</sup> All G-matrices in all  $V(p-h)$ 's should be, but are not in this calculation, off the energy shell by  $2\hbar\omega$ .

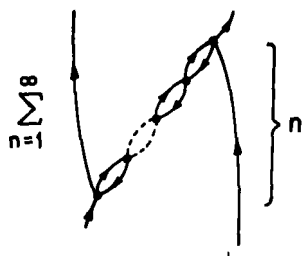


FIG. 9. Diagrams summed in extending the core polarization to include particle-hole interactions in the core. The number  $n$  of particle-hole bubbles is summed to all orders. Each order differs from the preceding one by a factor  $-V_{p-h}/\Delta E_{p-h}$ , where  $V_{p-h}$  is the particle-hole interaction and  $\Delta E_{p-h}$  the particle-hole excitation energy.



FIG. 10. Effect of ground-state correlations on core polarization. The basic correlation vertex, at left, corresponds to spontaneous excitation of two particle-hole pairs from the core, and can always be put on the energy shell. Such excitations make possible core polarization contributions like that on the right, which must be summed to all orders.

not interfere with one another, because of the conservation of angular momentum, parity and isospin in each interaction, but propagate independently. The multipole analysis of second-order core polarization indicates that even- $J$  multipoles play a dominant role, particularly the  $2^+0$  vibration, which is equivalent to a quadrupole-quadrupole effective interaction. In going to TDA, most multipoles are quite unaffected, the exceptions being just those which are generally regarded as being collective – the  $0^+0$  and the  $2^+0$ . This tends to reinforce the identification of core polarization with core vibrations.

It now becomes interesting to see what RPA would do. This can also be achieved by summing diagrams, by allowing for ground-state correlations in the core (see Fig. 10). Once again, this can be done by summing geometric series. Factorization plays a vital role in allowing each TDA-like sequence to be summed independently. The identification of the summed series with the use of RPA vibrations in the core can again be confirmed algebraically, though it is somewhat more complicated than the TDA case [23]. In somewhat schematic form, the propagator of the vibration becomes  $[H_0(p-h) + V(p-h) - B[H_0(p-h) + V(p-h) + E]^{-1}B]^{-1}$ , where  $B$  is the usual ground-state correlation vertex of the RPA and  $E$  is the RPA eigenvalue for the vibration. The effect on the core polarization is dramatic [23, 24] (see Table V and Figs 16a, 16b and 17). The  $0^+0$  and  $2^+0$  vibrations are very strongly enhanced, the former by an order

of magnitude over the second-order result, and although the other multipoles are unaffected the resulting core polarization is much too strong. The suppression of the ground-state energy results in a mismatch with experiment of almost 3 MeV and the pattern of the spectrum is radically changed. There must clearly be other effects which counteract the explosive tendencies of the RPA. This need arises also in the treatment of vibrational excitations of closed-shell nuclei, where the RPA is too strong and even leads to instabilities (the  $0^+0$  excitation goes below the ground state [25]).

(ii) "Deformed" states - The second-order term with two particles excited out of the core, leaving two holes, introduces a four-particle-two-hole ( $4p-2h$ ) intermediate state. Such states have been identified with deformed states in several calculations [26], and have been found to play an important role in explaining observed spectra. They might thus be expected to be of some importance in obtaining the effective interaction. In fact, the second-order  $4p-2h$  diagram is quite important, though considerably smaller than the core polarization term. It affects mainly  $0^+1$  and  $1^+0$  states, depressing the ground-state energy (see Table II). Since deformation is a collective effect, it might be expected that the effect of the  $4p-2h$  states could also be enhanced by suitable summation of higher-order diagrams. Although very little has yet been done in this direction, preliminary indications are that there is no strong build-up of "deformed" contributions analogous to that for the core polarization.

(iii) Higher-order terms - The use of perturbation theory always involves some anxiety concerning the convergence of the expansion, and this anxiety is considerably greater than usual in the present case because of the strong enhancements found in the RPA treatment of the core polarization term. Again the simplest path to follow is to compare the total third-order contribution with the total second-order contribution, in the hope that the former will be much smaller than the latter. Such a result would give some hope that the perturbation series converges, or is at least a useful asymptotic series. However, it is not at all as easy to carry out this proposal as it is to make it. There are a tremendous number of third-order diagrams, even when attention is confined to two-body diagrams. This number is greatly reduced by again ignoring the absence of self-consistency and by limiting consideration to diagrams with only the lowest-energy intermediate states. Even then there remain sixteen distinct third-order diagrams, so that some care is needed in evaluating the results of the calculation.

Stated baldly, the results are that the total third-order contribution is comparable with the total second-order contribution [27], that it is

TABLE II. LOWEST EIGENVALUES FOR  $^{18}\text{O}$  ( $T=1$ ) AND  $^{18}\text{F}$  ( $T=0$ ) WITH  $G$  ALONE COMPARED WITH  $G$  PLUS LOWEST-ORDER "DEFORMED" CONTRIBUTION. ALL ENERGIES ARE IN MeV

	$J=0, T=1$	$J=1, T=0$
$G$	-2.271	-3.373
$G + \text{"deformed"}$	-2.575	-4.258

TABLE III. FEATURES OF THE THIRD-ORDER PERTURBATION THEORY CALCULATION [27]. THE MATRIX ELEMENTS, IN MeV, ARE  $\langle (0d_{5/2})^2 | \mathcal{V}_v (J=0, T=1) | (0d_{3/2})^2 \rangle$  FOR  $^{18}\text{O}$

G	-3.025
Total second order	-0.727
Total third order	1.109
Second order core polarization	-0.581
"Large" third order terms	1.161
First number-conserving set	0.242
Second number-conserving set	0.284

frequently even larger than second-order, and that it is opposite in sign - repulsive, while second order is attractive (see Table III). This is clearly a blow to expectations of rapid convergence, and a more detailed investigation of third order is warranted.

Of the sixteen third-order diagrams, eight fall into number-conserving sets [27, 28]. These are sets of diagrams related by a type of Ward's identity, as pointed out by Brandow, who predicted that such sets would tend to cancel in effective interaction calculations. They are grouped together because they correspond to diagrams in the expansion for the single-particle density of the system which must be kept together if the total number of particles is to be conserved in each order of perturbation theory. The numerical calculations confirm that, although not all individual diagrams are small, the sum of the contributions of all diagrams in any number-conserving set is small compared to G (see Table III). These sets include folded diagrams, which enter for the first time in third order. The folded diagrams play a role in the cancellation of the number-conserving sets. They also make the effective interaction slightly non-Hermitian.

Of the eight remaining third-order diagrams, six are themselves individually small (though the second-order TDA diagram is quite sizeable), but the remaining two are comparable in size but opposite in sign to the second-order diagrams (see Fig. 11 and Table III). These are clearly the ones responsible for the apparent divergence of the perturbation series. Careful study of the structure of these large third-order terms led to the identification of a suggestive classification of diagrams, according to their degree of "slashability" [27]. A diagram is not slashable (called zero-slashable) if it cannot be separated into two parts by cutting one internal particle line and one internal hole line. It is once slashable if it can be so separated into two zero-slashable parts. An n-slashable diagram can be successively divided, by cutting internal particle-hole lines, into  $(n+1)$  zero-slashable parts (see Fig. 12). It is observed that the set of zero-slashable diagrams appears to converge rapidly order by order in G, and that the same is true of the sets of once-slashable and twice-slashable diagrams. However, the sum over the degree of slashability

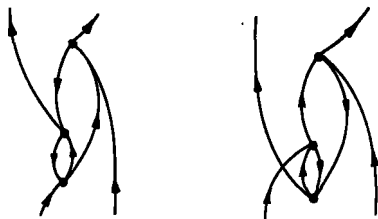


FIG. 11. Third-order diagrams which are found to give a large repulsive contribution to the effective interaction.

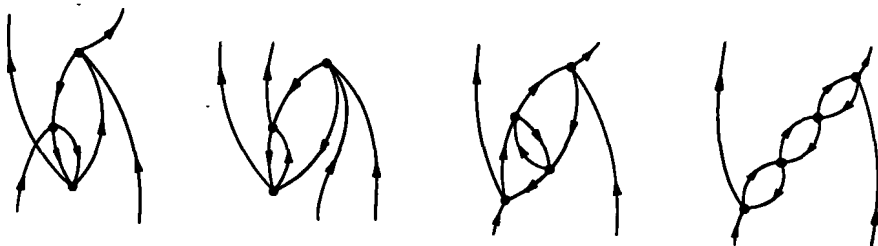


FIG. 12. Examples of the "slash" classification. The first diagram is once-slashable, the second zero-slashable, and the remaining two thrice-slashable. Compare also Fig. 11, where both diagrams are twice-slashable.

seems to diverge — the sum of twice-slashable diagrams is comparable to or bigger than the sum of once-slashable diagrams, and of opposite sign. Some method of summing all degrees of slashability in closed form is essential.

Several other classification schemes were tried [27], but all failed to converge order by order in  $G$  within each class. The particularly interesting feature of the slash classification is its connection with particle-hole pairs, which played such a role in the TDA and RPA enhancements. In fact, the large third-order diagrams are those with additional internal particle-hole pairs. This applies also to the zero-slashable third-order diagram in Fig. 12, which is comparable to the second-order "deformed" contribution from Fig. 7. It appears that core polarization, in the sense of particle-hole excitation of the core, is indeed very important, and that it is capable of modifying not only the propagation of core vibrations, but also the coupling of such vibrations to the valence nucleons. The large third-order diagrams are those in which the vertex coupling a valence nucleon to the valence-nucleon-plus-particle-hole-pair intermediate state contains a particle-hole pair. This suggests a possible new way of looking at core polarization.

Self-consistent particle-hole excitations: Since the third-order calculations suggest that the perturbation expansion may not converge order by order, it is attractive to seek a closed, non-perturbative formulation which has the same perturbation expansion as the original series. Although it is probably unreasonable to hope to find such a formulation for the whole



FIG. 13. Modification of the particle to two-particle-one-hole vertex. An incoming particle gives rise to an outgoing particle and a coupled particle-hole pair. The lowest-order vertex is a simple G-matrix, while the lowest-order modification has an internal particle-hole excitation of the core.

fully-linked folded diagram expansion, it may well be possible to do so for the most important diagrams, namely those of the highest degree of slashability in each order. In order to achieve this, it will be necessary to reformulate the results obtained so far.

As defined above, core polarization is the process in which a valence nucleon excites a core vibration, which then propagates independently of the valence nucleons and is finally de-excited by a different valence nucleon. This process is thus determined by two vertices – vibration production and vibration absorption – and a propagator for the vibration. What is required now is a suitable set of equations for the vertices and the propagator. The third order results have indicated the form of the vertex (see Fig. 13).

It must be either a simple G-matrix element between one particle and one particle plus a particle-hole pair, or it must have the excitation of a core vibration which propagates and then breaks up into a particle-hole pair, with the particle exchanging with the other nucleon present. Schematically,  $v = v_0 + v \mathcal{P} V_{p-h}$ , where  $v$  is the vertex,  $v_0$  the simple G-matrix vertex,  $\mathcal{P}$  the particle-hole propagator and  $V_{p-h}$  the G-matrix element leading to the breakup of the particle-hole pair. This equation must be solved self-consistently for  $v$ .

To get some feeling for this vertex modification effect, it is instructive to consider a first approximation for  $v$ , in which  $v$  is replaced by  $v_0$  in the right-hand side of the equation. The propagator  $\mathcal{P}$  is treated in TDA, because RPA turns out not to factorize, introducing overwhelming difficulties in the treatment of the energy denominators. (In general, factorization of a portion of a diagram requires that the relative ordering of interactions in the two parts of the diagram be varied completely freely in at least one direction – up or down. When the propagating vibration is contained between two fixed interactions, as in the case of the vertex modification, this freedom of ordering is lost, and factorization fails.) The resulting vertex is called a black-box vertex and can be used in calculating core polarization  $v \mathcal{P}_{RPA} v$ . The results are quite astonishing [27, 29]. The black-box vertex brings about a complete change in the coupling of the various vibrational multipoles, and dramatically reduces the RPA core polarization (see Table IV and Figs 16a, 16b and 17). The  $0^+0$  multipole is further enhanced, but the  $2^+0$  and  $4^+0$  are greatly reduced, while such non-collective vibrations as  $3^+$  and  $5^+$  are considerably enhanced. As far as core polarization is concerned, the black box vertex is a strong damping factor. This is precisely the kind of effect that was hoped for – a reduction in the explosiveness of the RPA.

TABLE IV. COMPARISON OF SOME MATRIX ELEMENTS (IN MeV) OF VARIOUS PORTIONS OF THE EFFECTIVE INTERACTION FOR MASS-18 NUCLEI  
(In the last row, the single-particle energy splitting is changed from 14 to 17.5 MeV.)

	$\langle (0d_{5/2})^2   0^+1   (0d_{5/2})^2 \rangle$	$\langle (0d_{5/2})^2   1^+0   (0d_{3/2})^2 \rangle$	$\langle 0d_{5/2} 0d_{3/2}   3^+1   0d_{5/2} 0d_{3/2} \rangle$
G	-1.236	+2.097	-0.403
Second-order "deformed"	-0.254	-0.043	-0.000
Second-order core polarization	-0.755	-0.543	+0.604
TDA	-1.232	-0.525	+0.898
RPA	-1.955	-0.574	+1.514
Nested RPA	-1.345	-0.458	+0.986
Black box RPA	-0.413	-0.764	+1.270
scce	-0.163	-0.628	+0.672
scce (17.5)	-0.218	-0.493	+0.505

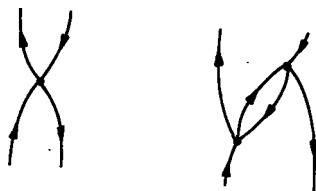


FIG. 14. The particle-hole interaction. At left, the simple G-matrix; at right, the contribution of lowest-order core polarization.

Unfortunately, the situation now attained does not yet satisfy the maximum slashability criterion. It is further subject to the criticism of inconsistency. Both of these criticisms are related to the absence of a certain set of diagrams from those taken into account so far. Pictorially, the type of modification employed both in the lowest-order core polarization and in the black box vertex modification has been the replacement of the simple black-dot G interaction by a particle-hole pair between two black-dot interactions. Since this replacement has been found to produce significant changes wherever it is used, it should be used consistently throughout. But there is one place where it has been omitted - in the black-dot interaction  $V_{p-h}$ . In the particle-hole interaction, this "standard" replacement leads to a self-screened interaction, with propagating particle-hole pairs mediating the interaction of a particle-hole pair (see Fig. 14). Such self-screening effects have been found to play an important role in moderating the RPA for vibrations of closed-shell nuclei [30]. In particular, they very much reduce the tendency to instability of the  $0^+ 0$  multipole which has been so dominant in the present results. The self-screening diagrams are also of the same degree of slashability as the TDA diagrams (see Fig. 12), and should thus be taken into account to all orders. Again schematically, a self-screened  $V_{p-h}$  should satisfy the equation  $V_{p-h} = V_{p-h}^{(0)} + \mathcal{P} V_{p-h}$ , where  $V_{p-h}^{(0)}$  is the simple G-matrix interaction and the other symbols have been previously defined. Since the propagator  $\mathcal{P}$  includes  $V_{p-h}$ , this equation is non-linear.

Again to get a feeling for the importance of this effect, it is useful to consider the first approximation  $V_{p-h} = V_{p-h}^{(0)} + \mathcal{P}_{TDA} V_{p-h}$ , a non-linear equation for  $V_{p-h}$ , but with simple vertices. The resulting "nested"  $\mathcal{P}_{RPA}$  (as indicated in Fig. 15, the iteration expansion of this equation reproduces all diagrams with strings of particle-hole pairs inside strings of particle-hole pairs inside strings of particle-hole pairs inside ...) is used in the core polarization,  $\mathcal{P}_{RPA} \mathcal{P}_{RPA}$ , and the results are again quite astonishing [23]) (see Table IV and Figs 16a, 16b and 17). Multipole by multipole, matrix element by matrix element, energy level by energy level, nested RPA is very similar to TDA! The strong RPA enhancement of the collective vibrations is damped by the nesting to produce much weaker, TDA-like enhancements. All other multipoles are essentially unaffected. There is a probable physical explanation for this phenomenon. The RPA requires very special ground-state correlations. The ground state of the closed shell nucleus must be a vacuum for the particular RPA vibration considered, i. e. it must contain only zero-point motion for that vibration. This imposes stringent phase relations on the ground-state wave-function.

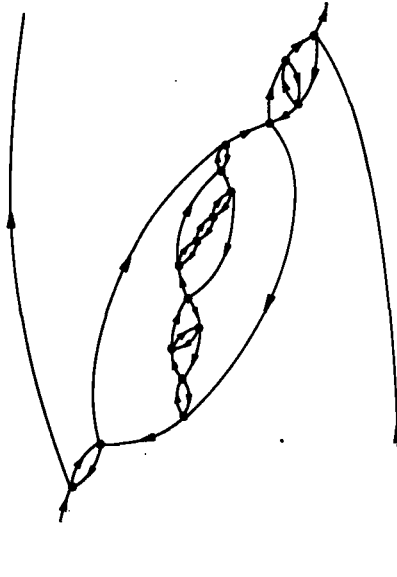


FIG. 15. A typical "nested-screening" diagram included in the self-consistent self-screened core polarization process.

In any situation where different vibrations must be considered at the same time, the phase relations imposed by the zero-point motion of one will generally compete with those required by the other. Some kind of destructive interference is at work. When many such zero-point vibrations must exist together, none of the phase relations will be satisfied, the ground-state will be uncorrelated, as far as vibrations are concerned, and TDA propagation will result. This is the physical content of the self-screening effect.

The final step is to demand complete self-consistency of vertices and propagators, namely the simultaneous satisfaction of the coupled non-linear equations

$$\omega = \omega_0 + \omega \mathcal{P}(V_{p-h}) V_{ph}^{(0)}$$

$$V_{p-h} = V_{p-h}^{(0)} + \omega \mathcal{P}(V_{p-h}) \omega$$

These will be called the self-consistent coupled equations (scc). They involve both damping effects – the screening of the propagator and the black-box vertex – so it is not too surprising that the overall effect is near-cancellation of the core polarization. The fully self-consistent core polarization is much smaller than simple second order [23] (see Table IV and Figs 16(a), 16(b) and 17), and the beautiful fit to experiment has been lost. The contributions of many multipoles, not all of them collective, are important and tend to cancel. However, a very selective choice of diagrams has been made – all diagrams contained in the perturbation expansion of the scc have been included, and all others excluded. This

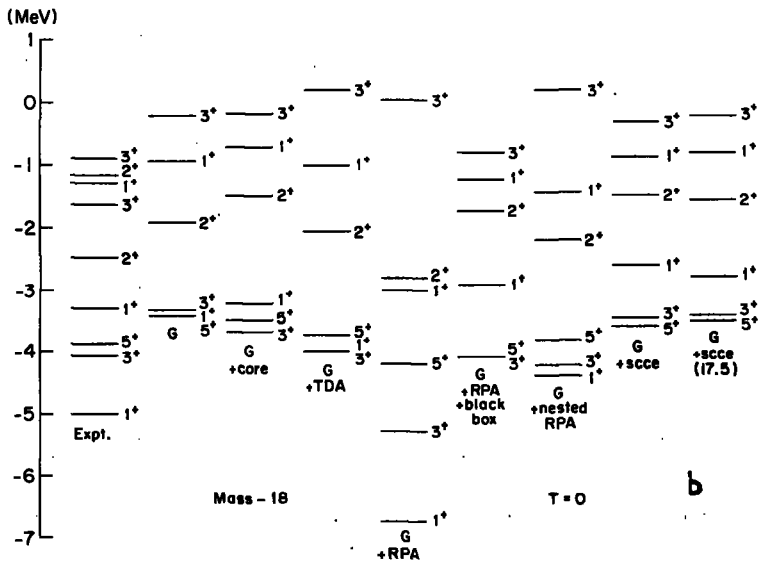
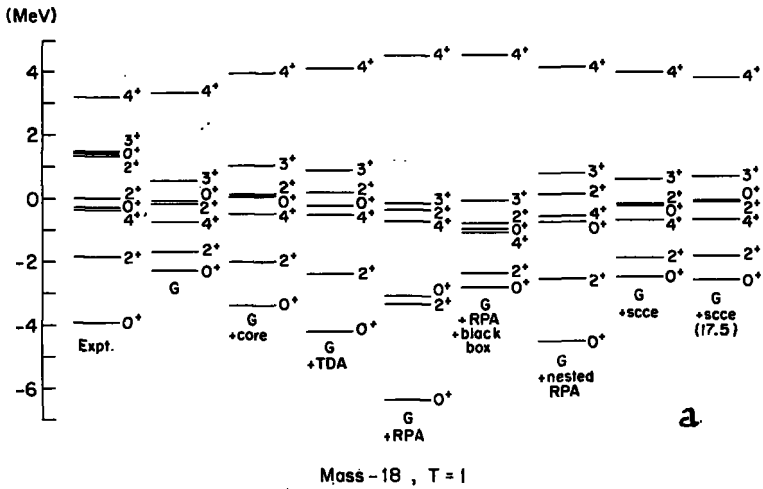


FIG. 16. Spectra in the mass-18 nuclei, with different prescriptions for the effective interaction. The order of the columns follows the order in which effects are described in the text. (a)  $T=1$ ; (b)  $T=0$ .

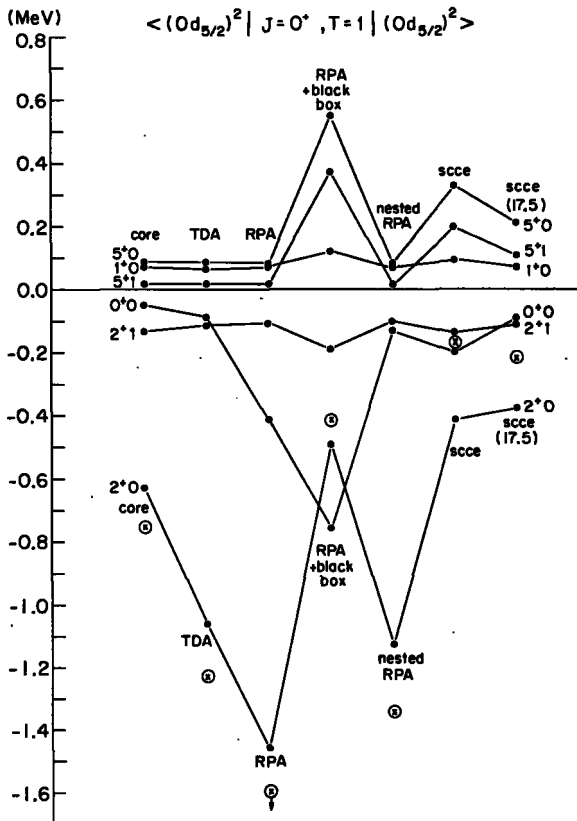


FIG. 17. Contributions of selected particle-hole multipoles to the core polarization for an effective interaction matrix element in  $^{16}\text{O}$ . The small crosses represent the total matrix element (which is off scale for RPA!). The different calculations are described in the text.

selectivity is partly justified by the slash classification, since it corresponds to the sum of all terms of lowest order in  $G$  for every degree of slashability. This argument must also be invoked to justify neglect of diagrams which cancel Pauli-violating terms in scce. In any case, the reasonable physical significance of scce justifies regarding it as the "correct" way to handle core polarization.

The way ahead: It is still reasonable on physical grounds to introduce diagrams omitted by scce and having evident physical significance. The "deformed" four-particle-two-hole diagrams are a case in point. They aid the now greatly weakened core polarization in lowering the energy of the ground state, but don't go quite far enough. However, it can now be argued that the effects under consideration are quite small, but still have a significant effect on the calculated spectrum, so that previously-neglected "small" corrections may be of some importance. Improved

G-matrix elements, better single-particle wave-functions<sup>10</sup> and energies (the single-particle self-consistency problem again), better treatment of intermediate states (the continuum does exist [19]), careful handling of off-energy-shell effects – all of these could affect the final results. As a very simple example, an increase of the harmonic oscillator energy  $\hbar\omega$  for the single-particle energies (but not the wave-functions) from 14 MeV to 17.5 MeV appears to reduce the black-box vertex effect more than the propagator screening effect, producing a net increase in the core polarization. However, the effect of this 25% shift in the single-particle energies is seen to be quite small (see Table IV and Figs 16(a), 16(b) and 17), insofar as the spectrum is concerned.

Since most of the calculations given in detail above make use of one set of G-matrix elements, and in particular a set acknowledged to have quantitative defects [32], the conclusions drawn should properly refer only to relative effects – screened versus unscreened RPA, black box vertex versus simple vertex, etc. – and not to close agreement or disagreement with experiment. As previously mentioned, many different calculations of reaction-matrix elements have been carried out to date, and there are often considerable differences between the results of different calculations. The qualitative effects, however, appear to remain the same – second-order core polarization is always sizeable and attractive, second-order "deformed" contributions are smaller, but also attractive, the large third-order terms are comparable to second-order core polarization and repulsive – when calculated with different nucleon-nucleon forces and different methods of computing G [27]. It thus remains possible that all effects beyond the simple G-matrix are comparatively small, as found in the present calculations, but that the "correct" nucleon-nucleon potential and/or the "correct" single-particle wave-functions and energies will produce agreement with experiment.

There remains one additional effect which could well affect the relative importance of different renormalizations, and which is intimately tied in with the choice of single-particle potential. The factorization arguments used in defining a single-particle potential also produce occupation probability factors on all internal particle and hole lines [6, 18, 33]. These factors express the probability that the single-particle state considered is actually occupied (particle) or unoccupied (hole), and are always between zero and one. They must necessarily reduce the contribution of any intermediate state to any diagram, and could lead to a revision of conclusions involving competition between different diagrams. A rough estimate of their effect leads to a reduction of the second-order core polarization by about ten percent.

It is quite clear that the above considerations, though here applied so far exclusively to the two-particle effective interaction, also affect many other properties. Obvious examples are the two-hole effective interaction, the particle-hole effective interaction (directly involving the core vibrations themselves), the single-particle energies, effective charges, etc. Some of these involve special problems of their own – the single-particle energies require a very careful diagram analysis to avoid serious over-counting problems; the particle-hole calculations for even parity vibrations

---

<sup>10</sup> Kahana and collaborators have shown [31] that the use of Woods-Saxon wave-functions for the states between which matrix elements are evaluated can have a considerable effect on the G-matrix.

TABLE V. NEUTRON AND PROTON EFFECTIVE CHARGES (TO BE ADDED TO  $e_n^{(0)} = 0$  AND  $e_p^{(0)} = 1$ ) FOR ONE PARTICLE OUTSIDE A  $^{16}\text{O}$  CORE. EACH COLUMN IS HEADED BY THE SYMBOLS FOR THE TWO STATES BETWEEN WHICH MATRIX ELEMENTS OF THE E2 OPERATOR ARE TAKEN

	$0d_{5/2}, 0d_{5/2}$		$1s_{1/2}, 0d_{5/2}$		$0d_{3/2}, 0d_{5/2}$		$0d_{3/2}, 1s_{1/2}$		$0d_{3/2}, 0d_{3/2}$	
	p	n	p	n	p	n	p	n	p	n
Lowest order	0.103	0.329	0.119	0.269	0.187	0.371	0.053	0.239	0.099	0.331
TDA	0.315	0.501	0.277	0.404	0.431	0.581	0.167	0.322	0.285	0.474
RPA	0.477	0.655	0.394	0.517	0.632	0.775	0.232	0.381	0.428	0.608
Nested RPA	0.341	0.513	0.291	0.412	0.461	0.599	0.177	0.322	0.314	0.486
Black box RPA	0.190	0.435	0.212	0.379	0.372	0.551	0.000	0.209	0.122	0.354
scce	0.143	0.353	0.158	0.300	0.285	0.429	0.028	0.204	0.119	0.311

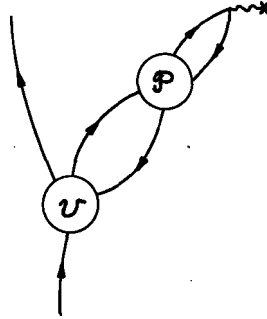


FIG. 18. Core polarization contribution to the E2 effective charge. The wiggly-line-and-cross represents the E2 operator,  $\rho$  the propagator of the core vibration and  $\nu$  the particle-vibration vertex.

are complicated by the presence of two-particle-two-hole states degenerate with the particle-hole states — but others are straightforward. The E2 effective charge, for instance (see Fig.18), simply selects the  $2^+$  multipole from the above development, and its behaviour closely parallels that found above. The damping due to the black box is less dramatic because of the absence of competing  $3^+$  and  $5^+$  multipoles, but all other effects are as expected. The net result here, too, is that self-consistent core polarization is too weak to produce the observed effective charges with the present G-matrix elements (see Table V).

It is appropriate to mention here two variations on the formalism which warrant attention. One is an extreme version of "double partitioning" [6], which sees as a first step the definition of a space 1 containing those states with all particles in single-particle orbits below a high-energy cutoff [34]. Such a space has no core, but folded diagrams would still be required to eliminate energy-dependence. The effective interaction in this model space would be mainly the G-matrix, all excitations outside the space fitting naturally into a cluster scheme, probably with small three-body (and higher) contributions. The model space would then be further subdivided into a space 1' of a core plus a few valence particles, and a space 2' of all core-excited states and all states with valence particles outside the valence states. The effective interaction in space 1' would be calculated by the methods described here. The chief new features would be the appearance of "up-ladders" (within space 1 but outside space 1') and the confident use of plane waves for states outside space 1.

The second variation is the extreme opposite of this model-space approach. It considers space 1 to be an inert core, with valence particles anywhere outside the core. The only diagram without core excitation is a single  $\nu$ -interaction. For the particular case of two particles beyond the core, the Bloch-Horowitz equation, with no core excitation, is identical to a Schrödinger equation for two particles in an external potential, interacting by way of the bare nucleon-nucleon interaction, but excluded from any of the core states. The eigenvalues give directly the spectrum, without core excitation, of the nucleus with two particles outside the core, and the eigenvectors are the projection of the true eigenvectors on the space 1 [35].

There is evidently much still to be done to understand even the simple two-body effective interaction. The application of the same formalism to other operators and more complicated systems allows for extensive calculations of nuclear properties from first principles. Perhaps even more useful are the qualitative conclusions to be drawn. For example, excellent fits to spectra are possible with very poor model wave-functions – the projection of the true wave-function on the model space may be only a small part of the whole, but all the rest can be absorbed in a suitable effective interaction. As a corollary, effective operators must always be used in shell-model calculations. Computations of quantities such as mean square radii, magnetic moments, transition rates, etc., using shell-model wave-functions must always be supplemented by higher order calculations testing the effect of the neglected part of the wave-function. Many-body effective forces may be necessary in certain calculations. The simple structure of nuclei with many particles outside of closed shells may be a reflection of "double partitioning" – sixteen neutrons outside  $^{100}\text{Sn}$  interacting through effective forces can themselves be treated by many-body methods, generating effective self-consistent fields, effective closed shells, effective effective forces, and so on. The possibilities appear to be boundless.

#### REFERENCES†

† The choice of references is far from complete, and no effort has been made to assign priorities nor to ascribe relative importance. The references cited are meant to give a convenient entry to the literature. Each contains references to earlier work.

- [1] TALMI, I., *Rev. mod. Phys.* 34 (1962) 704; FEDERMAN, P., TALMI, I., *Physics Letts* 19 (1965) 490.
- [2] REID, R.V., Jr., *Ann. Phys. (N.Y.)* 50 (1968) 411; International Conference on the Nucleon-Nucleon Interaction (GREEN, A.E.S., MACGREGOR, M.H., WILSON, R., Eds) *Rev. mod. Phys.* 39 (1967) 495.
- [3] CLARK, J.W., WESTHAUS, P., *Phys. Rev.* 141 (1966) 833; JASTROW, R., *Phys. Rev.* 98 (1955) 1479.
- [4] VILLARS, F.M.H., *Rendiconti S.I.F., Course 3*, New York (1963); CIOFI DEGLI ATTI, C., GRYPEOS, M.E., *Lett. Nuov. Cim.* 2 (1969) 587; GRYPEOS, M.E., these Proceedings.
- [5] THOULESS, D.J., *Rep. Prog. Phys.* 27 (1964) 53.
- [6] BRANDOW, B.H., *Rev. mod. Phys.* 39 (1967) 771; *Phys. Rev.* 152 (1966) 863.
- [7] JOHNSON, M.B., BARANGER, M., *Ann. Phys. (N.Y.)* 62 (1971) 172.
- [8] LÖWDIN, P.-O., in "Perturbation Theory and its Applications in Quantum Mechanics", (WILLCOX, C.H., Ed.), Wiley, New York (1966).
- [9] BLOCH, C., HOROWITZ, J., *Nucl. Phys.* 8 (1958) 91.
- [10] BARRETT, B.R., *Nucl. Phys.* A109 (1968) 129; AGASSI, D., Ph. D. thesis, Weizmann Institute, Rehovot, 1967.
- [11] QUESNE, C., *Physics Letts* 31B (1970) 7.
- [12] BERTSCH, G.F., *Phys. Rev. Letts* 21 (1968) 1694.
- [13] DAY, B.D., *Rev. mod. Phys.* 39 (1967) 719.
- [14] BARANGER, M., *Proc. Int. School of Physics "Enrico Fermi", Course 40*, 1967, Academic Press, New York (1969) 511.
- [15] KIRSON, M.W., *Physics Letts* 32B (1970) 33.
- [16] BETHE, H.A., BRANDOW, B.H., PETSCHKE, A.G., *Phys. Rev.* 129 (1963) 225.
- [17] RAJARAMAN, R., BETHE, H.A., *Rev. mod. Phys.* 39 (1967) 745; DAY, B.D., *Phys. Rev.* 187 (1969) 1269.
- [18] KIRSON, M.W., *Nucl. Phys.* A115 (1968) 49.
- [19] BARANGER, M., *Nucl. Phys.* A149 (1970) 225; JONES, R.W., MOHLING, F., *Nucl. Phys.* A151 (1970) 420; ARPONEN, J., *Nucl. Phys.* A155 (1970) 597.
- [20] STINGL, M.M., KIRSON, M.W., *Nucl. Phys.* A137 (1969) 289.

- [21] BERTSCH, G.F., Nucl. Phys. 74 (1965) 234; KUO, T.T.S., BROWN, G.E., Nucl. Phys. 85 (1966) 40.
- [22] KUO, T.T.S., Nucl. Phys. A103 (1967) 71; KUO, T.T.S., BROWN, G.E., Nucl. Phys. A114 (1968) 241; KUO, T.T.S., Nucl. Phys. A122 (1968) 325; LAWSON, R.D., MACFARLANE, M.H., KUO, T.T.S., Physics Letts 22 (1966) 168.
- [23] KIRSON, M.W., Ann. Phys. (N.Y.), 66 (1971) 624.
- [24] OSNES, E., WARKE, C.S., Physics Letts 30B (1969) 306; ZAMICK, L., Phys. Rev. Letts 23 (1969) 1406.
- [25] BLOMQUIST, J., Nucl. Phys. A103 (1967) 644.
- [26] BROWN, G.E., GREEN, A.M., Nucl. Phys. 85 (1966) 87; FEDERMAN, P., Nucl. Phys. A95 (1967) 443.
- [27] BARRETT, B.R., KIRSON, M.W., Nucl. Phys. A148 (1970) 145.
- [28] BRANDOW, B.H., in Lectures in Theoretical Physics, vol.11-B, (MAHANTHAPPA, K.T., BRITTIN, W.E., Eds) Gordon and Breach, New York (1969) 55; BARRETT, B.R., KIRSON, M.W., Physics Letts 30B (1969) 8.
- [29] KIRSON, M.W., ZAMICK, L., Ann. Phys. (N.Y.) 60 (1970) 188.
- [30] BLOMQUIST, J., KUO, T.T.S., Physics Letts 29B (1969) 544; ZAMICK, L., Physics Letts 31B (1970) 160.
- [31] KAHANA, S., LEE, H.C., SCOTT, C.K., Phys. Rev. 180 (1969) 956.
- [32] WILDENTHAL, B.H., HALBERT, E.C., McGRORY, J.B., KUO, T.T.S., Physics Letts 32B (1970) 339.
- [33] BECKER, R.L., Phys. Rev. Letts 24 (1970) 400.
- [34] BROWN, G.E., Rev. mod. Phys. 43 (1971) 1.
- [35] LAWSON, R.D., SOPER, J.M., Nucl. Phys. A133 (1969) 473; LAWSON, R.D., Nucl. Phys. A148 (1970) 401.

#### NOTE ADDED IN PROOF

Since these lectures were delivered, some errors in computer programs have been found and corrected. The effect is to change some of the numbers quoted in Tables IV and V and Figs 16 and 17, without changing any of the qualitative features. The numerical values in these tables and figures should be regarded as illustrative only, and not exact.



# HARTREE-FOCK THEORY OF FINITE NUCLEI IN THE LOCAL DENSITY APPROXIMATION

J. NÉMETH

Eötvös University, Budapest,  
Hungary

## Abstract

### HARTREE-FOCK THEORY OF FINITE NUCLEI IN THE LOCAL DENSITY APPROXIMATION

1. Introduction; 2. Definition of an effective interaction in nuclear matter; 3. Definition of effective forces in finite nuclei; 4. Renormalization and starting-energy correction; 5. Separation of volume and residual surface terms of potential energy; 6. Hartree-Fock equations with density-dependent forces; 7. Results with different density-dependent effective forces.

## 1. INTRODUCTION

A nucleus cannot be treated by the usual perturbation theory because of the strong interactions acting among the particles. A convergent perturbative series was worked out for nuclear matter as a result of almost twenty years of investigations. The terms of this series are the sums of all the two-hole, three hole, etc. interactions. The convergence of the series seems to be reasonably fast, so, as a first approximation, one can take into account only the first-order term, the sum of the two-hole diagrams. The summation of these ladder diagrams can be performed by the Brueckner method. The Brueckner-Goldstone theory introduces an effective two-body operator instead of the two-body forces and determines the potential energy of the nuclear matter as the sum of the matrix elements of this G-operator taken among unperturbed plane-wave wave-functions. Present calculations underestimate the binding energy of nuclear matter by 3 - 5 MeV per particle [1]. This underestimation might partly be due to the lack of the three-hole, four-hole diagrams, partly to the approximate solution of the G-matrix equations, and partly to our unsatisfactory knowledge of the nuclear forces.

The Brueckner-Goldstone theory has been applied to finite nuclei [2] as well as to nuclear matter. The results of the finite-nucleus calculations are similar to the infinite-nucleus calculations: they underestimate the value of the nuclear binding energy by about 4 - 5 MeV per particle. They also give too small root-mean-square radii of charge. Better agreement with experiments should be obtained from a theory which accounts for the nuclear-matter binding energy derived from the Weizsäcker formula.

It is more convenient for nuclear calculations to use an effective interaction instead of the G-operator. There are several attempts in the literature to derive an approximate state-dependent or state-independent but density-dependent effective interaction in nuclear matter which trivially reproduces the nuclear-matter saturation curve calculated in the Brueckner approximation [1, 3]. We can generalize this effective interaction for the case of finite nuclei by applying the local density approximation [4 - 7].

Such a force was successfully used for Hartree-Fock calculations of spherical nuclei [6 - 8] and deformed light nuclei [27].

Density-dependent effective forces have been applied already twenty years ago by Skyrme [9]. He used a force containing three-body forces in addition to two-body forces. Such a force can be transformed into a density-dependent effective two-body interaction. Skyrme's force is a  $\delta$ -function force, depending on the density and its derivatives. The advantage of such a force is the simple treatment of the exchange terms, when applied to Hartree-Fock calculations [10].

## 2. DEFINITION OF AN EFFECTIVE INTERACTION IN NUCLEAR MATTER

Brueckner's G-matrix, which sums all the ladder diagrams, satisfies the equation

$$G(W) = v - v \frac{Q}{e(W)} G(W) \quad (2.1)$$

where  $Q$  is the Pauli operator projecting into unoccupied states,  $e$  is the energy denominator,  $W$  the starting energy and  $v$  the two-body potential. The operator equation (2.1) defines a two-body wave function through the equation

$$G\phi = v\psi \quad (2.2)$$

$$\psi = \phi - \frac{Q}{e} v\psi \quad (2.3)$$

It is convenient to expand  $\phi$  and  $\psi$  into partial waves

$$\phi(r) = \sum_{j\ell} i^\ell \sqrt{4\pi(2\ell+1)} (\ell s 0 m_s | j m_s) j_\ell(kr) \mathcal{Y}_{\ell s j}^{m_s}(\hat{k}\hat{r}) \quad (2.4)$$

$$\psi(r) = \sum_{j\ell\ell'} i^\ell \sqrt{4\pi(2\ell+1)} (\ell s 0 m_s | j m_s) \frac{u_{\ell\ell'}^{js}(kr)}{r} \mathcal{Y}_{\ell s j}^{m_s}(\hat{k}\hat{r}) \quad (2.5)$$

where the  $(\ell s 0 m_s | j m_s)$ -terms are the Clebsch-Gordan coefficients,  $\mathcal{Y}_{\ell s j}^{m_s}$  are the generalized spherical harmonics,  $j_\ell$  are Bessel functions,  $k$  represents the relative momentum, and  $s$  the spin. The wave functions  $u_{\ell'\ell}^{js}$ , according to Eq. (2.3), satisfy the equations

$$u_{\ell'\ell}^{js} = \delta_{\ell'\ell} j_\ell(kr) - \frac{Q_{av}}{e} \sum_{\ell''} v_{\ell'\ell''}^{js} u_{\ell''\ell}^{js} \quad (2.6)$$

where  $Q_{av}$  is the spherically averaged Pauli operator. From Eqs (2.1)-(2.6) we obtain the expansion of the G-matrix elements

$$\langle k' s m_s' | G | k s m_s \rangle = \sum_{j \ell \ell'} i^{\ell - \ell'} \sqrt{4\pi(2\ell + 1)} (\ell' s (m_s - m_s') m_s' | j m_s) \\ \times (\ell s 0 m_s | j m_s) Y_{\ell' m_s'}^{m_s m_s'} (\hat{k} \hat{k}') G_{\ell' \ell}^{j s} (\vec{k}, \vec{k}') \quad (2.7)$$

where

$$G_{\ell' \ell}^{j s} (\vec{k}, \vec{k}') = 4\pi \sum_{\ell''} \int_0^{\infty} r j_{\ell'}(k' r) v_{\ell' \ell''}^{j s}(r) u_{\ell'' \ell}^{j s}(k, r) \quad (2.8)$$

is the partial-wave G-matrix element.

To derive Eqs (2.7) and (2.8) we made use of the fact that

$$Y_{\ell' 0}(\hat{k}') \chi_{s m_s'} = \sqrt{\frac{4\pi}{2\ell' + 1}} \sum_m Y_{\ell' m}^*(\hat{k}) Y_{\ell' m}(\hat{k}, \hat{k}') \chi_{s m_s'} \\ = \sqrt{\frac{4\pi}{2\ell' + 1}} \sum_m (\ell' m s m_s' | j m_j) \mathcal{G}_{\ell' j s}^{m_j}$$

and the matrix element

$$(\mathcal{G}_{\ell' j s}^{m_j} | v | \mathcal{G}_{\ell'' j s}^{m_s}) = \delta_{m_j m_s} v_{\ell' \ell''}^{j s}$$

is diagonal in  $m_j$ ,  $m_s$  and independent of them.

The definition of an effective force means that the G-matrix elements should be expressed as the matrix elements of an effective potential in the Born approximation. This means that

$$G_{\ell' \ell}^{j s} (\vec{k}', \vec{k}) = 4\pi \int_0^{\infty} r j_{\ell'}(k' r) V_{\ell' \ell}^{j s}(r) r j_{\ell}(k r) dr \quad (2.9)$$

Comparing (2.8) and (2.9) one sees that to get an effective potential it is sufficient to require that

$$V_{\ell' \ell}^{j s}(r) = \sum_{\ell''} v_{\ell' \ell''}^{j s}(r) u_{\ell'' \ell}^{j s}(k, r) / r j_{\ell}(k r) \quad (2.10)$$

To satisfy Eq. (2.10) we have to introduce the approximation

$$u_{\ell'' \ell}^{j s}(k, r) = f_{\ell'' \ell}^{j s}(r) r j_{\ell}(k r) \quad (2.11)$$

which gives the effective potential

$$V_{\ell' \ell}^{j s} = \sum_{\ell''} v_{\ell' \ell''}^{j s}(r) f_{\ell'' \ell}^{j s}(r) \quad (2.12)$$

Equation (2.11) represents clearly a requirement which is strong and somewhat arbitrary, namely that the  $k$ -dependence of  $u_{\ell''\ell}^{js}$  should be parametrized in the way described by this equation. Clearly, Eq. (2.11) cannot be fulfilled for every  $k$ -value. Brandow [11] suggested that  $f(r)$  should be defined at an average  $k$ -value:

$$f_{\ell''\ell}^{js}(r) = u_{\ell''\ell}^{js}(k_{av}, r) / r j_{\ell}(k_{av}, r) \quad (2.11a)$$

Instead of the definition (2.11a), one can define, as Sprung [3] has pointed out, a  $k$ -dependent effective potential which is clearly already sufficient, but not easy to treat:

$$V_{\ell'\ell}^{js}(r, k, P, W) = \sum_{\ell''} v_{\ell'\ell''}^{js}(r) u_{\ell''\ell}^{js}(k, r) / r j_{\ell}(k, r) \quad (2.12a)$$

Since  $u$  depends on the starting parameters used for the solution of the  $G$ -matrix equation ( $k_F, P, W$ , where  $W$  is the starting energy and  $P$  is the centre-of-mass momentum), the effective potential defined in expression (2.12a) will depend on them, too. Banerjee and Sprung showed [12] in their paper that it is a good approximation to replace  $P$  by its average value for a given  $k$ . The effective potential defined in expression (2.11b) goes over into the free potential as  $r$  increases and the zeroes of the denominator occur at those points where this approximation is already true.

Siemens [1] has used an alternative approximation for  $f_{\ell}(r)$ . He required that the nuclear-matter binding energy calculated with the effective interaction in the Born approximation reproduce the Bruckner values. This requirement suggests an average over the relative momentum  $\vec{k} = \frac{1}{2}(\vec{k}_1 - \vec{k}_2)$ :

$$f_{\ell''\ell}^{js}(r, k_F, W) = \frac{\sum_{k_1 < k_F} \sum_{k_2 < k_F} \left(\frac{1}{k^2}\right) r j_{\ell'}(kr) u_{\ell''\ell}^{js}(r, k)}{\sum_{k_1 < k_F} \sum_{k_2 < k_F} \frac{1}{k^2} j_{\ell'}(kr) j_{\ell}(kr)} \quad (2.13)$$

Expression (2.13) together with relation (2.12) supplies the effective potential:

$$V_{\ell'\ell}^{js}(r, k_F, W) = \frac{\int_0^{k_F} P(k, k_F) j_{\ell'}(kr) \sum_{\ell''} v_{\ell'\ell''}^{js}(r) r u_{\ell''\ell}^{js}(r, k) dk}{\int_0^{k_F} P(k, k_F) j_{\ell'}(kr) j_{\ell}(kr) dk} \quad (2.14)$$

where  $P(k, k_F)$  is the weight function coming from the replacement of the double summation in Eq. (2.13) by a single integral in Eq. (2.14):

$$P(k, k_F) = \frac{64\pi^2}{3} (2k_F^3 + k^3 - 3k_F^2 k) \quad (2.15)$$

It is easy to prove that the effective force defined in expression (2.14) gives exactly the Brueckner value in the first-order Born approximation. From expression (2.7) we see that

$$\begin{aligned}
 & \frac{1}{2} \sum_{k_1 < k_F} \sum_{k_2 < k_F} \langle \vec{k}_1 \vec{k}_2 | G | \vec{k}_1 \vec{k}_2 \rangle \\
 &= \frac{1}{2} \sum_{\ell \ell'} (2\ell + 1) \int dk P(k, k_F) \int dr r j_{\ell}(kr) v_{\ell \ell}^{j s} u_{\ell' \ell}^{j s}(r, k) \quad (2.16) \\
 &= \frac{1}{2} \sum_{\ell} (2\ell + 1) \int dk P(k, k_F) \int j_{\ell}^2(kr) V_{\ell \ell}^{j s}(r, k_F) dr \\
 &= \frac{1}{2} \sum_{k_1 < k_F} \sum_{k_2 < k_F} \langle \vec{k}_1 \vec{k}_2 | V | \vec{k}_1 \vec{k}_2 - \vec{k}_2 \vec{k}_1 \rangle
 \end{aligned}$$

where for nuclear-matter binding one needs only the diagonal  $\ell = \ell'$  forces.

In many applications it is convenient to further simplify expression (2.16) and use an effective interaction which depends only on spin and isospin. We can achieve this aim by averaging first over the total angular momentum variable in the triplet cases

$$\begin{aligned}
 G_{\ell}^{s=1} &= \sum_{j=\ell-1}^{\ell+1} (2j+1) V_{\ell \ell}^{j, s=1} / \sum_{j=\ell-1}^{\ell+1} (2j+1) \\
 G_{\ell}^{s=0} &= V_{\ell \ell}^{j, s=0}
 \end{aligned} \quad (2.17)$$

and then defining the effective  $g^{ST}$  interaction acting in an S, T spin, isospin channel by taking the average

$$g^{ST}(r, k_F, W) = \frac{\sum_{\ell} \frac{1}{2} \left[ 1 - (-1)^{\ell+S+T} \right] (2\ell + 1) G_{\ell}^S(r, k_F, W) \int dk P(k, k_F) j_{\ell}^2(kr)}{\sum_{\ell} \frac{1}{2} \left[ 1 - (-1)^{\ell+S+T} \right] (2\ell + 1) \int dk P(k, k_F) j_{\ell}^2(kr)} \quad (2.18)$$

In the first step, the averaging projected out the  $j$ -independence for a given  $\ell$ , while in the second step we obtain an  $\ell$ -independent force, which differs, however, for odd and even, singlet and triplet cases.

Another way of defining an effective interaction was proposed by Sprung and Banerjee [3]. Elliot et al. and others [13] defined an  $f_{\ell}(kr)$  function which is the inverse operator to  $j_{\ell}^2(kr)$ . Using this  $f_{\ell}(kr)$  an effective interaction

$$V_{\ell}^{jST} = \int f_{\ell}^{jST}(kr) \langle k | G_{\ell}^{jST} | k \rangle dk \quad (2.19)$$

is obtained which precisely reproduces the diagonal G-matrix elements. To evaluate  $V_{\ell}^{jST}$  one needs, however, the G-matrix elements for all values of  $k$ , while the nuclear-matter calculations give them only for  $k \lesssim k_F$ . Sprung and Banerjee propose that one should admit that these high- $k$  diagonal matrix elements are somewhat arbitrary, and one should determine them by improving the approximation for the off-diagonal elements:

$$\langle k' | V_{\ell}^{jST} | k \rangle = 4\pi \int j_{\ell}(k'r) V_{\ell}^{jST}(r) j_{\ell}(kr) r^2 dr \quad (2.20)$$

They assumed a functional shape for  $V_{\ell}^{jST}$  and changed the parameters in such a way as to fit the following data:

- (a) The diagonal G matrix elements in the Fermi sea.
- (b) The Negele force in the  $r$ -space, except for  $r \leq 0.4$  fm.
- (c) The OPEP-potential for large values of  $r$ .

The reason for the second requirement was that Negele's force probably reproduces the off-diagonal matrix elements on the average well enough.

No matter which way one defines the effective interaction in nuclear matter, when one wishes to use this effective force in finite nuclei, an extension for a medium with different neutron and proton Fermi momenta is necessary. It is reasonable to assume, as was pointed out by Brueckner and Dąbrowsky [14], that the proton-proton and neutron-neutron interaction contributions to the G-matrix elements should be evaluated from the nuclear-matter calculations at  $k_F = k_p$  and  $k_N$ , respectively, while the neutron-proton interaction is to be taken at

$$k_A = \left( \frac{k_N^2 + k_p^2}{2} \right)^{1/2} \quad (2.21)$$

where  $k_N$  is the neutron,  $k_p$  the proton Fermi momentum. There are other alternative proposals instead of relation (2.21): Sprung [3] and Siemens [1] proposed

$$k_A = \left( \frac{k_N^3 + k_p^3}{2} \right)^{1/3} \quad (2.21a)$$

while one can take also the simple geometrical mean

$$k_A = (k_N \cdot k_p)^{1/2} \quad (2.21b)$$

With this last assumption, the effective force can be written as [7]

$$g_{\tau\tau'}^{ST} = g^{ST}(r, \sqrt{k_{F\tau} k_{F\tau'}}, W) \quad (2.22)$$

where  $\tau$  and  $\tau'$  mean neutrons and protons, respectively.

### 3. DEFINITION ON EFFECTIVE FORCES IN FINITE NUCLEI

In finite nuclei, one wants to define an effective interaction similarly to that used in nuclear matter. In a finite nucleus, the density is not

constant but a function of the radius. One may, however, assume that an effective finite nuclear interaction can be evaluated at a given local density in the same way as in nuclear matter. This approximation is called the local density approximation.

The validity of the local density approximation has not yet been checked quantitatively. The assumption that the approximation can be applied is motivated by the fact that the two-body correlations are relatively short-range compared to the range of nuclear forces and nuclear sizes. The effective forces defined in expression (2.14) go over into the bare two-body forces at large distances, and only for short distances ( $r \leq 1$  fm) do they differ from them significantly. It is thus reasonable to assume that, at a given point, the short-range interactions of two particles are influenced only by the local density, and they are not too sensitive to the behaviour of the wave-functions far from the place of the interaction. The approximation is better in the centre of the nucleus than at the surface where the density changes rapidly.

Accepting the validity of the local density approximation it is easy to show [6] that the effective finite nuclear interaction has the same functional form as the infinite nuclear matter interaction. Let us denote by  $\phi_{NL}$ , the relative finite nuclear wavefunctions and by  $R_{NL}(r)$  their radial parts. The central  $G_F$ -matrix elements for a finite nucleus are then given by [6]

$$\begin{aligned} \langle \phi_{NL} | G_F^{ST} | \phi_{N'L} \rangle &= \sum_{kk'} \langle \phi_{NL} | \phi_k \rangle \langle \phi_k | G_F^{ST} | \phi_{k'} \rangle \langle \phi_{k'} | \phi_{N'L} \rangle \\ &= \int d\mathbf{d} d\mathbf{d}' d\mathbf{r}'' \sum_{kk'} R_{NL}(r) j_L(kr) j_L(kr'') v_L^{ST}(r'') u_L^{ST}(r'', k') j_L(k'r') R_{N'L}(r') \\ &= \int dr dr' R_{NL}(r) R_{N'L}(r) V_L^{ST}(r, k_F, \omega) \end{aligned} \quad (3.1)$$

where  $V_L^{ST}$  is the effective force

$$V_L^{ST}(r, k_F, \omega) = v_L^{ST} f_L^{ST}(r, k_F, \omega) \quad (3.2)$$

and  $f_L$  is defined in expression (2.11a).

As one sees from expression (3.1), the local density approximation consists in substituting the finite  $G_F$ -matrix operator

$$G_F^{ST} = v^{ST} - \sum_{NL}^{(ST)} v^{ST} | \phi_{NL} \rangle \langle \phi_{NL} | \left| \frac{Q}{e_F} \right| | \phi_{NL} \rangle \langle \phi_{NL} | G^{ST} \quad (3.3)$$

by its nuclear matter value:

$$G_{NM}^{ST} = v^{ST} - \sum_k^{(ST)} v^{(ST)} | \phi_k \rangle \langle \phi_k | \left| \frac{Q}{e_{NM}} \right| | \phi_k \rangle \langle \phi_k | G^{ST} \quad (3.3a)$$

The most serious approximation in this substitution is the starting-energy problem. In the energy denominators  $e$ , one has the finite nuclear and the infinite nuclear-matter single-particle energies, respectively. The single-particle energies, however, differ widely from each other in the two cases. To take into account this difference, one has to use different starting energies for finite nuclei and for nuclear matter.

Another approximation which is introduced by using expression (3.3a) instead of expression (3.3) is the approximation of the Pauli operator  $Q$  by its nuclear-matter value. Wong has shown [15] in his calculations that the error introduced is not too significant.

As a result of the local density approximation one can define a finite nuclear effective force which has the same functional dependence on the local density and the starting energy as the nuclear-matter one, given by (2.18). The method for evaluating expression (2.18) at a given local density is, however, not unique. The local density in the effective force can be chosen in various ways, such as the density of the centre-of-mass position of the interacting nucleons, the arithmetic mean density between the two local densities corresponding to the two interacting particles [3] or the geometrical mean between them [7]. The last two forms are more convenient for computational purposes. Using the last assumption we can write the final effective force as

$$\mathcal{G}_{\tau\tau'}^{ST} = \mathcal{G}_{\tau\tau'}^{ST}(r, \omega_{\tau\tau'}, [k_{\tau}(r_1)k_{\tau'}(r_1)k_{\tau}(r_2)k_{\tau'}(r_2)]^{1/2}) \quad (3.4)$$

where the local Fermi momentum  $k_{F\tau}(r)$  is defined by the local density

$$k_{F\tau}(r) = [3\pi^2 \rho_{\tau}(r)]^{1/3} \quad (3.5)$$

and  $\omega_{\tau\tau'}$  is the starting energy.

#### 4. RENORMALIZATION AND STARTING-ENERGY CORRECTION

To deduce a nuclear effective force in a finite nucleus one has to start from nuclear-matter calculations. Present nuclear calculations, however, as mentioned above, underestimate the value of the nuclear-matter binding energy by 2.5 - 4.5 MeV. Since the higher-order corrections to finite nuclear energies are determined in the same way as in nuclear matter, a similar underestimation is to be expected. To avoid this error, Bethe [5, 17] proposed the renormalization of the effective interaction so as to obtain 16 MeV binding energy per particle in nuclear matter. If one renormalizes the force to give greater binding energy, the saturation density tends to increase. To obtain an unchanged saturation density one has to adjust the density dependence of the interaction simultaneously. Sprung and Banerjee [3] found that a convenient form for writing this renormalization is the following:

$$g^{ST}(r, k_F) = [1 - \alpha^{ST} F(r)] g_0^{ST}(r) + [1 - \beta^{ST} F(r)] g_1^{ST}(r) [k_F^{\lambda} - 1.36^{\lambda}] \quad (4.1)$$

where  $\lambda$  characterizes the density dependence of the force, and  $g_0$  and  $g_1$  are the density-independent and the density-dependent parts of the forces

$$g^{ST}(r, k_F) = g_0^{ST}(r) + g_1^{ST}(r) [k_F^\lambda - 1.36^\lambda] \quad (4.2)$$

$F(r)$  is an operator projecting into the short-range part of the forces and  $\alpha, \beta$  are the density-independent and density-dependent renormalization parameters. Since we believe that the long-range parts of the effective forces are fairly well known and the value of the short-range correlation is uncertain in nuclear-matter calculations, we want to renormalize the short-range forces only. One of the  $\alpha, \beta$  parameters is adjusted to obtain the correct binding, the other parameter to obtain the required saturation densities. For more sophisticated calculations one can use different  $\alpha^{ST}, \beta^{ST}$  values, reproducing the correct symmetry energy with them.

The adjustment of the renormalization parameters is somewhat arbitrary. One cannot avoid this difficulty: the contributions of some higher-order interactions are unknown even for the simple nuclear-matter case. Probably less arbitrariness is involved if we require that the nuclear-matter saturation density and symmetry energy remain unchanged by adding this missing part. There are, of course, no definite reasons for making this assumption, and Negele arbitrarily changed the saturation density to achieve better agreement with the experiments. In this way, however, he had to choose a very large  $\beta$ -value, as Sprung and Banerjee [3] have pointed out. In the next section, we shall give a renormalization method which seems to be slightly less arbitrary than other procedures.

The other question which we have to consider in detail is that of the starting-energy correction. Negele [6] has observed that a significant part of the density dependence of the G-matrix is, in fact, its starting-energy dependence. In nuclear matter, the starting-energy dependence can easily be transformed to density dependence since the starting energy can be expressed in terms of Fermi momentum. In finite nuclei, this correspondence is not so clear. Negele calculated the effective interaction at different densities but with a fixed starting energy, separating thereby the starting energy and density dependence of the g-matrix elements.

Another way of defining the starting-energy correction as proposed by many authors [3, 5, 7, 16] is through the BBP-integral equation. According to Bethe, Brandow and Petschek (BBP) [18], the g-matrix at a given starting energy  $\omega$  can be expressed by the matrix at another starting energy  $W$  through the equation

$$g(\omega) = g(W) + g(W) + \left( \frac{Q}{e(W)} - \frac{Q}{e(\omega)} \right) g(\omega) \quad (4.3)$$

which gives the relation between the g-matrix elements

$$\langle kk' | G(\omega) | kk' \rangle = \langle kk' | G(W) | kk' \rangle + \langle \chi_{kk'} | e(\omega) - e(W) | \chi_{kk'} \rangle \quad (4.4)$$

where

$$\chi_{kk'} = \phi_{kk'} - \Psi = \frac{Q}{e} G \phi_{kk'} \quad (4.5)$$

is the defect wave-function. Taking into account that  $e(W) = H_0 - W$ , and assuming that the difference between the starting energies is state-independent, expression (4.4) can be written as

$$\langle kk' | G(\omega) | kk' \rangle = \langle kk' | G(W) | kk' \rangle - (\bar{\omega}' - \bar{W}) \langle \chi_{kk'} | \chi_{kk'} \rangle \quad (4.6)$$

Sprung and Banerjee proposed the use of Eq. (4.6) for defining a correction to the effective force,

$$\dot{V}(r, \omega) = V(r, \bar{\omega}) - (\bar{\omega} - \overline{\bar{\omega}}) V^{(2)}(r) \quad (4.7)$$

where

$$V_{L'L}^{(2)JS}(r) = \frac{\sum_{L''} \chi_{L''L}^{JS}(r, k) \chi_{L''L}^{JS}(r, k)}{r^2 j_{L''}(kr) j_L(kr)} \quad (4.8)$$

is analogous to the effective forces defined in Eq. (2.10). All the averages can be carried out over  $k$  and  $L$ ,  $J$  as discussed above. They found that a  $\delta$ -function is a good approximation for  $V^{(2)}$ .

However, the question of what is the best approximation for the  $\bar{\omega} - \overline{\bar{\omega}}$  average starting-energy difference in finite nuclei and in nuclear matter still remains to be solved. One must be sure to use the same-single particle energies in both cases, i. e. one either includes the rearrangement terms both in nuclear matter and in finite nuclei, or one omits them in both cases.

Kohler estimated the difference  $\bar{\omega} - \overline{\bar{\omega}}$  in the two cases [19] and he found that the numerical values are very near to each other. Since it is more convenient to include the rearrangement terms in the finite nuclear single-particle potentials one generally includes them in evaluating the difference (4.7).

Another method of taking into account the starting energy will be given in the following section.

## 5. SEPARATION OF VOLUME AND RESIDUAL SURFACE TERMS OF POTENTIAL ENERGY

The effective forces deduced in the previous sections reproduce the infinite G-matrix elements as far as possible. In the following we shall proceed in a different way, i. e. we want to use the nuclear-matter calculations as far as possible and consider the finite nuclei as nuclear matter with some corrections due to the finite size of the nucleus. The procedure has the advantage that all errors introduced in the deduction of the effective force are of only secondary importance since they occur only in a correction term, the bulk of the effective force coming from the exact nuclear-matter calculations without any approximation. The outline of this section follows section 4 of Ref. [7].

Following an idea of Bethe [5] we separate the total potential energy into a volume term, which is completely determined from nuclear-matter calculations and a residual term which we call the residual surface term (RST). The first expression accounts for most of the potential energy while the second term vanishes for a constant-density system. It contains both a residual surface energy (RSE) and a starting-energy correction (STE). In the following we shall restrict ourselves to nuclei which have the same neutron and proton orbits and which have spin-saturated closed shells.

The generalization to nuclei with different neutron and proton orbits and spin-unsaturated shells can be found in Ref. [7].

Let

$$\left. \begin{aligned} \rho(\vec{r}_1, \vec{r}_2) &= \sum_{\alpha} \varphi_{\alpha}^*(\vec{r}_1) \varphi_{\alpha}(\vec{r}_2) \\ \rho(\vec{r}) &= \sum_{\alpha} |\varphi_{\alpha}(\vec{r})|^2 \end{aligned} \right\} \quad (5.1)$$

be the mixed and total densities of the Hartree-Fock state, respectively.

We define a nuclear-matter potential-energy density

$$\begin{aligned} D[\rho(r_1), \omega(r_1)] &= \frac{1}{2} \rho^2(r_1) \int d\vec{r}_2 g^D[r, k_F(r_1), \omega(r_1)] \\ &+ \frac{1}{2} \int d\vec{r}_2 |\rho_{NM}(\vec{r}_1, \vec{r}_2)|^2 g^X[r, k_F(r_1), \omega(r_1)] \end{aligned} \quad (5.2)$$

In expression (5.2) the direct and exchange interactions  $g^D$  and  $g^X$  are the following linear combinations of the effective interaction:

$$\left. \begin{aligned} g^D &= \frac{1}{16} \sum_{S,T} (2S+1)(2T+1) g^{ST} \\ g^X &= \frac{1}{16} \sum_{S,T} (2S+1)(2T+1)(-1)^{S+T+1} g^{ST} \end{aligned} \right\} \quad (5.3)$$

The nuclear-matter mixed density  $\rho_{NM}(\vec{r}_1, \vec{r}_2)$  is defined as

$$\rho_{NM}(\vec{r}_1, \vec{r}_2) = \rho(r_1) \frac{3j_1[k_F(r_1)r]}{(k_F(r_1)r)^3} \quad (5.4)$$

The energy density (5.2) is the potential energy per unit volume of nuclear matter at a density equal to the local density  $\rho(\vec{r}_1)$  and calculated with a starting energy  $\omega(r_1)$  in the effective interaction  $g$ . The starting energy  $\omega(r_1)$  is an average local starting energy of the finite nucleus which depends on the local density. The nuclear-matter potential energy can be determined from the equation:

$$D[\rho(r_1), \omega(r_1)] = \frac{1}{2\Omega} \sum_{k_1 \in k_F(r_1)} \sum_{k_2 \in k_F(r_1)} \langle k_1 k_2 | g[r_1, k_F(r_1), \omega(r_1)] | k_1 k_2 \rangle \quad (5.5)$$

where the sums over the plane waves include the spin and isospin variables. If one uses the nuclear-matter self-consistent starting energies instead of the finite nuclear ones the potential becomes independent of the starting energy and it is then defined as  $\tilde{D}[\rho(r_1)]$ .

The potential energy of a nucleus can be written as

$$\langle V \rangle = \frac{1}{2} \sum_{\alpha, \beta} \langle \alpha \beta | g(\epsilon_\alpha + \epsilon_\beta) | \alpha \beta \rangle \quad (5.6)$$

where  $g(\epsilon_\alpha + \epsilon_\beta)$  is the effective interaction calculated with self-consistent starting energies  $\epsilon_\alpha + \epsilon_\beta$  which we shall specify later on. We may write expression (4.6) in the following way:

$$\begin{aligned} \langle V \rangle = & \int d\vec{r} \tilde{D}[\rho(r)] + \left[ \frac{1}{2} \sum_{\alpha, \beta} \langle \alpha \beta | g(\epsilon_\alpha + \epsilon_\beta) | \alpha \beta \rangle - \int d\vec{r} D[\rho(r), \omega(r)] \right] \\ & + \int d\vec{r} \left\{ D[\rho(r), \omega(r)] - \tilde{D}[\rho(r)] \right\} = \int d\vec{r} \tilde{D}[\rho(r)] + (\text{RSE}) + (\text{STE}) \end{aligned} \quad (5.7)$$

The first term in (5.7) is the volume term, the second term represents the residual surface energy (RSE) while the last term is the starting-energy correction (STE).

As one sees from expressions (4.6) and (5.5) that the starting-energy correction can be written as

$$D[\rho, \omega_1] - D[\rho, \omega_2] = -(\bar{\omega}_1 - \bar{\omega}_2) \kappa(\rho) \rho / 2 \quad (5.8)$$

where the integral  $\kappa(\rho)$  is defined as

$$\kappa(\rho) = \frac{1}{\rho \Omega} \sum_{k_1 k_2} \langle \chi_{k_1 k_2} | \chi_{k_1 k_2} \rangle \quad (5.9)$$

Taking into account the fact that the starting energy is twice an average single-particle energy, and a single-particle energy is the sum of the single-particle kinetic and potential energy, we assume that the STE can be written as

$$\int d\vec{r} \left[ D[\rho(r), \omega(r)] - \tilde{D}[\rho(r)] \right] = - \int \left[ U_R^F(r) - U_R^{NM}(r) \right] \kappa[\rho(r)] \rho(r) d\vec{r} \quad (5.10)$$

where  $U_R^F$  is the finite  $U_R^{NM}$  the nuclear-matter single-particle energy, including the rearrangement terms.

The average finite single-particle potential is defined as the equivalent local potential

$$U^F(\vec{r}) = \sum_{\alpha} \varphi_{\alpha}^*(\vec{r}) \int d\vec{r}' U(\vec{r}, \vec{r}') \varphi_{\alpha}(\vec{r}') / \sum_{\alpha} \varphi_{\alpha}^*(\vec{r}) \varphi_{\alpha}(\vec{r}) \quad (5.11)$$

where  $U(\vec{r}, \vec{r}')$  is the non-local potential defined by the  $g$ -matrix as

$$\langle \alpha | U^F | \alpha \rangle = \sum_{\beta} \langle \alpha \beta | g(\epsilon_{\alpha} + \epsilon_{\beta}) | \alpha \beta \rangle \quad (5.12)$$

From relations (5.11) and (5.12) it follows, that

$$\int d\vec{r} \rho(r) \kappa[\rho(r)] U_R^F(r) = \sum_{\alpha\beta} \langle \alpha\beta | \kappa[\rho(r_1)] \left[ g(\epsilon_\alpha + \epsilon_\beta) + \frac{dg(\epsilon_\alpha + \epsilon_\beta)}{d\rho(r_1)} \rho(r_1) \right] \alpha\beta \rangle \quad (5.13)$$

The average nuclear-matter potential is defined as

$$U_R^{NM}(r_1) = \rho(r_1) \int d\vec{r}_2 \left[ g^D(r, k_F(r_1), \omega(r_1) + \rho(r_{11}) \frac{dg^D(r, k_F(r_1)\omega(r_1))}{d\rho(r_1)}) \right. \\ \left. + \int d\vec{r}_2 |\rho(\vec{r}_1, \vec{r}_2)|_{NM}^2 / \rho(r_1) \left[ g^X(r, k_F(r_1)\omega(r_1) \right. \right. \\ \left. \left. + \rho(r_1) \frac{dg^X(r, k_F(r_1)\omega(r_1))}{d\rho(r_1)} \right] \right] \quad (5.14)$$

and it has the property that

$$\rho(r) \kappa[\rho(r)] U_R^{NM}(r) = 2\kappa[\rho(r)] \rho(r) \left[ D[\rho(r), \omega(r)] + \delta D[\rho(r), \omega(r)] \right] \quad (5.15)$$

where  $\delta D[\rho(r), \omega(r)]$  is a similar expression as  $D$ , only that in expression (5.5) we substitute  $g[r, k_F(r_1), \omega(r_1)]$  by  $\rho(r_1) (dg[r, k_F(r_1), \omega(r_1)]/d\rho(r_1))$ .

With Eqs (5.13) and (5.15) we find the following expression for the starting-energy correction (5.10):

$$(STE) = - \sum_{\alpha\beta} \langle \alpha\beta | \kappa(\rho(r_1)) \left[ g(\epsilon_\alpha + \epsilon_\beta) + \frac{dg(\epsilon_\alpha + \epsilon_\beta)}{d\rho(r_1)} \rho(r_1) \right] + \alpha\beta \rangle \\ + \int d\vec{r}_1 2\kappa(\rho(r_1)) \left[ D[\rho(r_1), \omega(r_1)] + \delta D[\rho(r_1), \omega(r_1)] \right] \quad (5.16)$$

Including expression (5.16) into the second expression (5.7) we obtain

$$\langle V \rangle = \int d\vec{r} \tilde{D}[\rho(r)] + \frac{1}{2} \sum_{\alpha\beta} \langle \alpha\beta | \left\{ \left( 1 - 2\kappa(\rho(r_1)) \right) g(\epsilon_\alpha + \epsilon_\beta) \right. \right. \\ \left. \left. - 2\kappa(\rho(r_1)) \frac{dg(\epsilon_\alpha + \epsilon_\beta)}{d\rho(r_1)} \rho(r_1) \right\} | \alpha\beta \rangle \right. \\ \left. - \int d\vec{r} \left[ \left( 1 - 2\kappa(\rho(r)) \right) D[\rho(r), \omega(r)] - 2\kappa(r) \delta D[\rho(r), \omega(r)] \right] \right. \\ \left. = \int d\vec{r} \tilde{D}[\rho(r)] + (RST) \quad (5.17)$$

where the second expression (5.17) represents the residual surface term.

To evaluate the residual surface term we first approximate it by replacing the effective interaction  $g(\epsilon_\alpha + \epsilon_\beta)$  by the effective interaction  $\tilde{g}$  calculated with nuclear matter self-consistent energies and likewise the potential-energy density  $D$  by  $\tilde{D}$ . This can be done in two steps. First, we replace  $g(\epsilon_\alpha + \epsilon_\beta)$  by  $g(\omega(r))$ , i. e. we replace the starting energy by an average local starting energy. In the second step, we replace in both terms of the (RST) the starting energy  $\omega(r)$  by the nuclear-matter self-consistent starting energy. This may be justified by the fact that the (RST) is sensitive to the long-range part of the effective interaction  $V^D, V^X$  only. For short-range force the RST term vanishes as can be seen from expression (5.18). Since we mentioned in section 4 that a small change in the starting energy may be replaced by a short-range interaction, it is clear from the above argument that the (RST) is not sensitive to the starting energy used in the effective interaction:

$$\begin{aligned}
 (\text{RST}) &= \frac{1}{2} \sum_{\alpha\beta} \langle \alpha\beta | [1 - 2\kappa(\rho(r_1))] \tilde{g} | \alpha\beta \rangle - \int d\vec{r} [1 - 2\kappa(\rho(r))] \tilde{D}[\rho(r)] \\
 &= \frac{1}{2} \int d\vec{r}_1 d\vec{r}_2 \left\{ \rho(r_1)\rho(r_2) V^D[r, \rho(r_1); \rho(r_2)] \right. \\
 &\quad \left. - \rho(r_1)^2 V^D[r, \rho(r_1), \rho(r_1)] \right\} \\
 &\quad + \frac{1}{2} \int d\vec{r}_1 d\vec{r}_2 \left\{ |\rho(\vec{r}_1, \vec{r}_2)|^2 V^X[r, \rho(r_1), \rho(r_2)] \right. \\
 &\quad \left. - |\rho_{\text{NH}}(\vec{r}_1, \vec{r}_2)|^2 V^X[r, \rho(r_1), \rho(r_1)] \right\} \tag{5.18}
 \end{aligned}$$

where  $V^D$  and  $V^X$  are the effective interactions defined as

$$\begin{aligned}
 V^D[r, \rho(r_1), \rho(r_2)] &= [1 - 2\kappa[\rho(r_1)]] \tilde{g}^D[r, k_F(r_1), k_F(r_2)] \\
 &\quad - 2\kappa[\rho(r_1)] \rho(r_1) \frac{d\tilde{g}^D[r, k_F(r_1), k_F(r_2)]}{d\rho(r_1)} \\
 V^X[r, \rho(r_1), \rho(r_2)] &= [1 - 2\kappa[\rho(r_1)]] \tilde{g}^X[r, k_F(r_1), k_F(r_2)] \\
 &\quad - 2\kappa[\rho(r_1)] \rho(r_1) \frac{d\tilde{g}^X[r, k_F(r_1), k_F(r_2)]}{d\rho(r_1)} \tag{5.19}
 \end{aligned}$$

As we have pointed out before, the inclusion of the rearrangement terms in expression (5.19) is not necessary. Since they are always multiplied by  $\rho$ , they act mostly in the high-density region in which the difference  $U^F - U^{\text{NM}}$  is small. They contribute only little to the starting-energy correction and to the (RST). The starting-energy correction used this way differs from that of Negele [6] but agrees with that given by Sprung and Banerjee [3].

Equations (5.17) and (5.18) provide a convenient way of writing the potential energy in terms of a single effective interaction  $\mathcal{V}^{D,X}$

$$\langle V \rangle = \frac{1}{2} \int d\vec{r}_1 d\vec{r}_2 \left\{ \rho(r_1) \rho(r_2) \mathcal{V}^D + |\rho(\vec{r}_1, \vec{r}_2)|^2 \mathcal{V}^X \right\} \quad (5.20)$$

where

$$\mathcal{V}^{D,X} = \frac{1}{2} \Gamma(r_1, \rho(r_1)) \delta(\vec{r}_1 - \vec{r}_2) + V^{D,X}[r, \rho(r_1), \rho(r_2)] \quad (5.21)$$

$$\Gamma[r_1, \rho(r_1)] = 2\tilde{D}[\rho(r_1)]/\rho(r_1)^2 - \int d\vec{r}_2 V^D[r, \rho(r_1), \rho(r_1)] \\ - \int d\vec{r}_2 \left[ |\rho_{NM}(\vec{r}_1, \vec{r}_2)|^2 / \rho(r_1)^2 \right] V^X[r, \rho(r_1), \rho(r_1)] \quad (5.22)$$

Equations (5.19), (5.21) and (5.22) define an effective force for finite nuclear calculations.  $\tilde{D}$ ,  $\tilde{g}$  and  $\kappa$  can be determined from nuclear-matter calculations. Since  $V^{D,X}$  acts in the (RST)-term, which vanishes for very-short-range forces, one can define  $V^{D,X} = 0$  for  $r < d$ , where  $r = d$  is a cut. A reasonable value for  $d$  is somewhere between 0,6 and 1 fm.

Equation (5.17) supplies a direct method for the renormalization discussed in section 4. The potential energy is divided into two parts: one is the nuclear-matter energy density – as the function of  $\rho(r)$  – and the other one is the (RST)-term which vanishes for small distances. Since the renormalization is due to the short-range contributions, one does not change the long-range forces, i. e. the (RST)-term, at all, only the nuclear-matter energy-density function is changed in such a way as to supply good infinite nuclear-matter binding. There is, of course, still an arbitrariness as to how one changes the  $\tilde{D}(\rho)$ -function, but if one keeps the saturation density and the symmetry energy fixed, this exact shape of the  $\tilde{D}(\rho)$ -function does not influence the results too much.

## 6. HARTREE-FOCK EQUATIONS WITH DENSITY-DEPENDENT FORCES

In the previous sections, a density-dependent effective interaction has been derived with the help of the local density approximation. We now wish to determine the orbit wave-functions by using a variational principle, i. e. by minimizing the total energy. The total energy can be written as

$$E = \sum_{\alpha} \langle \alpha | t | \alpha \rangle + \frac{1}{2} \sum_{\alpha, \beta} \langle \alpha \beta | \mathcal{V}(\rho) | \alpha \beta - \beta \alpha \rangle \quad (6.1)$$

where  $t$  is the single-particle kinetic energy. Expanding the orbits  $\alpha$  in the orthonormal basis system

$$\varphi_{\alpha} = \sum_i c_i \alpha \varphi_i \quad (6.2)$$

the variational principle yields the equations

$$\frac{\partial}{\partial c_i^{\alpha*}} \left[ E - e_\alpha \sum_i c_i^* c_i \right] = 0 \quad (6.3)$$

Differentiating expression (6.1) as a function of  $c_i^\alpha$  one has to take into account the fact that because of relations (5.1) and (6.2)  $\mathcal{V}_{\text{eff}}$  depends on the  $c_i^\alpha$  coefficients too. Equations (6.3) yield the Hartree-Fock (HF) equations [20]:

$$\sum_j \langle i | h | j \rangle c_j^\alpha = e_\alpha c_i^\alpha \quad (6.4)$$

where  $h$  is the Hartree-Fock Hamiltonian, given by its matrix elements

$$h_{ij} = \langle i | t | j \rangle + \sum_\alpha \langle i\alpha | \mathcal{V}(\rho) | j\alpha - \alpha j \rangle + \frac{1}{2} \sum_{\alpha\beta} \langle \alpha\beta | (\varphi_i^* \varphi_j) \frac{d\mathcal{V}(\rho)}{d\rho} | \alpha\beta - \beta\alpha \rangle \quad (6.5)$$

The diagonal elements of Eq. (6.4) yield the HF-equations:

$$\langle \alpha | t | \alpha \rangle + \sum_\lambda \langle \alpha\lambda | v | \alpha\lambda \rangle + \frac{1}{2} \sum_{\lambda\mu} \langle \lambda\mu | \delta\rho_\alpha \frac{d\mathcal{V}(\rho)}{d\rho} | \lambda\mu \rangle = e_\alpha \quad (6.6)$$

In these equations we have omitted the spin and isospin indices.

In Eq. (6.5) we have included the rearrangement terms in the definition of the single-particle energies. A variational principle automatically yields such a single-particle potential; however, the use of a variational principle is not warranted by the present theory. Assuming the local density approximation to be exact, a strict application of Brueckner theory in the finite nucleus would amount to a use of Eq. (6.5) without its last term. The inclusion of the rearrangement terms in the HF-field, however, seems physically reasonable and successful. Not only does it yield good binding energies and single-particle separation energies, but it also considerably improves the charge distributions observed in elastic scattering, which suggests that it gives an improved shell-model potential.

Another argument in favour of including the rearrangement terms in the HF-field is that, in this case, the eigenenergies of the HF-Hamiltonians are equal to the nucleon separation energies [20]:

$$\begin{aligned} S_\alpha &= E_{A+1} - E_\alpha = \langle \phi | a_\alpha H(\rho + \delta\rho_\alpha) a_\alpha^\dagger | \phi \rangle - \langle \phi | H(\rho) | \phi \rangle \\ &= \langle \phi | a_\alpha \delta\rho_\alpha \frac{d\mathcal{V}(\rho)}{d\rho} a_\alpha^\dagger | \phi \rangle + \langle \phi | a_\alpha H(\rho) a_\alpha^\dagger | \phi \rangle - \langle \phi | H(\rho) | \phi \rangle \\ &= \langle \alpha | t | \alpha \rangle + \sum_\lambda \langle \alpha\lambda | \mathcal{V} | \alpha\lambda \rangle + \frac{1}{2} \sum_{\lambda\mu} \langle \lambda\mu | \delta\rho_\alpha \frac{d\mathcal{V}(\rho)}{d\rho} | \lambda\mu \rangle \end{aligned}$$

$$+ \sum_{\lambda} \langle \alpha \lambda | \delta \rho_{\alpha} \frac{d\mathcal{V}(\rho)}{d\rho} | \alpha \lambda \rangle \quad (6.7)$$

Here  $a_{\alpha}$  and  $a_{\alpha}^{\dagger}$  are the absorption and creation operators of a nucleon, respectively, and

$$H(\rho + \delta \rho_{\alpha}) = H(\rho) + \delta \rho_{\alpha} \frac{d\mathcal{V}(\rho)}{d\rho} \quad (6.8)$$

is the modified Hamiltonian. Neglecting the last term which represents the change in the interaction of the extra nucleon with the core nucleons due to its own density, expression (6.7) can be rewritten, with the help of relation (6.6), as

$$S_{\alpha} = e_{\alpha} \quad (6.9)$$

The inclusion of the rearrangement term in the single-particle potential solves the usual contradiction in the HF-calculations. Without rearrangement energies, the total HF-energy of a nucleus is

$$E = \frac{1}{2} \sum_{\alpha} \left[ \langle \alpha | t | \alpha \rangle + e_{\alpha} \right] \quad (6.10)$$

The single-particle energies  $e_{\alpha}$  can be determined experimentally. The different models yield very similar kinetic energies, so that we can determine the right-hand side of Eq. (6.10), which differs, however, significantly from the experimental total energy of a nucleus. Including the rearrangement terms, Eq. (6.10) can be written as

$$E = \frac{1}{2} \sum_{\alpha} \left[ \langle \alpha | t | \alpha \rangle + e_{\alpha} \right] - \frac{1}{2} \sum_{\alpha} \langle \phi | \delta \rho_{\alpha} \frac{d\mathcal{V}}{d\rho} | \phi \rangle \quad (6.11)$$

i. e. one can obtain both good single-particle and total energies.

The eigenstates of the HF-Hamiltonian are obtained by solving the HF-integro-differential equations in co-ordinate space by the method used by Vautherin [21]. We shall outline his derivation in the following:

Let us, in a doubly-closed-shell nucleus, denote by  $\alpha$ , the quantum-number set  $n_{\alpha} \ell_{\alpha} j_{\alpha} m_{\alpha}$  and  $\tau_{\alpha}$ , where  $\tau_{\alpha}$  means the nucleon charge. The radial wave-function  $u_{\alpha}$  of orbit  $\alpha$  depends on  $n_{\alpha} \ell_{\alpha} j_{\alpha}$  and  $\tau_{\alpha}$ . The neutron or proton density is given by

$$\rho_{\tau}(\mathbf{r}) = \frac{1}{4\pi r^2} \sum_{\alpha}^{(\tau, m)} (2j_{\alpha} + 1) u_{\alpha}^2(r) \quad (6.12)$$

where  $\sum_{\alpha}^{(\tau, m)}$  means a sum over all the quantum numbers of the occupied

TABLE I. ENERGIES AND CHARGE ROOT-MEAN-SQUARE RADII OF SPHERICAL NUCLEI FROM FIVE DIFFERENT CALCULATIONS AND THE EXPERIMENT

	$^{16}\text{O}$		$^{40}\text{Ca}$		$^{48}\text{Ca}$		$^{90}\text{Zr}$		$^{208}\text{Pb}$	
	E/A	$r_c$	E/A	$r_c$	E/A	$r_c$	E/A	$r_c$	E/A	$r_c$
Ref.[6]	-6.75	2.83	-7.49	3.51	-7.48		-7.85		-7.53	
Ref.[22]	-7.73	2.76	-8.32	3.45	-7.87	3.52	-8.07	4.23	-7.31	5.44
Ref.[23]	-8.22	2.68	-8.64	3.41	-8.93	3.46	-8.81	4.22	-7.89	5.44
Ref.[2]	-3.84	2.61	-4.20	3.12	-3.73	3.14				
Ref.[24]	-6.05	2.77	-6.43	3.52	-6.10	3.60	-6.28	4.32	-5.52	5.50
Experimental value	-7.98	2.70	-8.55	3.50	-8.67	3.49	-8.71	4.30	-7.87	5.45

orbits except  $\tau$  and  $m$ . The density due to orbits with quantum numbers  $S_\alpha \equiv \ell_\alpha, j_\alpha, \tau_\alpha$  is thus written as

$$\rho_{s_\alpha}^{(r)} = \frac{1}{r^2} \sum_{n_\alpha} u_\alpha^2(r) \quad (6.13)$$

while the corresponding mixed density is

$$\rho_{s_\alpha}(r, r') = \frac{1}{rr'} \sum_{n_\alpha} u_\alpha(r) u_\alpha(r') \quad (6.14)$$

The radial wave-function  $u_\alpha$  satisfies the HF-equation

$$\frac{\hbar^2}{2m} \left[ -u_\alpha''(r) + \frac{\ell_\alpha(\ell_\alpha + 1)}{r^2} u_\alpha(r) \right] + \int_0^\infty rr' H_{s_\alpha}(r, r') u_\alpha(r') dr' = e_\alpha u_\alpha(r) \quad (6.15)$$

where the HF-potential  $H_{s_\alpha}$  has a local direct and a non-local exchange term:

$$H_{s_\alpha}(r, r') = \frac{1}{r^2} H_{r_\alpha}^D(r) \delta(r - r') + H_{s_\alpha}^X(r, r') \quad (6.16)$$

The calculation of  $H_{s_\alpha}(r, r')$  can be found in Ref. [21] for density-independent forces. In the case of density dependence the only change is that one has always to add the rearrangement terms to the different components of the potential energy. Reference [7] gives the detailed formula for density-dependent effective forces.

Finally, one has to include the Coulomb interaction and a single-particle spin-orbit field, in the HF-equation (6.15) as it was done in Ref. [21]. The equations can be solved by the method of equivalent local potentials proposed by Vautherin [21].

## 7. RESULTS WITH DIFFERENT DENSITY-DEPENDENT EFFECTIVE FORCES

In Table I we collect the results of different calculations for spherical nuclei. The following calculations are compared:

1. Negele [6],
2. Németh and Vautherin [22],
3. Vautherin and Brink [23],
4. Davies, Baranger, Tarbuton and Kuo [2],
5. Vautherin and Veneroni [24].

The first two of these authors use density-dependent effective forces deduced from nuclear-matter calculations employing the Reid soft-core potentials [25] with the help of the local density approximation. The third author uses the Skyrme force [9], i. e. a density-dependent  $\delta$ -force. The calculation of Vautherin and Veneroni used the Brink [26] interaction which

does not depend on density,<sup>3</sup> while the calculation of Davies et al. is a Brueckner-Hartree-Fock (BHF) calculation in which the  $g$ -matrix elements are self-consistently calculated in the finite nucleus. It does not include rearrangement terms.

The results of each of the density-dependent calculations are similar, giving binding energies and root-mean-square radii close to the experimental values. The BHF-calculation gives too small binding energy and too small radii, while the Brink interaction gives good radii but generally underestimates the binding energy of the nuclei.

## REFERENCES

- [1] SIEMENS, P., Nucl. Phys. A141 (1970) 225 and references therein.
- [2] DAVIES, K.R.R., BARANGER, M., TARBUTTON, R.M., KUO, T.T.S., Phys. Rev. 177 (1969) 1519 and references therein.
- [3] SPRUNG, P.W.L., BANERJEE, P.K., to be published.
- [4] BRUECKNER, K.A., GÄMMEL, J.L., WEITZNER, H., Phys. Rev. 110 (1958) 431.
- [5] BETHE, H.A., Phys. Rev. 167 (1968) 879.
- [6] NEGELE, J.W., Phys. Rev. C1 (1970) 1260.
- [7] NÉMETH, J., RIPKA, G., to be published.
- [8] NÉMETH, J., VAUTHERIN, D., Phys. Letts 32B (1970) 561.
- [9] SKYRME, T.H.R., Nucl. Phys. 9 (1959) 615.
- [10] VAUTHERIN, D., BRINK, D.M., Phys. Letts 32B (1970) 149.
- [11] BRANDOW, B.H., in Proceedings of the International Summer School of Physics "Enrico Fermi" Course 36, Academic Press, New York (1966).
- [12] BANERJEE, P.K., SPRUNG, D.W.L., to be published.
- [13] ELLIOT, J.P., MAVROMATIS, H.A., SANDERSON, E.A., Phys. Letts 24B (1967) 358; SRIVASTAVA, M.K., JOPKO, A.M., SPRUNG, D.W.L., Can. J. Phys. 47 (1969) 2459; MAVROMATIS, H.A., SCHLCHER, K., J. Math. Phys. 9 (1968) 1627.
- [14] BRUECKNER, K.A., DABROWSKI, J., Phys. Rev. 134 (1964) 8722.
- [15] WONG, C.W., Nucl. Phys. A91 (1967) 399.
- [16] NÉMETH, J., Acta Phys. Hung., to be published.
- [17] NÉMETH, J., BETHE, H.A., Nucl. Phys. A116 (1968) 241.
- [18] BETHE, H.A., BRANDOW, B.H., PETSCHER, A.G., Phys. Rev. 129 (1963) 225.
- [19] KÖHLER, H.S., Nucl. Phys. A128 (1969) 273.
- [20] RIPKA, G., Fast Neutrons and Nuclear Structure, to be published by Gordon and Breach.
- [21] VAUTHERIN, D., in Theory of Nuclear Structure, (Proc. Trieste lectures, 1969) IAEA, Vienna, 767.
- [22] NÉMETH, J., VAUTHERIN, D., Phys. Letts 32B (1970) 561.
- [23] VAUTHERIN, D., BRINK, D.M., Phys. Letts 32B (1970) 149.
- [24] VAUTHERIN, D., VENERONI, M., Phys. Letts 25B (1967) 175.
- [25] REID, R.V., Ann. Phys., New York 50 (1968) 411.
- [26] BRINK, D.M., BOEKER, E., Nucl. Phys. A91 (1967)
- [27] ZOFKA, J., RIPKA, G., Phys. Letts 34B (1971) 10.

## PART II: NUCLEAR STRUCTURE

### 2. Shell-model configuration mixing



# MICROSCOPIC DESCRIPTION OF THE 2p-1f SHELL NUCLEI

A. RIMINI

Istituto di fisica teorica,  
Università di Trieste,  
Trieste, Italy

## Abstract

### MICROSCOPIC DESCRIPTION OF THE 2p-1f SHELL NUCLEI.

The construction is described, from a smooth nucleon-nucleon interaction, of an effective Hamiltonian suitable for shell-model calculations in the complete 2p-1f shell of  $^{56}\text{Ni}$  and the nuclei around. A preliminary application to  $^{56}\text{Ni}$  is made, using a 2p-2h approximation.

## 1. SOME PROBLEMS IN THE 2p-1f SHELL

We shall describe here some calculations which are being done by our group in the spirit of the shell model with configuration mixing for the nuclei in the middle of the 2p-1f shell, i. e.  $^{56}\text{Ni}$  and the nuclei around it. Some preliminary results have recently been published [1]. The interest of these calculations is, in my opinion, that they provide a simple (or simplified?) example of a consistent application of the concept of effective Hamiltonian. In the shell model with configuration mixing one assumes few shell-model single-particle (sp) levels as active or valence levels. For some of these levels it may be convenient to use a description in terms of holes. The Hamiltonian for the valence system is written

$$H^{\text{SM}} = \sum_{\alpha}^{\text{valence}} \bar{\epsilon}_{\alpha} : a_{\alpha}^{\dagger} a_{\alpha} : + \frac{1}{4} \sum_{\alpha\beta\gamma\delta}^{\text{valence}} \bar{V}_{\alpha\beta\gamma\delta} : a_{\alpha}^{\dagger} a_{\beta}^{\dagger} a_{\delta} a_{\gamma} : \quad (1)$$

where  $a_{\alpha}^{\dagger}$  is the creation operator of a nucleon in the "spherical" sp level  $\alpha$ . The Greek index  $\alpha$  summarizes the quantum numbers  $n, \ell, j, m$  and  $q$ , while Latin  $a$  will indicate  $n, \ell$  and  $j$  only. The condition of invariance under rotations in space and isospin space implies  $\bar{\epsilon}_{\alpha} = \bar{\epsilon}_a$  and

$$\begin{aligned} \bar{V}_{\alpha\beta\gamma\delta} &= \sum_{\substack{\text{IN} \\ \text{SV}}} \langle j_a m_{\alpha} j_b m_{\beta} | \text{IN} \rangle \langle j_c m_{\gamma} j_d m_{\delta} | \text{IN} \rangle \\ &\times \langle \frac{1}{2} q_{\alpha} \frac{1}{2} q_{\beta} | \text{SV} \rangle \langle \frac{1}{2} q_{\gamma} \frac{1}{2} q_{\delta} | \text{SV} \rangle \bar{G}(abcd | S) \end{aligned} \quad (2)$$

The symbol  $:\ :$  is relevant only if hole valence levels are present and means normal ordering with respect to the reference state in which all hole levels are occupied and all particle levels are empty. The single-particle energies  $\bar{\epsilon}_a$  and the interaction  $\bar{V}_{\alpha\beta\gamma\delta}$  are understood to be effective

in the sense that they contain corrections which compensate for the neglecting of the non-active core and upper levels. One of the aims of our calculations is to give a description as microscopic as possible of the nuclei under consideration. Therefore, we have tried to calculate all quantities appearing in expression (1) from the assumed nucleon-nucleon potential rather than attempting to determine them by fitting to the experimental data on the considered nuclei.

The interest in  $^{56}\text{Ni}$  arises from the studies of heavier nickel isotopes. These nuclei were treated extensively in the framework of the shell model by assuming a closed  $^{56}\text{Ni}$  core and distributing the remaining neutrons in the levels  $2p_{3/2}$ ,  $1f_{5/2}$ ,  $2p_{1/2}$  (and sometimes  $1g_{9/2}$ ). When this assumption is made, one is in a good position. First, the single-particle energies are easily determined in a phenomenological way. In fact, they are directly given by the levels of  $^{57}\text{Ni}$  since only the first term in expression (1) survives for this nucleus. Secondly, the subsequent shell-model problems involve only identical nucleons and are therefore rather easy to treat both in exact and in approximate form. The effective nucleon-nucleon interaction was either phenomenologically determined by fitting the experimental nuclear levels or microscopically derived from various nucleon-nucleon potentials. As a whole, these treatments had considerable success. Then one became curious about the  $^{56}\text{Ni}$  core: to what extent is it actually closed?  $^{56}\text{Ni}$  has an excited state at rather low energy (2.6 MeV), and  $^{57}\text{Ni}$  has an excited state indicated as an excitation from the  $1f_{7/2}$  level at approximately the same energy. Moreover, the neutron effective charges in nickel isotopes are large, indicating that protons play an important role in the low-lying states. The proposed question has a sense only if one includes the  $1f_{7/2}$  level among the valence levels. This has been done by several authors in the last few years [2].

The first problem met by such authors was that of the sp-energies  $\bar{\epsilon}_a$ . These quantities are not directly related to the levels of any nucleus, when the problem is treated in the complete  $2p-1f$  shell. For example, if one describes the  $1f_{7/2}sp$  level in terms of holes and the remaining levels in terms of particles, the energy levels of  $^{57}\text{Ni}$  are to be obtained by diagonalizing the Hamiltonian (1) in the space of all the  $n$ -hole  $(n+1)$ -particle states. Clearly, the  $\bar{\epsilon}_a$  values no longer coincide with the energy levels. The attitude assumed by the abovementioned authors was the following: the old values were assumed for  $\bar{\epsilon}_{3/2}$ ,  $\bar{\epsilon}_{5/2}$ ,  $\bar{\epsilon}_{1/2}$  lacking any better indication; the value of  $\bar{\epsilon}_{7/2}$  was treated as a parameter. The values of the  $\bar{\epsilon}_{3/2} - \bar{\epsilon}_{7/2}$  separation proposed by the various authors range from 1.5 to 5 MeV. The differences are probably due mainly to the different approximations to the exact shell model which were adopted. One can say, in our opinion, that the situation is not satisfactory.

Let us try to give a microscopic definition of the sp-energies to be used in a shell-model calculation of  $^{56}\text{Ni}$  and neighbouring nuclei in the  $2p-1f$  shell. We start by assuming a smooth N-N interaction. In our preliminary calculation we have used the Tabakin force with new  $^1P_1$  parameters [3]. One could equally well use an effective interaction deduced from a non-smooth potential as a consequence of the elimination of the very-high-lying levels (e.g. a reaction matrix or the Yale-Shakin force). We secondly assume that for all the nuclear states which we shall consider the following is a rough but reasonable approximation: a  $^{56}\text{Ni}$  core (in a spherical basis) plus few particles and/or holes in levels not too high or

deep lying. This assumption would be invalid in the case of strong deep deformation or in that of large superconductivity effect. One can then define the sp-energies which should be used if the non-active levels were completely negligible. The nuclear Hamiltonian in the second-quantized form is written

$$H = \sum_{\alpha\beta} T_{\alpha\beta} a_{\alpha}^{\dagger} a_{\beta} + \frac{1}{4} \sum_{\alpha\beta\gamma\delta} V_{\alpha\beta\gamma\delta} a_{\alpha}^{\dagger} a_{\beta}^{\dagger} a_{\delta} a_{\gamma} \quad (3)$$

Let

$$|\phi_0\rangle = \left( \prod_{\alpha}^{\text{hole}} a_{\alpha}^{\dagger} \right) |0\rangle \quad (4)$$

be the  $^{56}\text{Ni}$  reference state introduced above and put the Hamiltonian (3) in normal form with respect to such a state. We have

$$\begin{aligned} H &= H_0 + H_1 + H_2 \\ H_1 &= \sum_{\alpha\beta} \left( T_{\alpha\beta} + \sum_{\gamma}^{\text{hole}} V_{\alpha\gamma\beta\gamma} \right) : a_{\alpha}^{\dagger} a_{\beta} : = \sum_{\alpha\beta} \epsilon_{\alpha\beta} : a_{\alpha}^{\dagger} a_{\beta} : \\ H_2 &= \frac{1}{4} \sum_{\alpha\beta\gamma\delta} V_{\alpha\beta\gamma\delta} : a_{\alpha}^{\dagger} a_{\beta}^{\dagger} a_{\delta} a_{\gamma} : \end{aligned} \quad (5)$$

$H_0$  is a constant which can be dropped for spectroscopic calculations.  $H_1$  contains, besides the kinetic energy, a term representing the interaction of a particle (or a hole) with the particles in  $|\phi_0\rangle$ . The quantities  $\epsilon_{\alpha\beta}$  contained in  $H_1$  have the property

$$\epsilon_{\alpha\beta} = \epsilon_{ab} \delta_{j_a j_b} \delta_{l_a l_b} \delta_{m_a m_b} \delta_{q_a q_b} \quad (6)$$

and are therefore diagonal within the valence levels. We could assume  $H_1 + H_2$  as the shell model Hamiltonian (1) but, in so doing, one would neglect the coupling between the active and the non-active levels caused by the off-diagonal elements of  $\epsilon_{ab}$  and by  $V_{\alpha\beta\gamma\delta}$ .

Of course, the one-body potential appearing in expressions (5) has a physical meaning only if  $|\phi_0\rangle$  is an acceptable first approximation. This depends on the properties of the nuclei we are considering and on the sp basis which one uses. This basis has so far been left unspecified. The simplest theoretical definition is that of Hartree-Fock (HF), given by the condition  $\epsilon_{\alpha\beta} = \epsilon_{\alpha\alpha} \delta_{\alpha\beta}$ . This condition implies that  $|\phi_0\rangle$  is decoupled from the most elementary 1p-1h excitations and this fact puts one in a good position for the successive calculations. However, a considerable computational price must be paid in order to construct and use a HF-basis. For this reason, harmonic oscillator (ho) states of suitable size parameter are most frequently used in shell model calculations. We will also use such a sp basis. This assumption is justified by the fact that the HF- and ho-states do not differ very much in practice, at least, for not too high-lying states. Those ho-states which would lie in the continuum of the HF-potential should be interpreted as corresponding to resonances of the HF-potential. The fact that we use a ho-basis does not mean that we

simply forget the off-diagonal elements of  $\epsilon_{\alpha\beta}$ . These elements introduce a coupling between states in and outside the model space, and we shall consider such a coupling (as well as that introduced by  $H_2$ ) in going from the Hamiltonian (5) to the shell-model Hamiltonian.

## 2. THE EFFECTIVE HAMILTONIAN

We have first calculated the diagonal and off-diagonal elements  $\epsilon_{ab}$  up to the 3p-2f-1h oscillator major shell. We have used the value  $b = (\hbar/M\omega)^{1/2} = 2.063F$  for the ho size parameter corresponding to  $\hbar\omega = 9.74$  MeV. The number of elements  $G(abcd|S)$  required for the calculation is 1282. A part of the resulting  $\epsilon_{ab}$ 's are shown in Table I. It can be seen from the table that there is a large cancellation between the kinetic and potential energy parts in the off-diagonal elements, showing that the ho-wave functions provide a reasonable substitute to the HF-wave-functions. The off-diagonal elements are small when compared with the difference between the corresponding diagonal elements. The largest of these ratios is about 0.1 and their root mean square is 0.074. We also note that the differences between the diagonal elements tend to be larger than those given by the  $\hbar\omega$  rule.

Since we limit the configuration mixing to the 2p-1f shell, we cannot use simply the Hamiltonian (5). Let  $H$  be split into two terms

$$H = K_0 + K_1 \quad (7)$$

TABLE I. DIAGONAL AND OFF-DIAGONAL ELEMENTS  $\epsilon_{ab}$  (in MeV) FOR THE SINGLE-PARTICLE p-STATES. THE THREE COLUMNS GIVE THE KINETIC AND POTENTIAL ENERGY PARTS AND THE TOTAL ENERGY, RESPECTIVELY.

a	b	T	V	$\epsilon_{ab}$
1p <sub>3/2</sub>	1p <sub>3/2</sub>	12.18	-49.95	-37.77
1p <sub>1/2</sub>	1p <sub>1/2</sub>	12.18	-48.94	-36.76
1p <sub>3/2</sub>	2p <sub>3/2</sub>	7.70	-10.55	-2.84
1p <sub>1/2</sub>	2p <sub>1/2</sub>	7.70	-9.85	-2.15
2p <sub>3/2</sub>	2p <sub>3/2</sub>	21.92	-25.72	-3.80
2p <sub>1/2</sub>	2p <sub>1/2</sub>	21.92	-23.99	-2.07
2p <sub>3/2</sub>	3p <sub>3/2</sub>	12.89	-12.26	0.63
2p <sub>1/2</sub>	3p <sub>1/2</sub>	12.89	-11.51	1.38
3p <sub>3/2</sub>	3p <sub>3/2</sub>	31.67	-16.03	15.63
3p <sub>1/2</sub>	3p <sub>1/2</sub>	31.67	-14.37	17.29

such that the model space is an invariant manifold of  $K_0$ . According to the most frequently used definition [4], the effective Hamiltonian is given by

$$H^{SM} = K_0 + K_1^{eff}. \quad (8)$$

$$K_1^{eff.} = K_1 + K_1 \frac{Q}{E - K_0} K_1^{eff.}$$

where  $E$  is the energy of the state under consideration and  $Q$  is the operator projecting outside the model space. With such a definition the model wave-function  $|\psi_M\rangle$  is related to the true wave-function by

$$|\psi_M\rangle = (1 - Q)|\psi\rangle \quad (9)$$

We take for  $K_0$  the diagonal part of  $H_1$ , and for  $K_1$  the off-diagonal part of  $H_1$  plus  $H_2$ . We limit the complete Hilbert space to the configurations which can be built on the sp levels up to the 3p-2f-1h shell. Furthermore, we calculate the correction in expression (8) in the lowest order

$$K_1^{eff.} = K_1 + K_1 \frac{Q}{E - K_0} K_1 \quad (10)$$

This approximation is reasonable if the energy denominators are large enough compared to the matrix elements of  $K_1$ , i. e. if the states outside the model space are well separated from the energy region in which we are interested. As already mentioned, we choose the model space to be spanned by all the states in which the 2s-1d shell is closed ( $^{40}\text{Ca}$  core) and the 3s-2d-1g shell is unoccupied. Note that the core levels do not coincide with the hole levels. The approximation (10) makes life easy. In the domain of its validity, small variations of the energy denominators are allowed. To make  $K_1^{eff.}$  energy-independent, we replace  $E$  by the energy of the unperturbed initial state. The resulting  $K_1^{eff.}$  is then non-Hermitian. To avoid this, we further replace in the energy denominators the valence sp-energies pertaining to the unperturbed initial (and also final) state by their average value. The lowest-order  $H^{SM}$  defined above can be written

$$H^{SM} = K_0 + K_1^{eff.} = \text{constant} + \bar{H}_1 + \bar{H}_2 + \text{three-body term}$$

$$\bar{H}_1 = \sum_{\alpha} \bar{\epsilon}_{\alpha} : a_{\alpha}^{\dagger} a_{\alpha} : \quad (11)$$

$$\bar{H}_2 = \frac{1}{4} \sum_{\alpha\beta\gamma\delta} \bar{V}_{\alpha\beta\gamma\delta} : a_{\alpha}^{\dagger} a_{\beta}^{\dagger} a_{\delta} a_{\gamma} :$$

The constant term can be dropped for spectroscopic calculations. As is customary, we neglect the three-body term, even though, as we shall see later, there is at least one respect in which it is important. The expressions for  $\bar{\epsilon}_{\alpha}$  and  $\bar{V}_{\alpha\beta\gamma\delta}$  in terms of  $\epsilon_{ab}$  and  $V_{\alpha\beta\gamma\delta}$  are easily found. The two-body matrix elements  $\bar{V}_{\alpha\beta\gamma\delta}$  are not automatically antisymmetric, so that one must antisymmetrize them in order to retain all the usual features

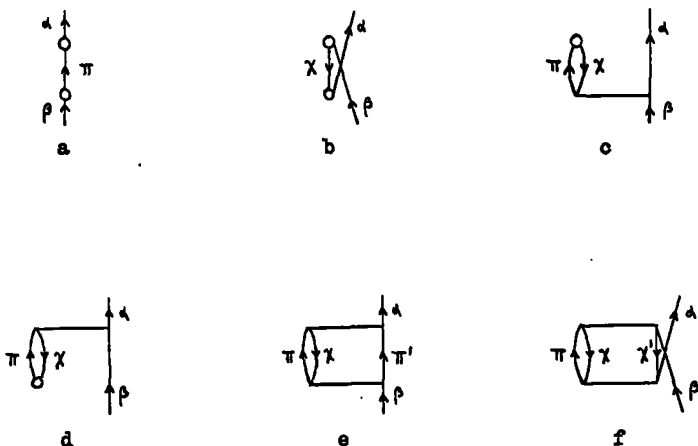


FIG. 1. Processes contributing to  $\bar{H}_1$ . Circles represent the one-body operator  $\epsilon_{ab}$  and horizontal lines represent the interaction  $V_{\alpha\beta\gamma\delta}$ . The graphs are drawn for the case in which all external lines are particle lines.

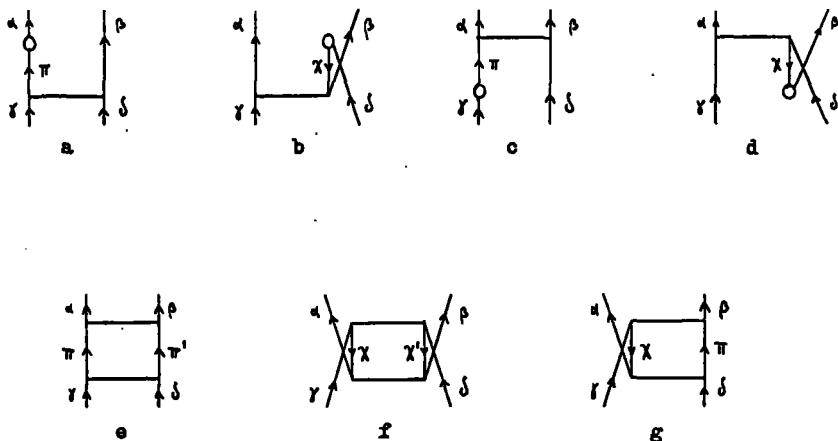


FIG. 2. Processes contributing to  $\bar{H}_2$ . The graphs are drawn for the case in which all external lines are particle lines.

of the shell-model interaction. Of course, all expressions are used, in practice, in the coupled form. The various processes which contribute to  $\bar{H}_1$  and  $\bar{H}_2$  are illustrated by graphs in Figs 1 and 2, respectively. All the processes which contain at least one one-body circle would be zero if a HF-basis were used. The number of independent  $G(abcd|S)$  elements requested to perform the calculation is 7653.

Let us see now what happens if some particle valence levels are occupied (a similar situation arises when some hole valence levels are empty). Let us take into account, e.g. the process represented in Fig. 3a,



FIG. 3. Two processes forbidden by the Pauli principle.

FIG. 4. A process possible when the valence level  $\mu$  is occupied. a and b represent the same process using a particle and a hole description for  $\mu$ , respectively.

where  $\nu$  is an upper level and  $\mu$  is a valence level already occupied by a freely propagating particle. Such a process is forbidden by the Pauli principle and actually its contribution is cancelled by the process represented in Fig. 3b. On the other hand, new processes become possible because the level  $\mu$  is occupied, e.g. that represented in Fig. 4a using the description in which  $\mu$  is a hole level. The same process, in the description in which  $\mu$  is a particle level, is represented in Fig. 4b. We see that the three-body term in  $H_2^{\text{SM}}$  would automatically take into account both the exclusion principle and the new processes. Since, however, we drop the three-body term, this should, in principle, be compensated by introducing a dependence of  $\bar{H}_2$  on the state of the valence system. We can hope that the state dependence discussed here is smooth enough so that it can be properly taken into account through factors depending on the average occupation probabilities of the particle and hole valence levels. There would remain, however, a dependence on such average occupation probabilities, i.e. on the particular nucleus which is taken into account. Such an effect may be important when a large number of nucleons is added to or taken away from our reference nucleus  $^{56}\text{Ni}$ . For this reason we say that our effective Hamiltonian is suitable for  $^{56}\text{Ni}$  and the nuclei containing only few nucleons less or more.

The values of the valence sp energies we get are given in Table II. The three columns give the bare values of Eq. (5), the "effective HF" values containing the processes of Figs 1a-d, and the completely renormalized values, respectively. It can be seen that both corrections are important. The final values are reasonable and are in favour of the small  $1f_{7/2}-2p_{3/2}$  gap.

For the two-body part  $\bar{H}_2$  of the shell-model Hamiltonian, the corrections can be divided into four classes: 3p-1h (Fig. 2g), 2p (Fig. 2e),

TABLE II. SHELL-MODEL  $sp$ -ENERGIES  $\bar{\epsilon}_a$  (in MeV). THE THREE COLUMNS GIVE THE BARE VALUES, THE "EFFECTIVE HF" VALUES AND THE FINAL VALUES, RESPECTIVELY

a	$\epsilon_a$	$\epsilon_a^{\text{HF}}$	$\bar{\epsilon}_a$
7/2	-2.41	-2.57	-2.15
3/2	0	0	0
5/2	0.22	1.02	1.57
1/2	1.73	1.74	1.79

TABLE III. NORMALIZED SHELL-MODEL INTERACTION MATRIX ELEMENTS  $G(aabb|I=0S=1)$  (in MeV). THE TWO COLUMNS GIVE THE VALUES OF REFS [1] AND [5], RESPECTIVELY

a	b	G	K
7/2	7/2	-1.351	-1.807
7/2	3/2	-0.767	-0.783
7/2	5/2	-2.795	-2.788
7/2	1/2	-0.656	-0.714
3/2	3/2	-0.967	-1.206
3/2	5/2	-0.825	-0.777
3/2	1/2	-1.032	-1.465
5/2	5/2	-0.627	-0.860
5/2	1/2	-0.455	-0.392
1/2	1/2	-0.295	-0.249

HF (Figs 2a-d), 4p-2h (Fig. 2f). This nomenclature is non-symmetric in particles and holes because it makes reference to Fig. 2 which is drawn for the case in which all the external lines are particle lines. On the whole, the above order is that of decreasing importance. None of the corrections is negligible. The corrections, though important, never become overwhelming. Only in few cases they are of the same size of the bare element and only in one case (7/2, 7/2, 7/2, 7/2, I=0, S=1) this happens for a large element.

Our calculated  $\bar{H}_2$  can be compared with the effective interaction in the 2p-1f shell calculated by Kuo and Brown [5] for a  $^{40}\text{Ca}$  core from the Hamada-Johnston potential. In Table III we compare the I=0, S=1 normalized two-body matrix elements. The agreement for the remaining 185 elements is not essentially different. The two sets are surprisingly similar in spite of the different N-N potentials and slightly different values of b which were used. Moreover, Kuo and Brown assume the 1f<sub>7/2</sub> sub-shell to be unoccupied and include only the 3p-1h corrections.

### 3. TWO-PARTICLE TWO-HOLE SHELL-MODEL CALCULATION

As a general feature, the interaction we have obtained looks rather strong and, having in mind the small calculated  $1f_{7/2}-2p_{3/2}$  gap, a large configuration mixing should be expected in the shell-model description of  $^{56}\text{Ni}$ . In fact, the Tamm-Dancoff and RPA-treatments fail. The Tamm-Dancoff spectrum is completely unrealistic and the RPA gives imaginary energies. More complete shell-model treatments are therefore necessary. We have started by calculating the  $J = 0, 2, 4$  levels of  $^{56}\text{Ni}$  including up to the 2p-2h excitations from the  $1f_{7/2}$  to the  $2p_{3/2}$ ,  $1f_{5/2}$  and  $2p_{1/2}$  levels. The results are shown in Table IV. It can be seen that the spacings between excited states are in essential agreement with experiment. It should be remembered that no adjustable or phenomenologically determined parameter is present in our description. The ground state is too much depressed by more than 1 MeV. Counting the excitation energies from the calculated ground state is, however, incorrect because of higher excitations not included in the model space, whose effect would be different on ground state and excited states as discussed by Ellis and Zamick [6] and Padjen and Ripka [7]. But the prescription of Ref.[7] for calculating consistently the energy shift of the unperturbed ground state and 2p-2h states cannot be used in our case because the 2p-2h admixtures in the ground state are large (the vacuum is only 54% of the calculated ground state). We hope that the explicit inclusion of higher order excitations will push down the excited states by a larger amount than the ground state, bringing the results near to the observed values.

The inspection of the calculated wave functions shows that few components exhaust more than 95% of the total wave function. But the nature of the important components is completely different, e. g. in the  $2_1^+$  and  $4_1^+$  states. The  $2_1^+$  case seems to suggest a kind of pairing scheme with holes coupled to  $J_h = 0$ . The  $2_1^+$  wave function is 8.7% 1p-1h and 87% 2p-2h with  $J_h = 0$ . On the contrary, the  $4_1^+$  case suggests a kind of aligned scheme with holes coupled to maximum  $J_h$ . The  $4_1^+$  wave function is 40% 1p-1h, 34% 2p-2h with  $J_h = 7$  and 15% 2p-2h with  $J_h = 6$ . On the basis of these results, it seems difficult to use a unique model assumption to select the most important higher excitations. Still we hope that the problem of truncations can be handled numerically starting from the lowest diagonal elements and including the most important couplings in the Hamiltonian matrix. This kind of treatment can be successful if it is possible to find out some simple-minded representation in which the wave functions of the low-lying states have a limited number of important components.

TABLE IV. ENERGIES (in MeV) FOR THE LOW-LYING STATES OF  $^{56}\text{Ni}$ . THE TWO COLUMNS GIVE THE 2p-2h CALCULATED VALUES AND THE EXPERIMENTAL VALUES, RESPECTIVELY

$J_h$	2p-2h	Expt.
$0_1^+$	-1.207	0
$2_1^+$	2.483	2.64
$4_1^+$	4.077	3.90
$0_2^+$	4.950	4.95

## REFERENCES

- [1] BOITI, A., GMITRO, M., RIMINI, A., WEBER, T., *Physics Letts* 33B (1970) 553.
- [2] WONG, S.S.M., DAVIES, W.G., *Physics Letts* 28B (1968) 77; PITTEL, S., *Physics Letts* 33B (1970) 158; GAMBHIR, Y.K., GMITROVA, E., GMITRO, M., *Physics Letts* 30B (1969) 382; JAFFRIN, A., *Physics Letts* 32B (1970) 448.
- [3] CLEMENT, D.M., BARANGER, E.U., *Nucl. Phys. A* 108 (1968) 27.
- [4] MACFARLANE, M.H., Lectures given at the International School of Physics Enrico Fermi, 40th Course, Varenna (1967).
- [5] KUO, T.T.S., BROWN, G.E., *Nucl. Phys. A* 114 (1968) 241.
- [6] ELLIS, P.J., ZAMICK, L., *Ann. Phys. (N.Y.)* 55 (1969) 61.
- [7] PADJEN, R., RIPKA, G., *Nucl. Phys. A* 149 (1970) 273.

# NUMBER-CONSERVING QUASI-PARTICLE CALCULATIONS

T. WEBER

Istituto di Fisica Teorica,  
Università di Trieste,  
Italy

## Abstract

### NUMBER-CONSERVING QUASI-PARTICLE CALCULATIONS.

The physical grounds and main features of the broken pair approximation (BPA) are presented. This formalism is introduced as a number-conserving approximation to the lowest-seniority shell model and is applied to the nickel isotopes, using a phenomenological and a realistic interaction. Comparison with the lowest-seniority and the exact-shell-model results shows that the BPA is a much more reliable approximation than the quasi-particle Tamm-Dancoff approximation.

The broken pair approximation is a number-conserving approximation to the shell model. It has been developed by Lorazo [1] for the  $J=0$ -case and completely worked out for all  $J$ 's by Gambhir, Rimini and Weber [2, 3]. Let us limit ourselves to the study of the even single-closed-shell medium and heavy nuclei and try to apply the shell model (ESM) techniques to reproduce the low-lying part of the spectra. If we want to use the shell-model procedure, we have to construct the model space as a first step. In practice, we start by choosing a system of single-particle energies and wave functions. In principle, this should be done by some Hartree-Fock type procedure, i. e. by determining the single-particle Hamiltonian (and therefore the residual interaction) and the single-particle wave-functions in a self-consistent way, so that the independent-particle-model results are as good as possible. Therefore the interaction between nucleons is as low as possible and one forgets (at least, for the moment) the levels defining the closed major shell, assuming that they form a completely filled and inert core. Then we distribute the nucleons not contained in the closed major shell, i. e. the "valence" nucleons, among a few of the remaining single-particle levels (valence levels). As a next step, we construct for each  $J$  a complete set of antisymmetric states belonging to the configurations  $(j_1^{k_1} j_2^{k_2} \dots j_n^{k_n})_J$  (where  $1, 2, \dots, n$  are the  $n$  valence levels and  $k_1 + k_2 + \dots + k_n = k$  is the number of active nucleons). We note that, because we are considering only single-closed-shell nuclei, the valence nucleons are all neutrons or protons. The last step of the calculation is to build up an effective Hamiltonian and to diagonalize it in the above-mentioned basis. This effective Hamiltonian should take into account, in some way, the effect of the neglected single-particle levels (below and above the valence levels); it can be determined by imposing the condition that its lowest eigenvalues coincide with those of the true Hamiltonian and that the model eigenvectors are the projections on the model space of the true eigenstates [4]. Unfortunately, such a program can be performed in practice only in a very limited number of cases because of the explosive dimensions of the bases. Therefore we are compelled to look for some approximation to the shell model.

Let us consider two nucleons in a valence level and suppose that they interact through a short-range interaction. If it is attractive, their binding energy is maximum when the overlap of their wave functions is maximum [5]. This happens when the resulting angular momentum of the two particles is maximum ( $J=2j$ , they are aligned) or is zero (they are paired). In our case, the valence nucleons are identical and the Pauli principle prevents the possibility of alignment. Therefore the configuration  $(j^2)_0$  is the most favoured one and forming a configuration  $(j^2)_{J \neq 0}$  requires a large amount of energy which tends to produce a gap between the state with  $J=0$  and those with  $J \neq 0$ . Let us now consider a system of  $n$  valence levels. The previous considerations suggest that the ground state of an even single-closed-shell nucleus must contain a large number of zero-coupled pairs (or simply pairs). On the other hand, the largest matrix elements of the interaction are the so-called "pairing" matrix elements of the type  $\langle aa J = 0 | V | bb J = 0 \rangle$ . Let us now define the seniority of a state of identical nucleons as the number of unpaired particles after all the pairs have been removed. Then one is tempted to introduce an approximation in which only the basis states up to seniority two or four are used. This is the lowest seniority shell model (LSSM). Also here we encounter on dimension difficulties. Let us consider, for example, a  $2^+$  state of  $\text{Sn}^{116}$ . The shell-model configurations are obtained by distributing the 16 neutrons out of the inert core in the five valence orbits  $2d_{5/2}$ ,  $1g_{7/2}$ ,  $3s_{1/2}$ ,  $2d_{3/2}$  and  $1h_{11/2}$ . If we limit the space up to the seniority - two states, only two neutrons can couple to  $J = 2$  and there are only nine possibilities for it. But the remaining 14 neutrons in the five valence shells can be arranged in pairs in so many ways that the number of seniority-two states approaches a thousand. Therefore, also the use of LSSM is limited to specific cases in practice.

A way of overcoming this difficulty is to introduce a new type of object, called quasi-particle, which contains in it the effects of the main part of the interaction, i. e. of the pairing part. We obtain this result if we are able to define the quasi-particle creation and destruction operators in such a way that the Hamiltonian, in terms of these, becomes as much as possible a free Hamiltonian. If this happens we can hope that states with few quasi-particles will provide a good space for the description of the low-energy levels. We can proceed as follows. Let us call  $a_{jm}$  and  $a_{jm}^\dagger$  the particle destruction and creation operators, respectively, and look for some other operators  $\alpha_{jm}$  and  $\alpha_{jm}^\dagger$  connected with the preceding ones by means of a unitary transformation (this requirement preserves the anticommutation relations). It is well known [6] that if we choose this unitary transformation as a rotation in the quasi-spin space we obtain the Bogolyubov-Valatin transformation

$$\begin{aligned}\alpha_{jm}^\dagger &= U_j a_{jm}^\dagger - (-)^{j-m} V_j a_{j-m} \\ \alpha_{jm} &= U_j a_{jm} - (-)^{j-m} V_j a_{j-m}^\dagger\end{aligned}\quad (1)$$

with

$$U_j^2 + V_j^2 = 1 \quad (2)$$

The  $U_j$  and  $V_j$  coefficients can be determined by imposing that the residual interaction between quasi-particles be as weak as possible, i. e. that the

quasi-particles be the elementary excitations of our nuclear system. It can be seen [6] that this condition is perfectly equivalent to minimizing the Hamiltonian in the quasi-particle vacuum, i. e. to imposing that the quasi-particle vacuum be a good approximate ground state for the even nucleus under consideration. To make sure that we are considering a specific nucleus, we must add the condition that the expectation value of the number operator in the quasi-particle vacuum gives the right valence nucleon number. This is the BCS-procedure. Then the excited states will be found by diagonalizing the residual interaction in the space (for example) of the two-quasi-particle states, i. e. of the states

$$|(r s)JM\rangle = (\alpha_r^\dagger \otimes \alpha_s^\dagger)_{JM} |BCS\rangle \quad (3)$$

where  $|BCS\rangle$  is the quasi-particle vacuum or BCS-state. These states are particular superpositions of  $v = 2$  (or  $v = 0$  for  $J = 0$ ) states, because  $|BCS\rangle$  contains only pairs, distributed in a fixed way. This procedure (called quasi-particle Tamm-Dancoff approximation, QTD) is conceptually very simple and, at least for the two-quasi-particle approximation, the relative calculations are easy to do in practice. Unfortunately, it presents a very disturbing feature, the non-conservation of the nucleon number. In fact, the Hamiltonian matrix in the truncated Hilbert space containing few quasi-particles does not commute with the particle number operator, so that the energy eigenstates do not have a well-determined particle number. Indeed, they are superpositions of states with different number of particles. Furthermore, the Hilbert space contains spurious states which would not appear in a number-conserving theory. These states must be projected out of our space before diagonalization, but nevertheless some non-valuable contamination from the higher-order spurions cannot be avoided. At this point, one could pick out of the quasi-particle states the components with the right number of particles. The corresponding formulae can be found (see, for example, Ref. [6]) and many ways of doing this "particle-number projection" can be chosen. The simplest procedure is to project on the right particle number the QTD-eigenstates and then to calculate the relative energy levels as expectation values of the Hamiltonian. Because of this procedure, the obtained states are not eigenstates of the Hamiltonian. A more serious way of doing it is to project before diagonalization. We calculate the  $U$ 's and  $V$ 's using BCS-theory; then we know the quasi-particle operator and can project the quasi-particle basis states and diagonalize the Hamiltonian in this projected space. Clearly this type of calculation is an approximation to the procedure in which the  $u$ 's and  $v$ 's are determined by minimizing the mean value of  $H$  in the projected BCS-state. This has been done by Ottaviani and Savoia and applied to the tin isotopes [7] by them.

These procedures, though successful, are not satisfactory from a conceptual point of view. The quasi-particles are very useful because they provide a simple scheme in which to perform calculations: when the projection is carried out this simplicity is lost. Moreover, the quasi-particle technique cannot be the most direct way to arrive at a number-conserving theory. There must be a way of doing such calculations without having to introduce quasi-particles.

We can interpret the quasi-particle theory as a way of doing LSSM-calculations. The reason why the dimensions are very low is that the

pairs are contained in the BCS-state in a well-defined way. Let us then introduce an approximate ground state containing the right number of pairs distributed among the valence levels in a fixed way. We first consider a particular case of two identical nucleons in the valence levels. In this case, we can construct a state which exactly diagonalizes the pairing part of the Hamiltonian. Let us write the shell-model Hamiltonian

$$H = - \sum_a \epsilon_a \sqrt{2j_a + 1} U_{00}(aa) + \frac{1}{4} \sum_{\substack{abcd \\ JM}} G(abcdJ) A_{JM}^\dagger(ab) A_{JM}(cd) \quad (4)$$

where  $\epsilon_a$  are the single-particle energies and

$$U_{JM}(ab) = \sum_{m_a m_b} \langle j_a j_b m_a m_b | JM \rangle (-)^{j_b - m_b} a_{j_a m_a}^\dagger a_{j_b - m_b} \quad (5)$$

$$A_{JM}^\dagger(ab) = \sum_{m_a m_b} \langle j_a j_b m_a m_b | JM \rangle a_{j_a m_a}^\dagger a_{j_b m_b}^\dagger \quad (6)$$

$$A_{JM}(ab) = [A_{JM}^\dagger(ab)]^\dagger \quad (7)$$

$$G(abcdJ) = \sum_{\substack{m_a m_b \\ m_c m_d}} \langle j_a j_b m_a m_b | JM \rangle \langle j_c j_d m_c m_d | JM \rangle \langle ab | V | cd \rangle_A \quad (8)$$

Then the pairing Hamiltonian is

$$H_p = - \sum_a \epsilon_a \sqrt{2j_a + 1} U_{00}(aa) + \frac{1}{4} \sum_{ab} G(aabb0) A_{00}^\dagger(aa) A_{00}(bb) \quad (9)$$

If we introduce the state

$$|\varphi_{00}\rangle = \sum_a \frac{\sqrt{2j_a + 1}}{2} \varphi_a A_{00}^\dagger(aa) |0\rangle \quad (10)$$

the distribution coefficients  $\varphi_a$  can be determined in such a way that

$$H_p |\varphi_{00}\rangle = E_p |\varphi_{00}\rangle \quad (11)$$

Let us define the operator

$$S_+ = \sum_a \frac{\sqrt{2j_a + 1}}{2} \varphi_a A_{00}^\dagger(aa) \quad (12)$$

The state  $S_+^p |0\rangle$  is then a particular seniority-zero state, containing  $p$  pairs, which reduces to  $|\varphi_{00}\rangle$  in the case of  $p = 1$ . Moreover, if we put  $\varphi_a = V_a/U_a$  with the condition  $U_a^2 + V_a^2 = 1$ ,  $S_+^p |0\rangle$  has exactly the same structure as the projected BCS-state, which is a very good approximation

to the  $v=0$  ground state [6]. Therefore we can think that it takes well into account the pairing part of the Hamiltonian and can assume it to be a trial ground state for a system of  $2p$ -valence nucleons. We must determine the coefficients  $\varphi_a$  by minimizing  $H$ , i. e. by imposing the condition

$$\delta \left\{ \frac{\langle 0 | S^p H S^p | 0 \rangle}{\langle 0 | S^p S^p | 0 \rangle} \right\} = 0 \quad (13)$$

Let us put  $|\phi_0\rangle = S_+^p |0\rangle$ . Then the condition (13) can be written

$$\frac{\partial}{\partial \varphi_a} \frac{\langle \phi_0 | H | \phi_0 \rangle}{\langle \phi_0 | \phi_0 \rangle} = 2 \frac{\langle \phi_0 | H \frac{\partial}{\partial \varphi_a} | \phi_0 \rangle}{\langle \phi_0 | \phi_0 \rangle} - 2 \frac{\langle \phi_0 | \frac{\partial}{\partial \varphi_a} | \phi_0 \rangle \langle \phi_0 | H | \phi_0 \rangle}{\langle \phi_0 | \phi_0 \rangle^2}$$

i. e.

$$\langle \phi_0 | H \frac{\partial}{\partial \varphi_a} | \phi_0 \rangle \langle \phi_0 | \phi_0 \rangle - \langle \phi_0 | \frac{\partial}{\partial \varphi_a} | \phi_0 \rangle \langle \phi_0 | H | \phi_0 \rangle = 0 \quad (13')$$

On the other hand, it is easy to show that

$$\frac{\partial}{\partial \varphi_a} | \phi_0 \rangle = p \frac{\sqrt{2j_a + 1}}{2} | \phi(a) \rangle \quad (14)$$

where

$$| \phi(a) \rangle = S_+^{p-1} (a_a^\dagger \otimes a_a^\dagger)_{00} | 0 \rangle$$

We can also put

$$\frac{\partial}{\partial \varphi_a} | \phi_0 \rangle = C | \phi_0 \rangle + | \phi_a^\perp \rangle \quad (15)$$

with  $\langle \phi_0 | \phi_a^\perp \rangle = 0$ . Then, using relation (14) or (15), the conditions (13') become, respectively,

$$\langle \phi_0 | H | \phi(a) \rangle \langle \phi_0 | \phi_0 \rangle - \langle \phi_0 | H | \phi_0 \rangle \langle \phi_0 | \phi(a) \rangle = 0 \quad (16)$$

$$\langle \phi_0 | H | \phi_a^\perp \rangle = 0 \quad (17)$$

Conditions (16) can be used to calculate the coefficients  $\varphi_a$ . Conditions (17) will be used later. We can now construct the other basis states by removing one distributed pair (one operator ( $S_+$ ) from the ground state and replacing it by a two-particle state (an operator  $A_{JM}^\dagger(ab)$ ). In this manner, we obtain particular seniority-two (or zero for  $J=0$ ) states of the type

$$S_+^{p-1} A_{JM}^\dagger(ab) | 0 \rangle \quad (18)$$

We shall call the states (18) the one-broken-pair (1BP) states. For  $J=0$ , these states coincide with the previously defined  $|\phi(a)\rangle$  states; they are not orthogonal and must be orthogonalized. We note that conditions (17) imply that  $|\phi_0\rangle$  is not coupled to the 1BP-states, i. e. that it is the ground

state of the 1BP-approximation. It is easy to show that the space spanned by the state  $|\phi_0\rangle$  and the states (18) coincides with the space spanned by the projected zero- and two-quasi-particle states, if the coefficients  $U_a$  and  $V_a$  are assumed equal in the two theories. In fact the following relations hold [2]:

$$|\text{BCS}\rangle_{2p} = \frac{K}{p!} S_+^p |0\rangle, \quad (19)$$

$$\begin{aligned} \left[ (\alpha_a^\dagger \otimes \alpha_b^\dagger)_{JM} |\text{BCS}\rangle \right]_{2p} &= \frac{1}{U_a U_b} \frac{\tilde{K}}{(p-1)!} S_+^{p-1} A_{JM}^\dagger(ab) |0\rangle \\ &- \frac{\tilde{K}}{p!} \delta_{J0} \delta_{ab} \sqrt{2j_a+1} \frac{V_a}{U_a} S_+^p |0\rangle \end{aligned} \quad (20)$$

where

$$\tilde{K} = \prod_a U_a^{(j_a + \frac{1}{2})} \quad (21)$$

At this point we have to orthonormalize states (18) and diagonalize the Hamiltonian in this basis. Therefore we must calculate the scalar products of states (18) and the matrix elements of  $H$  between states (18). If we face the first problem from a general point of view, we can solve both problems together. Obviously, the approximation described above is the first which we can construct. In general, we can consider a broken-pair state of the type

$$S_+^{p-b} X_{JM}^\dagger(d, K) |0\rangle \quad (22)$$

where  $X_{JM}^\dagger$  is a vector-coupled product of  $2b$  creation operators,  $d$  is the set of quantum numbers necessary to specify the valence levels and  $K$  is the set of intermediate angular momenta. Even if the states  $X_{JM}^\dagger(d, K) |0\rangle$  are orthogonal (in general, they are not) for different  $d$  and  $K$ , states (22) can be non-orthogonal. Therefore, we must orthogonalize them and this requires the knowledge of the scalar products of states (22). To calculate them we first expand the states  $X_{JM}^\dagger(d, K) |0\rangle$  in terms of the orthonormal states  $\chi_{JM}^\dagger(n_i, \nu_i, \alpha) |0\rangle$ , where  $n_i$  are the occupation numbers for the valence orbits,  $\nu_i$  are the seniorities and  $\alpha$  contains all the additional quantum numbers necessary to specify the state uniquely. For two, three or four particles (which are the cases in which we are interested) this expansion is very easy to carry out [6]. Then the states  $S_+^{p-b} \chi_{JM}^\dagger(n_i, \nu_i, \alpha) |0\rangle$  can be expanded in terms of the states  $|2p_1+n_1, \dots, 2p_k+n_k\rangle$  ( $p_1+p_2+\dots+p_k=p-b$ ) and the scalar products can be evaluated immediately. The procedure is explicitly shown in Ref. [2].

Let us turn now to the evaluation of the matrix elements of the type

$$\langle 0 | A_{JM}(a'b') S_+^{p-1} H S_+^{p-1} A_{JM}^\dagger(ab) | 0 \rangle \quad (23)$$

We observe that the Hamiltonian can be written

$$\begin{aligned}
 H = & \sum_a \left\{ (2j_a + 1) \epsilon_a + \frac{1}{2} \sqrt{2j_a + 1} \sum_b \sqrt{2j_b + 1} F(aabb0) \right\} \\
 & - \sum_a \left\{ \epsilon_a + \frac{1}{\sqrt{2j_a + 1}} \sum_b \sqrt{2j_b + 1} F(aabb0) \right\} \sum_{m_a} a_{j_a m_a} a_{j_a m_a}^\dagger \\
 & + \sum_{\substack{a \leq b \\ a' \leq b'}} \frac{G(aba'b'I)}{(1 + \delta_{ab})(1 + \delta_{a'b'})} \sum_M A_{IM}(a'b') A_{IM}^\dagger(ab)
 \end{aligned} \quad (24)$$

where

$$F(ab'a'bJ) = \sum_I (2I + 1) \left\{ \begin{matrix} a & b & I \\ a' & b' & J \end{matrix} \right\} G(aba'b'I) \quad (25)$$

If we use expression (24) for the Hamiltonian, the matrix elements (23) become scalar products of states of type (22), and the relative procedure to calculate them can be applied directly. The explicit formulae for scalar products and Hamiltonian matrix elements are shown in Ref. [2]. The same method can be used to evaluate matrix elements of any other one- or two-body operator and therefore to calculate electromagnetic transition rates, static moments and spectroscopic factors.

To check the validity of this approximation, the broken-pair method (BPA) in its first approximation has been applied to the even nickel isotopes [2]. The case of nickel is particularly significant because exact shell-model and lowest-seniority shell-model calculations are possible for nickel and, therefore, these theories are directly comparable with BPA. We used two kinds of forces for these applications. The first one is the Argonne effective interaction, obtained by Cohen et al. [8] fitting the experimental levels of the even and odd isotopes from  $^{58}\text{Ni}$  to  $^{62}\text{Ni}$ . In this case, the valence levels are  $2p_{3/2}$ ,  $1f_{5/2}$ ,  $2p_{1/2}$  and the corresponding single-particle energies we used are, respectively, 0, 0.78 and 1.08 MeV. These values were deduced from the experimental spectrum of  $^{57}\text{Ni}$ . The results are shown in Table I. The comparison between BPA and  $v \leq 2$  results shows that they agree very well: BPA presents itself as a very good approximation to LSSM. In all cases the difference between the two spectra is less than 100 keV, except for the states  $0_3^+$  and  $2_3^+$  of  $^{60}\text{Ni}$ , which contain appreciable percentages of two broken pairs with seniority two. On the other hand, the comparison of the  $v \leq 2$  and ESM spectra and the inspection of the seniority-two percentages in the ESM states show that LSSM is a good approximation to ESM, at least for the low levels and with the exception of  $3^+$  states. On the other hand, the two-quasi-particle Tamm-Dancoff results show a complete failure of the quasi-particle theory in this case.

The second interaction we used is the non-local, energy-dependent Tabakin potential [9]. In this case, we include the  $1g_{9/2}$  subshell among the valence levels, in order to construct negative-parity states too. The energy of the  $1g_{9/2}$  level is taken equal to 3.5 MeV. The effective interaction is obtained by appropriately renormalizing the Tabakin interaction for one-particle-one-hole excitations of the core [10, 11]. Holes run on the six core shells  $1p_{3/2}$ ,  $1p_{1/2}$ ,  $1d_{5/2}$ ,  $2s_{1/2}$ ,  $1d_{3/2}$ ,  $1f_{7/2}$  and particles on the four

TABLE I. ENERGY LEVELS (in MeV) CALCULATED ACCORDING TO THE EXACT SHELL MODEL (ESM), LOWEST SENIORITY SHELL MODEL ( $v \leq 2$ ), FIRST BROKEN PAIR APPROXIMATION (BPA), AND TWO-QUASIPARTICLE APPROXIMATION (QTD)

$J^\pi$	$^{60}\text{Ni}$				$^{62}\text{Ni}$			$^{64}\text{Ni}$			
	ESM	$v \leq 2$	BPA	QTD	ESM	BPA	QTD	ESM	$v \leq 2$	BPA	QTD
$0^+$	0. (99.8)	0.	0.	0.	0. (99.7)	0.	0.	0. (99.8)	0.	0.	0.
	2.32 (95.8)	2.41	2.46	1.93	2.01 (87.3)	2.19	1.69	2.16 (98.8)	2.18	2.19	1.72
	3.27 (86.7)	3.42	3.65	2.98	2.61	3.62	3.03	3.56 (81.2)	3.66	3.77	3.42
$2^+$	1.42 (99.8)	1.42	1.42	0.95	1.53 (99.4)	1.53	1.07	1.56 (99.7)	1.56	1.56	1.11
	2.17 (76.6)	2.43	2.53	2.07	2.25 (89.1)	2.41	1.86	2.37 (78.7)	2.48	2.49	2.08
	2.58	2.87	3.48	2.99	2.70	3.45	2.88	2.60 (64.9)	3.28	3.31	2.75
$3^+$	2.76 (55.5)	3.44	3.51	2.99	2.84 (40.6)	3.59	3.03	3.07 (36.6)	3.45	3.45	2.95
	3.37 (30)	3.87	3.98	3.51		3.63	3.10	3.48 (72.7)	3.77	3.80	3.34
$4^+$	2.21 (91.9)	2.30	2.30	1.86	2.20 (92.9)	2.30	1.84	2.26 (96.3)	2.29	2.31	1.84
	2.80 (23.9)	3.50	3.57	3.21	2.76	3.48	2.91	2.73 (34.1)	3.35	3.40	2.86

The effective interaction of Cohen et al. (Ref.[ 8]) is used. The numbers in parentheses in the columns ESM are the percentages of seniority two in ESM vectors. The ESM values for  $^{62}\text{Ni}$  are taken from Ref.[8].

TABLE II. SAME AS TABLE I, BUT FOR EFFECTIVE TABAKIN INTERACTION

$J^\pi$	$^{60}\text{Ni}$				$^{62}\text{Ni}$		$^{64}\text{Ni}$	
	ESM	$v \leq 2$	BPA	QTD	BPA	QTD	BPA	QTD
$0^+$	0. (99.2)	0.	0.	0.	0.	0.	0.	0.
	2.39 (98.4)	2.51	2.50	2.16	1.95	1.68	2.59	2.18
	3.35 (58.9)	3.79	3.85	3.27	4.61	3.78	4.99	4.59
$2^+$	1.62 (95.2)	1.70	1.77	1.57	2.03	1.81	2.08	1.84
	2.58 (91.9)	2.69	2.80	2.54	3.14	2.51	3.38	3.12
	3.03 (94.4)	3.10	3.10	2.61	3.52	3.13	3.74	3.27
$3^+$	2.88 (91.3)	2.99	3.03	2.96	3.10	2.91	3.58	3.27
	3.75 (22.2)	4.19	4.17	3.51	3.62	3.35	4.28	3.89
$4^+$	2.63 (95.3)	2.68	2.67	2.64	3.27	3.01	3.34	3.14
	3.67 (20.0)	4.23	4.22	3.94	3.83	3.44	3.94	3.62
$3^-$	4.34 (90.8)	4.46	4.49	4.28	4.27	3.97	3.63	3.46
	5.48 (76.8)	5.66	5.73	5.09	4.83	4.25	4.01	3.98

valence shells and on the four upper shells  $1g_{7/2}$ ,  $2d_{5/2}$ ,  $2d_{3/2}$ ,  $3s_{1/2}$ . Because of the small occupation of the valence shells we do not take into account the partial inhibition of the core-valence transitions due to the Pauli principle and we neglect the valence-upper processes. The results are shown in Table II. In the case of  $^{60}\text{Ni}$ , we again find very good agreement between BPA and  $v \leq 2$  and between  $v \leq 2$  and ESM. On the other hand, the difference with the QTD-spectra is now less appreciable, and this happens also for  $^{62}\text{Ni}$  and  $^{64}\text{Ni}$ .

## REFERENCES

- [1] LORAZO, B., thesis, Orsay 1968 (unpublished); Phys. Letts 29B (1969) 150; Nuclear Physics A153 (1970) 255.
- [2] GAMBHIR, Y.K., RIMINI, A., WEBER, T., Phys. Rev. 188 (1969) 1573; Phys. Rev. C 3 5 (1971) 1965.
- [3] RIMINI, A., WEBER, T., Phys. Rev. C2 (1970) 324.
- [4] MACFARLANE, M.H., The Reaction Matrix in Nuclear Shell Theory, International School of Physics "Enrico Fermi", Course 40, Varenna (1967).
- [5] BARANGER, M., Theory of Finite Nuclei, 1962 Cargèse Lectures in Theoretical Physics, Benjamin (1963).
- [6] MACFARLANE, M.H., Shell Model Theory of Identical Nucleons, Lectures in Theoretical Physics, University of Colorado Press, Boulder, Colorado (1966).
- [7] OTTAVIANI, P.L., SAVOLA, M., Phys. Rev. 178 (1969) 1594; Lett. Nuovo Cim. 1 (1969) 766; Phys. Rev. 187 (1969) 1306; Nuovo Cim. 67 (1970) 630.
- [8] COHEN, S., LAWSON, R.D., MACFARLANE, M.H., PANDYA, S.P., SOGA, M., Phys. Rev. 160 (1967) 903.
- [9] TABAKIN, F., Ann. Phys. (N.Y.) 30 (1964) 51.
- [10] KUO, T.T.S., BROWN, G.E., Nucl. Phys. 85 (1966) 40; A92 (1967) 481; KUO, T.T.S., *ibid.* A90 (1967) 199.
- [11] GMITRO, M., HENDEKOVIĆ, J., SAWICKI, J., Phys. Rev. 169 (1968) 983.



# GROUND-STATE PROPERTIES OF LIGHT NUCLEI AS DEDUCED FROM VARIATIONAL CALCULATIONS

S. BOFFI

Istituto di Fisica dell' Università, Pavia,  
Istituto Nazionale di Fisica Nucleare, Gruppo di Pavia,  
Italy

## Abstract

GROUND-STATE PROPERTIES OF LIGHT NUCLEI AS DEDUCED FROM VARIATIONAL CALCULATIONS.

A review is presented of recent work done in Pavia on ground-state properties of light nuclei as deduced from variational calculations. Special attention is devoted to the single-particle density; three methods are analysed to deduce it. In the framework of Hartree-Fock theory, first-order contributions to the ground-state function are shown to be negligible in the case of  ${}^4\text{He}$ . The projection of good quantum numbers from the initial Slater determinant before variation has been compared with the Hartree-Fock method in the case of parity, and considerable energy gain has been achieved. A variational procedure has been proposed to determine the single-particle reduced density matrix by a best fit to the experimental data, with the conclusion that, in the case of  ${}^4\text{He}$ , even a finite linear combination of Slater determinants seems inadequate to describe all ground-state properties.

In the microscopic description of ground-state (g. s.) properties of nuclei the Hartree-Fock (HF) approximation is the most widely used. A large number of calculations in recent years have shown the possibility of reproducing the gross features of nuclei as light as  ${}^4\text{He}$ . However, as Kerman pointed out [1], a second-order contribution to the total energy is always required. Thus, it is generally assumed that HF-solutions should only serve to define a convenient basis in which a perturbation calculation can be carried out. This argument holds for the g. s. energy, as well as for the total state function. It is well known, indeed, that wave functions based on an independent-particle model do not reproduce the charge form factor at high  $q$ -values, which has been recently measured [2, 3] in elastic electron scattering on  ${}^4\text{He}$  and  ${}^{16}\text{O}$ . Only Woods-Saxon wave functions seem to reproduce the form factor of  ${}^{16}\text{O}$  reasonably [4], but they also predict a second diffraction dip in the form factor of  ${}^{12}\text{C}$  which was not observed [3].

As far as  ${}^4\text{He}$  is concerned, Radhakant et al. [5] have shown that HF-like single-particle (s. p.) wave functions fitting the charge form factor are not able to give the correct energy, and vice versa. So, if one believes in the HF-method and wishes to describe all the g. s. properties of a nucleus in a coherent way, one is forced to use perturbed HF-wave functions.

This idea has been developed by the author in collaboration with Rimini and Weber [6]. Let  $|0\rangle$  be the (non-degenerate) HF g. s., which is not an eigenstate of the total Hamiltonian  $H$ . To approach the true eigenfunction of  $H$  we add to  $|0\rangle$  the first-order contribution in a perturbation treatment of the residual interaction  $V$ :

$$|1\rangle = -\frac{1}{4} \sum_{mni j} c_{mni j} |mni j\rangle \quad (1)$$

where

$$c_{mni j} = \langle mni j | V | 0 \rangle (\epsilon_m + \epsilon_n - \epsilon_i - \epsilon_j)^{-1} \quad (2)$$

The indices  $m, n, p, \dots$  are used for particle labels, and the indices  $i, j, k, \dots$  for hole labels;  $\epsilon_\alpha$  is the s. p. energy corresponding to the HF-orbital  $|\alpha\rangle$ .

Then the normalized g. s. wave function is given by

$$|\psi\rangle = N^{-1/2} (|0\rangle + |1\rangle) \quad (3)$$

where

$$N = 1 + \frac{1}{4} \sum_{mni j} |c_{mni j}|^2 \quad (4)$$

A knowledge of the admixture coefficients  $c_{mni j}$  is possible after solving the HF-equations with a specific interaction in a sufficiently large s. p. basis: the size of these coefficients depends on the strength of the 2p-2h interaction and on the spacing between particle and hole energy levels. It has been usually assumed that higher-lying s. p. states enter with lower weight in the calculation; however, Bassichis and Strayer [7] have shown that this assumption is correct only in the pure harmonic-oscillator (h. o.) shell model. In the HF-approximation, on the contrary, because of a phase conspiracy in the unoccupied orbitals, the probability of 2p-2h configurations is smeared out over the whole excitation spectrum, whereas in the pure shell model it is strongly peaked at the lowest 2p-2h excitations.

Thus, significant alterations with respect to the zero-order approximation can be expected in the average value of a s. p. operator  $Q$  computed with the state function (3):

$$\langle \psi | Q | \psi \rangle = \sum_{i=1}^A q_{ii} + \frac{1}{2N} \sum_{mni j} c_{mni j} \left[ \sum_p c_{mpij}^* q_{pn} - \sum_k c_{mnik}^* q_{jk} \right] \quad (5)$$

In the case of the charge form factor (neglecting nuclear recoil and proton size) we have

$$q_{\alpha\beta} = \frac{1}{Z} \langle \alpha | j_0(qr) | \beta \rangle \delta_{\tau_\alpha \tau_\beta} \left( \frac{1}{2} + \tau_\alpha \right) \quad (6)$$

Bassichis et al. [7, 8] have published HF-calculations for  ${}^4\text{He}$  in a suitably large basis (up to the h. o. level  $i_{13/2}$ ) using the Tabakin interaction [9]. A zero-order g. s. energy of -0.10 MeV and a second-order contribution of -20.46 MeV are found: taking into account the Coulomb repulsion and the c. m. correction this gives a g. s. binding energy of about 31 MeV (experimental value: 28.3 MeV). The r. m. s. radius turns out to be 1.91 fm, which seems too large (experimental value: 1.61 fm); however, this result can be attributed to the large value of the oscillator constant used in the HF-calculation ( $b^2 = 2.6 \text{ fm}^2$ ).

In Fig. 1 we report the charge form factor as computed according to Eqs (5) and (6) with the same large basis, the same interaction and the

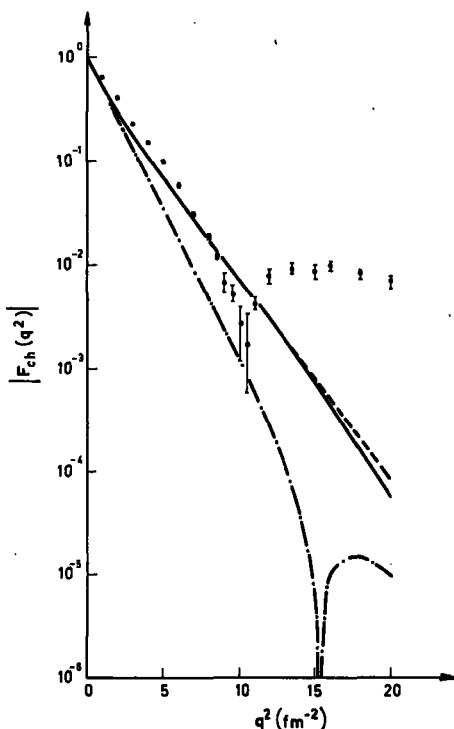


FIG. 1. The charge form factor of  ${}^4\text{He}$ . The dashed line is obtained with HF-orbitals, the full line is the result of first-order perturbation; the dot-dashed line represents the approximation with pure shell model as described in the text. Experimental points are taken from Ref. [2].

same  $b$  as in Refs [7, 8] (full line): no diffraction dip is present. For comparison, the dot-dashed curve is drawn: it represents the result obtained by approximating HF-orbitals by h. o. wave functions.

This result seems thus to be at variance with the feeling that HF-orbitals are convenient for a zero-order s. p. basis set.

There is now another problem, which is fundamental in HF-technology. Among the very many possible solutions of HF-equations, only those with some given consistent symmetry have been investigated, as a matter of computational simplification. However, the consistent symmetry group of the HF-Hamiltonian  $H_0$  need not necessarily be the same group of symmetry as that of the total Hamiltonian  $H$ . Let  $\Omega$  be an operator which commutes with  $H$ , and  $\omega$  the relative quantum number associated with the symmetry properties described by  $\Omega$ . In principle, the Slater determinant (SD) solution of the HF-problem is not an eigenstate of  $\Omega$ . Several values of  $\omega$  are mixed together in the solution; and the description of a nuclear level requires the use of a projection operator  $\mathcal{P}_\Omega$  which extracts from the HF-wave function the component of a good quantum number  $\omega$ . This method can be called "projection after variation" (PAV). It does not, in general, give the same results as "projection before variation" (PBV), i. e. a variational calculation based on trial wave functions obtained after projecting the good quantum number  $\omega$  from the initial SD.

Let  $K_\alpha$  be an  $m$ -dimensional vector space formed by the complex linear combination of a set  $\{|\alpha\rangle\}$  of  $m$  linearly independent s. p. wave functions; then

$$|i\rangle = \sum_{\alpha=1}^m X_\alpha^i |\alpha\rangle \quad (7)$$

is an element of  $K_\alpha$ . Let  $K_N$  be the space formed by all the SD's of order  $A$  which can be constructed, each starting from  $A$  linearly independent s. p. wave functions  $|i\rangle$ . The HF-approximation restricts the variation of the trial wave function to the set of functions belonging to  $K_N$ .

Let us denote by  $K_P$  the space of all state functions obtained by applying the projection  $\mathcal{P}_\Omega$  to all the elements of  $K_N$ . Furthermore, let us suppose that  $K_C$  is the set of all state functions belonging both to  $K_N$  and to  $K_P$ :

$$K_C = K_N \cap K_P \quad (8)$$

The solution of the PBV-method, which must be found in  $K_P$ , will not necessarily be in  $K_C$ . It is still an antisymmetric state function (as SD's) and, in addition, has the required symmetry (i. e.  $\omega$  is a good quantum number).

From a theoretical point of view, the advantage of using the PBV method is evident, even when the HF-solution lies in  $K_C$ , i. e. when no PAV is required. Indeed, when performing the PBV method, the same solution (in  $K_C$ ) or one with lower energy (in that part of  $K_P$  complementary to  $K_C$ ) must be found.

In the case of  $\Omega$  being the total angular momentum, the PBV-method has already been extensively and successfully used [10] and also compared with the corresponding PAV method [11]. Here, the HF-solution is not in  $K_C$  (except for spherical nuclei), and PAV is not trivial.

Let us now consider the case of parity symmetry. If the functions of the set  $\{|\alpha\rangle\}$  are not all of the same parity, the corresponding SD's have no definite parity. The possible presence of parity mixing in s. p. orbitals is suggested by the existence of tensor forces and one-pion-exchange contributions in a complete realistic nucleon-nucleon interaction.

However, in a  $4n$ -nucleus with s. p. density which is invariant under the usual consistent symmetries (i. e. time reversal, reflection through a plane, rotation by  $\pi$  about an axis in the plane of reflection symmetry) good-parity solutions are indeed energetically favoured [12, 13]. Under these conditions, therefore, HF and PAV are equivalent, the final solution being in  $K_C$ . When some of the above symmetries are relaxed, and/or a nucleus is considered which is not of the  $4n$ -type, parity mixing in s. p. orbitals may be present in the final solution. In any case, it is interesting to compare the results of a PBV-calculation with those of the corresponding HF and PAV ones.

Pacati and the author [14, 15] have studied the general structure of the parity-projected solution and its relation with the original SD without definite parity. The application of the parity PBV method to actual nuclei is very laborious, from a computational point of view: the choice of the particular nuclear system is very limited by the number of parameters (i. e. the  $X$ -coefficients of Eq. (7)) varying in the calculation of the energy minimum. Therefore, to have a reasonably large s. p. space  $K_\alpha$ , we have

studied spherical nuclei [15], such as  $^4\text{He}$  and  $^{16}\text{O}$ , and very light odd nuclei [14], such as  $^3\text{H}$  and  $^3\text{He}$ .

With the exception of  $^{16}\text{O}$ , an energy gain of about one MeV is achieved by the PBV-method compared to the HF-approximation. Moreover, the HF-solution is always parity-conserving, while the PBV-solution shows large parity mixing in s.p. orbitals; in the case of  $^4\text{He}$ , e.g. the dominant expansion coefficients  $X_{nl}$  of the PBV-solution are  $X_{00} = 0.972$  and  $X_{01} = 0.230$  i. These results are obtained although two-body interaction was simulated by the effective force derived by Elliott et al. [16], whose central character is well known [17]. This fact, together with the argument given by Rowe [18] about the origin of the energy gap, may explain the stability (with respect to parity deformation) of the energy minimum of  $^{16}\text{O}$  with a spherical shape. In this case, indeed, the absolute energy minimum (with parity mixing) should be obtained if sphericity is relaxed [19].

At first sight, a large difference exists between HF- and PBV-state functions. However, accurate investigation of the s.p. density matrix

$$\rho = \sum_{\alpha\beta} \rho_{\alpha\beta} |\alpha\rangle\langle\beta| \quad (9)$$

shows that only differences of 5 + 10% are to be expected when computing average values of s.p. operators. As an example, let us consider the case of  $^4\text{He}$ . For a state function  $|\psi\rangle \in K_p$  (with positive parity) the charge- and bond-order matrix [20] of Eq. (9) becomes:

$$\rho_{\alpha\beta}^P = \frac{1}{2} \langle\psi|\psi\rangle^{-1} \left[ \rho_{\alpha\beta}^N + \pi_\beta \sum_i X_\alpha^{i*} X_\beta^i k_i \right] \quad (10)$$

where

$$k_i = \prod_{\ell \neq i} \sum_\alpha \pi_\alpha |X_\alpha^\ell|^2 \quad (11)$$

and  $P|\alpha\rangle = \pi_\alpha|\alpha\rangle$ . In Eq. (10),  $\rho_{\alpha\beta}^N$  is obtained from a total state function  $|\Phi\rangle \in K_N$ :

$$\rho_{\alpha\beta}^N = \sum_i X_\alpha^{i*} X_\beta^i \quad (12)$$

Owing to the smallness of the elements  $k_i$  ( $\approx 1$ , but  $\ll 1$  for large A) expression (12) does not differ strikingly from expression (10). Indeed, in the charge form factor of  $^4\text{He}$  computed both with our PBV and HF solutions, no remarkable difference is present.

Moreover, the qualitative behaviour is similar to the standard h.o. shell model, thus deviating strongly from the experimental data.

The same situation prevails for the magnetic moment of  $^3\text{H}$  and  $^3\text{He}$  and for the charge form factor of  $^{16}\text{O}$  (see Refs [14, 15]).

We are tempted to conclude that HF-like calculations are inadequate for a microscopic description of such light nuclei.

We shall now report some results of a work still in progress [21] on the problem of a coherent microscopic description of finite nuclei, which seems to support the idea that, at least for  $^4\text{He}$ , a s.p. description is very difficult.

Let  $|\psi_0\rangle$  be the exact g. s. eigenstate of a finite nucleus:  $H|\psi_0\rangle = E_0|\psi_0\rangle$ . According to Thouless [22], we define the one-particle Green's function:

$$G_{\alpha\beta}(\tau) = \begin{cases} \langle \psi_0 | a_{\beta} e^{i(H-E_0)\tau} a_{\alpha}^{\dagger} | \psi_0 \rangle, & \text{for } \tau < 0 \\ -\langle \psi_0 | a_{\alpha}^{\dagger} e^{-i(H-E_0)\tau} a_{\beta} | \psi_0 \rangle, & \text{for } \tau > 0 \end{cases} \quad (13)$$

where  $a_{\alpha}^{\dagger}$  creates a particle in the state  $|\alpha\rangle$ . Then

$$\rho_{\alpha\beta} = -\lim_{\tau \rightarrow 0^+} G_{\alpha\beta}(\tau) \quad (14)$$

and the expectation value of a s. p. operator  $Q$  on the g. s.  $|\psi_0\rangle$  is given by

$$\langle \psi_0 | Q | \psi_0 \rangle = \sum_{\alpha\beta} q_{\alpha\beta} \rho_{\alpha\beta} \quad (15)$$

The g. s. energy (sum of the kinetic energy  $T$  and the potential energy  $V$ , with the centre-of-mass motion subtracted) is given by

$$E_0 = \langle T \rangle + \langle V \rangle = \frac{1}{2} \sum_{\alpha\beta} T_{\alpha\beta} \rho_{\alpha\beta} + \frac{1}{2} i \lim_{\tau \rightarrow 0^+} \sum_{\alpha} \frac{dG_{\alpha\alpha}(\tau)}{d\tau} \quad (16)$$

Evaluating the derivative of the Green's function in terms of the advanced part of  $G_{\alpha\beta}$  [22], one has:

$$\frac{1}{2} i \lim_{\tau \rightarrow 0^+} \sum_{\alpha} \frac{dG_{\alpha\alpha}(\tau)}{d\tau} = -\frac{1}{2} \sum_{\alpha} \sum_n \langle \Phi_n | a_{\alpha} | \psi_0 \rangle^2 (E_n^1 - E_0) \quad (17)$$

where  $E_n^1$  is the energy of the excited state  $|\phi_n\rangle$  of the nucleus with one nucleon missing.

In the case of  ${}^4\text{He}$ , the right-hand side of Eq. (17) can be approximated by the sum  $\Omega_p + \Omega_n$ , where  $\Omega_p = E_0({}^4\text{He}) - E_0({}^3\text{H}) = -19.6$  MeV and  $\Omega_n = E_0({}^4\text{He}) - E_0({}^3\text{He}) = -20.6$  MeV.

The unknown quantities  $\rho_{\alpha\beta}$  can be obtained by a variational procedure, fitting the experimental data on the energy, the root-mean-square radius and the charge form factor in a force-independent way.

Preliminary results of such a calculation in a s. p. basis set with  $l = 0, 1$  and  $n \leq 5$  show that the simultaneous fit is not possible under the condition

$$\rho^2 = \rho \quad (18)$$

which is necessary and sufficient for  $|\psi_0\rangle$  to be a SD: if the charge form factor is reproduced, the energy turns out to be positive; conversely, a

negative, reasonable value of the ground-state energy corresponds to a pure-shell-model-like charge form factor.

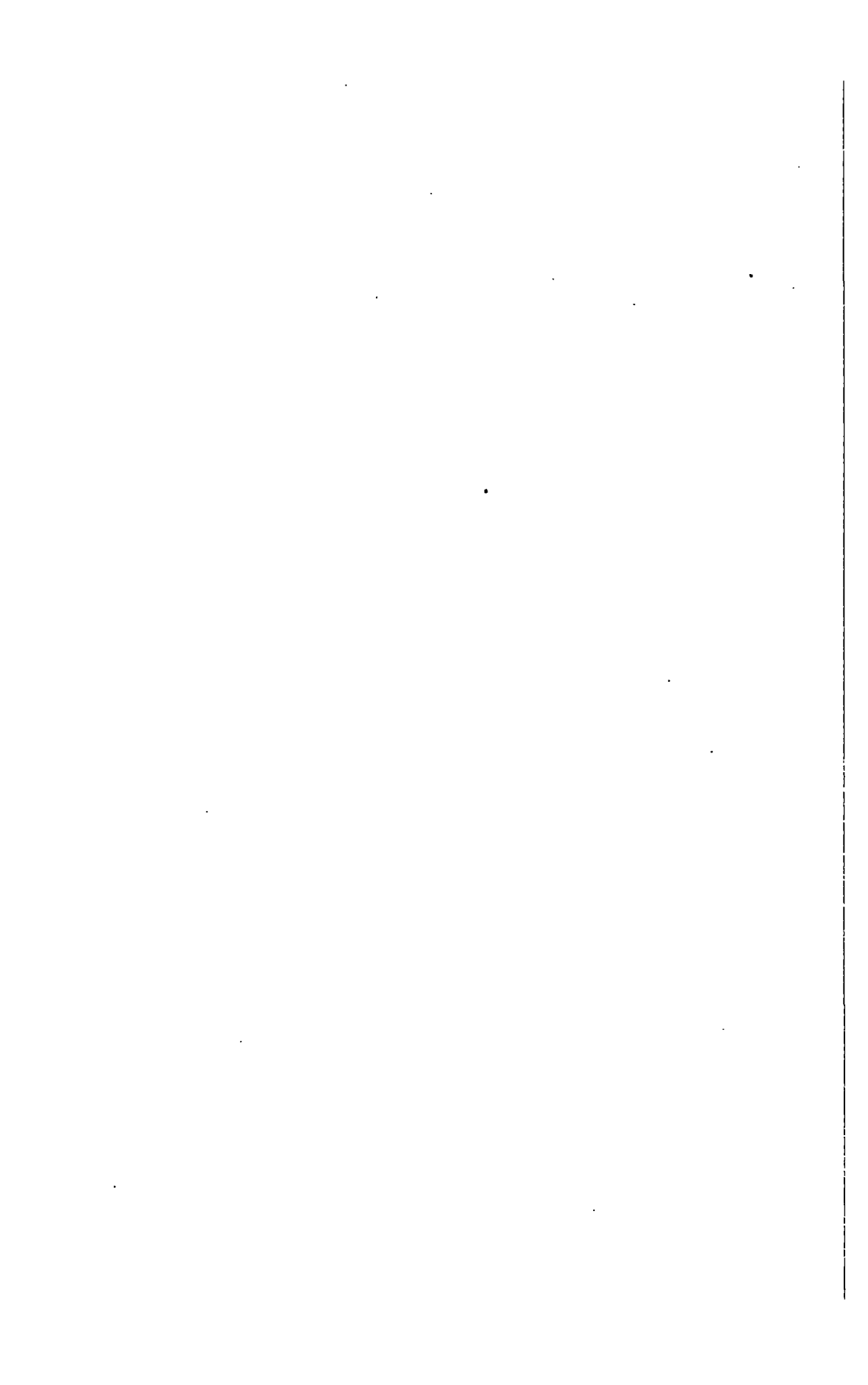
A very satisfactory fit can be reached, on the contrary, if only the (less stringent) condition

$$\text{Tr } \rho = A \quad (19)$$

is satisfied. In this case, however, some eigenvalues of  $\rho$  are negative or greater than one. This implies further investigation of the problem of the N-representability of the density matrix [23], which will be published elsewhere [21].

#### REFERENCES

- [1] KERMAN, A.K., in *Cargèse Lectures in Physics* (JEAN, M., Ed.) 3, Gordon and Breach, New York (1969) 395.
- [2] FROSCH, R.F., McCARTHY, J.S., RAND, R.E., YEARIAN, M.R., *Phys. Rev.* 160 (1967) 874.
- [3] SICK, I., McCARTHY, J.S., *Nucl. Phys.* A150 (1970) 631.
- [4] DONNELLY, T.W., WALKER, G.E., *Phys. Rev. Letts* 22 (1969) 1121.
- [5] RADHAKANT, S., KHADKIKAR, S.B., BANERJEE, B., *Nucl. Phys.* A142 (1970) 81.
- [6] BOFFI, S., *Nuovo Cim. Lett.* 2 (1969) 538; BOFFI, S., RIMINI, A., WEBER, T., *Nuovo Cim. Lett.* 4 (1970) 988.
- [7] BASSICHIS, W.H., STRAYER, M.R., *Phys. Rev. Letts* 23 (1969) 30 and M.I.T. preprint.
- [8] BASSICHIS, W.H., POHL, B.A., KERMAN, A.K., *Nucl. Phys.* A112 (1968) 360.
- [9] TABAKIN, F., *Ann. Phys.* 30 (1964) 51.
- [10] BOUTEN, M., VAN LEUVEN, P., DEPUYDT, H., *Nucl. Phys.* A94 (1967) 687; BOUTEN, M., in *Theory of Nuclear Structure* (Proc. Trieste Lectures, 1969) IAEA, Vienna (1970) 361; WARKE, C.S., GUNYE, M.R., *Phys. Rev.* 155 (1967) 1084.
- [11] DREIZLER, R., FEDERMAN, P., GIRAUD, B., OSNES, E. *Nucl. Phys.* A113 (1968) 145.
- [12] BANERJEE, M.K., LEVINSON, C.A., STEPHENSON, G.J., Jr.; *Phys. Rev.* 178 (1969) 1709.
- [13] BASSICHIS, W.H., SVENNE, J.P., *Phys. Rev. Letts* 18 (1967) 80; PAL, M.K., STAMP, A.P., *Phys. Rev.* 158 (1967) 924.
- [14] PACATI, F.D., BOFFI, S., *Phys. Rev.* 2c (1970) 1205.
- [15] BOFFI, S., PACATI, F.D., *Nuovo Cim.* 6A (1971) 465; *ibid.* 8A (1972) 470.
- [16] ELLIOTT, J.P., JACKSON, A.D., MAVROMATIS, H.A., SANDERSON, E.A., SINGH, B., *Nucl. Phys.* A121 (1968) 241.
- [17] KAKKAR, I., WAGHMARE, Y.R., *Phys. Rev.* 2c (1970) 1191.
- [18] ROWE, D.J., *Nucl. Phys.* A140 (1970) 74.
- [19] ULLAH, N., WONG, S.S.M., *Phys. Rev.* 188 (1969) 1645.
- [20] LÖWDIN, P.O., *Phys. Rev.* 97 (1955) 1474.
- [21] BOFFI, S., *Nuovo Cim. Lett.* 1 (1971) 931.
- [22] THOULESS, D.J., *Quantum Mechanics of Many-Body Systems*, Academic Press, New York (1961) 60.
- [23] See, e.g. "Reduced Density Matrices With Applications to Physical and Chemical Systems" (COLEMAN, A.J., ERDAHL, R.M., Eds, Kingston, Ontario (1968). The author is grateful to Dr. P. Nunberg for this reference.



## PART II: NUCLEAR STRUCTURE

### 3. Theory of collective motion and fission



# ANHARMONICITIES AND THE PARTICLE-VIBRATION COUPLING

L. ŠIPS

Institute "Ruder Bošković"  
Zagreb, Yugoslavia

## Abstract

ANHARMONICITIES AND THE PARTICLE-VIBRATION COUPLING.

1. Introduction; 2. Phenomenological description of nuclear vibrations; 3. The particle-vibration coupling; 4. Triangular diagrams and the quadrupole moments.

## I. INTRODUCTION

Since the early identification of the pattern of the low-lying states in some nuclei with the collective quadrupole vibrations, it has been clear that the harmonic description should prove to be insufficient. The splitting in the energy of the degenerate many-phonon multiplets, deviations from the simple harmonic rule for the transition intensities and, finally, the successful measurement of the signs and magnitudes of the quadrupole moments, have provided necessary information on the relevance of the question of what type and magnitude of anharmonicities are required by the experimental observations. The phenomenological description of the nuclear vibrations has been substantiated by the random-phase approximation [1] (there are a number of similar though differently named approximations which yield the same result in the lowest order) for it provides a means of understanding the collective vibrational states in terms of particle degrees of freedom.

To the lowest order, the random-phase approximation and similar approximations are basically harmonic; consequently, the anharmonic terms are expected in higher orders from which it may be difficult to extract the most important contributions.

The essential geometry of the problem is contained in the phenomenological description, as well. This, together with the strong evidence of the fundamentality of particle-vibration coupling [2], suggests the possibility of analysing the anharmonicities in terms of the polygonal particle-vibration coupling diagrams [1, 3]. Additional support is provided by the possibility of explaining the occurrence of quadrupole moments together with the correct other electromagnetic properties by the phenomenological description [3, 4].

In section 2, the phenomenological description will be briefly reviewed and the geometrical structure of the anharmonicities will be shown. Section 3 contains the concept of particle-vibration coupling and its relevance to the problem of anharmonicities. Finally, in section 4 triangular graphs will be shown to give the possibility of evaluating the magnitude of the third-order anharmonicities, and an explicit calculation for the isotopes of cadmium will be presented.

## 2. PHENOMENOLOGICAL DESCRIPTION OF NUCLEAR VIBRATIONS

Assuming constant rectangular density  $\rho_0$  of the incompressible matter within the radius  $R_0$  of a spherical nucleus, small deviations from sphericity can be parametrized conveniently in terms of  $\alpha_{\lambda\mu}$  such that

$$R(\theta, \varphi) = R_0 \left[ 1 + \sum_{\lambda\mu} \alpha_{\lambda\mu}^* Y_{\lambda\mu}(\theta, \varphi) \right]$$

The transformation properties of the  $\alpha_{\lambda\mu}$ 's are determined by the reality of the radius  $R(\vartheta, \varphi)$ .  $Y_{\lambda\mu}(\vartheta, \varphi)$  are spherical harmonics. Volume-conserving changes of the shape lead, in the lowest order for small  $\alpha_{\lambda\mu}$ , to the harmonic oscillator Hamiltonian:

$$H = \frac{1}{2} \sum_{\lambda} B_{\lambda} \sum_{\mu} |\dot{\alpha}_{\lambda\mu}|^2 + \frac{1}{2} \sum_{\lambda} C_{\lambda} \sum_{\mu} |\alpha_{\lambda\mu}|^2 \quad (1)$$

$\dot{\alpha}_{\lambda\mu}$  are associated velocities, while the parameters  $B_{\lambda}$  and  $C_{\lambda}$  are conveniently referred to as the inertial and the restoring force parameter of the  $\lambda$ -pole vibration, respectively. They can be calculated by assuming a definite model (e. g. a liquid drop) or else can be taken as parameters from experiment. In expression (1) parameters  $B_{\lambda}$  and  $C_{\lambda}$  are taken to be independent of  $\alpha_{\lambda\mu}$  and  $\dot{\alpha}_{\lambda\mu}$ , and it should be noted that the vibrations corresponding to different multipole characters are uncoupled and therefore qualified as normal modes. The quantization of (1) is achieved by requiring that

$$[\alpha_{\lambda\mu}, B_{\lambda}, \dot{\alpha}_{\lambda'\mu'}] = i\hbar \delta_{\lambda\lambda'} \delta_{\mu\mu'}$$

The transformation to the occupation number representation, which often proves convenient, is given by

$$\begin{aligned} \alpha_{\lambda\mu} &= \sqrt{\frac{\hbar\omega_{\lambda}}{2C_{\lambda}}} [b_{\lambda\mu}^{\dagger} + (-)^{\mu} b_{\lambda-\mu}] \\ \dot{\alpha}_{\lambda\mu} &= i\sqrt{\frac{\hbar\omega_{\lambda}}{2B_{\lambda}}} [b_{\lambda\mu}^{\dagger} - (-)^{\mu} b_{\lambda-\mu}] \end{aligned} \quad (2)$$

$b_{\lambda\mu}^{\dagger}$  and  $b_{\lambda\mu}$  are the phonon creation and annihilation operators, respectively, and the phonon vacuum  $|0\rangle$  is defined such that  $b_{\lambda\mu}|0\rangle = 0$  is fulfilled. Hamiltonian (1) assumes the form

$$H = \sum_{\lambda} \hbar\omega_{\lambda} \sum_{\mu} (b_{\lambda\mu}^{\dagger} b_{\lambda\mu} + \frac{1}{2}) = \sum_{\lambda} \hbar\omega_{\lambda} (N_{\lambda} + \frac{2\lambda+1}{2}) \quad (3)$$

Bilinear combination  $\sum_{\mu} b_{\lambda\mu}^{\dagger} b_{\lambda\mu} = N_{\lambda}$  counts the number of phonons of energy

$\hbar\omega_\lambda = \hbar(C_\lambda/B_\lambda)^{1/2}$  in a given state and it is immediately seen that (3) yields the familiar equidistant spectrum for each multipole  $\lambda$ .

The same assumptions give for the electric multipole operator the following expression:

$$M(E\lambda, \mu) = \frac{3}{4\pi} Ze R_0^\lambda \alpha_{\lambda\mu} + O(a^2) \quad (4)$$

for the uniform charge density within the nucleus. By virtue of transformation (2) it is clear that the electromagnetic transitions occur only between the states differing in phonon number  $N$  by one. Therefore, only so-called cascade transitions are allowed, whereas all the other transitions as well as the static electric moments are zero. Relative ratios of the reduced transition probabilities yield the simple  $N^1/N$  ratio when summed over the final spins;  $N^1$  and  $N$  are the phonon numbers of the initial states in question. This completes the harmonic picture.

The anharmonicities which appear in departing from the lowest-order approximation can be conveniently separated into two groups: i) the anharmonicities within a given normal mode  $\lambda$  which distort the harmonic pattern but leave the normal modes uncoupled, and ii) anharmonicities which arise from the coupling of the different normal modes.

Respecting the rotational and time-reversal invariance as well as the parity conservation, the construction of the anharmonic terms is straightforward. Note the implication of the time-reversal invariance that only the even number of associated velocities  $\dot{\alpha}_{\lambda\mu}$  appears (from  $\alpha_\lambda(-t) = \alpha_\lambda(t)$  follows  $\dot{\alpha}_\lambda(-t) = -\dot{\alpha}_\lambda(t)$ ). For the first kind of anharmonicities, cubic and quartic terms are, for example,

$$C_\lambda^c \sum_{\mu\nu\rho} \begin{bmatrix} \lambda & \lambda & \lambda \\ \mu & \nu & \rho \end{bmatrix} \alpha_{\lambda\mu} \alpha_{\lambda\nu} \alpha_{\lambda\rho} + B_\lambda^c \sum_{\mu\nu\rho} \begin{bmatrix} \lambda & \lambda & \lambda \\ \mu & \nu & \rho \end{bmatrix} \dot{\alpha}_{\lambda\mu} \alpha_{\lambda\nu} \dot{\alpha}_{\lambda\rho} \quad (5a)$$

and

$$C_\lambda^q \sum_L f(\lambda, L) [(\alpha_\lambda \alpha_\lambda)_L (\alpha_\lambda \alpha_\lambda)_L]_0 + D_\lambda^q \sum_L f'(\lambda, L) [(\dot{\alpha}_\lambda \dot{\alpha}_\lambda)_L (\alpha_\lambda \alpha_\lambda)_L]_0 + B_\lambda^q \sum_L f(\lambda, L) [(\dot{\alpha}_\lambda \dot{\alpha}_\lambda)_L (\dot{\alpha}_\lambda \dot{\alpha}_\lambda)_L]_0 \quad (5b)$$

respectively, [ ] is the 3-j symbol ensuring the symmetry and rotational invariance in (5a), whereas in (5b) it is  $f(\lambda, L)$  and by brackets are denoted couplings.  $f(\lambda, L)$  can be directly related to the symmetric fractional grandparentage coefficients [5]. Parity conservation would immediately set equal to zero terms (5a) for odd multipoles  $\lambda$ .

The cubic terms of the second group of anharmonicities coupling the different normal modes are of the form:

$$\begin{aligned}
 C^c(\lambda\lambda\lambda') & \sum_{\mu\nu\rho} \begin{bmatrix} \lambda & \lambda & \lambda' \\ \mu & \nu & \rho \end{bmatrix} \alpha_{\lambda\mu} \alpha_{\lambda\nu} \alpha_{\lambda'\rho} \\
 B^c(\dot{\lambda}\dot{\lambda}\dot{\lambda}') & \sum_{\mu\nu\rho} \begin{bmatrix} \lambda & \lambda & \lambda' \\ \mu & \nu & \rho \end{bmatrix} \dot{\alpha}_{\lambda\mu} \dot{\alpha}_{\lambda\nu} \dot{\alpha}_{\lambda'\rho} \\
 B^c(\dot{\lambda}\lambda\dot{\lambda}') & \sum_{\mu\nu\rho} \begin{bmatrix} \lambda & \lambda & \lambda' \\ \mu & \nu & \rho \end{bmatrix} \dot{\alpha}_{\lambda\mu} \alpha_{\lambda\nu} \dot{\alpha}_{\lambda'\rho}
 \end{aligned} \tag{6}$$

There are many fourth-order or quartic terms which can be easily constructed following the above-mentioned rules. However, the main concern here will be the anharmonicities within a given normal mode, more specifically with  $\lambda = 2$  quadrupole vibrations.

A few general remarks are in order. Rewriting expressions (5a) and (5b) by making use of transformation (2), it becomes apparent that the two expressions obtained will have different effects on the properties of the vibrator. Their diagrammatic expression is as follows:

$$A_0[\Psi + \Lambda] + A_1[\Upsilon + \Lambda] \tag{5a'}$$

$$D_0[\Psi + \Lambda] + D_1[\Upsilon + \Lambda] + D_2[\times] \tag{5b'}$$

$A_0$ ,  $A_1$  as well as  $D_0$ ,  $D_1$  and  $D_2$  are expressed in terms of  $C_\lambda^c$ ,  $B_\lambda^c$  and  $C_\lambda^q$ ,  $D_\lambda^q$  and  $B_\lambda^q$ , respectively, and the broken line represents phonon. Neglecting the contributions from the terms containing  $\dot{\alpha}_{\lambda\mu}$  (extreme adiabatic limit) thereby retaining only the "potential energy" terms, there are simple relations between the constants. If the order of the anharmonicity is  $n$ , then there are  $\binom{n}{r}$  (binomial coefficient) diagrams with  $r$  phonon lines coming in. Now  $\binom{n}{r} = \binom{n}{n-r}$  and it is, of course, true that the Hermitian conjugate diagrams have the same weight. For example, in (5a')  $A_1 = 3A_0$  and in (5b')  $D_2 : D_1 : D_0 = 6 : 4 : 1$ .

It is clear that the odd and the even power anharmonicities form two separate chains. While the even chain (see (5b) and (5b')) contributes to the energy in the first order of perturbation and admixes to a state with given  $N$  states with  $N$ ,  $N \pm 2$ ,  $N \pm 4$ , etc., the odd chain will give second-order energy corrections and admix  $N \pm 1$ ,  $N \pm 3$ , etc., states to a given state  $N$ . Therefore, in view of expression (4) the even chain will produce neither static moment nor cross-over transition. The odd chain will give both non-zero, but it has been shown [4] that the large moments do not necessarily imply large cross-over transitions. It should also be noted that, although the quartic anharmonicity is an order of magnitude ( $\sqrt{\hbar\omega}/2C \approx 0.1$ ) smaller than the cubic one, it is necessary to take it into account if the energies are to be reproduced. In other words, with each odd-power anharmonicity one should incorporate one order higher even-

power anharmonicity, otherwise the nucleus becomes unstable. For the purpose of investigating the origin of the static moments it is, however, sufficient to consider the cubic anharmonicity only.

The constants in Eqs (5a) and (5b) are parameters to be fixed by comparison with experiment. This leads, of course, to a multi-parameter analysis which is neither an easy nor a very enlightening procedure. Therefore, it is very instructive to try and calculate the respective constants, a possibility which has been offered by the success of the particle-vibration coupling.

### 3. THE PARTICLE-VIBRATION COUPLING

When an incompressible nucleus vibrates, its density will clearly undergo changes in shape. Assuming that the changes in the density are followed by changes in the potential and that the equipotential surfaces have the shape of the nuclear surface, it follows that under the small amplitude  $\alpha_{\lambda\mu}$  vibrations, each point  $r$  is subject to the change

$$r \rightarrow r \left[ 1 + \sum_{\lambda,\mu} \alpha_{\lambda\mu}^* Y_{\lambda\mu} \right]$$

Therefore for the potential one has to put

$$V(r) \rightarrow V \left[ r / \left( 1 + \sum_{\lambda\mu} \alpha_{\lambda\mu}^* Y_{\lambda\mu} \right) \right]$$

Smallness of the vibrational amplitude allows one to expand around  $\alpha_{\lambda\mu} = 0$

$$V \left[ r / \left( 1 + \sum_{\lambda,\mu} \alpha_{\lambda\mu}^* Y_{\lambda\mu} \right) \right] = V \left[ r \left( 1 - \sum_{\lambda,\mu} \alpha_{\lambda\mu}^* Y_{\lambda\mu} \right) \right] = V(r) - r \frac{\partial V(r)}{\partial r} \sum \alpha_{\lambda\mu}^* Y_{\lambda\mu} \quad (7)$$

The second term in expression (7) represents the change of the potential felt by the particle and can conveniently be written as

$$H_{pv} = \kappa(r) \sum_{\lambda} (2\lambda + 1)^{\frac{1}{2}} \sum_{\mu} (\alpha_{\lambda} Y_{\lambda})_0 \quad (8)$$

where  $H_{pv}$  stands for the particle-vibration coupling and the bracket  $( )_0$  denotes symbolically the angular momentum coupling [1].  $\kappa(r) = -r(\partial V(r))/\partial r$  is the radial dependence of the coupling. If the potential is well described by the square well,  $\kappa(r)$  is simply  $V_0 R_0 \delta(r-R_0)$  where  $R_0$  is nuclear radius and  $\delta(r-R_0)$  the usual delta function. For the harmonic oscillator potential  $\kappa(r)$  will be proportional to  $r^2$ , therefore having the same form as the original potential. In the case of the more realistic Woods-Saxon potential

$\kappa(r)$  will be surface-peaked, though slightly asymmetric owing to the weighting with  $r$ . The Woods-Saxon potential is conveniently represented as

$$V(r) = -V_0 f(r) = -V_0 \left[ 1 / \left( 1 + e^{\frac{r-R_0}{a}} \right) \right]$$

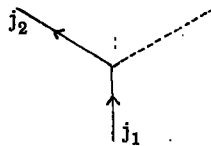
with  $R_0$  being the nuclear radius,  $V_0$  the depth of the potential and  $a$  the diffuseness parameter.  $\kappa(r)$  is then given by

$$\kappa(r) = -V_0 \frac{r}{a} \frac{e^{\frac{r-R_0}{a}}}{\left[ 1 + e^{\frac{r-R_0}{a}} \right]^2}$$

Now, for the last bound particle  $R_0^3 \varphi^2(R_0) \approx 1.4$  [6] ( $\varphi(R_0)$  is the value of the radial wave function at the surface  $R_0$ ) so that if  $V_0 = 48$  MeV and  $a = 0.6$  fm the value of the radial integral at the surface will be  $\sim 2.8$  MeV. The integration over the spread contributes to the final average value of  $\sim 50$ -60 MeV [3].

By virtue of transformation (2) it is seen that the strength of the particle-vibration coupling depends also on the amplitude of the vibration  $\sqrt{\hbar\omega_\lambda/2C_\lambda}$ . In practical calculations (see, e.g. section 4) the amplitude of the vibration can be determined from the ground-state transition with an accuracy corresponding to the degree of the validity of the approximations invoked in deriving expression (4).

The matrix element representing the scattering of the particle off the phonon due to the  $H_{pv}$  will be calculated explicitly. The corresponding diagram is



where the vertex is the particle-vibration coupling  $H_{pv}$  (8):

$$\begin{aligned} \langle (j_2\lambda) j_1 | H_{pv} | j_1 \rangle &= (j_2 | \kappa(r) | j_1) (2j_2 + 1)^{-\frac{1}{2}} \langle j_2 || Y_\lambda || j_1 \rangle \\ &\times \sum_{m_2, \mu, \nu} \langle j_2 m_2 \lambda \mu | j_1 m_1 \rangle \langle j_1 m_1 \lambda - \nu | j_2 m_2 \rangle (-)^{\lambda - \nu} \langle \lambda \mu | \alpha_{\lambda\nu} | 0 \rangle \end{aligned}$$

where  $\langle | \rangle$  are the vector coupling coefficients,  $\langle || \rangle$  the radial matrix element  $\langle || || \rangle$  the reduced matrix element. Making use of transformation (2),

$$\langle \lambda \mu | \alpha_{\lambda\nu} | 0 \rangle = \sqrt{\frac{\hbar\omega_\lambda}{2C_\lambda}} \langle \lambda \mu | (b_{\lambda\nu}^\dagger + (-)^\nu b_{\lambda-\nu}) | 0 \rangle = \sqrt{\frac{\hbar\omega_\lambda}{2C_\lambda}} \delta_{\mu\nu}$$

and performing the summation, one obtains:

$$\langle (j_2 \lambda) j_1 | H_{pv} | j_1 \rangle = (-)^{\lambda+j_2-j_1} (j_2 | \kappa(r) | j_1) (2j_1 + 1)^{-\frac{1}{2}} \sqrt{\frac{\hbar \omega_\lambda}{2C_\lambda}} \langle j_2 || Y_\lambda || j_1 \rangle$$

The reduced matrix element is

$$\langle j_2 || Y_\lambda || j_1 \rangle = (-)^{\lambda+j_2-j_1} \left[ \frac{(2j_1 + 1)(2\lambda + 1)}{4\pi} \right]^{\frac{1}{2}} \langle j_1 \frac{1}{2} \lambda 0 | j_2 \frac{1}{2} \rangle$$

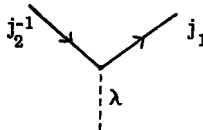
which, together with the definition [3],

$$a(r) = \frac{1}{\sqrt{4\pi}} \sqrt{\frac{\hbar \omega_\lambda}{2C_\lambda}} \kappa(r)$$

yields finally

$$\langle (j_2 \lambda) j_1 | H_{pv} | j_1 \rangle = (j_2 | a(r) | j_1) (2\lambda + 1)^{\frac{1}{2}} \langle j_1 \frac{1}{2} \lambda 0 | j_2 \frac{1}{2} \rangle \equiv H_{21} \quad (9)$$

Expression (9) denoted by the  $H_{21}$  in Ref. [2] is one of the basic building blocks for the particle-vibration coupling diagrams. Remembering that in the random-phase approximation the phonon represents many scatterings of the particle-hole (quasi-particle) pairs, another important building block corresponds to the diagram



and is related to expression (9) by

$$\langle (j_1 j_2^{-1}) \lambda | H_{pv} | \lambda \rangle = \sqrt{\frac{2j_2 + 1}{2\lambda + 1}} H_{12} \quad (10)$$

In the case of the open-shell quasi-particles expressions (9) and (10) are multiplied by the factors  $(U_1 U_2 - V_1 V_2)$  and  $(U_1 V_2 + U_2 V_1)$ , respectively [2], and the corresponding diagrams bear no arrows on the particle (hole) lines. Note that (9) and (10) represent the matrix elements of the respective diagrams; the energy denominators have not been exhibited.

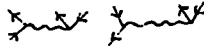
The relation of the particle-vibration coupling and the anharmonicities can be understood as follows. Given a certain basis (Hartree-Fock or shell model, for example) the random-phase approximation means taking from the Hamiltonian

$$H = \sum_{\alpha\beta} T_{\alpha\beta} a_\alpha^\dagger a_\beta + \frac{1}{4} \sum_{\alpha\beta\gamma\delta} V_{\alpha\beta\gamma\delta} a_\alpha^\dagger a_\beta^\dagger a_\gamma a_\delta$$

terms which correspond to the particle-hole pair scattering by the interaction  $V$ . In the case of the pairing vibrations, it is particle-particle and hole-hole pairs. For the particle-hole random-phase approximation this can be represented as the summation of the diagrams



where the wavy line is the interaction  $V$ . By inspecting expression (9) and the corresponding diagram it is clear that the diagrams of the type



are included by the particle-vibration coupling. To make them identical one has to replace the particle-hole pair by the phonon line (random-phase approximation summation at the particle-hole pair scattering) and the interaction wavy line by the  $H_{pv}$ . The tensorial property is correct, as can be established by the fact that the particle-hole pair carries the angular momentum  $\lambda$  of the vibration requiring the particle vertex to have the same transformation property. This is manifestly so in expression (8) of  $H_{pv}$ .

Therefore one can say that the particle-vibration coupling takes more of the dynamics of the total Hamiltonian. The diagrams associated with expression (9) are the ones responsible for the non-linearity in the problem of vibrations, or, as usually phrased, for the anharmonicities in the vibrational motion [2]. Their magnitude will depend on the shell structure in the nucleus in question, as will be seen in the next section where the connection between the triangular graphs and the quadrupole moment is discussed.

#### 4. TRIANGULAR DIAGRAMS AND THE QUADRUPOLE MOMENTS

Assuming that in the first excited state of the vibrator  $|N\lambda\rangle \equiv |12\rangle$  ( $N$  stands for the number of phonons) there is an admixture of the two-phonon state  $|22\rangle$  with the amplitude  $a_{21}$ , the diagonal matrix element of the electric multipole operator  $M(E\lambda, \mu)$  of (4) for  $\lambda = 2$  in the state  $|2_1\rangle = |12\rangle + a_{21}|22\rangle$  is

$$\langle 2_1 | M(E2, \mu) | 2_1 \rangle = 2 a_{21} \langle 12 | M(E2, \mu) | 22 \rangle$$

The definition of the quadrupole moment

$$eQ(I) = \begin{pmatrix} 1 & 2 & 1 \\ -1 & 0 & 1 \end{pmatrix} \sqrt{\frac{16\pi}{5}} \langle I || M(E2) || I \rangle$$

gives immediately the relation between the quadrupole moment and the amplitude  $a_{21}$  of the admixture as

$$eQ(2_1) = 2a_{21} \sqrt{\frac{16\pi}{5}} \begin{pmatrix} 2 & 2 & 2 \\ -2 & 0 & 2 \end{pmatrix} \langle 12 || M(E2) || 22 \rangle$$

Now as  $\langle 12 || b || 2R \rangle = \sqrt{2(2R+1)}$ , by virtue of expression (4) and the transformation (2) we obtain

$$eQ(2_1) = 2\sqrt{10} a_{21} \sqrt{\frac{16\pi}{5}} \begin{pmatrix} 2 & 2 & 2 \\ -2 & 0 & 2 \end{pmatrix} \cdot \frac{3}{4\pi} Ze R_0^2 \sqrt{\frac{\hbar\omega_2}{2C_2}} \quad (11')$$

Remembering, however, that in the harmonic picture the reduced transition probability for the ground state transition is

$$B(E2, 12 \rightarrow 00) = \left( \frac{3}{4\pi} Ze R_0^2 \right)^2 \frac{\hbar\omega_2}{2C_2}$$

it is seen that, for the small amplitudes of the admixture  $a_{21}$ , the last factor in expression (11') can be extracted from the experiment in a given nucleus. The expression for the quadrupole moment is then

$$eQ(2_1) = 2\sqrt{10} a_{21} \sqrt{\frac{16\pi}{5}} \begin{pmatrix} 2 & 2 & 2 \\ -2 & 0 & 2 \end{pmatrix} (B(E2, 12 \rightarrow 00))^{\frac{1}{2}} \quad (11)$$

The knowledge of the amplitude  $a_{21}$  provides the sign and the magnitude of the quadrupole moment. This is of course in the lowest order of perturbation. Higher order terms, however, for reasonable values of  $a_{21}$  do not change appreciably the values obtained (see, e.g. Ref. [4]).

The amplitude  $a_{21}$  can be determined in the phenomenological approach by relating it to the magnitude of the third-order anharmonicity ( $A_1$  of (5a'))

$$a_{21} = -\sqrt{\frac{2}{5}} \frac{A_1}{\hbar\omega}$$

This, however, is the relation of one unknown to another and it is important to be able to calculate the amplitude  $a_{21}$ . Such a possibility is suggested by expressions (9) and (10) and respective diagrams.

The particle-vibration coupling  $H_{pv}$  (8) changes the number of phonons by one and therefore the lowest-order expression for  $a_{21}$  is given by the third-order perturbation

$$a_{21} = \sum_{a, b \neq i} \frac{\langle 2 \text{ phon} | H_{pv} | b \rangle \langle b | H_{pv} | a \rangle \langle a | H_{pv} | i \equiv 1 \text{ phon} \rangle}{(\hbar\omega - E_a)(\hbar\omega - E_b)(-\hbar\omega)} \quad (12)$$

For the particle scattering off the phonon the diagrammatic expression of (12) is shown in Fig.1. There are three terms whose matrix elements (numerators of (12)) are the same:

$$M_p = -\sqrt{\frac{2}{5}} (4\pi)^{\frac{1}{2}} \langle j_1 || a(r) Y_2 || j_2 \rangle \langle j_2 || a(r) Y_2 || \bar{j}_2 \rangle \langle \bar{j}_2 || a(r) Y_2 || j_1 \rangle \left\{ \begin{matrix} 2 & 2 & 2 \\ j_1 & j_2 & \bar{j}_2 \end{matrix} \right\} \quad (13)$$

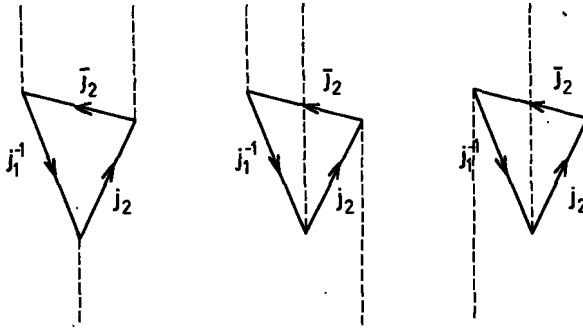


FIG. 1. Triangular diagrams for particle scattering (13). The sum of their energy denominators is given by expression (13').

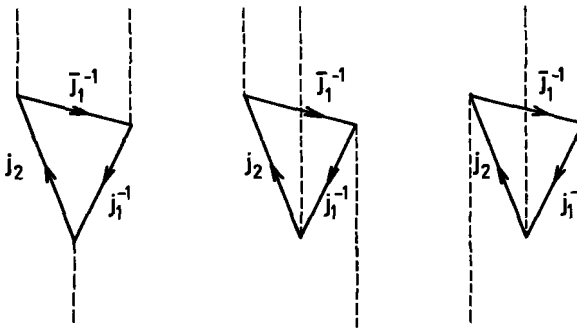


FIG. 2. Triangular diagrams for hole scattering (14). The sum of their energy denominators is given by expression (14').

The subscript p denotes particle scattering, { } is the 6-j symbol and the definition  $\langle j_1 \| a(r) Y_2 \| j_2 \rangle \equiv (j_1 | a(r) | j_2) \langle j_1 \| Y_2 \| j_2 \rangle$  is used for the sake of brevity. The summed energy denominator is

$$E_p^{-1} = - \frac{\hbar\omega (\epsilon(j_2) - \epsilon(\bar{j}_2)) + 3 (\epsilon(j_1^{-1}) + \epsilon(j_2)) (\epsilon(j_1^{-1}) + \epsilon(\bar{j}_1) + \hbar\omega)}{\hbar\omega (\epsilon(j_1^{-1}) + \epsilon(\bar{j}_2)) (\epsilon(j_1^{-1}) + \epsilon(j_2) - \hbar\omega) (\epsilon(j_1^{-1}) + \epsilon(j_2) + \hbar\omega) (\epsilon(j_1^{-1}) + \epsilon(\bar{j}_2) + 2\hbar\omega)}$$

(13')

where  $\epsilon(j)$  and  $\epsilon(j^{-1})$  are single-particle and single-hole energies, respectively. The amplitude  $a_{21}$  is then simply  $a_{21} = M_p E_p^{-1}$ . In the case of the hole scattering off the phonon (see Fig.2), the respective expressions are:

$$M_h = \sqrt{\frac{2}{5}} (4\pi)^{\frac{1}{2}} \langle j_1 \| a(r) Y_2 \| \bar{j}_1 \rangle \langle \bar{j}_1 \| a(r) Y_2 \| j_2 \rangle \langle j_2 \| a(r) Y_2 \| j_1 \rangle \left\{ \begin{matrix} 2 & 2 & 2 \\ j_2 & j_1 & \bar{j}_1 \end{matrix} \right\}$$

(14)

and

$$E_h^{-1} = - \frac{\hbar\omega (\epsilon(j_1^{-1}) - \epsilon(\bar{j}_1^{-1})) + 3 (\epsilon(j_2) + \epsilon(j_1^{-1})) (\epsilon(j_2) + \epsilon(\bar{j}_1^{-1}) + \hbar\omega)}{\hbar\omega (\epsilon(j_2) + \epsilon(\bar{j}_1^{-1})) (\epsilon(j_2) + \epsilon(j_1^{-1}) - \hbar\omega) (\epsilon(j_2) + \epsilon(\bar{j}_1^{-1}) + \hbar\omega) (\epsilon(j_2) + \epsilon(\bar{j}_1^{-1}) + 2\hbar\omega)} \tag{14'}$$

The relation  $\langle j^{-1} \| Y_\lambda \| j^{-1} \rangle = (-)^{\lambda+1} \langle j \| Y_\lambda \| j \rangle$  has been employed [6]. In the particular case when the particle and the hole remain in the same state after the scattering off the phonon, expressions (13) and (14) have to be taken when evaluating the amplitude  $a_{21}$ . The reason is that then both the particle and the hole can experience the particle-vibration coupling  $H_{pv}$ . The corresponding diagrams are shown in Fig.3 and the expressions for the  $M_{ph}$  and  $E_{ph}$  are

$$M_{ph} = (-)^{j_1+j_2} (4\pi)^{3/2} \sqrt{\frac{2}{5}} \langle j_1 \| a(r) Y_2 \| j_2 \rangle^2 \left[ \langle j_2 \| a(r) Y_2 \| j_2 \rangle \left\{ \begin{matrix} 2 & 2 & 2 \\ j_1 & j_2 & j_2 \end{matrix} \right\} \right. \\ \left. - \langle j_1 \| a(r) Y_2 \| j_1 \rangle \left\{ \begin{matrix} 2 & 2 & 2 \\ j_2 & j_1 & j_1 \end{matrix} \right\} \right] \tag{15}$$

and

$$E_{ph}^{-1} = -3 [\hbar\omega (\epsilon(j_1^{-1}) + \epsilon(j_2) - \hbar\omega) (\epsilon(j_1^{-1}) + \epsilon(j_2) + 2\hbar\omega)]^{-1} \tag{15'}$$

respectively.

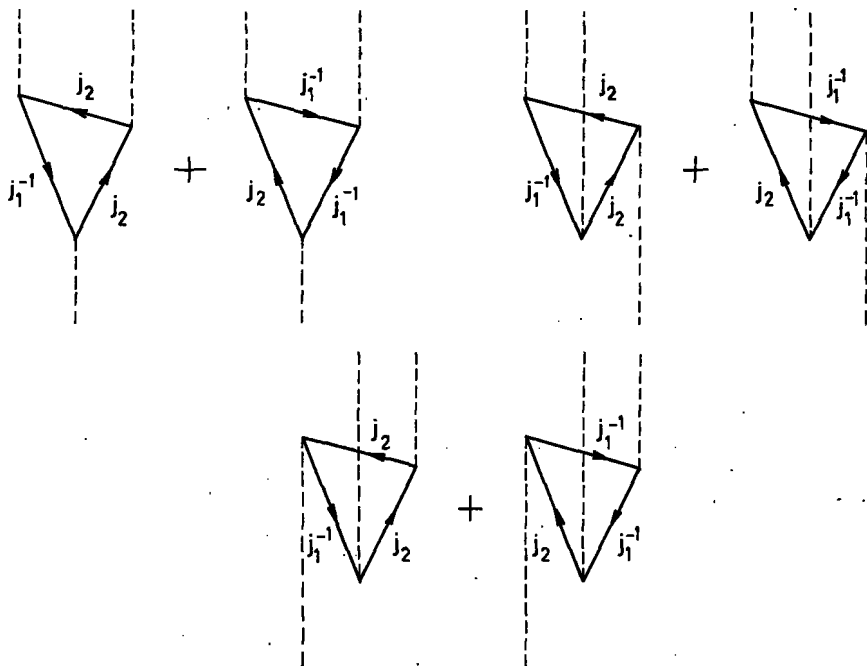
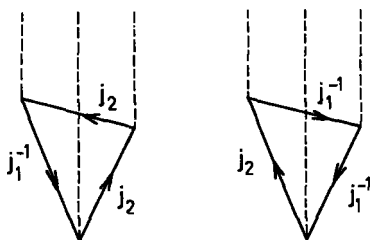


FIG. 3. Triangular diagrams illustrating expressions (15) and (15').

FIG. 4. Diagrams contributing to the  $a_{30}$  amplitude.

It is possible to relate this calculated amplitude  $a_{21}$  to the magnitude of the equivalent cubic anharmonicity  $A_1$  (5a'). However, it will now depend on  $\omega$ . According to the amplitude  $a_{21}$  of (15) and (15'),  $A_1(\omega)$  is given by

$$A_1(\omega) = (-)^{j_1+j_2} (4\pi)^{3/2} \frac{3 \langle j_1 \| a(r) Y_2 \| j_2 \rangle^2}{(\epsilon(j_1^{-1}) + \epsilon(j_2) - \hbar\omega)(\epsilon(j_1^{-1}) + \epsilon(j_2) + 2\hbar\omega)} \\ \times \left[ \langle j_2 \| a(r) Y_2 \| j_2 \rangle \left\{ \begin{matrix} 2 & 2 & 2 \\ j_1 & j_2 & j_2 \end{matrix} \right\} - \langle j_1 \| a(r) Y_2 \| j_1 \rangle \left\{ \begin{matrix} 2 & 2 & 2 \\ j_2 & j_1 & j_1 \end{matrix} \right\} \right]$$

By evaluating the diagrams (Fig. 4) corresponding to the admixture of the three-phonon state to the ground state whose amplitude is  $a_{30}$ , one finds for  $A_0(\omega)$  (5a')

$$A_0(\omega) = (-)^{j_1+j_2} (4\pi)^{3/2} \frac{\langle j_1 \| a(r) Y_2 \| j_2 \rangle^2}{(\epsilon(j_1^{-1}) + \epsilon(j_2) + \hbar\omega)(\epsilon(j_1^{-1}) + \epsilon(j_2) + 2\hbar\omega)} \\ \times \left[ \langle j_2 \| a(r) Y_2 \| j_2 \rangle \left\{ \begin{matrix} 2 & 2 & 2 \\ j_1 & j_2 & j_2 \end{matrix} \right\} - \langle j_1 \| a(r) Y_2 \| j_1 \rangle \left\{ \begin{matrix} 2 & 2 & 2 \\ j_2 & j_1 & j_1 \end{matrix} \right\} \right]$$

Consequently, there is the relation

$$A_1(\omega) = 3 \frac{\epsilon(j_1^{-1}) + \epsilon(j_2) + \hbar\omega}{\epsilon(j_1^{-1}) + \epsilon(j_2) - \hbar\omega} A_0(\omega)$$

which for  $\hbar\omega \ll \epsilon(j_1^{-1}) + \epsilon(j_2)$  reduces to  $A_1 = 3A_0$  found for the extreme adiabatic case in section 2.

The expressions for the open-shell quasi-particles are obtained following the prescription given with the basic building blocks (9) and (10). The second term in the square bracket of expression (15), however, comes with the opposite sign, for the particle hole difference is contained in the appropriate values of the  $U_j$  and  $V_j$  coefficients for the state in question. The particle energies  $\epsilon(j)$  in the energy denominators are, of course, to be replaced by the quasi-particle energies  $E_j$ .

In nuclei where either protons or neutrons are near the closed shell it has been known [7] that the BCS-solution becomes poor and, therefore, the expressions for triangles involving the seniority [5]  $v=0$  to  $v=2$  two-

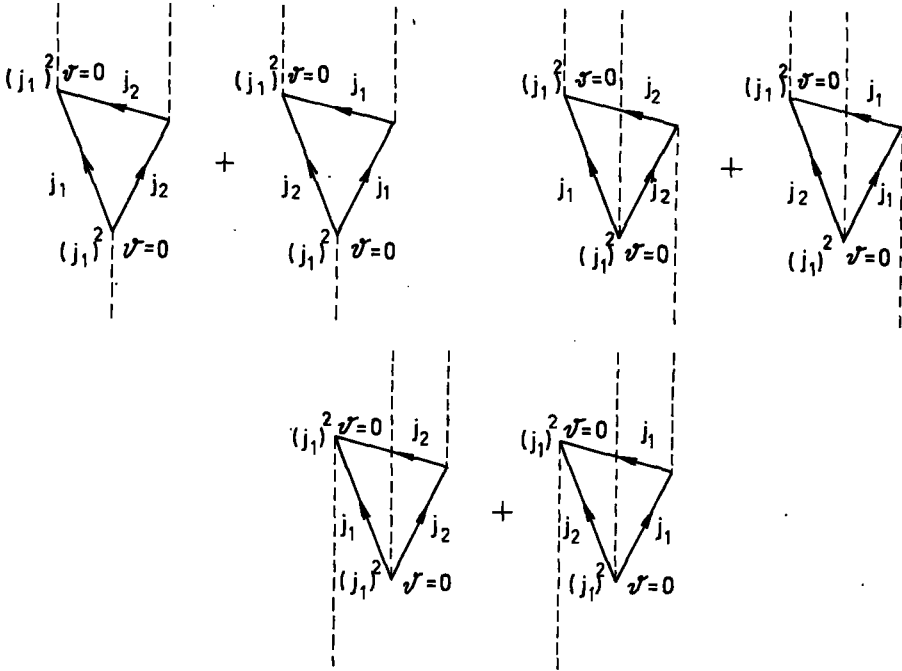


FIG. 5. Particle triangular diagrams for  $(j_1)^2 0 \rightarrow (j_1)^2 0$  corresponding to expressions (16) and (16').

particle (hole) states are considered. The corresponding diagrams are shown in Fig. 5 and the matrix element and the energy denominator are

$$M = (-)^{j_1 + j_2} (4\pi)^{3/2} \sqrt{\frac{2}{5}} \frac{\langle j_1 \| a(r) Y_2 \| j_2 \rangle^2}{2j_1 + 1} \left[ \langle j_1 \| a(r) Y_2 \| j_1 \rangle \begin{Bmatrix} 2 & 2 & 2 \\ j_2 & j_1 & j_1 \end{Bmatrix} \right. \\ \left. + \langle j_2 \| a(r) Y_2 \| j_2 \rangle \begin{Bmatrix} 2 & 2 & 2 \\ j_1 & j_2 & j_2 \end{Bmatrix} \right] \quad (16)$$

and

$$E^{-1} = -3 [\hbar\omega (\epsilon(j_1) + \epsilon(j_2)) - \hbar\omega (\epsilon(j_1) + \epsilon(j_2) + 2\hbar\omega)]^{-1} \quad (16')$$

respectively, for particles, and the same expression except for the general minus sign in the matrix element  $M$  for holes. The factor  $(2j_1 + 1)^{-1}$  comes from the fact that there are only two particles (holes) whereas it did not appear in the particle-hole case, Eq. (15), because of the  $\sqrt{n} = \sqrt{(2j_1 + 1)}$  normalization when one particle is taken out of the closed subshell  $j_1$ . In the case of the difference in the initial and the final  $\nu = 0$   $j$ -value, expression (16) is to be multiplied by the appropriate statistical factor. Equation (16) has been evaluated (see Fig. 5) for  $(j_1)^2 0, \nu = 0 \rightarrow (j_1)^2 0, \nu = 0$ , consequently, for  $(j_1)^2 0, \nu = 0 \rightarrow (j_2)^2 0, \nu = 0$  it should be multiplied by the factor  $[(2j_1 + 1)/(2j_2 + 1)]^{1/2}$ . When pairing among these two particles (holes) is

taken into account, it is clear that the gap  $\Delta_j$  will appear in the energy denominators. For example, in the case of a single-(j)<sup>2</sup> configuration with pairing the amplitude  $a_{21}$  assumes a very simple form:

$$a_{21} = (4\pi)^{3/2} \sqrt{\frac{2}{5}} \frac{24}{\hbar\omega(\Delta_j - \hbar\omega)(\Delta_j + 2\hbar\omega)} \frac{\langle j \| a(r) Y_2 \| j \rangle^3}{2j+1} \begin{Bmatrix} 2 & 2 & 2 \\ j & j & j \end{Bmatrix} \quad (17)$$

Before the amplitudes  $a_{21}$  are explicitly evaluated for chosen examples, an approximate selection rule for the vertices should be mentioned. From expression (8) for the particle-vibration coupling  $H_{pv}$  follows, that, in the case of density fluctuations,  $H_{pv}$  acts only on the orbital motion which implies the difference between the spin-flip and the non-spin-flip vertices [2, 3]. The larger the single-particle j-value the greater the difference. As an illustration several reduced matrix elements are listed:

$$\langle 9/2 \| Y_2 \| 9/2 \rangle = -\frac{1}{\sqrt{4\pi}} 3.4, \quad \langle 9/2 \| Y_2 \| 5/2 \rangle = -\frac{1}{\sqrt{4\pi}} 3.8 \rightarrow \text{non-spin flip}$$

$$\langle 9/2 \| Y_2 \| 7/2 \rangle = -\frac{1}{\sqrt{4\pi}} 0.94, \quad \langle 7/2 \| Y_2 \| 5/2 \rangle = -\frac{1}{\sqrt{4\pi}} 1.04 \rightarrow \text{spin flip}$$

Upon inspection of expressions (13) - (16) and the corresponding triangular diagrams, Figs 1-5, it is seen that the spin-flip vertices come twice and therefore the reduction of the spin-flip diagrams compared to the values of the non-spin-flip diagrams is approximately given by the ratio of the reduced matrix elements squared. As an example, possible diagrams for the closed shell  $Z = 50$  are considered. The hole will be made in the states  $p_{1/2}$ ,  $p_{3/2}$ ,  $f_{5/2}$  and  $g_{9/2}$  of the 28-50 major shell. In evaluating the triangular diagrams, one of the particles is promoted to the major shell 50-82 containing the  $s_{1/2}$ ,  $d_{3/2}$ ,  $d_{5/2}$ ,  $g_{7/2}$  and  $h_{11/2}$  single-particle states. Simple angular-momentum and parity considerations show that only the  $g_{9/2}$  particle is to be promoted to either the  $d_{5/2}$  or the  $g_{7/2}$  orbit. This still yields 18 triangular diagrams (see Figs 1 and 3). Taking for the radial matrix elements of  $a(r)$  an average value  $a$  it is simple to see that the non-spin-flip diagrams are by a factor 12-16 greater than the spin-flip ones. The difference in the energy denominators ( $\epsilon(9/2) = 0$ ,  $\epsilon(5/2) = 4.5$  MeV and  $\epsilon(7/2) = 5.2$  MeV) is small. In practical calculations, provided the particle angular momenta are not small, this approximate selection rule considerably reduces the number of triangular diagrams to be evaluated.

<sup>114</sup>Cd has been the first vibrational-like nucleus in which a large quadrupole moment has been found experimentally [8]. Many experiments have been performed on different nuclei since [9] using the same higher-order Coulomb excitation process. Recent experiments [10, 11] are of particular interest for they (Ref. [10]) represent relative measurements providing the data on <sup>108</sup>Cd - <sup>116</sup>Cd nuclei. This gives the possibility of observing the change in the quadrupole moments due to the difference in neutron number. Relevant experimental data are given in Table I.

Cd isotopes have the proton number  $Z = 48$  and therefore the proton part of the wave function will be represented by two holes in the 28-50 proton shell. It is noted that the particle-hole triangles in this case are multiplied by the square of the fractional parentage coefficient [5]  $\langle (9/2)^2 0, 9/2; 9/2 \rangle \langle 9/2 \rangle^2 \theta = 1 \langle 9/2 \rangle^2 = 4/15$  and can be neglected, being

TABLE I. EXPERIMENTAL DATA OF REF. [10]

Isotope	$E(2_1^+)$ MeV	$B(E2; 2_1^+ \rightarrow 0_1^+)e^2b^2$	$Q(2_1^+)eb$
$^{106}\text{Cd}$	0.633	0.084	$-0.84 \pm 0.28$
$^{108}\text{Cd}$	0.633	0.084	$-0.84 \pm 0.28$
$^{110}\text{Cd}$	0.656	0.087	$-0.24 \pm 0.09$
$^{112}\text{Cd}$	0.618	0.097	$-0.15 \pm 0.07$
$^{114}\text{Cd}$	0.558	0.112	-0.38
$^{116}\text{Cd}$	0.517	0.131	$-0.88 \pm 0.25$

Note that the value  $-0.38$  eb of the  $^{114}\text{Cd}$  quadrupole moment has been used as a reference for relative measurements.

TABLE II. CALCULATED QUADRUPOLE MOMENTS IN eb COMPARED WITH EXPERIMENTAL VALUES OF REFS [10, 11]

Isotope	$Q_{\text{exp}}$ in eb	$Q_{\text{calc}}$ in eb
$^{106}\text{Cd}$	$-0.76 \pm 0.15^b$	-
$^{108}\text{Cd}$	$-0.84 \pm 0.28^a$	-0.14
$^{110}\text{Cd}$	$-0.24 \pm 0.09^a$	-0.16
$^{112}\text{Cd}$	$-0.15 \pm 0.07^a$	-0.26
$^{114}\text{Cd}$	$-0.38^a$ $-0.32 \pm 0.11^b$	-0.48
$^{116}\text{Cd}$	$-0.88 \pm 0.25^a$	-0.69

<sup>a</sup> See Ref. [10]

<sup>b</sup> See Ref. [11]

of the order of  $0.03 a^3$ . Throughout the calculation an average value for the radial integrals  $(nlj | a(r) | n'l'j')$  =  $a = -0.5$  MeV is used. The triangles based on the  $(9/2)^{-2}$  configuration with  $\Delta_{9/2} = 2$  MeV ( $6^+$  and  $8^+$  states are not observed below that energy) are evaluated using expression (17) with the general minus sign because of holes. The effect of  $p_{1/2}^{-1}$  and  $p_{3/2}^{-1}$  hole states [12] is mocked by multiplying the amplitudes obtained with 0.9 ( $^{108}\text{Cd}$ ), 0.85 ( $^{110}\text{Cd}$ ) and 0.8 ( $^{112}\text{Cd}$ - $^{116}\text{Cd}$ ).  $A_1(\omega)$ 's related to  $a_{21}$  then assumes values 0.166, 0.157, 0.147, 0.147 and 0.147 MeV for  $^{108}\text{Cd}$  -  $^{116}\text{Cd}$ , respectively. From their sign it is seen by virtue of (11) that they yield a negative quadrupole moment.

Neutrons are particles in the shell 50-82. As their number ranges from 8 ( $^{106}\text{Cd}$ ) to 18 ( $^{116}\text{Cd}$ ) it is clear that the BCS-solution is to be used. Then the expressions (13) - (15) are to be multiplied by appropriate combinations of U and V factors as indicated. BCS-solutions<sup>1</sup> with the best

<sup>1</sup> We are grateful to Dr. A. Rimini for kindly providing the BCS-solutions.

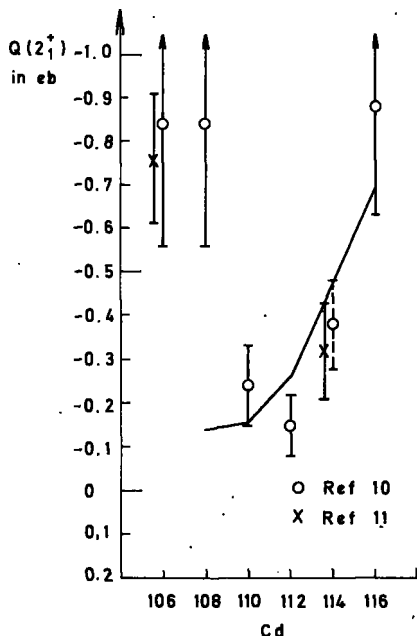


FIG. 6. Graphical presentation of Table II is given. The dashed error bar for  $^{114}\text{Cd}$  is an estimate of an error not indicated in Ref. [10]. The full line joins the calculated points.

single-particle energies of the Bonn group and the core-polarization-renormalized Yale-Shakin interaction of Ref. [13] have been used. The calculated  $A_1(\omega)$  are  $-0.06$ ,  $-0.03$ ,  $0.05$ ,  $0.14$  and  $0.19$  MeV for  $^{108}\text{Cd}$  -  $^{116}\text{Cd}$ , respectively. Adding the neutron and the proton contribution,  $A_1(\omega)$  is connected into the amplitude  $a_{21}$  and the respective quadrupole moments are evaluated making use of expression (11). The results are shown in Table II together with the experimental ones of Refs [10, 11]. For the sake of illustration they are shown in Fig. 6. The general variation with the particle number is seen to be reproduced although it seems unlikely that the value for  $^{106}\text{Cd}$ , which has not been calculated, would increase sufficiently. However, the results presented confirm the notion [1, 2] of particle-vibration coupling being the basic anharmonicity of the vibrational motion. The magnitude and the sign of the triangular diagrams depend on the shell structure featuring the anharmonicities as shell effects. A similar calculation [14] for Te-isotopes also shows satisfactory results. However, there remains the question of predicting the positions of the two-phonon triplet states. They are not degenerate, and their positions are known in many cases. To account for this, it is necessary to evaluate, besides the triangular diagrams, the quadrangular ones which would correspond to a quartic anharmonicity. Quadrangular diagrams will have a first-order contribution to the energy and, although one order higher in  $H_{pv}$ , will therefore favourably compete with the second-order contribution from the triangular diagrams (see section 2). This should be done for a

further confirmation of the confidence gained so far, namely that particle-vibration coupling is the key to the solution of the problem of nuclear vibrations.

#### REFERENCES

- [1] BOHR, A., MOTTELSON, B.R., Nuclear Structure, volumes 2 and 3, (to be published by Benjamin, New York-Amsterdam); LANE, A.M., Nuclear Theory, Benjamin, New York - Amsterdam (1964).
- [2] MOTTELSON, B.R., Topics in Nuclear Structure Theory, Nikko Summer School Lectures (1967).
- [3] ALAGA, G., Vibrational States in Nuclei, Nuclear Theoretical Physics (Proc. Summer School, Predeal, Romania, 1969).
- [4] ŠIPS, L., LOPAC, V., Physics Letts 32B (1970) 649.
- [5] De-SHALIT, A., TALMI, I., Nuclear Shell Theory, Academic Press, New York (1963).
- [6] BOHR, A., MOTTELSON, B.R., Nuclear Structure, vol.1, Benjamin, New York-Amsterdam (1969).
- [7] MANGER, J., EVANS, J.A., Nucl. Phys. A167 (1971) 16.
- [8] DeBOER, J., STOKSTAD, R.G., SYMONS, G.D., WINTHER, A., Phys. Rev. Letts 14 (1965) 564.
- [9] CLINE, D., Bull. Am. Phys. Soc. 14 (1969) 726 and references quoted therein.
- [10] STEADMAN, S.G., KLEINFELD, A.M., SEAMAN, G.C., deBOER, J., WARD, D., Nucl. Phys. A155 (1970) 1.
- [11] KLEINFELD, A.M., ROGERS, J.D., GASTEBOIS, J., STEADMAN, S.G., deBOER, J., Nucl. Phys. A158 (1970) 81.
- [12] CONJEAUD, M., HARAR, S., THURIERE, E., Nucl. Phys. A129 (1969) 10.
- [13] GMITRO, M., RIMINI, A., SAWICKI, J., WEBER, T., Phys. Rev. 173 (1968) 964.
- [14] ŠIPS, L., ICTP, Trieste, preprint IC/71/34 (submitted to Physics Letts).

#### NOTE ADDED IN PROOF

After completing the article it became clear that the sign of the neutron contribution corresponds to pure isovector particle-vibration coupling. The isoscalar particle-vibration coupling which is certainly dominant yields the opposite sign of the neutron contribution, thus worsening the agreement considerably. Further investigations are under way.



# QUASI-PARTICLE VIBRATION COUPLING

W. RYBARSKA\*

Joint Institute for Nuclear Research, Dubna,  
Union of Soviet Socialist Republics

## Abstract

### QUASI-PARTICLE VIBRATION COUPLING.

A complete system of coupled equations necessary for describing the nuclear rotational excitation is obtained from a variational principle without use of the equations of motion.

The quasi-particle approach and the random phase approximation (RPA) are the methods used [1] in the nuclear model called the microscopic model. The starting point of this model is the model Hamiltonian

$$H = H_0 + H_{\text{pair}} + H_{\text{QQ}}$$

where  $H_0$  is one-particle energy of all nucleons moving in a self-consistent potential, and the last two terms describe the interaction of particles. As a rule, in spherical nuclei only particles over closed shells interact.

Unfortunately, [2], this model in pure RPA has been found insufficient to describe the vibrational collective excitations higher than  $2^+$  in even nuclei, and it was possible to describe only a few nearest excited levels in odd nuclei.

Subsequently, some progress has been made in deriving methods by which the RPA defects could be eliminated. Various anharmonic corrections have been introduced either by modifying the RPA equations of motion and enlarging the Hilbert space of the admissible states (two-boson excitation, for example [3]) or by making use of boson expansions [4]. The problem we should like to discuss in this paper is the following:

In all these methods, higher accuracy is required and various corrections to RPA are calculated but the conventional RPA as a zero-order approximation is always used. In this connection, let us once more verify RPA, taking into account that in this simplification not only part of the interaction was omitted but also the Pauli principle was violated. Therefore our task will be to find the best quasi-bosons taking, approximately of course, the Pauli principle into account. As a result, we shall obtain the coupled system of equations for all parameters necessary to describe the quasi-particle and collective excitations of nuclei.

What will be new in my calculations was obtained last year at Dubna in collaboration with Dr. R.V. Jolos [6]. The idea worked out by us was first stated by K. Hara in 1964 [5], but he solved only part of the problem.

---

\* Permanent address: Institute for Theoretical Physics, Wrocław University, Poland.

The individual terms in the model Hamiltonian given above are defined as

$$H_0 = \sum_{jm} (\epsilon_j - \lambda) a_{jm}^\dagger a_{jm}$$

where  $\epsilon_j$  is the one-particle energy and  $\lambda$  the chemical potential (we use the spherical-nuclei quantum numbers). The next term is defined as

$$H_{\text{pair}} = -\frac{G}{4} \mathcal{P}^\dagger \mathcal{P}$$

where

$$\mathcal{P}^\dagger = \sum_{jm} (-1)^{j-m} a_{jm}^\dagger a_{j-m}^\dagger$$

$$H_{\text{QQ}} = -\frac{1}{2} \sum_{LM} \chi_L Q_{LM}^\dagger Q_{LM} \quad L = 2, \dots$$

$$Q_{LM} = \sum_{j_1 m_1 j_2 m_2} \langle 1 | Q_{LM} | 2 \rangle a_{j_1 m_1}^\dagger a_{j_2 m_2}$$

$$Q_{LM}(X) = r^L Y_{LM}(\vartheta, \varphi)$$

$$\langle 1 | Q_{LM} | 2 \rangle = \int \psi_1^\dagger(x) Q_{LM}(x) \psi_2(x) dx$$

We perform the u-v transformation by passing from a,  $a^\dagger$ -fermion particle operators to c,  $c^\dagger$ -fermion quasi-particle operators:

$$\begin{aligned} a_{jm}^\dagger &= u_j c_{jm}^\dagger + (-1)^{j-m} v_j c_{j-m} \\ a_{jm} &= u_j c_{jm} + (-1)^{j-m} v_j c_{j-m}^\dagger \end{aligned} \quad u_j^2 + v_j^2 = 1$$

After this transformation our Hamiltonian can be written as:

$$H_0 = \sum_j (\epsilon_j - \lambda) \left[ 2\Omega_j v_j^2 + \sqrt{2\Omega_j} (u_j^2 - v_j^2) \alpha_j^\dagger + \sqrt{4\Omega_j} u_j v_j (A_j^\dagger + A_j) \right]$$

$$H_{\text{pair}} = -\frac{G}{4} \left\{ \left( \sum_j 2\Omega_j u_j v_j \right)^2 - 4 \sum_{jj'} 2\Omega_j \sqrt{2\Omega_{j'}} u_j v_j u_{j'} v_{j'} \alpha_j^\dagger \right\}$$

$$\begin{aligned}
& + \sum_{jj'} 2\Omega_j \sqrt{4\Omega_j} u_j v_j (u_j^2 - v_j^2) (A_{j'}^\dagger + A_{j'}) \\
& - \sum_{jj'} \sqrt{2\Omega_j} \sqrt{4\Omega_{j'}} u_j v_{j'} \alpha_j^\dagger (u_{j'}^2 A_{j'} - v_{j'}^2 A_{j'}^\dagger) \\
& - 2 \sum_{jj'} \sqrt{4\Omega_j} \sqrt{2\Omega_{j'}} (u_j^2 A_j^\dagger - v_j^2 A_j) u_j v_{j'} \alpha_{j'}^\dagger \\
& + \sum_{jj'} \sqrt{4\Omega_j} \sqrt{4\Omega_{j'}} \left[ \frac{1}{4} (u_j^2 - v_j^2) (u_{j'}^2 - v_{j'}^2) (A_j^\dagger + A_j) (A_{j'}^\dagger + A_{j'}) \right. \\
& \left. - \frac{1}{4} (A_j^\dagger - A_j) (A_{j'}^\dagger - A_{j'}) - \frac{1}{2} \delta_{jj'} (u_j^2 - v_j^2) (1 - \sqrt{2\Omega_j} \alpha_j^\dagger) \right] \\
& + 4 \sum_{jj'} \left\{ \sqrt{2\Omega_j} \sqrt{2\Omega_{j'}} u_j v_j u_{j'} v_{j'} \alpha_j^\dagger \alpha_{j'}^\dagger \right\}
\end{aligned}$$

where

$$A_j^\dagger = \frac{1}{\sqrt{4\Omega_j}} \sum_{jm} c_{jm}^\dagger c_{j-m}^\dagger (-1)^{j-m}$$

$$\alpha_j^\dagger = \alpha_j = \frac{1}{\sqrt{2\Omega_j}} \sum_m c_{jm}^\dagger c_{jm} \quad 2\Omega_j = 2j + 1$$

and

$$\begin{aligned}
H_{QQ} &= \frac{1}{2} \sum_{LM11'22'} \chi_L Q_L [11'] Q_L [22'] (A_{LM}^\dagger [11'] A_{LM} [22'] \\
& + (-1)^{L-M} A_{L-M} [11'] A_{LM} [22'] + (-1)^{L-M} A_{LM}^\dagger [11'] A_{LM}^\dagger [22'] + A_{L-M} [11'] A_{L-M}^\dagger [22']) \\
& - \frac{1}{2} \sum_{LM11'22'} \chi_L Q_L [11'] q_L [22'] \left( A_{LM}^\dagger [11'] + (-1)^{L-M} A_{L-M} [11'] \right) \alpha_{LM}^\dagger [22'] \\
& - \frac{1}{2} \sum_{LM11'22'} \chi_L Q_L [22'] q_L [11'] \alpha_{LM}^\dagger [11'] \left( A_{LM} [22'] + (-1)^{L-M} A_{L-M}^\dagger [22'] \right) \\
& - \frac{1}{2} \sum_{LM11'22'} \chi_L q_L [11'] q_L [22'] \alpha_{LM}^\dagger [11'] \alpha_{LM}^\dagger [22']
\end{aligned}$$

(the shell-model state  $N_1 \ell_1 j_1 m_1$  is simply abbreviated as 1) where

$$A_{LM}^\dagger [12] = \frac{1}{\sqrt{2}} \sum_{m_1 m_2} \langle 12 | LM \rangle c_1^\dagger c_2^\dagger$$

$$\alpha_{LM}^\dagger [12] = \sum_{m_1 m_2} \langle 1-2 | LM \rangle (-1)^{j_1 - m_2} c_1^\dagger c_2$$

$$Q_L [12] = \frac{1}{\sqrt{2}} (u_1 v_2 + v_1 u_2) \frac{\langle 1 || Q_L || 2 \rangle}{\sqrt{2\Omega_L}}$$

$$q_L [12] = (u_1 u_2 - v_1 v_2) \frac{\langle 1 || Q_L || 2 \rangle}{\sqrt{2\Omega_L}}$$

These quantities do not depend on magnetic quantum numbers  $m_1$  and  $m_2$ ; to indicate this fact we used the bracket [12]. The matrix element  $\langle 1 | Q_{LM} | 2 \rangle$  is written with the help of the Wigner-Eckart theorem as

$$\langle 1 | Q_{LM} | 2 \rangle = \frac{\langle 1 || Q_L || \rangle}{\sqrt{2\Omega_L}} \langle 2, LM | 1 \rangle$$

and  $\langle 2, LM | 1 \rangle$  is short for the Clebsch-Gordan coefficient  $\langle j_2 m_2 LM | j_1 m_1 \rangle$ . The operators  $A, A^\dagger$  satisfy the commutation relations:

$$\begin{aligned} [A_{1'}, A_{1'}^\dagger] &= \delta_{11'} \left( 1 - \frac{2}{\sqrt{2\Omega_{j'}}} \alpha_{1'}^\dagger \right) \left[ \sum_{22'} Q_L [22'] A_{LM} [22'], \sum_{11'} f_\lambda [11'] A_{\lambda\mu}^\dagger [11'] \right] \\ &= \delta_{\lambda L} \delta_{\mu M} \sum_{11'} Q [11'] f_\lambda [11'] \\ &\quad - 2 \sum_{11' L'} \sqrt{4\Omega_L} \sqrt{4\Omega_{L'}} \langle L' M' LM | \lambda \mu \rangle G_{\lambda L L'} [11'] \alpha_{L' M'}^\dagger [11'] \end{aligned}$$

where

$$G_{\lambda L L'} [11'] = \sum_2 f_\lambda [12] Q_L [21'] W(11' \lambda L; L' 2)$$

and

$$W(11' \lambda L; L' 2) = W(j_1 j_1' \lambda L; L' j_2)$$

represents a Racah coefficient;  $Q_L [22']$ ,  $f_\lambda [11']$  are arbitrary coefficients.

Our approximation is based on the replacement of the operators of the right-hand side of the last relations by their ground-state averages

$$\langle |\alpha_j^\dagger| \rangle = \sqrt{2\Omega_j} \rho_j$$

where

$$\rho_1 = \langle |\frac{\hat{n}_1}{2\Omega_1}| \rangle, \quad \hat{n}_1 = \sum_{m_1} c_1^\dagger c_1$$

$$\langle |\alpha_{LM}^\dagger [11']| \rangle = \delta_{L0} \delta_{11'} \sqrt{2\Omega_1} \rho_1$$

In other words, we do not neglect the fact that the occupation numbers of the quasi-particle states are different from zero in the RPA-ground state. If we assume  $\langle |\alpha_{LM}^\dagger [11']| \rangle = 0$ , we obtain  $\alpha^\dagger [11']| \rangle \approx 0$  or  $c_1| \rangle = 0$ . From this it follows that the boson vacuum is approximately equal to the quasi-particle vacuum, which is not very reasonable. To avoid this contradiction we assume that the approximate commutation relations are

$$\begin{aligned} [A_1, A_1^\dagger] &= \delta_{11'} (1 - 2\rho_1) \left[ \sum_{22'} Q_L [22'] A_{LM} [22'], \sum_{11'} f_\lambda [11'] A_{\lambda\mu}^\dagger [11'] \right] \\ &= \delta_{\lambda L} \delta_{\mu M} \sum_{33'} (1 - \rho_{33'}) Q_L [33'] f_\lambda [33'], \quad \text{where } \rho_{11'} = \rho_1 + \rho_{1'} \end{aligned}$$

We now define the bosons by

$$B_n^\dagger = \sum_1 (a_{n1} A_1^\dagger - b_{n1} A_1)$$

$$B_{\lambda\mu}^\dagger [\alpha] = \sum_{11'} \left( f_\lambda^\alpha [11'] A_{\lambda\mu}^\dagger [11'] - g_\lambda^\alpha [11'] (-1)^{\lambda-\mu} A_{\lambda-\mu} [11'] \right)$$

with the following conditions for the co-efficients:

$$f_\lambda^\alpha [11'] = - (-1)^{j_1+j_1'+\lambda} f_\lambda^\alpha [1'1]$$

$$g_\lambda^\alpha [11'] = - (-1)^{j_1+j_1'+\lambda} g_\lambda^\alpha [1'1]$$

Using the approximate commutation relations we obtain the orthonormality conditions:

$$\sum_1 (1-2\rho_1)(a_{n1}a_{m1} - b_{n1}b_{m1}) = \delta_{nm}$$

$$\sum_n (1-2\rho_1)(a_{n1}a_{n2} - b_{n1}b_{n2}) = \delta_{12}$$

$$\sum_1 (1-2\rho_1)(a_{n1}b_{m1} - a_{m1}b_{n1}) = 0$$

$$\sum_n (1-2\rho_1)(a_{n1}b_{n2} - b_{n1}a_{n2}) = 0$$

$$\sum_{11'} (1-\rho_{11'}) \left( f_\lambda^\alpha [11'] f_\lambda^\beta [11'] - g_\lambda^\alpha [11'] g_\lambda^\beta [11'] \right) = \delta_{\alpha\beta}$$

$$\sum_\alpha (1-\rho_{11'}) \left( f_\lambda^\alpha [11'] f_\lambda^\alpha [22'] - g_\lambda^\alpha [11'] g_\lambda^\alpha [22'] \right) = \frac{1}{2} \left( \delta_{12} \delta_{1'2'} - (-1)^{j_2 + j_2 - \lambda} \delta_{12} \delta_{1'2'} \right)$$

$$\sum_{11'} (1-\rho_{11'}) \left( f_\lambda^\alpha [11'] g_\lambda^\beta [11'] - g_\lambda^\alpha [11'] f_\lambda^\beta [11'] \right) = 0$$

$$\sum_\alpha (1-\rho_{11'}) \left( f_\lambda^\alpha [11'] g_\lambda^\alpha [22'] - g_\lambda^\alpha [11'] f_\lambda^\alpha [22'] \right) = 0$$

Having set up these conditions, we can simply perform the inverse transformation

$$A_1^\dagger = \sum_n (1-2\rho_1)(a_{n1}B_n^\dagger + b_{n1}B_n)$$

$$A_{\lambda\mu}^\dagger [11'] = (1-\rho_{11'}) \sum_\alpha \left( f_\lambda^\alpha [11'] B_{\lambda\mu}^\dagger [\alpha] + (-1)^{\lambda-\mu} g_\lambda^\alpha [11'] B_{\lambda-\mu} [\alpha] \right)$$

Now, we proceed to the formulation of the problem as a variational principle which is our basic approach. We construct the functional  $\mathcal{L}$  as

$$\mathcal{L} = \langle |H| \rangle - \sum_1 \mu_1 (v_1^2 + u_1^2)$$

$$- \sum_{\alpha, \lambda, 11'} \omega_{\lambda}^{\alpha} (1 - \rho_{1r}) \left( (f_{\lambda}^{\alpha} [11'])^2 - (g_{\lambda}^{\alpha} [11'])^2 \right) \\ - \sum_{1, n} \omega_0^n (1 - 2\rho_1) (a_{n1}^2 - b_{n1}^2)$$

where  $\langle |H| \rangle$  is the expectation value of the Hamiltonian in the ground state. We require

$$\delta \mathcal{L} = 0$$

and we assume the ground state of the system  $| \rangle$  to be a vacuum of bosons

$$B_n | \rangle = 0$$

$$B_{\lambda\mu} [\alpha] | \rangle = 0$$

We have now explicitly

$$\mathcal{L} = \frac{G}{4} \sum_1 2\Omega_1 + \sum_1 2\Omega_1 \left( \epsilon_1 - \lambda - \frac{G}{2} \right) v_1^2 - \frac{G}{4} \left( \sum_1 2\Omega_1 u_1 v_1 (1 - 2\rho_1) \right)^2 \\ + \sum_1 \left( \epsilon_1 - \lambda - \frac{G}{2} \right) (u_1^2 - v_1^2) 2\Omega_1 \rho_1 - \sum_1 \mu_1 (v_1^2 + u_1^2) \\ - \frac{G}{4} \sum_{11'} \sqrt{4\Omega_1} \sqrt{4\Omega_{1'}} (1 - 2\rho_1) (1 - 2\rho_{1'}) \frac{1}{4} (u_1^2 - v_1^2) (u_{1'}^2 - v_{1'}^2) \\ \times \sum_n (a_{n1} a_{n1'} + b_{n1} b_{n1'} + a_{n1} b_{n1'} + b_{n1} a_{n1'}) \\ - \frac{G}{4} \sum_{11'} \sqrt{4\Omega_1} \sqrt{4\Omega_{1'}} (1 - 2\rho_1) (1 - 2\rho_{1'}) \frac{1}{4} \sum_n (a_{n1} a_{n1'} + b_{n1} b_{n1'} - a_{n1} b_{n1'} - b_{n1} a_{n1'}) \\ - \frac{1}{2} \sum_{L \alpha 11'} \chi_L 2\Omega_L Q_L [11'] Q_L [22'] (1 - \rho_{1r}) (1 - \rho_{2r}) \\ \times \left( f_L^{\alpha} [11'] f_L^{\alpha} [22'] + g_L^{\alpha} [11'] g_L^{\alpha} [22'] + f_L^{\alpha} [11'] g_L^{\alpha} [22'] + g_L^{\alpha} [11'] f_L^{\alpha} [22'] \right) \\ - \sum_{L \alpha 11'} \omega_L^{\alpha} (1 - \rho_{1r}) \left( (f_L^{\alpha} [11'])^2 - (g_L^{\alpha} [11'])^2 \right) - \sum_{n1} \omega_0^n (1 - 2\rho_1) (a_{n1}^2 - b_{n1}^2)$$

(In  $\mathcal{L}$  only terms quadratic in  $\rho_i$  have been omitted). The system of equations for all the parameters characterizing the quasi-particle and collective excitations

$$\begin{aligned} \frac{\partial \mathcal{L}}{\partial u_k} = 0, \quad \frac{\partial \mathcal{L}}{\partial v_k} = 0, \quad \frac{\partial \mathcal{L}}{\partial a_{nk}} = 0, \quad \frac{\partial \mathcal{L}}{\partial b_{nk}} = 0 \\ \frac{\partial \mathcal{L}}{\partial f_L^\gamma[33]} = 0, \quad \frac{\partial \mathcal{L}}{\partial g_L^\gamma[33]} = 0 \end{aligned}$$

is just the set of conditions necessary for  $\mathcal{L}$  to be minimum. As we see,  $\mathcal{L}$  depends on the so far unknown parameters  $\rho_i$  which are the occupation numbers of the quasi-particle levels in the ground state. For these parameters we should find additional equations.

Let us assume that

$$|\rangle = \mathcal{U} |\Phi_0\rangle$$

where  $|\Phi_0\rangle$  is the quasi-particle vacuum

$$\mathcal{U} = Ne^{\mathcal{B}}, \quad N \text{ is a constant.}$$

Since

$$B|\rangle = 0$$

we have

$$S = \frac{1}{2} \sum_{LM1'2'} \chi_L S_L[11', 22'] (-1)^{L-M} A_{LM}^\dagger[11'] A_{L-M}^\dagger[22']$$

and  $S_L$  has the following symmetry properties:

$$S_L[11', 22'] = (-1)^{j_1+j_1'+L} S_L[1'1, 2'2] \quad \text{etc.}$$

From the condition  $B|\rangle = 0$  we also obtain

$$(*) \sum_{11'} \left\{ f_\lambda^\alpha[11'] \mathcal{U}^{-1} A_{\lambda\mu}[11'] \mathcal{U} - g_\lambda^\alpha[11'] (-1)^{\lambda-\mu} A_{\lambda-\mu}^\dagger[11'] \right\} |\Phi_0\rangle = 0$$

$$(\mathcal{U}, \mathcal{U}^{-1} \text{ commute with } A_{\lambda\mu}^\dagger)$$

On the other hand, a well-known identity holds for any two operators A and B:

$$e^{-B} A e^B = A - [B, A] + \frac{1}{2} [B, [B, A]] \dots$$

Therefore the left-hand side of (\*) can be calculated and the result is

$$\sum_{11'} \left\{ \chi_\lambda \sum_{22'} (1 - \rho_{22'}) S_\lambda [11', 22'] f_\lambda^\alpha [22'] - g_\lambda^\alpha [11'] \right\} (-1)^{\lambda - \mu} A_{\lambda - \mu}^+ [11'] | \Phi_0 \rangle = 0$$

Thus we obtain a system of equations

$$(**) \quad g_\lambda^\alpha [11'] = \chi_\lambda \sum_{22'} (1 - \rho_{22'}) S_\lambda [11', 22'] f_\lambda^\alpha [22']$$

Let us now return to  $\rho_1$ :

$$\langle | \hat{n}_1 \rangle \rangle = N \langle | \hat{n}_1 e^S | \Phi_0 \rangle = N \langle | [\hat{n}_1, e^S] | \Phi_0 \rangle$$

We use the algebraic relation

$$[\hat{n}_1, e^S] = [\hat{n}_1, S] e^S$$

which we are going to prove immediately:

$$N_1(\vartheta) = [\hat{n}_1, e^{\vartheta S}]$$

$$N_1(0) = 0$$

Differentiating  $\hat{N}_1(\vartheta)$   $m$  times with respect to  $\vartheta$  we obtain

$$\frac{d^m}{d\vartheta^m} \hat{N}_1(\vartheta) = m [\hat{n}_1, S] S^{m-1} e^{\vartheta S} + S^m N_1(\vartheta)$$

which can be verified by mathematical induction. Thus, we have

$$\hat{N}_1(\vartheta) = \sum_{m=1}^{\infty} \frac{\vartheta^m}{m!} \left( \frac{d^m}{d\vartheta^m} \hat{N}_1(\vartheta) \right)_{\vartheta=0} = \vartheta [\hat{n}_1, S] e^{\vartheta S}$$

and hence from

$$[\hat{n}_1, e^{\vartheta S}] = \vartheta [\hat{n}_1, S] e^{\vartheta S}$$

we have our identity if we put  $\vartheta = 1$ .

Then we have

$$\langle | \hat{n}_1 \rangle \rangle = \langle | [\hat{n}_1, S] | \rangle$$

On the other hand;  $[\hat{n}_1, S]$  is evaluated as

$$\begin{aligned} [\hat{n}_1, S] &= 2 \sum_{233^*LM} \chi_L S_L [12, 33'] (-1)^{L-M} A_{LM}^\dagger [12] A_{L-M}^\dagger [33'] \\ &= 2 \sum_{233^*LM\alpha\beta} \chi_L S_L [12, 33'] (1-\rho_{12}) (1-\rho_{33'}) \\ &\quad \times \left\{ f_L^\alpha [12] B_{LM}^\dagger [\alpha] + g_L^\alpha [12] (-1)^{L-M} B_{L-M} [\alpha] \right\} (-1)^{L-M} \\ &\quad \times \left\{ f_L^\beta [33'] B_{L-M}^\dagger [\beta] + g_L^\beta [33'] (-1)^{L-M} B_{LM} [\beta] \right\} \end{aligned}$$

and

$$\langle |\hat{n}_1| \rangle = 2 \sum_{233^*LM\alpha} 2\Omega_L \chi_L (1-\rho_{12}) (1-\rho_{33'}) S_L [12, 33'] g_L^\alpha [12] f_L^\alpha [33']$$

Taking into account equations (\*\*) we obtain

$$\langle |\hat{n}_1| \rangle = 2 \sum_2 (1-\rho_{12}) \sum_{L\alpha} 2\Omega_L (g_L^\alpha [12])^2$$

We can now use the orthonormality condition and add pairing vibrations. Finally

$$\begin{aligned} \rho_1 &= \frac{1}{2\Omega_1} \sum_{L\alpha 2} (1-\rho_{12}) 2\Omega_L \left( (f_L^\alpha [12])^2 + (g_L^\alpha [12])^2 - 1 \right) \\ &\quad + \frac{1}{2\Omega_1} (1-2\rho_1) \sum_n (a_{n1}^2 + b_{n1}^2 - 1) \end{aligned}$$

remembering that  $\rho_{ik} = \rho_i + \rho_k$ .

We now reduce the system of equations for  $u_k, v_k$  by the usual method to

$$2 R_k u_k v_k - r_k (u_k^2 - v_k^2) = 0$$

where

$$\begin{aligned} R_k &= \left( \epsilon_k - \lambda - \frac{G}{2} \right) (1-2\rho_k) 2\Omega_k \\ &\quad + \frac{G}{4} \sqrt{4\Omega_k} (1-2\rho_k) \sum_{1n} \sqrt{4\Omega_1} (1-2\rho_1) (u_1^2 - v_1^2) (a_{n1} a_{nk} + b_{n1} b_{nk} + a_{n1} b_{nk} + b_{n1} a_{nk}) \end{aligned}$$

$$r_k = \frac{G}{2} 2\Omega_k(1-2\rho_k) \sum_1 2\Omega_1 u_1 v_1 (1-2\rho_1)$$

$$+ 2 \sum_{L\alpha 22'} \chi_L \langle 1 \| Q_L \| k \rangle \langle 2 \| Q_L \| 2' \rangle (u_2 v_2' + v_2 u_2') (1-\rho_{k1})(1-\rho_{22'})$$

$$\times \left( f_L^\alpha [1k] f_L^\alpha [22'] + g_L^\alpha [1k] g_L^\alpha [22'] + g_L^\alpha [1k] f_L^\alpha [22'] + f_L^\alpha [1k] g_L^\alpha [22'] \right)$$

The quantities  $R_k$  play the role of the renormalized quasi-particle energies, the renormalization being due to pairing vibrations. The quantities  $r_k$  are the renormalized energy gap, the renormalization being due to multipole vibrations. Using these formulae we can write the formal solutions for  $u_k, v_k$  simply as

$$u_k^2 = \frac{1}{2} \left( 1 + \frac{R_k}{\sqrt{r_k^2 + R_k^2}} \right)$$

$$v_k^2 = \frac{1}{2} \left( 1 - \frac{R_k}{\sqrt{r_k^2 + R_k^2}} \right)$$

To derive the equations for the collective-vibration amplitudes we use the equations for  $\rho_i$ . Generally, we also obtain non-linear terms but we shall omit them. Thus we have

$$\frac{\partial \mathcal{L}}{\partial a_{nk}} = (2E_k - \omega_0^n) a_{nk}$$

$$- \frac{G}{4} \sqrt{4\Omega_k} (u_k^2 - v_k^2) \sum_1 \sqrt{4\Omega_1} (1-2\rho_1) (u_1^2 - v_1^2) \frac{1}{2} (a_{n1} + b_{n1})$$

$$- \frac{G}{4} \sqrt{4\Omega_k} \sum_1 \sqrt{4\Omega_1} (1-2\rho_1) \frac{1}{2} (a_{n1} - b_{n1}) = 0$$

$$\frac{\partial \mathcal{L}}{\partial b_{nk}} = (2E_k + \omega_0^n) b_{nk}$$

$$- \frac{G}{4} \sqrt{4\Omega_k} (u_k^2 - v_k^2) \sum_1 \sqrt{4\Omega_1} (1-2\rho_1) (u_1^2 - v_1^2) \frac{1}{2} (a_{n1} + b_{n1})$$

$$+ \frac{G}{4} \sqrt{4\Omega_k} \sum_1 \sqrt{4\Omega_1} (1-2\rho_1) \frac{1}{2} (a_{n1} - b_{n1}) = 0$$

$$\frac{\partial \mathcal{L}}{\partial f_L^\gamma [33']} = (E_3 + E_{3'} - \omega_L^\gamma) f_L^\gamma [33'] - \chi_L Q_L [33'] \sum_{11'} Q_L [11'] (1 - \rho_{11'}) (f_L^\gamma [11'] + g_L^\gamma [11']) = 0$$

$$\frac{\partial \mathcal{L}}{\partial g_L^\gamma [33']} = (E_3 + E_{3'} + \omega_L^\gamma) g_L^\gamma [33'] - \chi_L Q_L [33'] \sum_{11'} Q_L [11'] (1 - \rho_{11'}) (f_L^\gamma [11'] + g_L^\gamma [11']) = 0$$

where

$$E_k = \left( \epsilon_k - \lambda - \frac{G}{2} \right) (u_k^2 - v_k^2) + G u_k v_k \sum_1 2\Omega_1 u_1 v_1 (1 - 2\rho_1)$$

The equations for  $f, g$  are formally identical with the equations obtained by Hara if we identify  $E_k$  with the quasi-particle energy. In our case, the parameters  $u_k, v_k$  satisfy some other equations. From our formulae follows the secular equation for the multipole excitations

$$1 = 2\chi_L \sum_{11'} \frac{(1 - \rho_{11'}) Q_L^2 [11'] (E_1 + E_{1'})}{(E_1 + E_{1'})^2 - (\omega_L^\gamma)^2}$$

and, for the pairing vibration energies, a similar one. Thus we have a coupled system of equations describing the excitations of our system. Obviously, it is not possible to solve it in the general case. We can only try to use some iteration procedure.

We shall now give some simple examples by which we shall demonstrate the corrections characteristic of our method.

#### a) Simplified equations for $u_k$ and $v_k$

Let us neglect, for the sake of simplicity, the second terms in the formulae for  $R_k$  and  $r_k$ . In this case we put

$$\Delta = G \sum_1 2\Omega_1 (1 - 2\rho_1) u_1 v_1$$

and the equation for the  $\Delta$  assumes the form

$$\frac{2}{G} = \sum_1 \frac{\Omega_1 (1 - 2\rho_1)}{\sqrt{\Delta^2 + (\tilde{\epsilon}_1 - \lambda)^2}}, \quad \tilde{\epsilon}_1 = \epsilon_1 - \frac{G}{2}$$

From the condition

$$\langle |\tilde{N}| \rangle = N_0 = \sum_1 (2\Omega_1 v_1^2 + 2\Omega_1 (u_1^2 - v_1^2) \rho_1)$$

we can also determine  $\lambda$ :

$$\Omega - N_0 = \sum_1 \frac{\Omega_1 (\tilde{\epsilon}_1 - \lambda) (1 - 2\rho_1)}{\sqrt{\Delta^2 + (\tilde{\epsilon}_1 - \lambda)^2}}$$

In this crude approximation, we see that the coupling with the vibrations leads to blocking-type corrections in the energy-gap equation, i.e. the energy gap decreases. This effect is rather large in nuclei in which there are strongly collective low-lying states and small where such states are absent.

### b) Pairing vibrations

From the equations

$$\frac{\partial \mathcal{L}}{\partial a_{nk}} = 0, \quad \frac{\partial \mathcal{L}}{\partial b_{nk}} = 0$$

we have

$$(2E_k - \omega_0^n) a_{nk} - \frac{G}{4} \sqrt{4\Omega_k} (u_k^2 - v_k^2) \Phi_n - \frac{G}{4} \sqrt{4\Omega_k} \Psi_n = 0$$

$$(2E_k + \omega_0^n) b_{nk} - \frac{G}{4} \sqrt{4\Omega_k} (u_k^2 - v_k^2) \Phi_n + \frac{G}{4} \sqrt{4\Omega_k} \Psi_n = 0$$

so that we obtain

$$a_{nk} = \frac{G \sqrt{4\Omega_k} [(u_k^2 - v_k^2) \Phi_n + \Psi_n]}{4(2E_k - \omega_0^n)}$$

$$b_{nk} = \frac{G \sqrt{4\Omega_k} [(u_k^2 - v_k^2) \Phi_n - \Psi_n]}{4(2E_k + \omega_0^n)}$$

where

$$\Phi_n = \sum_1 \frac{\sqrt{4\Omega_1}}{2} (1 - 2\rho_1) (u_1^2 - v_1^2) (a_{n1} + b_{n1})$$

$$\Psi_n = \sum_1 \frac{\sqrt{4\Omega_1}}{2} (1 - 2\rho_1) (a_{n1} - b_{n1})$$

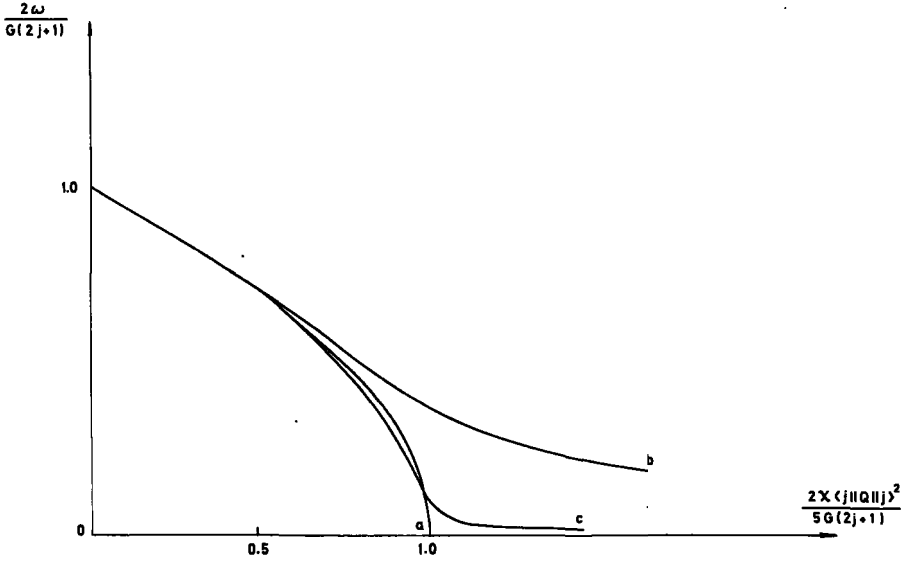


FIG. 1. The energy of the first collective excitation plotted as a function of the coupling constant  $\chi$   
 a) in the RPA;  
 b) in the Hara approximation;  
 c) in our approximation.

Using the simplified expression for the  $\Delta$  we obtain the following secular equation:

$$\begin{aligned}
 (\omega_0^n)^2 \left\{ \left( \sum_1 \frac{\Omega_1(1-2\rho_1)}{E_1(4E_1^2 - (\omega_0^n)^2)} \right) \left( \sum_1 \frac{\Omega_1(1-2\rho_1)((\omega_0^n)^2 - 4\Delta^2)}{E_1(4E_1^2 - (\omega_0^n)^2)} \right) \right. \\
 \left. - \left( \sum_1 \frac{\Omega_1(1-2\rho_1) 2(\tilde{\epsilon}_1 - \lambda)}{E_1(4E_1^2 - (\omega_0^n)^2)} \right)^2 \right\} = 0
 \end{aligned}$$

This equation differs from the usual one in two respects:

- 1) there are corrections of the  $(1-2\rho_1)$ -type;
- 2)  $E_k$ , which here plays the rôle of a one-quasi-particle energy, differs from the analogous term in the formulae for  $u_k, v_k$  by renormalization.

### c) One-level model

Let us take the isolated level as the last unfilled shell. In this model our formulae are simplified:

$$1 = \frac{G}{2} \frac{(j + \frac{1}{2})(1 - 2\rho_1)}{E_j}$$

$$E_j = \sqrt{(\tilde{\epsilon}_j - \lambda)^2 + \Delta^2}$$

$$N_0 = (j + \frac{1}{2}) - (j + \frac{1}{2}) \frac{\tilde{\epsilon}_j - \lambda}{E_j} (1 - 2\rho_j)$$

$$1 = 2\chi \frac{(1 - 2\rho_j) Q^2 [jj] 2 E_j}{4 E_j^2 - \omega^2}$$

$$Q [jj] = \frac{\Delta}{\sqrt{2} E_j \sqrt{s}} \langle j | Q | j \rangle$$

We assume  $2j + 1 = 2\Omega_j = 40$ ,  $N_0 = 18$ . We have taken into account the  $L = 2$  vibrations only. Solving this system numerically we obtain the result shown in Fig. 1 (Remark: The list of references is not complete. The last three papers are monographs where exhaustive references can be found).

### CONCLUSIONS

A. A complete system of coupled equations which is necessary for describing the nuclear non-rotational excitation has been obtained from a vibrational principle without using the equation of motion.

B. The expressions playing the roles of one-quasi-particle energies are different in the secular equations and in the equations for  $u_k, v_k$ . In the latter case, these expressions are being changed:

- 1) by one-particle energy renormalization which depends upon pairing vibrations only;
- 2) by the energy-gap renormalization which is induced by the multipole vibrations.

C. The appearance of factors  $(1 - 2\rho_1)$  in the energy-gap equation means that in this approach some blocking effect of the one-particle levels is taken into account.

## REFERENCES

- [1] BARANGER, M., Phys.Rev. 120 (1960) 957; 122 (1961) 992.
- [2] TAMURA, T., UDAGAWA, T., Progr.theor.Phys. (Kyoto) 26 (1961) 947.
- [3] FANO, G., SAWICKI, J., Nuovo Cim. 25 (1962) 586; TAMURA, T., UDAGAWA, T., Nucl.Phys. 53 (1964) 33; Phys.Rev. 150 (1966) 783; KERMAN, A.K., KLEIN, A., Phys.Rev. 132 (1964) 1326; DO DANG, G., KLEIN, A., Phys.Rev. 133B (1964) 257; 140B (1965) 245; PAL, M.K., GAMBHIR, Y.K., RAY, Ram, Phys.Rev. 155 (1967) 1144; GOSWAMI, A., NALCIOGLU, O., SHERWOOD, A.I., "Bootstrap theory of vibrations" (preprint); ROWE, D.J., Rev.mod.Phys. 40 (1968) 153.
- [4] BELIAEV, S.T., ZELEVINSKY, V.G., Nucl.Phys. 39 (1962) 582; MARUMORI, T., YAMAMURA, M., TOKUNAGA, A., Progr.theor.Phys. (Kyoto) 31 (1964) 1009; SØRENSEN, B., Nucl.Phys. A97 (1967) 1; SØRENSEN, B., Progr.theor.Phys. (Kyoto) 39 (1968) 1468.
- [5] HARA, K., Progr.theor.Phys. (Kyoto) 32 (1964) 88; IKEDA, K., UDAGAWA, T., YAMAURA, H., Progr.Theor.Phys. (Kyoto) 33 (1965) 22.
- [6] JOLOS, R.V., RYBARSKA, W., (preprint Dubna in press); PAL, M.K., "Theory of Nuclear Vibrations" in Theory of Nuclear Structure (Proc.Trieste Course, 1969) IAEA, Vienna (1970) 547; in Nuclear Theoretical Physics (Proc.Summer School Predeal, Romania (September 1969)); Advances in Nuclear Physics 2 (1969); BES, D.R., SØRENSEN, R.A., The Pairing Plus Quadrupole Model.

# NUCLEAR FISSION

K. DIETRICH

University of Heidelberg

and

Kernforschungszentrum Karlsruhe,

Federal Republic of Germany

## Abstract

### NUCLEAR FISSION.

1. Introduction; 2. The cranking approach applied to nuclear fission; 3. The method of Strutinski; 4. Application of the Strutinski method; 5. Conclusions.

## 1. INTRODUCTION

After the basic paper by N. Bohr and J.A. Wheeler [1] had appeared, progress in the theory of nuclear fission was relatively slow. The development of the nuclear shell model [2] concentrated attention on phenomena which are dominated by single-particle degrees of freedom. On the other hand, the collective model [3] which provided a successful description of rotations and vibrations, was restricted to harmonic or almost harmonic vibrational modes. The process of nuclear fission, however, implies a continuous change of the nuclear shape from the original nucleus via strongly deformed shapes to the final state of separated fragments, i. e. it represents a non-harmonic collective motion. Bohr and Wheeler [1] used the liquid-drop model (LDM) for the description of this process. The model has two great merits:

(i) It provides a simple means of introducing collective variables as parameters defining the shape of the droplet surface.

(ii) By keeping the volume of the droplet constant and independent of the nuclear shape, the saturation property can be taken into account in a very simple way.

Calculations within the static LDM could explain certain gross features of the fission process, like the existence of a potential barrier which protects the fissile nuclei against rapid disintegration, but they failed to account for the details. There were mainly three basic difficulties which hindered the further development of the phenomenological theory:

(i) There is experimental evidence for the influence of nuclear-shell structure on the fission process, like the asymmetric mass division for low-energy fission of nuclei heavier than Ra, or the average number of emitted neutrons as a function of the fragment mass. Thus the problem posed itself of how to include nuclear-shell effects in a theory based on the liquid-drop model.

(ii) A dynamical theory of fission requires not only the knowledge of the potential energy  $\mathcal{V}(q)$  but also the knowledge of the kinetic energy  $\mathcal{T}(q)$  as a function of the collective variables  $q$ . The kinetic energy depends

on the "mass tensor" ("inertial tensor")  $g_{\mu\nu}(q)$ . In the original version of the collective model [2], the inertial tensor was calculated assuming a non-viscous, incompressible, irrotational fluid. Since this leads to moments of inertia about an order of magnitude smaller than the observed ones, a different method of determining the kinetic energy had to be found.

(iii) Assuming that the kinetic energy  $\mathcal{T}(q)$  can be obtained by some reliable method, we face the problem of quantizing the classical Hamiltonian function

$$\mathcal{H}(q) = \mathcal{T}(q) + \mathcal{V}(q)$$

where  $q$  is a set of collective co-ordinates  $q^1 \dots q^f$ . There is no unique prescription to do this, as we shall see.

As to the first difficulty, an important break-through was achieved by W. Strutinski [4] who devised a method of applying a shell correction term to the LD-energy. The importance of adding shell-correction terms to the energy of the static LD was recognized rather early by a number of authors in the attempts of formulating accurate mass formulas. As we shall see, the significance of the Strutinski term is that it can be derived from an adiabatic microscopic approach under certain assumptions, that it is valid for arbitrary nuclear shapes, and that it does not depend on new parameters other than the ones specifying the phenomenological shell-model potential.

Assuming that the fission process is approximately adiabatic, i. e. \*) that the collective velocities  $\dot{q}$  are small compared to the velocities of intrinsic motion, the cranking model suggests itself for a calculation of the inertial tensor. In recent times, Kumar and Baranger [5] constructed collective Hamiltonians for vibrational and rotational motion using the cranking approach and studied the corresponding spectrum of collective states. Similar work has been performed by Mosel and Greiner [6] and Gneuss [7]. Several authors [8, 9] used the same approach for calculating the mass tensor in a Hamiltonian for the fission process. The quality of the adiabatic approximation is still an open question, especially for the dynamical behaviour beyond the saddle point [10].

As to the problem of quantization, we can only display the difficulties without presenting a solution to them. One usually applies the quantization procedure proposed by Schrödinger [11] without further justification.

In section 2 we shall derive a classical Hamiltonian function in the cranking approximation and we shall comment on the quantization problem. In section 3, the "Strutinski method" will be developed. In section 4, we shall discuss the qualitative effect of the shell-correction term, and we shall mention specific forms of phenomenological nuclear-shell-model potentials for strongly deformed nuclei. Finally, in section 5, we shall point out a number of open problems in the present stage of the theory of fission.

## 2. THE CRANKING APPROACH APPLIED TO NUCLEAR FISSION

We assume that the system of  $A$  nucleons may be described by a many-body Hamiltonian  $H(1 \dots A; q^1 \dots q^f)$  which depends on the co-ordinates  $1 \dots A$  of the  $A$  nucleons and on a set of parameters  $q^1 \dots q^f \equiv q$

\*) d.h.: Bewegung d. Kerns als pausen (Vibrationen, Deformation) viel langsamer als die d. ein einzelner Nucleonen

which are to specify the nuclear shape [12]. As an example, the  $q^i$  may be the ratios of half axes of an ellipsoidal nucleus, or some multipole moments of the nuclear density distribution. As an example, such a Hamiltonian could be obtained as a result of a Hartree-Fock method subject to constraints. We imagine that the parameters  $q^i$  are classically given functions of the time  $t$ . The explicit form of this dependence will not be needed. It will be assumed that the "velocities"  $\dot{q}^i(t)$  are low compared to the intrinsic velocities or, equivalently, that the energies of collective excitations are much smaller than the typical energies of intrinsic excitations. It is due to this assumption that we hope to be justified to use superfluous ( $> 3A$ ) co-ordinates. We derive a "collective Hamiltonian" by studying the reaction of the system with respect to slow changes of the collective parameters in time ("cranking"). We write  $q(t)$  for the set of shape parameters  $q^1(t) \dots q^f(t)$  and  $X$  for the set of variables  $1, \dots, 3A$ . The bracket symbol  $\langle \rangle$  means integration over the variables  $X$ . We expand the solution  $\Psi(X, q(t); t)$  of the time-dependent problem

$$H(X; q(t)) \Psi = i\hbar \dot{\Psi} \quad (1)$$

in terms of the stationary solutions  $u_k(x, q(t))$  at fixed time  $t$  ("adiabatic states")

$$H u_k = \mathcal{E}_k(q(t)) u_k \quad (2)$$

$$\Psi(X, q(t); t) = \sum_k c_k(t) u_k e^{-\frac{i}{\hbar} \int^t \mathcal{E}_k(\tau) d\tau} \quad (3)$$

Insertion of the factor  $\exp\left(-\frac{i}{\hbar} \int^t \mathcal{E}_k(\tau) d\tau\right)$  has the consequence that the coefficients  $c_k$  become independent of time in the limit  $\dot{q}(t) = 0$ . We substitute expression (3) into Eq. (1), multiply the resulting equation with  $u_k^*$  and integrate over  $X$ . This results in the equations

$$\dot{c}_\ell(t) = - \sum_k c_k(t) \left\langle u_\ell \left| \frac{\partial u_k}{\partial q^\mu} \right. \right\rangle \dot{q}^\mu e^{-\frac{i}{\hbar} \int^t d\tau (\mathcal{E}_k - \mathcal{E}_\ell)} \quad (4)$$

Here and in the following equations, summation from  $1 \dots f$  over repeated Greek indices is implied. The summation  $\sum_k$  usually contains a discrete as well as a continuous part. Thus the Eqs (4) represent an infinite set of integro-differential equations, and our procedure is only useful if there is a simple approximate solution to Eqs (4).

We assume that  $\dot{q}(t)$  is small enough such that terms containing the time-derivative of a collective variable may be treated as a perturbation. Calling the ordering parameter  $\eta$ , we have

$$\begin{aligned} \dot{c}_\ell^{(0)} + \eta \dot{c}_\ell^{(1)} + \dots = & - \sum_k \left[ c_k^{(0)} + \eta c_k^{(1)} + \dots \right] \\ & \times \left\langle u_\ell \left| \frac{\partial u_k}{\partial q^\mu} \right. \right\rangle \eta \dot{q}^\mu e^{-\frac{i}{\hbar} \int^t d\tau (\mathcal{E}_k - \mathcal{E}_\ell)} \end{aligned} \quad (5)$$

To the lowest order in  $O(\eta)$  we obtain

$$\dot{c}_\ell^{(0)} = 0 \quad (6)$$

Since the system should be in the lowest possible state for vanishing  $\dot{q}$ , Eq. (6) is equivalent to

$$c_\ell^{(0)} = \delta_{\ell 0} \quad (7)$$

To first order ( $\eta^1$ ) we obtain

$$\dot{c}_\ell^{(1)} = - \left\langle u_\ell \left| \frac{\partial u_0}{\partial q^\mu} \right. \right\rangle \dot{q}^\mu e^{-\frac{i}{\hbar} \int^t (\mathcal{E}_0 - \mathcal{E}_\ell) d\tau} \quad (8)$$

for  $\ell \neq 0$  and

$$\dot{c}_0^{(1)} = 0 \quad (8')$$

because  $\left\langle u_0 \left| \frac{\partial u_0}{\partial q^\mu} \right. \right\rangle = 0$  follows from  $\langle u_0 | u_0 \rangle = 1$ .

Since we must have  $c_0^{(1)} = 0$  for  $\dot{q}^\mu = 0$  and since relation (8') holds independently of the value of  $\dot{q}^\mu$ , we must have

$$c_0^{(1)} = 0 \quad (9)$$

Equation (8) is equivalent to its integrated form

$$c_\ell^{(1)}(t) = (1 - \delta_{\ell 0}) i \hbar \frac{\left\langle u_\ell \left| \frac{\partial u_0}{\partial q^\mu} \right. \right\rangle}{\mathcal{E}_\ell - \mathcal{E}_0} \dot{q}^\mu e^{-\frac{i}{\hbar} \int^t d\tau (\mathcal{E}_0 - \mathcal{E}_\ell)} \quad (10)$$

This is easily seen by differentiating Eq. (10) with respect to time if we observe that  $\dot{\mathcal{E}}_\ell = \frac{\partial \mathcal{E}_\ell}{\partial q^\mu} \cdot \dot{q}^\mu$  is of the order  $O(\eta^1)$  and assume that  $\dot{q}^\mu$  is of the order  $O(\eta^1)$ . We also note that the condition

$$\lim_{\dot{q}^\mu \rightarrow 0} c_k = \delta_{k0}$$

excludes the addition of a time-independent term on the right-hand side of Eq. (10).

We now calculate the total energy  $E(t)$  of the system as a function of time:

$$\begin{aligned} E &= \langle \Psi(t) | H | \Psi(t) \rangle \\ &= \mathcal{E}_0 |c_0|^2 + \sum_{k \neq 0} \mathcal{E}_k |c_k|^2 \end{aligned} \quad (11)$$

$$= \mathcal{E}_0 + \sum_{k \neq 0} (\mathcal{E}_k - \mathcal{E}_0) |c_k|^2$$

Substituting the result (10) of perturbation theory into expression (11) we obtain

$$E = \mathcal{E}_0 + \frac{1}{2} \sum_{\mu, \nu} g_{\mu\nu} \dot{q}^\mu \dot{q}^\nu + O(\eta^3) \quad (12)$$

where the "mass tensor"  $g_{\mu\nu}$  is given by

$$g_{\mu\nu} = 2\hbar^2 \sum_{k \neq 0} \frac{\langle \frac{\partial u_0}{\partial q^\nu} | u_k \rangle \langle u_k | \frac{\partial u_0}{\partial q^\mu} \rangle}{\mathcal{E}_k - \mathcal{E}_0} \quad (13)$$

One can write  $g_{\mu\nu}$  in alternative ways by using trivial manipulations: For  $k \neq 0$  we have

$$\begin{aligned} (\mathcal{E}_k - \mathcal{E}_0) \langle u_k | \frac{\partial u_0}{\partial q^\mu} \rangle &= \langle \mathcal{E}_k u_k | \frac{\partial u_0}{\partial q^\mu} \rangle - \langle u_k | \frac{\partial (\mathcal{E}_0 u_0)}{\partial q^\mu} \rangle \\ &= \langle u_k | \left[ H, \frac{\partial}{\partial q^\mu} \right] u_0 \rangle \\ &= - \langle u_k | \frac{\partial H}{\partial q^\mu} | u_0 \rangle \end{aligned} \quad (14)$$

Substituting the result (14) into expression (13) we obtain the inertial tensor in the form

$$g_{\mu\nu} = 2\hbar^2 \sum_{k \neq 0} \frac{\langle \frac{\partial H}{\partial q^\nu} u_0 | u_k \rangle \langle u_k | \frac{\partial H}{\partial q^\mu} u_0 \rangle}{(\mathcal{E}_k - \mathcal{E}_0)^3} \quad (15)$$

The derivation of Eq. (15) follows closely a chapter in Ref. [12]. The total energy  $E$  must be identified with the classical Hamiltonian function  $\mathcal{H}$ :

$$E = \mathcal{H} = \frac{1}{2} \sum_{\mu, \nu} g_{\mu\nu} \dot{q}^\mu \dot{q}^\nu + \mathcal{E}_0 \quad (16)$$

$$\mathcal{H} = \frac{1}{2} \sum_{\mu, \nu} g^{\mu\nu} p_\mu p_\nu + \mathcal{V}(q) = \mathcal{F}(q, \dot{q}) + \mathcal{V}(q) \quad (16')$$

The potential energy  $\mathcal{V}(q)$  is given by the energy of the lowest adiabatic state

$$\mathcal{V}(q) = \mathcal{E}_0 \quad (17)$$

and  $p_\mu$  are the canonically conjugate momenta. In order to obtain a quantum-mechanical Hamiltonian  $\mathcal{H}$  depending on the collective variables  $q$ , we have to quantize the classical system described by (16). Schrödinger has given the general prescription that the classical kinetic energy ought to be replaced by

$$\mathcal{T} \rightarrow \mathcal{K} = -\frac{\hbar^2}{2} \Delta(q^1 \dots q^f) \quad (18)$$

where  $\Delta$  is the  $f$ -dimensional Laplacian in curvilinear co-ordinates:

$$\Delta(q^1 \dots q^f) = \sum_{\mu, \nu=1}^f \frac{1}{\sqrt{g}} \frac{\partial}{\partial q^\mu} \sqrt{g} g^{\mu\nu} \frac{\partial}{\partial q^\nu} \quad (19)$$

Here we have defined

$$g = |\det \{g_{\kappa\lambda}\}|$$

and

$$\sum_\nu g^{\mu\nu} g_{\nu\rho} = \delta^\mu_\rho$$

The Hamiltonian is thus given by

$$\mathcal{H}(q^1 \dots q^f) = -\frac{\hbar^2}{2} \Delta(q^1 \dots q^f) + \mathcal{V}(q^1 \dots q^f) \quad (20)$$

Although this quantization rule may appear to be a natural generalization of the well-known quantization in three-dimensional Euclidean space, it is not proved to be correct:

(i) In general, the metric defined by the tensor  $g_{\mu\nu}$  is non-Euclidean and the quantization rules to be applied in non-Euclidean spaces could be different from the ones in a Euclidean metric.

(ii) By describing the  $A$ -body system by  $f < 3A$  collective co-ordinates, we have, so to speak, "frozen" the  $(3A - f)$  additional degrees of freedom. Thus we have to quantize in a space which is embedded in a higher-dimensional space. It can be demonstrated [13] that the resulting Hamiltonian depends on the way in which we "freeze" the additional degrees of freedom. The Hamiltonian proposed by Schrödinger can be shown to be one of the possible results.

Returning to our special example of a collective Hamiltonian for the fissioning nucleus, we propose to argue as follows: The approximations underlying the derivation of our classical Hamiltonian  $\mathcal{H}$  are only valid if the coupling between the collective degrees  $q^1 \dots q^f$  and the remaining

(3A - f) degrees is negligibly small. Let  $G_{\mu\nu}(q^1 \dots q^{3A})$  be the mass tensor for some choice of the complete set of 3A independent variables and  $W(q^1 \dots q^{3A})$  the total potential term formulated in these co-ordinates. Let us assume that the variables  $q^1 \dots q^{3A}$  are related to the original Cartesian variables  $X^1 \dots X^{3A}$  by some contact transformation. It is then consistent with the hypothesis of weak coupling to assume that, for our choice of collective variables, the total 3A-dimensional tensor  $G(q^1 \dots q^f; q^{f+1} \dots q^{3A})$  should have the form

$$G = \begin{pmatrix} g_{\mu\nu}(q^1 \dots q^f) & 0 \\ 0 & \tilde{g}_{\kappa\lambda}(q^{f+1} \dots q^{3A}) \end{pmatrix} \quad (22)$$

$$\mu, \nu = 1 \dots f$$

$$\kappa, \lambda = f+1, \dots, 3A$$

and the total interaction term  $W$  should separate into two parts:

$$W = \mathcal{V}(q^1 \dots q^f) + \tilde{\mathcal{V}}(q^{f+1}, \dots, q^{3A}) \quad (23)$$

In this case, we obviously obtain a complete decoupling of the Hamiltonian  $\underline{H}(q^1 \dots q^f)$  from the Hamiltonian depending on the remaining co-ordinates and  $\underline{H}(q^1 \dots q^f)$  must have the form (20) [14]. So, to justify the quantization method applied, we have to assume that there is complete decoupling as postulated by Eqs (22) and (23).

### 3. THE METHOD OF STRUTINSKI

The method of Strutinski [4] consists in representing the potential energy  $\mathcal{V}(q)$  in terms of the liquid-drop energy plus a "shell-correction term". If we choose as zero of the energy the intrinsic energy of the nucleus in the spherical state, the potential energy  $\mathcal{V}(q)$  is the difference between the intrinsic energy of the nucleus with some shape  $q$  and the intrinsic energy of the spherical nucleus. We, therefore, refer to  $\mathcal{V}(q)$  as "deformation energy". While there are many properties of the nucleus which are mainly determined by the nucleons in the topmost, partially filled levels near the Fermi energy, we have to expect that all the nucleons contribute to the deformation energy. The contribution of the bulk of nucleons will be determined by the saturation property of nuclear matter. Because of the low compressibility of nuclear matter, a small violation of nuclear saturation may grossly falsify the deformation energy. Thus, if we wish to calculate  $\mathcal{V}(q)$  within a microscopic many-body theory, we must use saturating nuclear forces and we cannot restrict ourselves to the nucleons in the topmost shells. Since this is a technically difficult problem, it is desirable to find a simpler method. As we have already mentioned in the introduction, the LDM takes nuclear saturation into account simply by keeping the volume of the nuclear droplet independent of its shape. So we ask the question: Is it possible to write the potential energy  $\mathcal{V}(q)$  as a sum of a liquid-drop energy and a correction to it?

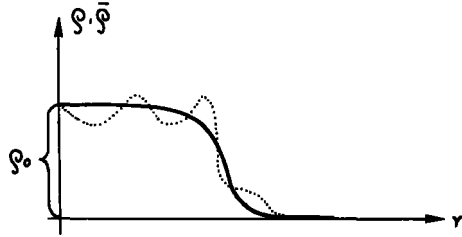


FIG. 1. Density  $\rho$  (....) and average density  $\bar{\rho}$  (—) as a function of distance  $r$ .

The LDM describes a system with a smooth density distribution  $\bar{\rho}$ . This smooth density  $\bar{\rho}$  should be about equal to the nuclear matter density  $\rho_0$  in the interior of the nucleus and should drop to zero in a surface layer of thickness  $d$  (much less than the nuclear radius  $R$ ) around the hypothetical surface of a classical droplet (Fig. 1).

Let us, therefore, define the density  $\rho$  corresponding to the lowest adiabatic state  $u_0$  by

$$\rho(X_1; q) = A \int d\tau_2 \dots d\tau_A u_0^*(X_1, X_2, \dots, X_A; q) u_0(X_1, \dots, X_A; q) \quad (24)$$

where  $X_i$  is the total set of co-ordinates of the nucleon  $i$  (we neglect spin for simplicity).

Because of the factor  $A$  in Eq. (24), the density  $\rho$  is normalized to  $A$ :

$$\int d\tau \rho(y; q) = A \quad (25)$$

where  $d\tau$  is the volume element corresponding to the three co-ordinates  $y$  of one arbitrary nucleon. We assume that the intrinsic energy  $\mathcal{V}(q) = \mathcal{E}_0(q)$  can be represented as a functional of the density  $\rho$  in the following way:

$$\mathcal{V}(q) = \int d\tau \mathcal{E}[\rho(y); y] \rho(y) \quad (26)$$

The quantity  $\mathcal{E}$  is an energy density per particle. Note that  $\mathcal{E}$  as well as  $\rho$  depend on the shape parameters  $q$ . We omit these variables in order to keep the notation simple. A representation of the form (26) can be proved under very general conditions [15]. All that is required is a one-to-one relationship between the density distribution and the energy density  $\mathcal{E}$ . We then assume that there exists an average density  $\bar{\rho}(y)$  such that replacing  $\rho$  by  $\bar{\rho}$  in the functional of Eq. (26) leads to the energy given by the LDM:

$$E_{LD} = \int d\tau \mathcal{E}[\bar{\rho}(y); y] \bar{\rho}(y) \quad (27)$$

As we shall see later, this is correct if the energy density  $\mathcal{E}[\bar{\rho}; y]$  turns out to be approximately constant in the nuclear interior, and if  $\bar{\rho}$  drops sufficiently rapidly to zero in the nuclear surface.

We now write the true density  $\rho$  as a sum of the smooth density  $\bar{\rho}$  and the fluctuating part  $\delta\rho$ :

$$\rho(y) = \bar{\rho}(y) + \delta\rho(y) \quad (28)$$

and expand the functional in Eq. (26) up to terms linear in  $\delta\rho$ :

$$\mathcal{V} = E_{LD} + \int d\tau \left\{ \left( \frac{\delta \mathcal{E}}{\delta \rho} \right)_{\bar{\rho}} \bar{\rho}(y) + \mathcal{E}[\rho; y] \right\} \delta\rho + O(\delta\rho^2) \quad (29)$$

We call the term linear in  $\delta\rho$  a "Strutinski term". If the nuclear radius were large compared to the average wave-length of occupied single-particle states, the fluctuation  $\delta\rho$  of the density would be negligible and, consequently, the LDM would be an excellent representation of the nuclear system. In this limit, the single-particle energies would be closely and regularly spaced so that the density of single-particle levels could be replaced by a smooth function of the energy. This means that the Thomas-Fermi model which is equivalent to the LDM for large particle numbers should be applicable in this limit.

In realistic nuclei, the nuclear radius is not very much larger than the average wave-length of occupied single-particle states, and, therefore, the density fluctuation is not negligible, at all. In terms of the density of single-particle energies, this means that there are fluctuations of the level density around a smooth average trend which is defined by the Thomas-Fermi model. Consequently, the Strutinski term contains the effect on the total energy of fluctuations of the density of shell-model levels and it is referred to as a "shell correction term"  $E_{SC}$ . The existence of this term is thus due to the finite size of nuclei while its detailed value is expected to be a function of the nuclear shape, possibly of the spin-orbit coupling, a. s. o. The Strutinski term

$$E_{SC} = \int d\tau \left\{ \left( \frac{\delta \mathcal{E}}{\delta \rho} \right)_{\rho=\bar{\rho}} \bar{\rho}(y) + \mathcal{E}[\bar{\rho}; y] \right\} \delta\rho \quad (30)$$

is seen to depend on the nuclear model, i. e. finally on the Hamiltonian used in Eq. (1) and on the average density  $\bar{\rho}$ . We shall now show that the shell correction term proposed by Strutinski [4] is obtained if we calculate  $E_{SC}$  in the Hartree-Fock approximation and if we generate the smooth part  $\bar{\rho}$  of the density by way of a hypothetic, smooth distribution of single particle levels. This is motivated by the very fact that the fictitious system with the average density  $\bar{\rho}(y)$  ought to be equivalent to a nucleus treated in the Thomas-Fermi approach, i. e. to a system which can be described by a smooth continuous density of single-particle energies. Since we wish to use the Strutinski method for any given nuclear shape, we have to consider the Hartree-Fock method with constrictive conditions. For simplicity we consider only one subsidiary condition; the generalization to several ones is straightforward. If  $\phi$  is a Slater determinant of  $A$  single-particle wave-functions  $\varphi_\nu$ :

$$\phi = \frac{1}{\sqrt{A!}} \mathcal{A} \left\{ \varphi_1(1) \dots \varphi_A(A) \right\}$$

and if we demand that the expectation value of the quadrupole operator should be equal to a given quantity  $q$ :

$$\langle \phi | \sum_{i=1}^A r_i^2 Y_{20}(\theta_i) | \phi \rangle = \langle \phi | \sum_{i=1}^A Q(i) | \phi \rangle = q \quad (31)$$

the Hartree-Fock equations arise from the variational principle

$$\delta \langle \phi | \hat{H} - E - \lambda \sum_{i=1}^A Q(i) | \phi \rangle = 0 \quad (32)$$

Here,  $\hat{H}$  is the many-body Hamiltonian<sup>1</sup>

$$\hat{H} = \sum_{i=1}^A T(i) + \sum_{i<j}^A v(i, j)$$

and the quantities  $E$  and  $\lambda$  are Lagrange multipliers to be chosen such that the normalization of  $\phi$  and the constraint (31) are taken into account. The variation leads to the following set of Hartree-Fock equations:

$$[T(1) + U^{HF}(1) + U^{ext}(1)] \varphi_\nu(1) = \epsilon_\nu \varphi_\nu(1) \quad (33)$$

where  $U^{HF}$  is the usual Hartree-Fock potential

$$U^{HF}(1) \varphi_\nu(1) = \sum_{\rho=1}^A \int d2 \varphi_\rho^*(2) v(1, 2) [\varphi_\nu(1) \varphi_\rho(2) - \varphi_\nu(2) \varphi_\rho(1)] \quad (34)$$

and  $U^{ext}$  is an additional external field which is created by the constraint (31):

$$U^{ext}(1) = \lambda r_1^2 Y_{20}(\theta_1) \quad (35)$$

We note that the Lagrange parameter  $\lambda$ , the single-particle energies  $\epsilon_\nu$ , and the wave-functions  $\varphi_\nu$  are all functions of the "collective variable"  $q$ . The total energy  $E$  in the Hartree-Fock approximation turns out to be

$$E = \sum_{\rho=1}^A \langle \rho | T | \rho \rangle + \frac{1}{2} \sum_{\rho, \nu=1}^A \langle \rho \nu | v | \rho \nu \rangle \quad (36)$$

where

$$\begin{aligned} \langle y | \rho \rangle &= \varphi_\rho(y) \\ \langle y_1 y_2 | \rho \nu \rangle &= \frac{1}{\sqrt{2}} \left( \varphi_\rho(y_1) \varphi_\nu(y_2) - \varphi_\nu(y_1) \varphi_\rho(y_2) \right) \end{aligned}$$

<sup>1</sup> The Hamiltonian  $H$  of Eq. (1) can be thought to be obtained from the basic Hamiltonian  $\hat{H}$  by applying the Wick theorem. The contractions are to be defined with respect to  $\phi$  as "vacuum state". Consequently,  $H$  will be a function of  $q$ .

and the density  $\rho$  has the form

$$\rho(y) = \sum_{\nu=1}^A |\varphi_{\nu}(y)|^2 = \sum_{\nu=1}^A \rho_{\nu}(y) \quad (37)$$

It is now useful to define a spectral density  $\overset{\circ}{g}(\epsilon)$  by

$$\overset{\circ}{g}(\epsilon) := \sum_{\nu} \delta(\epsilon - \epsilon_{\nu}) \quad (38)$$

We, furthermore, define a smooth level density  $g(\epsilon)$  which is generated from  $\overset{\circ}{g}(\epsilon)$  by a "smearing function"  $f(\epsilon, \epsilon')$ :

$$g(\epsilon) := \int_{-\infty}^{+\infty} d\epsilon' f(\epsilon, \epsilon') \overset{\circ}{g}(\epsilon') \quad (39)$$

We assume that  $f(\epsilon, \epsilon')$  varies very little in an energy interval  $\Delta\epsilon$  which contains a relatively large number of shell-model energies  $\epsilon_{\nu}$ , i. e. in an energy range which is of the order of several times the average distance between neighbouring levels. As a consequence, the level density is a smooth function of the energy  $\epsilon$ . The function  $f(\epsilon, \epsilon')$  will be specified later. Using the spectral density  $\overset{\circ}{g}(\epsilon)$  (Eq. (38)) we may write the density  $\rho(y)$  in the form

$$\rho(y) = \int_{-\infty}^{\epsilon_F} d\epsilon \overset{\circ}{g}(\epsilon) |\varphi(\epsilon, y)|^2 = \sum_{\nu=1}^{\infty} \int_{-\infty}^{\epsilon_F} d\epsilon \delta(\epsilon - \epsilon_{\nu}) |\varphi(\epsilon_{\nu}, y)|^2 \quad (40)$$

where  $\varphi(\epsilon, y)$  may be thought to be the analytic continuation of  $\varphi_{\nu}(y) \equiv \varphi(\epsilon_{\nu}, y)$ . It should, however, be noted that in expression (40) as well as in all the following expressions,  $\varphi(\epsilon, y)$  is actually only used for  $\epsilon = \epsilon_{\nu}$ , i. e. for the discrete eigenvalues. Consequently, only normalized eigenfunctions  $\varphi(\epsilon, y)$  enter our derivation. The form of expression (40) suggests the following definition of a smooth density  $\bar{\rho}(y)$ :

$$\bar{\rho}(y) := \sum_{\nu=1}^{\infty} \int_{-\infty}^{\Lambda} d\epsilon f(\epsilon, \epsilon_{\nu}) |\varphi(\epsilon_{\nu}, y)|^2 = \int_{-\infty}^{\Lambda} d\epsilon f(\epsilon, \epsilon') \overset{\circ}{g}(\epsilon') \varphi(\epsilon', y) \quad (41)$$

The parameter  $A$  is defined by the requirement of conservation of particle number

$$\int_{-\infty}^{\Lambda} d\epsilon g(\epsilon) = A \quad (42)$$

Since, by construction,  $g(\epsilon)$  is just the result of smearing the singular spectral density  $\overset{\circ}{g}(\epsilon)$ , the parameter  $\Lambda$  is expected to be close to the Fermi energy  $\epsilon_F$ . It will be convenient to introduce the following conventions:

(i) We formally extend the bracket symbols to continuous values of the energy

$$\langle y | \epsilon \rangle = \varphi(\epsilon, y) \quad (43)$$

$$\langle y_1 y_2 | \epsilon_1 \epsilon_2 \rangle = \frac{1}{\sqrt{2}} \left[ \varphi(\epsilon_1, y_1) \varphi(\epsilon_2, y_2) - \varphi(\epsilon_1, y_2) \varphi(\epsilon_2, y_1) \right] \quad (43')$$

(ii) We introduce the notation

$$\begin{aligned} \int_{-\infty}^{\Lambda} d\epsilon g(\epsilon) \cdot q[\varphi(\epsilon, y)] &:= \int_{-\infty}^{\Lambda} d\epsilon f(\epsilon, \epsilon') \int_{-\infty}^{+\infty} d\epsilon' \mathring{g}(\epsilon') q[\varphi(\epsilon', y)] \\ &= \sum_{\nu=1}^{\infty} \int_{-\infty}^{\Lambda} d\epsilon f(\epsilon, \epsilon_{\nu}) q[\varphi(\epsilon_{\nu}, y)] \end{aligned} \quad (44)$$

where  $q[\varphi(\epsilon, y)]$  is some functional of the single-particle wave-function  $\varphi(\epsilon, y)$ , for instance the density  $|\varphi(\epsilon, y)|^2$ . We shall use the following applications of this notation:

$$\int_{-\infty}^{\Lambda} d\epsilon g(\epsilon) \cdot \langle \epsilon | Q | \epsilon \rangle := \sum_{\nu=1}^{\infty} \int_{-\infty}^{\Lambda} d\epsilon f(\epsilon, \epsilon_{\nu}) \langle \nu | Q | \nu \rangle \quad (45)$$

$$\int_{-\infty}^{\Lambda} d\epsilon_1 \int_{-\infty}^{\epsilon_1^F} d\epsilon_2 \mathring{g}(\epsilon_2) g(\epsilon_1) \cdot \langle \epsilon_1 \epsilon_2 | V | \epsilon_1 \epsilon_2 \rangle = \int_{-\infty}^{\Lambda} d\epsilon_2 \int_{-\infty}^{\epsilon_2^F} d\epsilon_1 \mathring{g}(\epsilon_1) g(\epsilon_2)$$

$$\langle \epsilon_1 \epsilon_2 | V | \epsilon_1 \epsilon_2 \rangle := \sum_{\nu=1}^{\Lambda} \sum_{\rho=1}^{\infty} \int_{-\infty}^{\Lambda} d\epsilon f(\epsilon_1, \epsilon_{\rho}) \langle \rho \nu | V | \rho \nu \rangle \quad (45')$$

$$\int_{-\infty}^{\Lambda} d\epsilon_1 \int_{-\infty}^{\Lambda} d\epsilon_2 g(\epsilon_1) g(\epsilon_2) \cdot \langle \epsilon_1 \epsilon_2 | V | \epsilon_1 \epsilon_2 \rangle := \sum_{\nu=1}^{\infty} \sum_{\rho=1}^{\infty} \int_{-\infty}^{\Lambda} d\epsilon_1 \int_{-\infty}^{\Lambda} d\epsilon_2$$

$$\times f(\epsilon_1, \epsilon_{\rho}) f(\epsilon_2, \epsilon_{\nu}) \langle \rho \nu | V | \rho \nu \rangle \quad (45'')$$

$$\int_{-\infty}^{\Lambda} d\epsilon g(\epsilon) \cdot \epsilon := \int_{-\infty}^{\Lambda} d\epsilon \int_{-\infty}^{+\infty} d\epsilon' f(\epsilon, \epsilon') \mathring{g}(\epsilon') \epsilon' = \sum_{\nu=1}^{\infty} \int_{-\infty}^{\Lambda} d\epsilon f(\epsilon, \epsilon_{\nu}) \epsilon_{\nu} \quad (45''')$$

With the help of the spectral density  $\mathring{g}(\epsilon)$ , we may formally write the total energy  $E$  in terms of integrals:

$$E = \int_{-\infty}^{\epsilon_F} d\epsilon \mathring{g}(\epsilon) \langle \epsilon | T | \epsilon \rangle + \frac{1}{2} \int_{-\infty}^{\epsilon_F} d\epsilon_1 \int_{-\infty}^{\epsilon_F} d\epsilon_2 \mathring{g}(\epsilon_1) \mathring{g}(\epsilon_2) \langle \epsilon_1 \epsilon_2 | V | \epsilon_1 \epsilon_2 \rangle \quad (46)$$

We now replace  $\overset{\circ}{g}$  by  $[(\overset{\circ}{g} - g) + g]$  in the different terms of (46):

$$\overset{\circ}{g}(\epsilon) = \delta g(\epsilon) + g(\epsilon)$$

with

$$\delta g(\epsilon) = \overset{\circ}{g}(\epsilon) - g(\epsilon)$$

This leads to<sup>2</sup>

$$\begin{aligned} E = & \int_{-\infty}^{\Lambda} d\epsilon g(\epsilon) \cdot \langle \epsilon | T | \epsilon \rangle + \frac{1}{2} \int_{-\infty}^{\Lambda} d\epsilon_1 \int_{-\infty}^{\Lambda} d\epsilon_2 g(\epsilon_1) g(\epsilon_2) \cdot \langle \epsilon_1 \epsilon_2 | V | \epsilon_1 \epsilon_2 \rangle \\ & + \int d\epsilon \delta g(\epsilon) \cdot \langle \epsilon | T | \epsilon \rangle + \int d\epsilon_1 \delta g(\epsilon_1) \cdot \int d\epsilon_2 \overset{\circ}{g}(\epsilon_2) \langle \epsilon_1 \epsilon_2 | V | \epsilon_1 \epsilon_2 \rangle \\ & + O(\delta g^2) \end{aligned} \quad (47)$$

Using the symmetry

$$\langle \epsilon_1 \epsilon_2 | V | \epsilon_1 \epsilon_2 \rangle = \langle \epsilon_2 \epsilon_1 | V | \epsilon_2 \epsilon_1 \rangle$$

Eq. (47) represents the Taylor expansion (29) for the case of the Hartree-Fock model. The terms in 0th order of  $\delta g$  represent the Hartree-Fock approximation to the smooth (i. e. LD) part of the energy

$$E_{LD}^{\text{Hartree-Fock}} = \int_{-\infty}^{\Lambda} d\epsilon g(\epsilon) \cdot \langle \epsilon | T | \epsilon \rangle + \frac{1}{2} \int_{-\infty}^{\Lambda} d\epsilon_1 \int_{-\infty}^{\Lambda} d\epsilon_2 g(\epsilon_1) g(\epsilon_2) \cdot \langle \epsilon_1 \epsilon_2 | V | \epsilon_1 \epsilon_2 \rangle$$

while the term linear in  $\delta g(\epsilon)$  constitute the "shell-correction term"  $E_{SC}$ . From (33) to (35), we see that the single-particle energies  $\epsilon_\nu$  may be written as

$$\epsilon_\nu = \langle \nu | T | \nu \rangle + \sum_{\rho=1}^A \langle \nu \rho | V | \nu \rho \rangle + \lambda \langle \nu | Q | \nu \rangle \quad (47a)$$

Comparing expression (47a) with the terms linear in  $\delta g$  of Eq. (47), we see that the following equation holds:

$$\begin{aligned} & \int d\epsilon \delta g(\epsilon) \cdot \left\{ \langle \epsilon | T | \epsilon \rangle + \int d\epsilon' \overset{\circ}{g}(\epsilon') \langle \epsilon \epsilon' | V | \epsilon \epsilon' \rangle \right\} \\ & = \int d\epsilon \delta g(\epsilon) \left\{ \epsilon - \lambda \langle \epsilon | Q | \epsilon \rangle \right\} \end{aligned}$$

<sup>2</sup> The integration limits are  $\int_{-\infty}^{\Lambda}$ , if the variable occurs as an argument of  $g(\epsilon)$  and  $\int_{-\infty}^{\epsilon F}$  if it occurs as an argument of  $\overset{\circ}{g}(\epsilon)$ .

We may rewrite the term which contains the contribution of the external potential as

$$\begin{aligned} \lambda \int d\epsilon \delta g(\epsilon) \cdot \langle \epsilon | \underline{Q} | \epsilon \rangle &= \lambda \int_{-\infty}^{\Lambda} d\epsilon g(\epsilon) \cdot \int d\tau \underline{Q}(y) |\varphi(\epsilon, y)|^2 \\ &\quad - \lambda \int_{-\infty}^{\epsilon_F} d\epsilon \overset{\circ}{g}(\epsilon) \cdot \int d\tau \underline{Q}(y) |\varphi(\epsilon, y)|^2 \\ &= \lambda \left\{ \int d\tau \underline{Q}(y) \bar{\rho}(y) - \int d\tau \underline{Q}(y) \rho(y) \right\} \end{aligned} \quad (48)$$

We see from Eq. (48) that the terms arising from the external potential are proportional to the difference between the quadrupole moment of the true and the average density distribution. Now, clearly, the average density  $\bar{\rho}(y)$  must display the same multipole moments as the true density  $\rho(y)$ . If we identify  $\bar{\rho}$  with the density distribution in a LDM, it is exactly this requirement which serves to relate the shape of the droplet to the shape of the actual nuclear density. Thus the contributions from the constrictive potential cancel in expression (47a) and the "shell-correction term" is seen to be

$$E_{SC} = \int d\epsilon \delta g(\epsilon) \cdot \epsilon = \sum_{\nu=1}^{\Lambda} \epsilon_{\nu} - \int_{-\infty}^{\Lambda} d\epsilon g(\epsilon) \cdot \epsilon$$

Using the definition (45<sup>m</sup>), we have the explicit form

$$E_{SC} = \sum_{\nu=1}^{\Lambda} \epsilon_{\nu} - \sum_{\nu=1}^{\infty} \int_{-\infty}^{\Lambda} d\epsilon f(\epsilon, \epsilon_{\nu}) \epsilon_{\nu} \quad (49)$$

It is seen from expression (49) that only the energies  $\epsilon_{\nu}$  in the interval  $\epsilon_F - \gamma < \epsilon_{\nu} < \epsilon_F + \gamma$  around the Fermi energy contribute to the shell correction  $E_{SC}$ . The smooth term in Eq. (49) can be written as

$$\begin{aligned} \sum_{\nu=1}^{\infty} \int_{-\infty}^{\Lambda} d\epsilon f(\epsilon, \epsilon_{\nu}) \epsilon_{\nu} &= \int_{-\infty}^{\Lambda} d\epsilon \int_{-\infty}^{+\infty} d\epsilon' f(\epsilon, \epsilon') \overset{\circ}{g}(\epsilon') \epsilon \\ &\quad + \int_{-\infty}^{\Lambda} d\epsilon \int_{-\infty}^{+\infty} d\epsilon' f(\epsilon, \epsilon') \overset{\circ}{g}(\epsilon') (\epsilon' - \epsilon) \\ &= \int_{-\infty}^{\Lambda} d\epsilon \epsilon g(\epsilon) + \sum_{\nu=1}^{\infty} \int_{-\infty}^{\Lambda} d\epsilon f(\epsilon, \epsilon_{\nu}) (\epsilon_{\nu} - \epsilon) \end{aligned}$$

The second term in this equation is expected to be very small if the number of shell-model levels in an interval of length  $2\gamma$  (see Eq. (59)) around the Fermi energy ( $\epsilon_F - \gamma < \epsilon_\nu < \epsilon_F + \gamma$ ) is large. Since the Strutinski theory should only be applied to sufficiently large nuclei, this condition is usually fulfilled. We wish to emphasize the following point: The summation of single-particle energies as well as the cancellation of the effects of the external potential result from the fact that the Strutinski term is defined as a correction to the smooth part of the energy functional which is linear in the fluctuation  $\delta\rho$  of the density. We thus arrive at the result

$$\mathcal{V}(q) = E_{LD} + E_{SC} \quad (50)$$

$$E_{SC} = \sum_{\nu=1}^A \epsilon_\nu - \int_{-\infty}^{\Lambda} d\epsilon \epsilon g(\epsilon)$$

$$E_{SC} = \int d\epsilon \epsilon [\overset{\circ}{g}(\epsilon) - g(\epsilon)] \quad (51)$$

This is the shell-correction term introduced by Strutinski [4]. We note that because of the cancellation of the contributions of  $U^{\text{ext}}$ :

$$\lambda \int d\tau \mathcal{Q} \bar{\rho}(y) - \lambda \int d\tau \mathcal{Q} \rho(y) = 0$$

we may replace the energies  $\epsilon_\nu$  in expression (51) by

$$\overset{\circ}{\epsilon}_\nu := \langle \varphi_\nu | T + U^{\text{HF}} | \varphi_\nu \rangle$$

and thus also by the eigenenergies of a phenomenological potential which replaces the self-consistent potential  $U^{\text{HF}}$ .

We now turn to the problem of specifying the "smoothing function"  $f(\epsilon, \epsilon')$ : In principle, the smoothing function should be determined in such a way that it produces an average density  $\bar{\rho}$  which, when substituted in expression (26), leads to the liquid-drop energy. It is difficult to carry out this prescription, because it implies that we specify the energy functional and carry through the actual LD expansion of the smooth part  $\int d\tau w[\bar{\rho}; y] \bar{\rho}$  as a function of  $A^{-1/3}$ . We, therefore, use the fact that for large particle numbers the LDM is equivalent to the Thomas-Fermi theory. A basic ingredient of the Thomas-Fermi model is the replacement of the actual density of single-particle energies by a smooth continuous one. We shall, therefore, determine the smoothing function  $f(\epsilon, \epsilon')$  such that it produces, through Eq. (39), a level density  $g(\epsilon)$  which is equal to the smooth part of the actual level density  $\overset{\circ}{g}(\epsilon)$  [4, 16]:

Let  $\Delta\epsilon$  be an energy interval sufficiently large for containing a relatively large number of single-particle energies  $\epsilon_\nu$ . So,  $\Delta\epsilon$  should be large compared to the average distance of neighbouring single-particle levels, but smaller than the distance between major shells (see Fig. 2). We now calculate from  $\overset{\circ}{g}(\epsilon)$  a continuous level density by integrating  $\overset{\circ}{g}(\epsilon)$  over intervals of length  $\Delta\epsilon$ . This new level density is composed of a smooth

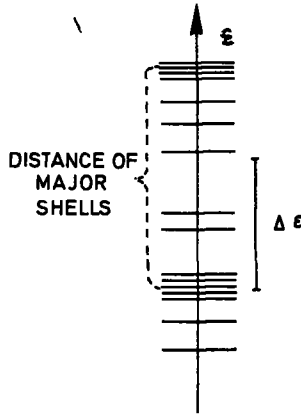


FIG. 2. Level distances.

part  $g_S(\epsilon)$  which varies slowly with the energy  $\mathcal{E}$  and a rapidly varying part  $g_R(\mathcal{E})$  which reflects the irregular fluctuations of the number of levels contained in an interval of length  $\Delta\epsilon$  as its center  $\mathcal{E}$  is moved through the spectrum:

$$g_S(\mathcal{E}) + g_R(\mathcal{E}) = \frac{1}{\Delta\epsilon} \int_{\mathcal{E} - \frac{\Delta\epsilon}{2}}^{\mathcal{E} + \frac{\Delta\epsilon}{2}} d\epsilon \mathring{g}(\epsilon) \quad (52)$$

We now require that the level distribution  $g(\epsilon)$  which is calculated from Eq. (39) should agree with the smooth part  $g_S(\mathcal{E})$  of the actual level distribution:

$$g(\epsilon) = g_S(\epsilon) = \int_{-\infty}^{+\infty} d\epsilon' f(\epsilon, \epsilon') \mathring{g}(\epsilon') \quad (53)$$

Assuming that the smearing function  $f(\epsilon, \epsilon')$  can be considered to be constant in an energy interval of length  $\Delta\epsilon$ , we may write instead of (53):

$$\begin{aligned} \int_{-\infty}^{+\infty} d\epsilon' f(\epsilon, \epsilon') \mathring{g}(\epsilon') &= \int_{-A}^{-A+\Delta\epsilon} d\epsilon' f\left(\epsilon, -A + \frac{\Delta\epsilon}{2}\right) \mathring{g}(\epsilon') \\ &+ \int_{-A+\Delta\epsilon}^{-A+2\Delta\epsilon} d\epsilon' f\left(\epsilon, -A + \frac{\Delta\epsilon}{2} + \Delta\epsilon\right) \mathring{g}(\epsilon') + \dots \\ &+ \int_{A-\Delta\epsilon}^A d\epsilon' f\left(\epsilon, A - \frac{\Delta\epsilon}{2}\right) \mathring{g}(\epsilon') \end{aligned} \quad (54)$$

where  $A$  is a sufficiently large positive energy such that the contributions  $\int_{-\infty}^{-A}$  and  $\int_A^{+\infty}$  to the integral are negligible. Substituting expression (52) into relation (54) we obtain

$$\begin{aligned} \int_{-\infty}^{+\infty} d\epsilon' f(\epsilon, \epsilon') \overset{\circ}{g}(\epsilon') &= \Delta\epsilon \left\{ f\left(\epsilon, -A + \frac{\Delta\epsilon}{2}\right) \left[ g_S\left(-A + \frac{\Delta\epsilon}{2}\right) + g_R\left(-A + \frac{\Delta\epsilon}{2}\right) \right] \right. \\ &+ \dots + f\left(\epsilon, A - \frac{\Delta\epsilon}{2}\right) \left[ g_S\left(A - \frac{\Delta\epsilon}{2}\right) + g_R\left(A - \frac{\Delta\epsilon}{2}\right) \right] \left. \right\} \\ &= \int_{-\infty}^{+\infty} d\epsilon' f(\epsilon, \epsilon') \left[ g_S(\epsilon') + g_R(\epsilon') \right] \end{aligned} \quad (55)$$

Combining Eq. (55) with requirement (53), we obtain the following conditions for the determination of the smoothing function  $f$ :

$$\int_{-\infty}^{+\infty} d\epsilon' f(\epsilon, \epsilon') g_S(\epsilon') = g_S(\epsilon) \quad (56)$$

$$\int_{-\infty}^{+\infty} d\epsilon' f(\epsilon, \epsilon') g_R(\epsilon') = 0 \quad (57)$$

It is important to note with respect to the conditions (56) and (57) that  $g_S$  is supposed to be a smooth function of the energy and  $g_R$  a rapidly varying function. We have to specify these properties in greater detail: For given  $\epsilon$ , the smoothing function  $f(\epsilon, \epsilon')$  is substantially different from zero in an interval  $I(\epsilon)$  of  $\epsilon'$  values centred around  $\epsilon$  with a length comparable to the energy difference between major shells. We assume that in this range of  $\epsilon'$ -values the smooth density  $g_S(\epsilon')$  may be represented by the first  $m$  terms of its Taylor expansion around  $\epsilon' = \epsilon$ :

$$\int_{-\infty}^{+\infty} d\epsilon' f(\epsilon, \epsilon') \left[ g_S(\epsilon) + (\epsilon' - \epsilon) \frac{\partial g_S}{\partial \epsilon} + \dots + \frac{(\epsilon' - \epsilon)^m}{m!} \frac{\partial^m g_S}{\partial \epsilon^m} \right] = g_S(\epsilon) \quad (58)$$

We imagine that in each interval  $I(\epsilon)$  the rapidly varying density  $g_R(\epsilon')$  is expanded in a Fourier series [16]. Then "rapid" variation should mean that the longest "wave length"  $\lambda$  in this expansion is given by the interval  $\Delta\epsilon$ , i. e. several times the average distance between neighbouring shell model levels. If condition (57) is well fulfilled for the Fourier component with  $\lambda = \Delta\epsilon$ , then it is certainly fulfilled for all shorter wave lengths. We can thus specify condition (57) by demanding

$$\int_{-\infty}^{+\infty} d\epsilon' f(\epsilon, \epsilon') e^{i \frac{\epsilon'}{\Delta\epsilon}} = 0 \quad (57')$$

The requirements (58) and (57') can certainly be met by a variety of smoothing functions. Following Strutinski, we choose the following function:

$$f(\epsilon, \epsilon') = \frac{1}{\sqrt{\pi}\gamma} e^{-\left(\frac{\epsilon - \epsilon'}{\gamma}\right)^2} P_m\left(\frac{\epsilon - \epsilon'}{\gamma}\right) \quad (59)$$

where  $P_m$  is an  $m$ -th order polynomial

$$P_m\left(\frac{\epsilon - \epsilon'}{\gamma}\right) = \sum_{k=0}^m a_k \cdot \left(\frac{\epsilon - \epsilon'}{\gamma}\right)^k \quad (60)$$

According to our preceding discussion, the parameter  $\gamma$  should be approximately equal to the distance between major shells. Substituting expression (59) into relation (58) and introducing as an integration variable

$$u = \frac{\epsilon' - \epsilon}{\gamma}$$

we obtain

$$g_S(\epsilon) = \frac{1}{\sqrt{\pi}} \int_{-\infty}^{+\infty} du e^{-u^2} P_m(u) \left\{ g_S(\epsilon) + \sum_{k=1}^m \frac{(\gamma u)^k}{k!} \frac{\partial^k g_S}{\partial \epsilon^k} \right\} \quad (61)$$

Eq. (61) can be fulfilled for arbitrary (smooth) functions  $g_S(\epsilon)$  if the following set of equations hold:

$$\frac{1}{\sqrt{\pi}} \int_{-\infty}^{+\infty} du e^{-u^2} P_m(u) u^\ell = \delta_{\ell 0} \quad (62)$$

where  $\ell = 0, 1, \dots, m$ .

Substituting expression (60) into relation (62) yields a linear system of equations for the coefficients  $a_k$  of the polynomial  $P_m$ :

$$\sum_{k=0}^m a_k I_{k\ell} = \delta_{\ell 0} \quad (\ell = 0, 1, \dots, m) \quad (63)$$

with

$$I_{k\ell} := \frac{1}{\sqrt{\pi}} \int_{-\infty}^{+\infty} du e^{-u^2} u^{\ell+k} \quad (64)$$

The quantities  $I_{k\ell}$  can be calculated analytically. They vanish if  $(\ell+k)$  is an odd number. Consequently, Eqs (63) are composed of a homogeneous set of linear equations for the coefficients  $a_k$  with odd  $k$  and an inhomogeneous set of linear equations for the coefficients  $a_k$  with even  $k$ . The homogeneous equations have only the trivial solution

$$a_k = 0 \text{ for odd } k \quad (65)$$

The inhomogeneous equations yield a non-trivial solution for the coefficients  $a_k$  with even  $k$ . Note that the coefficients  $a_k$  of the polynomial  $P_m$  depend, only on the order  $m$  of the polynomial, but not on the special form of  $g_S(\epsilon)$ . The order  $m$  of the polynomial must be sufficiently high such that the smooth density  $g_S(\epsilon')$ , in an interval of length  $\gamma$  around  $\epsilon$ , may be described by the  $m$  first terms of the Taylor expansion around  $\epsilon$  (see Eq. (58)). On the other hand, the order  $m$  must not be too high in view of condition (57) or (57') which, for given value of  $\gamma$ , is fulfilled the better the lower the order  $m$ . The optimal compromise between the two requirements (57') and (58) depends on  $\gamma$ . Tsang [16] (see also Ref. [8]) used  $\gamma = 1.2 \hbar \omega_0$  and  $m = 6$  ( $\omega_0$  = frequency of spherical oscillator potential). Strutinski et al. [9] and Andersen et al. [17] used a somewhat smaller  $\gamma$  and polynomials of order 2-4. It can be seen from actual calculations [3] that the shell correction  $E_{SC}$  does not critically depend on the choice of the "compromise".

We wish to conclude this section by indicating very crudely how the LD expansion can be derived from the smooth part of the energy [16]. As already mentioned, we must assume that the average density  $\bar{\rho}$  generates an energy density  $w[\bar{\rho}; y]$  which is almost constant in the interior of the nucleus:

$$w[\bar{\rho}(y); y] \approx w_0 = \text{const for } y \in \text{interior of the nucleus,} \quad (66)$$

where  $y$  are the co-ordinates of an arbitrary point in space.

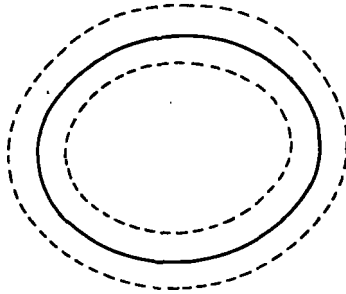


FIG.3. — ... surface S of fictitious classical droplet;  
 --- ... surface layer.

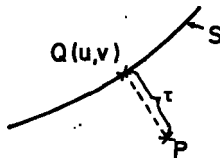


FIG.4. Choice of variables.

We may thus write:

$$E[\bar{\rho}] = \int d\tau w[\bar{\rho}(y); y] \bar{\rho}(y) = \int d\tau [w - w_0] \bar{\rho} + w_0 \int \bar{\rho} d\tau \quad (67)$$

$$E[\bar{\rho}] = w_0 A + \int d\tau \left\{ w[\bar{\rho}; y] - w_0 \right\} \bar{\rho}(y)$$

The first term on the right side of Eq. (67) is the volume term of the LD expansion. If Eq. (66) holds, the integrand of the second term in expression (67) is unequal to zero only in the surface layer of the nucleus.

Let us now use as the co-ordinates of an arbitrary point P in the surface layer the distance  $\tau$  of the point from the fictitious surface S of the classical droplet, and a pair of orthogonal surface co-ordinates  $(u, v)$  which specify the position of the surface point Q closest to P (Figs 3, 4). We then have

$$\int d\tau \left\{ w[\bar{\rho}; y] - w_0 \right\} \bar{\rho}(y) = \int du dv d\tau (1 + 2\kappa\tau + \kappa_1 \kappa_2 \tau^2) \cdot F(u, v, \tau) \quad (68)$$

where  $\kappa_{1,2}(u, v)$  are the principal curvatures at point Q  $(u, v)$ ,  $\kappa$  is the average curvature

$$\kappa = \frac{1}{2} (\kappa_1 + \kappa_2)$$

and F is the integrand as a function of the co-ordinates  $u, v, \tau$

$$F(u, v, \tau) = \left\{ w[\bar{\rho}] - w_0 \right\} \bar{\rho}$$

We now assume that the function F depends on  $u, v$  only by way of the principal curvatures  $\kappa_1, \kappa_2$ . Using the same symbol F for simplicity, this means

$$\left\{ w[\bar{\rho}] - w_0 \right\} \bar{\rho} = F(\kappa_1(u, v), \kappa_2(u, v), \tau) \quad (69)$$

F is thus a functional of the principal curvatures  $\kappa_{1,2}$  and can be expanded around<sup>3</sup>  $\kappa_1 = \kappa_2 = 0$

$$F[\kappa_1, \kappa_2, \tau] = F(0, 0, \tau) + (\kappa_1 + \kappa_2) \left( \frac{\partial F}{\partial \kappa_1} \right)_{\kappa_1 = \kappa_2 = 0} + \dots \quad (70)$$

Substituting expression (70) into relations (68) and (67) we obtain

$$E[\bar{\rho}] = w_0 A + a \cdot S + b \cdot K + O(\kappa^3) \quad (71)$$

<sup>3</sup> For symmetry reasons we must have

$$\left( \frac{\partial F}{\partial \kappa_1} \right)_{\kappa_1 = \kappa_2 = 0} = \left( \frac{\partial F}{\partial \kappa_2} \right)_{\kappa_1 = \kappa_2 = 0}$$

where  $S = \int du dv$  is the surface of classical droplet, and

$K = \int du dv \kappa(u, v)$  is the average curvature of droplet surface, and the constants  $a$  and  $b$  are given by

$$a = \int d\tau F(0, 0, \tau)$$

$$b = 2 \int d\tau \left[ F(0, 0, \tau) + \left( \frac{\partial F}{\partial \kappa_1} \right)_{00\tau} \right]$$

Equation (71) represents the LD-expansion. Since the nuclear radius  $R \propto A^{1/3}$ , the formula is seen to be an expansion in terms of  $A^{-1/3}$ . The LD-expansion is seen to converge if the curvature of the classical droplet surface is small. It should be noted that the constants  $a$ ,  $b$  are independent of the nuclear shape. The dependence on the nuclear shape is only contained in the surface  $S$  and the average curvature  $K$ .

#### 4. APPLICATION OF THE STRUTINSKI METHOD

In the actual applications of the Strutinski method, one does not calculate the single particle energies  $\epsilon_\nu$  from a Hartree-Fock method. Instead one generates these single particle energies from a phenomenological shell-model potential. The shape of this potential must be related to a given shape of the nuclear droplet in such a way that the multipole moments of the actual density and the droplet density are equal (see Eq. (48) and following discussion). The way this is achieved depends on the choice of the phenomenological potential. Calculations were performed with essentially three types of phenomenological potentials: Strutinski et al. [9, 31] use a deformed Saxon-Woods potential

$$U = U_1 + U_2 = \frac{V_0}{1 + e^{\ell/a}} - \frac{\kappa}{\hbar^2} \text{grad } U_1 (\vec{\sigma} \times \vec{p}) \quad (72)$$

where  $\ell$  is defined by

$$\ell := \frac{\pi(z, r)}{|\nabla \pi(z, r)|} \quad (72')$$

The function  $\pi(z, r)$  defines the surface of the rotationally symmetric droplet through:  $\pi(z, r) = 0$  ( $z$ -axis = symmetry axis). The parameters  $V_0$ ,  $\kappa$ ,  $a$  are self-explanatory.

S.G. Nilsson et al. [8] use a Nilsson potential which is generalized by the addition of higher multipoles<sup>4</sup>

$$U = U_0 + U_{\text{corr}} \quad (73)$$

$$U_0 = \frac{\hbar\omega_0}{2} r^2 \left[ 1 - \frac{2\epsilon_2}{3} P_2 + 2 \sum_{i=3}^5 \epsilon_i P_i \right] \quad (73')$$

<sup>4</sup> R. Nix et al. generate the shell-model potential from a Thomas-Fermi theory (private communication, to be published).

$$U_{\text{corr}} = \kappa \hbar \omega_0 \left[ \vec{l} \vec{\sigma} - \mu \left( \vec{l}^2 - \frac{N(N+3)}{2} \right) \right] \quad (73'')$$

The parameters  $\epsilon_i$  define the shape of the potential.  $U_{\text{corr}}$  is the well-known correction term in the Nilsson potential. For details we refer to Ref. [8]. In this case one requires that an equipotential surface given by

$$U = \kappa_0 = \text{const} \quad (74)$$

should coincide with the given surface of the LD.

Andersen et al. [17] use a potential composed of two oscillators which are smoothly joined by an inverted oscillator.

$$U = U_0 + U_{\text{corr}} = \frac{m\omega^2}{2} \rho^2 + V(z) + U_{\text{corr}} \quad (75)$$

$$V(z) = \begin{cases} \frac{m\omega_1^2}{2} (z+z_1)^2 & \text{for } z < -z_0 \\ V_0 - \frac{m\omega_0^2}{2} z^2 & \text{for } -z_0 < z < z_0 \\ \frac{m\omega_1^2}{2} (z-z_1)^2 & \text{for } z > z_0 \end{cases} \quad (76)$$

The definition of potential  $V_{\text{corr}}$  in (75) differs from the one in (73''); the angular momentum  $\vec{l} = \vec{r} \times \vec{p}$  is replaced by  $\nabla \vec{V}_0 \times \vec{p}$  and the trace term is generalized [17, 19].

The results obtained for the potential energy on the basis of the above-mentioned shell-model potentials are published in several papers (see Refs [8, 9, 17 - 19]). Here, we restrict ourselves to a discussion of a few general points which we believe to be noteworthy:

#### (i) The qualitative effect of the shell correction

It can easily be seen that the effect of the shell correction

$$E_{\text{SC}} = \int_{-\infty}^{\epsilon_F} d\epsilon \dot{g}(\epsilon) \epsilon - \int_{-\infty}^{\Lambda} d\epsilon g(\epsilon) \epsilon$$

depends sensitively on the density of shell-model levels just above the Fermi energy  $\epsilon_F$ . The Fermi energy  $\epsilon_F$  and the upper bound  $\Lambda$  of the integrated part of the smooth spectrum are given by conservation of particle number  $A$ :

$$\int_{-\infty}^{\epsilon_F} d\epsilon \dot{g}(\epsilon) = \int_{-\infty}^{\Lambda} d\epsilon g(\epsilon) = A \quad (77)$$

We compare two typical situations: In Fig. 5 we show the case that the last occupied level of the true spectrum is just the topmost of a bunch of filled

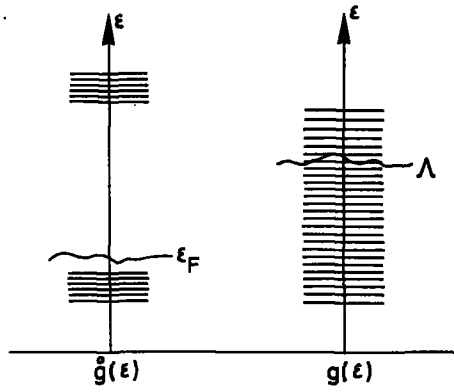


FIG. 5. Case 1 of shell corrections.

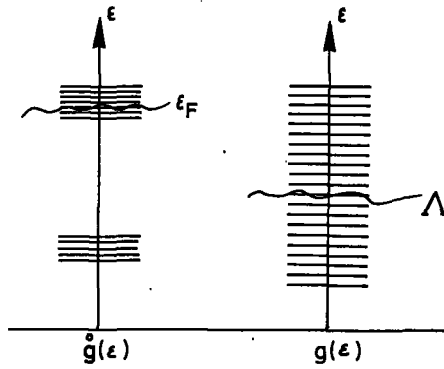


FIG. 6. Case 2 of shell corrections.

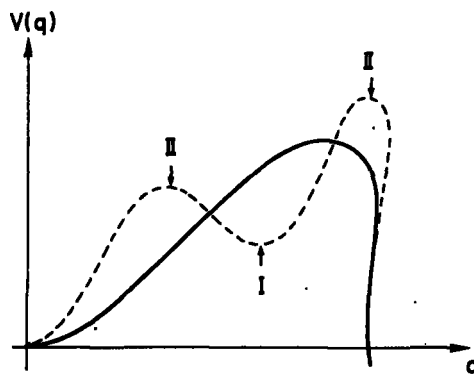


FIG. 7. LD-energy —; LD-energy + shell correction - - - - -; I corresponds to Fig. 5, II to Fig. 6.

levels and separated from the next group of (unoccupied) levels by a gap. Because of Eq. (77) and because, for sufficiently large energy intervals, the number of levels of the true and the smooth spectrum must be equal, this leads to  $\Lambda > \epsilon_F$  (see Fig. 5), and consequently a negative shell correction term  $E_{SC} < 0$ . In Fig. 6, we show the opposite case that the Fermi energy is in the middle of a group of narrowly spaced shell-model levels. Now, the condition of particle number conservation (Eq. 77) leads to  $\Lambda < \epsilon_F$  (see Fig. 6) and consequently a positive shell correction  $E_{SC} > 0$ . Thus, if the density of shell-model levels above the Fermi energy  $\epsilon_F$  is low, the shell correction increases the binding; if the density of shell model levels above the Fermi energy  $\epsilon_F$  is high, the shell correction decreases the binding.

The bunching of the actual level spectrum is a function of the nuclear shape. Thus, for given particle number, situations as depicted in Figs 5 and 6 are expected to occur as a function of nuclear shape. The shell-correction produces fluctuations of the potential energy  $\mathcal{V}(q)$  around the smooth LD-energy. The magnitude of the shell-correction term may amount to several MeV, i. e. it provides a substantial "renormalization" of the LD energy. In favourable cases the shell correction may produce a "second valley" in the potential landscape (see schematic picture in Fig. 7). As is well-known such a second valley leads to the phenomenon of shape isomers [4]. A high level density above the Fermi energy  $\epsilon_F$  means that a small perturbation may lead the system into a state of different deformation, while, on the contrary, a low density of levels above may correspond to a stable equilibrium.

## (ii) The use of phenomenological shell-model potentials

From the form of the shell correction (Eq. 51) it follows that the part of the single-particle spectrum below  $(\epsilon_F - \gamma)$  ( $\gamma$  = width of the Gaussian in Eq. (59)) does not contribute to the shell correction, at all. Only the levels in an interval of  $\pm \gamma$  around the Fermi-energy  $\epsilon_F$  determine the magnitude of the shell-correction. Consequently, it is only in this energy interval that the phenomenological shell-model potential is required to provide a good representation of the true shell-model level density. The actual Hartree-Fock potential is non-local and state-dependent. In a sufficiently narrow energy range, this potential may be replaced by a local, state-independent approximation [21]. Thus there is hope that the simple local phenomenological potentials (Eqs (72), (73), and (75)) which are used in the calculations of  $\mathcal{V}(q)$ , do, in fact, represent sufficiently good approximations. It should be noted that this is only due to the special form of the Strutinski term  $E_{SC}$ . Since it is only the level density near the Fermi energy which determines  $E_{SC}$ , the special form of the phenomenological potential is not very important as long as the shape of this potential is related to the given shape of a liquid drop as was indicated above. Only in the last state of fission (scission) where a potential barrier develops between the nascent fragments, the two-centre model seems to be superior to the generalized Nilsson potential and possibly even to the deformed Saxon-Woods. It should, however, be noted that near the scission point we should consider the "adiabatic approach" with great suspicion [10].

### (iii) Qualitative effect of variable inertia

It should be kept in mind that it is not  $\mathcal{V}(q)$  but the total Hamiltonian  $\mathcal{H}(q)$  (see Eq. (20)) which determines the dynamics of fission. In particular we may expect important effects from the fact that the inertia is a function of the collective variables [22]. The magnitude of the different components of the inertial tensor (15, 13) are seen to depend most sensitively on the low-lying excited states of the system. If the density of excited states above the groundstate is high, many energy denominators in Eq. (13) are small and, consequently, the inertia is large. Correspondingly, the inertia tends to be small, if there are few excited states above the groundstate. Since, in any nuclear model, the density of actual excitations is correlated to the density of shell model levels, the elements of the inertial tensor tend to be large if the shell correction  $E_{SC}$  is larger than zero ( $E_{SC} > 0$ ) and small if it is smaller than zero ( $E_{SC} < 0$ ) [9].

According to calculations [8, 9], the influence of the shell structure on the inertial tensor is substantial. If one calculates life-times for spontaneous fission within the WKB-approach [20] as a function of the mass number of the fissile nucleus, one realizes a very strong influence of the variable inertia on the results. It can be shown [23] that variable inertia acts like a scale in the potential landscape: Large inertia stretches the scale, small inertia contracts it.

## 5. CONCLUSIONS

We would like to conclude this short review of recent developments in the theory of nuclear fission by pointing at what we believe to be the most urgent unresolved problems:

### (i) Validity of the adiabatic approximation

It is not clear at all whether we may trust in the adiabatic approximation. The successful explanation of shape isomers within the Strutinski theory and the striking success of the transition state hypothesis of A. Bohr [24] lend support to the assumption that the adiabatic approach may provide a useful zero-order approximation. At higher energies, the coupling to intrinsic excitations (dissipation) is sure to be of paramount importance. Furthermore, deviations from adiabaticity should be expected near the scission point.

### (ii) Validity of the cranking formula for the inertial tensor

The inertial tensor was so far calculated within the adiabatic theory using a constant pairing interaction acting in the deformed average field [8, 9, 20]. This approach could be considerably improved, even within a strictly adiabatic theory.

### (iii) Accuracy of the Strutinski theory

Hartree-Fock or Hartree-Bogoliubov calculations based on realistic forces could provide a test on the validity of the Strutinski method, especially

the neglect of terms of second order in the density fluctuation  $\delta\rho$ . An analysis of the actual level distribution in a deformed shell-model potential may provide a deeper understanding of the smoothing procedure proposed by Strutinski. In this respect, I would like to draw attention to the most interesting recent work of Balian and Bloch [25]. Furthermore, we should like to note a recent investigation of the Strutinski method by Tyapin [26] which is similar to the one presented here. The derivation of the Strutinski method from Hartree-Fock theory was already given by Strutinski [20], but without consideration of the role of constraints.

#### (iv) Dynamics of fission

Within an adiabatic approach, the dynamics of fission was so far only treated in the WKB-approach [8, 20]. More complete calculations were performed within a pure dynamical LDM [27, 28]. Hasse [29] combined the dynamical LD-model with phenomenological shell corrections calculated according to the Myers-Swiatecki theory [29]. These last-mentioned investigations [27-29] are subject to the criticism that the inertial tensor was essentially obtained from the irrotational flow assumption, which is not realistic.

#### (v) Problem of introducing collective variables

Finally, the theory of nuclear fission is tied to the fundamental problem of introducing collective variables in the description of a many-body system. The cranking theory is only one of different ways to do this. A more basic approach is possibly provided by the method of generator co-ordinates. In this respect, we should like to point out a recent work by Nörenberg [30].

### REFERENCES

- [1] BOHR, N., WHEELER, J.A., Phys. Rev. 56 (1939) 426.
- [2] GÖPPERT-MAYER, M., JENSEN, J.H.D., Elementary Theory of Nuclear Shell Structure, J. Wiley, New York (1955).
- [3] BOHR, A., Mat. Fys. Medd. 26 14 (1952).
- [4] STRUTINSKI, V.M., Nucl. Phys. A95 (1967) 420.
- [5] KUMAR, K., BARANGER, M., Nucl. Phys. A122 (1968) 273.
- [6] GNEUSS, G., MOSEL, U., GREINER, W., Physics Letts 30B (1969) 397.
- [7] GNEUSS, G., GREINER, W., MOSEL, U., Physics Letts 31B (1970) 269.
- [8] NILSSON, S.G., TSANG, C.F., SOBICZEWSKI, A., SZYMANSKI, Z., WYCECH, S., GUSTAFSON, C., LAMM, I.L., MØLLER, P., NILSSON, B., Nucl. Phys. A131 (1969) 1; TSANG, C.F., NILSSON, S.G., Nucl. Phys. A140 (1970) 289.
- [9] STRUTINSKI, V.M., PAULI, H.C., in Physics and Chemistry of Fission (Proc. Symp. Vienna, 1969) IAEA (1959) 155.
- [10] GRIFFIN, J., *ibid.*, 3.
- [11] PAULI, W., Handbuch der Physik, Bd 24/1, Springer, Berlin, (1933) 120.
- [12] WILETS, L., Theories of Nuclear Fission, Clarendon Press (1964).
- [13] JENSEN, H., KOPPE, H., Anns Phys. 63 (1971), to appear soon; JENSEN, H., KOPPE, H., Sitzungsber Akad. Wiss. Heidelberg.
- [14] SOMMERFELD, A., Atombau und Spektrallinien, 2, Appendix.
- [15] HOHENBERG, P., KOHN, W., Phys. Rev. 136B (1964) 864.
- [16] TSANG, C.F., UCRL-18899 (May 1969).
- [17] ANDERSEN, B.L., DICKMANN, F., DIETRICH, K., Nucl. Phys. A159 (1971) 337.

- [18] MOSEL, U., SCHMITT, H.W., to be published in Nuclear Physics
- [19] DEMEUR, M., REIDEMEISTER, G., Ann. Phys. 1 (1966) 181;  
SCHARNWEBER, D., MOSEL, U., GREINER, W., Phys. Rev. Letts 24 (1970) 601.
- [20] BRACK, M., DAMGAARD, J., PAULI, H.C., STENHOLM-JENSEN, A., STRUTINSKI, V.M.,  
WONG, C.Y., "Funny Hills", to be submitted to Rev. mod. Phys.
- [21] STINGL, M., Nucl. Phys. A138 (1969) 353.
- [22] GRIFFIN, J., University of Maryland, Technical Reports No.805 (March 1968) and No.810 (April 1968).
- [23] HOFMANN, H., DIETRICH, K., to be published in Nucl. Phys. 1971.
- [24] BOHR, A., Int. Conf. peaceful Uses atom. Energy (Proc. 1st Conf. Geneva, 1955), 2 (1955) 151.
- [25] BALIAN, R., BLOCH, C., "Distribution of eigenfrequencies for the wave equation in a finite domain",  
DPh-T 17016; Service de Physique Théorique BP No.2 - 91 Gif-sur-Yvette.
- [26] TYAPIN, A.S., Sov. Phys. J. nucl. Phys. 11 (1970) 53.
- [27] NIX, J.R., SWIATECKI, W.J., Nucl. Phys. 71 (1965) 1
- [28] NIX, J.R., Nucl. Phys. A130 (1969) 241.
- [29] HASSE, R.W., Nucl. Phys. A128 (1969) 609.
- [30] NÖRENBERG, W., "Zur mikroskopischen Beschreibung der Kernspaltung", Habilitationsschrift,  
University of Heidelberg (1970).
- [31] DAMGAARD, J., PAULI, H.C., PASHKEVICH, V.V., STRUTINSKI, V.M., Nucl. Phys. A135  
(1969) 432.



# QUADRUPOLE COUPLING CONSTANT FOR LARGE DEFORMATIONS

M. ZIELIŃSKA-PFABÉ

Institute for Nuclear Research, Warsaw, Poland

Z. BOCHNACKI, S. GABRAKOV

Joint Institute for Nuclear Research, Dubna,

Union of Soviet Socialist Republics

## Abstract

QUADRUPOLE COUPLING CONSTANT FOR LARGE DEFORMATIONS.

1. Introduction; 2. Determination of the quadrupole force strength from the position of the  $0^+$  and  $2^+$  vibrational states of deformed nuclei; 3. Deformation dependence of the multipole-multipole interaction; 4. Vibrational states for large deformation.

## 1. INTRODUCTION

In 1955 A. Bohr [1] proposed the channel theory of fission. According to this theory, the fissioning nucleus in the saddle point of its deformation may exhibit the excited states which are similar to those at the equilibrium deformation. The different excited states correspond to the different fission channels. Some experiments have been made in order to find the position of this transition-state spectrum. Britt's group [2] measured the probability of fission as a function of the excitation energy. The experimental results indicated the presence of a low-lying vibrational spectrum. They also measured the angular correlations for  $(\alpha, pf)$  and  $(\alpha, tf)$  reactions for  $^{233}\text{U}$ ,  $^{235}\text{U}$  and  $^{239}\text{Pu}$  and found the position of some collective vibrational states at the saddle point (the octupole and  $\gamma$ -vibrational states). It is therefore interesting to look at the theoretical estimate of the energy of the  $\gamma$ -vibrational  $2^+$  state in the saddle point. If one carries out, for example, a microscopic calculation (described in detail in the next section) one finds that at the saddle point the nucleus seems to be extremely stiff with respect to the non-axial quadrupole deformation, i. e. the calculated energy is about 2 MeV while the experimental one is about 0.6 MeV. In this kind of calculation there is only one free parameter – the strength of the quadrupole force which is responsible for the existence of this vibrational level and the value of this parameter is usually fitted so as to account for the energies of the equilibrium deformation.

The simplest way making the nucleus softer with respect to the non-axial  $\gamma$ -vibrations at the saddle point is to increase the value of the strength of the quadrupole coupling constant. This means that one needs this value to be deformation-dependent. We are thus faced with one of the central problems in every microscopic calculation of the collective nuclear phenomena: the choice of the effective two-body interaction.

This problem becomes especially important when an effective interaction is used in the study of collective processes taking place far from the equilibrium, e. g. at deformations much larger than the equilibrium

deformation. Fine effects, such as the density dependence of the effective interaction, which are often accounted for at equilibrium by the choice of the phenomenological parameters of the two-body force, lead to non-negligible changes of the interaction strength. In many cases these changes play an important role in understanding the nuclear properties far from equilibrium.

Thus it is important to test different approaches to the problem of the dependence of the effective interaction strength on parameters defining the density distribution in the nucleus.

The approach to the effective interaction problem, which is tested here, is that of Bohr and Mottelson [3] generalized to include the deformation dependence of the interaction strength [4, 5].

The strength of the two-body force can be obtained from the experimental data as a function of the parameters which define the density distribution by fitting calculated (e. g. by the RPA method) energies of the collective excitations to the experimental values for a number of nuclei and a number of excitations. The calculation must include all transitions which give significant contribution (e. g.  $\Delta N = 0, 2$  transitions for a sufficiently large number of shells in the case of quadrupole excitations) in order to make "renormalization" of the force strength negligibly small. This is essential not only for testing the strength of the force but also for its dependence on deformation which can be strongly affected by large renormalization.

First, we present this kind of calculation performed for quadrupole excitations in deformed nuclei with the use of the Nilsson model potential. Afterwards we calculate the effective two-body force direct from a given single-particle potential; we discuss the deformation-dependence of the multipole-multipole interaction and compare the results obtained by both methods.

In the last section, we use the calculated values of the strength of the non-axial quadrupole force in estimating the position of the  $\gamma$ -vibrational state for large deformations (for the saddle point and in the second potential-energy well).

## 2. DETERMINATION OF THE QUADRUPOLE FORCE STRENGTH FROM THE POSITION OF $0^+$ AND $2^+$ VIBRATIONAL STATES OF DEFORMED NUCLEI

To connect the strength of the quadrupole force with the energies of  $0^+$  and  $2^+$  vibrational states, the method described in detail by Bès [6] and used in Ref. [7] has been applied.

Nucleons are assumed to move in a single-particle field approximated by the "new" Nilsson potential [8] and interact through the pairing and quadrupole two-body forces. Thus the Hamiltonian has the form

$$H = H_0 + H_{\text{pair}} - \frac{1}{2} \kappa \hat{Q}^+ \hat{Q} \quad (1)$$

where  $H_0$  is the Nilsson model Hamiltonian,  $H_{\text{pair}}$  represents pairing interaction in its standard form [9].  $\kappa$  is the strength of the quadrupole

force and  $\hat{Q}$  is defined as  $\hat{Q} = \sum_{i=1}^A \hat{q}_i$  where

$$\hat{q} = \begin{cases} \sqrt{\frac{16\pi}{5}} r^2 Y_{20} & \text{in the case of } \beta\text{-vibration} \\ \frac{1}{\sqrt{2}} \sqrt{\frac{16\pi}{5}} r^2 (Y_{22} + Y_{2-2}) & \text{in the case of } \gamma\text{-vibration} \end{cases} \quad (2)$$

The energies of the vibrational state are obtained in the adiabatic approximation by calculating the stiffness and mass parameters C and B:

$$B = \hbar^2 \frac{\Sigma_3}{2\Sigma_1^2} \quad (3)$$

$$C = \frac{1}{2\Sigma_1} - \kappa$$

where

$$\Sigma_1 = \sum_{\nu\nu'} \frac{|g_{\nu\nu'}|^2 (u_\nu v_{\nu'} + u_{\nu'} v_\nu)^2}{E_\nu + E_{\nu'}} \quad (4)$$

$$\Sigma_3 = \sum_{\nu\nu'} \frac{|g_{\nu\nu'}|^2 (u_\nu v_{\nu'} + u_{\nu'} v_\nu)^2}{(E_\nu + E_{\nu'})^3} \quad (5)$$

In the present calculation the sums in expression (4) and (5) were extended over all the single-particle states with positive magnetic quantum number values of  $N = 0, 1, \dots, 7$  and  $N = 0, 1, \dots, 8$  harmonic oscillator shells for protons and neutrons, respectively, in the rare earth region and of  $N = 0, 1, \dots, 8$  and  $N = 0, 1, \dots, 9$  oscillator shells, respectively, in the actinide region.

In the case of  $\gamma$ -vibrations the matrix elements of  $\hat{q}$  between states with the opposite signs of the magnetic quantum numbers were also included. The  $E_\nu$  are the quasi-particle energies and  $u_\nu, v_\nu$  are pairing amplitudes of the state  $\nu$ . The parameters of the Nilsson potential are those of Ref.[8]. The pairing force was diagonalized by the BCS method within 24 double-degenerated single-particle states with pairing force strength  $G_p = 32.2/A$  MeV for protons and  $G_n = 26.5/A$  MeV or  $G_n = 26.04/A$  MeV for neutrons in the rare earth or actinide regions, respectively.

The relation

$$E = \hbar \sqrt{\frac{C}{B}} = \sqrt{\frac{1}{2\Sigma_1} - \kappa} \quad (6)$$

relates  $\kappa$ , which is the only free parameter of this calculation, to the vibrational energy values.

TABLE I. STRENGTH OF K=0-COMPONENT OF QUADRUPOLE FORCE

Nucleus	$\epsilon$	$\epsilon_4$	$E_\beta(\text{MeV})$	$\kappa_{20}^0 \text{ exp}$	$\kappa_{20}^0 \text{ th}$
$^{152}_{62}\text{Sm}$	0.25	-0.02	0.685	0.173	0.191
$^{154}_{62}\text{Sm}$	0.29	-0.02	1.100	0.166	0.188
$^{154}_{64}\text{Gd}$	0.24	-0.04	0.680	0.173	0.199
$^{156}_{64}\text{Gd}$	0.28	-0.02	1.048	0.172	0.194
$^{158}_{64}\text{Gd}$	0.30	-0.02	1.449	0.162	0.189
$^{156}_{66}\text{Dy}$	0.25	-0.02	0.674	0.171	0.202
$^{158}_{66}\text{Dy}$	0.27	-0.01	0.993	0.174	0.199
$^{162}_{68}\text{Er}$	0.27	0.00	1.081	0.179	0.202
$^{164}_{68}\text{Er}$	0.27	0.02	1.245	0.187	0.208
$^{166}_{68}\text{Er}$	0.28	0.02	1.460	0.193	0.205
$^{176}_{72}\text{Hf}$	0.25	0.07	1.250	0.238	0.227
$^{178}_{72}\text{Hf}$	0.24	0.07	1.199	0.253	0.230
$^{188}_{76}\text{Os}$	0.17	0.09	1.086	0.276	0.258
$^{188}_{78}\text{Pt}$	0.17	0.05	0.800	0.256	0.246
$^{190}_{78}\text{Pt}$	0.15	0.05	0.922	0.253	0.252
$^{192}_{78}\text{Pt}$	0.15	0.05	1.195	0.247	0.252
$^{194}_{78}\text{Pt}$	0.15	0.05	1.267	0.250	0.252
$^{196}_{78}\text{Pt}$	0.12	0.05	1.135	0.259	0.262

The first four columns give the nucleus, the quadrupole deformation parameter  $\epsilon$ , the hexadecapole deformation parameter  $\epsilon_4$  and the experimental position of the  $\beta$ -vibrational state, respectively. In column five we present the  $\kappa_{20}^0$  value calculated from the experimental value of the energy of the  $\beta$ -vibration while the last column gives the value of  $\kappa_{20}^0$  obtained from formula (22).

By taking the experimental values of  $E$  we obtain

$$\kappa = \frac{1}{2\Sigma_1} \left( 1 - \frac{\Sigma_3}{\Sigma_1} E_{\text{exp}}^2 \right) \quad (7)$$

The calculations were performed for experimental values of quadrupole deformation  $\epsilon$ . The experimental values of the hexadecapole deformation  $\epsilon_4$  were used in the rare earth region only [10]. The values of  $\epsilon_4$  in the actinide region were taken from calculations of Ref. [6].

The results of our calculations are presented in Tables I and II where the values of

$$\kappa^0 = \kappa A^{4/3} \left( \frac{\hbar}{M\omega_0} \right)^2 (\hbar\omega_0)^{-1} \quad (8)$$

TABLE II. STRENGTH OF THE K=2-COMPONENT OF QUADRUPOLE FOR CE

Nucleus	$\epsilon$	$\epsilon_4$	$E_\gamma$ (MeV)	$\kappa_{22}^0 \text{ exp}$	$\kappa_{22}^0 \text{ th}$
$^{152}_{62}\text{Sm}$	0.25	-0.02	1.090	0.465	0.405
$^{154}_{62}\text{Sm}$	0.29	-0.02	1.450	0.486	0.428
$^{160}_{66}\text{Dy}$	0.26	-0.02	0.970	0.486	0.410
$^{164}_{68}\text{Er}$	0.27	0.02	0.840	0.485	0.419
$^{170}_{68}\text{Er}$	0.27	0.04	0.950	0.488	0.421
$^{170}_{70}\text{Yb}$	0.27	0.06	1.230	0.481	0.422
$^{172}_{70}\text{Yb}$	0.27	0.06	1.470	0.475	0.422
$^{176}_{70}\text{Yb}$	0.27	0.07	1.260	0.457	0.423
$^{188}_{76}\text{Os}$	0.17	0.09	0.633	0.424	0.371
$^{232}_{90}\text{Th}$	0.193	-0.021	0.790	0.459	0.374
$^{232}_{92}\text{U}$	0.200	-0.024	0.870	0.456	0.378
$^{234}_{92}\text{U}$	0.209	-0.022	0.920	0.459	0.383
$^{238}_{94}\text{Pu}$	0.216	-0.019	1.030	0.467	0.387
$^{240}_{94}\text{Pu}$	0.230	-0.015	0.940	0.486	0.394

The first four columns give the nucleus, the quadrupole deformation parameter  $\epsilon$ , the hexadecapole deformation parameter  $\epsilon_4$  and the experimental position of the  $\gamma$ -vibrational state, respectively. In column five we give the  $\kappa_{22}^0$  value calculated from the experimental energy of the  $\gamma$ -vibrational state while the last column presents the value of  $\kappa_{22}^0$  obtained from formula (23).

are given. Column 5 of Table I gives the strength  $\kappa_{20}^0$  of the K = 0 component of the quadrupole force which is responsible for  $\beta$ -vibrations, while column 5 of Table II shows the strength  $\kappa_{22}^0$  of the K = 2 component responsible for  $\gamma$ -vibrations.

### 3. DEFORMATION DEPENDENCE OF THE MULTIPOLE-MULTIPOLE INTERACTION

According to Ref. [4], the field-producing two-body force used in the RPA-calculation of collective excitations with a self-consistent single-particle potential U is

$$F_{12} = F(r_1, r_2) = \frac{\delta \bar{U}(r_1)}{\delta \rho(r_2)} \quad (9)$$

where  $\rho$  is the density distribution of the nucleus.

The components of  $F_{12}$  corresponding to collective modes of given symmetry ( $\lambda\mu$ ) may be obtained by restricting the variation of the density distribution to the variation having this symmetry. For a self-consistent

potential  $U$  a deformation parameter determines both the density variation and the corresponding distortion of the potential. Thus relation (9) may be rewritten in the form [11]

$$F_{12}^{(\lambda\mu)} = \frac{\partial U_1}{\partial \alpha_{\lambda\mu}} \cdot \frac{\delta \alpha_{\lambda\mu}}{\delta \rho_2} \quad (10)$$

It is convenient to define the deformation parameter  $\alpha_{\lambda\mu}$  by the relation

$$U_1^{\lambda\mu} = f(\alpha_{\lambda\mu}) \hat{q}_{\lambda\mu}(1) \quad (11)$$

where

$$\hat{q}_{\lambda\mu} = g(r) Y_{\lambda\mu}(\theta, \varphi) \quad (12)$$

and  $f(\alpha_{\lambda\mu})$  is such a function of  $\alpha_{\lambda\mu}$  that the equipotential surfaces of the distorted potential are given by

$$r = r_0 \left( 1 + \sum_{\lambda\mu} \alpha_{\lambda\mu} Y_{\lambda\mu} \right) \quad (13)$$

we have then

$$F_{12} = \frac{\partial f(\alpha_{\lambda\mu})}{\partial \alpha_{\lambda\mu}} \frac{\partial \alpha_{\lambda\mu}}{\partial Q_{\lambda\mu}} \frac{\delta Q_{\lambda\mu}}{\delta \rho_2} \hat{q}_{\lambda\mu}(1) = \frac{\partial f(\alpha_{\lambda\mu})}{\partial \alpha_{\lambda\mu}} \frac{\partial \alpha_{\lambda\mu}}{\partial Q_{\lambda\mu}} \hat{q}_{\lambda\mu}(1) \hat{q}_{\lambda\mu}(2) \quad (14)$$

where

$$Q_{\lambda\mu} = \int \hat{q}_{\lambda\mu}(2) \rho_2 dV_2 \quad (15)$$

is the average value of the operator  $\hat{q}_{\lambda\mu}$ .

Thus the multipole force strength is given by

$$\kappa_{\lambda\mu} = \frac{\partial f(\alpha_{\lambda\mu})}{\partial \alpha_{\lambda\mu}} \frac{\partial \alpha_{\lambda\mu}}{\partial Q_{\lambda\mu}} \quad (16)$$

where the derivatives should be taken at the value of the deformation parameters  $\alpha$  which correspond to the nuclear state just considered.

In general, both the  $f(\alpha_{\lambda\mu})$  and  $Q_{\lambda\mu}$  are not linear in  $\alpha_{\lambda\mu}$  so the strength parameter  $\kappa_{\lambda\mu}$  changes with the deformation of the nucleus. It should be stressed that, as a rule, the parameters  $\kappa_{\lambda\mu}$  change differently with deformation not only for different  $\lambda$  components but also for different  $\mu$  components of the same  $\lambda$ . For example, in the quadrupole case,  $\kappa_{22}$  increases while  $\kappa_{20}$  decreases with the increasing quadrupole deformation [5].

To avoid calculating the derivatives of expression (16) for given values of deformation, one can define the operators

$$\hat{q}_{\lambda\mu}(\tilde{r}) = g(\tilde{r}) Y_{\lambda\mu}(\tilde{\theta}, \tilde{\varphi}) \quad (17)$$

in such a stretched co-ordinate system  $(\tilde{x}, \tilde{y}, \tilde{z})$  in which the potential and the density distribution become spherical again. In this co-ordinate system we have

$$F_{12} = \frac{\partial f(\tilde{\alpha}_{\lambda\mu})}{\partial \tilde{\alpha}_{\lambda\mu}} \frac{\partial \tilde{\alpha}_{\lambda\mu}}{\partial Q_{\lambda\mu}} \hat{q}_{\lambda\mu}(\tilde{r}_1) \hat{q}_{\lambda\mu}(\tilde{r}_2) \quad (18)$$

where the derivatives should be taken at  $\tilde{\alpha}_{\lambda\mu} = 0$ .

For  $g(\tilde{r}) = \tilde{r}^\lambda$  the value of

$$\kappa_{\lambda\mu} = \left( \frac{\partial f(\tilde{\alpha}_{\lambda\mu})}{\partial \tilde{\alpha}_{\lambda\mu}} \frac{\partial \tilde{\alpha}_{\lambda\mu}}{\partial Q_{\lambda\mu}} \right)_{\tilde{\alpha}_{\lambda\mu} = 0} \quad (19)$$

coincides with the estimate of Bohr and Mottelson [3] for the multipole force strength of spherical nuclei.

The deformation dependence of the force given by expression (14) is determined by the transformation of expression (18) from the  $(\tilde{x}, \tilde{y}, \tilde{z})$  - to the  $(x, y, z)$  - space.

In the case of an ellipsoidal nucleus with the semi-axes

$$\begin{aligned} a_1 &= R_0 e^{-\sigma/2} \\ a_2 &= R_0 e^{-\sigma/2} \\ a_3 &= R_0 e^{\sigma} \end{aligned} \quad (20)$$

described by the harmonic oscillator potential, this transformation has the form

$$\begin{aligned} \tilde{x} &= x e^{\sigma/2} \\ \tilde{y} &= y e^{\sigma/2} \\ \tilde{z} &= z e^{-\sigma} \end{aligned} \quad (21)$$

where

$$\sigma = 0.631 \beta (1 + 0.045 \beta + \dots)$$

and

$$\epsilon \approx 0.95 \beta$$

The quadrupole force dependence on  $\sigma$  in the  $(x, y, z)$ -system implied by this transformation is given in Ref. [5].

A static hexadecapole deformation introduces additional distortion of the density. In the  $(x, y, z)$ -space this introduces the dependence of the multipole force strength on the hexadecapole deformation parameter  $\epsilon_4$ . In the formula (14) this dependence is determined by the dependence of the multipole moment  $Q_{\lambda\mu}$  on  $\epsilon_4$ . In the case of a quadrupole force with

$g(r) = r^2$  the complete formulas for the strength with  $\epsilon_4$ -dependence included have the form

$$\kappa_{20}^0 = \frac{4\pi}{3} \frac{M\omega_0^2}{AR_0^2} \frac{2e^{-2\sigma} + e^\sigma}{2e^{2\sigma} + e^{-\sigma}} \left[ 1 + \epsilon_4 \frac{1.12 + 2.7\sigma}{1 + \sigma} \right] \quad (22)$$

$$\kappa_{22}^0 = \frac{4\pi}{3} \frac{M\omega_0^2}{AR_0^2} e^{2\sigma} [1 + 0.19 \epsilon_4] \quad (23)$$

where  $R_0$  is the radius of the nucleus.

The values of  $\kappa_{20}^0$  and  $\kappa_{22}^0$  obtained from Eqs (22) and (23) are listed in column 6 of Tables I and II, respectively.

The quadrupole force strength values calculated from the experimental energies of  $\beta$ - and  $\gamma$ -vibrational states are in good agreement with the values predicted on the basis of the simple oscillator model according to formulas (22) and (23). Both the absolute values of the strengths and their deformation dependence agree within the accuracy of a few per cent with the predicted numbers. In particular, the calculation shows the opposite tendencies in the deformation dependence of  $\kappa_{20}^0$  and  $\kappa_{22}^0$  in accordance with formulas (22) and (23). Both methods of calculation give nearly the same difference between these two components of the quadrupole force.

It is interesting to notice that even the slight dependence on  $\epsilon_4$  predicted by formula (22) appears in the values of the strength calculated from the experimental data. It appears quite clearly in the splitting of  $\kappa_{20}^0$  value for nuclei with the same quadrupole deformation  $\epsilon$  but different hexadecapole deformation  $\epsilon_4$ .

The results obtained above support the conclusion that the force extracted from the phenomenological potentials may be used in the calculations of the collective nuclear properties.

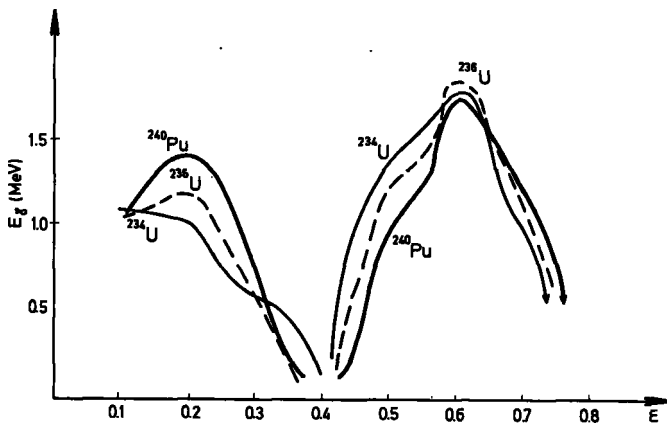


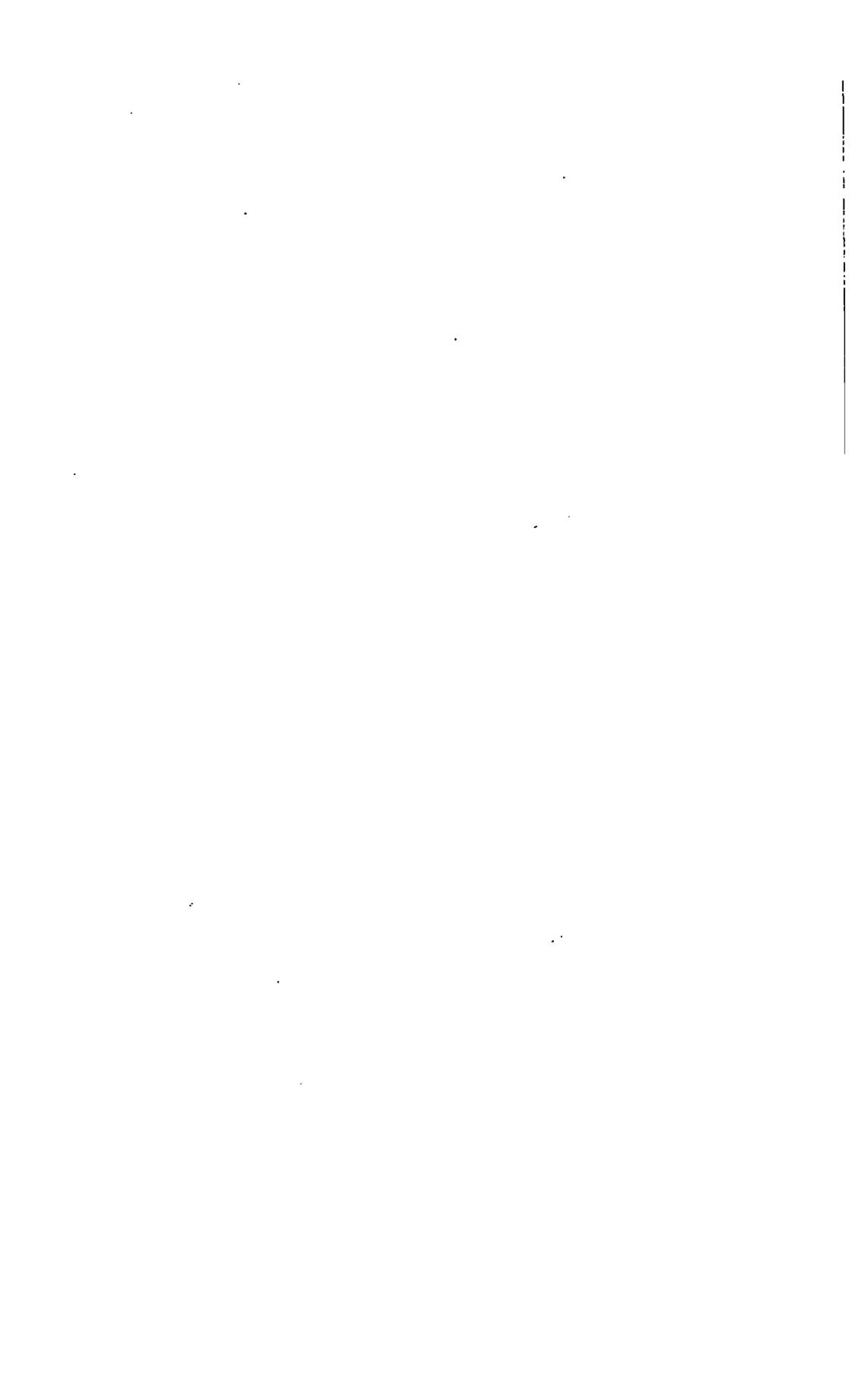
FIG. 1. The energy of the  $\gamma$ -vibrational state for  $^{234}\text{U}$ ,  $^{236}\text{U}$  and  $^{240}\text{Pu}$  is drawn as a function of the deformation parameter  $\epsilon$  for the  $\kappa_{22}^0$  value calculated from formula (23). The hexadecapole deformation parameter is given by  $\epsilon_4 = 0.06$ .

## 4. VIBRATIONAL STATES FOR LARGE DEFORMATION

The method described in section 2 was used to study the behaviour of the  $\gamma$ -vibrational state for large deformation. The quadrupole coupling constant  $\kappa_{22}$ , was taken from formula (23). In this case we took into account nine harmonic oscillator shells for protons and ten for neutrons. The pairing force was diagonalized within Z and N double degenerate levels for protons and neutrons, respectively, and the pairing force strength was assumed to be proportional to the surface of the nucleus [12]. The results of these calculations are shown in Fig. 1. We see that the energy of the  $2^+$  vibrational state has two maxima which correspond very nicely to the minima of the total energy of the nucleus calculated with the use of the Nilsson potential by the method of Strutinsky [13]. The position of the  $2^+$  vibrational state in the second minimum is of the same order of magnitude as at the equilibrium. It seems very interesting to notice that we have no real solution at the deformation corresponding to the saddle point. It seems to be in agreement with the result obtained by Pashkevich [14] who calculated the total energy of the nucleus with the inclusion of the  $\gamma$ -deformation parameter. He concluded that while in both minima the nucleus seems to be axially symmetric, the saddle point occurs for  $\gamma \neq 0$ , so if there is some experimental evidence about the  $\gamma$ -vibrational state at the saddle point [2] this kind of vibration may exist only if  $\gamma \neq 0$ .

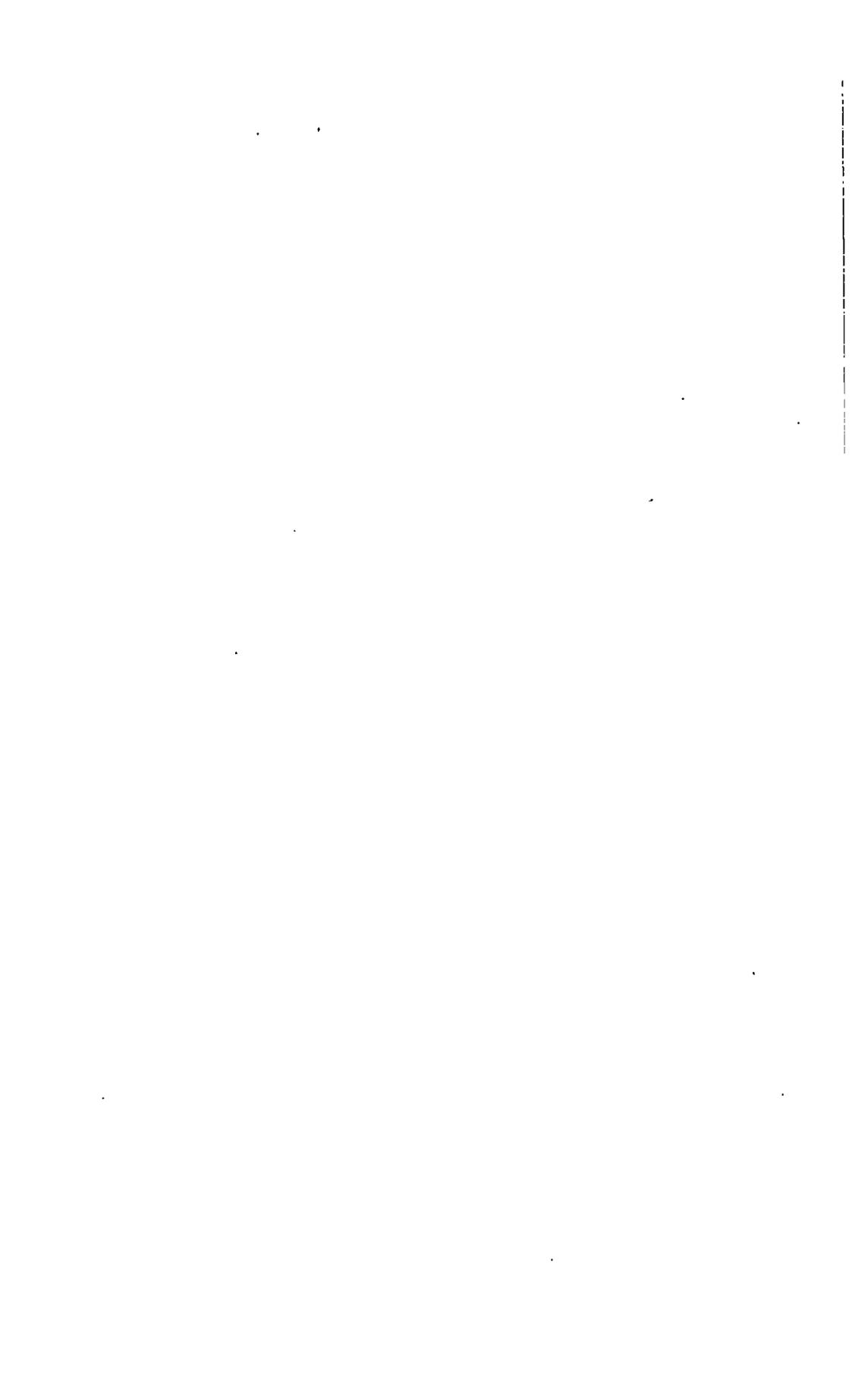
## REFERENCES

- [1] BOHR, A., Int. Conf. peaceful Uses atom. Energy (Proc. Conf. Geneva, 1955).
- [2] BRITT, H.C., et al., Phys. Rev. 175 (1968) 1525.
- [3] BOHR, A., MOTTELSON, B.R., Lectures on Nuclear Structure and Energy Spectra, Benjamin, New York, to be published.
- [4] BOCHNACKI, Z., HOLBAN, I.N., MIKHAILOV, I.N., Nucl. Phys. A97 (1967) 33.
- [5] BOCHNACKI, Z., Physics Letts 31B (1969) 175.
- [6] BÈS, D.R., Mat. Fys. Medd. Dan. Vid. Selsk. 33 2 (1961).
- [7] ZIELIŃSKA-PFABÉ, M., Physics Letts 33B (1970) 153.
- [8] NILSSON, S.G., Lectures given at International School of Physics "Enrico Fermi", Varenna (1967).
- [9] BELIAEV, S.D., Mat. Fys. Medd. Dan. Vid. Selsk. 31 11 (1959).
- [10] HENDRIE, D.L., et al., Physics Letts 26B (1968) 127.
- [11] MIKHAILOV, I.N., in Nuclear Structure (Proc. Symp. Dubna, 1968) 549.
- [12] STĘPIEŃ, W., SZYMAŃSKI, Z., Physics Letts 26B (1968) 181.
- [13] NILSSON, S.G., et al., Nucl. Phys. A131 (1969) 1.
- [14] PASHKEVICH, V.V., Nucl. Phys. A133 (1969) 400.



## PART II: NUCLEAR STRUCTURE

### 4. Short-range correlations



# JASTROW CORRELATIONS - DIAGRAMMATIC EXPANSIONS \*

G. RIPKA\*\*

International Centre for Theoretical Physics, Trieste, Italy

## Abstract

JASTROW CORRELATIONS - DIAGRAMMATIC EXPANSIONS.

1. Introduction; 2. Definition of Jastrow wave-function and of one- and two-body correlation functions; 3. Calculation of the normalization constant; 4. Calculation of the one-body correlation function; 5. The two-body correlation function; 6. The effect of Jastrow correlations on the charge density of  $^{40}\text{Ca}$ .

## 1. INTRODUCTION

In this paper we shall develop a perturbation expansion of the expectation value of one- and two-body operators calculated with a Jastrow wave-function in terms of linked diagrams and discuss some of the applications of Jastrow wave-functions which have been made in nuclei.

Since the Jastrow wave-functions were proposed [1] they have been widely used, especially in the theory of condensed matter. The use of Jastrow wave-functions in nuclei has developed greatly after the original work of Iwamoto and Yamada [2]. Although the Jastrow wave-function is simple to write down it is very difficult to calculate exactly the expectation value of one- and two-body operators. This is why various cluster expansions have been proposed. They are reviewed in a recent monograph by Feenberg [3].

Jastrow wave-functions are used for strongly interacting systems. In nuclei it is the strongly repulsive short-range interaction between the nucleons which requires a special treatment because it forbids the use of perturbation theory where a Slater determinant or a superposition of a finite number of Slater determinants is taken as the zero-order approximation. Jastrow wave-functions have been used either as variational wave-functions which are required to minimize the total energy of the nucleus or as wave-functions the parameters of which are determined to fit experimental data such as electron and proton scattering at high momentum transfer or the absorption of  $\pi$ -mesons by nuclei. The use of the Jastrow wave-function as a variational wave-function is exposed to the following problem: unless the energy is calculated exactly, an expansion which is cut off at a certain number of terms (for example, cut off at two-body clusters) does not, in general, give an energy with a lower bound. This is why subsidiary conditions are required on the correlation factor. Many calculations have been made with such subsidiary conditions [4]. We shall

---

\* These lecture notes were written by L. Döhnert (on leave of absence from Universidad Central de Venezuela, Caracas, Venezuela) and J. Tepel (on leave of absence from Atomic Energy Board, Pretoria, South Africa).

\*\* On leave of absence from CEN de Saclay, 91 Gif-sur-Yvette, France.

not discuss these calculations here, but the expansion of the correlations in terms of linked diagrams which we develop here may help in finding such re-summations of diagrams with which no subsidiary condition is required.

The fitting of elastic electron and proton scattering with Jastrow wave-functions [5-11] has raised many discussions on their meaning. First, the central point of these discussions was the question: do these experiments show short-range correlations? It is generally agreed that they do not, because a measure of the charge distribution alone cannot possibly measure the two-body correlation function. The question is then weakened: would short-range correlations affect the charge distribution and its Fourier transform, the form factor? This question can be answered theoretically by calculating the effect of short-range correlations on the form factor. The result is positive: short-range correlations do contribute to the form factor, especially at large momentum transfer of  $q > 2.5 \text{ fm}^{-1}$ . Unfortunately, the form factor has a large contribution due to the uncorrelated Slater determinant even at the large momentum transfer of  $q \sim 3 \text{ fm}^{-1}$ . It is therefore not possible by a measurement of the form factor alone to disentangle the contribution arising from the uncorrelated Slater determinant from that arising from the short-range correlations. In principle, many measurements could give information on the existence of correlations. A complete set of ground state measurements would provide a complete determination of the one-body density matrix  $\bar{\rho}_{ij}$ . It could then be checked if  $\bar{\rho}^2 = \bar{\rho}$ , that is, if the ground state can be described by a Slater determinant, and, if so, what the orbits are. Even this would only tell us that there are correlations, but it would tell us nothing about their nature. Furthermore, a simple pick-up of  $l = 3$  nucleons from  $^{40}\text{Ca}$  will tell us that the ground state of  $^{40}\text{Ca}$  is not a pure closed shell. What would be very useful is a measure of the short-range correlations; even a crude measure such as the volume of the space which two nucleons keep out of because of the short-range repulsion, commonly called the volume of the "wound" in the two-nucleon wave-function, would enable us to discriminate between various potentials which give the same scattering and deuteron properties [12]. For this, clever experiments will have to be devised. The absorption of  $\pi$ -mesons by nuclei has been studied for this purpose [13].

Finally, one can also encounter theorists who, with model wave-functions such as the Jastrow wave-function or with approximate theories such as the Brueckner theory, differ as to the definition of the effect of correlations on one-body operators such as the charge density or the form factor. There are as many definitions as there are ways of separating the charge distribution into correlated and uncorrelated parts. It is a matter of convenience to choose one Slater determinant rather than another to represent the uncorrelated part. A Jastrow wave-function (see section 2) is a product of a Slater determinant and a correlation factor. It has been shown [14], for example, that the Slater determinant of the Jastrow wave-function is not the uncorrelated state which approximates the charge distribution best. Another determinant may be constructed which approximates it better.

We shall make also a comparison between Jastrow and Brueckner correlations. This comparison will show the importance which the Pauli operator has in Brueckner theory. It is not necessary, a priori, to include

the Pauli operator in the Jastrow correlation factor. But the inclusion of it will be shown to affect strongly the evaluation of one-body operators. We shall also discuss the use of oscillating correlation factors, which correspond to an exchange of rather high momentum between the nucleons [11, 12] and which can also affect strongly the evaluation of one-body operators.

## 2. DEFINITION OF JASTROW WAVE-FUNCTION AND OF ONE- AND TWO-BODY CORRELATION FUNCTIONS

The Jastrow wave-function for a system of N nucleons is given by

$$\psi(\vec{r}_1, \dots, \vec{r}_N) = \frac{1}{\sqrt{C_N}} \prod_{1 \leq i < j \leq N} f(r_{ij}) \phi(\vec{r}_1, \dots, \vec{r}_N) \quad (2.1)$$

$C_N$  is a normalization constant such that

$$\int |\psi(\vec{r}_1, \dots, \vec{r}_N)|^2 d\vec{r}_1, \dots, d\vec{r}_N = 1 \quad (2.2)$$

where  $\vec{r}$  stands for  $\vec{r} = (\vec{r}, \sigma, \tau)$ ,  $d\vec{r}$  designates spatial integration plus sums over spins and isospins, and  $r_{ij}$  stands for  $|\vec{r}_i - \vec{r}_j|$ .

$\phi(\vec{r}_1, \dots, \vec{r}_N)$  is a Slater determinant made up of N single-particle wave functions  $\{\varphi_\alpha(\vec{r})\}$ , the ensemble of which is called the Fermi sea F:

$$\phi(\vec{r}_1, \dots, \vec{r}_N) = \det |\phi_\alpha(\vec{r}_i)| \quad \alpha \in F, \quad i \in [1, N] \quad (2.3)$$

The quantity

$$f(r_{ij}) = f(|\vec{r}_i - \vec{r}_j|) \quad (2.4)$$

is the two-body correlation factor.

The object of the factor  $f(r_{ij})$  is to give us finite matrix elements of the free two-nucleon interaction. It is expected to reproduce the "healing" of the wave function describing two nucleons in a Fermi sea, as in Brueckner theory [15], i. e. the fact that for relative distances larger than the so-called "healing distance" this wave-function becomes equal to the unperturbed two-body wave-function.

These two conditions can be stated as follows:

- 1)  $f(r_{ij}) = 0$  when  $r_{ij} < c$ , where  $c$  is the range of the repulsive hard core of the nucleon-nucleon force, and
- 2)  $f(r_{ij}) \xrightarrow[r_{ij} \text{ large}]{} 1$ .

$f(r_{ij})$  should therefore be of the form shown in Fig. 1. It may also oscillate about the value one at not too large distances.

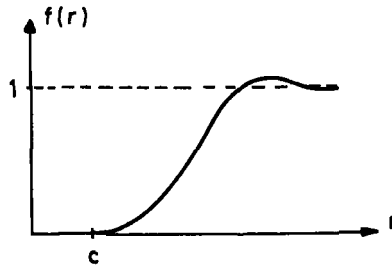


FIG. 1. General form of two-body correlation factor.

If the two-body forces are singular only at the origin, condition 1) can be replaced by

$$f(r_{ij}) \xrightarrow{r_{ij} \rightarrow 0} 0$$

The fact that we do not choose  $f$  to be state-dependent, as suggested by De Shalit and Weisskopf [16], will give us a perturbation expansion which differs from the Brueckner-Goldstone theory. We shall compare the theories later.

In most applications, we are interested in calculating the expectation values of one- and two-body operators in the state described by the Jastrow wave-function (2.1). For this it is sufficient to know the one- and two-body correlation functions, which are defined as follows:

i) One-body correlation function:

$$G_1(\vec{r}_1, \vec{r}_1) = N \int \psi^*(\vec{r}_1, \dots, \vec{r}_N) \psi(\vec{r}_1, \vec{r}_2, \dots, \vec{r}_N) d\vec{r}_2, \dots, d\vec{r}_N \quad (2.5)$$

The expectation value of one-body operators  $\Theta_1(\vec{r})$  is then given by

$$\langle \Theta_1 \rangle = \int [\Theta_1(\vec{r}_1) G(\vec{r}_1, \vec{r}_1)]_{\vec{r}_1 = \vec{r}_1} d\vec{r}_1 \quad (2.6)$$

ii) Two-body correlation function:

$$G_2(\vec{r}_1, \vec{r}_2; \vec{r}_1, \vec{r}_2) = N(N-1) \int \psi^*(\vec{r}_1, \vec{r}_2, \vec{r}_3, \dots, \vec{r}_N) \psi(\vec{r}_1, \vec{r}_2, \vec{r}_3, \dots, \vec{r}_N) d\vec{r}_3, \dots, d\vec{r}_N \quad (2.7)$$

The expectation value of a two-body operator  $\Theta_2(\vec{r}_1, \vec{r}_2)$  is then

$$\langle \Theta_2 \rangle = \frac{1}{2} \iint [\Theta_2(\vec{r}_1, \vec{r}_2) G_2(\vec{r}_1, \vec{r}_2; \vec{r}_1', \vec{r}_2')]_{\vec{r}_1' = \vec{r}_1, \vec{r}_2' = \vec{r}_2} d\vec{r}_1 d\vec{r}_2 \quad (2.8)$$

We now proceed to develop the perturbation expansion formalism for the quantities we want to calculate.

### 3. CALCULATION OF THE NORMALIZATION CONSTANT

One of the factors which appears in the Jastrow wave-function (2.1) is the normalization constant  $C_N$ . Its evaluation will serve us to illustrate the methods used to obtain the perturbation series for the correlation functions.

From condition (2.2) we have

$$C_N = \int \prod_{i < j} |f(r_{ij})|^2 |\phi(\vec{r}_1, \dots, \vec{r}_N)|^2 d\vec{r}_1, \dots, d\vec{r}_N \quad (3.1)$$

The exact integral is, in general, quite difficult to evaluate since the product of the correlation factors depends on the co-ordinates of all the particles. We shall therefore proceed in the following way. First, we obtain a cluster expansion for the product of correlation factors, in which each cluster involves a certain number  $p \leq N$  of co-ordinates and which will be represented graphically by means of Yvon-Meyer diagrams [17]. Then we integrate  $|\phi|^2$  over all co-ordinates not contained in the respective cluster. This integration will give us a determinant of lower order which we shall represent by diagrams of oriented lines, which, when drawn in the Yvon-Meyer diagram, will give us a graphical representation of a cluster expansion for  $C_N$  in terms of the modified Yvon-Meyer diagrams.

#### A. Expansion of the product of correlation factors

We introduce the auxiliary correlation factor

$$g(r_{ij}) = |f(r_{ij})|^2 - 1 \quad (3.2)$$

Figure 2 shows that  $g(r)$  is zero outside the region in which  $f(r)$  differs from zero. We can expand the product

$$\prod_{i < j} |f(r_{ij})|^2 = \prod_{i < j} (1 + g(r_{ij})) = 1 + \sum_{i < j} g(r_{ij}) + \sum_{i < j} \sum_{k < l} g(r_{ij}) g(r_{kl}) + \dots \quad (3.3)$$

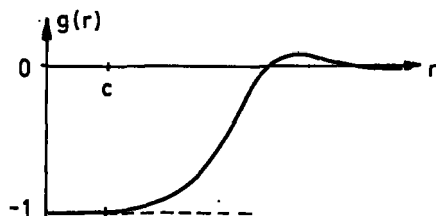


FIG. 2. General form of auxiliary correlation factor.

and re-group the terms in this series so as to group the terms which depend on a given number of co-ordinates:

$$\prod_{i < j} |f(r_{ij})|^2 = 1 + \sum_{i < j} W_2(\vec{r}_i, \vec{r}_j) + \sum_{i < j < k} W_3(\vec{r}_i, \vec{r}_j, \vec{r}_k) + \dots \quad (3.4)$$

This is called a cluster expansion.  $W_2(\vec{r}_i, \vec{r}_j)$  represents the terms in expression (3.3) that depend only on the two co-ordinates  $\vec{r}_i$  and  $\vec{r}_j$ . We see easily that

$$W_2(\vec{r}_i, \vec{r}_j) = g(r_{ij}) \quad (3.5)$$

In the same way,  $W_3(\vec{r}_i, \vec{r}_j, \vec{r}_k)$  contains all the terms in (3.3) that depend only on the three points  $\vec{r}_i \neq \vec{r}_j \neq \vec{r}_k$ . Therefore, we have

$$W_3(\vec{r}_i, \vec{r}_j, \vec{r}_k) = g(r_{ij})g(r_{ik}) + g(r_{ij})g(r_{jk}) + g(r_{ik})g(r_{jk}) + g(r_{ij})g(r_{jk})g(r_{ki}) \quad (3.6)$$

The common feature for all the clusters in Eq. (3.4) is that each point is related to at least one other point of the same cluster by at least one correlation factor. It is easy to represent all the terms that make up a given cluster of order  $p$ , that is, all the terms of  $W_p(\vec{r}_1, \dots, \vec{r}_p)$  by means of Yvon-Meyer diagrams. We proceed in the following way:

- 1) We draw  $p$ -points labelling them  $\vec{r}_1, \dots, \vec{r}_p$ .
- 2) We join the points by dashed lines representing the correlation factor  $g(r_{ij})$  in such a way that each point is joined to at least one other point.
- 3) We draw all the diagrams joining the points in a different way every time, until we have exhausted all possibilities.

All the graphs obtained in this way represent the cluster  $W_p(\vec{r}_1, \dots, \vec{r}_p)$ . Examples are shown in Fig. 3.

$$W_2(\vec{r}_1, \vec{r}_j) = \begin{array}{c} \vec{r}_j \\ \diagup \\ \text{---} \\ \diagdown \\ \vec{r}_1 \end{array} = g(r_{ij})$$

$$W_3(\vec{r}_1, \vec{r}_2, \vec{r}_3) = \begin{array}{c} \vec{r}_3 \\ \diagup \quad \diagdown \\ \text{---} \quad \text{---} \\ \vec{r}_1 \quad \vec{r}_2 \end{array} \quad \begin{array}{c} \vec{r}_3 \\ \diagup \quad \text{---} \\ \text{---} \quad \text{---} \\ \vec{r}_1 \quad \vec{r}_2 \end{array} \quad \begin{array}{c} \vec{r}_3 \\ \text{---} \quad \diagdown \\ \text{---} \quad \text{---} \\ \vec{r}_1 \quad \vec{r}_2 \end{array} \quad \begin{array}{c} \vec{r}_3 \\ \diagup \quad \diagdown \\ \text{---} \quad \text{---} \\ \vec{r}_1 \quad \vec{r}_2 \end{array}$$

$$= g(r_{12})g(r_{23}) + g(r_{13})g(r_{12}) + g(r_{13})g(r_{23}) + g(r_{12})g(r_{23})g(r_{13})$$

FIG. 3. Examples for clusters. The dashed lines are called correlation lines.

### B. Expansion of the squared Slater determinant

The unperturbed density matrix is given by

$$\rho(\vec{r}_1, \vec{r}_j) = \sum_{\alpha \in F} \varphi_{\alpha}^*(\vec{r}_1) \varphi_{\alpha}(\vec{r}_j) \quad (3.7)$$

The Slater determinant squared may then be written as

$$|\phi(\vec{r}_1, \dots, \vec{r}_N)|^2 = \det |\rho(\vec{r}_i, \vec{r}_j)| \quad (i, j) \in [1, N] \quad (3.8)$$

that is, it is equivalent to an  $N \times N$  determinant whose elements are  $\rho(\vec{r}_i, \vec{r}_j)$ . If we also want to specify a given number of co-ordinates  $p \leq N$ , we define the determinant of dimensions  $(p \times p)$

$$\Delta_p(\vec{r}_1, \dots, \vec{r}_p) = \det |\rho(\vec{r}_i, \vec{r}_j)| \quad \text{with } (i, j) \in [1, p] \quad (3.9)$$

With these definitions we easily obtain the following identities:

$$\int |\phi(\vec{r}_1, \dots, \vec{r}_N)|^2 d\vec{r}_1, \dots, d\vec{r}_N = N!$$

$$\int |\phi(\vec{r}_1, \dots, \vec{r}_N)|^2 d\vec{r}_2, \dots, d\vec{r}_N = (N-1)! \Delta_1(\vec{r}_1)$$

$$\int |\phi(\vec{r}_1, \dots, \vec{r}_N)|^2 d\vec{r}_3, \dots, d\vec{r}_N = (N-2)! \Delta_2(\vec{r}_1, \vec{r}_2)$$

and, in general,

$$\int |\phi(\vec{r}_1, \dots, \vec{r}_N)|^2 d\vec{r}_{p+1}, \dots, d\vec{r}_N = (N-p)! \Delta_p(\vec{r}_1, \dots, \vec{r}_p) \quad (3.10)$$

It is possible to construct a simple graphical representation for the terms that make up the expansion of the determinant  $\Delta_p$  by representing  $\rho(\vec{r}_i, \vec{r}_j)$  by an oriented line that leaves the point  $\vec{r}_i$  and enters the point  $\vec{r}_j$

$$\rho(\vec{r}_i, \vec{r}_j) = \begin{matrix} \times & \longrightarrow & \times \\ r_i & & r_j \end{matrix} \quad (3.11)$$

The expansion of  $\Delta_p(\vec{r}_1, \dots, \vec{r}_p)$  is then obtained in the following way:

- 1) Draw  $p$  labelled points  $(\vec{r}_1, \dots, \vec{r}_p)$ . Then join them by means of oriented lines such that at each point one (and only one) line enters it and one (and only one) line leaves it. Each line gives a factor  $\rho(\vec{r}_i, \vec{r}_j)$ .
- 2) The sign which corresponds to the term in the expansion characterized by this graph is given by

$$(-)^{p+\ell}$$

where  $p$  is the order of graph or number of points, and  $\ell$  is the number of closed loops formed by the oriented lines.

- 3) Draw all diagrams until all different ways of joining the  $p$  points are exhausted. The sum of all possible diagrams multiplied by their respective signs gives then  $\Delta_p(\vec{r}_1, \dots, \vec{r}_p)$ .

Examples are shown in Fig. 4. We can now represent each term of a cluster expansion for the normalization constant  $C_N$  in a straightforward way.

$$\begin{aligned} \Delta_1(\vec{r}_1) &= \textcircled{\vec{r}_1} = g(\vec{r}_1, \vec{r}_1) (-)^{1+1} \\ \Delta_2(\vec{r}_1, \vec{r}_2) &= \left( \textcircled{\vec{r}_1} \textcircled{\vec{r}_2} \right) + \begin{matrix} \vec{r}_1 & \longleftarrow & \vec{r}_2 \\ \vec{r}_1 & \longrightarrow & \vec{r}_2 \end{matrix} \\ &= g(\vec{r}_1, \vec{r}_1) g(\vec{r}_2, \vec{r}_2) - g(\vec{r}_1, \vec{r}_2) g(\vec{r}_2, \vec{r}_1) = \begin{vmatrix} g(\vec{r}_1, \vec{r}_1) & g(\vec{r}_1, \vec{r}_2) \\ g(\vec{r}_2, \vec{r}_1) & g(\vec{r}_2, \vec{r}_2) \end{vmatrix} \\ \Delta_3(\vec{r}_1, \vec{r}_2, \vec{r}_3) &= \left( \textcircled{\vec{r}_1} \textcircled{\vec{r}_2} \textcircled{\vec{r}_3} \right) + \left( \textcircled{\vec{r}_3} \begin{matrix} \vec{r}_1 & \longleftarrow & \vec{r}_2 \\ \vec{r}_1 & \longrightarrow & \vec{r}_2 \end{matrix} \right) + \left( \begin{matrix} \vec{r}_3 & \longleftarrow & \vec{r}_1 \\ \vec{r}_1 & \longrightarrow & \vec{r}_2 \end{matrix} \right) \\ &+ \left( \begin{matrix} \vec{r}_3 & \longleftarrow & \vec{r}_2 \\ \vec{r}_1 & \longrightarrow & \vec{r}_3 \end{matrix} \right) + \left( \begin{matrix} \vec{r}_3 & \longleftarrow & \vec{r}_1 \\ \vec{r}_1 & \longrightarrow & \vec{r}_3 \end{matrix} \right) + \left( \begin{matrix} \vec{r}_3 & \longleftarrow & \vec{r}_2 \\ \vec{r}_1 & \longrightarrow & \vec{r}_3 \end{matrix} \right) = \begin{vmatrix} g(\vec{r}_1, \vec{r}_1) & \dots & g(\vec{r}_1, \vec{r}_3) \\ \dots & & \dots \\ g(\vec{r}_3, \vec{r}_1) & & g(\vec{r}_3, \vec{r}_3) \end{vmatrix} \end{aligned}$$

FIG. 4. Examples for expansion of  $\Delta_p(\vec{r}_1, \dots, \vec{r}_p)$ .

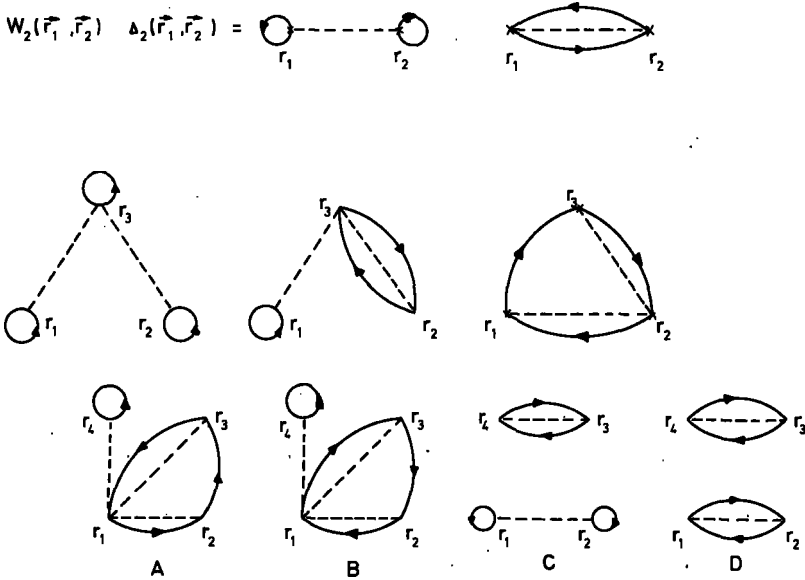


FIG. 5. Third- and fourth-order diagrams. A, B are "linked", CD "unlinked" diagrams.

From expressions (3.1) and (3.4) we have

$$C_N = \int \left[ 1 + \sum_{i < j} W_2(\vec{r}_i, \vec{r}_j) + \sum_{i < j < k} W_3(\vec{r}_i, \vec{r}_j, \vec{r}_k) + \dots \right] |\phi(\vec{r}_1, \dots, \vec{r}_N)|^2 d\vec{r}_1, \dots, d\vec{r}_N \quad (3.12)$$

We can reduce this expression to:

$$C_N = \int \left[ 1 + \binom{N}{2} W_2(\vec{r}_1, \vec{r}_2) + \binom{N}{3} W_3(\vec{r}_1, \vec{r}_2, \vec{r}_3) + \dots \right. \\ \left. + \binom{N}{p} W_p(\vec{r}_1, \dots, \vec{r}_p) + \dots \right] |\phi(\vec{r}_1, \dots, \vec{r}_N)|^2 d\vec{r}_1, \dots, d\vec{r}_N \quad (3.13)$$

Integrating over all co-ordinates not contained in  $W_p$ , we can use expression (3.10) and obtain by dividing by  $N!$

$$\frac{C_N}{N!} = 1 + \sum_{p=2}^N \left\{ \frac{1}{p!} \int W_p(\vec{r}_1, \dots, \vec{r}_p) \Delta_p(\vec{r}_1, \dots, \vec{r}_p) d\vec{r}_1, \dots, d\vec{r}_p \right\} \quad (3.14)$$

Each term of this expansion can be represented by a modified Yvon-Meyer diagram, i. e. an Ivon-Meyer diagram contributing to  $W_p$  in which one draws the diagram contributing to  $\Delta_p$  (see Fig. 5). The prescription for obtaining the diagrammatic representation of  $\int W_p \Delta_p d\vec{r}_1, \dots, d\vec{r}_p$  is then:

- 1) Take  $p$  distinct and labelled points  $\vec{r}_1, \dots, \vec{r}_p$ .
- 2) Join them by means of correlation lines according to the rules given in section 3. A.
- 3) Join them by means of oriented lines according to the rules given in section 3. B.
- 4) Sum all the possible diagrams.

To calculate the contribution of each diagram of order  $p$ , we have the following rules:

- 1) For each interaction line between  $(\vec{r}_i, \vec{r}_j)$  we have a factor  $g(r_{ij})$ .
- 2) For each oriented line going from  $\vec{r}_i$  to  $\vec{r}_j$  we have a factor  $\rho(\vec{r}_i, \vec{r}_j)$ .
- 3) The overall sign of the graph is  $(-)^{p+\ell}$  where  $\ell$  is the number of closed loops.
- 4) Integrate over all co-ordinates  $\vec{r}_1, \dots, \vec{r}_p$  (including sums over spin and isospin variables).

The integral  $\int W_p \Delta_p d\vec{r}_1, \dots, d\vec{r}_p$  is thus equal to the summed contribution of all such diagrams  $\Gamma_p$  of order  $p$ :

$$\int W_p \Delta_p d\vec{r}_1, \dots, d\vec{r}_p = \sum_{\Gamma_p} \Gamma_p \quad (3.15)$$

### C. Exponential formula for the normalization constant $C_N$

As we see from the fourth-order diagrams in Fig. 5, a diagram in general contains both linked and unlinked parts. A diagram  $\Gamma_p$  of order  $p$  will therefore consist of

- A linked labelled part  $\Gamma_A$  repeated  $\nu_A$  times  
 B linked labelled part  $\Gamma_B$  repeated  $\nu_B$  times, etc.,

so that the contribution of the diagram is equal to

$$\Gamma_p = (\Gamma_A)^{\nu_A} (\Gamma_B)^{\nu_B} (\Gamma_C)^{\nu_C} \dots \quad \Gamma_A \neq \Gamma_B \neq \Gamma_C \neq \dots \quad (3.16)$$

There are

$$N(\Gamma_A, \Gamma_B, \Gamma_C, \dots) = \frac{p!}{(p_A!)^{\nu_A} (p_B!)^{\nu_B} \dots \nu_A! \nu_B! \dots} \quad (3.17)$$

different ways of distributing the linked diagrams  $\Gamma_A, \Gamma_B, \dots$  among the  $p$  points of the diagram. Therefore, we have

$$\sum_{\Gamma_p} \frac{1}{p!} \Gamma_p = \sum_{\nu_A=0}^{N_A} \sum_{\nu_B=0}^{N_B} \dots \frac{1}{p!} N(\Gamma_A, \Gamma_B, \Gamma_C, \dots) (\Gamma_A)^{\nu_A} (\Gamma_B)^{\nu_B} \dots \quad (3.18)$$

Substituting into expression (3.14) we obtain

$$\begin{aligned} \frac{C_N}{N!} &= 1 + \sum_{p=2}^N \frac{1}{p!} \int W_p \Delta_p d\vec{r}_1, \dots, d\vec{r}_p \\ &= \sum_{\nu_A=0}^{N_A} \sum_{\nu_B=0}^{N_B} \dots \frac{1}{p!} N(\Gamma_A, \Gamma_B, \dots) (\Gamma_A)^{\nu_A} (\Gamma_B)^{\nu_B} \dots \\ &= \sum_{\nu_A=0}^{N_A} \sum_{\nu_B=0}^{N_B} \frac{1}{\nu_A!} (\Gamma_A)^{\nu_A} \frac{1}{\nu_B!} (\Gamma_B)^{\nu_B} \dots \\ &= e^{\Gamma_A} e^{\Gamma_B} \dots \end{aligned} \quad (3.19)$$

It is possible to extend the sum over  $p$  in expression (3.14) or (3.19) to infinity, because  $\Delta_p = 0$  when  $p > N$ , as one cannot put more than  $N$  fermions into  $N$  different single-particle orbits. This means that the sum over  $\nu_A, \nu_B, \dots$ , etc., can also be extended to infinity, because the sum of all graphs of order  $p > N$  gives zero contributions.

We then obtain

$$\frac{C_N}{N!} = \exp \left\{ \sum_{p=2}^{\infty} \frac{1}{p!} \int [W_p \Delta_p]_L d\vec{r}_1, \dots, d\vec{r}_p \right\} \quad (3.20)$$

where  $[W_p \Delta_p]_L$  means: "include only the linked diagrams of order  $p$ ".

We are able to reduce further the number of diagrams when we realize that topologically equivalent graphs give the same contribution. For example, diagrams which may be distinguished only through the exchange of the position of points or through the direction of the arrows making up closed loops are topologically equivalent (example: in Fig. 5 diagrams A and B). For  $t$  topologically equivalent diagrams, we define the symmetry factor  $s$  in the following way:

$$s = \frac{p!}{t} \quad (3.21)$$

It can be seen that  $s$  is the number of substitutions, including the identity, which leave the given diagram invariant.

#### Example:

Let us take as an example the diagrams of order three. All diagrams are linked. We shall now draw all the topologically different graphs and

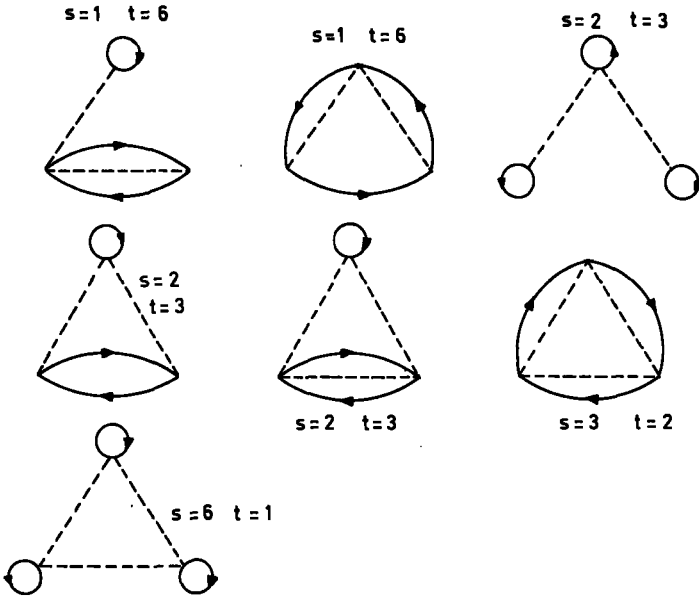


FIG. 6. Topologically different graphs of order three.

indicate the corresponding symmetry factor  $s$  and the number of topologically equivalent diagrams (Fig. 6). The sum over all  $t$  gives the total number of diagrams of order three:

$$6 + 6 + 3 + 3 + 3 + 2 + 1 = 24$$

We can rewrite the diagrammatic expansion for the normalization constant thus:

$$\frac{C_N}{N!} = \exp \left\{ \sum_{p=2}^{\infty} \int \frac{1}{s} [W_p \Delta_p]_{L, TD} d\vec{r}_1, \dots, d\vec{r}_p \right\} \quad (3.22)$$

where

$$[W_p \Delta_p]_{L, TD}$$

stands for: "include only linked and topologically distinct diagrams".

Example: As an example, let us look at diagram A of Fig. 5. It is of fourth order:  $p = 4$ . There is no substitution but the identity which leaves A invariant:  $s = 1$ . In fact, the number of topologically equivalent diagrams in this case is:  $t =$  (number of ways of joining one point with the other

three)  $\otimes$  (number of ways of placing the bubble)  $\otimes$  (number of changes of direction of the arrows in the large loop) =  $(4) \otimes (3) \otimes (2) = 24$ ;

$$s = \frac{p!}{t} = \frac{24}{24} = 1$$

The total contribution is therefore given by

$$\iiint d\vec{r}_1 d\vec{r}_2 d\vec{r}_3 d\vec{r}_4 g(\vec{r}_{12})g(\vec{r}_{13}) g(\vec{r}_{14}) \rho(\vec{r}_1, \vec{r}_2) \rho(\vec{r}_2, \vec{r}_4) \rho(\vec{r}_4, \vec{r}_1) \rho(\vec{r}_3, \vec{r}_3)$$

#### 4. CALCULATION OF THE ONE-BODY CORRELATION FUNCTION

Using the Jastrow wave-function (2.1) and (2.5) we find for the one-body correlation function

$$G_1(\vec{r}_1, \vec{r}'_1) = \frac{N}{C^N} \int \prod_{2 \leq i \leq N} f^*(|\vec{r}_1 - \vec{r}_i|) f(|\vec{r}'_1 - \vec{r}_i|) \prod_{2 \leq i < j \leq N} |f(r_{ij})|^2 \\ \times \phi^*(\vec{r}_1, \dots, \vec{r}_N) \phi(\vec{r}'_1, \dots, \vec{r}_N) d\vec{r}_2, \dots, d\vec{r}_N \quad (4.1)$$

As before, we introduce the correlation factor

$$g(r_{ij}) = |f(r_{ij})|^2 - 1 \quad (3.2)$$

and an additional correlation factor

$$h(r_{ij}) = f(r_{ij}) - 1 \quad (4.2)$$

We distinguish

external points:  $\vec{r}_1, \vec{r}'_1$

internal points:  $\vec{r}_2, \dots, \vec{r}_p$

##### A. Expansion of the correlation factors

Using the correlation factors (3.2) and (4.2) we can rewrite the product of correlation factors in expression (4.1) as a sum of clusters. The order of each cluster is given by the number of internal points which it contains:

$$\prod_{2 \leq i \leq N} [1 + h^*(r_{1i})] [1 + h(r_{1'i})] \prod_{2 \leq i < j \leq N} [1 + g(r_{ij})] \\ = 1 + \sum_{2 \leq i \leq N} \tilde{W}_1(\vec{r}_i) + \sum_{2 \leq i < j \leq N} \tilde{W}_2(\vec{r}_i, \vec{r}_j) + \dots \quad (4.3)$$

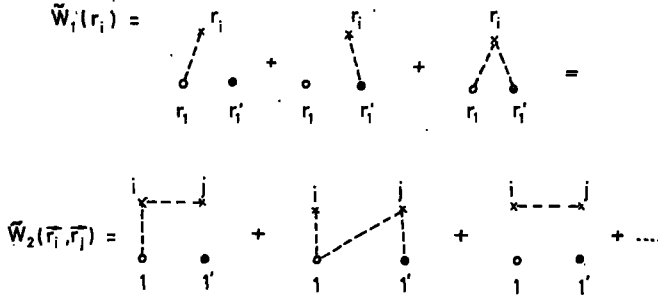


FIG. 7. Expansion of correlation factors.

The common feature of these clusters is that each internal point is connected through a correlation factor with, at least, one other point of the same cluster, be it internal or external.

The external points are never connected with each other by a correlation line and there are cases where they are not even connected to internal points.

- If now
- o ----- x stands for  $h^*(\vec{r}_1 - \vec{r}_i) = h^*(r_{1i})$
  - ----- x stands for  $h(\vec{r}_1' - \vec{r}_i) = h(r_{1'i})$  and
  - x ----- x stands for  $g(r_{ij})$

we can immediately write down the Yvon-Meyer diagrams which represent the members of a cluster of order p using the following rules:

- 1) Draw 2 external points  $\vec{r}_1, \vec{r}_1'$  and p internal points  $(\vec{r}_2, \dots, \vec{r}_{p+1})$ ;
- 2) connect each internal point by means of a correlation line with at least one other point, be it external or internal;
- 3) do not connect the external points to each other with a correlation line;
- 4) draw all such diagrams.

For examples, see Fig. 7.

B. Expansion of the determinant and rules for calculating  $G_1(\vec{r}_1, \vec{r}_1')$

We have now transformed the product of correlation factors appearing in expression (4.1) into a cluster expansion. To carry out the integrations in expression (4.1) it is convenient to generalize the functions  $\Delta_p$  given by expression (3.9). We define

$$(N-p)! \tilde{\Delta}_p \left( \begin{matrix} \vec{r}_1, \vec{r}_1', \dots, \vec{r}_p \\ \vec{r}_1, \vec{r}_2, \dots, \vec{r}_p \end{matrix} \right) = \int \phi^*(\vec{r}_1, \vec{r}_2, \dots, \vec{r}_p, \vec{r}_{p+1}, \dots, \vec{r}_N) \times \phi(\vec{r}_1', \dots, \vec{r}_p', \vec{r}_{p+1}, \dots, \vec{r}_N) d\vec{r}_{p+1}, \dots, d\vec{r}_N \tag{4.4}$$

$$\delta_1 \begin{pmatrix} \vec{r}_1 \\ \vec{r}_1 \end{pmatrix} = g(\vec{r}_1, \vec{r}_1) = \begin{array}{c} \text{---} \longrightarrow \text{---} \\ \vec{r}_1 \qquad \qquad \vec{r}_1' \end{array}$$

$$\delta_2 \begin{pmatrix} \vec{r}_1 & \vec{r}_2 \\ \vec{r}_1 & \vec{r}_2 \end{pmatrix} = \begin{vmatrix} g(\vec{r}_1, \vec{r}_1) & g(\vec{r}_1, \vec{r}_2) \\ g(\vec{r}_2, \vec{r}_1) & g(\vec{r}_2, \vec{r}_2) \end{vmatrix} =$$

$$= \begin{array}{c} \text{---} \longrightarrow \text{---} \\ \vec{r}_1 \qquad \qquad \vec{r}_1' \end{array} + \begin{array}{c} \text{---} \nearrow \text{---} \\ \text{---} \searrow \text{---} \\ \vec{r}_1 \qquad \qquad \vec{r}_1' \end{array}$$

$$\delta_3 \begin{pmatrix} \vec{r}_1 & \vec{r}_2 & \vec{r}_3 \\ \vec{r}_1 & \vec{r}_2 & \vec{r}_3 \end{pmatrix} = \begin{vmatrix} g(\vec{r}_1, \vec{r}_1) & g(\vec{r}_1, \vec{r}_2) & g(\vec{r}_1, \vec{r}_3) \\ g(\vec{r}_2, \vec{r}_1) & g(\vec{r}_2, \vec{r}_2) & g(\vec{r}_2, \vec{r}_3) \\ g(\vec{r}_3, \vec{r}_1) & g(\vec{r}_3, \vec{r}_2) & g(\vec{r}_3, \vec{r}_3) \end{vmatrix} =$$

FIG. 8. Expansion of the determinant.

Again we can calculate the functions  $\tilde{\Delta}_p$  in terms of the unperturbed single-particle density matrix

$$\tilde{\Delta}_p \begin{pmatrix} \vec{r}_1, \dots, \vec{r}_p \\ \vec{r}'_1, \dots, \vec{r}'_p \end{pmatrix} = \det |\rho(\vec{r}_i, \vec{r}'_j)| \quad (i, j) \in [1, p] \quad (4.5)$$

We can also find a diagrammatic representation of these determinants. As examples, see Fig. 8. The rules for drawing the diagrams representing  $\tilde{\Delta}_{(p+1)}$  are the following:

- 1) Draw two external points ( $\vec{r}_1, \vec{r}'_1$ ) and p labelled internal points  $\vec{r}_2, \dots, \vec{r}_{p+1}$ .
- 2) Connect all the points with directed lines such that:
  - i) there is one (and only one) line entering each internal point and one (and only one) line leaving it.
  - ii) One line must leave  $\vec{r}_1$  and one line must enter  $\vec{r}'_1$  so that one must be able to go from  $\vec{r}_1$  to  $\vec{r}'_1$  along a continuous line.
- 3) The sign corresponding to each graph is  $(-)^{\ell+p}$  where
  - p = number of external points
  - $\ell$  = number of closed loops.

- 4) Draw all diagrams until all the different ways of joining the  $(p+2)$  points are exhausted. The sum of all diagrams multiplied by their respective sign then represents

$$\Delta_{(p+1)} \left( \begin{array}{c} \vec{r}_1 \vec{r}_2, \dots, \vec{r}_{p+1} \\ \vec{r}_1 \vec{r}_2, \dots, \vec{r}_{p+1} \end{array} \right)$$

We now substitute expression (4.3) into relation (4.1) and find

$$\begin{aligned} G_1(\vec{r}_1, \vec{r}_1) &= \frac{N}{C_N} \int \left[ 1 + \sum_{2 \leq i \leq N} \tilde{W}_1(\vec{r}_i) + \sum_{2 \leq i < j \leq N} \tilde{W}_2(\vec{r}_i, \vec{r}_j) + \dots \right] \\ &\quad \times \phi^*(\vec{r}_1 \vec{r}_2, \dots, \vec{r}_N) \phi(\vec{r}_1 \vec{r}_2, \dots, \vec{r}_N) d\vec{r}_2, \dots, d\vec{r}_N \\ &= \frac{N}{C_N} \int \left[ 1 + \binom{N-1}{1} \tilde{W}_1(\vec{r}_1) + \binom{N-1}{2} \tilde{W}_2(\vec{r}_1, \vec{r}_2) + \dots \right] \\ &\quad \times \phi^*(\vec{r}_1 \vec{r}_2, \dots, \vec{r}_N) \phi(\vec{r}_1 \vec{r}_2, \dots, \vec{r}_N) d\vec{r}_2, \dots, d\vec{r}_N \\ &= \frac{N!}{C_N} \left[ \tilde{\Delta}_1 \binom{r_1}{r_1} + \sum_{p=1}^{(N-1)} \frac{1}{p!} \int \tilde{W}_p \tilde{\Delta}_{(p+1)} d\vec{r}_2, \dots, d\vec{r}_{p+1} \right] \end{aligned} \quad (4.6)$$

As  $\Delta_p = 0$  where  $p > N$ , we can extend this sum to infinity. Each term in expression (4.6) can be represented by combining the graphs contributing to  $\tilde{W}_p$  and  $\tilde{\Delta}_{(p+1)}$ , respectively. If we limit ourselves to linked diagrams, the factor  $N!/C_N$  cancels out and we are left with

$$G_1(\vec{r}_1, \vec{r}_1) = \rho(\vec{r}_1, \vec{r}_1) + \sum_{p=1}^{\infty} \frac{1}{p!} \int \left[ \tilde{W}_p \tilde{\Delta}_{(p+1)} \right]_L d\vec{r}_2, \dots, d\vec{r}_{p+1} \quad (4.7)$$

As we integrate over the internal points, all diagrams which distinguish themselves only by the re-labelling of the points will give the same contribution. These graphs are called topologically equivalent diagrams. By limiting ourselves to topologically distinct diagrams, we rewrite expression (4.7) as

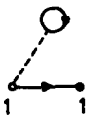
$$G_1(\vec{r}_1, \vec{r}_1) = \rho(\vec{r}_1, \vec{r}_1) + \sum_{p=1}^{\infty} \int \frac{1}{S} \left[ \tilde{W}_p \tilde{\Delta}_{(p+1)} \right]_{L, TD} d\vec{r}_2, \dots, d\vec{r}_{p+1} \quad (4.7')$$

where  $[\tilde{W}_p \tilde{\Delta}_{(p+1)}]_{L, TD}$  stands for: "include only linked and topologically distinct diagrams".  
 $s$  is the symmetry factor of the diagram.

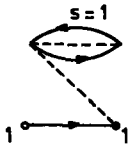
Once one has drawn a diagram of order  $p$ , following the rules given in sub-sections 4.A and 4.B, we obtain the contributions of this diagram to (4.7') by means of the following rules:

- 1) Each correlation line between internal points gives a factor  $g(r_{ij})$ ;
- 2) each correlation line between an internal point  $\vec{r}_i$  and an external point gives either a factor  $h^*(r_{1i})$  or  $h(r_{1i})$ ;
- 3) each directed line from point  $\vec{r}_i$  to point  $\vec{r}_j$  contributes a factor  $\rho(\vec{r}_i, \vec{r}_j)$ ;
- 4) the sign of the graph is  $(-)^{\ell+p}$  where  $p$  is the order of graph or number of internal points; and  $\ell$  is the number of closed loops;
- 5) integrate over internal points.

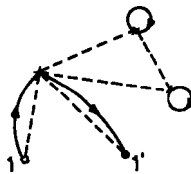
Let us give some examples (Fig. 9).

$s=1$   


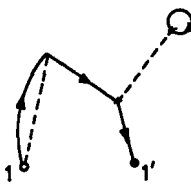
$= g(\vec{r}_1, \vec{r}_1) \int h^*(\vec{r}_2) g(\vec{r}_2, \vec{r}_2) d\vec{r}_2$

$s=1$   


$= (-) g(\vec{r}_1, \vec{r}_1) \int \int h(\vec{r}_2) g(\vec{r}_2, \vec{r}_3) g(\vec{r}_3, \vec{r}_2) d\vec{r}_2 d\vec{r}_3$

$s=2$   


$= -\frac{1}{2} \iiint h^*(r_{12}) h(r_{12}) g(r_{23}) g(r_{24}) g(r_{34}) g(\vec{r}_1, \vec{r}_2) g(\vec{r}_2, \vec{r}_3) g(\vec{r}_3, \vec{r}_4) g(\vec{r}_4, \vec{r}_1) d\vec{r}_2 d\vec{r}_3 d\vec{r}_4$



$= \iiint h^*(r_{12}) g(r_{24}) g(\vec{r}_1, \vec{r}_2) g(\vec{r}_2, \vec{r}_3) g(\vec{r}_3, \vec{r}_4) g(\vec{r}_4, \vec{r}_1) d\vec{r}_2 d\vec{r}_3 d\vec{r}_4$

FIG. 9. Contributions to expression (4.7') - examples.

### C. Rules for calculating the density

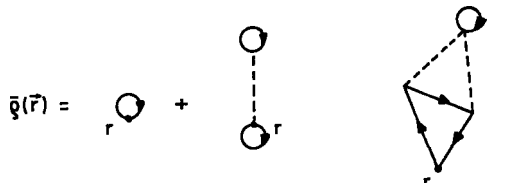
The density  $\bar{\rho}(\vec{r})$  is given in terms of the one-body correlation function  $G(\vec{r}, \vec{r}')$  by

$$\bar{\rho}(\vec{r}) = G(\vec{r}, \vec{r}) \quad (4.8)$$

It is obtained by summing all diagrams consisting of one external point  $\vec{r}$  and any number of internal points. The rules for calculating the contribution of a diagram are the same as those used for calculating the one-body correlation function, with the following exceptions:

- 1) All correlation lines contribute a factor  $g$ ;
- 2) the overall sign is  $(-1)^{p+l+1}$  where  $p$  is the number of internal points and  $l$  is the number of closed loops formed by the oriented lines

For an example, see Fig. 10.



$$\begin{aligned} \bar{g}(\vec{r}) &= \text{diagram 1} + \text{diagram 2} + \text{diagram 3} \\ &= g(\vec{r}, \vec{r}) = \int d\vec{r}_1 g(\vec{r}, \vec{r}_1) g(\vec{r}_1, \vec{r}_1) g(\vec{r} - \vec{r}_1) \\ &\quad + \int d\vec{r}_1 d\vec{r}_2 d\vec{r}_3 g(\vec{r}, \vec{r}_1) g(\vec{r}_1, \vec{r}_2) g(\vec{r}_2, \vec{r}) g(\vec{r}_3, \vec{r}_3) g(\vec{r}_1 - \vec{r}_3) g(\vec{r}_3 - \vec{r}_2) \end{aligned}$$

FIG. 10. Calculation of density.

Unless the subset of diagrams is chosen correctly, which is always possible, the contribution of a subset of diagrams contributing to  $G(\vec{r}_1, \vec{r}_2)$  will not go continuously into a subset of diagrams contributing to  $\bar{\rho}(\vec{r})$ .

## 5. THE TWO-BODY CORRELATION FUNCTION

The techniques used to derive a cluster expansion for the two-body correlation function  $G_2(\vec{r}_1, \vec{r}_2; \vec{r}_1', \vec{r}_2')$  are the same as those employed in the previous section. We limit ourselves, therefore, to indicating the essential steps followed in the derivation. Substituting the Jastrow wavefunction (2.1) into the expression (2.6) for the two-body correlation function we obtain

$$G_2(\vec{r}_1, \vec{r}_2; \vec{r}_1', \vec{r}_2') = \frac{N(N-1)}{C_N} f(r_{1'2'}) f^*(r_{12}) \int \prod_{2 \leq i \leq N} f^*(r_{1i}) f^*(r_{2i}) f(r_{1'i}) f(r_{2'i}) \\ \times \prod_{3 \leq i < j \leq N} |f(r_{ij})|^2 \phi^*(\vec{r}_1, \vec{r}_2, \vec{r}_3, \dots, \vec{r}_N) \phi(\vec{r}_1', \vec{r}_2', \vec{r}_3, \dots, \vec{r}_N) d\vec{r}_3, \dots, d\vec{r}_N \quad (5.1)$$

Using the correlation factors defined previously, (3.2) and (4.2), we obtain a cluster expansion for the product of correlation factors in the integral (5.1):

$$\prod f^* f^* f f \prod |f|^2 = 1 + \sum_{3 \leq i \leq N} X_1(\vec{r}_i) + \sum_{3 \leq i < j \leq N} X_2(\vec{r}_i, \vec{r}_j) + \dots \quad (5.2)$$

where the  $X_p(r_1, \dots, r_p)$  are symmetric p-body operators. These are represented by all possible Yvon-Meyer diagrams one can obtain by joining the internal points to each other and to external points. No correlation line joins any two external points. Making use of the determinants defined in (4.6) we obtain for  $G_2(\vec{r}_1, \vec{r}_2; \vec{r}_1', \vec{r}_2')$

$$G_2(\vec{r}_1, \vec{r}_2; \vec{r}_1', \vec{r}_2') = \frac{N!}{C_N} f^*(r_{12}) f(r_{1'2'}) \left[ \tilde{\Delta}_2 \left( \begin{matrix} \vec{r}_1' & \vec{r}_2' \\ \vec{r}_1 & \vec{r}_2 \end{matrix} \right) + \sum_{p=1}^{\infty} \frac{1}{p!} \int X_p \tilde{\Delta}_{(p+2)} d\vec{r}_3, \dots, d\vec{r}_p \right] \quad (5.3)$$

where we have extended the sum to  $\infty$  due to the properties of  $\tilde{\Delta}_p$ . Each term of order p in this expression can be represented, as in previous cases, by modified Yvon-Meyer diagrams, according to the following rules:

- 1) Draw four external points  $\vec{r}_1, \vec{r}_2, \vec{r}_1', \vec{r}_2'$  and p internal points;
- 2) connect them by means of correlation lines in such a way that each internal point is connected with at least one other point, be it internal or external;
- 3) connect all points by means of oriented lines in such a way that one (and only one) line enters an internal point and one (and only one) line leaves an internal point. Two lines must leave  $\vec{r}_1$  and  $\vec{r}_2$  and two lines must enter  $\vec{r}_1'$  and  $\vec{r}_2'$ ;
- 4) draw all diagrams until all the different possibilities of joining all points by correlation lines and oriented lines are exhausted.

Rule 3 has the following consequence:

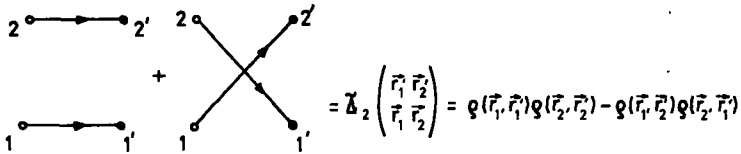
If we leave  $\vec{r}_1$  (or  $\vec{r}_2$ ) then we reach, along two continuous lines,  $\vec{r}_1'$  and  $\vec{r}_2'$  (or  $\vec{r}_1$ ). To obtain the contribution of these diagrams we have the following rules:

- 1) Each correlation line joining two internal points contributes a factor  $g(r_{ij})$ ;
- 2) each correlation line joining the external points  $(\vec{r}_1, \vec{r}_2, r_1', r_2')$  with an internal point  $\vec{r}_i$  contributes factors  $[h^*(r_{1i}), h^*(r_{2i}), h(r_{1'i}), h(r_{2'i})]$ , respectively;

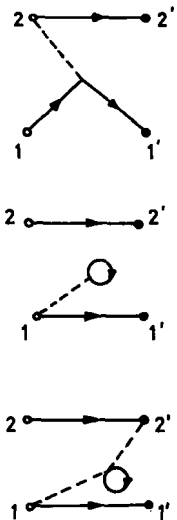
- 3) each oriented line going from  $\vec{r}_i$  to  $\vec{r}_j$  gives a factor  $\rho(\vec{r}_i, \vec{r}_j)$ ;
- 4) the sign of a graph is  $\epsilon(-)^{p+l}$ , where  $p$  is the number of internal points,  $l$  the number of closed loops formed by the oriented lines, and  $\epsilon$  is + or - according to whether the continuous line leaving the external point  $\vec{r}_1$  enters the external  $\vec{r}'_1$  or  $\vec{r}'_2$ ;
- 5) integrate over all internal points.

If we limit ourselves to linked and topologically distinct diagrams it can be shown, as in section 4, that the factor  $N!/C_N$  cancels and the factor  $1/p!$  is replaced by the symmetry factor  $1/s$ .

**Important:** Diagrams in which pairs of external points, for example  $(\vec{r}_1, \vec{r}'_1)$  and  $(\vec{r}_2, \vec{r}'_2)$ , are not joined by any line, are not necessarily unlinked diagrams.



$$= \Delta_2 \left( \begin{matrix} \vec{r}'_1 & \vec{r}'_2 \\ \vec{r}_1 & \vec{r}_2 \end{matrix} \right) = \rho(\vec{r}_1, \vec{r}'_1)\rho(\vec{r}_2, \vec{r}'_2) - \rho(\vec{r}_1, \vec{r}'_2)\rho(\vec{r}_2, \vec{r}'_1)$$



$$= (-) \int \rho(\vec{r}_1, \vec{r}_3)\rho(\vec{r}_3, \vec{r}'_1) h^s(r_{23})\rho(\vec{r}_2, \vec{r}'_2) d\vec{r}_3$$

$$= \rho(\vec{r}_1, \vec{r}'_1)\rho(\vec{r}_2, \vec{r}'_2) \int h(r_{13})\rho(\vec{r}_3, \vec{r}_3) d\vec{r}_3$$

$$= \rho(\vec{r}_1, \vec{r}'_1)\rho(\vec{r}_2, \vec{r}'_2) \int h^s(r_{13})h(r_{23})\rho(\vec{r}_3, \vec{r}_3) d\vec{r}_3$$

FIG. 11. Two-body correlation functions.

We have therefore:

$$G_2(\vec{r}_1, \vec{r}_2; \vec{r}_1', \vec{r}_2') = f^*(r_{12}) f(r_{1_2'}) \left[ \tilde{\Delta}_2 \left( \begin{array}{cc} \vec{r}_1' & \vec{r}_2' \\ \vec{r}_1 & \vec{r}_1 \end{array} \right) + \sum_{p=1}^{\infty} \int \frac{1}{S} \right. \\ \left. \times [X_p \tilde{\Delta}_{(p+2)}]_{L,TD} d\vec{r}_3, \dots, d\vec{r}_p \right] \quad (5.4)$$

Let us give some examples for the first few orders. Remember that the diagrams only represent the clusters, that is, the factor  $f^*(r_{12}) f(r_{1_2'})$  is not included (Fig. 11).

By means of the expansions (4.7') and (5.4) we are now able to calculate the one- and two-body correlation functions approximately in the sense that we have derived a perturbation expansion for them. Lowest-order contributions with respect to the correlation functions are formally related to Brueckner theory. This relation and the differences are discussed in the next sections. Finally, we will discuss the effect of correlations on the particle density.

Each diagram has one continuous line leaving  $\vec{r}_1$  and entering  $\vec{r}_1'$  or  $\vec{r}_2'$ . Another continuous line joins the other pair of external points. The sum of all diagrams such that no line joins these two continuous lines is obviously equal to

$$f^*(r_{12}) f(r_{1_2'}) [G(\vec{r}_1, \vec{r}_1') G(\vec{r}_2, \vec{r}_2') - G(\vec{r}_1, \vec{r}_2') G(\vec{r}_2, \vec{r}_1')] \quad (5.5)$$

where  $G(\vec{r}_1, \vec{r}_1')$  is the one-body correlation function. This is a simple example of the resummation of an infinite subset of diagrams.

## 6. THE EFFECT OF JASTROW CORRELATIONS ON THE CHARGE DENSITY OF $^{40}\text{Ca}$ .

Let us calculate the form factor of the charge density. The form factor is the Fourier transform of the charge density:

$$f(q) = \int d\vec{r} e^{i\vec{q}\cdot\vec{r}} \bar{\rho}(r) \quad (6.1)$$

Elastic electron scattering experiments can measure the form factor provided the nucleus is not excited during the scattering process. We can calculate the density  $\bar{\rho}(r)$  by summing the diagrams shown in Fig. 12.

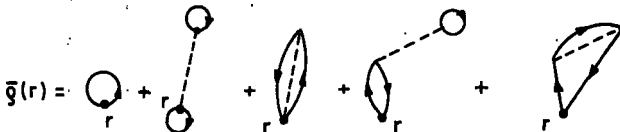


FIG. 12. Calculation of  $\bar{\rho}(r)$ .

These are the diagrams which are first order in the correlation factor  $g$ . Except for  ${}^4\text{He}$  [5] all the applications made so far [6-11] have been limited to the diagrams of the type shown in Fig. 12. They include what are called two-body cluster effects. The diagrams in Fig. 12 have another important property: they conserve the norm  $\int d\vec{r} \bar{\rho}(\vec{r})$  of the density and hence the number of particles. This would not be true if one of them was left out. In this section, for simplicity, we shall evaluate the total nucleon density; in  $N=Z$  nuclei such as  ${}^{12}\text{C}$ ,  ${}^{16}\text{O}$  and  ${}^{40}\text{Ca}$ , to which the Jastrow calculations have been applied most, the charge density is very nearly half of the total density.

The contribution of the graphs in Fig. 12 is

$$\begin{aligned} \bar{\rho}(\vec{r}) = & 4\rho(\vec{r}) + 16\rho(\vec{r}) \int d\vec{r}' g(\vec{r} - \vec{r}') \rho(\vec{r}') - 4 \int d\vec{r}' g(\vec{r} - \vec{r}') |\rho(\vec{r}, \vec{r}')|^2 \\ & - 16 \int d\vec{r}'_1 d\vec{r}'_2 |\rho(\vec{r}, \vec{r}'_1)|^2 \rho(\vec{r}_2) g(\vec{r}_1 - \vec{r}_2) \\ & + 4 \int d\vec{r}'_1 d\vec{r}'_2 \rho(\vec{r}, \vec{r}'_1) \rho(\vec{r}'_1, \vec{r}_2) \rho(\vec{r}_2, \vec{r}') g(\vec{r}_1 - \vec{r}_2) \end{aligned} \quad (6.2)$$

Expression (6.2) is that which has been used to analyse the elastic-electron-scattering data. It has been consistently observed [6-11] that the high-momentum-transfer data are better fitted with a density expression (6.2) than with an unperturbed density  $\rho(\vec{r})$  calculated with, say, Woods-Saxon orbitals. To see the effects of the various terms of Eq. (6.2) it is useful to make the following approximation: wherever in the integrands there appears a factor  $g(\vec{r}'_1 - \vec{r}'_2)$  we replace  $\vec{r}'_1$  and  $\vec{r}'_2$  by the centre-of-mass position  $\vec{R} = \frac{1}{2}(\vec{r}'_1 + \vec{r}'_2)$  in the other factors of the integrand. This approximation will be good if  $g(\vec{r}'_1 - \vec{r}'_2)$  is indeed short-ranged because for  $\vec{r}'_1 = \vec{r}'_2$  we have  $\vec{r}'_1 = \vec{r}'_2 = \vec{R}$ . The Fourier transform (6.1) of Eq. (6.2) reads:

$$\begin{aligned} f(\vec{q}) = & 4 \int d\vec{r} \rho(\vec{r}) e^{i\vec{q}\cdot\vec{r}} + 12 n(\vec{q}/2) \int d\vec{r} e^{i\vec{q}\cdot\vec{r}} \rho^2(\vec{r}) \\ & - 12 n(0) \int d\vec{r}'_1 d\vec{r}'_2 e^{i\vec{q}\cdot\vec{r}'_1} |\rho(\vec{r}'_1, \vec{r}'_2)|^2 \rho(\vec{r}_2) \end{aligned} \quad (6.3)$$

where

$$n(\vec{q}) = \int d\vec{r} e^{i\vec{q}\cdot\vec{r}} q(\vec{r}) = \int d\vec{r} e^{i\vec{q}\cdot\vec{r}} [ |f(\vec{r})|^2 - 1 ] \quad (6.4)$$

is the Fourier transform of the correlation factor  $g$ . We see that for  $\vec{q} = 0$ ,  $f(\vec{q}) = 4 \int \rho(\vec{r}) d\vec{r}$  so that the correction terms conserve the number of particles. We see also that the correction terms depend on the Fourier components of the correlation function. If a monotonic function

$$g_1(\vec{r}) = -\exp[-\beta^2 r^2] \quad (6.5)$$

is used [6-8], the Fourier transform  $n(q)$  is

$$n(q) = -\exp(-q^2/4\beta^2) \quad (6.6)$$

Typical values of  $\beta$  are  $\beta \sim 1.5 \text{ fm}^{-1}$ , so that  $n(q)$  is a slowly varying function of  $q$ .

Oscillating correlation factors have also been used [11] such as

$$g_2(r) = -j_0(q_0 r) \quad (6.7)$$

with  $q_0 \sim 1.5 \text{ fm}^{-1}$ .

This correlation factor has only Fourier components equal to  $q_0$  so that with this factor only the second term of Eq. (6.3) contributes. The form factor is only corrected for momentum transfer  $q = q_0/2$ . An oscillating correlation factor such as (6.7) was introduced to represent the exchange of relative momentum  $q_0$  between two nucleons. When an electron transfers momentum  $q$  to a nucleon, this nucleon will have a relative momentum of  $q/2$  with respect to another nucleon at rest and thus the correction to the form factor will peak at  $q = 2q_0$ .

Another useful way of writing the form factor of the charge distribution (6.2) is in terms of matrix elements between the single-particle states of the Slater determinant in the Jastrow wave-function. If we use the expressions

$$\begin{aligned} \rho(\vec{r}_1, \vec{r}_2) &= \sum_{\alpha \in F} \varphi_\alpha^*(\vec{r}_1) \varphi_\alpha(\vec{r}_2) \\ \rho(\vec{r}) &= \sum_{\alpha \in F} |\varphi_\alpha(\vec{r})|^2 \end{aligned} \quad (6.8)$$

where the sums extend over the orbits of the Slater determinant. The Fourier transform (6.1) of the charge density (6.2) is given by

$$\begin{aligned} f_j(q) &= \sum_{\alpha \in F} \langle \alpha | e^{i\vec{q} \cdot \vec{r}} | \alpha \rangle + \sum_{(\alpha, \beta) \in F} \langle \alpha \beta | e^{i\vec{q} \cdot \vec{r}_1} g(r) | \alpha \beta \rangle \\ &\quad - \sum_{(\alpha, \beta, \gamma) \in F} \langle \alpha | e^{i\vec{q} \cdot \vec{r}} | \beta \rangle \langle \alpha \gamma | g(r) | \beta \gamma \rangle \end{aligned} \quad (6.9)$$

In Eq. (6.10)  $\langle \alpha \beta | g | \alpha \beta \rangle$  are anti-symmetrized matrix elements of the operator  $g$ . Expression (6.9) allows a comparison of the effect of Brueckner and Jastrow contributions. In Brueckner theory [15] one solves the Bethe-Goldstone equation

$$\psi_{\alpha\beta} = \phi_{\alpha\beta} - \frac{Q}{e} \nabla \psi_{\alpha\beta} \quad (6.10)$$

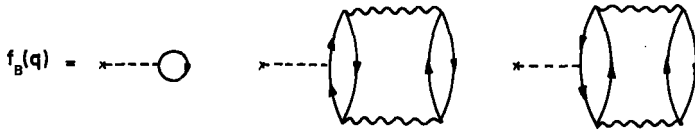


FIG. 13. Goldstone graphs for calculation of form factor.

$\psi_{\alpha\beta}$  represents the scattering wave-function of two nucleons in the nucleus;  $\phi_{\alpha\beta}$  is the unperturbed wave-function, an anti-symmetrized product of two single-particle orbits  $\alpha$  and  $\beta$ ,  $v$  is the nucleon-nucleon interaction. The operator  $Q$  is introduced in order to take into account the presence of the other nucleons which prevent the scattering of any nucleon pair into the states of the Fermi sea which is filled by the other nucleons. Thus the Pauli operator  $Q$  eliminates from any two-nucleon wave-function  $\psi$  its components in the Fermi sea

$$\begin{aligned} \langle ij|Q|\psi\rangle &= \langle ij|\psi\rangle \text{ if } [i,j] \notin F \\ &= 0 \quad \text{otherwise} \end{aligned} \quad (6.11)$$

We can calculate the form factor by summing the Goldstone graphs shown in Fig. 13. In the Goldstone graphs in Fig. 13 the dotted line represents the operator  $\exp(i\vec{q}\cdot\vec{r})$  and the wavy lines represent G-matrix interactions. A G-matrix is defined by

$$\langle ij|G|\alpha\beta\rangle = \langle ij|V|\psi_{\alpha\beta}\rangle \quad (6.12)$$

The contribution of the graphs of Fig. 13 to the form factor is given by

$$\begin{aligned} f_B(q) &= \sum_{\alpha \in F} \langle \alpha | e^{i\vec{q}\cdot\vec{r}} | \alpha \rangle + \sum_{\alpha, \beta \in F} \langle \chi_{\alpha\beta} | e^{i\vec{q}\cdot\vec{r}_1} | \chi_{\alpha\beta} \rangle \\ &\quad - \sum_{\alpha, \beta, \gamma \in F} \langle \alpha | e^{i\vec{q}\cdot\vec{r}} | \beta \rangle \langle \chi_{\alpha\gamma} | \chi_{\beta\gamma} \rangle \end{aligned} \quad (6.13)$$

where  $\chi_{\alpha\beta}$  is the defect wave-function defined as the difference

$$\chi_{\alpha\beta} = \phi_{\alpha\beta} - \psi_{\alpha\beta} \quad (6.14)$$

between the unperturbed and scattering wave-function.

Expressions (6.9) and (6.13) of the form factors calculated in Jastrow and Brueckner theory are formally very similar. But they may differ appreciably. Indeed, to compare them we assume that the defect wave-function in Brueckner theory is related to the Jastrow correlation factor by the approximate relation

$$\chi_{\alpha\beta} \sim (1-f)\phi_{\alpha\beta} \quad (6.15)$$

Relation (6.15) has the correct asymptotic values. At zero relative distance  $\chi_{\alpha\beta} = \phi_{\alpha\beta}$  and beyond the healing distance  $\chi_{\alpha\beta} = 0$ . Inserting relation (6.15) into the Brueckner contribution (6.13) we find that

$$f_B(\mathbf{q}) = f_J(\mathbf{q}) - 2 \sum_{(\alpha, \beta) \in F} \langle \alpha\beta | e^{i\vec{q} \cdot \vec{r}_1} (f-1) | \alpha\beta \rangle + 2 \sum_{\alpha, \beta, \gamma \in F} \langle \alpha | e^{i\vec{q} \cdot \vec{r}} | \beta \rangle \langle \alpha\gamma | f-1 | \beta\gamma \rangle \quad (6.16)$$

so that unless

$$\sum_{\alpha, \beta \in F} \langle \alpha\beta | e^{i\vec{q} \cdot \vec{r}_1} (f-1) | \alpha\beta \rangle - \sum_{\alpha, \beta, \gamma \in F} \langle \alpha | e^{i\vec{q} \cdot \vec{r}} | \beta \rangle \langle \alpha\gamma | f-1 | \beta\gamma \rangle = 0 \quad (6.17)$$

the contributions of Brueckner and Jastrow correlations to the form factor will differ. With the usual correlation factors such as (6.5) and (6.6), Eq. (6.17) will not be satisfied. The difference may be traced to the absence of the Pauli operator in the Jastrow correlation factor. In Brueckner theory, the defect wave-function has no components in the Fermi sea so that

$$(Q-1) \chi_{\alpha\beta} = 0 \quad (6.18)$$

The equivalent Jastrow defect wave-function (6.17) does not, in general, satisfy the Pauli condition

$$(Q-1)(1-f) \phi_{\alpha\beta} = 0 \quad (6.19)$$

The wave-function  $(1-f)\phi_{\alpha\beta}$  will have, in general, particle-hole components. It is easy to check that if the correlation factor  $1-f$  did satisfy the Pauli condition (6.19) then Eq. (6.17) would be satisfied so that Brueckner and Jastrow correlations would give the same contribution to the form factor.

There is no reason, a priori, to require the Jastrow correlation factor  $f-1$  to satisfy the Pauli condition (6.19). But unless it does it is not possible to make a fair comparison between the contribution of Brueckner and Jastrow correlations. Note, in particular, that the Brueckner contribution depends on  $\langle \chi_{\alpha\beta} | \chi_{\alpha\beta} \rangle$ , i. e. on  $(f-1)^2$ , which is positive whereas the Jastrow contribution depends on  $(f^2-1)$ , which for monotonic correlation factors such as (6.5) is negative and for oscillating correlation factors such as (6.7) will oscillate in sign. Finally, when the Pauli condition (6.19) is not satisfied the effects of Jastrow correlations on the form factor may differ very much according to the definition used for the uncorrelated part [14].

#### ACKNOWLEDGEMENTS

Most of the theory and applications discussed in this paper are the result of a collaboration with M. Gaudin and J. Gillespie. The author also

thanks C. Ciofi degli Atti, M. E. Grypeos, L. Döhnert, J. Tepel and the many other physicists of the International Centre for Theoretical Physics, Trieste, who helped to clarify some points in discussions. He also thanks M. Danos and M. G. Huber for useful discussions.

## REFERENCES

- [1] BIJL, A., *Physica* 7 (1940) 869; DINGLE, R. B., *Phil. Mag.* 40 (1949) 573; JASTROW, R., *Phys. Rev.* 98 (1955) 1479.
- [2] IWAMOTO, F., YAMADA, M., *Progr. theor. Phys. (Kyoto)* 17 (1957) 543.
- [3] FEENBERG, E., *The Theory of Quantum Fluids*, Academic Press, New York and London (1969).
- [4] BACKMAN, S.-O., CHAKKALAKAL, D. A., CLARK, J. W., *Nucl. Phys.* A130 (1969) 635; BRINK, D. M., GRYPEOS, M. E., *Nucl. Phys.* A97 (1967) 81; RISTIG, M. L., TER LOUW, W. J., CLARK, J. W., Washington University Preprint, St. Louis, Missouri (1971); WONG, C. W., UCLA preprint, 1970, "A possible connection between the IY cluster expansion and the reaction matrix perturbation theory".
- [5] CZYŻ, W., LESNIAK, L., *Physics Letts* 25B (1967) 319.
- [6] GERACE, W. J., SPARROW, D. A., *Physics Letts* 30B (1969) 71.
- [7] KHANNA, F. C., *Phys. Rev. Letts* 20 (1968) 871.
- [8] CIOFI DEGLI ATTI, C., KABACHNIK, N. M., *Phys. Rev.* C1 (1970) 809.
- [9] GRYPEOS, M. E., CIOFI DEGLI ATTI, C., *Nuovo Cim. Letts* 2 (1969) 587.
- [10] TUAN, S. T., WRIGHT, L. E., HUBER, M. G., *Phys. Rev. Letts* 23 (1969) 174.
- [11] WRIGHT, L. E., TUAN, S. T., HUBER, M. G., *Nuovo Cim. Letts* 3 (1970) 253.
- [12] HAFTEL, M. I., TABAKIN, F., Naval Research Laboratory preprint, Oct. 1970.
- [13] CHUNG, K. N., HUBER, M. G., DANOS, M., *Z. Physik* 240 (1970) 195 and references therein.
- [14] RIPKA, G., GILLESPIE, J., *Phys. Rev. Letts* 25 (1970) 1624.
- [15] See BROWN, G. E., *Unified Theory of Nuclear Models and Forces*, North-Holland, Amsterdam, and J. WILEY, New York (1967).
- [16] DE SHALIT, A., WEISSKOPF, V. F., *Ann. Phys. (NY)* 5 (1958) 282.
- [17] YVON, J., *Acta Sc. Ind.* 203 (1935); MEYER, J. E., MEYER, M. G., *Statistical Mechanics*, J. WILEY, New York and London (1966).
- [18] See THOULESS, D. J., *The Quantum Mechanics of Many-Body Systems*, Academic Press, New York and London (1961).

# VARIATIONAL DETERMINATION OF THE EFFECTIVE INTERACTION IN NUCLEI

M. E. GRYPEOS\*

Physics Department, N.R.C. "Democritos",

Aghia Paraskevi Attikis,

Athens, Greece

and

International Centre for Theoretical Physics,

Trieste, Italy

## Abstract

VARIATIONAL DETERMINATION OF THE EFFECTIVE INTERACTION IN NUCLEI.

1. Introduction. 2. The model operator and the effective nuclear Hamiltonian; 3. The variational method with the separation condition; 4. The continuity of the derivative of  $\psi_{nGS}$  at the separation distance; 5. The variational method with the healing condition; 6. Non-central forces; 7. Applications and remarks.

## 1. INTRODUCTION

In the last few years, extensive use of effective-interaction matrix elements has been made in various nuclear-structure calculations [1-5].

These matrix elements are derived from the free nucleon-nucleon potential which is assumed to be a local potential with short-range strong repulsion.

Two general many-body approaches have been followed in determining the two-nucleon wave functions and the matrix elements of effective interaction from such a "realistic" nucleon-nucleon potential. The first is the reaction matrix  $G$  and is based on perturbation theory<sup>1</sup>. The second is the cluster-expansion variational approach.

Both general approaches (which originated from the study of infinite nuclear matter [6, 7a, b]) and the various versions of each of them have their limitations, but the first has been much more popular so far, and it might appear that the second approach is less suitable for the treatment of the nuclear many-body problem. This, however, may not necessarily be the case. Quite a number of the limitations of the second approach are not likely to be inherent in it but they can be removed if sufficient effort is made. The recent developments in the cluster-expansion variational approach, which we are going to discuss in this paper, indicate such a possibility.

In the following, we shall first discuss the unitary model operator suggested by Villars, and we shall describe two variational methods for determining the two-nucleon relative wave functions and the matrix elements of the effective interaction. More details can be found in Refs [8-11].

\* Present address: Department of Theoretical Physics, University of Thessaloniki, Greece.

<sup>1</sup> To avoid misunderstanding, we should note that the matrix elements determined by means of this method are usually referred to as "reaction-matrix elements" and not as effective-interaction matrix elements.

## 2. THE MODEL OPERATOR AND EFFECTIVE NUCLEAR HAMILTONIAN

Following Villars [8] we write the model operator which introduces short-range correlations in the form  $\exp(iS)$ . An eigenstate  $\Phi$  of the model system corresponds to an eigenstate

$$\Psi = e^{iS} \Phi \quad (1)$$

of the true system.

Let  $H$  be the Hamiltonian of the original system, which contains single-particle kinetic energies  $t_i$  and two-body interactions represented by the potential  $v_{ij}$ :

$$H = T + V = \sum_{\alpha\beta} a_{\alpha}^{\dagger} a_{\beta} \langle \alpha | t_1 | \beta \rangle + \frac{1}{2!} \sum_{\alpha\beta\gamma\delta} a_{\alpha}^{\dagger} a_{\beta}^{\dagger} a_{\delta} a_{\gamma} \langle \alpha\beta | v | \gamma\delta \rangle \quad (2)$$

The quantities  $a_{\alpha}^{\dagger}$  and  $a_{\alpha}$  are creation and annihilation operators for the single-particle states  $\alpha$ . The effective Hamiltonian for the model system is

$$H_{\text{eff.}} = e^{-iS^{\dagger}} H e^{iS} \quad (3)$$

The aim is to choose the model operator in such a way that the model eigenfunctions  $\Phi$  may be well approximated by a single Slater determinant or a linear combination of a few Slater determinants. Short-range correlations would be absorbed on the model operator, to which certain general restrictions are made:

- (1) The model operator is (left) unitary [8, 12]. If a state  $\Phi$  of the model system is normalized then the corresponding state  $\Psi$  of the original system is also normalized;
- (2)  $S$  is a two-body operator:  $S = \sum_{i < j} S_{ij}$ ;
- (3)  $S$  depends only on the spins, isospins and relative co-ordinates and momenta of the particles in the system;
- (4)  $S$  is a scalar with respect to rotations.

These restrictions make it impossible to include all correlations in the model operator. Hence if  $\Phi$  is a proper model wave function then  $\Psi$  is no longer the true wave function of the system, but can only be considered as trial wave function.

The original Hamiltonian Eq. (2) is a sum of one- and two-body operators, but the model or effective Hamiltonian Eq. (3) contains three body and many-body parts [8, 9] also:

$$H_{\text{eff.}} = H_{\text{eff.}}^{(1)} + H_{\text{eff.}}^{(2)} + H_{\text{eff.}}^{(3)} + \dots \quad (4)$$

where

$$H_{\text{eff.}}^{(1)} = \sum_{\alpha\beta} a_{\alpha}^{\dagger} a_{\beta} \langle \alpha | t_1 | \beta \rangle \quad (5)$$

$$H_{\text{eff}}^{(2)} = \frac{1}{2!} \sum_{\alpha\beta\gamma\delta} a_{\alpha}^{\dagger} a_{\beta}^{\dagger} a_{\delta} a_{\gamma} [\langle \alpha\beta | e^{-iS_{12}^{\dagger}} (t_1 + t_2 + v_{12}) e^{iS_{12}} - (t_1 + t_2) | \gamma\delta \rangle] \quad (6)$$

etc.

The one-body part of the effective Hamiltonian is the same as that of the original Hamiltonian by restriction [2].

We try to determine the model operator by a variational principle. We shall assume that this operator should be chosen to make

$$\langle E \rangle = \langle \Psi | H | \Psi \rangle = \langle \Phi | H_{\text{eff.}} | \Phi \rangle \quad (7)$$

a minimum, for a suitable wave function  $\Phi$ . Such a procedure is reasonable if  $\Psi$  represents a trial wave function for the ground state of the nucleus. If we wish to apply the variational principle keeping the many-body terms in (4), we are faced with an extremely complicated task. In order to avoid this complication we consider explicitly only the first and second terms. The omission of the other terms will be compensated by the following:

(1) First, by adding the term  $H_{\text{eff.}}^{(2)}$

$$H_{\text{eff.}}^{(2)} = \frac{1}{2!} \sum_{\alpha\beta\gamma\delta} a_{\alpha}^{\dagger} a_{\beta}^{\dagger} a_{\delta} a_{\gamma} [\langle \alpha\beta | e^{-iS_{12}^{\dagger}} (U_1 + U_2) e^{iS_{12}} - (U_1 + U_2) | \gamma\delta \rangle] \quad (8)$$

This additional term is a two-body term which contains an average contribution from the three-body terms and takes some account of the effect of the other nucleons on the motion of nucleons 1 and 2. Da Providencia and Shakin have shown that  $U_1$  should be taken as the Hartree-Fock single-particle potential defined by Eq. (36) of Ref. [9]. In the present study this H-F potential is approximated as in Ref. [4] by a harmonic-oscillator potential

$$U_1 = \frac{\hbar^2}{2M} \frac{r_1^2}{b_1^4}, \quad b_1 = \left( \frac{\hbar}{M\omega} \right)^{\frac{1}{2}} \quad (9)$$

(2) Secondly, by introducing subsidiary conditions which can restrict the correlation to having a sufficiently short range. We describe these subsidiary conditions in the following sections.

The calculation of the two-particle matrix elements of the two-body parts ( $H_{\text{eff.}}^{(2)} + H_{\text{eff.}}^{(2)}$ ) can be simplified by making a transformation to relative co-ordinates of the two interacting nucleons. This is exhibited in detail in Ref. [10].

If the model wave function is a single Slater determinant, the trial energy of the nucleus can be written in the above approximations as

$$\langle E \rangle = \sum_{\alpha} \langle \alpha | t | \alpha \rangle + \frac{1}{2} \sum_{\alpha\beta} [\langle \alpha\beta | v_{\text{eff.}} | \alpha\beta \rangle - \langle \alpha\beta | v_{\text{eff.}} | \beta\alpha \rangle] \equiv \langle T \rangle + \langle V_{\text{eff.}} \rangle \quad (10)$$

where

$$v_{\text{eff.}} = e^{-iS_{12}} \left( t_{\text{rel.}} + \frac{\hbar^2 r^2}{M b^4} + v_{12} \right) e^{iS_{12}} - \left( t_{\text{rel.}} + \frac{\hbar^2 r^2}{M b^4} \right) \quad (11)$$

In this expression  $b$  is the harmonic-oscillator parameter of the relative motion ( $b = 2\hbar/M\omega$ )<sup>1/2</sup>.

For central forces and with harmonic-oscillator wave functions the two-body matrix elements can be written as sums of diagonal matrix elements between relative wave functions (see sections 3 and 4 of Ref. [10a] for details). Therefore, in order to vary  $\langle E \rangle$ , we can vary the diagonal matrix elements of  $v_{\text{eff.}}$ , which can be written:

$$\begin{aligned} \langle n\ell, S | v_{\text{eff.}} | n\ell, S \rangle \equiv M_{n\ell S} &= \int_0^\infty \left[ \frac{\hbar^2}{M} \left( \left| \frac{d\psi_{n\ell S}}{dr} \right|^2 + \frac{\ell(\ell+1)}{r^2} |\psi_{n\ell S}|^2 + \frac{r^2}{b^4} |\psi_{n\ell S}|^2 \right) \right. \\ &\left. + v_{\ell, S}(r) |\psi_{n\ell S}|^2 \right] dr - \frac{\hbar^2}{M} \int_0^\infty \left[ \left( \frac{d\phi_{n\ell}}{dr} \right)^2 + \frac{\ell(\ell+1)}{r^2} \phi_{n\ell}^2 + \frac{r^2}{b^4} \phi_{n\ell}^2 \right] dr \quad (12) \end{aligned}$$

where  $n$  is the principal harmonic-oscillator quantum number for the relative motion,  $\ell$  the orbital angular momentum quantum number of the relative motion and  $S$  the total-spin quantum number of the nucleon-nucleon system.

The statement in the preceding paragraph about the variation of  $M_{n\ell S}$  follows by considering  $\langle E \rangle$  as a functional of the correlated radial, relative, two-nucleon wave functions

$$\psi_{n\ell S}(r) = e^{iS_{12}} \phi_{n\ell}(r) : \langle E \rangle = \langle E \rangle_{(\psi_{000}, \psi_{001}, \psi_{100}, \dots)} = \langle T \rangle + \sum_{n\ell S} C_{n\ell S} M_{n\ell S}(\psi_{n\ell S})$$

Variation of  $\langle E \rangle$  is equivalent to

$$\frac{\delta \langle E \rangle}{\delta \psi_{n\ell S}} = \frac{\delta M_{n\ell S}}{\delta \psi_{n\ell S}} = 0$$

for every  $\psi_{n\ell S}$  appearing in the trial energy of the nucleus.

In the two variational methods which will be discussed in Sections 3-5 the variational principle is applied to the matrix element (12) of the effective interaction, with the subsidiary condition that  $\psi_{n\ell S}$  is normalized (or approximately normalized), which goes some way towards satisfying the (left) unitary condition of the model operator in the two-body approximation.

### 3. THE VARIATIONAL METHOD WITH THE SEPARATION CONDITION

In this method we assume that there are no correlations beyond a separation distance  $d = d_{n\ell S}$ , which is determined later. In other words we assume that

$$\psi_{n\ell S}(r) = \phi_{n\ell}(r) \quad \text{for } r > d_{n\ell S} \quad (13)$$

Using this restriction we can write expression (12) as follows:

$$\begin{aligned} M_{n\ell S} = & \int_0^{d_{n\ell S}} \left[ \frac{\hbar^2}{M} \left( \left| \frac{d\psi_{n\ell S}}{dr} \right|^2 + \frac{\ell(\ell+1)}{r^2} |\psi_{n\ell S}|^2 + \frac{r^2}{b^4} |\psi_{n\ell S}|^2 \right) + v_{\ell S}(r) |\psi_{n\ell S}|^2 \right] dr \\ & - \frac{\hbar^2}{M} \int_0^{d_{n\ell S}} \left[ \left( \frac{d\phi_{n\ell}}{dr} \right)^2 + \frac{\ell(\ell+1)}{r^2} \phi_{n\ell}^2 + \frac{r^2}{b^4} \phi_{n\ell}^2 \right] dr + \int_{d_{n\ell S}}^{\infty} v_{\ell S}(r) \phi_{n\ell}^2 dr \end{aligned} \quad (14)$$

We shall minimize this matrix element by varying the relative two-body wave function  $\psi_{n\ell S}$ , with boundary conditions

$$\psi_{n\ell S}(c) = 0, \quad \psi_{n\ell S}(d_{n\ell S}) = \phi_{n\ell}(d_{n\ell S}) \quad (15)$$

The first is due to the possible existence of a hard core in the inter-nucleon potential. Obviously, there is no difficulty if there is a soft core, instead. The only difference is that in this case  $c=0$ . The second condition is due to restriction (13). In addition, we require that  $\psi_{n\ell S}$  be normalized:

$$\int_0^{\infty} |\psi_{n\ell S}|^2 dr = 1 \quad (16)$$

The Euler equation of our variational problem is

$$-\frac{\hbar^2}{M} \frac{d^2 \psi_{n\ell S}}{dr^2} + \frac{\hbar^2}{M} \frac{\ell(\ell+1)}{r^2} \psi_{n\ell S} + \frac{\hbar^2}{M} \frac{r^2}{b^4} \psi_{n\ell S} + v_{\ell S}(r) \psi_{n\ell S} = \epsilon_{n\ell S} \psi_{n\ell S} \quad (17)$$

$$c < r < d_{n\ell S}$$

The Lagrange multiplier  $\epsilon_{n\ell S}$  is due to the normalization condition (16).

Multiplying Eq. (17) by  $\psi_{n\ell S}$  and integrating from  $c$  to  $d$ , we obtain the following expression for the stationary value of  $M_{n\ell S}$ :

$$\begin{aligned} M_{n\ell S} = & \frac{\hbar^2}{M} \psi_{n\ell S}(d_{n\ell S}) \psi'_{n\ell S}(d_{n\ell S}) - \frac{\hbar^2}{M} \int_0^{d_{n\ell S}} \left[ \left( \frac{d\phi_{n\ell}}{dr} \right)^2 + \frac{\ell(\ell+1)}{r^2} \phi_{n\ell}^2 + \frac{r^2}{b^4} \phi_{n\ell}^2 \right] dr \\ & + \epsilon_{n\ell S} \int_0^{d_{n\ell S}} \phi_{n\ell}^2 dr + \int_{d_{n\ell S}}^{\infty} v_{\ell S}(r) \phi_{n\ell}^2 dr \end{aligned} \quad (18)$$

The first terms in this expression, i. e. the boundary term with the "uncorrelated energy term" and the normalization term, are short-range contributions while the last term comes from the long-range part of the two-nucleon potential.

Finally, a criterion can be found for the stationary value of  $M_{n\ell S}$  to be a minimum. This is given in Ref. [10].

#### 4. THE CONTINUITY OF THE DERIVATIVE OF $\psi_{n\ell S}$ AT THE SEPARATION DISTANCE

We may first note that, while the continuity of  $\psi_{n\ell S}(r)$  at  $r = d_{n\ell S}$  can be guaranteed by the boundary condition imposed in applying the variational principle, the derivative of  $\psi_{n\ell S}(r)$  at  $r = d_{n\ell S}$  is not continuous in general since, we cannot require in addition

$$\psi'_{n\ell S}(r) \Big|_{r=d_{n\ell S}} = \phi'_{n\ell}(r) \Big|_{r=d_{n\ell S}} \quad (19)$$

for arbitrary values of  $d_{n\ell S}$ .

The actual two-body relative wave function and its derivative are not expected to have any discontinuity in the interval  $c < r < \infty$  and therefore we should investigate whether we can choose  $d_{n\ell S}$  in such a way that the continuity of  $\psi'_{n\ell S}(r) \Big|_{r=d_{n\ell S}}$  is also satisfied.

If for a value of the separation distance  $d_{n\ell S} : d_{n\ell S} = d_{n\ell S}^{M.S.}$  the condition

$$\frac{\psi'_{n\ell S}(d_{n\ell S}^{M.S.})}{\psi_{n\ell S}(d_{n\ell S}^{M.S.})} = \frac{\phi'_{n\ell}(d_{n\ell S}^{M.S.})}{\phi_{n\ell}(d_{n\ell S}^{M.S.})} \quad (20)$$

is satisfied, we shall call this separation distance "(variational) Moszkowski and Scott separation distance", in analogy to the corresponding definition of the Moszkowski and Scott separation distance in the reaction matrix approach [13]. Note that  $d_{n\ell S}^{M.S.}$  is state dependent.

In the case  $d_{n\ell S} = d_{n\ell S}^{M.S.}$  the expression for  $M_{n\ell S}$  becomes extremely simple:

$$M_{n\ell S} = (\epsilon_{n\ell S} - E_{n\ell}) \int_0^{d_{n\ell S}^{M.S.}} \phi_{n\ell}^2 dr + \int_{d_{n\ell S}^{M.S.}}^{\infty} v_{\ell S} \phi_{n\ell}^2 dr \quad (21)$$

where

$$E_{n\ell} = \left( 2n + \ell + \frac{3}{2} \right) \hbar\omega \quad (22)$$

The results of the numerical calculations based on this method (see sections 2 and 3 of Ref. [11] show that only in a few cases can the wave function  $\psi_{n\ell S}(r)$  also have continuous derivative at  $r = d_{n\ell S}$ . It was found, however, that one could guarantee continuity of  $\psi'_{n\ell S}$  at  $r = d_{n\ell S}$  if one does not impose the normalization (16), but instead the condition

$$\int_0^{\infty} |\psi_{n\ell S}|^2 dr = N_{n\ell S} \quad (23)$$

where  $N_{n\ell S}$  is a number different from one, but very close to it. A discussion of such an approach is given in Ref. [11]. We should finally note that corrections due to the lack of exact normalization could also be calculated. This has been done recently [11b] and it is expected that in certain cases improved results will be obtained.

## 5. THE VARIATIONAL METHOD WITH THE HEALING CONDITION

In this section the variational principle is again applied to the matrix element of the effective interaction  $M$  but with a restriction different from Eq. (13). Namely, the wave function  $\psi$  is required to satisfy the following two conditions:<sup>2</sup>

$$i) \int_0^{\infty} |\psi|^2 dr = 1 \quad (24)$$

$$ii) \int_0^{\infty} P(r) |\psi - \phi|^2 dr = \eta^2 (= \text{constant}), \quad P(r) > 0 \quad (25)$$

where  $P(r)$  is an appropriate weighting function. We shall be mainly interested in the simplest case in which  $P(r)$  is taken equal to one.

The second condition, which has been called the "healing condition", is introduced so that the relative radial wave function of the two particles in the nucleus may approach the unperturbed wave function rapidly. With conditions (24) and (25) variation of the diagonal matrix element  $M_{n\ell S}$  is equivalent to variation of the integral

$$\int_c^{\infty} \left[ -\frac{\hbar^2}{M} \psi^* \frac{d^2 \psi}{dr^2} + \frac{\hbar^2}{M} \frac{\ell(\ell+1)}{r^2} |\psi|^2 + \frac{\hbar^2}{M} \frac{r^2}{b^4} |\psi|^2 + v(r) |\psi|^2 + \lambda_1 |\psi|^2 + \lambda_2 P(r) |\psi - \phi|^2 \right] dr - \int_0^{\infty} \frac{\hbar^2}{M} \left[ \phi \frac{d^2 \phi}{dr^2} + \frac{\ell(\ell+1)}{r^2} \phi^2 + \frac{r^2}{b^4} \phi^2 \right] dr \quad (26)$$

where  $\lambda_1$  and  $\lambda_2$  are Lagrange multipliers.

The Euler equation is

$$\frac{d^2 \psi}{dr^2} - \frac{\ell(\ell+1)}{r^2} \psi - \frac{r^2}{b^4} \psi - \frac{M}{\hbar^2} v(r) \psi - (\beta_1 + \beta_2 P(r)) \psi = -\beta_2 P(r) \phi, \quad c < r < \infty \quad (27)$$

<sup>2</sup> In the following we shall omit in most cases the indices  $n\ell S$  for simplicity.

The boundary conditions are  $\psi(c) = 0$ ,  $\psi(\infty) = \phi(\infty) = 0$ . In Eq. (27) we have put

$$\beta_1 = \frac{M}{\hbar^2} \lambda_1, \quad \beta_2 = \frac{M}{\hbar^2} \lambda_2 \quad (28)$$

The above Eq. (27) is linear and inhomogeneous. It differs from the usual Schrödinger equation because it contains the terms  $-(r^2/b^4)\psi$ ,  $-\beta_2 P(r)\psi$  and the inhomogeneous term  $-\beta_2 P(r)$ .

A simple expression for the matrix element  $M_{n\ell S}$  can now be derived by multiplying Eq. (27) by  $-(\hbar^2/M)\psi$ , integrating and substituting into the original expression for  $M_{n\ell S}$ . We obtain

$$M = -\frac{\hbar^2}{M} \beta_1 - \frac{\hbar^2}{M} \beta_2 \int_c^\infty P(r) \psi(\psi - \phi) dr - \left(2n + \ell + \frac{3}{2}\right) \hbar \omega \quad (29)$$

The nature of the above stationary value of  $M_{n\ell S}$  can easily be investigated. It is found that this is indeed a minimum unless the eigenvalue problem

$$-\frac{\hbar^2}{M} \frac{d^2 h(r)}{dr^2} + \frac{\hbar^2}{M} \frac{\ell(\ell+1)}{r^2} h(r) + \frac{\hbar^2}{M} \frac{r^2}{b^4} h(r) + v(r) h(r) + \frac{\hbar^2}{M} \beta_1 h(r) + \frac{\hbar^2}{M} \beta_2 P(r) h(r) = \lambda h(r) \quad (30)$$

$$h(c) = 0, \quad h(\infty) = 0$$

has a non-positive eigenvalue (see Ref. [15b]).

In the case  $P(r) = 1$  a simple relation between  $M_{n\ell S}$  and  $\eta^2$  can be derived. This relation is

$$M_{n\ell S} = -\frac{\hbar^2}{M} \left( \beta_1 + \beta_2 \frac{\eta^2}{2} \right) - \left( 2n + \ell + \frac{3}{2} \right) \hbar \omega \quad (31)$$

Numerical calculations have been performed in order to obtain the wave functions  $\psi$  and the matrix element  $M_{n\ell S}$ . In these calculations the extra h. o. potential energies were omitted. The Kallio-Kolltveit potential [14] was used and for each value of  $\beta_2$  the parameter  $\beta_1$  (Lagrange multiplier due to the normalization condition) was varied until  $\psi$  was normalized. In choosing the various values of  $\beta_2$  one must be careful not to use a value for  $\beta_2$  such that<sup>3</sup>  $(\beta_1 + \beta_2) \equiv \beta^2 > 0$  is an eigenvalue of the homogeneous equation. This is not allowed unless the inhomogeneous part of the differential equation happens to be orthogonal to the eigenfunction of the homogeneous equation.

The way in which  $M$  and  $\eta^2$  for the  $^1S_0$  state with  $n=0$  vary with  $\beta_2$  is shown in Fig. 1. It is seen that  $M$  becomes more negative for the smaller values of  $\beta_2$  for which the restriction on  $\psi$  due to condition (25) is weaker. On the other hand,  $\eta^2$  becomes larger for small  $\beta_2$ . Note also that  $\beta_1$  turns out to be quite small and also a slowly varying function of  $\beta_2$  for  $0.5 \lesssim \beta_2 \lesssim 14$ .

<sup>3</sup> We have taken  $P(r) = 1$

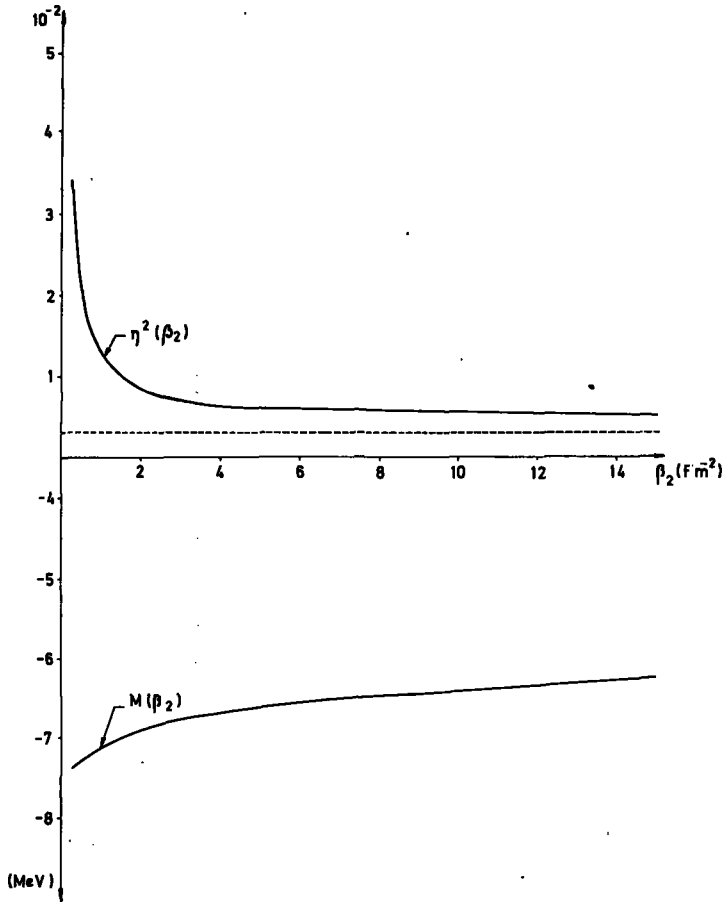


FIG. 1. The diagonal matrix element of the effective interaction  $M = M_{000}$  and the corresponding healing integral  $\eta^2$  as functions of the parameter  $\beta_2$ . ( $\hbar\omega = 13.3$  MeV, Kallio-Kolltveit potential).

TABLE I. VALUES OF THE MATRIX ELEMENTS  $M_{nLS}$  (IN MeV) CALCULATED WITH THE HEALING CONDITION VARIATIONAL METHOD USING THE KALLIO-KOLLTVEIT POTENTIAL AND  $\hbar\omega = 13.3$  MeV

State	$\beta_2 = 7 \text{ fm}^{-2}$	$\beta_2 = 15 \text{ fm}^{-2}$
$^1S_0, n = 0$	- 6.6	- 6.3
$^3S_1, n = 0$	- 10.4	- 9.9

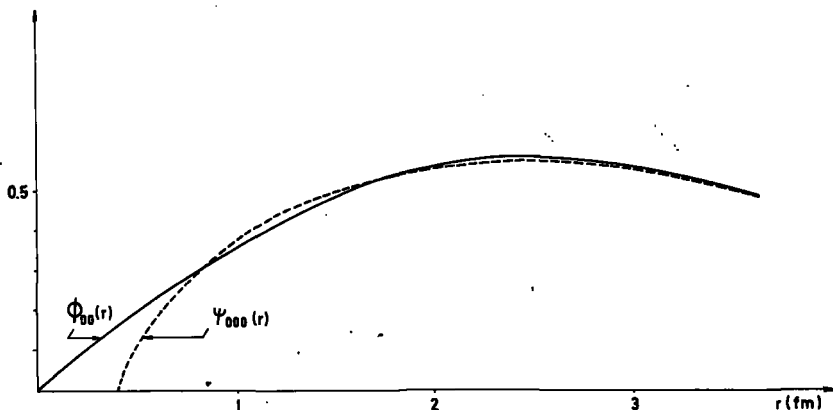


FIG. 2. Uncorrelated (solid line) and correlated (dashed line) relative wave functions obtained with the healing condition variational method ( $\hbar\omega = 13.3$  MeV,  $\beta_2 = 11.5$  fm<sup>-2</sup>, Kallio-Koltveit potential).

Among the possible values of  $\beta_2$  it is necessary to choose one for which the value of  $\eta^2$  is small because then  $\psi$  would heal rapidly and the neglected many-body terms would not be very important. We must note, however, that there is a lower bound for  $\eta^2 \equiv \eta_{n\ell S}^2 : \eta_{n\ell S}^2 > \int_0^{\epsilon} \phi_{n\ell}^2 dr$ . This lower bound is shown by a dotted line in Fig. 1. A reasonable value for  $\beta_2$  should be one for which the value of  $\eta^2(\beta_2)$  is not very far from its lower bound. Therefore the region of very small values of  $\beta_2$  should be excluded. From Fig. 1 it is also obvious that for the larger values the matrix element does not vary very much with  $\beta_2$ . Consequently, the effect on the value of the matrix element will not be very serious if different but rather large values of  $\beta_2$  are chosen. We may also expect that very large values of  $\beta_2$  are not appropriate either. An estimate of the three-body terms (or a suitable approximate treatment of higher terms) should enable us to determine the best values of  $\beta_2 = \beta_{2, n\ell S}$  in analogy with other similar cases.

In Table I some typical values of the matrix elements are given, while in Fig. 2 the uncorrelated ( $\phi_{00}$ ) and correlated  $\psi_{000}(r)$  wave functions are plotted.

## 6. NON-CENTRAL FORCES

The method of the previous section can easily be extended to cover the case of non-central forces. In the general case, the model operator introduces more complicated correlations. A diagonal reduced matrix element of the effective interaction will be

$$\begin{aligned} \langle n\ell SJ | v_{\text{eff}} | n\ell SJ \rangle = & \langle n\ell SJ M_J | e^{-iS_{12}} \left( t_{\text{rel.}} + \frac{\hbar^2}{M} \frac{r^2}{b^4} + v \right) e^{iS_{12}} \\ & - \left( t_{\text{rel.}} + \frac{\hbar^2}{M} \frac{r^2}{b^4} \right) | n\ell SJ M_J \rangle \end{aligned} \quad (32)$$

$$= \langle \psi | t_{\text{rel.}} + \frac{\hbar^2}{M} \frac{r^2}{b^4} + v | \psi \rangle - \langle \phi | t_{\text{rel.}} + \frac{\hbar^2}{M} \frac{r^2}{b^4} | \phi \rangle$$

where now

$$\phi = |n\ell S J M_J\rangle \quad \text{and} \quad \psi = e^{iS_{12}} |n\ell S J M_J\rangle \quad (33)$$

stand for the uncorrelated and correlated wave functions, respectively. The spin  $S$  has been coupled to the relative orbital angular momentum. Also, the isospin quantum numbers have not been written explicitly because they are redundant if the interaction  $v$  and the correlation operator are charge-independent. Following the procedure for central forces, the diagonal matrix elements (32) are minimized subject to the "healing condition"

$$\langle \psi - \phi | P | \psi - \phi \rangle = \eta^2 \quad (34)$$

analogous to Eq. (25) where  $P$  is some positive-definite operator and a normalization condition

$$\langle \psi | \psi \rangle = 1 \quad (35)$$

The variational principle leads to an Euler equation for the correlated wave function

$$\left( t_{\text{rel.}} + \frac{\hbar^2}{M} \frac{r^2}{b^4} + v \right) \psi + \lambda_1 \psi + \lambda_2 P(\psi - \phi) = 0 \quad (36)$$

This equation is analogous to Eq. (27). When  $\psi$  satisfies the Euler equation the matrix element (32) becomes

$$\langle n\ell S J | v_{\text{eff.}} | n\ell S J \rangle = -\lambda_1 - \lambda_2 \langle \psi | P | \psi - \phi \rangle - \langle \phi | t_{\text{rel.}} + \frac{\hbar^2}{M} \frac{r^2}{b^4} | \phi \rangle \quad (37)$$

To solve Eq. (36) it is convenient to separate the radial parts of the wave functions  $\phi$  and  $\psi$  from the spin-angle parts. The functions

$$\psi_{\ell S J}^{M_J} = \sum_{m M_S} \langle \ell S m M_S | J M_J \rangle | \ell m \rangle | S M_S \rangle \quad (38)$$

form a convenient orthonormal set of spin-angle wave functions. We shall assume the operator  $P = P(r) > 0$ ,  $0 < r < \infty$  is a function of the radial coordinate only and that the two-body potential contains central, tensor and spin-orbit parts:

$$v = v_c(r) + v_T(r) \hat{S}_{12} + v_{\ell S}(r) \vec{\ell} \cdot \vec{S} \quad (39)$$

Other parts, e. g. a quadratic spin-orbit potential, could be included in an obvious way. The spin-orbit and tensor parts of the interaction do not contribute when two interacting nucleons are in a singlet state and the analysis of correlations is the same as before. Several possibilities occur for the interaction in triplet states (see Ref. [10a]). Here we give the results for  $S = 1$ ,  $\ell = J \pm 1$ . The uncorrelated and correlated wave functions are

$$\phi = |n\ell 1JM_J\rangle = \frac{1}{r} \phi_{n\ell}(r) \mathcal{Y}_{\ell 1J}^{M_J}, \quad \ell = J \pm 1 \quad (40)$$

$$\psi = e^{iS_{12}} |n\ell 1JM_J\rangle = \frac{1}{r} \left( X_{n\ell}^{(\pm)}(r) \mathcal{Y}_{J+1,1J}^{M_J} + Y_{n\ell}^{(\pm)}(r) \mathcal{Y}_{J-1,1J}^{M_J} \right), \quad \ell = J \pm 1 \quad (41)$$

The correlated radial wave functions  $X_{n\ell}^{(\pm)}$  and  $Y_{n\ell}^{(\pm)}$  satisfy the coupled equations

$$\left[ \frac{d^2}{dr^2} - \frac{(J+1)(J+2)}{r^2} - \frac{r^2}{b^4} - \frac{M}{\hbar^2} \left( v_c(r) - \frac{2(J+2)}{2J+1} v_T(r) - (J+2)v_{\ell S}(r) \right) \right] X_{n\ell}^{(\pm)}(r) - \frac{M}{\hbar^2} \frac{6\sqrt{J(J+1)}}{2J+1} v_T(r) Y_{n\ell}^{(\pm)}(r) = \beta_1 X_{n\ell}^{(\pm)}(r) + \beta_2 P(r)(X_{n\ell}^{(\pm)}(r) - \xi_{n\ell}^{(\pm)}(r)) \quad (42)$$

$$\left[ \frac{d^2}{dr^2} - \frac{J(J-1)}{r^2} - \frac{r^2}{b^4} - \frac{M}{\hbar^2} \left( v_c(r) - \frac{2(J-1)}{2J+1} v_T(r) + (J-1)v_{\ell S}(r) \right) \right] Y_{n\ell}^{(\pm)}(r) - \frac{M}{\hbar^2} \frac{6\sqrt{J(J+1)}}{2J+1} v_T(r) X_{n\ell}^{(\pm)}(r) = \beta_1 Y_{n\ell}^{(\pm)}(r) + \beta_2 P(r)(Y_{n\ell}^{(\pm)}(r) - \theta_{n\ell}^{(\pm)}(r))$$

where we have put

$$\xi_{n\ell}^{(+)} = \phi_{n\ell}, \quad \theta_{n\ell}^{(+)} = 0 \quad (43a)$$

$$\xi_{n\ell}^{(-)} = 0, \quad \theta_{n\ell}^{(-)} = \phi_{n\ell} \quad (43b)$$

The radial correlated wave functions satisfy the boundary conditions

$$X_{n\ell}^{(\pm)}(c) = Y_{n\ell}^{(\pm)}(c) = X_{n\ell}^{(\pm)}(\infty) = Y_{n\ell}^{(\pm)}(\infty) = 0 \quad (44)$$

and should be normalized so that

$$\int_c^\infty [(X_{n\ell}^{(\pm)}(r))^2 + (Y_{n\ell}^{(\pm)}(r))^2] dr = 1 \quad (45)$$

A diagonal matrix element of the effective interaction reduces to

$$\begin{aligned} \langle n\ell 1J | v_{\text{eff}} | n\ell 1J \rangle = & -\frac{\hbar^2}{M} \beta_1 - \frac{\hbar^2}{M} \beta_2 \int_c^\infty P(r) X_{n\ell}^{(\pm)}(r) (X_{n\ell}^{(\pm)}(r) - \xi_{n\ell}^{(\pm)}(r)) dr \\ & - \frac{\hbar^2}{M} \beta_2 \int_c^\infty P(r) Y_{n\ell}^{(\pm)}(r) (Y_{n\ell}^{(\pm)}(r) - \theta_{n\ell}^{(\pm)}(r)) dr - \left(2n + \ell + \frac{3}{2}\right) \hbar\omega \end{aligned} \quad (46)$$

Analogous expressions can be derived for off-diagonal matrix elements. The Eqs (42) are very similar to the equations of the deuteron or of nucleon-nucleon scattering and reduce to them if  $\beta_2$  is put equal to zero and the terms  $-(r^2/b^4)X_{n\ell}^{(\pm)}(r)$  and  $-(r^2/b^4)Y_{n\ell}^{(\pm)}(r)$  are omitted.

## 7. APPLICATIONS AND REMARKS

Certain applications of the matrix elements of the effective interaction determined in the previous sections have been made. We mention them here very briefly.

The ground-state energy of the  $^{16}\text{O}$  nucleus has been calculated by using the matrix elements obtained with both methods [15]. The following expression has been used:

$$\begin{aligned} E_{(^{16}\text{O})} = & T + V_c + 21[\langle 00, 0 | v_{\text{eff}} | 00, 0 \rangle + \langle 00, 1 | v_{\text{eff}} | 00, 1 \rangle] \\ & + 6[\langle 01, 0 | v_{\text{eff}} | 01, 0 \rangle + 9\langle 01, 1 | v_{\text{eff}} | 01, 1 \rangle] + 7.5[\langle 02, 0 | v_{\text{eff}} | 02, 0 \rangle \\ & + \langle 02, 1 | v_{\text{eff}} | 02, 1 \rangle] + 1.5[\langle 10, 0 | v_{\text{eff}} | 10, 0 \rangle + \langle 10, 1 | v_{\text{eff}} | 10, 1 \rangle] \end{aligned} \quad (47)$$

The first term in this expression is the kinetic-energy term, in which the correction due to the centre-of-mass motion is included:

$$T = 17.25 \hbar\omega \quad (48)$$

The second term is the Coulomb energy of the  $^{16}\text{O}$  nucleus. This was calculated with the uncorrelated wave function:

$$V_c = \frac{83e^2}{2\sqrt{\pi}} \cdot \frac{1}{b} \quad (49)$$

The value  $E_{(^{16}\text{O})} = -143.3$  MeV was obtained using the Kallio-Kolltveit potential and the healing condition variational method with  $\beta_2 = 5 \text{ fm}^{-2}$  and  $b = 2.494$  fm. If  $\beta_2$  is chosen  $8 \text{ fm}^{-2}$ ,  $E_{(^{16}\text{O})}$  is  $-132.4$  MeV. These values are quite close to the experimental one ( $-127.56$  MeV).

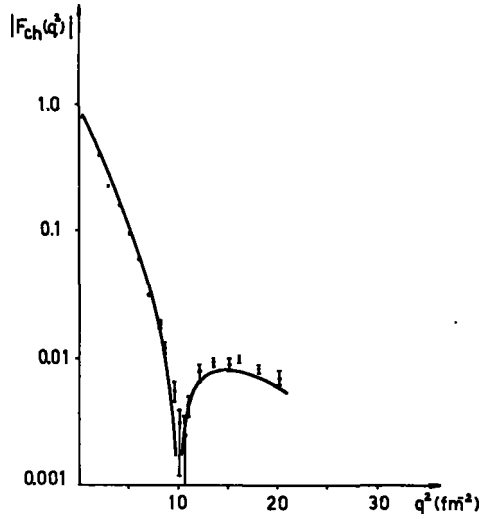


FIG. 3. The absolute value of the charge form factor of  ${}^4\text{He}$  fitted to the experimental points. The healing-condition variational method was used and  $b_1 = b/\sqrt{2}$  and  $\beta_2$  were treated as adjustable parameters.

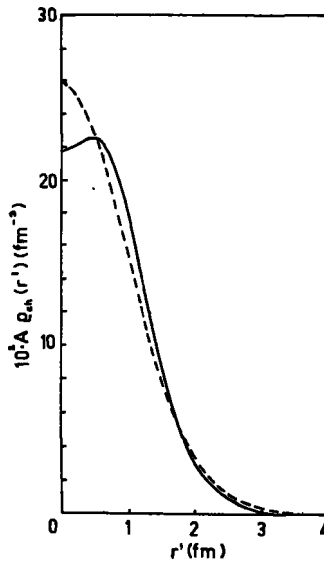


FIG. 4. The solid line is  $A$  ( $\approx 4$ ) times the nuclear-charge-density distribution  $\rho_{\text{ch}}(r')$  of  ${}^4\text{He}$ , obtained with the healing condition variational method using the best fit values of  $b_1$  and  $\beta_2$ . The dashed line is  $A$  ( $\approx 4$ ) times the harmonic-oscillator shell-model nuclear-charge-density distribution with the best fit value of  $b_1$  (see Ref. [16b]).

The matrix elements of the effective interaction obtained with a preliminary version of the separation condition variational method (in which the normalization had been neglected) has been used in calculations of hyper-nuclei [17] and in calculations of nucleon separation energies [18].

In addition, the two-body wave functions determined with the healing condition variational method have been used in calculating the charge form factor of nuclei in Born approximation [16]. The calculated charge form factor of  ${}^4\text{He}$  has been fitted to the experimental one by using again the Kallio-Kolltveit potential and treating the oscillator strength  $b_1 = b/\sqrt{2}$  and the "healing parameter"  $\beta_2$  as adjustable parameters. The fit is very good even in the region of high momentum transfers (see Fig. 3). The calculated charge form factor of  ${}^4\text{He}$  has subsequently been used in obtaining the charge density distribution of this nucleus. This is shown in Fig. 4. It is seen that the maximum of the density distribution is not at the centre. This sort of behaviour, although common for the charge-density distributions of heavier nuclei as, for example,  ${}^{12}\text{C}$ , was found for  ${}^4\text{He}$  for the first time.

We conclude with the following remarks concerning the two-body correlations by means of which the effective interaction matrix elements are determined from the free nucleon-nucleon potential in the way we have described:

(1) There is a similarity of the differential equations in both variational methods (which are characterized by a sort of inhomogeneity [10]) with the corresponding equations of the simplified versions of Brueckner's reaction matrix theory, namely the Moszkowski and Scott separation method [13] (see Eq. (2.21) of Ref. [1]) and the reference spectrum method [19], applied to finite nuclei [1]. The differential equation in the latter case is

$$\frac{d^2\psi^R}{dr^2} - \frac{\ell(\ell+1)}{r^2}\psi^R - \gamma^2\psi^R - \frac{M}{\hbar^2}v(r)\psi^R = -\left(\frac{M}{\hbar^2}E_{n\ell} + \gamma^2\right)\phi_{n\ell} + \frac{r^2}{b^2}\phi_{n\ell} \quad (50)$$

$$c < r < \infty$$

However, as has already been pointed out by Baranger (see Ref. [20], p. 609) in spite of this "striking superficial similarity, the formalism is basically different".

(2) The correlations are state-dependent. In the standard Jastrow method [7, 21] they are state-independent, and, in addition, non-central forces are not treated.

(3) The shape of the correlated two-nucleon wave functions (which have been determined by means of functional variation) depends upon the nucleon-nucleon potential. Again, this is not the case in most calculations performed with Jastrow wave functions.

#### ACKNOWLEDGEMENTS

I would like to thank Drs F. Palumbo and G. Ripka for useful discussions and comments.

#### REFERENCES

- [1] KUO, T.T.S., BROWN, G.E., Nucl. Phys. **85** (1966) 40.  
 [2] KALLIO, A., DAY, B.D., Nucl. Phys. **A124** (1969) 177.

- [3] BANERJEE, B., PARIKH, J.C., RAO, Y.S.T., Nucl. Phys. A94 (1967) 481.
- [4] SHAKIN, C.M., WAGHMARE, Y.R., TOMASELLI, M., HULL, M.H., Jr., Phys. Rev. 161 (1967) 1015.
- [5] KIRSON, M.W., these Proceedings.
- [6] BRUECKNER, K., in The Many-Body Problem, Les Houches (1958), published by Dunod, Paris.
- [7] a) JASTROW, R., Phys. Rev. 98 (1955) 1479;  
b) IWAMOTO, F., YAMADA, H., Progr. Theor. Phys. (Kyoto) 17 (1957) 543;  
c) CLARK, J.W., WESTHAUS, P., Phys. Rev. 141 (1966) 833;  
d) RIPKA, G., these Proceedings.
- [8] VILLARS, F., Proc. Int. School of Physics Enrico Fermi, Course 23, Academic Press, New York (1963).
- [9] DA PROVIDENCIA, J., SHAKIN, C.M., Ann. Phys. (NY) 30 (1964) 95.
- [10] a) BRINK, D.M., GRYPEOS, M.E., Nucl. Phys. A97 (1967) 81;  
b) GRYPEOS, M.E., Proc. Int. School of Physics Enrico Fermi, Course 40, Academic Press, New York (1969).
- [11] a) GRYPEOS, M.E., Nucl. Phys. A141 (1970) 400.  
b) GRYPEOS, M.E., (in preparation).
- [12] PALUMBO, F., Phys. Rev. C1 (1970) 129.
- [13] MOSZKOWSKI, S., SCOTT, B., Ann. Phys. (NY) 11 (1960) 65.
- [14] KALLIO, A., KOLLTVEIT, K., Nucl. Phys. 53 (1964) 87.
- [15] GRYPEOS, M.E., a) Nuovo Cim. Letts 2 (1969) 117;  
b) Phys. Letts 34B (1971) 481.
- [16] GRYPEOS, M.E., a) Phys. Rev. Letters 23 (1969) 793; b) Nuovo Cim. Letts 3 (1970) 31.
- [17] BRINK, D.M., GRYPEOS, M.E., Nucl. Phys. 80 (1966) 681.
- [18] BRINK, D.M., SHERMAN, N., Nucl. Phys. A94 (1967) 385.
- [19] BETHE, H.A., BRANDOW, B.H., PETSCHKE, A.G., Phys. Rev. 129 (1963) 225.
- [20] BARANGER, M., Proc. Int. School of Physics Enrico Fermi, Course 40, Academic Press, New York (1969).
- [21] DĄBROWSKI, J., Proc. Phys. Soc. 71 (1958) 658.

**PART III: SLOWING-DOWN AND  
IMPLANTATION OF IONS IN SOLIDS**



# ION IMPLANTATION AND CHANNELLING

J. A. DAVIES

Chalk River National Laboratory  
Chalk River, Canada

## Abstract

### ION IMPLANTATION AND CHANNELLING.

1. Heavy-ion ranges in solids; 1.1. Introduction; 1.2. Anodizing-stripping method; 1.3 Range measurements; 1.4. Comparison with theory; 1.5. Stopping-power ( $dE/dx$ ) studies; 2. Ranges in single crystals; 2.1. Historical introduction; 2.2. Experimental techniques; 2.3. Qualitative features of channelled range distributions; 2.4. Factors affecting range profiles; 2.5. Quantitative features of channelled range distributions; 2.6.  $Z_1$ -oscillations for channelled ions; 3. Channelling behaviour of low-Z ions (protons, helium, etc.) at MeV energies; 3.1. Introduction, 3.2. Theoretical framework; 3.3. Experimental technique; 3.4. General features of axial (and planar) channelling experiments; 3.5. Comparison of various close-encounter processes; 3.6. "Blocking" experiments; 3.7. Positron channelling; 3.8. Comparison with theory at zero depth; 3.9. Depth dependence of  $\psi_1$  and  $\chi_{\min}$ ; 4. Applications of channelling to solid-state science; 4.1. Introduction; 4.2. Channelling-effect technique of atom location; 4.3. Foreign-atom detection; 4.4. Applications in ion-implanted silicon; 4.5. Yb in silicon case; 4.6. Lattice disorder and surface contamination; 4.7. Foreign-atom location on the surface; 4.8. Surface structure of clean crystals; 5. Problems of ion implantation; 5.1. General features; 5.2. Advantages of implantation; 5.3. Penetration depth; 5.4. Radiation damage; 5.5. Foreign-atom location; 5.6. Electrical behaviour of implanted dopants; 6. Nuclear and crystallographic applications of channelling; 6.1. Introduction; 6.2. Crystal-alignment techniques; 6.3. Nuclear life-time studies; 6.4. Fission life-times; 6.5. Life-times of the (p, p') reaction; 6.6. Doppler-shift life-time studies; 6.6. Polarized deuteron beams.

### INTRODUCTORY REMARKS

This is a series of lectures — to be called sections henceforth — on the experimental aspects of ion implantation and channelling. It is intended to be a complementary contribution to the theoretical paper by Professor Lindhard, which is, however, not published in these Proceedings. At the outset, we shall give a brief outline of what we intend to cover in the individual sections.

The first two sections will consider the available experimental information on the question, "How deep does an ion penetrate in a solid?" In this section, we confine ourselves to penetration phenomena (ranges, etc.) in the absence of lattice-steering effects such as channelling. For want of a better word, these are often referred to as amorphous-target ranges, although they include polycrystalline material and even, to a first approximation, ranges in non-aligned (random) directions of single crystals. Subsequently, we shall discuss how the crystal lattice can gently steer or "channel" an ion beam, and thus greatly enhance its range.

Both sections will be restricted to the low-velocity region, i. e. to velocities  $v \ll v_0 Z_1^{2/3}$  where  $v_0 = 2.2 \times 10^8$  cm/s, and  $Z_1$  is the atomic number of the projectile. We also confine ourselves to heavy ions, namely to  $Z_1$  values between something like 10 and 92.

This particular region of  $Z_1$  and  $v$  is presently attracting a great deal of interest in the frontier area between nuclear, solid-state, and atomic-collision physics. One of the main reasons is the recent emergence of

ion implantation as a practical process for introducing specific foreign atoms into various types of solid substrate — such as doping semiconductors, implanting radioactive nuclei in magnetic crystals, etc.

In sections 3 and 4, we shall continue to look at channelling effects but in a completely different region of velocity and atomic number: i. e. the region of  $Z_1 < 10$ , and  $v > v_0 Z_1^{2/3}$ . In this high-velocity region, one observes some very strong channelling effects, and in section 3 we shall examine the experimental evidence for the influence that the crystal lattice exerts on all violent-collision processes — such as nuclear-reaction yields, Rutherford scattering, Coulomb excitation. We shall also see how well these channelling effects compare with the predicted behaviour from Lindhard's theoretical description.

It turns out that channelling also has useful applications in crystallography and other fields — and in sections 4, 5 and 6 we shall discuss some of the more interesting ones that have appeared. For example, channelling provides us with a probe for observing atomic displacements on a distance scale of about one-tenth of an ångström. If an atom is displaced from the regular lattice site by more than 0.1 - 0.2 Å (i. e. 2 - 5% of the lattice spacing) channelling effects are able to observe and quantitatively measure this displacement. Many interesting applications of channelling to solid-state problems are based on this ability to pinpoint where atoms are sitting in crystals: One can determine substitutional content, radiation damage, the location of impurity atoms on crystal surfaces, and so forth. Sections 4 and 5, therefore, will deal with the applications of channelling in various solid-state studies, and section 5 will also consider in more detail the specific case of ion-implanted semiconductors — as this is certainly the most extensive (and probably the most exciting) application to date.

It turns out that channelling effects can also be used to determine the position of a recoiling atom at the moment it undergoes some sort of charged-particle decay. So, the same process of channelling enables us to observe extremely short nuclear life-times: in ideal cases, life-times from  $10^{-14}$  s down to  $10^{-18}$  s or even less. This and other applications in nuclear physics plus some simple applications in crystallography, will be described in section 6.

The above is a brief review of what each section will contain. The reader may be wondering what convenient references are available: unlike the theoretical side, it is difficult to select one individual paper or review article that covers the same material as this contribution. Probably the best general reference at present is the book "Ion Implantation in Semiconductors" (Academic Press, 1970) by J. W. Mayer, L. Eriksson and myself. Here, the reader will find a rather extensive list of references to all of the topics covered (except section 6); also, at least 50% of the illustrations used in this contribution are taken from figures in this book.

Another interesting reference is the paperback "New Uses of Low Energy Accelerators", published by the US Academy of Sciences in 1968, with the objective of providing a simple guide to people with rather limited research budgets who are looking for interesting problems to tackle with low-energy ( $\approx 5$  MeV) accelerators. On the same theme, there is also a good review article in ORNL Conf. 680411 (1968): "Particle channelling experiments using small accelerators", by W. M. Gibson.

Finally, for those who wish to delve more deeply into the original literature, we should suggest as a starting point the published proceedings

of a series of conferences entitled, "Atomic Collisions in Solids". These conferences have been held every two years:

- 1) in 1965 — University of Aarhus, Denmark — published in Nuclear Instruments and Methods, 38.
- 2) in 1967 — Chalk River Nuclear Laboratory, Canada — published in Canadian Journal of Physics, 46.
- 3) in 1969 — University of Sussex, England — published as a book by North-Holland Publishing Company.

The next conference in this series was held in September 1971 in Norway; the proceedings are expected to appear early in 1972 in Radiation Effects.

## 1. HEAVY-ION RANGES IN SOLIDS

### 1.1. Introduction

Why are we interested in measuring the range of heavy ions? We have already indicated that one reason is the recent upsurge in ion-implantation work: if you wish to implant semiconductors, for example, with various dopant species, you need information on how deep the ions penetrate. Similarly, in many other branches of science — such as nuclear spectroscopy or radiation damage studies — the distance that an energetic recoil atom travels through a solid is one of the important experimental parameters. A more fundamental reason for measuring heavy-ion ranges is to provide accurate experimental data for testing the theoretical predictions of Lindhard and others on the slowing-down behaviour. In the low-velocity ( $v \ll v_0 Z_1^{2/3}$ ) region, there was virtually no experimental information available on heavy-ion ranges prior to 1960. And, of course, any field where no experimental information exists is interesting 'per se'. It was to remedy this paucity of data that several groups, including our own at Chalk River, decided to enter the ion penetration field.

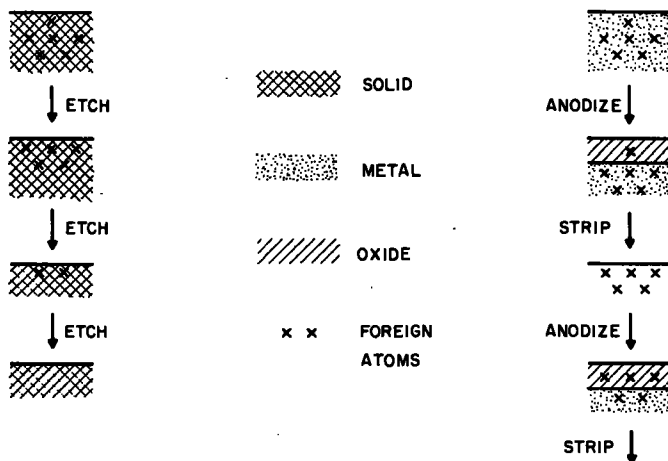
The main reason for the lack of experimental information was simply the practical problem of how to measure the rather small penetration depths involved. The principle is simple: you take a solid target, bombard it with a beam of ions (preferably radioactive ones) of atomic number  $Z_1$  and energy  $E$ , and then measure the resulting depth distribution by sectioning the target into a series of thin uniform slices and measuring the radioactive content of each slice. The practical difficulty is that the mean range  $R$  of, say, a 10-keV Xe ion is only  $\sim 30$  Å.

During the early 1960's many different experimental techniques for measuring small penetration depths were proposed and tested. Not all of these techniques turned out to be successful, but in Fig. 1.1 are summarized the ones that have achieved sufficient sensitivity and reliability to be used for depth-probing measurements. The methods can be divided into two categories — chemical and physical — although the physical methods might better be described as "nuclear physical" methods.

In the chemical method, one injects radioactive ions into a solid (as described above), and then determines the depth distribution of these radioactive ions by removing successive uniform layers from the surface of the solid and measuring the residual radioactivity in the target. There are various ways of accomplishing this: simple chemical etching of the target

## LOCATION OF ATOMS AT SMALL DEPTHS

## A. CHEMICAL METHODS



## B. PHYSICAL METHODS

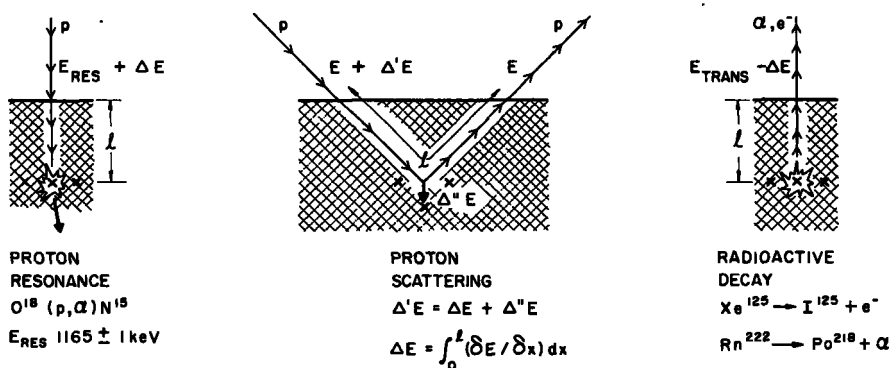


FIG. 1.1. Techniques for measuring the depth distribution of foreign atoms at shallow depths in a solid.

can be used, as shown on the left-hand side of Fig. 1.1. However, etching processes are not noted for their uniformity or reproducibility.

There are ways in which one can improve the uniformity. The chemical method which we shall discuss here is one developed at Chalk River in which the etching process is subdivided into two steps. The first step is an electrochemical one in which one converts a surface layer of the target into a protective oxide by electrochemical oxidation (known as anodizing). For certain elements (such as Al, Si, Ta and W) these anodic oxides are quite uniform,

and their thickness increases almost linearly with anodizing voltage, at a rate of  $\sim 10$  Å per volt. The second step consists in dissolving off the anodized layer chemically with a reagent that does not attack the underlying material. This 2-step cycle may then be repeated as often as necessary and thus the entire range profile can be obtained. For the above group of targets, the method works extremely well, and has been extensively applied [1]. It is described in more detail later in this section.

There are several other variations of the chemical approach: for example, Whitton [2] has developed a method based on a sensitive mechanical polishing unit known as a vibratory polisher, with which he can actually polish 50 - 100 Å layers off the surface of any material that is sufficiently hard, using an aluminium oxide paste, with quite good reproducibility; also, a group in Munich under Sizmann [3] has used low-energy ion-sputtering to erode the surface at a controlled rate. So, there are various ways in which one can remove thin uniform layers.

There are also several variations of what one might call the nuclear-physics approach: i. e. the use of some other radiation or high-energy particle (for which we know the rate of energy loss) to identify the depth of the implanted foreign atom. For example, suppose the implanted foreign atom on the bottom right-hand side of Fig. 1.1 is a radioactive atom, which decays by giving off monoenergetic electrons or alpha particles. Since one knows the initial energy with which the particle starts and since one can measure accurately the energy with which it is emitted from the solid, then from the difference,  $\Delta E$ , one can calculate the depth at which that particular atom was located, provided, of course, the rate of energy loss ( $dE/dx$ ) of the particles is known.

Even if the atom is not radioactive, one can use an external beam, provided there is some nuclear reaction in the atom that has a very sharp resonance. For instance, if one wants to obtain a range distribution of oxygen, one can use the isotope  $^{18}\text{O}$  which has a very sharp ( $p, \alpha$ ) resonance at 1165 keV (bottom left-hand side of Fig. 1.1); hence, the incident proton energy must be increased above 1165 keV in order to be at the resonance energy when it penetrates to the depth of the oxygen atoms. By measuring accurately this excess energy  $\Delta E$  and knowing the rate of energy loss of protons, one again obtains the depth distribution.

The method illustrated in the lower centre of Fig. 1.1 has been the most extensively used of the nuclear-physical methods. It is similar to the proton-resonance method, but uses Rutherford backscattering instead of a nuclear reaction. A proton, or helium ion, scattering off a foreign atom in a target loses energy on the way in and again on the way back out of the target. So if one knows the incident energy and measures accurately the emitted energy, then (after subtracting the calculated elastic energy loss on scattering) one can again determine the depth. This is illustrated better in Fig. 1.2 - a schematic diagram depicting the energy spectrum of backscattered helium from a thick silicon target containing a small amount of an embedded foreign atom (antimony). A sharp threshold is observed, - in this case at  $0.59 E_0$ , since a helium atom (mass 4) on being scattered through  $\sim 150^\circ$  by a silicon atom (mass 28) loses approximately 41% of its energy. So the backscattered spectrum off the silicon target consists of a sharp edge at  $0.59 E_0$  and then a continuum extending to lower energies, corresponding to scattering from progressively larger depths into the silicon substrate. Suppose the silicon substrate contains some foreign atoms that we have injected and whose depth

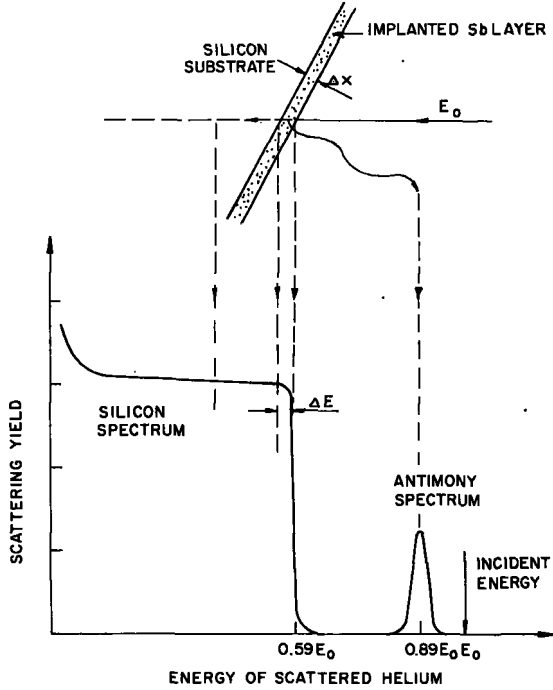


FIG.1.2. Schematic representation of the energy spectrum of a helium beam (incident energy,  $E_0$ ) backscattered from a thick silicon target in which some heavy atoms (Sb) are embedded at a shallow depth.

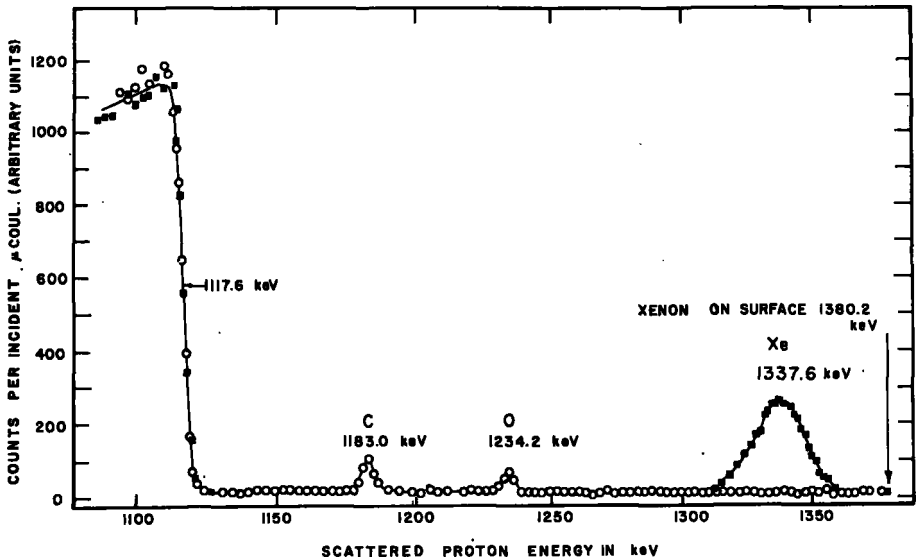


FIG.1.3. Energy spectrum of protons scattered  $90^\circ$  from a beryllium target into which had been injected  $5 \times 10^{15}$  Xe atoms/cm<sup>2</sup> at 1.0 MeV. Incident proton energy: 1401.7 keV (from Powers et al., Ref.[4]).

distribution we are trying to determine. The energy loss on backscattering off a heavy foreign atom (such as antimony) will be considerably less than 41%, and so its spectrum will occur as a peak at much higher energy than the silicon threshold. If the antimony atoms were located right on the surface, the helium would lose only 11% of its energy, and so the peak would occur at  $0.89 E_0$ . Thus, provided the foreign atom whose range we want to determine is heavier than the substrate atom, we can get a clearly differentiated signal for scattering off the foreign atom. If the antimony atoms, instead of being on the surface, had penetrated some finite depth, then this peak would be shifted to somewhat lower energy: from the magnitude of the shift we determine the mean range, and from the broadening of the peak we can determine the range straggling. This Rutherford scattering technique for measuring ion ranges has been extensively used by Powers et al. [4].

Figure 1.3 is one of his typical backscattered energy spectra: i. e. the Rutherford-scattered spectrum observed when a beam of  $\sim 1400$ -keV protons is injected into a beryllium target in which 1-MeV xenon atoms had previously been implanted. Protons scattering off a beryllium atom lose  $\sim 30\%$  of their energy, and thus there is a sharp threshold at 1117 keV for backscattering off the beryllium substrate. At a very much higher energy is the scattering from the xenon. The arrow near the right hand side indicates the calculated energy for backscattering off xenon atoms located right on the surface of the crystal. So, from the observed displacement of the xenon peak, one obtains the mean depth of the xenon (in this particular case, it is  $\sim 8000 \text{ \AA}$ ); and, from the width of the peak, one gets the range straggling. As an added bonus in Fig. 1.3, one also observes several small peaks at intermediate energies; these correspond to scattering from carbon and oxygen atoms on the surface of the beryllium target. In fact, one of

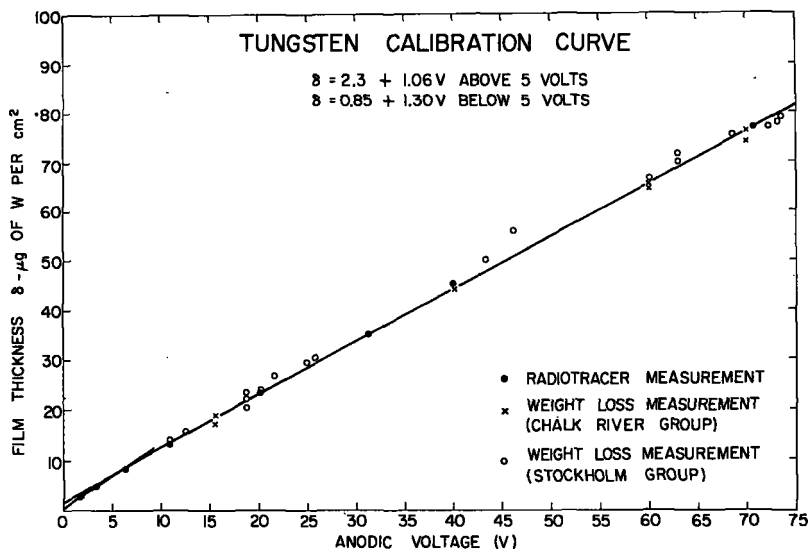


FIG. 1.4. Calibration curve of the thickness of tungsten converted to anodic oxide ( $\text{WO}_3$ ) as a function of the anodizing voltage (from Ref. [5]).

the advantages of Rutherford scattering is that it gives you a detailed mass analysis of the surface contamination — and in many of these problems dealing with ions recoiling into a solid, surface cleanliness is one of the vital questions to be considered. The areas of these two small peaks in Fig. 1.3 indicate that there are  $\sim 10$  atomic layers of oxygen and  $\sim 30$  atomic layers of carbon on the surface of this particular target.

One advantage of the Rutherford scattering technique for measuring ranges — its greatest advantage, in our opinion — is the fact that one can re-determine the range as often as one likes without destroying the sample. Hence, it can be used to study changes in the depth distribution with temperature, oxide film growth, etc. Also, it can be used to analyse for any implanted ion that is heavier than the substrate. Its main limitations (compared with the 2-step anodizing method) are that the depth resolution is not so good, and that it requires a rather large concentration of foreign atoms. The best depth resolution attainable with the scattering technique is  $\sim 50 - 100 \text{ \AA}$  (compared to better than  $5 \text{ \AA}$  with the anodizing method); since the range of a 10-keV Xe is only  $\sim 30 \text{ \AA}$ , the scattering technique has not been of much use below 100 keV. Data such as those in Fig. 1.3 require a foreign-atom concentration of at least 0.1 - 1 atom%. For single-crystal channelling studies, such a high concentration would usually introduce an unacceptable amount of radiation damage; for measuring ranges in non-crystalline material, however, this is usually not a problem.

## 1.2. Anodizing-stripping method

We shall now look in more detail at the most extensively used chemical method for measuring ranges, namely the anodic oxidation-chemical stripping method. As we noted earlier, there is a group of elements (the so called 'valve' metals) that form highly protective oxides when subjected to anodic oxidation. Furthermore, they have the very nice feature that the oxide thickness is quite uniform and increases almost linearly with the applied voltage at a rate of 10 - 15  $\text{\AA}$  per volt. The voltage can be varied from less than one volt up to several hundred volts; hence, by selecting the appropriate voltage, one can form a surface-oxide film whose thickness can be adjusted from  $\lesssim 10 \text{ \AA}$  up to several thousand  $\text{\AA}$ . Having done this, one then searches for a reagent which will dissolve the oxide layer without attacking the underlying metal; for example, in the case of tungsten, the anodic oxide  $\text{WO}_3$  is very soluble in alkaline solution, such as potassium hydroxide, whereas the metal is unattacked.

One limitation of the method is that one destroys the range distribution in the process of measuring it, so that one cannot go back and measure changes in distribution with temperature and so on. However, this is not a serious limitation in most range studies. A more significant one is that it can be used only for those targets that have the property of forming thin protective oxide films. At present there are about 8 elements that have been successfully tested: Al, Si, V, Mo, Nb, Ta, W and Au.

One of the major advantages is that virtually any foreign ion can be studied, since almost all heavy ions (above mass 20) have a suitable radio-tracer. The depth sensitivity of the method is extremely high, as can be seen from the calibration curve in Fig. 1.4. This shows the thickness of tungsten converted to oxide as a function of the anodizing voltage. The three sets of calibration data are all in reasonable agreement, and indicate

a roughly linear relationship with a slope of  $\sim 1 \mu\text{g}/\text{cm}^2/\text{V}$ . Note  $1 \mu\text{g}$  of tungsten per  $\text{cm}^2$  is equivalent to about  $5 \text{ \AA}$  — so the slope of this line is about  $5 \text{ \AA}$  per volt. There is a small intercept at zero voltage, and the thinnest layer that can be removed is  $\sim 10 \text{ \AA}$ . But the reproducibility is considerably better than this: i. e.  $\sim 1 - 2 \text{ \AA}$ . So it is a very sensitive and a very reproducible method of obtaining range profiles. Another advantage of this and of all the chemical methods is that, by implanting radio-tracers, one may use much smaller concentrations of foreign atoms than in the Rutherford scattering case. For Rutherford scattering, we noted above that one needed 0.1 - 1 atom% in order to observe a reasonable scattered peak; on the other hand, for anodizing (using radiotracers), one can quite readily decrease the foreign-atom concentration by another 3 or 4 orders of magnitude — i. e. to  $\sim 1 \text{ ppm}$ .

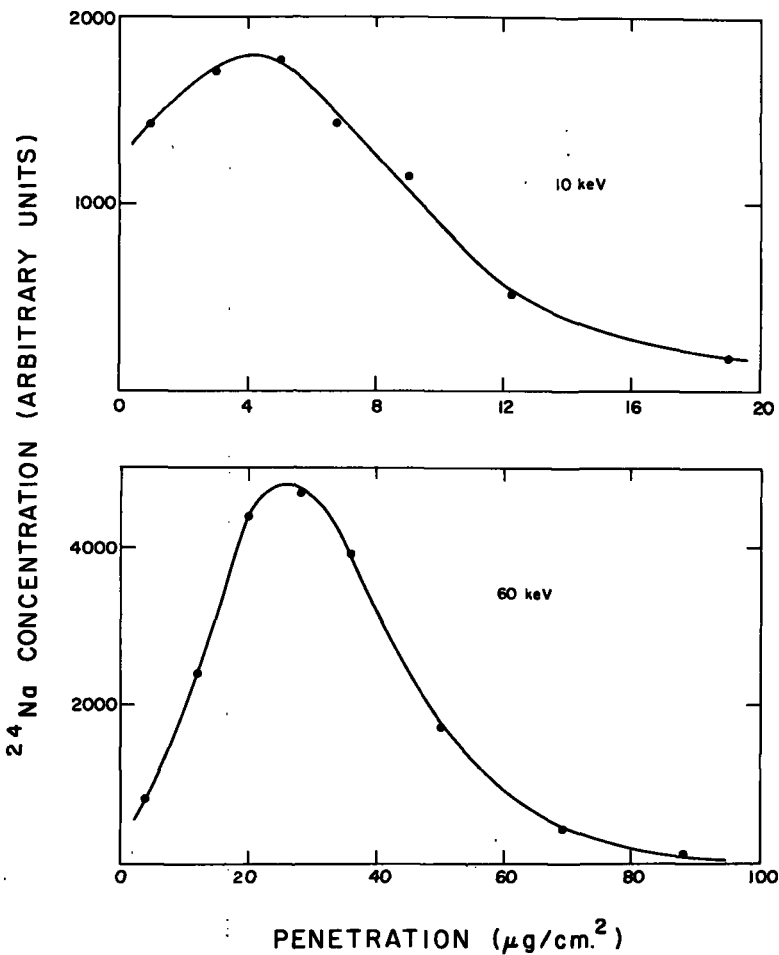


FIG. 1.5. Range distributions for  $^{24}\text{Na}$  in polycrystalline aluminium (from Ref. [6]).

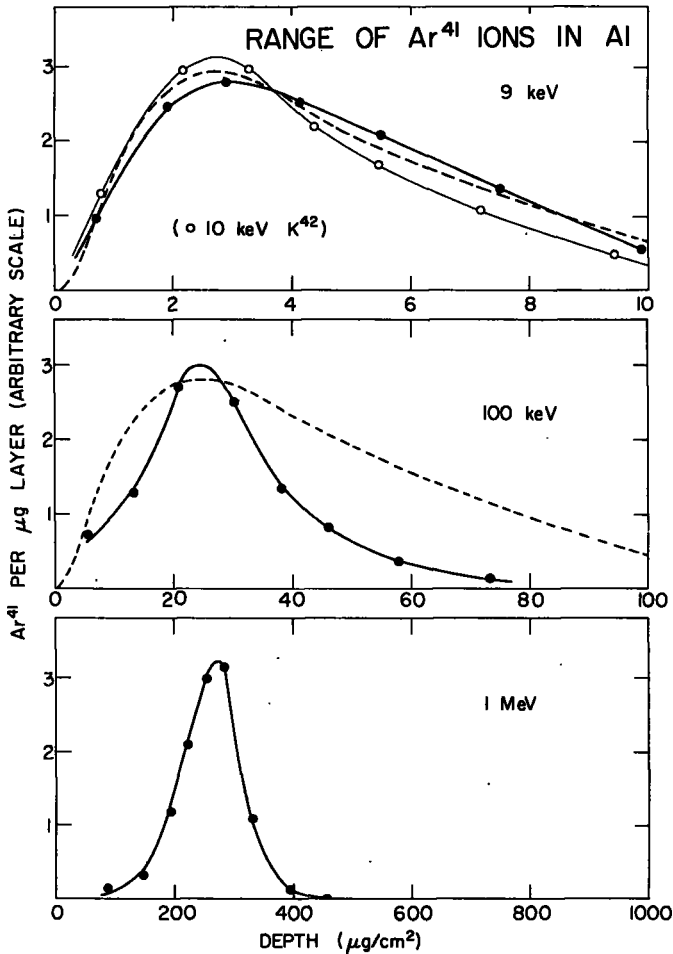


FIG.1.6. Range distributions for  $^{41}\text{Ar}$  (and  $^{42}\text{K}$ ) in polycrystalline aluminum (from Ref. [1]).

### 1.3. Range measurements

Figure 1.5 illustrates the type of range profile that one obtains by means of this anodizing technique. In aluminium, a depth of  $1\ \mu\text{g}/\text{cm}^2$  is equivalent to about  $40\ \text{\AA}$ , and so the position of the peak in the upper (10-keV) curve corresponds to a depth of  $\sim 150\ \text{\AA}$ .

As far as range profiles are concerned, there are two qualitative features to note in Fig. 1.5. Firstly, as the energy of the  $^{24}\text{Na}$  is increased from 10 to 60 keV, we see that the relative width of the range distribution becomes much sharper. This is due largely to a gradual transition, with increasing energy, from nuclear scattering to electronic scattering; and it is the nuclear collisions which give rise to most of the range straggling. Secondly, we should like you to note that the distributions in Fig. 1.5 are

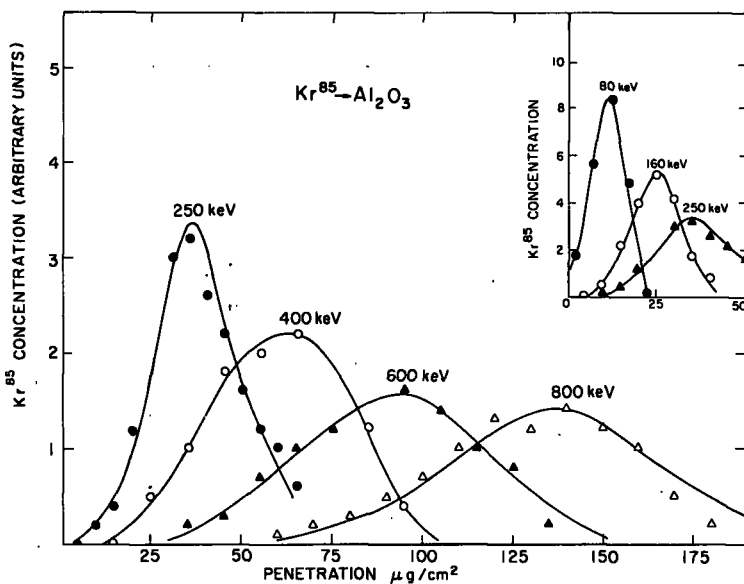


FIG. 1.7. Range distributions for  $^{85}\text{Kr}$  in amorphous  $\text{Al}_2\text{O}_3$  (from Ref. [8]). In  $\text{Al}_2\text{O}_3$ ,  $1 \mu\text{g}/\text{cm}^2$  is equivalent to  $\sim 30 \text{ \AA}$ .

not symmetric, but contain a rather prominent tail in the distribution, especially for the 10-keV case. These experiments were carried out in 1959-60 a few years before the channelling effect had been recognized or even seriously proposed. It turned out afterwards that this was one of the first experimental evidences of ion-channelling, although we did not recognize it as such at the time. The measurements had been carried out in polycrystalline aluminium foil, and these tails in the distribution were explained a few years later by Robinson and Oen [7] as being associated with that small fraction of the polycrystalline grains in the aluminium surface that were (by chance) aligned with the incoming beam direction: channelling of the incident ions in those grains then gives them an enhanced penetration.

These same qualitative features are seen also in Fig. 1.6, for a slightly heavier ion, argon, in polycrystalline aluminium at several different energies. Again, the peak becomes much sharper as the energy increases from 9 keV up to 1 MeV - due to the reduced importance of nuclear collisions. And again, in the low-energy region, we see a very pronounced tail (due to channelling) which has almost disappeared by the time the energy reaches 1 MeV.

Figure 1.7 illustrates another set of range profiles, using  $^{85}\text{Kr}$ , but injecting it into an amorphous target (aluminium oxide) instead of into polycrystalline aluminium. These profiles were obtained by a simple modification of the anodizing/stripping technique: i. e. forming the anodic oxide layer on the aluminium target first, then injecting the  $^{85}\text{Kr}$ , and finally removing chemically the  $\text{Al}_2\text{O}_3$  layer to determine what fraction of the  $^{85}\text{Kr}$

TABLE 1.1. RANGES IN POLYCRYSTALLINE TARGETS

Target	Projectile	Energy region (keV)	Precision	Reference
Be	C, N, O, F, Ne, Ar, Kr, Xe	500 - 2000	7%	Powers et al. [4]
C	O, Ne, Ar, Kr, Xe	500 - 2000	7%	Powers et al. [4]
Al	Ar, Kr, Xe	500 - 2000	7%	Powers et al. [4]
Al	Na, Ar, K, Kr	1 - 600	6%	Davies et al. [1,6]
W	Rb, Xe, Cs, Rn			

TABLE 1.2. RANGES IN AMORPHOUS TARGETS

Target ( $Z_2$ )	Projectile ( $Z_1$ )	Energy region (keV)	Precision	Reference
Al <sub>2</sub> O <sub>3</sub>	Na, K, Kr, Xe	1 - 1500	4%	Jespersgård and Davies [8]; Domeij et al. [9]
WO <sub>3</sub>	Na, Ar, Kr, Xe	1 - 160	6%	Domeij et al. [9]
Ta <sub>2</sub> O <sub>5</sub>	Na, K, Ar, Kr, Rb, In, Xe, Cs, Tl, Rn	0.5 - 160	1%	J.P.S. Pringle [10]

had been stopped in the oxide layer. The process can be repeated with a series of targets, each having a different thickness of oxide on the surface, and so the whole range distribution is obtained. It is known that these anodic oxides are essentially amorphous, and we see in Fig. 1.7 that the range distributions are quite symmetric and that the penetrating tails observed in the polycrystalline targets (Figs 1.5 and 1.6) are now completely absent. From a symmetrical profile such as these, one can easily extract the mean range, the root-mean-square straggling, and so on, for comparison with theory.

Tables 1.1. and 1.2 summarize the available range data in polycrystalline and amorphous targets, respectively, with an indication of the experimental accuracy that has been achieved. In this connection, we should like to draw attention to Pringle's recent range measurements in amorphous Ta<sub>2</sub>O<sub>5</sub>, where the accuracy is almost an order of magnitude better than the earlier work. He uses a modified version of the anodizing-stripping technique, combined with optical interference measurements to monitor accurately the oxide thickness and uniformity.

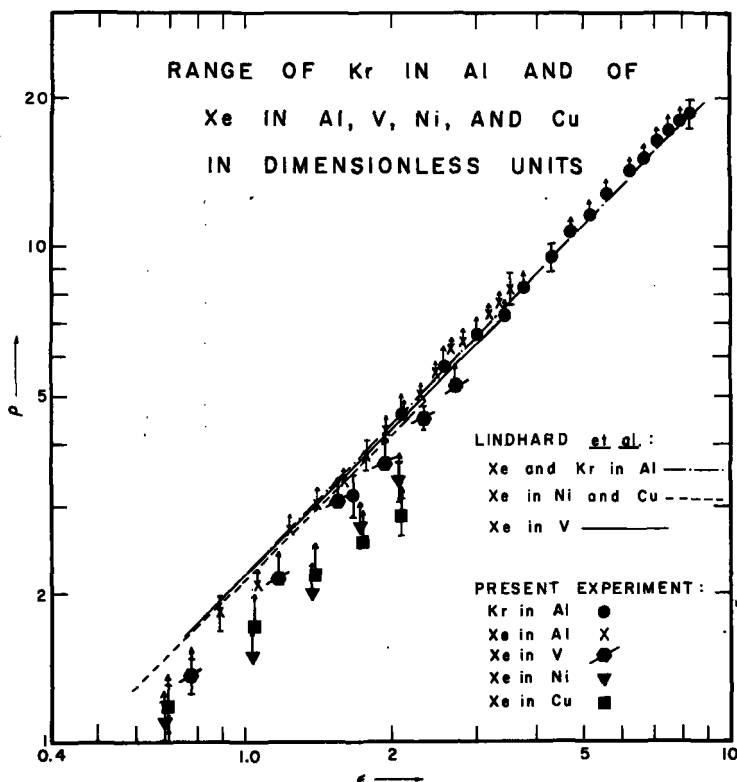


FIG. 1.8. Comparison of experimental range data in several polycrystalline targets with the theoretical curves given by Lindhard et al. [11]. The magnitude of the correction term from "projected range" to "total path length" is indicated by an arrow on each experimental point (from Powers et al., Ref. [4]).

#### 1.4. Comparison with theory

Let us now see how experimental data in polycrystalline targets (Fig. 1.8) and in amorphous targets (Fig. 1.9) compare with theoretical predictions. The theoretical range curves in these figures have been derived as outlined by Lindhard [11] i. e. by combining the curve for nuclear stopping with the appropriate one for electronic stopping, (Fig. 1.10) to obtain the total rate of energy loss, and then integrating this from the incident energy down to zero. Note that, in terms of Lindhard's reduced energy and length units,  $\epsilon$  and  $\rho$ , one obtains a single universal curve for nuclear stopping (Fig. 1.10); on the other hand for electronic stopping one gets a family of lines, each one characterized by a particular value of  $Z_1$  and  $Z_2$ . The energy region of interest in this section corresponds to  $\epsilon \lesssim 5$  (where nuclear stopping normally predominates) and hence in  $\rho$ - $\epsilon$  units one expects almost a universal range-energy curve — as can indeed be seen by the closely-spaced theoretical curves in Fig. 1.8 for quite a wide variety of targets and projectiles.

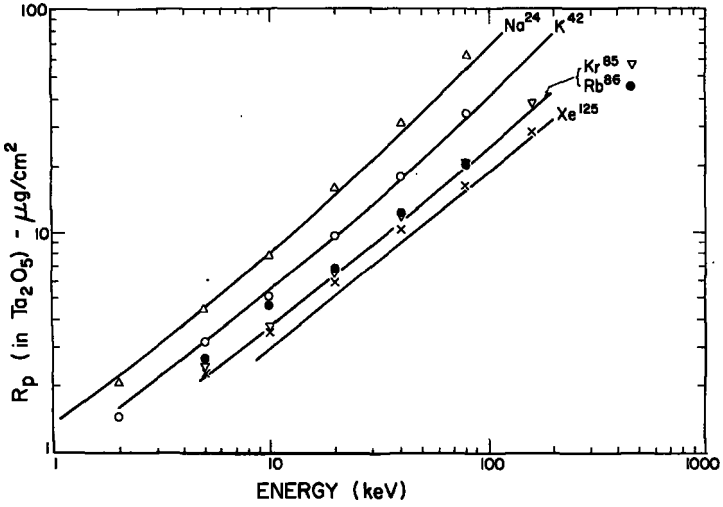


FIG.1.9. Comparison of experimental range data in amorphous  $Ta_2O_5$  with the theoretical "projected range" curves calculated by H.E. Schiøtt [12] (from Pringle, Ref.[10]).

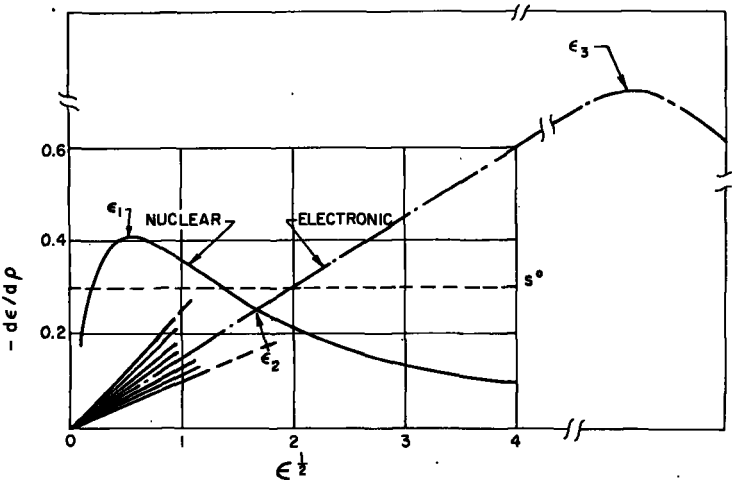


FIG.1.10. Theoretical nuclear and electronic stopping-power curves, expressed in terms of the reduced variables  $\rho$  and  $\epsilon$ . (Based on Lindhard et al. [11]). For electronic stopping, a family of lines (one for each combination of projectile and target) is obtained: the majority of cases fall within the limits shown. The dot-dash line represents the electronic stopping for  $k=0.15$ . The horizontal line labelled  $S^0$  represents the constant-stopping-power approximation suggested by Nielsen [13]). Values of the characteristic energies  $\epsilon_1$ ,  $\epsilon_2$  and  $\epsilon_3$  are given in Table 1.3.

TABLE 1.3. CHARACTERISTIC ENERGIES (IN keV) CORRESPONDING TO  $\epsilon_1$ ,  $\epsilon_2$ , AND  $\epsilon_3$  IN FIG. 1.10

Ion	$\epsilon_1$			$\epsilon_2$			$\epsilon_3$
	in Si	in Ge	in Sn	in Si	in Ge	in Sn	
B	3	7	12	17	18	10	$3 \times 10^3$
P	17	29	45	140	140	130	$3 \times 10^4$
As	73	103	140	800	800	800	$2 \times 10^5$
Sb	180	230	290	2000	2000	2000	$6 \times 10^5$
Bi	530	600	700	6000	6000	6000	$2 \times 10^6$

A theoretically predicted range is of course the total path length travelled by the ion in coming to rest, whereas what one measures experimentally is only the projected range perpendicular to the target surface. Hence, it is necessary to apply a small correction factor. In Fig. 1.9, this correction factor has been incorporated into the calculated range curves; however, in Fig. 1.8 the authors chose instead to represent it by a small vertical arrow on each of the experimental points.

In general, the agreement between experiment and theory is seen to be rather good: for example, in Fig. 1.9, the range data for all five ions in  $Ta_2O_5$  fit the predicted curves within a few percent over almost the entire energy region studied. For the heavier ions such as xenon, however, the data at very low energies lie systematically some 10-20% above the theoretical curve.

So far, we have compared only the mean range (i. e. the position of the peak in the range distribution) with theory, but of course one is often equally interested in obtaining information on the distribution or "straggling" about this mean value. Figure 1.11 summarizes the straggling information obtained from range data in polycrystalline targets, such as those in Fig. 1.8, and compares it with the semi-universal straggling-versus- $\epsilon$  curve of Lindhard, Scharff and Schiøtt [11]. These experimental straggling data were determined by fitting a Gaussian to the measured range profile, and thus determining the root-mean-square deviation ( $\Delta R/R$ ). At the higher energies the straggling data agree rather well with theory, but at lower energies the experimental points all lie significantly higher. Perhaps one reason why the low-energy data lie well above the theoretical curve is that these measurements were obtained in polycrystalline targets, and so have a penetrating tail due to channelling (see Fig. 1.5).

This point is illustrated rather nicely by Fig. 1.12 which shows similar straggling data, but for an amorphous target, aluminium oxide. Again, the data lie somewhat above Lindhard's theoretical curves at the lower energies, but the deviations are very much smaller than in the polycrystalline case. Note that in Fig. 1.12 we have plotted the square straggling, not the root-mean-square values.

Also, note that the energy scale is in laboratory (keV) units rather than in the universal  $\epsilon$ -units of Lindhard. For a light ion such as sodium

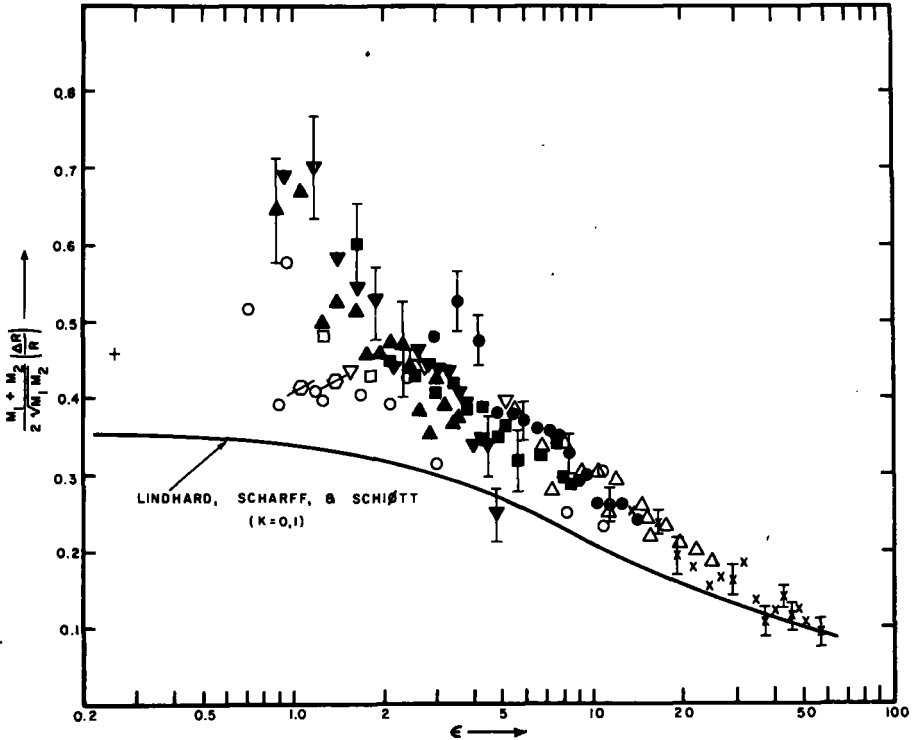


FIG. 1.11. Comparison of the experimental root-mean-square range straggling in polycrystalline targets with the theoretical  $\epsilon$ -dependence predicted by Lindhard et al. [11]. (From Powers et al., Ref.[4]).

or potassium the available energy region covers the transition from predominantly nuclear stopping up into the predominantly electronic-stopping region. In the electronic-stopping region, the predicted straggling is very much reduced, and this is confirmed experimentally by the data in Fig. 1.12. For heavy ions such as xenon, even 100-keV is still in the nuclear-stopping region, and so one predicts virtually a constant straggling throughout; except for a little bit of scatter, the experimental data are consistent with this.

### 1.5. Stopping-power ( $dE/dx$ ) studies

Up till now, we have discussed range measurements exclusively, but before leaving the amorphous-target case we should like to say a few words about stopping-power measurements. We have seen how ranges can be measured fairly accurately even in the purely nuclear-stopping region, and how quite a lot of useful information for comparison with stopping-power theory has thus become available. But if we want to study accurately the electronic-stopping contribution, ranges are not a very satisfactory method. Even if we use a sufficiently high incident energy that electronic collisions

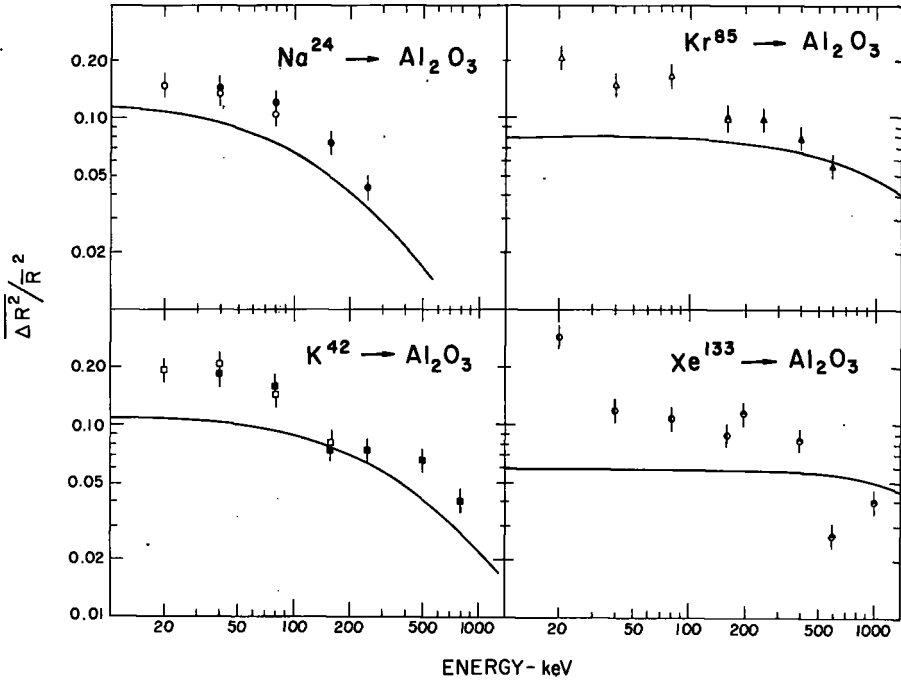


FIG.1.12. Comparison of mean square straggling data for several ions in amorphous  $\text{Al}_2\text{O}_3$  with the appropriate theoretical curves derived from the Lindhard treatment (from Ref.[8]).

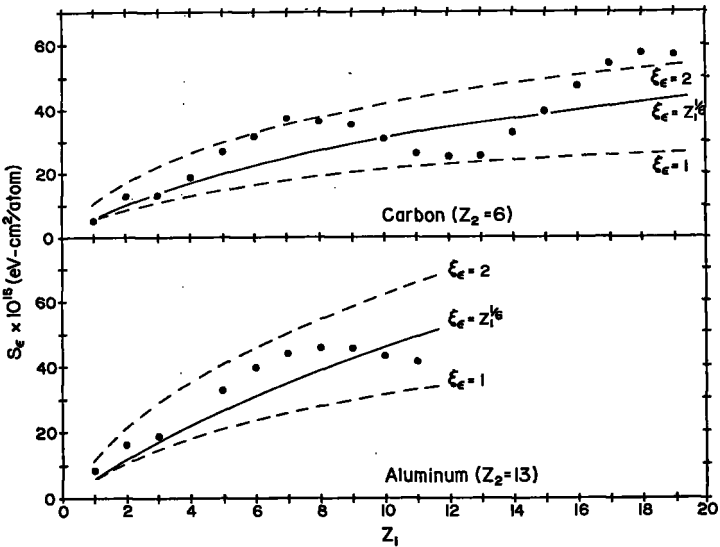


FIG.1.13. Electronic stopping cross-sections in carbon and aluminum as a function of the atomic number  $Z_1$  of the incident projectile (at a constant velocity  $v = 9 \times 10^7$  cm/s). Theoretical curves are from Lindhard et al. [11]. (Taken from Ormrod et al., Ref.[14]).

predominate initially, the range is still an integral effect involving collisions all the way down to zero energy. Hence, the measured quantity always contains a significant contribution from the lower-energy region where nuclear collisions are dominant.

To avoid this problem it is preferable to use a differential measurement, such as the rate of energy loss. Fortunately, at higher energies, the ranges are longer and it becomes possible to make self-supporting foils sufficiently thin that the ion beam can penetrate through. In such a case, an analysing magnet can be used to measure the transmitted energy and hence the energy loss ( $\Delta E$ ) in traversing the foil. Then, provided we know the thickness ( $\Delta x$ ) of the foil, we obtain directly the stopping power ( $dE/dx$ ). The main limitation is the difficulty in making self-supporting foils much thinner than a few hundred Å, and so for heavy ions, transmission techniques are generally restricted to energies greater than  $\sim 100$  keV.

There have been two particularly active groups making such ( $dE/dx$ ) measurements: Duckworth, Ormrod and McDonald [14] at McMaster University (Canada) and Fastrup, Sautter and Hvelplund [15] at Aarhus University (Denmark). Figure 1.13 illustrates a typical set of stopping-power data, for various ions (at a constant initial velocity) in thin carbon and aluminium foils. What one measures of course is the total stopping power — i. e. the sum of the electronic and nuclear contributions. But, if the energy is high enough, then the nuclear-stopping contribution is small and can be either neglected or corrected for. In this way, one obtains experimental values of the electronic stopping power,  $S_e$ .

The most interesting feature of these ( $dE/dx$ ) measurements is the oscillatory  $Z_1$ -dependence that occurs about the smooth monotonically-increasing Lindhard curve, as can be seen in Fig. 1.13. The magnitude of these oscillations is fairly large, with the peaks and valleys falling as much as 30-40% off the Lindhard curve. Subsequent experiments by the Aarhus group [15] have shown that the  $Z_1$ -oscillations continue with similar amplitude up to the heaviest ions. Qualitatively, one observes quite a good correlation between the positions of the maxima and minima and the ion size: i. e. the minima in  $S_e$  coincide roughly with minima in ion size and the maxima in  $S_e$  with maxima in ion size. It is therefore tempting to suggest that ion size is somehow responsible for the oscillations. On the other hand, there has not yet been a really quantitative explanation of the magnitude of the oscillations in terms of ion size, despite the efforts of several groups [16-19]. An alternative explanation [20] for the  $Z_1$ -oscillations, based on a Ramsauer-type effect, was outlined briefly by Lindhard in his lectures (which are not published here), and this too can predict correctly the positions of the maxima and minima. Furthermore, it has the additional advantage of retaining the self-consistent nature of the Thomas-Fermi treatment; however, it has not yet been developed sufficiently to permit quantitative estimates of the magnitude of the oscillations to be made.

Despite these rather large oscillations in electronic stopping power, the range measurements in Figs 1.8 and 1.9 seem to fit rather smoothly on the theoretical curve, even at the higher energies. The reason for this is simply the diluting effect that nuclear stopping has on a range measurement, where the stopping power is being integrated right down to zero energy. This is clearly illustrated in Table 1.4, in which the ratio of the range calculated from experimentally measured stopping-power values to the range predicted from the Lindhard theory is listed for various ions in

TABLE 1.4. EFFECT OF  $Z_1$  OSCILLATIONS  
IN "AMORPHOUS" SILICON

Ion	(k'/k)	$R_{\text{corrected}}/R_{\text{LSS}}$			
		1 keV	10 keV	100 keV	1 MeV
$^{11}\text{B}$	1.20	0.98	0.95	0.89	0.85
	1.5	0.95	0.89	0.76	0.69
$^{14}\text{N}$	1.30	0.98	0.95	0.86	0.79
$^{23}\text{Na}$	0.84	1.01	1.02	1.06	1.14
$^{27}\text{Al}$	0.90	1.00	1.01	1.05	1.09
$^{31}\text{P}$	1.14	0.99	0.99	0.96	0.92
$^{70}\text{Ga}$	0.55	1.01	1.02	1.05	1.21
$^{75}\text{As}$	0.60	1.01	1.02	1.05	1.18

silicon. The second column (k'/k) is the ratio of the experimentally observed electronic stopping power (k') to the value (k) used in the Lindhard theory [11]. A value of 1.0 therefore corresponds to the normal Lindhard estimate of electronic stopping. We have deliberately picked cases close to minima and maxima in  $S_e$ , and yet for the heavier ions, one has to go up to 1 MeV before the range correction due to  $Z_1$ -oscillations amounts to more than the typical experimental error of ~6%. Consequently, as far as ranges in amorphous targets are concerned, these  $Z_1$ -oscillations are not particularly important. For stopping-power measurements, of course, they certainly are significant, and (as we shall see in the next lecture), they become even more important for channelled ions.

The discovery of these prominent  $Z_1$ -oscillation effects in  $S_e$  a few years ago has made it fashionable in recent years to look for all kinds of oscillations in range and channelling studies. There has been a lot of speculation, and experimental evidence of varying degrees of reliability has been presented to suggest, for example, whether or not there are  $Z_2$ -oscillations in the electronic stopping power, or whether the nuclear stopping power also shows similar  $Z_1$ , or  $Z_2$  oscillations.

Varying  $Z_2$  is experimentally considerably more difficult than  $Z_1$  because it requires having a large series of different self-supporting targets. Nevertheless, some groups [21, 22] have obtained data suggesting there is a small (but experimentally significant)  $Z_2$ -oscillation effect: it is probably ~5-10% in magnitude, compared to 30-40% for the  $Z_1$ -oscillations.

The other suggestion - that of possible oscillations in nuclear stopping - has been rather convincingly refuted by some recent transmission experiments of Andersen et al. [23], who have measured not only the energy but also the angular distribution of the transmitted beam. Even at sufficiently high energies for electronic stopping to be the predominant slowing-down mechanism, the angular scattering of a transmitted beam arises almost entirely from nuclear collisions. Hence, the mean square scattering angle provides a direct measure of the nuclear-collision cross-section. They have measured the angular distribution of the transmitted beam for some

18 different elements transmitted through a thin carbon foil, and find a smooth monotonically increasing value for the mean scattering angle — indicating that any oscillations in nuclear scattering must be less than ~5%.

## SUMMARY

To sum up, we may conclude that in this low-energy region, in the absence of crystal structure, experimental range and stopping power data are in rather good agreement with the existing theoretical framework. Quite a wide region of energy and atomic number have been investigated and the only significant discrepancy that requires considerable further work is the  $Z_1$ -oscillation effect in the electronic stopping power.

## REFERENCES TO SECTION 1

- [1] DAVIES, J.A., BROWN, F., McCARGO, M., *Can. J. Phys.* 41 (1963) 829.
- [2] WHITTON, J.L., *J. appl. Phys.* 36 (1965) 3917.
- [3] LUTZ, H., SIZMANN, R., *Z. Naturforsch.* 19a (1964) 1079.
- [4] POWERS, D., CHU, W.K., BOURLAND, P.D., *Phys. Rev.* 165 (1968) 376.
- [5] McCARGO, M., DAVIES, J.A., BROWN, F., *Can. J. Phys.* 41 (1963) 1231.
- [6] DAVIES, J.A., SIMS, G.A., *Can. J. Chem.* 39 (1961) 601.
- [7] ROBINSON, M.T., OEN, O.S., *Phys. Rev.* 132 (1963) 2385.
- [8] JESPERSGÅRD, P., DAVIES, J.A., *Can. J. Phys.* 45 (1967) 2983.
- [9] DOMEIJ, B., BROWN, F., DAVIES, J.A., McCARGO, M., *Can. J. Phys.* 42 (1964) 1624.
- [10] PRINGLE, J.P.S., Chalk River, private communication (1968).
- [11] LINDHARD, J., SCHARFF, M., SCHIØTT, H.E., *Kgl. Danske Videnskab Selskab, Mat.-Fys. Medd.* 33 14 (1963).
- [12] SCHIØTT, H.E., *Can. J. Phys.* 46 (1968) 449.
- [13] NIELSEN, K.O., in "Electromagnetically Enriched Isotopes and Mass Spectroscopy" (SMITH, M.L., Ed.) Academic Press, New York (1956) 68.
- [14] ORMROD, J.H., MacDONALD, J.R., DUCKWORTH, H.E., *Can. J. Phys.* 43 (1965) 275.
- [15] FASTRUP, B., HVELPLUND, P., SAUTTER, C.A., *Kgl. Danske Videnskab. Selskab, Mat.-Fys. Medd.* 35 10 (1966);  
HVELPLUND, P., FASTRUP, B., *Phys. Rev.* 165 (1968) 408.
- [16] BHALLA, C.P., BRADFORD, J.N., *Physics Letts* 27A (1968) 318.
- [17] CHESHIRE, I.M., DEARNALEY, G., POATE, J.M., *Phys. Letts* 27A (1968) 304.
- [18] EL-HOSHY, A.H., GIBBONS, J.F., *Phys. Rev.* 173 (1968) 454.
- [19] WINTERBON, K.B., *Can. J. Phys.* 46 (1968) 2429.
- [20] LINDHARD, J., FINNEMANN, J., Aarhus University, unpublished report (1968).
- [21] WHITE, W., MUELLER, R.M., *Phys. Rev.* 187 (1969) 499.
- [22] CHU, W.K., POWERS, D., *Phys. Rev.* 187 (1969) 478.
- [23] ANDERSEN, H.H., BØTTIGER, J., *Phys. Rev.* B4 (1971) 2105.

## 2. RANGES IN SINGLE CRYSTALS

In this section, we are going to discuss range distributions in single crystals — and in particular the role that channelling plays. What exactly do we mean by channelling? A detailed description of the phenomenon has been provided by Lindhard in Ref. [1]. Basically, it is a gentle steering process arising from the correlated series of collisions that occur whenever

$$\text{CHANNELLING CONDITION: } \psi < \psi_{\text{crit}} = C\sqrt{\frac{2Z_1Z_2e^2}{Ed}}$$

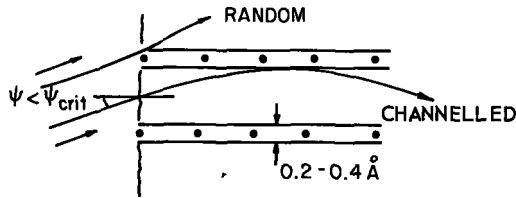


FIG. 2.1. Schematic diagram illustrating how a correlated sequence of collisions with an aligned row of atoms can gently steer (channel) a particle through a lattice, thus preventing violent collisions from occurring.

a beam of energetic ions moves through a crystal in a direction that is almost parallel to a major axis (or plane). As long as the angle between the beam and the crystal row is sufficiently small, the gradually increasing electrostatic repulsion between the ion and the screened field around each successive target nucleus (due to the gradually decreasing impact parameter at each successive collision) is sufficient to deflect the particle smoothly away from the row — as illustrated schematically in Fig. 2.1.

An obvious consequence of this steered motion is that it prevents the particle from having violent collisions with target atoms, and therefore the nuclear stopping is strongly attenuated. Consequently, the beam loses energy more slowly, it penetrates more deeply, it creates much less damage along its track, and it has much less probability of wide-angle scattering, or of participating in nuclear reaction yields. In short, almost all physical processes that can occur between moving particles and target atoms are drastically affected by such a steering process.

With such a wide-spread phenomenon that can produce (as we shall see) extremely large effects, people entering the field today may wonder why channelling was not recognized or even seriously postulated until about 10 years ago. It might therefore be of some interest to start with a brief historical introduction.

### 2.1: Historical introduction

Experimental evidence for the existence of channelling has now become particularly widespread. For a heavy ion such as krypton or iodine, channelling effects have been observed at energies as low as 250 eV and as high as 100 MeV: i. e. over an energy range spanning almost six orders of magnitude. Similarly, they have been observed not only for heavy ions but also for protons over an equally wide energy range, and even for much lower-mass particles such as positrons and electrons<sup>1</sup>. Hence, today we recognize that the channelling phenomenon is a significant factor whenever a charged-particle beam penetrates a crystal lattice. The channelling phenomenon is not really new. It was indeed postulated back in 1910 by

<sup>1</sup> In the electron case, an attractive potential is involved rather than a repulsive one — and this leads to a different and more complex type of steered motion, as was discussed briefly by Professor Lindhard.

Bragg [2] in an attempt to explain the X-ray diffraction patterns that had just been observed for the first time. Bragg suggested that the spots might be due to some sort of steering of the X-ray 'particles' (the wave nature of the X-ray had not yet been recognized) along the open "canals" that exist in a crystal lattice.

Shortly after Bragg's suggestion, Stark [3] actually proposed a channelling experiment involving a beam of protons in a single crystal, and the phenomena that he anticipated are very similar to what people observe today when they inject protons into crystals. It is interesting to speculate that if Stark's proposed experiment had actually been carried out in 1912, one would indeed have discovered channelling some 50 years earlier than was the case. If this had happened, the whole development of crystallography might have taken quite a different turn, since some of the channelling effects that one observes today provide in many respects a simpler and more direct way of studying lattice properties such as crystal structure, crystallographic orientation, mosaic spread, and so on. However, this did not happen — and probably the main reason it did not happen was that Bragg soon realized his mistake about the origin of the X-ray spot patterns. As the energy of the X-ray was varied, the position of each spot moved (due to the change in Bragg angle), and this led rapidly to the discovery of the wave-nature of X-rays and ultimately to the well-established field of X-ray diffraction. At that time, the intense interest in the wave nature of the X-ray completely over-shadowed Stark's proposed channelling experiment with protons and is probably the main reason why it was not attempted.

During the subsequent 50 years, scientists discovered that, not only X-rays, but particles such as electrons and neutrons also had wave properties, and one recognizes today the tremendous success that electron and neutron diffraction have achieved in solid-state studies.

By the mid 1950's, when people began to get interested in studying the penetration of energetic heavy ions in matter, one of the first questions asked was "Do we have to worry about crystal structure?" But most of us were so conditioned to thinking of crystal-lattice effects in terms of diffraction that we would immediately answer this question by working out the wave-length of the particle, and then seeing whether the Bragg angle was sufficiently large. Well, the wave-length of a 50-keV heavy ion (such as krypton or iodine) is typically about  $10^{-6}$  Å — and, for such a short wave-length, the Bragg diffraction angle would be of the order of  $10^{-5}$  degrees. This angle is at least 2-3 orders of magnitude smaller than readily available goniometers can achieve; it is also 2-3 orders of magnitude smaller than the mosaic spread that exists in high quality single crystals. Therefore, from a simple diffraction viewpoint, you quickly convince yourself that crystal-lattice effects are unimportant for heavy ions, and even for protons. Unfortunately, we did not consider (as we should have) the fact that a correlated sequence of collisions between atomic particles can be given a relatively simple classical description. And we did not uncover the early predictions of Stark until after we had stumbled accidentally upon experimental evidence for the existence of channelling. Anyway, that is now history, but there is surely an important lesson to be learned.

About the time that we started making accurate range studies (i. e. in the late 1950's), other types of heavy-ion experiments (such as sputtering and secondary electron emission) were showing strong crystal lattice effects that were obviously not due to diffraction, but which, on the other hand, did not

necessarily require a channelling mechanism. For example, Almen [4] at Goteborg observed that the yield of sputtered target atoms falls off very strongly when the beam is injected almost parallel to a crystal axis. Similarly, the number of secondary electrons emitted from a target was observed to be a strong function of the incident beam direction. Both types of measurement have often been interpreted as evidence for the existence of channelling. Here, we should like to draw a rather important distinction between channelling and purely geometrical transparency. Channelling is defined as a more or less stable, steered trajectory persisting for a significant depth into the crystal. In the absence of channelling, however, purely geometrical effects would still exist within the first few atomic spacings beneath a crystal surface: even a set of parallel linear trajectories would initially exhibit an enhanced transparency along low-index directions or planes — except, of course, for the occasional trajectory that enters the crystal too close to the end of an atomic row. Hence, the orientation dependence of processes (such as sputtering and secondary electron emission) which originate from collisions occurring within the first few atomic planes, can be attributed, at least qualitatively, to transparency effects, and are not necessarily evidence for the existence of a channelling mechanism.

The first unambiguous experimental evidence for channelling was probably the penetrating tail of the  $^{24}\text{Na}$  range distribution in polycrystalline aluminium (Fig. 1.5), although we did not at first identify it as such. These tails extend 1000 Å and more into the target, and are therefore far too deep to be merely a transparency effect.

The credit for correctly identifying the channelling mechanism belongs to the theoretical work of Robinson and Oen at Oak Ridge, who in 1961-62 attempted to simulate range distributions by means of a Monte-Carlo computer program [5]. First, to simulate an amorphous target, they selected the atomic positions in the target at random (by Monte-Carlo methods) and found that, with a fairly small number of collisions per trajectory they could fit the main part of the range distribution quite nicely. Then, they tried placing the target atoms (in their computer program) on fixed sites, namely in lattice positions, and selecting at random only the initial angle and point of incidence at which each incoming particle entered the crystal. In this case, whenever the incident trajectory was almost parallel to a row, the particle penetrated so deep in the computer program that the computer ran all night without reaching the end of that particle's track — thus, they discovered the existence of channelling from the large number of dollars they had to pay for the use of the computer!

As soon as channelling had been observed in the computer simulations, an obvious experimental test was to measure a range distribution in a carefully aligned single crystal. Such a test is illustrated in Fig. 2.2, in which we have measured the range distribution along four different directions in an aluminium single crystal. These four distributions were obtained on the same crystal — which had been cut in such a way that the three low-index directions were all inclined at the same angle to the crystal surface, (i.e. 28° away from the perpendicular). Note that there is a marked difference in the penetration profiles — with the  $\langle 110 \rangle$  exhibiting by far the strongest channelling effect. The curve corresponding to perpendicular incidence ( $\perp$ ) does not coincide with any crystallographic axis. However, it is only  $\sim 8^\circ$  off the  $\langle 112 \rangle$ , which is the second best crystal direction for channelling; this explains why the ( $\perp$ ) curve exhibits a rather pronounced tail. Similar

range studies in polycrystalline aluminium and amorphous  $\text{Al}_2\text{O}_3$  are included for comparison. As we saw in section 1, the penetrating tail is completely absent in the amorphous target.

Similar experimental confirmation for the existence of channelling was obtained independently and simultaneously by Lutz and Sizmann [7] who performed almost an identical range experiment, using  $^{85}\text{Kr}$  in a copper crystal, and also by Nelson and Thompson [8].

This concludes our brief introduction to the historical "discovery" of the phenomenon of channelling. For the rest of this section, we should like to discuss range distributions in single crystals, and their dependence on various experimental parameters.

## 2.2. Experimental techniques

The experimental techniques for measuring range distributions in single crystals are virtually the same as those used in the amorphous or polycrystalline case (section 1). Most of the data have been obtained by means of the electro-chemical method; i.e. by injecting radio-tracer ions, and then peeling off successive thin layers to find out how deeply the tracer ions had penetrated. The one difference is that, in the single-crystal experiment, of course, you need to align the crystal so that a given axis is parallel to the incoming beam direction. In the early measurements (such as those in Fig. 2.2), X-ray diffraction methods were used to obtain an alignment accuracy of  $0.5 - 1^\circ$ ; but later it became evident that a more accurate and convenient way of aligning a crystal is to use the channelling phenomenon itself. Hence, in most of the range studies we will be discussing here, the crystals were actually aligned in situ to  $0.1^\circ$  or better, using the channelling behaviour of a proton beam. This alignment technique will be discussed further in section 6 (see Figs 6.2 and 6.3).

## 2.3. Qualitative features of channelled range distributions

It is instructive to consider first the various types of trajectory that occur when a beam enters a single crystal. Figure 2.3 (a) illustrates the effect of varying the angle of incidence, for particles entering at the mid-point of a channel. Particle A, which enters at a large angle with respect to the row passes straight on through the row with just normal multiple scattering, and this would be very similar to what one might call a random trajectory; i.e. it would encounter a random stopping power and have approximately the same range as in an amorphous target. If you rotate the crystal so that the beam enters at a small enough angle for channelling to start occurring, you obtain a trajectory such as that of particle B which just avoids making violent contact with the aligned rows. On the other hand, if you reduce the angle still further, then you obtain a trajectory with a smaller amplitude of oscillation, such as that of particle C. Even if you go to the perfectly aligned case (Fig. 2.3 (b)) one still observes three different types, since the initial impact position of a particle also influences its trajectory. Those entering the crystal close to an atomic row are scattered immediately through an angle sufficiently large that they do not become channelled (trajectory A). Particles entering at a position slightly farther away are channelled (trajectory B), but with larger oscillations than particles near the centre of the channel (trajectory C). For convenience, therefore, the

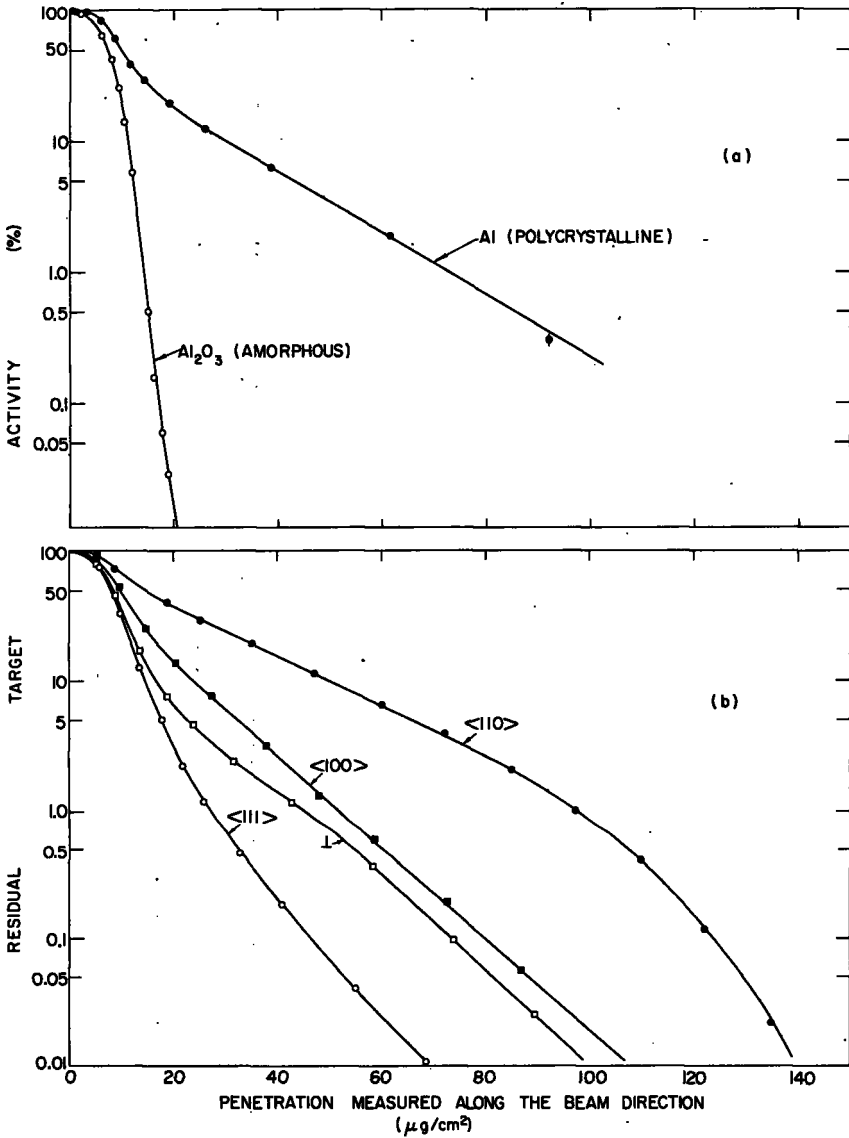


FIG. 2.2. Experimental range profiles of 40-keV  $^{86}\text{Kr}$ : a) in polycrystalline aluminium and amorphous  $\text{Al}_2\text{O}_3$ ; b) in monocrystalline aluminium (from Ref.[6]). Note: These distributions are integral range profiles such as those in Figs 1.5 - 1.7.

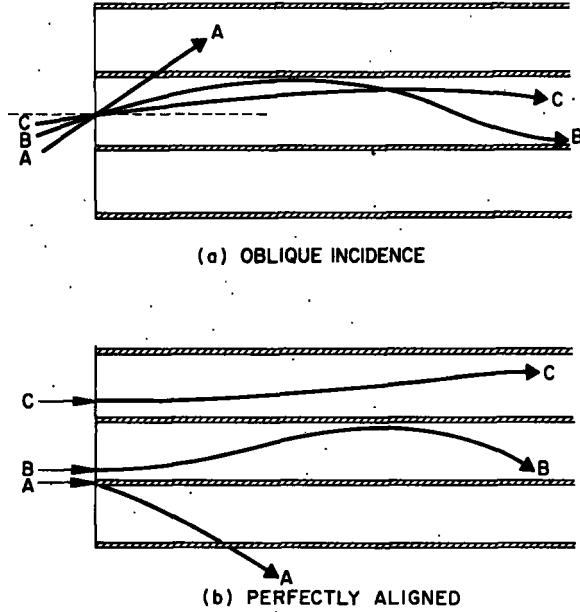


FIG. 2.3. Schematic representation of ion trajectories for axial channelling. The crystal lattice is depicted as a set of atomic "strings" of radius  $a$ , i.e. the shaded rows. (a) Trajectories B and C are for values of  $\psi$  less than the critical angle, and A is for values greater than the critical angle. (b) Trajectories for parallel incidence (i.e.  $\psi = 0$ ) as a function of impact position.

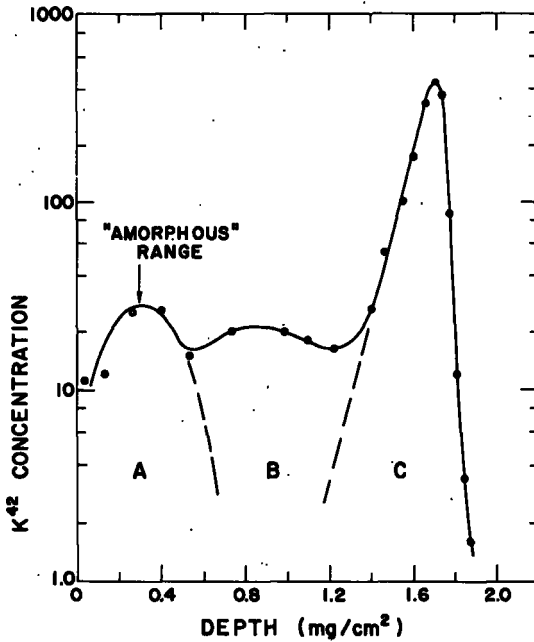


FIG. 2.4. The observed range distribution of 500-keV  $^{42}\text{K}$  ions injected at  $25^\circ\text{C}$  along the  $\langle 111 \rangle$  direction in tungsten (from Ref.[9]). Note that in tungsten,  $1 \text{ mg/cm}^2$  is equivalent to  $0.52 \text{ microns}$ .

incident particles may be divided into three broad categories, corresponding to the trajectories shown in Fig. 2.3:

- Group A, those particles that do not "feel" the lattice and so have a range distribution similar to that in amorphous material,
- Group B, those particles that start out with large oscillations in the channel. Such particles are probably scattered out of the preferred direction — i.e. are de-channelled — long before they become stopped, and so do not penetrate as deeply as those in Group C.
- Group C, those particles that start out "well-channelled" and thus have a better chance of remaining channelled throughout the slowing-down process.

Figure 2.4 illustrates the type of range distribution that is observed when a heavy-ion beam is implanted into a well-aligned tungsten crystal. Tungsten has been chosen as a rather ideal case in that the atomic vibrations of the crystal lattice are small at room temperature, and so de-channeling effects are minimized. We see that the experimental distribution curve does indeed consist of three clearly divided regions, which may be identified roughly with the three types of trajectory shown in Fig. 2.3 (b).

The two peaks, A and C, correspond to the amorphous and well-channelled ranges, respectively. The latter is due to those particles that remain channelled throughout their entire path, and is characterized by a sharp cut-off around  $1.9 \text{ mg/cm}^2$ . We define this cut-off as the maximum range  $R_{\text{max}}$  of a well-channelled ion.

In well-aligned tungsten crystals [9, 10], region C is usually the dominant feature of the range distribution, particularly at energies higher than  $\sim 100 \text{ keV}$ . In other crystals, however, de-channeling is often the dominant effect at room temperature — even for particles starting out initially in category C. De-channeling causes most of them to end up somewhere in the intermediate region B between the two peaks of the range distribution (Fig. 2.5). The resulting distribution then appears as a roughly exponential tail with an eventual cut-off at  $R_{\text{max}}$ ; in many cases, the distribution actually falls to an immeasurably low level before reaching  $R_{\text{max}}$ , so that the cut-off is not always observed. Several such distributions are illustrated in Fig. 2.6.

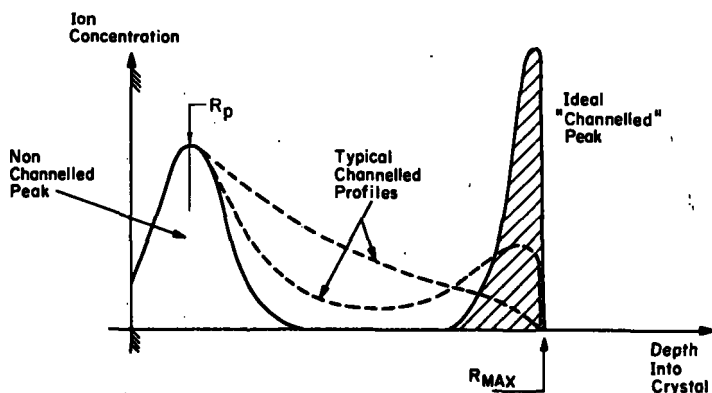


FIG. 2.5. Representative range profiles for an initially channelled beam. The solid curve represents an "ideal" case in which dechanneling is minimized. The dashed curves represent cases where dechanneling effects are large and only a small fraction of the implanted atoms penetrate to  $R_{\text{max}}$ .

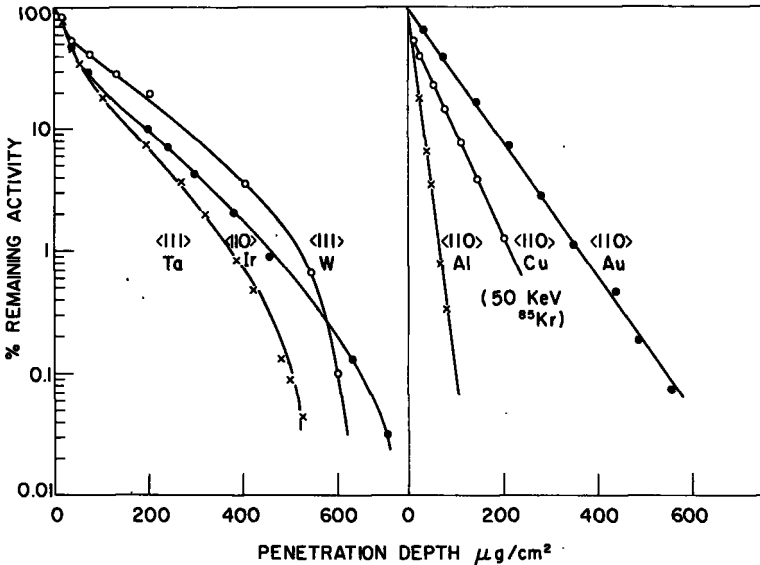


FIG. 2.6. Range distributions of 40-keV  $^{135}\text{Xe}$  injected at 25°C along the best channelling direction of various crystals (from Ref.[11]). Note: These distributions are integral range profiles and must be differentiated to give concentration profiles such as those, for example, in Figs 2.4 or 2.5.

The main reason for this enhanced de-channelling in other crystals is the fact that, at room temperature, their vibrational amplitude is very much greater than that of tungsten. In the case of gold, for example, you would have to cool the crystal to about 30°K in order to reduce its vibrational amplitude to the same magnitude as that for room-temperature tungsten. When this is done (Fig.2.7), one obtains a range profile similar in shape to that in tungsten at room temperature — except that the  $R_{\text{max}}$  in gold is considerably greater<sup>2</sup> than the tungsten value.

Even in an ideal crystal such as tungsten, there is a significant amount of de-channelling, and the observed distribution is very sensitive to many factors, such as crystal temperature, surface contamination, small mis-alignment, and angular divergence; some of these factors are often difficult to control. The amount of de-channelling also depends strongly on how far the ion must travel to reach  $R_{\text{max}}$  — i.e. on the magnitude of the electronic stopping power  $S_e$ . Thus  $^{42}\text{K}$  (for example) exhibits a much more pronounced channelled peak in tungsten than does  $^{64}\text{Cu}$ . The latter ion has a much smaller  $S_e$  value (see Fig.2.17) and hence a larger  $R_{\text{max}}$  than  $^{42}\text{K}$ , and so it exhibits a larger amount of de-channelling.

#### 2.4. Factors affecting range profiles

Let us now look briefly at some of the factors governing the detailed range distribution of channelled ions.

<sup>2</sup> The origin of this large difference in  $R_{\text{max}}$  values between tungsten and gold crystals is presumably linked closely to that of the  $Z_1$ -oscillations (Figs 2.16 and 2.17).

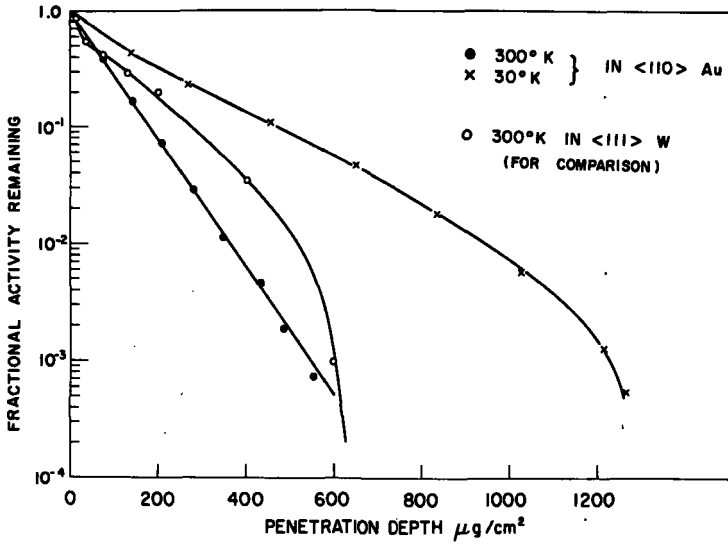


FIG. 2.7. Effect of temperature on the depth distribution of 40-keV  $^{135}\text{Xe}$  in gold (from Ref.[11]).

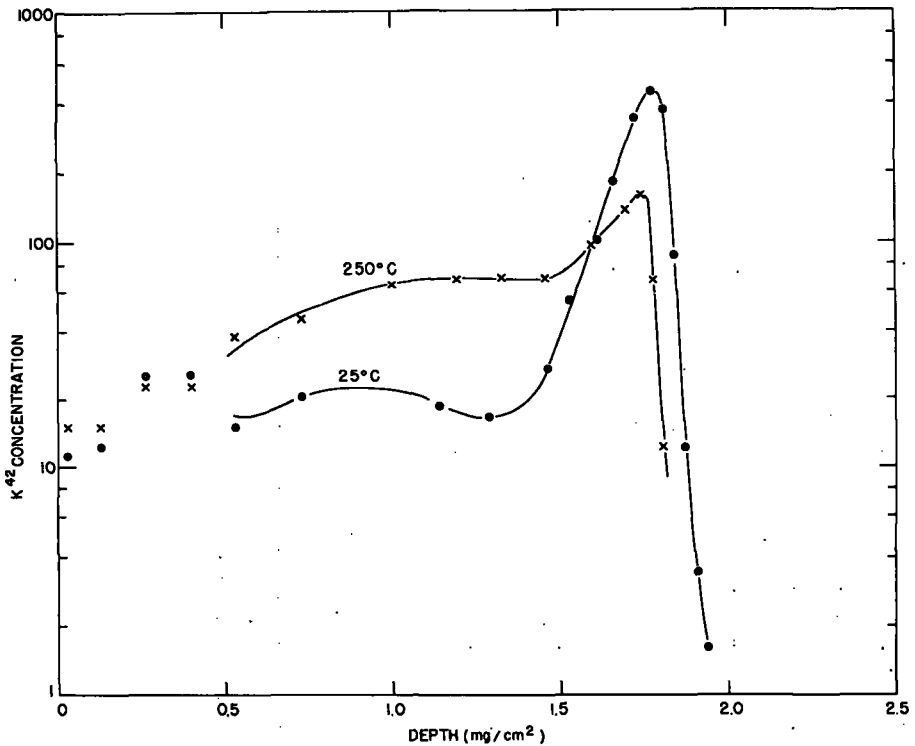


FIG. 2.8. The influence of target temperature on the range distribution of 500-keV  $^{42}\text{K}$  injected along the  $\langle 111 \rangle$  direction in tungsten (from Ref.[10]).

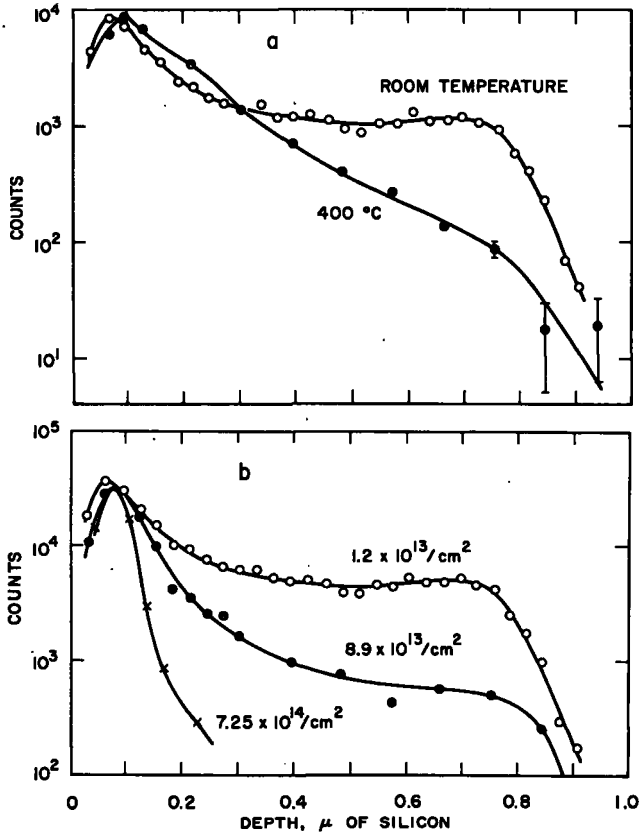


FIG. 2.9. Concentration profiles of  $^{32}\text{P}$  implanted into silicon at 40 keV along the  $\langle 110 \rangle$  direction (from Ref.[12]): a) distribution as a function of target temperature for a low-dose ( $1.2 \times 10^{13}$  ions/cm $^2$ ) implant; b) distribution as a function of total dose, normalized at the peak position.

#### a) Dependence on temperature

The effect of lattice vibration is illustrated in Fig. 2.8 for the case of 500-keV  $^{42}\text{K}$  ions injected into tungsten along the  $\langle 111 \rangle$  direction. At 250°C, the number of particles appearing in the well-channelled peak C is one-half to one-third smaller than at 25°C, presumably because of the increased scattering arising from the larger mean vibrational amplitude. As one might expect, there is no significant increase in the fraction of particles in the amorphous peak A. A similar temperature effect has also been observed in silicon (Fig. 2.9 (a)) by Dearnaley et al. [12]: by increasing the temperature from 25° to 400°C, you decrease the number of well-channelled particles by about an order of magnitude.

Note that, although the number of well-channelled (Group C) particles falls strongly with increasing temperature, the value of  $R_{\text{max}}$  is essentially temperature-independent. This point is illustrated clearly in Fig. 2.10 over a rather wide temperature region. As we shall see shortly (Fig. 2.14 and

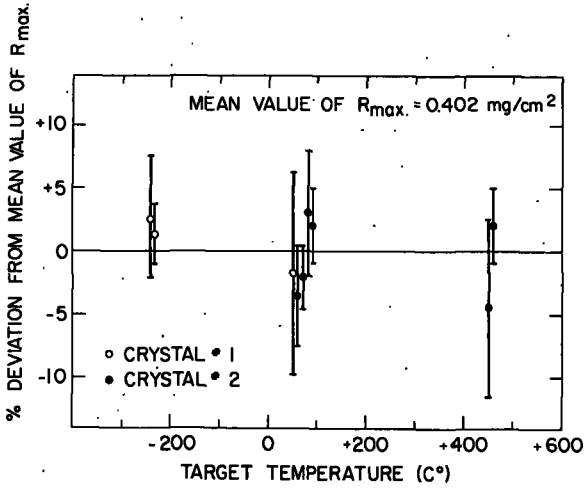


FIG. 2.10. The temperature dependence of  $R_{max}$  for 40-keV  $^{42}\text{K}$  injected along the  $\langle 100 \rangle$  direction in tungsten (from Ref. 13). The error bars indicate the maximum uncertainty in estimating  $R_{max}$  from the individual range distributions.

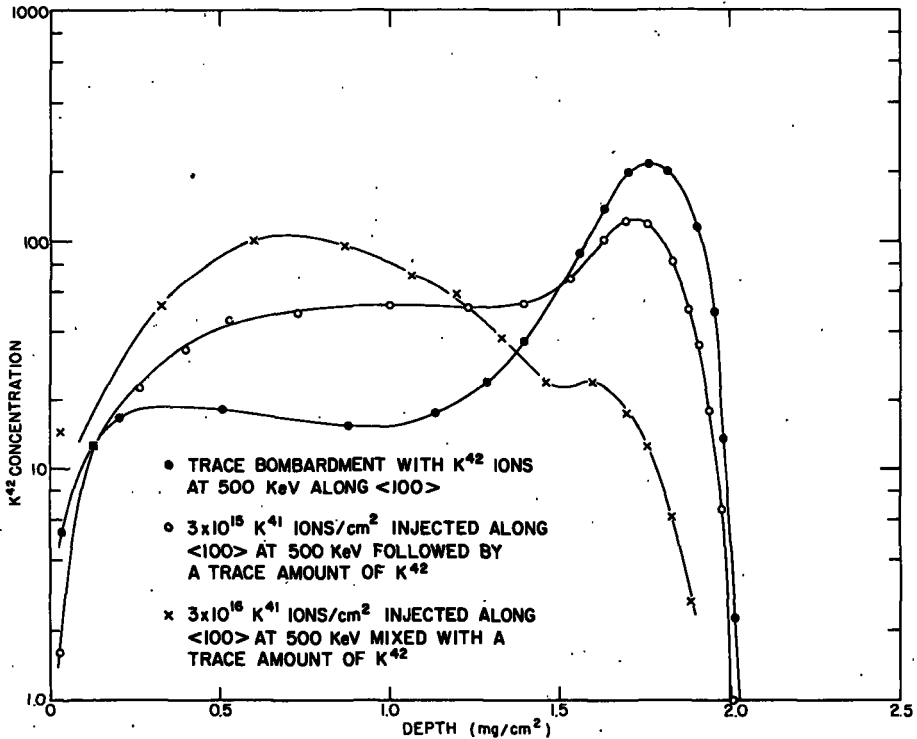


FIG. 2.11. The influence of pre-bombardment with a stable isotope ( $^{41}\text{K}$ ) on the range distribution of radio-tracer  $^{42}\text{K}$  ions in tungsten (from Ref. [10]). Both bombardments were made at 500 keV along the  $\langle 100 \rangle$  direction.

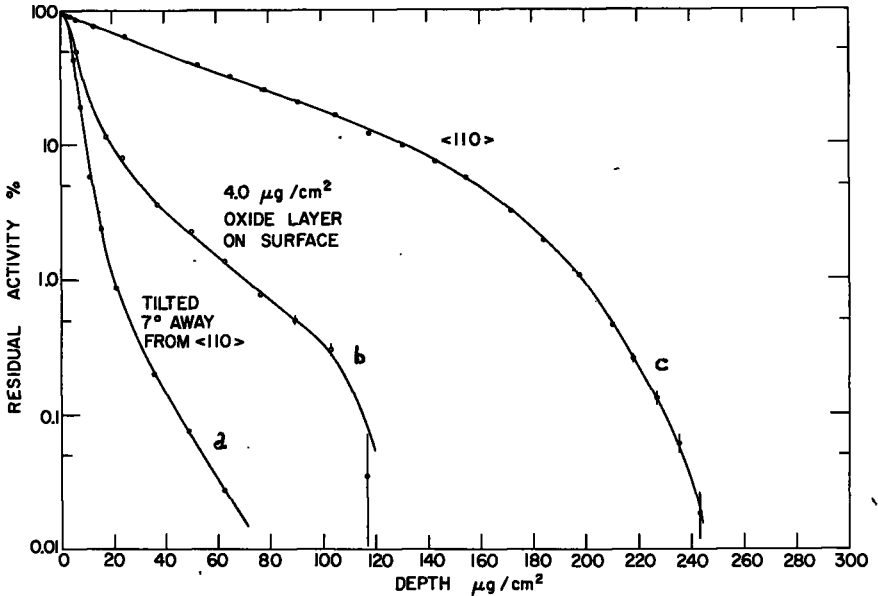


FIG. 2.12. Effect of misalignment and surface disorder on the integrated range distribution of 40-keV  $^{125}\text{Xe}$  injected into  $\langle 110 \rangle$  silicon at  $25^\circ\text{C}$ . (a) The crystal was tilted so that the beam entered at  $7^\circ$  from the  $\langle 110 \rangle$  direction. (b) The crystal has an anodic oxide layer  $4.0 \mu\text{g}/\text{cm}^2$  ( $\sim 160 \text{ \AA}$ ) thick on its surface. (c) The profile obtained in a well-aligned unanodized crystal is included for comparison. (From Ref. [15].)

2.15), the well-channelled ion loses energy almost entirely by electronic collisions; and, since the electron density near the middle of a channel should be relatively insensitive to lattice vibrations, it is not surprising to find that  $R_{\text{max}}$  does not depend on temperature.

#### b) Dependence on bombardment dose

The total ion dose can strongly influence the range profile, as can be seen in Fig. 2.9(b). The incident ions create a considerable amount of disorder and hence destroy the lattice structure necessary for channelling. A similar dose dependence has been observed in germanium crystals and also in gallium arsenide [14]. It should be noted that this sensitivity to bombardment dose does not occur in all crystals. In tungsten, for example, dose levels of  $\sim 10^{16}$  ions/ $\text{cm}^2$  at room temperature are required before drastic changes are observed (Fig. 2.11) in the range distribution of channelled ions. Most semiconductor lattices, however, seem to be rather sensitive to radiation damage and channelled profiles can be completely destroyed by doses of  $10^{14}$  ions/ $\text{cm}^2$  or even less.

#### c) Dependence on misalignment and surface disorder

Figure 2.12 shows the effect of a  $7^\circ$  misalignment and also of a surface oxide layer ( $\sim 160 \text{ \AA}$  thick) on the measured range distribution of  $^{125}\text{Xe}$  in a  $\langle 110 \rangle$  silicon crystal. In both cases, the number of well-channelled particles

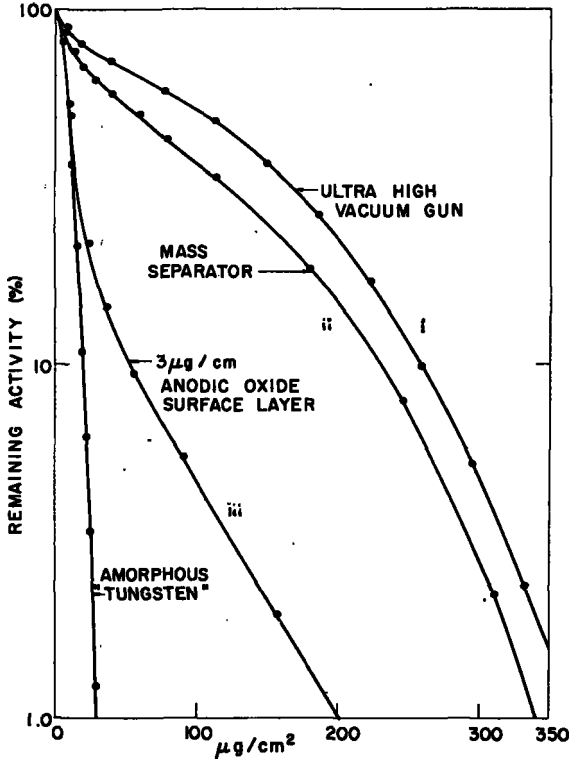


FIG. 2.13. Integral range profiles for 20-keV  $^{86}\text{Kr}$  ions in  $\langle 100 \rangle$  tungsten, illustrating the effect of surface contamination: (i) ultra-high-vacuum ( $10^{-10}$  torr) bombardment of a clean crystal - less than  $1/10$  of a monolayer of surface contamination; (ii) mass-separator bombardment ( $\sim 10^{-6}$  torr) - typically about  $10 \text{ \AA}$  of surface oxide; (iii) same as in (ii), but with a pre-formed oxide  $3 \mu\text{g}/\text{cm}^2$  (i.e.  $\sim 40 \text{ \AA}$ ) thick on the surface. (From Ref. [16].)

is reduced by some orders of magnitude. It should be noted that in this experiment we are not introducing new effects, but are merely increasing (by about a factor of 10) two effects that are present in all implantations. The drastic change in the observed penetration profile indicates that a misalignment of even  $0.5^\circ$  or the presence of some tens of  $\text{\AA}$  of surface oxide can affect significantly the shape of a channelled range distribution.

Another example of the serious de-channelling effect that even a few atomic layers of surface contamination can produce is shown in Fig. 2.13 in which three successive range measurements in the same tungsten crystal (but for different surface conditions) are compared. The significant difference between curves (i) and (ii) arises from  $\sim 10 \text{ \AA}$  of surface oxide. Since most crystals (aluminium, silicon, copper, iron, nickel, tantalum, etc.) have typically  $10\text{-}50 \text{ \AA}$  of oxide on their surface, it is evident that reproducible range profiles for channelled beams require special cleaning treatments and an ultra high vacuum environment.

Fortunately, when one uses high energy, low- $Z$  particles - such as the MeV protons and helium ions whose channelling behaviour we shall discuss in

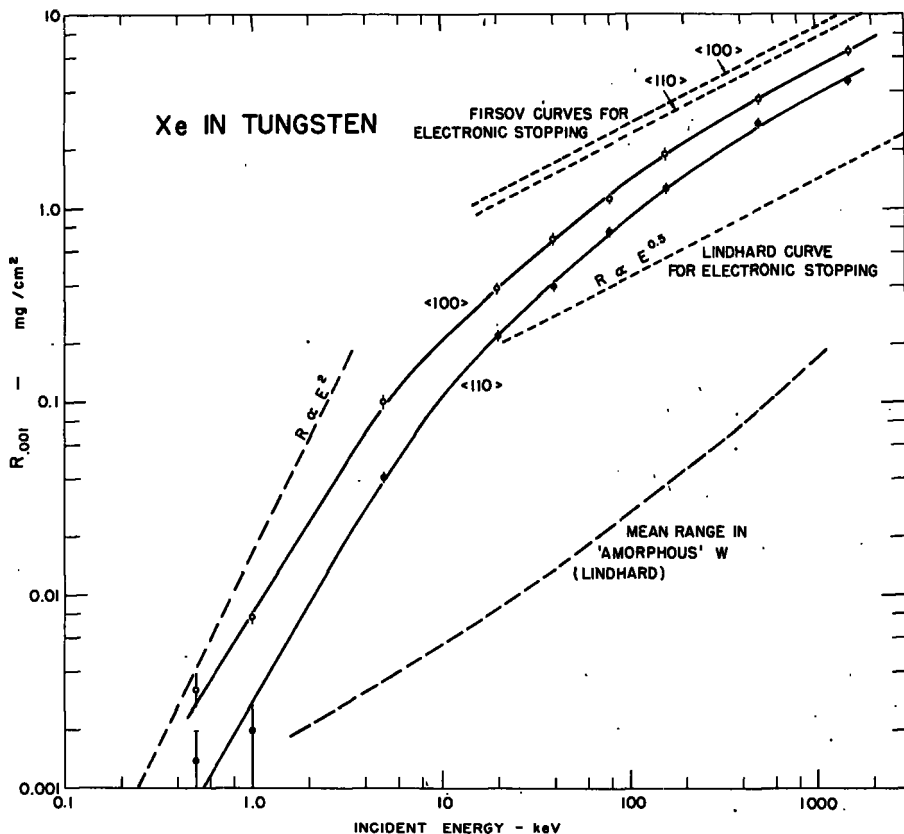


FIG.2.14. The "maximum range"  $R_{0.001}$  (i.e. the depth to which 0.1% of the beam penetrates) as a function of the incident energy of the Xe ions (from Ref.[17]). The dashed curves represent various theoretical estimates of R for random and well-channelled conditions.

the subsequent sections — this sensitivity to surface contamination, bombardment dose, and lattice temperature is considerably reduced, and reproducible data are therefore not so difficult to obtain.

### 2.5. Quantitative features of channelled range distributions

At present, the most reproducible experimental parameter for characterizing range distributions in single crystals is the maximum range  $R_{\max}$ . Studies in tungsten [9, 10, 16] over a wide range of experimental conditions have established that the measured values of  $R_{\max}$  depend only on the choice of the crystal, the crystal direction, the projectile and its energy.  $R_{\max}$  does not vary significantly with bombardment dose, lattice temperature (see Fig. 2.10), surface contamination, misalignment, or beam divergence. On the other hand, the number of particles approaching  $R_{\max}$  — i.e. the overall shape of the range distribution — is quite sensitive to all these factors, as we have seen in the preceding section.

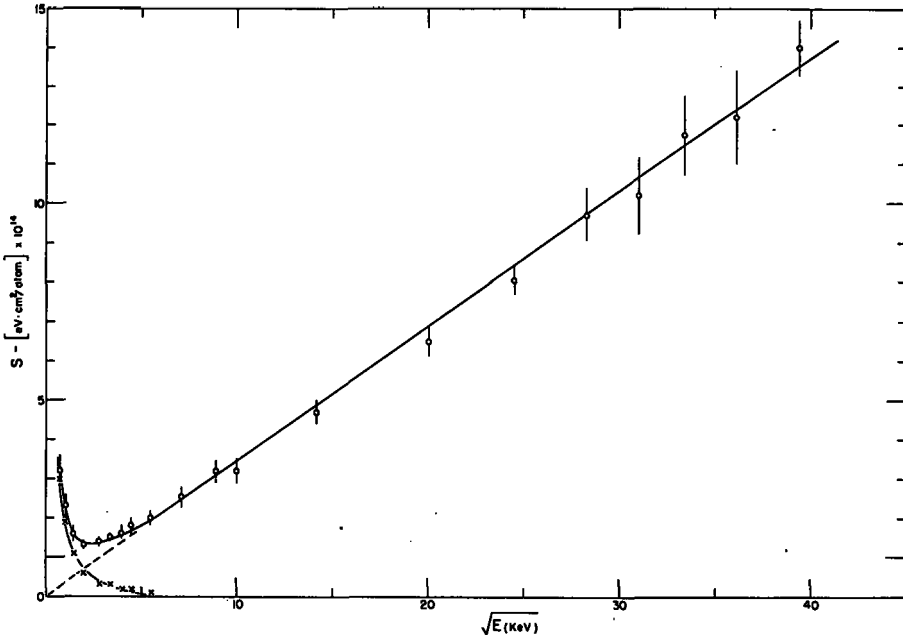


FIG.2.15. Experimentally derived values of the total stopping cross-section  $S$  versus  $E^{\frac{1}{2}}$  for well-channelled xenon ions injected into tungsten along the  $\langle 100 \rangle$  direction (from Ref.[9]). The dotted line is an extrapolation of the electronic-stopping contribution  $S_e$  to lower energies. Crosses indicate the nuclear stopping  $S_n$  derived by subtracting the extrapolated electronic-stopping line from the measured total values.

A detailed investigation of the energy dependence of  $R_{\max}$  has shown that it approximates closely the  $E^{\frac{1}{2}}$  dependence characteristic of electronic stopping (see Fig.1.10) down to energies of a few keV, thus confirming that for a well-channelled ion, electronic stopping is normally the dominant mechanism of energy loss. This is illustrated in Fig.2.15 in which the total stopping cross-section  $S$  of a well-channelled xenon beam, obtained by differentiating the experimental  $R_{\max}$  versus  $E$  curve of Fig.2.14 is plotted as a function of  $E^{\frac{1}{2}}$ . For such a channelled beam, nuclear stopping is seen to be negligible, except at energies below  $\sim 10$  keV. For a similar non-channelled beam in tungsten, the Lindhard theory [18] would predict that the transition energy  $\epsilon_2$  (Fig.1.10) between nuclear and electronic stopping occurs at  $\sim 2.7$  MeV, whereas in Fig.2.15 it occurs at about 4 keV: i.e. between channelled and non-channelled beams there is almost a factor of  $10^3$  difference in  $\epsilon_2$ . This predominance of electronic stopping leads to the observation that, for well-channelled ions of equal energy, the higher the mass, the lower the velocity, and hence the lower the stopping power. Therefore, contrary to the case for non-channelled beams (where nuclear stopping usually dominates), channelled particles of high mass often penetrate deeper than lower-mass particles. For example, a well-channelled bismuth or uranium ion at 100 keV actually has a longer range than a 100-keV channelled proton.

Several other interesting consequences arise from this drastic reduction in the nuclear-stopping contribution:

- (i) Electronic stopping can be investigated (for channelled ions) at much lower energies than would otherwise be possible.
- (ii) A well-channelled ion creates no damage along its trajectory, and so may come to rest as an interstitial atom in a completely undamaged region of the crystal. This has interesting solid-state possibilities and leads (for example) to unusual types of interstitial diffusion [13, 19].
- (iii)  $Z_1$ -oscillation effects in electronic stopping, which in amorphous targets (Fig. 1.13) rarely exceed 30%, are much enhanced for a channelled beam.

## 2.6 $Z_1$ oscillations for channelled ions

Eisen's recent measurements in silicon show peak-to-valley oscillations greater than a factor of ten (Fig. 2.16). Similar oscillations have also been studied in tungsten (Fig. 2.17) and in gold crystals [22]. The  $Z_1$ -values at which these maxima and minima in stopping power occur are almost identical in silicon and tungsten and also in amorphous carbon; hence the nature of the oscillations does not seem to depend strongly on the target material.

For non-channelled beams (Table 1.4), the effect of such stopping-power oscillations on the range distribution is considerably reduced by the dominant contribution of nuclear stopping over most of the energy region of interest.

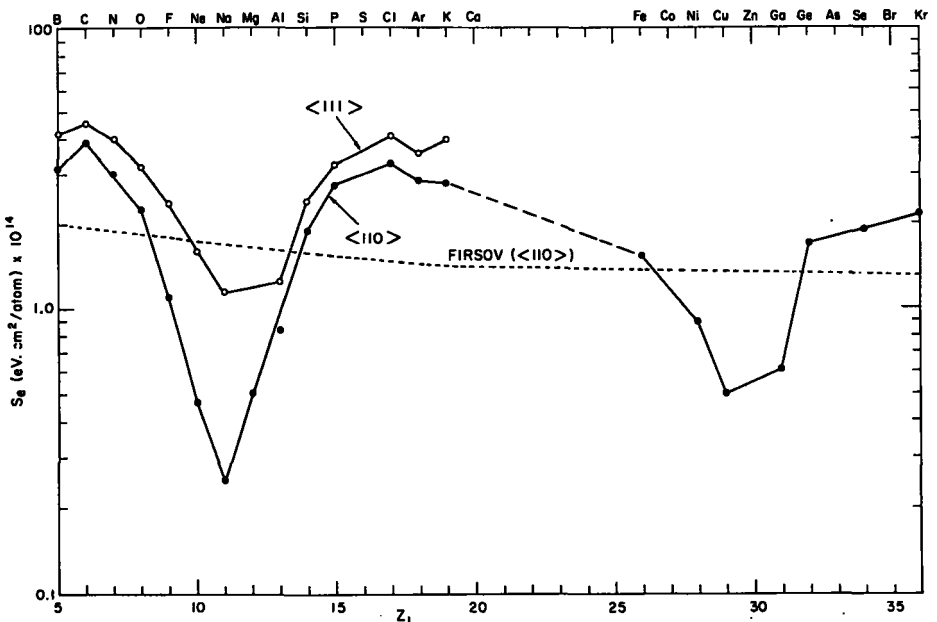


FIG. 2.16.  $Z_1$  dependence of  $S_e$  in silicon for well-channelled ions injected at constant energy (100 keV) along the  $\langle 110 \rangle$  direction (from Ref. [20]). The curve labelled "FIRSOV" is calculated from the electronic stopping equation given in Ref. [21].

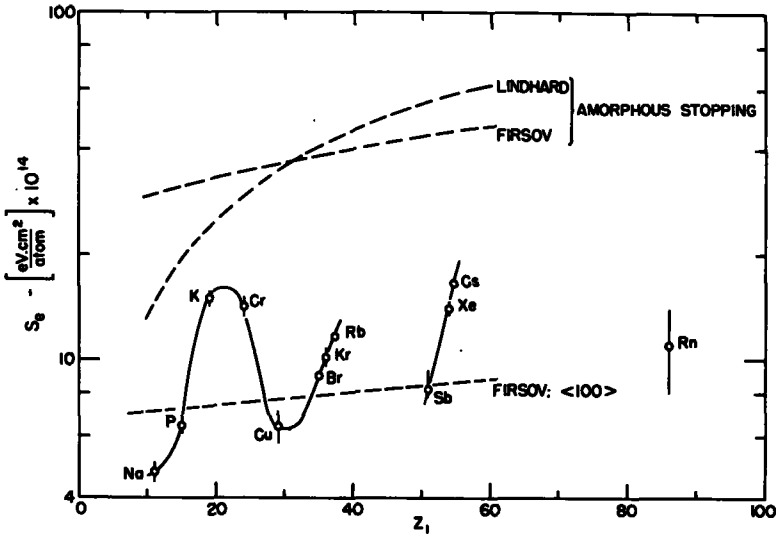


FIG. 2.17.  $Z_1$  dependence of the electronic stopping power ( $S_e$ ) in tungsten for well-channelled ions injected at a constant velocity ( $1.5 \times 10^8$  cm/s) along the  $\langle 100 \rangle$  direction (from Ref.[9]). The curve labelled "FIRSOV":  $\langle 100 \rangle$  is calculated from the electronic-stopping equation given by Firsov [21].

For channelled beams, however, nuclear stopping is negligible down to very low energies (Fig. 2.15) and so the  $R_{\max}$  values will exhibit  $Z_1$ -oscillations comparable in magnitude to those observed for the stopping powers (Figs 2.16 and 2.17): i.e. oscillations of as much as a factor of ten.

The theoretical curves labelled "Firsov" in Figs 2.14, 2.16 and 2.17 are derived from the velocity-proportional stopping-power equation of Firsov [21]. His treatment differs considerably from that used by Lindhard [18]; it has the advantage of expressing the stopping power as a function of impact parameter, and so can be used to estimate the stopping power for a well-channelled ion. As seen in Figs 2.16 and 2.17, Firsov's treatment predicts reasonably well the average attenuation in stopping power in going from the amorphous to the well-channelled case, but does not predict  $Z_1$  oscillations.

Recently, several theoretical groups (see Refs [16-20] in section 1) have looked into the question of these  $Z_1$  oscillations and have shown that the positions of the maxima and minima can be correlated roughly with ion size. Unfortunately, none of the theoretical treatments is yet able to predict accurately the magnitude of the oscillations, nor their dependence on energy or on impact parameter. Further theoretical work is obviously desirable to clarify the situation. In the meantime, the only reliable method for obtaining  $R_{\max}$  is by direct experimental measurement.

## SUMMARY

In non-crystalline targets (i.e. in the absence of channelling effects), the range profile of an implanted ion can be predicted with reasonable confidence. It is clear, however, that in a single-crystal substrate, channelling

phenomena exert a dominant influence on the distribution of the implanted ions. Unfortunately, the channelled part of a range profile is extremely sensitive to many factors that are often difficult to control; in such cases, the observed distribution is neither reproducible nor accurately predictable. In many applications, it is therefore desirable to suppress the channelled component as much as possible.

## REFERENCES TO SECTION 2

- [1] LINDHARD, J., Kgl. Danske Videnskab. Selskab, Mat.-Fys. Medd. 34 14 (1965).
- [2] Von LAUE, M., Historical Introduction to "International Tables for X-ray Crystallography", 1 (1952) (Kynoch Press).
- [3] STARK, J., Phys. Z. 13 (1912) 973.
- [4] ALMEN, O., BRUCE, G., Nucl. Instr. Meth. 11 (1961) 257.
- [5] ROBINSON, M. T., OEN, O. S., Phys. Rev. 132 (1963) 2385.
- [6] PIERCY, G. R., BROWN, F., DAVIES, J. A., McCARGO, M., Phys. Rev. Letts 10 (1963) 399.
- [7] LUTZ, H., SIZMANN, R., Physics Letts 5 (1963) 113.
- [8] NELSON, R. S., THOMPSON, M. W., Phil. Mag. 8 (1963) 1677.
- [9] ERIKSSON, L., DAVIES, J. A., JESPERSGÅRD, P., Phys. Rev. 161 (1967) 219.
- [10] ERIKSSON, L., Phys. Rev. 161 (1967) 235.
- [11] WHITTON, J. L., Can. J. Phys. 46 (1968) 581.
- [12] DEARNALEY, G., FREEMAN, J. H., GARD, G. A., WILKINS, M. A., Can. J. Phys. 46 (1968) 587.
- [13] DAVIES, J. A., ERIKSSON, L., WHITTON, J. L., Can. J. Phys. 46 (1968) 573.
- [14] WHITTON, J. L., CARTER, G., FREEMAN, J. H., GARD, G. A., J. Materials Sci. 4 (1969) 208.
- [15] DAVIES, J. A., BALL, G. C., BROWN, F., DOMEIJ, B., Can. J. Phys. 42 (1964) 1070.
- [16] KORNELSEN, E. V., BROWN, F., DAVIES, J. A., DOMEIJ, B., PIERCY, G. R., Phys. Rev. 136 (1964) A849.
- [17] DAVIES, J. A., ERIKSSON, L., JESPERSGÅRD, P., Nucl. Instr. Meth. 38 (1965) 245.
- [18] LINDHARD, J., SCHARFF, M., SCHIØTT, H. E., Kgl. Danske Videnskab Selskab. Mat.-Fys. Medd. 33 14 (1963).
- [19] DAVIES, J. A., JESPERSGÅRD, P., Can. J. Phys. 44 (1966) 1681.
- [20] EISEN, F. H., Can. J. Phys. 46 (1968) 561.
- [21] FIRSOV, O. B., Soviet Phys.-JETP (English Transl.) 9 (1959) 1076.
- [22] BØTTIGER, J., BASON, F., Rad. Effects 2 (1970) 105.

### 3. CHANNELLING BEHAVIOUR OF LOW-Z IONS (PROTONS, HELIUM, ETC.) AT MeV ENERGIES

#### 3.1. Introduction

In the previous section, we have seen how the motion of energetic heavy ions can be strongly influenced (i. e. channelled) by the regular arrangement of atoms composing a crystal lattice. For the relatively low velocities used in most implantations, this channelling effect depends strongly on implantation conditions, and so heavy-ion range distributions cannot be accurately predicted. On the other hand, experimental and theoretical studies have established that channelling is not confined to the lower-energy region where nuclear stopping normally predominates. The proton transmission experiments of Dearnaley [1], and the later work of Sattler and Dearnaley [2], and of Erginsoy et al. (Fig. 3.1) show clearly that protons and alpha particles, even at MeV energies, undergo as much

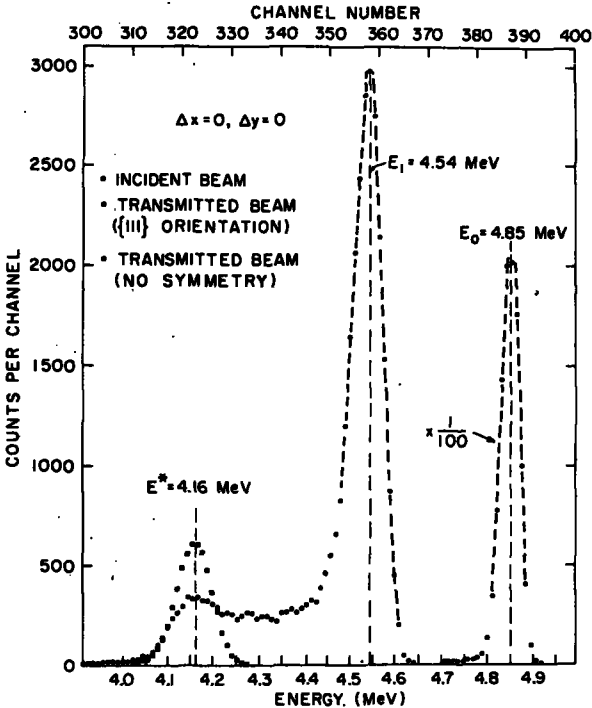


FIG. 3.1. Energy spectra of protons (incident energy 4.85 MeV) transmitted through a thin silicon crystal along the open  $\{111\}$  direction and in a direction of no symmetry. All three spectra are for the same number of incident protons using a 1-mm-diameter detector. The least deflected part of the beam (central spectrum) shows little energy straggling (from Ref. [3]).

as a threefold reduction in their rate of energy loss, if injected along a close-packed axis or plane. Similar reductions in energy loss have also been observed by Datz et al. [4] for heavy ions, such as  $^{79}\text{Br}$  and  $^{127}\text{I}$ , at energies up to 100 MeV. As a result of such experiments, we now recognize that channelling is a rather general phenomenon, occurring for all atomic projectiles in crystals at energies from below 1 keV up to at least 100 MeV.

Furthermore, for high-velocity particles (such as MeV protons or helium ions) the situation is quite different from the early heavy-ion case: here, the channelling behaviour is more reproducible, and the observed effects can be interpreted quantitatively in the theoretical framework given by Lindhard [5]. In the next section, we shall discuss, therefore, the experimental evidence for channelling in this high-velocity region.

### 3.2. Theoretical framework

One distinguishes three different types of particle trajectories (Fig. 3.2):

- (i) An energetic charged particle, moving through a lattice within a predictable critical angle  $\psi$  of an atomic row (or plane), is steered

by successive gentle collisions (trajectory A), and is thereby prevented from entering a forbidden region around each lattice row. The radius  $r_{\min}$  of this forbidden cylinder may be equated roughly to either the Thomas-Fermi screening distance,  $a$ , (which is typically 0.1 - 0.2 Å) or the vibrational amplitude  $\rho$  - whichever is larger.

- (ii) When the incident angle  $\theta$  is much larger than  $\psi$ , the particle has no "feeling" for the existence of a regular atomic lattice, and so has a random trajectory (trajectory C).
- (iii) On the other hand, if  $\theta$  is only slightly larger than  $\psi$ , then the particle trajectory (trajectory B) actually has an enhanced probability of being close to the atomic rows, and hence of undergoing violent collisions. For the case of axial channelling, the critical angle of approach  $\psi$  for such a steered motion is given by the formula

$$\psi = \alpha \left[ \frac{2Z_1Z_2e^2}{Ed} \right]^{\frac{1}{2}} \quad (3.1)$$

$Z_1e$  and  $Z_2e$  are the nuclear charges of the moving particle and the lattice atom, respectively,  $E$  is the energy of the projectile, and  $d$  is the atomic spacing along the lattice row. Here  $\alpha$  may be considered a proportionality constant, the value of which depends weakly on the vibrational amplitude

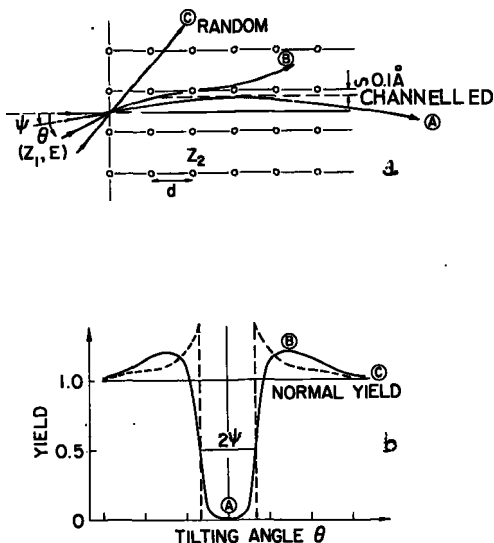


FIG. 3.2. a) Charged-particle trajectories for three typical values of the angle  $\theta$  between the incident beam and a close-packed row. Note that the channelled beam does not approach closer to the row than  $\approx 0.1$  Å (the Thomas-Fermi screening distance).

b) Angular dependence of the yield of any process requiring impact parameters less than 0.1 Å: --- perfect non-vibrating lattice: — lattice vibrations included.

of the lattice atoms, and hence on the temperature. Typical values of  $\alpha$  fall between 0.7 and 1.2. The value of  $\psi$  for 1-MeV protons or helium ions is typically of the order of  $1^\circ$ .

One simple but very important consequence of the above model is that all physical processes requiring smaller impact parameters than  $r_{\min}$  are completely prohibited for a channelled beam. Consequently, the yield of such a process is a quantitative measure of the non-channelled fraction of the beam, and so provides a very sensitive "detector" for studying the transition between channelled and non-channelled trajectories. The lower part of Fig. 3.2 illustrates the predicted orientation dependence for the yield of a typical close-encounter process.

Suitable close-encounter processes include wide-angle elastic (Rutherford) scattering, nuclear reactions, Coulomb excitation, and the production of inner-shell X-rays (K-, and in heavier atoms L- and even M-shell X-rays). Extremely strong attenuations (up to 100-fold) in the yields of such processes are expected to occur in the aligned case in comparison with the random case. The yield does not fall quite to zero, since even for  $\psi = 0$ , there is still a small random fraction (of the order of 1%), determined by the point of impact on the crystal surface: i. e. those particles which enter the crystal close enough to the end of a row — within the area  $\pi(r_{\min})^2$  — to be "de-channelled" during the initial impact.

Such pronounced directional effects have been observed in numerous experiments [6-8], and a typical example is illustrated in Fig. 3.3. Also shown in Fig. 3.3 is the predicted orientation dependence of the scattering yield, derived from the Lindhard theory (see Eq. 1), with the root-mean-square amplitude ( $\rho$ ) of the tungsten atoms set equal to 0.096 Å. We see that the agreement between the observed and the predicted angular dependence is really quite satisfactory. We see, too, that, at angles slightly greater than the critical angle (corresponding to trajectory B in Fig. 3.2), the observed yield actually rises somewhat above the random level, as predicted.

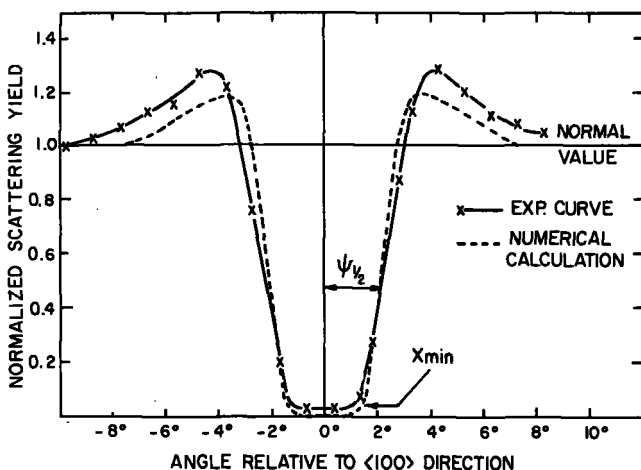


FIG. 3.3. Comparison between the experimental and calculated  $\langle 100 \rangle$  dip in scattering yield for 480-keV protons incident on a tungsten crystal (from Ref. [9]).

Experiments of this type have proved to be the most powerful method of studying the steering mechanism responsible for channelling; they also form the basis for most of the applications of the so-called "channelling-effect" technique to other fields. For both these purposes, wide-angle Rutherford scattering (such as that used in Fig. 3.3) is a particularly versatile close-encounter process because it enables the energy and atomic number of the projectile, and the atomic number of the target to be varied over a very wide range.

Note that at these high energies the stopping power of a channelled ion (Fig. 3.1) is only attenuated by about a factor of 2-3, since even in the middle of a channel there is still some energy loss to electrons. Consequently, stopping power (and range) measurements do not provide nearly as sensitive an indicator of the transition between channelled and random trajectories.

Let us now consider in more detail the advantages and limitations of various types of close-encounter measurements, what sort of effects are observed, and how they compare with theory.

### 3.3. Experimental technique

A standard goniometer assembly for investigating the yield of back-scattered particles is illustrated in Fig. 3.4. The incident beam (typically 1-MeV helium ions), collimated to  $0.1^\circ$  or better, is allowed to strike a crystal mounted on a suitable double-axis goniometer, which allows both a tilt motion ( $\theta$ ) and an azimuthal rotation ( $\phi$ ) around an axis perpendicular to the base plate of the goniometer. Particles that have undergone wide-angle ( $\sim 150^\circ$ ) scattering are detected by means of a solid state detector, and their energy spectrum is recorded on a multi-channel analyser. For investigating other close-encounter processes (such as  $\gamma$ -rays from a nuclear reaction, or X-ray emission) one merely substitutes an appropriate  $\gamma$ - or X-ray detector. Since Rutherford scattering has been by far the most widely used process to date, we will select it as our main example to illustrate what can be achieved.

Typical energy spectra for a 1-MeV helium beam backscattered from a silicon crystal are shown in Fig. 3.5 (a). The random spectrum is obtained by orienting the crystal so that the incident beam is not aligned with any crystal axis or plane. The aligned spectrum shows the large reduction in backscattered yield when a crystal axis,  $\langle 111 \rangle$  in this case, is parallel to the beam direction.

Particles of mass 4 scattered through  $150^\circ$  by  $^{28}\text{Si}$  atoms lose a certain amount (41%) of their energy in the elastic collision with the silicon; thus the spectra have a sharp threshold at  $0.59 E_0$  (where  $E_0$  is the energy of the incident beam), corresponding to backscattering from the surface layer of silicon. The probability of a backscattering event is extremely small; hence, most of the beam penetrates into the target, giving rise to a continuum of backscattered particles from greater depths in the crystal. These particles lose energy along their path in addition to the energy lost in the actual scattering event. They therefore emerge with lower energy, giving rise to an energy spectrum of scattered particles. If the stopping power is known, this energy spectrum can be converted into a depth scale in which each interval of energy corresponds to a depth interval in the crystal from

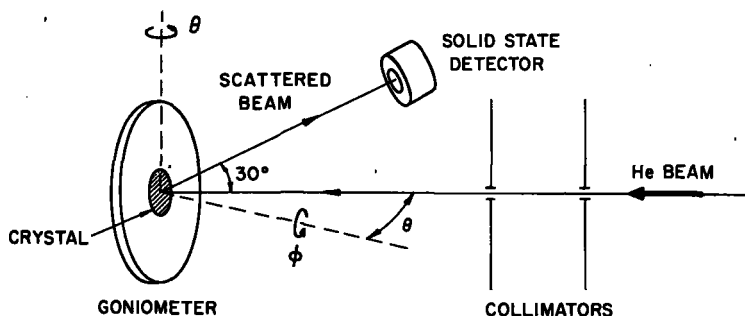


FIG. 3.4. Schematic diagram of the experimental assembly used for scattering experiments.

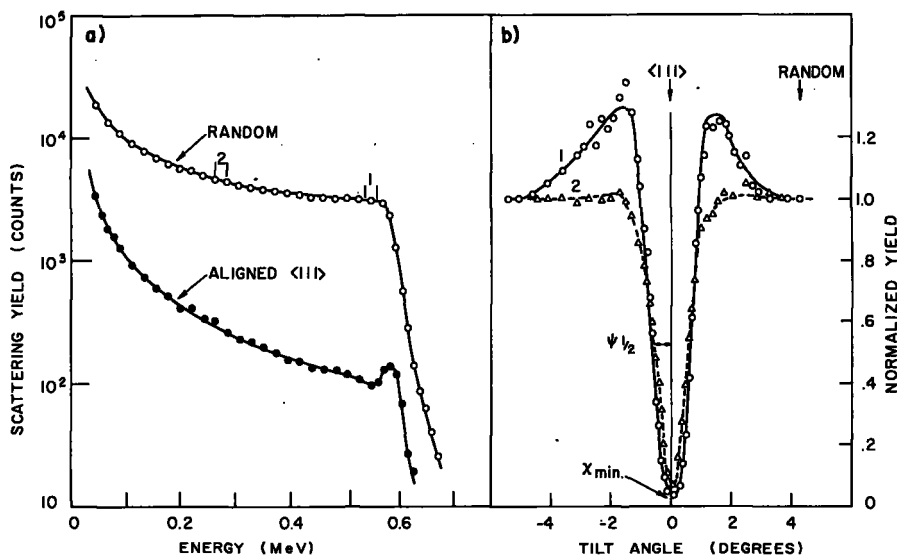


FIG. 3.5. a) Energy spectra for 1-MeV helium ions backscattered from a silicon crystal: ● - beam incident along the  $\langle 111 \rangle$ ; ○ - beam incident in a "random" direction. The energy regions 1 and 2 indicate the two single-channel-analyser settings used in (b). These correspond to depths of 900 and 6000 Å, respectively. b) Orientation dependence of the normalized yield obtained from the energy regions 1 and 2 in (a). Tilt angles marked " $\langle 111 \rangle$ " and "random" show the orientations at which the energy spectra in (a) were taken (from Ref. [10]).

which particles are scattered. With a 1-MeV beam of helium ions, one can probe depths of about 1 micron. The energy resolution of the detector is usually above 15 keV, which gives a depth resolution of  $\sim 300$  Å in the region near the surface.

### 3.4. General features of axial (and planar) channelling experiments

Detailed orientation scans from two different depths in silicon are shown in Fig. 3.5 (b). These are obtained by recording the yield in the

narrow energy regions 1 and 2 (Fig. 3.5 (a)), while tilting the  $\langle 111 \rangle$  axis through the beam direction.

The observed critical angle ( $\psi_{\frac{1}{2}}$ ) and minimum yield ( $\chi_{\min}$ ) both depend on the depth beneath the surface at which the measurements are made. The critical angle is determined by measuring the angular half-width ( $\psi_{\frac{1}{2}}$ ) at a level midway between the aligned and random levels. The minimum yield  $\chi_{\min}$  is defined as the ratio of the yield in the perfectly aligned direction to that in a random direction; it is therefore a direct measure of the unchannelled fraction of the beam. The depth dependence of  $\chi_{\min}$  can be obtained from the aligned and random spectra of Fig. 3.5 (a), and that of  $\psi_{\frac{1}{2}}$  from the detailed orientation scans of Fig. 3.5 (b).

From the results in Fig. 3.5, we see that even at a depth of 6000 Å, more than 90% of the particles in the beam are still channelled, indicating that de-channeling effects are much less serious than in the heavy-ion range distributions of section 2. On the other hand, the region of enhanced yield at angles slightly greater than  $\psi_{\frac{1}{2}}$  (the so-called "shoulder" region) decreases quite rapidly with increasing depth - and indeed has completely disappeared in the 6000 Å curve of Fig. 3.5 (b).

The area of the small peak at the high-energy edge of the aligned spectrum (Fig. 3.5 (a)) is a measure of the amount of disordered silicon in a surface oxide layer - in this case, it contains  $6 \times 10^{15}$  Si atoms/cm<sup>2</sup>, and is therefore equivalent to  $\sim 25$  Å of silicon oxide. Since this is much narrower than the detector resolution ( $\sim 300$  Å), the peak height does not rise to the random curve.

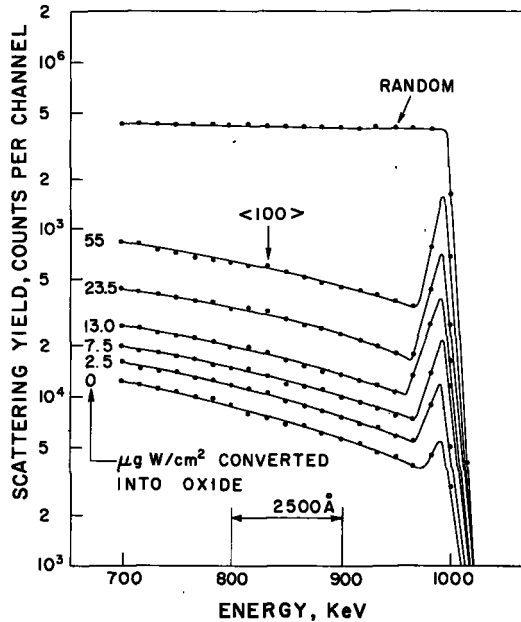


FIG. 3.6. Energy spectrum of 1-MeV protons scattered 150° in a tungsten crystal covered with anodically formed oxides of various thicknesses. The unit " $1 \mu\text{g of W/cm}^2$ " is equivalent to  $\sim 12$  Å of  $\text{WO}_3$  (from Ref. [11]).

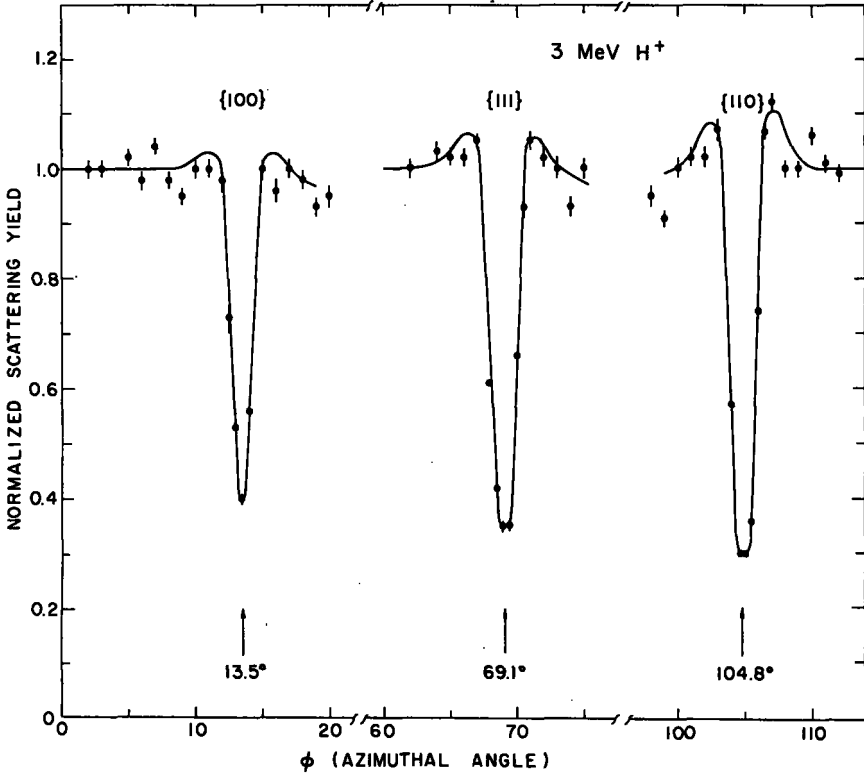


FIG. 3.7. Planar channelling of 3-MeV protons in Si, measured by rotating around a  $\langle 110 \rangle$  axis at a tilting angle  $\theta = 5.0^\circ$ . Experimental data are the yields measured just beneath the crystal surface (from Ref. [12]).

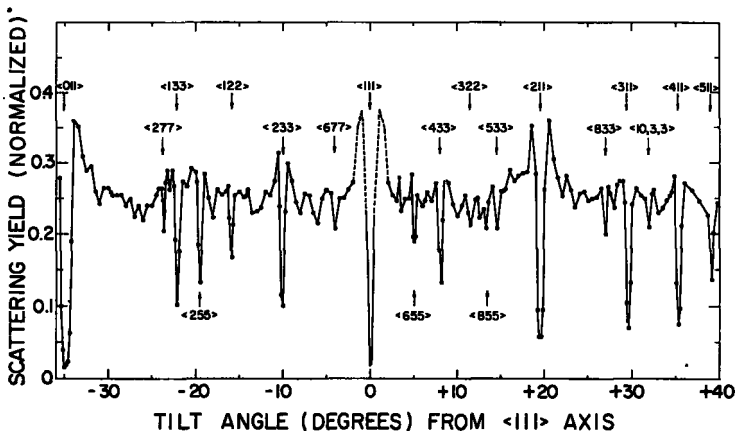


FIG. 3.8. High-index axial channelling effects for 1.0-MeV helium in the  $\{110\}$  plane of silicon. The measured yield is from a scattering zone about  $1000 \text{ \AA}$  beneath the crystal surface.

Figure 3.6 illustrates the effect of somewhat thicker oxide layers on the channelling of MeV protons in tungsten. Again, the peak area in the aligned ( $\langle 100 \rangle$ ) curves is a quantitative measure of the number of tungsten atoms in the oxide. We observe that the yield level from the underlying crystal (i. e. at lower energies) also increases with increasing oxide thickness, indicating that a significant amount of the beam becomes scattered through an angle greater than  $\sim \psi_{\frac{1}{2}}$  in traversing the amorphous surface oxide. However, comparison of the  $2.5 \mu\text{g}/\text{cm}^2$  curve in Fig. 3.6 with the corresponding ( $3 \mu\text{g}/\text{cm}^2$ ) curve in Fig. 2.13 shows clearly the marked difference in sensitivity to surface contamination between the two velocity regimes: i. e.  $< 2\%$  dechannelling for the 1-MeV proton case, compared to  $\sim 90\%$  dechannelling for 20-keV Kr ions.

So far, we have been considering only axial channelling, but similar effects also occur whenever the beam is aligned with one of the low-index planes in the crystal (Fig. 3.7). The attenuation in yield for the close-encounter processes is usually about a factor of 3-5 for a low-index plane: this is considerably weaker than for axial channelling. Again, as in the axial case, there is evidence of compensating shoulders at somewhat larger angles. Note that the angular widths in Fig. 3.7 are expressed in terms of the azimuthal angle  $\phi$  around a  $5^\circ$  cone, and hence the values appear rather large. To obtain the true angular width of the planar dips, it is of course necessary to project the observed angles in Fig. 3.7 on to an axis perpendicular to the plane. One then obtains values of 0.1-0.2° for the width at half minimum, compared to  $\sim 1^\circ$  for axial directions.

Planar channelling effects, therefore, are similar but somewhat weaker than those for the corresponding axial directions - and so in these lectures (for convenience) we shall restrict our discussion largely to axial channelling.

Figure 3.8 depicts the complexity that arises even in a simple cubic crystal, due to the large number of high-index directions (and planes) that produce significant channelling effects. Starting from a  $\langle 011 \rangle$  direction, a silicon crystal was rotated progressively through  $\sim 75^\circ$  in the  $\langle 110 \rangle$  plane, and at least twenty significant attenuations in scattering yield were observed at angles corresponding to identifiable higher-index directions. Admittedly, for an axis such as  $\langle 833 \rangle$ , the attenuation is a fairly small one, but nevertheless it raises a rather important question: i. e. how do you define a "random" direction, or measure a random yield curve (such as those in Figs 3.5 (a) and (b)) in a single crystal? If one merely tilts the crystal several degrees away from the low-index direction along some arbitrarily chosen azimuthal angle, there is roughly a 20% probability of being within the critical angle of some high-index direction. The best procedure is to search carefully for an angular region where the scattering yield exhibits a fairly constant plateau; even then, however, it is difficult to define more accurately than  $\sim 5\text{-}10\%$  the random-yield level for a single crystal. This uncertainty is often the main limitation to the accuracy achievable in certain applications of channelling, such as the determination of foreign-atom location (sections 4 and 5).

### 3.5. Comparison of various close-encounter processes

According to theory, the yield of any process requiring an impact parameter less than  $\sim 0.1 \text{ \AA}$  (Fig. 3.2) should show exactly the same orien-

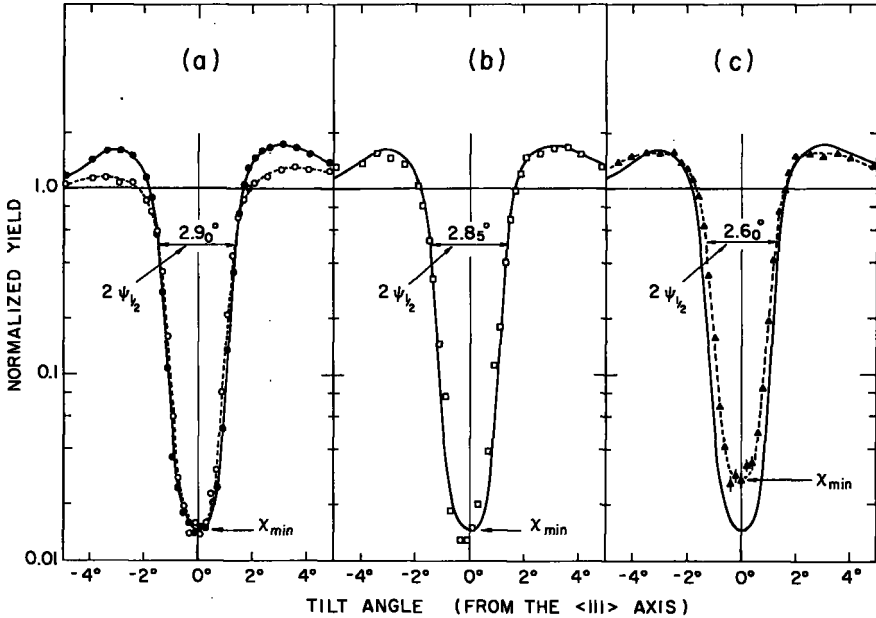


FIG. 3.9. Comparison of Rutherford scattering and of L and M X-ray yields in tungsten as a function of the angle between the incident beam (1.4-MeV helium) and the  $\langle 111 \rangle$  axis: (a) Rutherford-scattering yields -  $\circ$  at 1200 Å depth,  $\bullet$  at 5000 Å depth; (b) L X-ray yield ( $\square$ ) compared to the 1200 Å Rutherford-scattering curve (—); (c) M X-ray yield ( $\blacktriangle$ ) compared to the 1200 Å Rutherford scattering curve (—). All yield curves approach the value of 1.0 (i.e. the normal "random" yield) at larger tilt angles (from Ref. [13]).

tation dependence. Experimental confirmation of this point is provided in Fig. 3.9, in which simultaneous measurement of Rutherford scattering and of K- (not shown), L-, and M- X-ray yields were made.

Comparison of the X-ray yields with the 1200 Å Rutherford-scattering curve shows that (i) the orientation dependence of the yield of L X-rays (Fig. 3.9 (b)) is indistinguishable from that of the Rutherford-scattering yield, indicating that the channelled beam is unable to interact with the L-shell electrons, and (ii) the yield curve of M X-rays (Fig. 3.9 (c)) is slightly narrower and shallower than that of the other processes, indicating that a channelled beam does penetrate somewhat into the M-electron region, and that  $r_{\min}$  is therefore comparable in magnitude to the mean impact parameter for ejecting an M-shell electron. Note that the mean radii of the K-, L-, and M-shells in tungsten are 0.007, 0.04, and 0.10 Å, respectively.

Thus, we see that the different close-encounter processes can be used interchangeably in studying channelling effects - provided the impact parameters are all less than  $\sim 0.1$  Å. This flexibility is of particular advantage in investigating compound crystals - i.e. crystals containing two or more different atomic species - since it enables several different processes to be used to monitor simultaneously the interaction of a channelled beam with each atomic species. If, for example, one wishes to

study channelling in an  $\text{UO}_2$  crystal, then a beam of 0.975 MeV deuterons is an ideal choice. At this energy, the  $^{16}\text{O}(d,p)^{17}\text{O}$  reaction is selective for the oxygen sub-lattice, since the deuteron energy of 0.975 MeV is much too low to induce a (d,p) reaction with the heavy uranium atoms. Rutherford scattering, on the other hand, is equally selective for the uranium sub-lattice, since scattering from the low-Z oxygen atoms is far too weak, both in energy and intensity, to contribute significantly to the observed yield.

The protons from the above (d,p) reaction have an energy of  $\sim 1.4$  MeV, whereas the upper edge of the backscattered deuteron spectrum is only 0.94 MeV. Hence, in the energy spectrum from the solid-state detector, one can simultaneously observe both reaction yields. In practice, because of the much smaller cross-sections for the (d,p) reaction, it is better to use two detectors, A & B. Detector B is then placed much closer to the crystal to register protons; it is covered with a thin mylar film which prevents the more numerous (but less penetrating) deuterons from reaching it.

The results of such a channelling study are illustrated in Fig. 3.10. Two completely different types of behaviour are seen, depending on the axis chosen. Along the  $\langle 100 \rangle$  and  $\langle 110 \rangle$  (the latter is not shown here), the backscattering yield off the U-atoms exhibits a much wider and deeper attenuation than that for the protons of the  $^{16}\text{O}(d,p)$  reaction, whereas along the  $\langle 111 \rangle$  both processes exhibit identical orientation dependence. The reason for this difference is seen in Fig. 3.11: along the  $\langle 100 \rangle$  and  $\langle 110 \rangle$  there are in fact two different types of atomic rows (each containing one atomic species), but along the  $\langle 111 \rangle$  there is only one type of row (containing both oxygen and uranium atoms). Lindhard's theoretical description [5] of axial channelling has shown that the lattice can be treated as a series of isolated (parallel) "strings" of atoms; hence, each type of string, or row, will exhibit its own characteristic critical angle  $\psi_{1/2}$ , as given by Eq. (1).

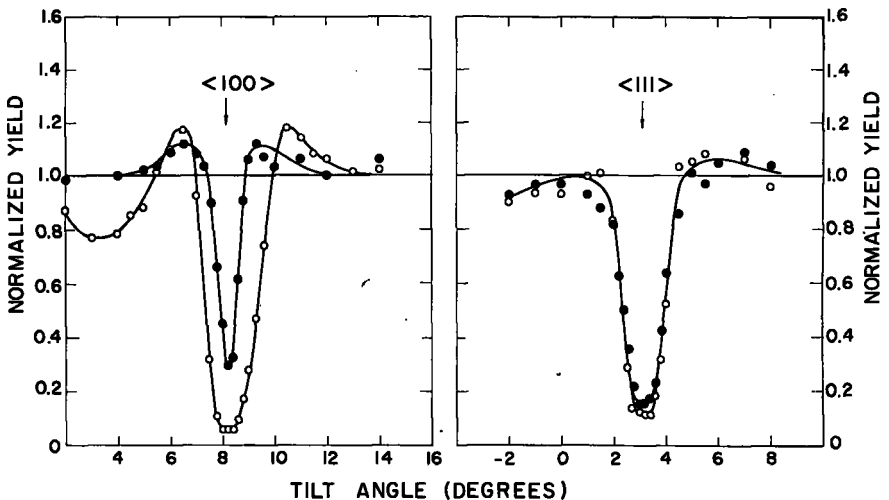


FIG. 3.10. Axial channelling of 0.975-MeV deuterons in  $\text{UO}_2$  at a mean depth of 4000 Å: O, backscattering yield from the uranium atoms; ●, proton yield from the  $^{16}\text{O}(d,p)^{17}\text{O}$  reaction (from Ref. [14]).

## THE $UO_2$ LATTICE

( $d = 5.47 \text{ \AA}$ )

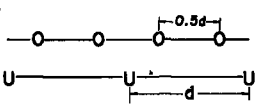
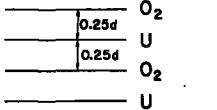
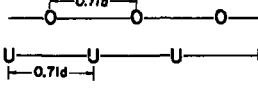
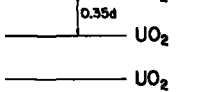
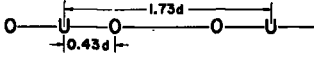
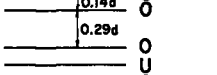
AXIAL CONFIGURATIONS	PLANAR CONFIGURATIONS
<p><b>&lt;100&gt;:</b></p> 	<p><b>{100}:</b></p> 
<p><b>&lt;110&gt;:</b></p> 	<p><b>{110}:</b></p> 
<p><b>&lt;111&gt;:</b></p> 	<p><b>{111}:</b></p> 

FIG. 3.11. Axial and planar atomic configurations in  $UO_2$ , in terms of the unit cell spacing  $d$ .

It is interesting to note that, along the  $\langle 100 \rangle$ , for example, one can tilt the crystal slightly so that the beam is no longer channelled with respect to the O-rows, and yet is still well within the critical steering angle of the U-rows. Under such conditions, the oxygen atoms behave essentially as interstitial scattering centres. Normal multiple scattering off these oxygen atoms causes a rather rapid de-channelling to occur with respect also to the uranium rows as the beam penetrates deeper into the crystal.

The data in Fig. 3.10 indicate that at shallow depths the  $\langle 100 \rangle$  direction exhibits considerably stronger channelling effects than the  $\langle 111 \rangle$ , as far as uranium atoms are concerned. On the other hand, at larger depths the  $\langle 111 \rangle$  becomes the preferred channelling direction, since it does not exhibit the rapid dechannelling effect described above. This is sometimes an important consideration in certain applications of channelling (cf. the fission lifetime studies in Lecture 6), where measurements are not being confined to the surface region.

### 3.6. "Blocking" experiments

Up to now, we have considered the channelling behaviour of particles approaching the crystal from the outside (the external-beam case). But, the same separation into allowed and forbidden trajectories occurs if the charged particles originate from a position inside the lattice: e. g. as a consequence of radioactive decay (Fig. 3.12) or of an elastic scattering event off lattice nuclei. If the trajectory originates from a position contained in a row of atoms (such as a lattice site), it cannot emerge from the crystal within the critical angle characteristic of that row - i. e. it cannot become channelled - since it started out from within one of the forbidden regions (Fig. 3.2 (a)) for channelled trajectories. Hence, a reduction in the number of emitted particles is observed in the direction of the row, and this phenomenon is usually termed "blocking". Lindhard [5]

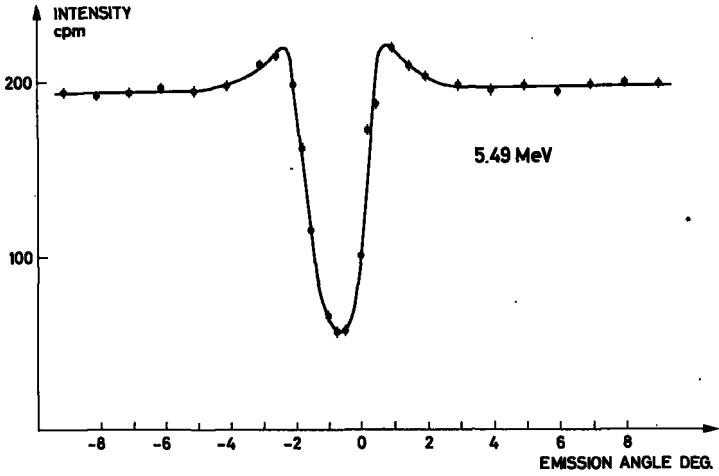


FIG. 3.12. Intensity as a function of emission angle for 5.49 MeV  $\alpha$ -particles from  $^{222}\text{Rn}$  atoms embedded (at 60 keV) into a tungsten crystal (from Ref. 15). Note that  $0^\circ$  on the abscissa scale corresponds roughly (i.e.  $\mp 1^\circ$ ) to the  $\langle 111 \rangle$  axial direction.

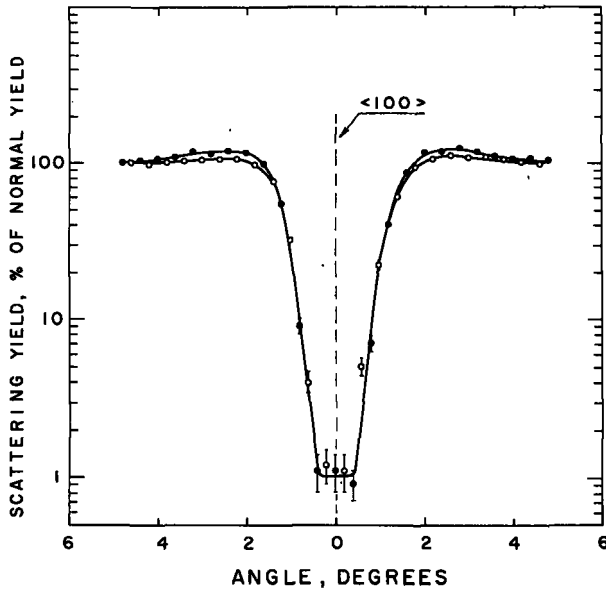


FIG. 3.13. Yield of protons scattered  $135^\circ$  in tungsten. Primary proton energy is 1 MeV. Depth of scattering zone is 3000-4000  $\text{\AA}$  beneath the surface. Solid circles denote channelling results; open circles, blocking results (from Bøgh and Whitton, Ref. [16]).

shows from reversibility arguments that channelling and blocking experiments are completely equivalent, provided depth effects are negligible, and this equivalence is illustrated quantitatively in the experimental work of Bøgh and Whitton (Fig. 3.13) in which the same crystal was used to investigate both processes.

One may well ask why the attenuation factor in Domeij's pioneering experiment on blocking (Fig. 3.12) is so much weaker than those in Fig. 3.13. In Domeij's experiment, an  $\alpha$ -emitting isotope  $^{222}\text{Rn}$  had been implanted into the tungsten crystal, and probably not all of the  $^{222}\text{Rn}$  atoms had ended up on lattice sites. In fact, by comparing the 5-fold attenuation in Fig. 3.12 with the  $\sim 100$ -fold attenuation in Fig. 3.13 (where all the emitted particles originate from lattice nuclei), one can deduce that only  $\sim 80\%$  of the Rn atoms in Domeij's experiment were substitutionally located. In the next two sections, we shall discuss more fully such uses of channelling and blocking to locate the site of foreign atoms in a lattice.

In the case of Rutherford scattering, it is possible to look at either the channelling or the blocking case, simply by aligning the crystal either with the incident-beam direction or with the detector, as seen in Fig. 3.13. In fact, as has been demonstrated by Bøgh [11] and by Feldman and Appleton [17], one can employ a double-alignment technique in order to combine in a single measurement both the channelling of the incident beam and the blocking of the emitted beam. The overall attenuation in the Rutherford-scattering yield is then determined by a geometrical combination of two attenuation factors, i. e. the attenuation factor due to channelling of the incoming beam, multiplied by the comparable attenuation factor for the blocking effect. In this way, attenuation factors of up to several thousand can actually be produced. We shall see later (Figs 5.4 and 5.6) how the enhanced attenuation due to double-alignment may be utilized in detecting low levels of lattice disorder.

### 3.7. Positron channelling

According to theory (see Eq. (1)), the steering process depends only on the atomic number — and not on the mass — of the projectile. Hence deuterons and protons of the same energy should have the same orientation dependence — as is indeed the case (Fig. 3.14). Even positrons would be expected to exhibit identical channelling behaviour to protons of similar energy. The first experimental evidence for positron channelling (Fig. 3.15) was obtained by injecting  $^{64}\text{Cu}$  atoms into a copper crystal and observing the blocking of the emitted positrons. Again, as in the  $^{222}\text{Rn}$  case (Fig. 3.12), only a 4-fold dip is observed — indicating that not all the implanted atoms are on lattice sites — but the angular width agrees rather well with calculations [19] based on the Lindhard theory.

The  $^{64}\text{Cu}$  isotope decays also by emitting electrons ( $\beta^-$ ), and on the left-hand side of Fig. 3.15 we see the effect of the crystal lattice on their emission pattern. Electrons of course have a negative charge, and so feel an attractive rather than a repulsive potential on approaching an aligned row of lattice atoms. As Lindhard pointed out in his lectures, the steering mechanism for electrons is considerably more complex than for positrons, and is further complicated by the need to include diffraction effects at these moderately low energies. However, qualitatively we note

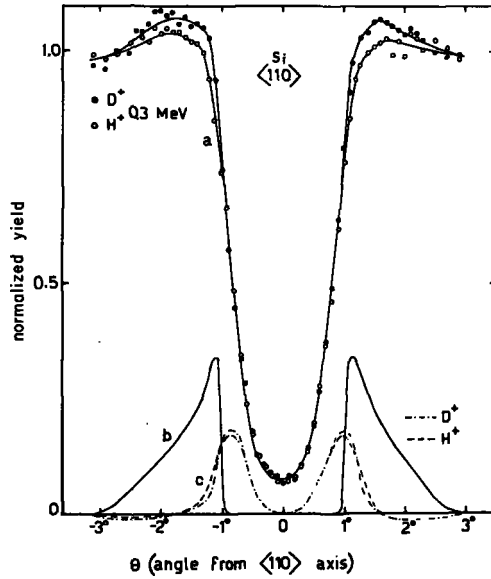


FIG. 3.14. Backscattered yields for 0.3-MeV  $H^+$  and  $D^+$  in silicon at a depth of 1000 Å (from Ref. [18]). Curves b and c represent the yield difference ( $D^+ - H^+$ ) and the angular derivative of the yields respectively.

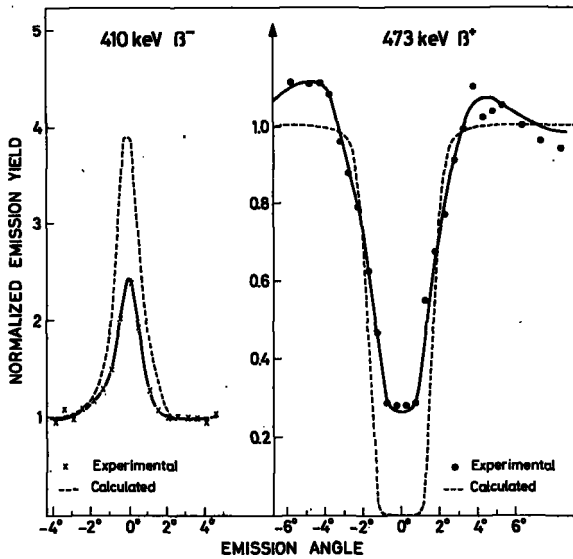


FIG. 3.15. Angular distribution (around a  $\langle 110 \rangle$  direction) of electrons ( $\beta^-$ ) and positrons ( $\beta^+$ ) emitted from  $^{64}\text{Cu}$  atoms implanted in a copper crystal (from Uggerhøj and Andersen, Ref. [19]).

that for electrons the orientation dependence is inverted (i.e. a peak instead of a dip in yield) and is much narrower in width. We will not discuss electron channelling further, except to point out (i) that MeV electron beams are readily available in many Van de Graaff accelerator laboratories; and (ii) that, since electron beams generally create much less damage than protons, they would be potentially more useful probes in many of the channelling applications to be discussed in sections 4-6. Unfortunately, at present, the theoretical basis for electron channelling is not nearly as quantitative as that for positively charged particles - but many laboratories are currently trying to improve our understanding.

As far as positrons are concerned, Lindhard has shown that their trajectory (at a given energy) is considerably more classical than that of an electron, and that in the MeV region the classical description should be quite adequate - at least for axial channelling. A striking confirmation of this has been provided recently by J.U. Andersen et al. [21], using an external beam of accelerated positrons, and studying the orientation dependence of their elastic scattering yield. As can be seen in Fig. 3.16, the orientation dependence for the positron yield curve at 1 MeV is almost identical to that for protons at 670 keV, except in the "shoulder" region. We should point out that in Eq. (1) it is not really the kinetic energy  $E$ , but rather one-half the product of (momentum)  $\times$  (velocity) - i.e.  $\frac{1}{2}pv$  - that should be used. For relativistic particles, such as 1-MeV positrons, a significant correction is involved, and it is for this reason that 670-keV protons are used for the comparison in Fig. 3.16.

Unfortunately, positron beams of high intensity are not readily available. The experiment in Fig. 3.16 was carried out by placing a suitable radioactive source in the terminal of a 1-MV accelerator, but the intensity was so weak that the experiment required several days. Consequently, the use of positron beams for various channelling applications (as a less damaging alternative to protons) is not yet a practical possibility.

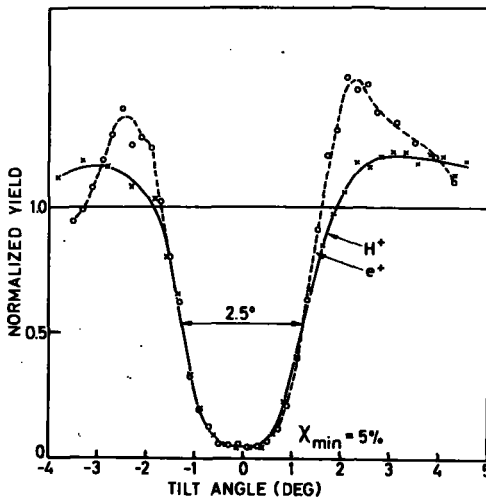


FIG. 3.16. Comparison of positron and proton dips in scattering yield along the  $\langle 110 \rangle$  axis in gold. The abscissa scale for the proton dip has been scaled from 1 MeV to 0.67 MeV (from Andersen et al., Ref. [21]).

## SUMMARY

To sum up, we see that there are many different types of close-encounter process (Rutherford scattering, nuclear reactions, inner-shell X-ray production, positron-blocking, etc.), involving violent collisions between MeV positive particles and crystal nuclei — and that they all exhibit identical orientation dependence. Consequently, for a given channelling experiment, one may select whichever process is most appropriate.

### 3.8. Comparison with theory at zero depth

As already seen in Figs 3.2 - 3.5, the two most commonly used experimental parameters for characterizing the orientation dependence of close-encounter processes such as Rutherford scattering are the minimum yield  $X_{\min}$  in the perfectly aligned direction and the angular width  $\psi_{1/2}$ , measured at a level mid-way between the random and perfectly-aligned yield values.

We will therefore compare experimental and predicted values for these two quantities as a function of energy, atomic number, lattice temperature, and lattice spacing.

In the preceding lecture, we saw that  $\psi_{1/2}$  in the axial case should be proportional to a characteristic angle  $\psi_1$  given by [5]

$$\psi_1 = (2Z_1Z_2e^2/Ed)^{1/2}, \text{ provided } \psi_1 < a/d. \quad (3.2)$$

$Z_1$  and  $Z_2$  are the atomic numbers of the energetic particle and lattice atom, respectively;  $a$  is the screening distance,  $E$  the particle energy and  $d$  the lattice spacing along the chosen axis. The proportionality constant  $\alpha$  relating  $\psi_{1/2}$  and  $\psi_1$  (i.e.  $\psi_{1/2} = \alpha\psi_1$ ) should be around 1.5 - 2.0 for a perfect non-vibrating crystal.

The theoretical treatment has been extended by Andersen [20] to include vibrational effects. He finds that  $\alpha$  for a real lattice is always significantly less than the value predicted for a perfect non-vibrating crystal, and that it decreases as the root-mean-square amplitude ( $\rho$ ) increases.

The simple theoretical framework given by Lindhard [5] does not include multiple scattering effects, and so should be compared with experimental data obtained at relatively shallow depths into a crystal: i.e. the so-called "zero-depth" values.

Such a comparison is shown in Fig.3.17 for various diamond-type lattices. A systematic deviation is observed between the diamond, silicon and germanium data (Fig.3.17(a)); but, when the effect of vibrational amplitude is incorporated into the abscissa, using the parameter  $\alpha$  obtained from Andersen's calculations, we see that the agreement between the different crystals is greatly improved (Fig.3.17(b)). Note that several compound semiconductors (GaP, GaAs and GaSb) are also included in this comparison.

While the axial critical angles in Fig.3.17 exhibit the predicted functional dependence on  $Z_1$ ,  $Z_2$ ,  $E$ , and  $d$ , their average value is about 25% lower in absolute magnitude than one obtains from the theory [dotted line]. To remove this 25% discrepancy would require an increase in the thermal vibrational amplitude of  $\sim 0.1 \text{ \AA}$  for C, Si, and Ge. This is equivalent to a value

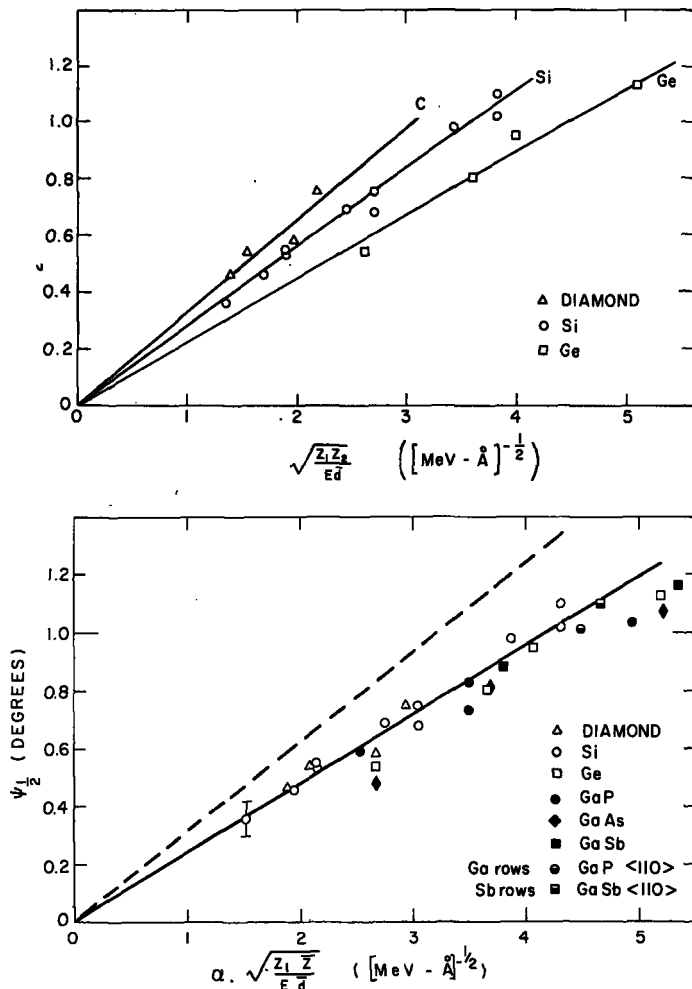


FIG.3.17. (a) The observed functional dependence of axial critical angles ( $\psi_{1/2}$ ) on energy ( $E$ ), atomic number ( $Z_1, Z_2$ ), and mean lattice spacing ( $d$ ) in various lattices;

(b) As in (a), but with Andersen's calculated dependence on lattice vibrations (Ref.[20]) included in the abscissa (from Ref.[10]).

of the vibrational amplitude approximately twice that calculated from the Debye temperatures and would be unrealistically large.

A similar discrepancy between experiment and theory has been observed in other crystals. For example, in tungsten (Table 3.1) the experimental values of  $\psi_{1/2}$ , for a wide variety of projectiles and energies, are consistently about 10% smaller than the predicted values. Hence, Eq.(3.2) again predicts accurately the functional dependence of  $\psi_{1/2}$ , but slightly overestimates its magnitude. Andersen [9] has also investigated the temperature dependence of  $\psi_{1/2}$  for 0.5 MeV  $H^+$  in tungsten, and Fig.3.18 shows that quite reasonable agreement is obtained between the measured and predicted slopes.

TABLE 3.1. CRITICAL ANGLES FOR AXIAL CHANNELLING IN TUNGSTEN AT 25°C. (Taken from Ref. [12])

Axis	Projectile	Energy (MeV)	Predicted values			Experimental values of $\psi_{1/2}$
			$\psi_1$	$\alpha^a$	$\psi_{1/2}^a$	
<100>	$^1\text{H}$	2.0	1.05°	1.03	1.08°	1.00°
		3.0	0.86°	1.03	0.88	0.79°
		6.0	0.61°	1.04	0.63	0.55°
	$^4\text{He}$	2.0	1.48°	1.00	1.48	1.39°
		10.0	0.66°	1.00	0.66	0.67°
	$^{12}\text{C}$	10.0	1.15°	0.99	1.14	1.10°
		30.0	0.66°	1.01	0.65	0.64°
	$^{16}\text{O}$	10.0	1.33°	0.99	1.32	1.23°
		30.0	0.77°	1.01	0.78	0.70°
	$^{36}\text{Cl}$	10.0	1.94°	0.95	1.84	1.82°
30.0		1.12°	0.97	1.09	1.00°	
<111>	$^1\text{H}$	3.0	0.92°	1.03	0.95	0.85°
		6.0	0.65°	1.04	0.68	0.52°
<210>	$^1\text{H}$	3.0	0.57°	1.04	0.59	0.51°
	$^4\text{He}$	10.0	0.44°	1.04	0.46	0.42°
	$^{12}\text{C}$	30.0	0.44°	1.01	0.44	0.36°
	$^{36}\text{Cl}$	30.0	0.75°	0.96	0.72	0.70°

<sup>a</sup> Andersen's calculations (Ref. [20]).

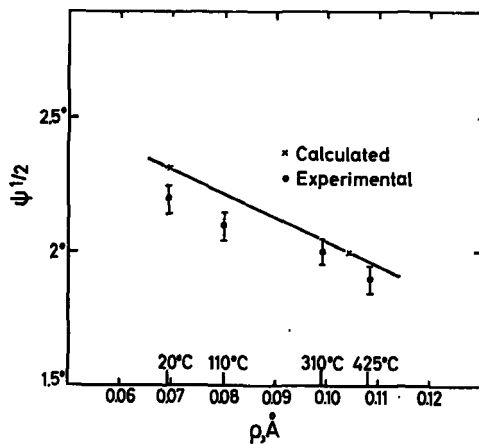


FIG. 3.18. Temperature dependence of  $\psi_{1/2}$  for the <100> dip for 400-keV protons incident on a tungsten crystal (from Andersen and Uggerhøj, Ref. [9]).

TABLE 3.2.  $\chi_{\min}$  VALUES ALONG THE  $\langle 110 \rangle$  AXIS (from Refs [10, 12])

Crystal	Projectile	Rough estimates of $\chi_{\min}$		$\chi_{\min}$ observed
		$Nd\pi(\rho_{\perp})^2$	$Nd\pi a^2$	
C (diamond)	H <sup>+</sup>	0.004	0.07	0.04
	He <sup>+</sup>	0.004	0.06	0.05
Si	He <sup>+</sup>	0.005	0.02	0.03
Ge	He <sup>+</sup>	0.005	0.01	0.03
GaP	He <sup>+</sup>	0.004 <sub>g</sub>	0.01 <sub>g</sub>	0.01 <sub>g</sub>
GaAs	He <sup>+</sup>	0.005	0.01	0.04
GaSb	He <sup>+</sup>	0.006	0.008	0.08
Al	H <sup>+</sup>	0.02	0.02	0.11
KCl ( $\langle 100 \rangle$ )		0.02	0.01	0.6
NaCl ( $\langle 100 \rangle$ )		0.015 <sup>a</sup>	0.02	0.02 <sup>a</sup>
W	H <sup>+</sup>	0.005	0.007	0.01 <sup>2</sup>
Au	H <sup>+</sup>	0.015	0.007	0.07 <sup>2</sup>

<sup>a</sup> At - 200 °C (from recent measurements by M.D. Hollis [22]).

It has sometimes been suggested that channelling measurements be used to study the mean vibrational amplitude of lattice atoms. However, a comparison of the slope of the calculated  $\psi_{1/2}$ -versus- $\rho$  curve in Fig.3.18 with the experimental error bars indicates that critical-angle measurements are not sufficiently sensitive to  $\rho$ . On the other hand, the minimum yield  $\chi_{\min}$  should be proportional to  $\rho^2$ , so that  $\chi_{\min}$  values may indeed offer sufficient sensitivity. Furthermore, the "double-alignment" yield  $\chi_{\min}$  is expected to increase as  $\rho^4$ , and should therefore be a particularly sensitive indicator.

The minimum yield  $\chi_{\min}$ , extrapolated to zero depth, is therefore a more useful experimental parameter for characterizing channelling behaviour — but unfortunately its absolute magnitude cannot yet be accurately predicted. An estimate (for axial channelling) may be obtained by substituting for  $r_{\min}$  in the following equation:

$$\chi_{\min} = Nd\pi(r_{\min})^2 \quad (3.3)$$

where  $N$  is the atomic density,  $d$  the spacing along the row, and  $r_{\min}$  is the closest distance of approach between a channelled beam and an aligned row. Lower limits for  $\chi_{\min}$  can be estimated: (i) for

a non-vibrating lattice, by setting  $r_{\min} \approx a$  (the Thomas-Fermi screening distance) and (ii) for a lattice in which the mean-square vibrational amplitude  $\rho_{\perp}$  (measured perpendicular to the row) is large, by setting  $r_{\min}$  equal to  $\rho_{\perp}$ . Measured and estimated values of  $\chi_{\min}$  are compared in Table 3.2. In most cases, the observed  $\chi_{\min}$  values are somewhat greater than either of these estimated lower limits, and this can probably be attributed to a small amount of de-channelling by surface contamination, lattice defects, etc. In a few cases, (Al, Au and KCl), the discrepancy is large, but subsequent work shows that this can usually be attributed to poor crystal quality. With alkali halides such as NaCl, for example, Hollis [22] has recently observed a  $\chi_{\min}$  value of 0.02 at low temperature ( $-200^{\circ}\text{C}$ ) — in good agreement with the theoretical limits — provided he uses a very low proton fluence to minimize radiation damage. (Alkali halide crystals are extremely sensitive to damage by ionizing radiation!)

### 3.9. Depth dependence of $\psi_{1/2}$ and $\chi_{\min}$

Using a series of single-channel analysers, one can observe simultaneously the orientation dependence of the scattering yield at several different depths beneath the crystal surface (see Fig. 3.5 (b)). The results of such a

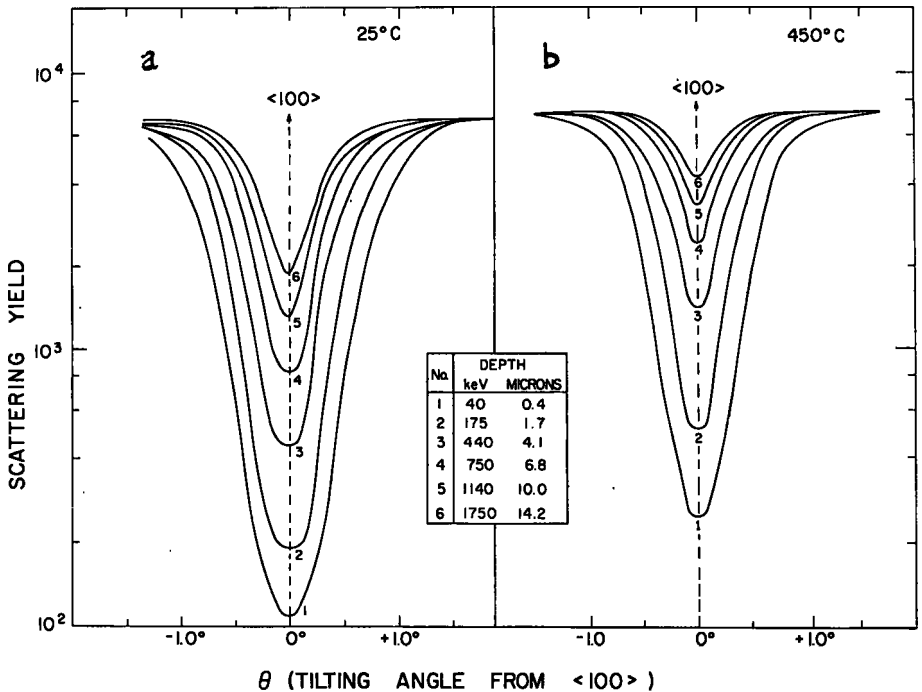


FIG. 3.19. Orientation scans of the scattering yield of 3-MeV protons through a  $\langle 100 \rangle$  axis in tungsten at various depths beneath the surface: (a) at  $25^{\circ}\text{C}$ ; (b) at  $450^{\circ}\text{C}$ . The depth in microns has been estimated from the observed  $\Delta E$  values, assuming that  $dE/dx$  for the channelled beam is  $1/3$  the "random" value; more recent work would suggest a somewhat higher value, and hence the depth scale should be reduced slightly (i.e. by  $\sim 20\%$ ) (from Ref. [12]).

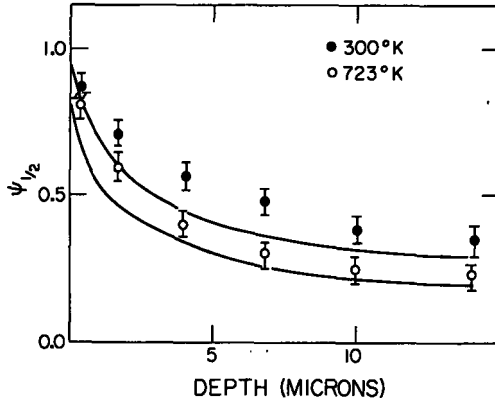


FIG. 3.20. Depth dependence of  $\psi_{1/2}$  for the channelling of 3-MeV protons along a  $\langle 100 \rangle$  axis in tungsten. The solid curves represent the theoretically predicted dependence, including both the nuclear and electronic contributions to the multiple scattering (from Ref. [23]).

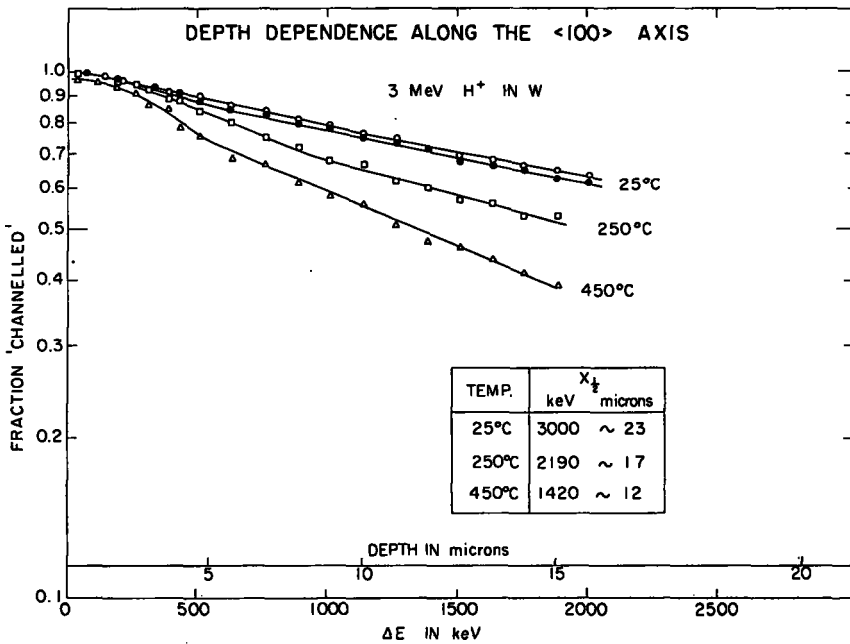


FIG. 3.21. Depth dependence of  $\chi_{\min}$  along a  $\langle 100 \rangle$  axis in tungsten using 3-MeV protons (from Ref. [12]).

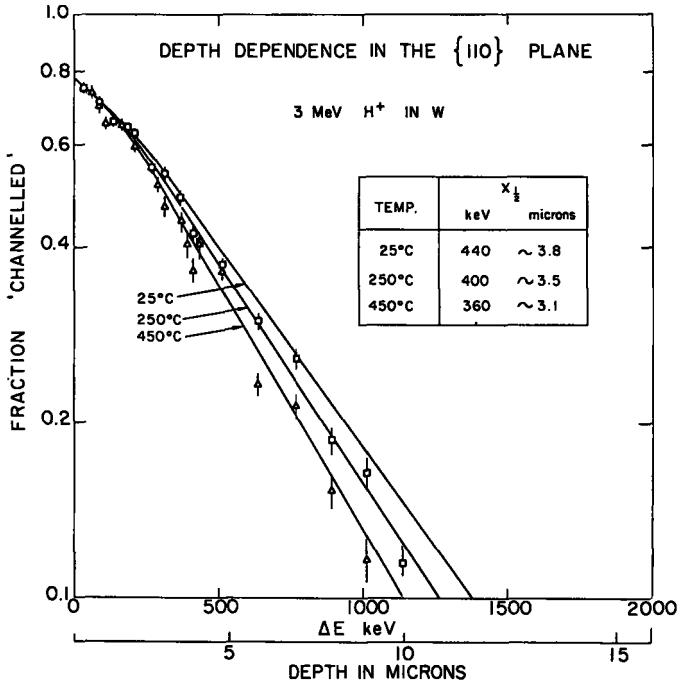


FIG.3.22. Depth dependence of  $\chi_{\min}$  along a {110} plane in tungsten, using 3-MeV protons (from Ref.[12]).

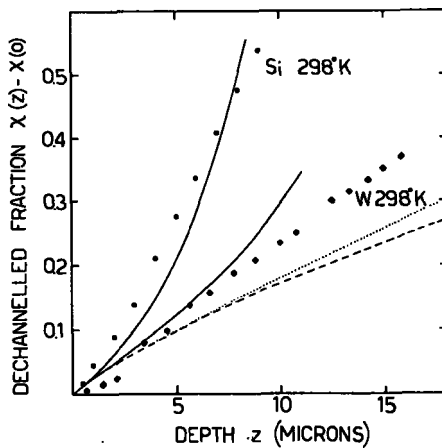


FIG.3.23. Dechannelled fraction versus penetration depth for 1.5-MeV protons on Si <111> and for 3-MeV protons on W <100> at 298°K. The full curves represent the calculated trends for the same conditions, including nuclear and electronic multiple-scattering contributions. Dotted (Si) and dashed (W) curves are calculated with the nuclear scattering term alone (from Ref.[24]).

measurement at two different temperatures are illustrated in Fig.3.19. We see that the minimum yield  $\chi_{\min}$  increases gradually with increasing depth, and that the angular width  $\psi_{1/2}$  at half-minimum decreases. The depth dependence of  $\psi_{1/2}$  is better illustrated in Fig.3.20. Both these effects may be attributed to a gradual de-channelling of the beam as a result of multiple scattering. In this regard, we note that the depth dependence becomes more pronounced at elevated temperatures, indicating that the rate of de-channelling depends strongly on the vibrational amplitude of the lattice atoms (as one might expect).

More detailed information about the rate of de-channelling along the  $\langle 100 \rangle$  axis in tungsten is contained in Fig. 3.21, in which the channelled fraction  $(1-\chi_{\min})$  is plotted as a function of depth for several different crystal temperatures. Except for a short initial period, the observed decrease is approximately exponential, with a slope that increases strongly with temperature.

Figure 3.22 shows a similar de-channelling study – but along one of the low-index planes. Again, the decrease in  $(1-\chi_{\min})$  is approximately exponential, but with a much steeper slope than for a low-index axis: for example, at 25°C, along the  $\langle 100 \rangle$  axis (Fig.3.21), ~70% of the beam remains channelled to a depth of 15  $\mu$  whereas along the (110) plane (Fig.3.22) the channelled component at this depth has become negligible. On the other hand, the temperature dependence is much weaker in the planar case.

Recent work particularly by the Catania group [23-25] has shown that Lindhard's theoretical framework may be extended to provide a reasonably accurate description of the depth dependence, as can be seen in Fig. 3.23. The solid curves, which include the multiple scattering contributions from electronic as well as from nuclear collisions, fit the experimental points in Si and also in W remarkably well. The dotted curves, on the other hand, (in which only the nuclear collisions have been considered) underestimate considerably the rate of de-channelling at large depths, thus indicating clearly that electronic collisions contribute significantly to the multiple scattering of a channelled beam and must therefore be included in the theoretical treatment. This is in marked contrast to the behaviour of non-channelled beams where, even at high energies, multiple scattering is normally dominated by the nuclear-collision contribution (see Ref. [23] in section 1).

It is interesting to note that the nuclear-scattering curves in Fig. 3.23 fit the initial slope reasonably well, indicating that at shallow depths de-channelling arises predominantly from those particles that enter the lattice fairly close to the forbidden region (of radius  $r_{\min}$ ) around each row, and that therefore undergo predominantly nuclear collisions.

The solid curves in Fig.3.20 indicate how well one can estimate also the depth dependence of the critical angle  $\psi_{1/2}$ . Strictly speaking, the critical steering angle inside the crystal remains constant and is not decreasing with depth. However, in order to maintain a beam channelled to a large depth (e.g. 10 microns), its initial transverse motion must be considerably less than the critical value (otherwise it becomes de-channelled before reaching this depth) – and  $\psi_{1/2}$  in Fig.3.20 represents the initial transverse motion, not the transverse motion at the actual depth.

An alternative method of comparing the experimental and calculated depth dependence is to search for suitable scaling factors that might enable the dependence of  $\chi_{\min}$  on depth, temperature, energy, etc. to be combined.

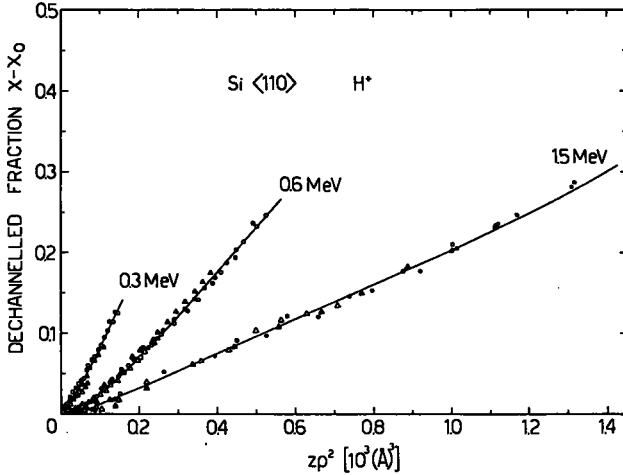


FIG.3.24. Depth ( $z$ ) and temperature ( $\rho^2$ ) dependence of the proton de-channelled fraction ( $\chi(z) - \chi_0$ ) along the  $\langle 100 \rangle$  axis of Si, indicating the use of  $z\rho^2$  as a scaling parameter;  $\Delta$  -  $80^\circ\text{K}$ ;  $\blacksquare$  -  $143^\circ\text{K}$ ;  $\blacktriangle$  -  $203^\circ\text{K}$ ;  $\circ$  -  $298^\circ\text{K}$ ;  $\square$  -  $363^\circ\text{K}$ ;  $\bullet$  -  $423^\circ\text{K}$  (from Ref.[25]).

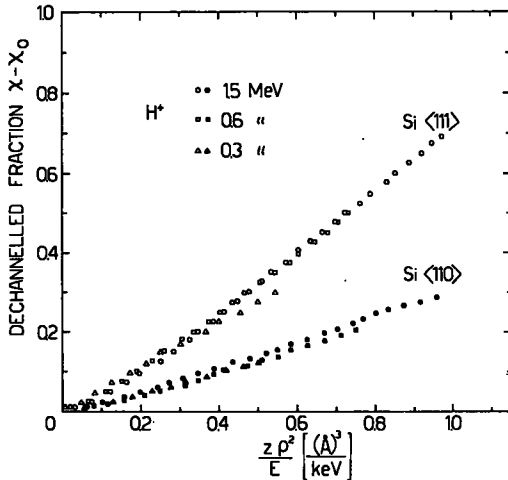


FIG.3.25. Depth ( $z$ ), temperature ( $\rho^2$ ) and energy ( $E$ ) dependence of the proton dechannelled fraction ( $\chi(z) - \chi_0$ ) in Si, indicating the use of  $z\rho^2/E$  as a scaling parameter (from Ref.[25]).

Again, the Catania group has been particularly active in pointing the way. Following Lindhard's suggestion [5] that for a channelled beam the nuclear contribution to multiple scattering should be proportional to  $\rho^2$  (where  $\rho$  is the mean vibrational amplitude) and to the penetration depth  $z$  along the channel, they first tested  $z\rho^2$  as a possible scaling parameter. As can be seen in Fig.3.24, the data for silicon at each energy fall on a single 'universal' curve over quite a wide temperature range; similar fits have been observed in several other crystals.

The agreement in Fig.3.24 is rather too good, since we have already seen that electronic collisions also play an important role in de-channelling (Fig.3.23) — and electronic collisions should be almost independent of temperature. Apparently, the fit of  $\chi_{\min}$  to a  $z\rho^2$  dependence arises somewhat fortuitously from two opposing effects: on the one hand, the contribution from electronic collisions tends to reduce the dependence to something less than  $\rho^2$ ; on the other hand, the decrease in the critical angle  $\psi_{1/2}$  at zero-depth (Fig.3.18) with increasing temperature tends to increase the  $\rho$ -dependence of  $\chi_{\min}$ , since at higher temperatures it requires less transverse energy to become de-channelled.

Theoretical considerations indicate that both the nuclear and electronic contributions to multiple scattering have approximately the same energy dependence: viz. that the de-channelling rate should be inversely proportional to the energy. Consequently, one might expect that  $z\rho^2/E$  would be an even more useful scaling factor — and Fig.3.25 shows that this is indeed the case.

Further simplifications, such as including the dependence on lattice spacing  $d$ , do not yet seem feasible. For example, Lindhard [26] has noted that the nuclear and electronic contributions to de-channelling should both increase linearly with  $d$ , and one would therefore expect the two sets of data in Fig.3.25 to collapse on to a single curve if plotted against  $(z\rho^2/E)$ . However, this is evidently not the case; the slope of the  $\langle 111 \rangle$  curve is almost 2.5 times greater than that of the  $\langle 110 \rangle$  curve, whereas the ratio of their  $d$ -spacings is less than 1.3.

## SUMMARY

This concludes our survey of experimental studies of the channelling behaviour of low-Z ions. We have seen that, within a predictable critical angle of a major axis or plane, extremely strong attenuations (up to a factor of 100 in the case of an axis) occur in the yields of all close-encounter processes — i.e. those processes that require a distance of closest approach smaller than  $\sim 0.1 \text{ \AA}$ . The magnitude and angular width of these attenuations can be described quite adequately at shallow depths by Lindhard's theoretical framework. Furthermore, unlike the low-velocity heavy-ion case treated in the first two sections, we find that at MeV energies the rate of de-channelling becomes relatively slow; it can also be estimated with fair accuracy from multiple-scattering theory as a function of depth, temperature and incident energy.

The agreement between experiment and theory is not quantitative, and there is still plenty of scope for further investigations — especially of the depth dependence. However, we have, at least, a semi-quantitative explanation for the large yield attenuations that are observed, and this is certainly good enough for many of the applications of channelling that are evolving in solid-state and nuclear science.

## REFERENCES TO SECTION 3

- [1] DEARNALEY, G., IEEE Trans. Nucl. Sci. NS11 (1964) 249.
- [2] SATTler, A.R., DEARNALEY, G., Phys. Rev. Letts 15 (1965) 59.
- [3] ERGINSOY, C., WEGNER, H.E., GIBSON, W.M., Phys. Rev. Letts 13 (1964) 530.

- [4] DATZ, S., NOGGLE, T.S., MOAK, C.D., Nucl. Instrum. Meth. 38 (1965) 221.
- [5] LINDHARD, J., Kgl. Danske Videnskab. Selskab, Mat.-Fys. Medd. 34 14 (1965).
- [6] ANDERSEN, J.U., DAVIES, J.A., NIELSEN, K.O., ANDERSEN, S., Nucl. Instrum. Meth. 38 (1965) 210.
- [7] BØGH, E., UGGERHØJ, E., Nucl. Instrum. Meth. 38 (1965) 216.
- [8] KHAN, J.M., POTTER, D.L., WORLEY, R.D., Phys. Rev. 148 (1966) 413.
- [9] ANDERSEN, J.U., UGGERHØJ, E., Can. J. Phys. 46 (1968) 517.
- [10] PICRAUX, S.T., DAVIES, J.A., ERIKSSON, L., JOHANSSON, N.G.E., MAYER, J.W., Phys. Rev. 180 (1969) 873.
- [11] BØGH, E., Can. J. Phys. 46 (1968) 653, and personal communication.
- [12] DAVIES, J.A., DENHARTOG, J., WHITTON, J.L., Phys. Rev. 165 (1968) 345.
- [13] DAVIES, J.A., ERIKSSON, L., JOHANSSON, N.G.E., MITCHELL, I.V., Phys. Rev. 181 (1969) 548.
- [14] ERIKSSON, L., DAVIES, J.A., Arkiv. Fysik 39 (1969) 439.
- [15] DOMEIJ, B., Nucl. Instrum. Meth. 38 (1965) 207.
- [16] BØGH, E., WHITTON, J.L., Phys. Rev. Letts 19 (1967) 553.
- [17] FELDMAN, L.C., APPLETON, B.R., Appl. Phys. Letts 15 (1969) 305.
- [18] FOTI, G., GRASSO, F., QUATTROCCHI, R., QUERCIA, I.F., RIMINI, E., Phys. Letts 31A (1970) 214.
- [19] UGGERHØJ, E., ANDERSEN, J.U., Can. J. Phys. 46 (1968) 543.
- [20] ANDERSEN, J.U., Kgl. Danske Videnskab. Selskab, Mat.-Fys. Medd. 36 7 (1967).
- [21] ANDERSEN, J.U., AUGUSTYNIAK, W.M., UGGERHØJ, E., Phys. Rev. B3 (1971) 705.
- [22] HOLLIS, M.J., private communication (1971).
- [23] CAMPISANO, S.U., FOTI, G., GRASSO, F., RIMINI, E., QUERCIA, I.F., Preprint (1971), presented at the Gausdal Conference on Atomic Collisions in Solids (Sept. 20-24, 1971).
- [24] FOTI, G., GRASSO, F., QUATTROCCHI, R., QUERCIA, I.F., RIMINI, E., Lett. al Nuovo Cim. 4 (1970) 707.
- [25] FOTI, G., GRASSO, F., QUATTROCCHI, R., RIMINI, E., Phys. Rev. B3 (1971) 2169.
- [26] LINDHARD, J., private communication (1970).

#### 4. APPLICATIONS OF CHANNELLING TO SOLID-STATE SCIENCE

##### 4.1. Introduction

It is almost axiomatic that any effect producing a 100-fold attenuation in a wide range of measurable processes (Rutherford scattering, nuclear reactions, X-ray emission, etc.) must have rather widespread application as an analytical tool in other investigations. It is therefore not too surprising to find that, in recent years, applications of channelling to other fields are attracting even more interest than the basic channelling studies themselves.

Most of these applications are based on the ability of a channelled beam to locate (with a precision of  $\sim 0.1 \text{ \AA}$ ) the site of specific atoms within the unit cell of a crystal lattice. This ability can be applied (for example) to measure such widely differing quantities as: (i) the distribution of foreign atoms between substitutional and various interstitial sites; (ii) the amount of lattice disorder near the surface of a crystal; (iii) the structure of a crystal surface; and (iv) the lifetime of extremely short-lived ( $10^{-16}$ - $10^{-18}$  s) recoiling nuclei.

First, let us discuss briefly the basic principle of the channelling technique for locating atoms, and then we will consider various examples of its application.

#### 4.2. Channelling-effect technique of atom location

The most important aspect of the channelling phenomenon for the present discussion is the existence of a well-defined distance of closest approach  $r_{\min}$  between a channelled beam and the aligned lattice rows. For low- $Z$  ions at MeV energies, we have seen already that the magnitude of  $r_{\min}$  (Table 4.2) is the larger of the Thomas-Fermi screening length  $a$ , and the vibrational amplitude  $\rho$ : i. e. typical values of  $r_{\min}$  fall between 0.1 and 0.2 Å. The crystal therefore is divided into allowed and forbidden regions, as shown in Fig. 4.1. Consequently, as we have already seen, all physical processes requiring a closer impact than  $\sim 0.1$  Å (such as wide-angle elastic scattering, nuclear reactions, or the production of inner-shell X-rays) are completely prohibited for channelled particles; hence, extremely strong attenuations (up to 100-fold) in the yields of such processes are observed for an aligned beam in comparison with a random one. The yield does not go completely to zero, since even for  $\psi = 0$ , there is still a small random fraction (of the order of 1 - 5%).

These large attenuations in interaction yield occur not only with the lattice atoms, but also with those foreign atoms that are located in the forbidden region for the channelled beam — for example, on lattice sites (the position marked  $\bullet$  in Fig. 4.1). On the other hand, foreign atoms located in the allowed region for the channelled beam (for example, the position  $x$  in Fig. 4.1) can interact with both the channelled and the random beam, and hence no attenuation in their interaction yield will be observed. In fact, as we shall see later (Fig. 4.10), the yield for such an interstitial atom actually increases when the beam becomes channelled, since (in order to conserve the total number of particles in the beam) one cannot have a decrease in flux in the forbidden region around the rows without having an increase in flux somewhere else. The magnitude of this yield increase for

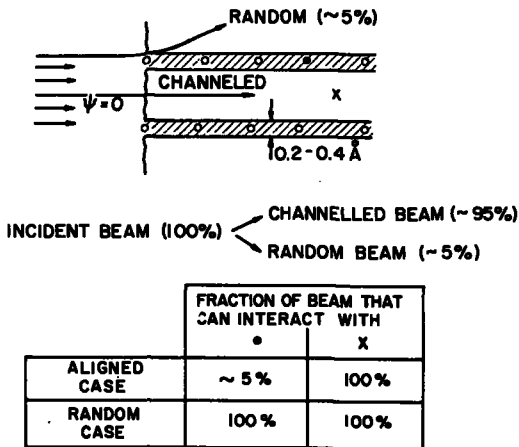


FIG. 4.1. The splitting of a perfectly aligned beam into channelled and random components in passing through the crystal surface.

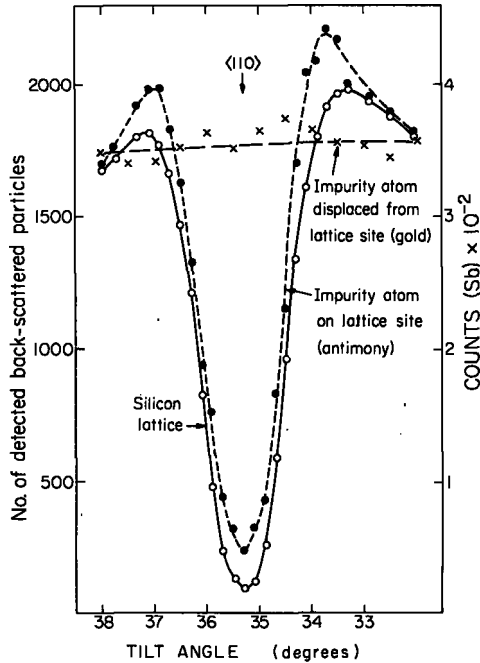


FIG. 4.2. Backscattering yield of 1.0-MeV helium ions from substitutionally located impurity atoms (antimony) and from randomly distributed atoms (gold) as a function of the angle of incidence relative to the  $\langle 110 \rangle$  direction. The corresponding yield from the lattice atoms (solid curve) is included for comparison.

mid-channel atoms is usually fairly small compared to the 100-fold attenuations that may occur for substitutional atoms. Nevertheless, in some cases enhancement factors of up to a 2-fold increase may occur.

Two examples of foreign-atom location are illustrated in Fig. 4.2. Antimony atoms ( $\bullet$ ) are located on lattice sites and hence show a large attenuation along the  $\langle 110 \rangle$  direction; gold atoms ( $x$ ), on the other hand, are distributed randomly throughout the lattice and so interact normally with both the channelled and the random beam.

Whenever a strong attenuation in yield is observed (as in the antimony case of Fig. 4.2), we cannot immediately conclude that the foreign atoms are on the substitutional sites, but only that they must be located somewhere within the shadow of that particular aligned row. Figure 4.3 illustrates how, for a simplified two-dimensional lattice, measurements along two or more directions may be combined in order to pinpoint the exact location of the foreign atom. If, for example, the foreign atom is substitutional ( $\bullet$ ), then it lies within the shadow of all close-packed rows in the lattice, and therefore large attenuations will be observed along both the  $\langle 01 \rangle$  and the  $\langle 11 \rangle$  directions. If, on the other hand, the atom lies at the intermediate position marked 'x' in Fig. 4.3, only 50% of the atoms will lie along the particular  $[01]$  direction, and the other 50% will lie on the completely equivalent set of  $[10]$  rows. Hence, the maximum attenuation that can occur is only 50%<sup>1</sup>.

<sup>1</sup> In the three-dimensional cubic lattice, there would, of course, be three equivalent sets of axes  $[100]$ ,  $[010]$ , and  $[001]$ , and hence the maximum attenuation at the edge interstitial position ( $x$ ) would be only 33%.

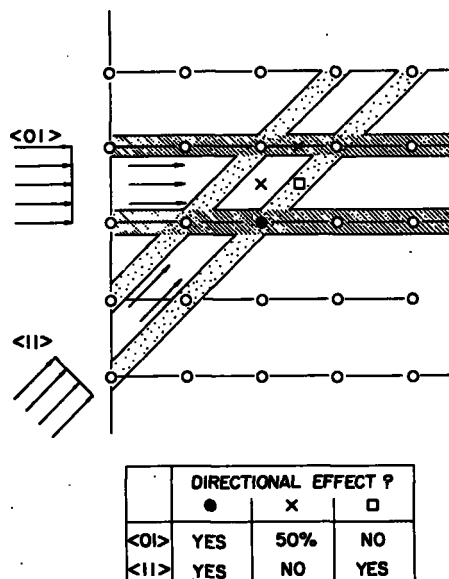


FIG. 4.3. A two-dimensional model illustrating how channelling phenomena can be used to locate foreign atoms in a crystal. As shown by the table, three typical sites for a foreign atom - ●, x, and □ - can be uniquely distinguished by studying the channelling behaviour firstly along the  $\langle 01 \rangle$  and then along the  $\langle 11 \rangle$  -direction.

Also, neither of the 'x' atoms lies in the shadow of the  $\langle 11 \rangle$  directions; hence, for this case, no directional effect would be observed. A third type of site, the position marked by the □ in Fig. 4.3, lies in the middle of the channel for the [01] and the completely equivalent [10] directions, but in the shadow of the [11] and the [11] directions. Hence, in this case, we would expect no attenuation in yield along the  $\langle 10 \rangle$  but a strong attenuation along the  $\langle 11 \rangle$ . Thus, in principle, by measuring orientation effects down two or more directions, and invoking lattice-symmetry arguments as in Fig. 4.3, it is possible to pin down the exact distribution of specific foreign atoms between substitutional and various types of interstitial site.

#### 4.3. Foreign-atom detection

To apply the channelling-effect technique, one must of course be able to detect the interaction of the beam with a small concentration of foreign atoms in the presence of a large excess of lattice atoms. Fortunately, there are many close-encounter processes available, and in the majority of cases, a satisfactory one can be found, provided the atomic concentration of foreign atoms exceeds approximately  $10^{-4}$ . For lighter atoms (such as lithium, boron, carbon, or oxygen), specific nuclear reactions are often available - such as  $(p, \alpha)$ ,  $(p, \gamma)$ , or  $(d, p)$ ; in such cases, Rutherford scattering can still be used to study the interaction of the beam with the lattice atoms. A typical example - the use of the  ${}^7\text{Li} (p, \alpha) {}^4\text{He}$  reaction to detect lithium in a silicon crystal - is illustrated in Fig. 4.4.

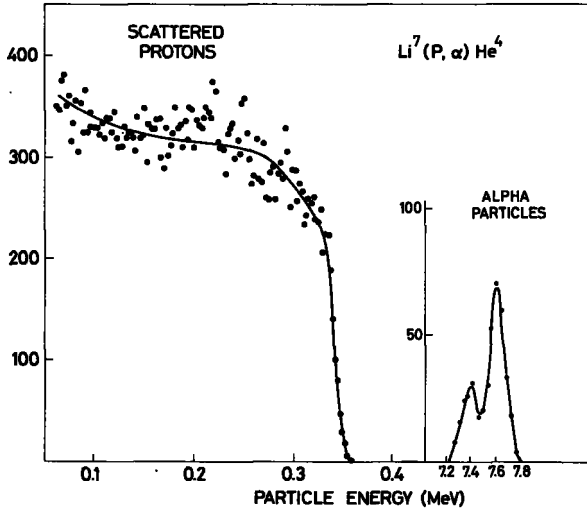


FIG. 4.4. Energy spectrum of particles measured at an angle of  $135^\circ$  to the direction of a 450-keV proton beam striking a silicon crystal that had previously been implanted with  $6 \times 10^{16}$  Li ions/cm<sup>2</sup>. Detected at high energy are the  $\alpha$ -particles from the  ${}^7\text{Li}(p, \alpha){}^4\text{He}$  reaction. (from Gibson et al., Ref. [2]).

In certain other cases, we can use the yields of characteristic inner-shell X-rays, or the emission behaviour (i.e. blocking) of charged particles from radioactive implants. So far, however, the most commonly chosen process for analyzing implanted layers has been the yield of backscattered particles, since this can be applied to almost all cases in which the implanted foreign atom is heavier than the substrate (see Fig. 1.2). It also has the advantage of measuring simultaneously the amount of lattice disorder introduced by the implantation, as we shall see in Fig. 4.6. For purposes of illustration, we may therefore select Rutherford scattering as our favourite close-encounter process for studying ion-implanted layers. It should always be remembered, however, that completely equivalent results can be obtained (where desirable) with other close-encounter processes, such as nuclear reactions and inner-shell X-ray production.

In order to achieve sufficient mass resolution in the backscattering energy spectrum, it is desirable to use a sufficiently heavy projectile that it will lose at least 40-50% of its energy in scattering off the lattice atoms. Thus, for a low-mass crystal such as silicon, a helium beam is the ideal choice (see Fig. 4.6), and provides a clear separation between the scattering peak from a heavy impurity (Bi) and the edge of the silicon spectrum. For a heavier crystal such as iron or germanium, however, a helium beam would lose only  $\sim 20\%$  of its energy in scattering off a lattice atom, and so the substrate spectrum would obscure almost all the available energy region. In this case, it is better to use a somewhat heavier projectile — such as, a 20-MeV oxygen beam (Fig. 4.5). Of course, not many laboratories have a 20-MeV accelerator at their disposal, and I might therefore point out that Eriksson and his colleagues [3] at Stockholm have shown that the energy of the oxygen beam can indeed be reduced to 2 MeV, without too much loss of mass resolution.

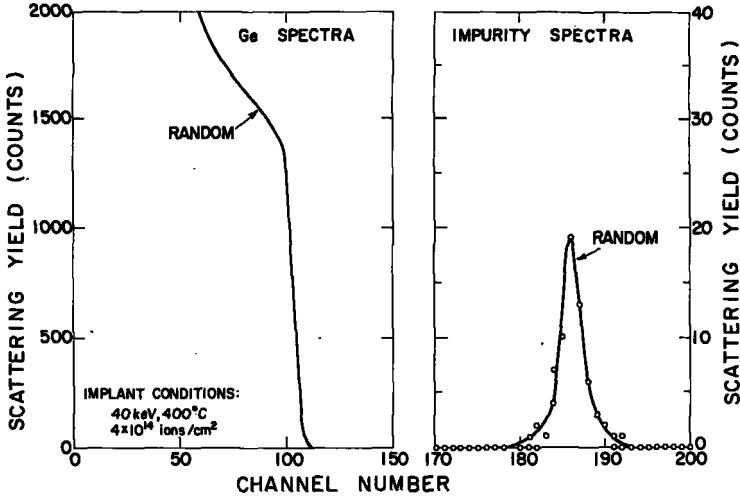


FIG. 4.5. Energy spectrum of 20-MeV  $^{16}\text{O}$  ions backscattered from a germanium crystal implanted with  $3 \times 10^{14}$  thallium ions/cm<sup>2</sup>, illustrating the mass resolution attainable with heavier projectiles (from Ref. [1]).

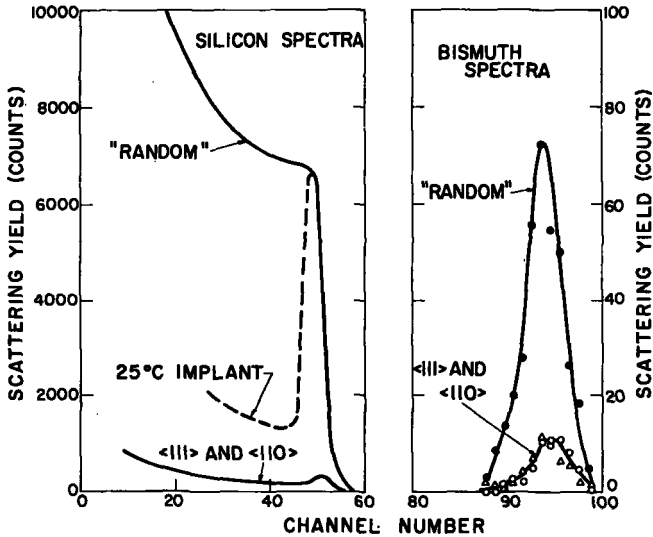


FIG. 4.6. Energy spectra (as recorded on a multichannel analyser) for the scattering yield of helium ions from silicon crystals implanted at 350°C with  $\sim 10^{14}$  bismuth ions/cm<sup>2</sup>. Spectra are given for the incident beam parallel to a  $\langle 111 \rangle$  and a  $\langle 110 \rangle$  axis as well as for a random direction. The dotted curve in the silicon region shows the aligned [ $\langle 111 \rangle$ ] spectrum for a similar unannealed room temperature implant; the surface peak (rising almost to the "random" curve) is due to the much larger amount of lattice disorder accumulated under these conditions (see section 5). In such a case, the lattice location of the bismuth atoms cannot be determined until this lattice disorder has been annealed. The experimental points have been omitted from the silicon spectra for the sake of clarity (from data in Ref. [4]).

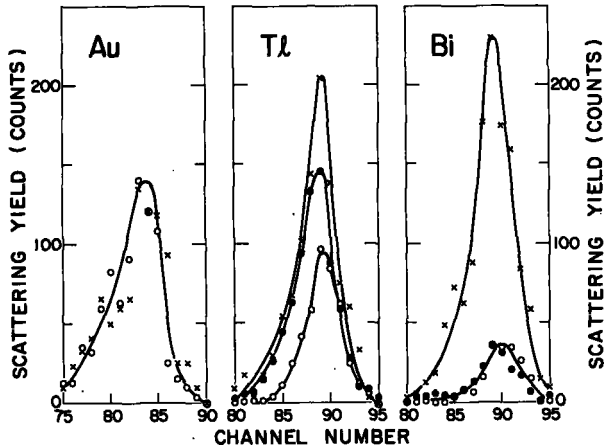


FIG. 4.7. High-energy (foreign atom) portion of the energy spectra of He ions scattered from various implanted silicon crystals. Spectra were taken with the beam incident along random (X),  $\langle 111 \rangle$  (O), and  $\langle 110 \rangle$  (●) directions. Implant conditions:  $\sim 10^{14}$  ions/cm<sup>2</sup> at 40 keV, with the substrate at 450°C. (from Ref.[4]).

So, by choosing the right combination of projectile and energy, one can detect almost any foreign atom that is heavier than the substrate atoms — provided, of course, that the foreign atom is located at a sufficiently shallow depth (i. e. a few microns, or less) beneath the crystal surface.

#### 4.4. Applications in ion-implanted silicon

Let us now look briefly at a few examples illustrating the use of the channelling-effect technique to locate specific foreign atoms implanted into a crystal lattice. These examples are all taken from the semi-conductor field, where ion implantation is currently attracting a great deal of interest. Here, one of the key factors determining the electrical characteristics is the type of site occupied by the implanted dopant atom — and this has led to a wide-spread use of the channelling-effect technique.

A typical set of energy spectra for random and various aligned directions of incidence is shown in Fig. 4.6 for a substitutionally located foreign atom (Bi). The strong attenuations in scattering yield from the Bi atoms, along both the  $\langle 111 \rangle$  and the  $\langle 110 \rangle$  directions, indicate that at least 90% of the Bi atoms lie in the shadow of both sets of atomic rows and therefore must be on the substitutional lattice sites. The significance of the peak in the unannealed room temperature implant (dotted curve) will be discussed under Lattice Disorder in sub-section 4.6.

Many different implanted ion/substrate combinations have been investigated by this channelling-effect technique. Figure 4.7 illustrates the most commonly observed types of behaviour. In the Bi case, as we have just discussed, the atoms are largely substitutional, and strong attenuations are observed along all major axes. In certain other cases, such as gold in silicon (see also Fig. 4.2), no significant attenuation is observed along any of the major axes, and one must therefore conclude that the foreign atoms

are distributed randomly throughout the lattice. In still other cases, illustrated here by thallium, one observes a significantly different attenuation along one axis than along another, indicating that some of the atoms, at least, must lie in well-defined interstitial sites - i.e. on sites that lie along the shadow of one particular set of atomic rows ( $\langle 111 \rangle$ ) but not along the shadow of another set ( $\langle 110 \rangle$ ). For the case of Tl in silicon, the tetrahedral interstitial sites in Fig. 4.8 fulfil this description.

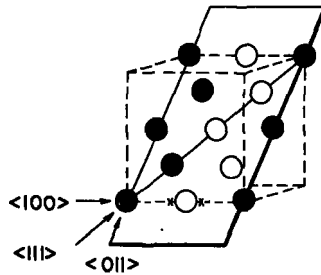


FIG. 4.8. Atomic configuration in the (011) plane of silicon: ● - lattice sites; ○ - regular interstitial holes grouped in pairs along the  $\langle 111 \rangle$  atomic rows (i.e. the tetrahedral-interstitial sites); X - probable location of the ytterbium atoms, as deduced from Fig. 4.10.

In such cases, where the foreign atom is located in a specific interstitial site, a quantitative interpretation of the measurements requires us to know the interaction yield of a channelled beam with a non-shadowed atom. Until recently, it has been assumed that this yield would be almost the same as the random-yield value, i.e. as the interaction yield for a non-channelled beam. However, the yield between a channelled beam and a non-shadowed atom must always be somewhat higher than the random value; this may be seen as a consequence of the general rule of spatial averages (conservation of particles) given by Lindhard [1], or, more directly, as being due to a flux-peaking of the channelled beam in the mid-channel region. For a channelled particle with a given transverse energy  $E_{\perp}$ , ( $E_{\perp} < E\psi_1^2$ ), a forbidden area exists around each string, namely the area within which the transverse potential exceeds  $E_{\perp}$ . Consequently, in the allowed area for this channelled particle, its probability density must be higher than that for a random beam.

Originally, the magnitude of this increase in yield was estimated to be only a few percent (i.e.  $\sim Nd\pi a^2$  where  $Nd$  is the density of the strings in the transverse plane and  $a$  the Thomas-Fermi radius) and such a small effect could safely have been neglected. For incidence parallel to a major axis, however, most particles have transverse energies considerably smaller than  $E\psi_1^2$  and correspondingly, a forbidden area much larger than  $\pi a^2$ , leading to a stronger flux-peaking than implied by the above estimate. Indeed, the recent experiments by Andersen et al. [5] on ytterbium implants (Fig. 4.9) and by Domeij et al. [6] for zirconium, hafnium, and thallium implants in silicon show an almost two-fold increase in scattering yield from the foreign atom along the  $\langle 110 \rangle$  direction compared to the value for random incidence. Similarly, the Harwell group [7] have observed approximately a three-fold flux-peaking in some recent computer simulations of channelled trajectories.

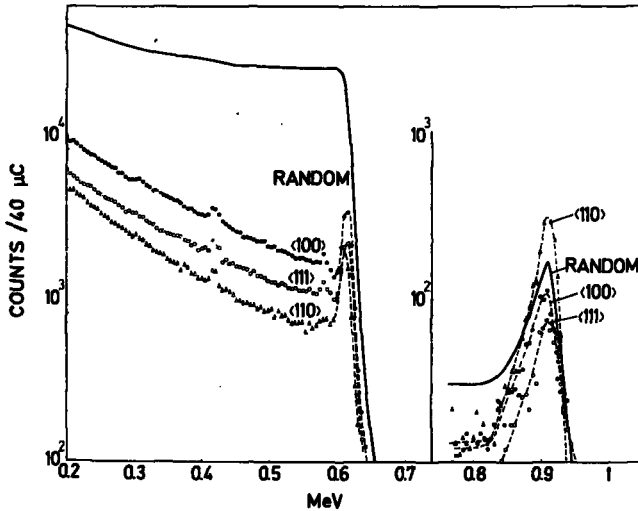


FIG. 4.9. Energy spectra for a 1-MeV helium beam scattered from a Yb-implanted silicon crystal with the beam incident as follows:

(—) along a random direction; (●) parallel to the  $\langle 100 \rangle$ ; (○) parallel to the  $\langle 111 \rangle$ ; and (Δ) parallel to the  $\langle 110 \rangle$ . Implantation conditions were  $10^{14}$   $^{89}\text{Yb}$  ions/cm<sup>2</sup> at 60 keV, 450 °C (from Ref.[5]).

#### 4.5. Yb in silicon case

Let us now consider the data in Fig. 4.9 in more detail in order to see how the exact location of an interstitial impurity can be deduced. For this purpose, a detailed angular scan (such as in Fig. 4.2) provides considerably more information than a mere comparison of the random and perfectly aligned spectra. Figure 4.10 therefore compares the angular dependence of the "Yb-peak" yield with that for the surface region of the silicon crystal. The most striking effect, of course, is the narrow peak in the ytterbium yield along the  $\langle 110 \rangle$ . The half-width of this peak is about a factor of three smaller than the critical angle for channelling, indicating that the flux-peaking effect should disappear when the beam acquires a transverse energy  $E\psi^2$  of only 10% of the maximum allowed transverse energy ( $E\psi_c^2$ ) for channelling.

Theoretical considerations show that the height of the flux-peaking alone does not pinpoint very accurately where the foreign atom is sitting within the channel. For example, the almost two-fold increase observed in Fig. 4.10 indicates only that the ytterbium atoms must be located within approximately 1.1 Å of the mid-channel axis. It turns out, however, that we can deduce quite a lot of information about the lattice location of the foreign atoms by comparing the orientation dependence along other axes as well. Along the  $\langle 100 \rangle$  and  $\langle 111 \rangle$  directions, the scattering yield from the ytterbium shows significant dips — but these dips are much weaker than the corresponding ones from the silicon lattice, indicating that most of the ytterbium atoms cannot be located on either the substitutional or the tetrahedral interstitial sites. We also note that along the  $\langle 111 \rangle$ , the angular width of the ytterbium

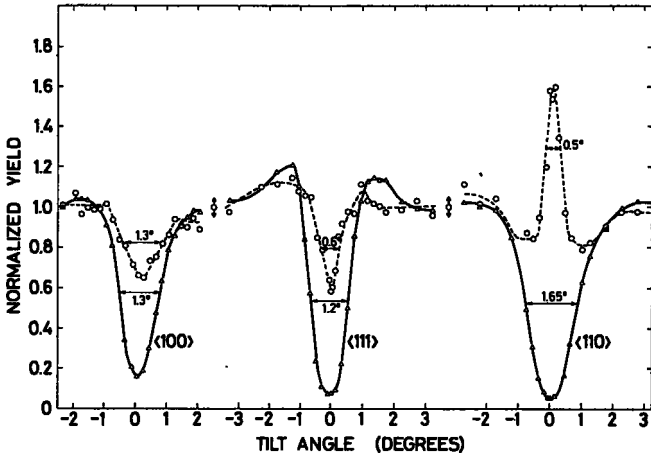


FIG. 4.10. Scattering yield from the Yb atoms (---○---) and from the Si atoms in the implanted region (—△—) as a function of the angle between the incident beam direction and various low-index axes. These yield values are obtained by integration over the appropriate energy regions (0.85–0.95 MeV and 0.55–0.58 MeV, respectively) in Fig. 4.9. The measured angular width ( $2\psi_{1/2}$ ) is indicated on each curve (from Ref. [5]).

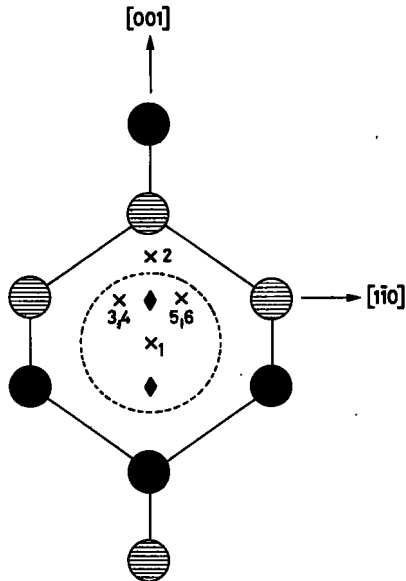


FIG. 4.11. The six equivalent ytterbium-atom sites (from Fig. 4.8) as viewed along a  $\langle 100 \rangle$  channel. The dotted circle indicates the maximum area over which a two-fold flux-peaking can occur.

dip is only 50% of the corresponding angular width for the silicon lattice, whereas along the  $\langle 100 \rangle$  direction, the two angular widths are comparable in magnitude.

If we assume that the ytterbium atoms are all located in one type of site, then the channelling-effect data in Fig. 4.10 lead to the following conclusions:

- (i) To explain the much narrower dip along the  $\langle 111 \rangle$ , the ytterbium atoms must be located  $0.5 - 0.7 \text{ \AA}$  from each of the four equivalent  $\langle 111 \rangle$  rows,
- (ii) To explain the broader but shallow  $\langle 100 \rangle$  dip,  $1/3$  of the ytterbium atoms must be located on each of the three equivalent  $\langle 100 \rangle$  rows, but approximately  $0.7 \text{ \AA}$  away from their intersection points - i.e.  $\sim 0.7 \text{ \AA}$  from either the tetrahedral interstitial or the substitutional sites.

There are two (equivalent) positions along each  $\langle 100 \rangle$  row that satisfy these requirements, namely the points indicated by the x's in Fig. 4.8.

The distribution of these six equivalent ytterbium-atom sites (i.e. two along each of the three equivalent  $\langle 100 \rangle$  directions), as viewed along one of the  $\langle 110 \rangle$  channels, is indicated by the numbered crosses in Fig. 4.11. We see that while only one of the positions (position 1) falls in the centre of the particular  $[110]$  channel, four more (positions 3-6) lie well within the central region ( $1.1 \text{ \AA}$  radius) required to account for the two-fold flux-peaking effect.

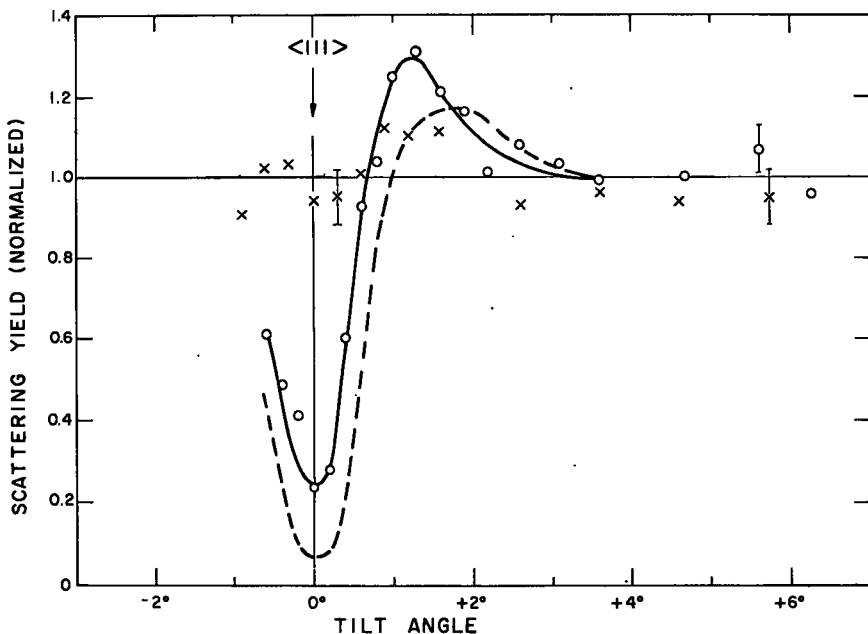


FIG. 4.12. Similar to Fig. 4.2 except that bismuth has replaced antimony as the 'substitutionally-located' foreign atom. The scattering yield from the bismuth atoms shows a significantly narrower dip than that from the lattice atoms (from Ref. [4]).

Each position lies exactly on one of the three equivalent  $\langle 100 \rangle$  axes and is displaced  $0.68 \text{ \AA}$  off the other two. Such a displacement is large enough to give negligible attenuation in yield for those ytterbium atoms (67%) lying along the other two axes and hence would explain the observed 30% dip in yield. Those ytterbium atoms contributing to the dip lie exactly on the particular aligned  $\langle 100 \rangle$  set of rows, and hence the angular width of this 30% dip is approximately the same as that for the silicon lattice (Fig. 4.10).

The proposed ytterbium sites all lie  $0.55 \text{ \AA}$  from each of the four sets of  $\langle 111 \rangle$  rows. This displacement is still small enough to produce a significant dip in scattering yield, but with a much narrower angular width than that for the corresponding silicon-lattice atoms (see the bismuth case in Fig. 4.12). A simple estimate of  $\psi_{1/2}$  for the dip in the ytterbium yield along the  $\langle 111 \rangle$  may be obtained by inserting  $r_{\min} = 0.55 \text{ \AA}$  into Lindhard's standard continuum potential for the critical angle; the resulting value is  $0.3^\circ$ , which agrees well with that observed in Fig. 4.10.

The main purpose of this rather detailed discussion of the specific lattice location of ytterbium in silicon has been to illustrate how angular widths and minimum-yield values pinpoint rather accurately where a non-substitutional atom is located in a crystal. Thus in the Yb case, we have established with a probable accuracy of  $\sim 0.1 \text{ \AA}$  where the foreign atoms must be located within the unit cell.

Even for supposedly substitutional dopants (such as the Bi in silicon case, illustrated in Fig. 4.6), a detailed angular scan (Fig. 4.12) sometimes shows a narrower dip in scattering yield from the implanted atoms than from the substrate — indicating that the foreign atom is not exactly on the lattice row. Again, as in Fig. 4.10, by means of the Lindhard continuum potential, we can estimate the magnitude of the displacement  $r_{\min}$  required to produce the observed reduction in angular width. For the Bi in silicon spectrum in Fig. 4.12, a displacement of  $\sim 0.25 \text{ \AA}$  is required to account for the observed reduction.

## SUMMARY

We have discussed briefly how the channelling behaviour of MeV particles provides a simple quantitative tool for determining the distribution of foreign atoms between substitutional and various interstitial sites in a crystal lattice. In the next section, we will consider other solid state applications of this channelling-effect technique.

### 4.6. Lattice disorder and surface contamination

In the preceding section, we saw how the channelling behaviour of MeV protons, helium ions, etc. may be used to pinpoint the exact location of specific foreign atoms implanted into a crystal lattice. But there is a bonus attached to this channelling-effect technique in that simultaneously it provides information about the perfection of the crystal lattice in the implanted region. Any lattice atom displaced from its regular site by more than  $0.1\text{--}0.2 \text{ \AA}$  is able to interact with the channelled beam, and so increases the measured value of  $\chi_{\min}$  (as shown by the dotted peak in the unannealed implant of Fig. 4.6). Figure 4.13 shows the aligned spectra for germanium crystals implanted at room temperature with various doses of 40-keV indium ions.

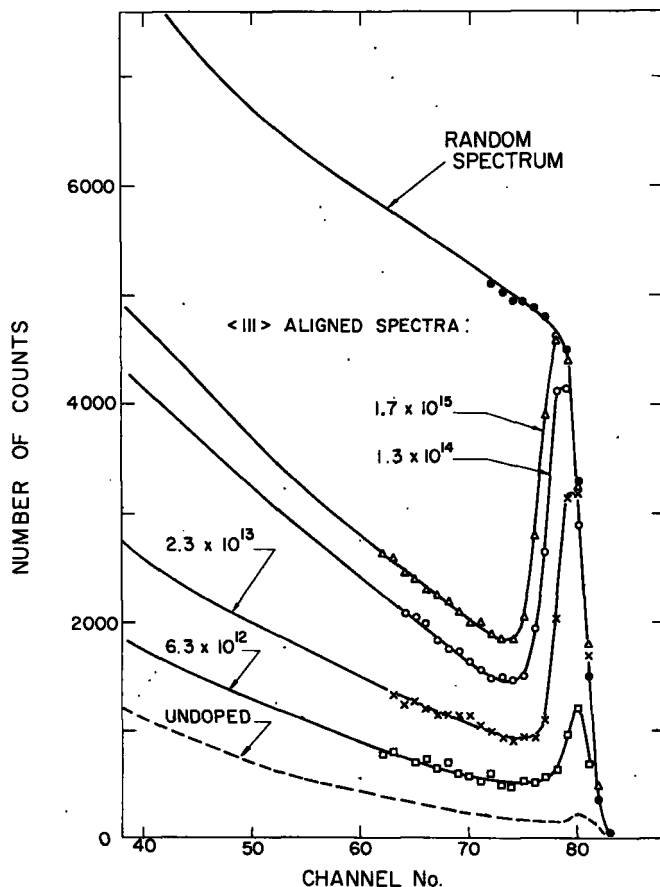


FIG.4.13. Aligned ( $\langle 111 \rangle$ ) and random spectra for backscattering of 1.0-MeV helium ions from germanium crystals implanted at room temperature with various doses of 40-keV indium ions (from Ref.[8]). Note that the high-energy region, due to scattering off the heavy In atoms, has been omitted; this would occur around channel 90.

A "random" spectrum (i.e. the spectrum obtained when the helium beam enters the crystal at a direction not coinciding with any of the major crystallographic axes) is included for comparison; it consists of a sharp edge around channel 80, corresponding to scattering from atoms in the surface region of the crystal, followed by a smooth, slowly increasing yield at lower energy, corresponding to scattering from atoms at greater depths. In the aligned direction, the unimplanted crystal exhibits a roughly 30-fold decrease in yield near the surface (due to channelling), and a somewhat smaller decrease at greater depths; the implanted crystals, in addition, exhibit a pronounced peak in the scattering yield from the implanted region of the crystal (i.e. channels 75-81), indicating that some of the lattice atoms have been displaced from their substitutional sites. The area of this peak is directly proportional to the number of displaced lattice atoms; as can be seen from

Fig. 4.13, it increases with increasing implantation dose. Similar measurements can also be made after various annealing treatments and thus one can study the annealing behaviour of lattice disorder.

You will notice that the aligned yield at lower energies (i. e. at greater depths) also increases continuously with increasing implantation dose. This does not mean that significant damage is extending to such great depths into the crystal. It arises simply from the fact that the aligned beam, in traversing the heavily damaged implanted region, undergoes appreciable multiple scattering. As a result, a significant fraction becomes scattered through an angle greater than the critical angle  $\psi_{1/2}$  and is therefore not channelled. The magnitude of this non-channelled fraction can also be related directly to the number of scattering centers (displaced atoms), and so one can use either the peak area or the level behind the peak as a quantitative measure of the amount of disorder in the implanted region.

A small surface peak in the aligned spectrum is observed even in the unimplanted crystal (Fig. 4.13). This may be attributed in part to the scattering yield from the first plane of atoms, since this yield does not depend on the direction of incidence (i. e. for the first plane of atoms there is no "shadowing" effect). In practice, the surface peak is usually enhanced by the presence of surface oxide layers, etc; this effect can be clearly seen in the aligned spectrum of Fig. 4.14, in which three distinct peaks have been resolved - corresponding to scattering from silicon, oxygen, and carbon atoms, respectively, in a disordered surface layer. For somewhat thicker oxide (or nitride) layers, one may actually use the relative areas of these surface peaks (assuming that the scattering cross-sections obey the Rutherford scattering law) to determine the stoichiometry of the layer, as has been recently demonstrated by Gyulai et al. [10]. Note that, in the "random" spectrum of Fig. 4.14, these low-mass impurity peaks (carbon and oxygen) are completely obscured by the high background from the silicon substrate.

The spectra in Figs 4.13 and 4.14 (and in most other studies so far) have been obtained with a solid-state detector, and thus have rather limited energy resolution (10-15 keV). For 1-MeV helium ions in silicon, this energy resolution is equivalent to a depth resolution of 200-300 Å. Since the range of implanted heavy ions is often less than 1000 Å, such a detector fails to provide much information on the depth distribution of the lattice disorder. Bøgh [11-13] has overcome this limitation by using a high-resolution magnetic spectrometer to increase the energy resolution, and therefore the depth resolution, by approximately one order of magnitude. This permits him to investigate the depth distribution of lattice disorder even at fairly low implantation energies, as can be seen in Fig. 4.15. Note too that this enhanced depth resolution enhances the sensitivity for detecting the surface peak in the unimplanted aligned spectrum. The mean depth of the disorder peak (curve b) in Fig. 4.15 is only  $\sim 500$  Å. It is interesting to observe that the damage is not uniformly distributed throughout the depth of the implanted region; on the contrary, in the first hundred Å or so there is relatively little disorder, and then it gradually increases to a maximum value around 500 Å (2750 G).

While the scattering technique may be a good method of measuring the total number of displaced atoms, it is not a particularly sensitive one. Even in an undamaged crystal, the yield attenuation due to channelling is no more than a factor of  $\sim 100$ . Hence, the background level is  $\sim 1\%$ , and we therefore require, at least, 1-2% of the lattice atoms to be displaced in order to

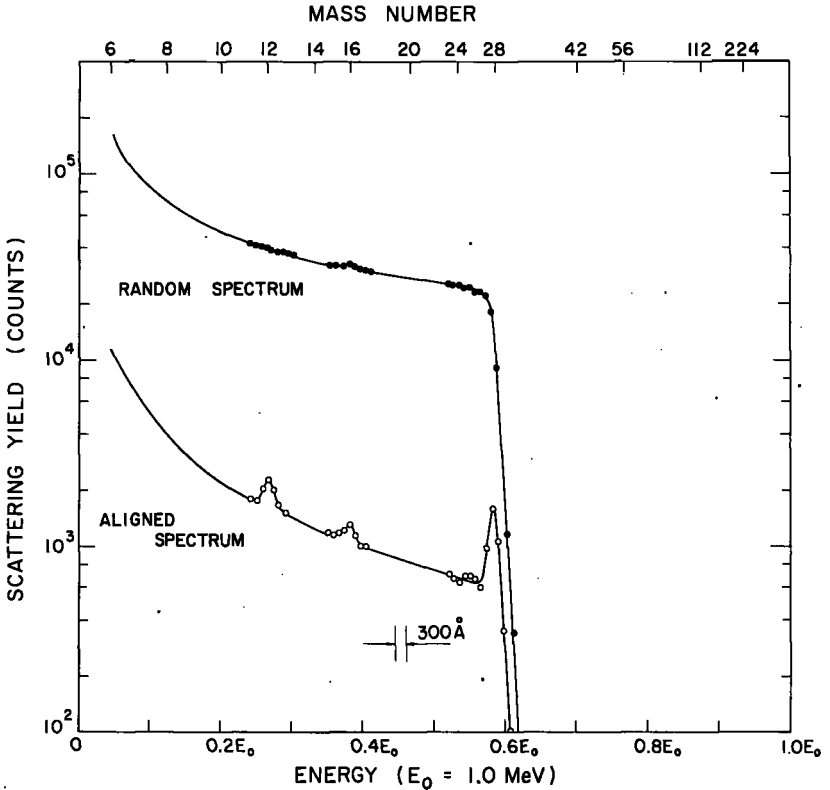


FIG.4.14. Aligned  $\langle 111 \rangle$  and random backscattering spectra for an undoped silicon crystal, recorded for the same dose of 1.0-MeV helium ions. The depth resolution for the aligned case (i.e.  $\sim 300 \text{ \AA}$ ) is indicated. A mass-number scale (for impurities located near the crystal surface) is also given. The three peaks in the aligned spectrum — at masses 12, 16, and 28 — indicate the amounts of carbon, oxygen, and silicon in the surface region that are not aligned with the underlying substrate. To simplify the figure, data points have been omitted except in the more important regions of the spectra (from Ref.[9]).

produce a reasonable signal/noise ratio. For many solid-state purposes, a 2% disorder level would be considered a severely damaged crystal.

However, the sensitivity of the channelling-effect technique can be enhanced considerably by utilizing the so-called "double-alignment" principle [13]. This requires simultaneous alignment of both the incident and the outgoing beam trajectories with major crystal axes. First, the incident beam is aligned with one axis in the crystal (as in any channelling experiment), thereby producing a 30-100 fold reduction in the total scattering yield. Then, a well-collimated detector is aligned with another axis in order to observe only those scattered particles that emerge parallel to a channelling direction. Particles originating from a lattice site are thus prevented, i.e. blocked, from emerging parallel to a lattice row or plane. This blocking phenomenon is related [13, 14] to that of channelling by the so-called rule of reversibility (see Fig. 3.13), and so produces an additional 30-100 fold attenuation in the

observed scattering yield from lattice atoms. Hence, with the double-alignment technique, an over-all attenuation factor of  $10^3$ - $10^4$  can be achieved in the unwanted background level from the undamaged substrate.

The exact relationship between the double-alignment attenuation  $\chi'_{\min}$  and that attainable for either channelling or blocking alone ( $\chi_{\min}$ ) is as follows:

$$\chi'_{\min} = k (\chi_{\min})^2$$

where  $k$  is a geometrical constant whose value lies between 1.5 and 2.0, depending on the angle  $\theta$  between the two axes [14].

The power of this double-alignment procedure is illustrated in Fig. 4.16, taken from the experimental work of Bøgh [13] on tungsten crystals. Even in such a heavy target as tungsten, we see that carbon and oxygen peaks, corresponding in this case to only  $\sim 1.0$  and  $\sim 0.3 \mu\text{g}/\text{cm}^2$ , respectively, are clearly resolved, indicating that with double alignment the sensitivity for low-mass impurities can be extended to less than one atomic layer. The unlabelled peak at 840 keV corresponds to about  $5 \times 10^{14}$  atoms/ $\text{cm}^2$ , i.e. about 0.5 monolayers of a surface contaminant around mass 40; it is probably due to potassium contamination, resulting from an aqueous potassium hydroxide treatment that had been used to clean the tungsten surface before this particular analysis.

Again, as in Fig. 4.14, we may use the ratios of the various surface-contaminant peaks in Fig. 4.16, after correcting for the  $Z^2$  dependence of the Rutherford-scattering cross-section, to derive the stoichiometry of the surface contamination.

The background level in between the surface-contaminant peaks in Fig. 4.16 is seen to be  $\sim 0.05\%$  of the normal random yield; hence, with such double alignment it should be possible to investigate lattice disorder down to at least the 0.1% level.

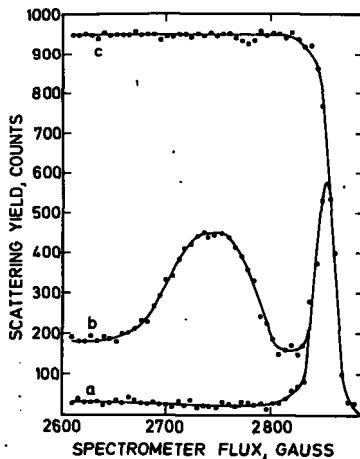


FIG. 4.15. Aligned ( $\langle 111 \rangle$ ) and random spectra for backscattering of 1.0-MeV helium ions from Sb-implanted silicon, using a magnetic analyser to obtain better depth resolution than in Fig. 4.13. The aligned spectrum for an unimplanted crystal (curve a) is included for comparison (from Ref. [12]).

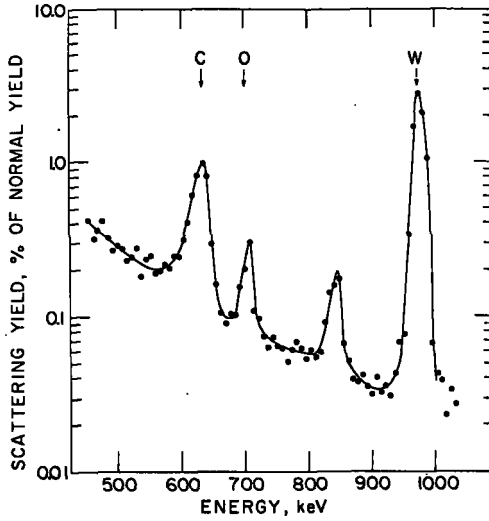


FIG.4.16. Energy spectrum of 1-MeV  $\text{He}^+$  ions in tungsten, under double aligned conditions. Incident direction:  $\langle 111 \rangle$  axis. Exit direction:  $\langle \bar{1}\bar{1}\bar{1} \rangle$  axis (taken from Ref.[13]). The unlabelled peak at  $\sim 840$  keV is attributed to  $^{89}\text{K}$  contamination from a previous chemical treatment.

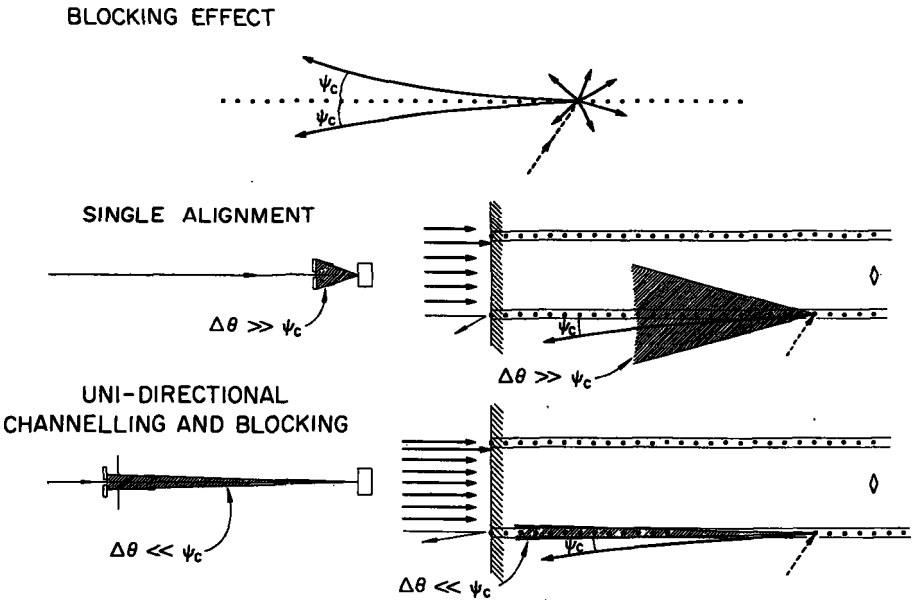


FIG.4.17. Schematic illustration of the uni-axial double-alignment technique. The single-alignment detector is sensitive to the reduction in scattering yield resulting from the channelling effect only, while the uni-axial detector is sensitive to the channelling and blocking effects (from Feldman and Appleton, Ref.[14]).

The area of the surface-tungsten peak in the aligned spectrum of Fig.4.16 corresponds to the scattering yield from  $\sim 1.5$  atomic planes of tungsten. It should be emphasized that, even in a perfect crystal with negligible surface disorder, this surface peak does not completely disappear. It has a limiting value corresponding to the yield from one atomic plane, since the first atom in each aligned row, i.e. the surface plane, must always exhibit the normal scattering yield. Evidently, the tungsten crystal in Fig.4.16 approaches rather closely this limiting case, indicating that the surface layers of C, O, and K are not displacing the tungsten atoms significantly.

Recently, Feldman and Appleton [14] have developed an experimental simplification to the double-alignment technique which they call "uni-axial double alignment". This simply means that they use the same crystal axis

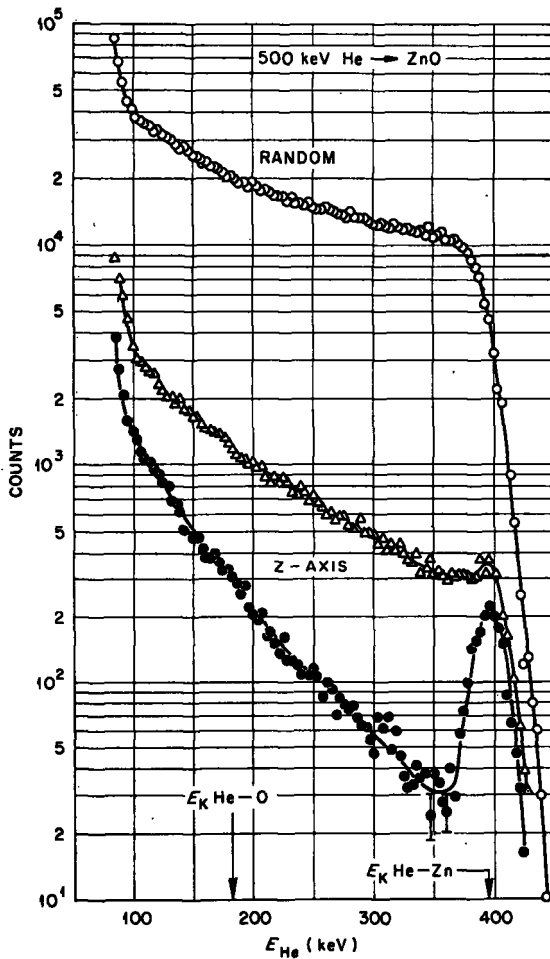


FIG.4.18. Energy spectra for 500-keV  $\text{He}^+$  ions Rutherford scattered to  $\sim 180^\circ$  from a ZnO single crystal. The spectra were obtained with the beam incident: (1) in a random direction (O); (2) parallel to the z axis, as recorded by the single-alignment detector ( $\Delta$ ); (3) parallel to the z axis as recorded by the double-alignment detector ( $\bullet$ ). All spectra are normalized to the same random spectrum. (From Feldman and Appleton, Ref.[14].)



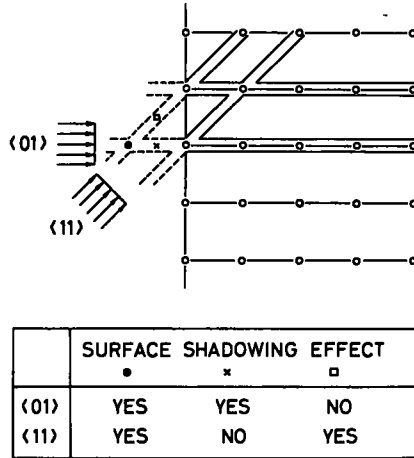


FIG. 4.20. A two-dimensional model illustrating how the channelling effect may be used to locate foreign atoms on the surface of a crystal. As shown by the table, three typical surface sites (●, X, and □) can in principle be distinguished by studying whether or not they are able to shadow the surface plane of lattice atoms when the incident beam enters (a) along the  $\langle 01 \rangle$  direction, or (b) along the  $\langle 11 \rangle$  direction.

atoms, as depicted schematically in Fig. 4.1. What happens, if the foreign atoms are sitting right on the crystal surface? We noted in discussing Fig. 4.16 that, for the surface plane of atoms, there can be no shadowing effect and the Rutherford-scattering yield therefore shows no orientation dependence. Moreover, it was this fact, namely the scattering from the unshadowed surface plane of tungsten atoms, that produced most of the observed W peak in the double-aligned spectrum of Fig. 4.16. Consequently, if such a crystal is then deliberately contaminated with a monolayer of foreign atoms on the surface, these contaminant atoms (if properly located) could shadow the first plane of the tungsten atoms, thereby attenuating the surface W peak. Hence, by looking at the orientation dependence of the scattering from the first plane of target atoms, it should be possible to determine where even a surface layer of foreign atoms is located. Again, the same principles of triangulation as were discussed in Fig. 4.3 can be used to pinpoint the exact location of the foreign atoms on the surface. For example, for the hypothetical two-dimensional lattice depicted in Fig. 4.20, measurements along the  $\langle 01 \rangle$  and  $\langle 11 \rangle$  directions can distinguish between the three sites represented by ●, □, and X. It should be emphasized that to date such surface location studies have not been attempted; this is mainly because of the unavailability of ultra-high-vacuum conditions in a target chamber suitably equipped for channelling studies. Nevertheless, several groups are presently developing such equipment, and hopefully it will not be long before results of this type become available.

#### 4.8. Surface structure of clean crystals

With a suitable ultra-high-vacuum target chamber for channelling studies, it may also be possible to use Rutherford scattering to obtain information about the atomic configuration in the first few planes of an uncontaminated crystal. A simple case to investigate would be one in which

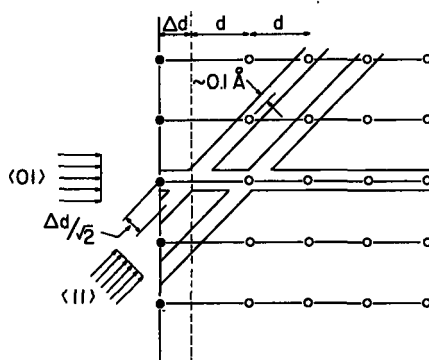


FIG. 4.21. A similar two-dimensional model to Fig. 5.8, illustrating how the channelling effect may be used to study the change ( $\Delta d$ ) in lattice spacing in the surface region of a crystal. Provided  $(\Delta d/\sqrt{2}) \geq 0.1 \text{ \AA}$ , the surface atoms (viewed along the  $\langle 11 \rangle$  direction) do not shadow the underlying plane.

the surface plane (or planes) of atoms are not properly lined up with the underlying bulk crystal — as, for example, in the reconstructed surface region of crystals such as silicon. The surface peak in the aligned back-scattering yield would then correspond to much more than one atomic plane, and from the area of the surface peak, one should be able to determine directly the number of atomic planes contributing to the reconstructed layer.

A somewhat more complicated problem is that of resolving whether or not the interplanar spacing is different in the surface region than in the bulk. But again, by looking down two or more axes in the crystal, it should be possible, in principle at least, to determine the interplanar spacing of the first atomic plane (Fig. 4.21), provided that it differs from the bulk spacing by more than  $\sim 0.1 \text{ \AA}$ .

## SUMMARY

To sum up, we have looked briefly at some of the ways in which channelling (in combination with Rutherford scattering) may be used to obtain precise geometrical information on the location of atoms in relation to the crystal lattice. This is one of the more difficult questions to answer from diffraction studies, and so offers an important supplement to these other techniques.

We should now like to discuss the problems of ion-implantation — particularly in semiconductors. In so doing, we shall see further examples of how the channelling-effect technique may be used for locating foreign atoms and for observing (simultaneously) the amount of lattice disorder.

## REFERENCES TO SECTION 4

- [1] For a more detailed description, see (for example) J. W. Mayer, L. Eriksson and J. A. Davies, "Ion Implantation in Semiconductors" (Academic Press, 1970) pp. 126-148.
- [2] GIBSON, W. M., ANDERSEN, J. U., UGGERHØJ, E., in Proc. Symp. Rad. Effects Semiconductor Components, Toulouse, France (1967).

- [3] ERIKSSON, L., FLADDA, G., BJÖRKQVIST, K., Appl.Phys.Letts 14 (1969) 195.
- [4] ERIKSSON, L., DAVIES, J.A., JOHANSSON, N.G.E., MAYER, J.W., J.appl.Phys. 40 (1969) 842.
- [5] ANDERSEN, J.U., ANDREASEN, O., DAVIES, J.A., UGGERHØJ, E., Rad.Effects 7 (1971) 25.
- [6] DOMEI, B., FLADDA, G., JOHANSSON, N.G.E., Rad.Effects 6 (1970) 155.
- [7] MORGAN, D.V., VAN VLIET, D., Private communication (1970).
- [8] MAYER, J.W., EIRKSSON, L., PICRAUX, S.T., DAVIES, J.A., Can.J.Phys. 46 (1968) 663.
- [9] DAVIES, J.A., DENHARTOG, J., ERIKSSON, L., MAYER, J.W., Can.J.Phys. 45 (1967) 4053.
- [10] GYULAI, J., MEYER, O., MAYER, J.W., RODRIQUES, V., Appl.Phys.Letts 16 (1970) 232.
- [11] BØGH, E., Can.J.Phys. 46 (1968) 653.
- [12] BØGH, E., private communication (1970).
- [13] BØGH, E., in Solid State Physics Research with Accelerators" (Proc.Int.Conf. BNL-50083 (1967) 76.
- [14] FELDMAN, L.C., APPLETON, B.R., Appl.Phys.Letts 15 (1969) 305.
- [15] MOORE, J., Brock University, Canada, private communication (1970).

## 5. PROBLEMS OF ION IMPLANTATION

### 5.1. General features

Ion implantation may be defined as the 'art' (or, more hopefully, as the 'science') of introducing atoms into the surface layers of a solid substrate by bombardment of the solid with accelerated ions, usually in the keV to MeV energy range. Ion implantation is finding widespread application in solid-state physics and in the fields of nuclear and atomic physics as well. For example, nuclear magnetic moments may be determined from studies of hyperfine interactions of atoms implanted into ferromagnetic materials; or, conversely, if the nuclear magnetic moments are known, these same hyperfine interactions may be used to investigate the strength of electromagnetic fields in solids.

The solid-state aspects of ion implantation are particularly broad because of the range of physical properties that are sensitive to the presence of a trace amount of foreign atoms. Mechanical, electrical, optical, magnetic, and superconducting properties are all affected and indeed may even be dominated by the presence of such foreign atoms. Recent interest in ion implantation has focused on the study of dopant behaviour in implanted semiconductors and has been stimulated by the possibilities of fabricating novel device structures in this way. The occurrence of three international conferences on ion implantation in semiconductors within the past year — i.e. at Thousand Oaks, California in May 1970; at the University of Reading, England in September 1970, and at Garmisch, Germany in May 1971 — is a clear indication of the current level of interest. We will therefore direct our attention primarily to those factors which affect the characteristics of implanted layers in silicon and germanium — such factors as range distributions of dopant species, lattice disorder, and the distribution of dopant species between substitutional and interstitial sites in the lattice.

### 5.2. Advantages of implantation

First we shall summarize briefly the principle advantages (and limitations) of ion implantation in comparison to the more widely used thermal-diffusion method of introducing dopant atoms into semiconductor lattices. There are at least four potential advantages:

(i) Use of implantation techniques affords the possibility of introducing a wide variety of atomic species, thus making it possible to obtain impurity concentrations and distributions of particular interest; in many cases, these distributions would not be otherwise attainable. Ordinary solubility limits do not apply to the implantation process, and so the upper limit to the concentration level that can be introduced is set only by the sputtering rate — this limit is typically of the order of 10 atom percent. Note, however, that solubility arguments may subsequently become important if a high-temperature anneal treatment is required.

(ii) Implantation provides a means of independently controlling the number  $N$  and the mean depth  $\bar{R}$  of the dopant species:  $N$  is determined by the integrated beam current, whereas the range  $\bar{R}$  is a function primarily of the accelerating voltage. In thermal diffusion, on the other hand, these two quantities are both related to the same experimental parameters (temperature and diffusion time) and so cannot be varied independently.

(iii) Implantation offers much more precise control, particularly of the number  $N$  of foreign atoms introduced into the lattice. Even for making such a routine item as a resistor in an integrated circuit on a silicon wafer, the precision achievable by ion implantation is an order of magnitude better than by standard diffusion techniques.

(iv) The depth profile produced by implantation (see Figs 1.5 - 1.7) is considerably different in shape than the monotonically decreasing one resulting from diffusion. Furthermore, by varying the accelerating voltage during the implantation, it should be possible (in principle, at least) to produce almost any shape of depth profile.

There are also, of course, some disadvantages — and by far the greatest one is the fact that ion implantation is a rather violent way of introducing an atom into a crystal lattice. In consequence, a large amount of disorder is created around the track of each implanted ion — for example, a 100-keV Sb ion introduced into a silicon crystal produces about 20 000 displaced silicon atoms along its trajectory — and so a subsequent annealing treatment is usually required. But, 20 000/1 is an extremely high ratio — and even after annealing away 99.9% of this disorder, the ratio of displaced silicon atoms to implanted dopant atoms would still be 20/1. Hence, if any of these residual damage centres are electrically active, they would completely mask the dopant behaviour of the implanted Sb atoms.

Historically, ion implantation was first proposed more than 20 years ago (when the semiconductor field was still in its infancy), as an alternative to diffusion for introducing the dopant atoms. A patent was taken out by Schottky in 1948, and an extensive series of experiments was reported a few years later by Kingsbury and Ohl [1], who implanted many different ions (varying in mass from protons up to arsenic) into silicon. They observed that the change in electrical properties was completely independent of the nature of the implanted ion, and depended only on the amount of deposited energy — i.e. on the amount of damage introduced. After this rather discouraging result, ion implantation remained dormant for many years. At that time, not much was known about the basic physics of the implantation process, but in recent years the picture has been improving very rapidly. However, even today, with our greatly improved understanding of the various collision processes associated with ion implantation, the radiation damage problem is still the major obstacle in almost all cases.

Successful exploitation of ion implantation in various solid-state fields requires answers to the following three questions: (i) how deep do the ions penetrate; (ii) how much radiation damage accompanies the implantation and what role does it play; and (iii) on what type of lattice site (substitutional, interstitial, etc.) do they come to rest. We will now briefly discuss a few of the more pertinent points that arise under each of these topics.

### 5.3. Penetration depth

One of the most important considerations, obviously, in any description of implantation processes is the depth (range) distribution of the implanted ions. In recent years, a large amount of experimental and theoretical work has been devoted to the task of understanding the energy-loss processes that govern the range distribution, and it is now possible to predict fairly accurately most of the factors involved (as we discussed in section 1). For example, a typical range distribution in an amorphous substrate is approximately Gaussian in shape, and may therefore be characterized by a mean range  $R_p$  and a straggling about this mean value. Typical values of the mean range for 100-keV ions are  $\sim 0.1$  micron, whereas diffusion doping usually produces a mean depth of 1-10 microns.

When channelling is present, the range distribution contains two distinct components, as shown in Fig. 5.1. Region A illustrates the range distribution of the non-channelled fraction of the beam. This always involves at least 20% of the dopant atoms (and often considerably more); it is characterized by essentially the same  $R_p$  and standard deviation as in an amorphous target. The more penetrating part (regions B and C) is due to the channelled ions; in most cases, it consists of a monotonically decreasing distribution (often an approximately exponential one), which is terminated eventually by a cut-off or maximum value  $R_{max}$  (section 2).

Occasionally, in certain types of well-aligned crystals, the dechannelling rate can be reduced to an almost negligible level. Region C then consists of a fairly sharp peak terminated at  $R_{max}$ , as indicated by the dotted curve in Fig. 5.10. Examples of a well-defined two-peaked range distribution are often observed in tungsten [2] and occasionally also in silicon [3].

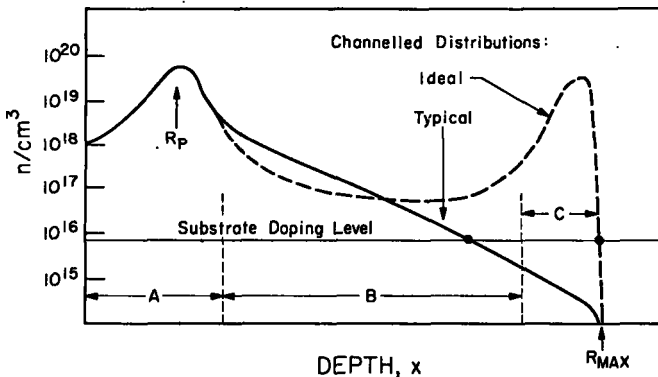


FIG. 5.1. Representative dopant profiles for an initially channelled beam. The dashed curve represents an "ideal" case in which de-channelling is minimized; the solid line represents the case where de-channelling effects are large and only a small fraction of the implanted atoms penetrate to  $R_{max}$ . The solid points (●) indicate the depth at which the junction would be located in the two cases.

For many implantation conditions in semiconductor crystals, the amorphous range-energy relations (section 1) may be used to estimate the location of the peak in the distribution of implanted atoms, and the average concentration near that point. This information is particularly useful in interpreting electrical measurements because both sheet-resistivity and Hall-effect measurements depend primarily on the concentration and mobility of the charge carriers in the region delineated by amorphous range distributions. Channelling phenomena, on the other hand, usually determine the junction location (as shown in Fig.5.1) and ultimately the current- and capacitance-voltage characteristics of the junction.

#### 5.4. Radiation damage

An ion incident on a single crystal will lose energy in both electronic and nuclear collision processes as it slows down and comes to rest in the crystal. Lindhard [4] has derived a comprehensive theoretical treatment of the partition of energy between electronic and nuclear processes. For the case of heavy ions, a large part of the ion energy will be lost in nuclear collision processes even up to ion energies of several hundred keV. These collisions are relatively violent, involving rather large energy transfers to atoms of the lattice and displacing them from their lattice sites. These atoms in turn displace others and the net result is the production of a disordered region around the path of the ion, as shown schematically in Fig.5.2. At sufficiently high doses, these individual disordered regions overlap to form a uniformly damaged area and eventually a "saturation-level" of damage will be reached.

This saturation effect has been studied extensively by the channelling-effect technique described earlier in this section, and a typical result is illustrated by the left-hand part of Fig. 5.3. Note that in this case the

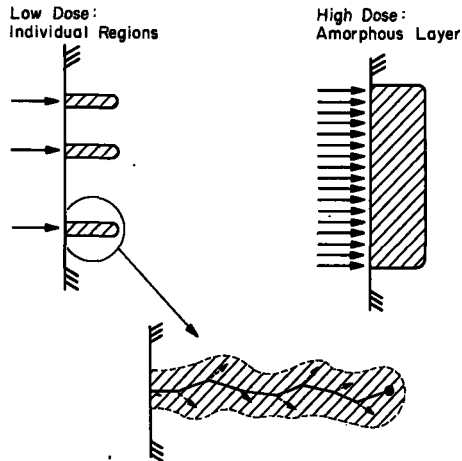


FIG. 5.2. A schematic representation of the disorder produced in room-temperature implantations of heavy ions, at energies of 10-100 keV. At low doses, the highly disordered regions around the tracks of the ions are spatially separated from each other. The volume of the disordered region is determined primarily by the stopping point of the ion and the range of the displaced lattice atoms (dashed arrows). At high doses, the disordered regions can overlap to form an amorphous layer (from Ref.[5]).

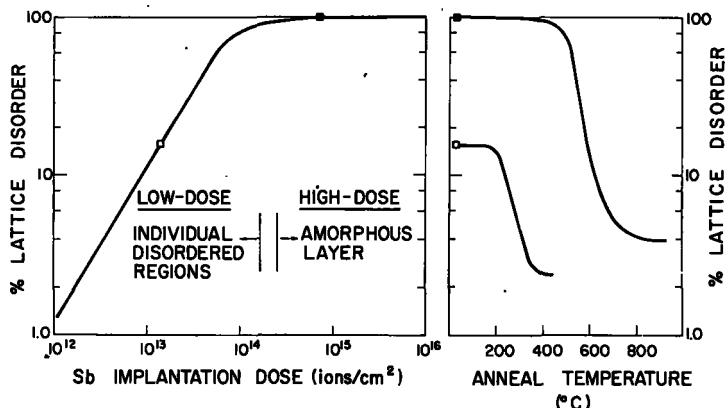


FIG. 5.3. Dose dependence and subsequent annealing behaviour of the lattice disorder produced in silicon by implantation at room temperature with 40-keV heavy ions (gallium, arsenic, antimony, or bismuth). Experimental points have been omitted for the sake of clarity. Squares (■, □) identify the two anneal curves chosen (from Ref.[8] of section 4.)

saturation level corresponds to 100% disorder; it is reached by an implant dose of  $\sim 10^{14}$  Sb ions/cm<sup>2</sup>. Electron microscopy studies indicate that the implanted region has indeed become amorphous. This formation of an amorphous layer at high doses is a characteristic feature of most semiconductor implantations, but does not often occur in other types of crystals.

In general, one might expect widely different anneal behaviour between the small isolated-disorder regions on the one hand and the saturation-level disorder on the other. This is indeed the case, as shown by the right hand part of Fig.5.3. At low implantation doses, one has small individual regions of disorder, surrounded on all sides by a perfect undamaged lattice, and so annealing can occur at a considerably lower temperature than that required to re-crystallize a completely amorphous slab several hundred Å thick. In silicon, for example, we observe a temperature difference of about 300° between the low-dose and high-dose annealing stages in Fig.5.3. A similar difference is observed also in the case of germanium.

This large difference in anneal temperatures suggests that, if one carries out the implantation at a temperature slightly above the low-dose anneal stage – for example, at 350°C in silicon – then the isolated disorder regions can anneal continuously during the bombardment, thus enabling the implantation to be extended to quite high doses without producing an amorphous layer. Figure 5.4 shows that at 350°C the build-up of gross lattice disorder has indeed been drastically suppressed, in comparison to that observed in a similar room-temperature implant (Fig.5.3). The gradual increase in disorder in Fig.5.4 at extremely high doses (i.e.  $\gg 10^{15}$  ions/cm<sup>2</sup>) is probably caused by the high concentration<sup>1</sup> of implanted ions in the lattice, rather than to inadequate annealing.

<sup>1</sup> At a dose of  $10^{16}$  ions/cm<sup>2</sup>, for example, the Sb concentration is about 5 atom percent. This must surely be considered as some sort of antimony/silicon alloy, not a doped silicon crystal.

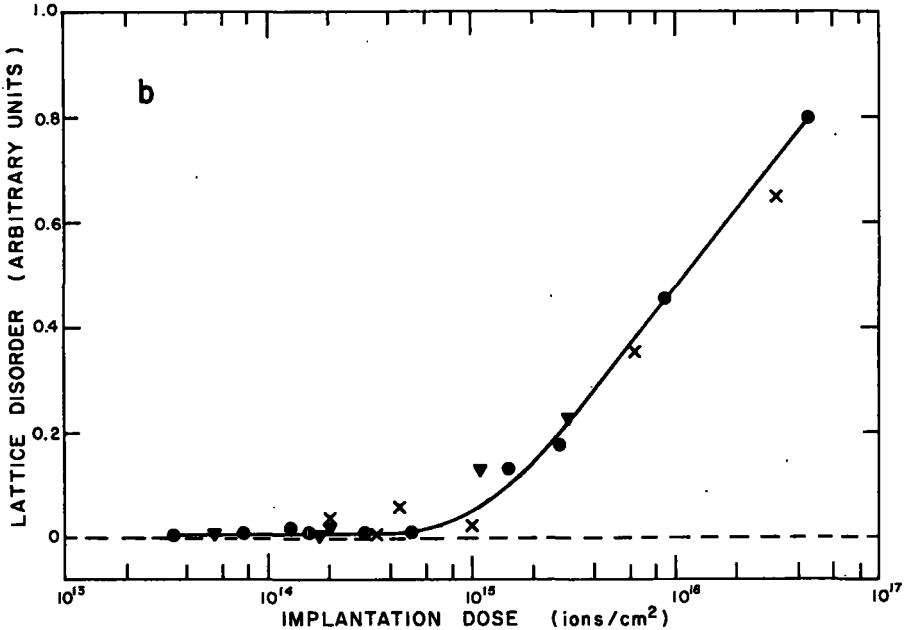


FIG. 5. 4. Dose dependence of the lattice disorder accompanying group-V implantations in silicon at 40-keV energy: X, As; O, Sb;  $\nabla$ , Bi (from Ref. [6]).

Thus, we see that the gross amount of disorder can be greatly reduced by carrying out implantations at elevated temperature. However, we are not so much interested in the amount of residual disorder as we are in its exact nature: i. e. in the effect that it will have on the electrical behaviour of the implanted dopant atoms. The anneal curves in Fig. 5.3 indicate that, even after annealing to 800°C or higher, several percent of the lattice atoms may still remain off their lattice sites and this represents a much higher concentration of defects than of implanted dopant atoms. So, the key question really is "What is the detailed nature of this residual damage, and what effect will it have on the electrical properties of the implanted layer?" This is a question that is currently attracting a great deal of attention. Ideally, one wants to be able to determine the individual contributions from all the different types of lattice defect (vacancies, interstitials, divacancies, various clusters, dislocations, A-centres, etc.) Already some progress has been made in identifying specific types of defect centres, using electron microscopy, electron-spin-resonance and infra-red absorption techniques. However, the lattice-disorder question is far from being fully resolved and as we shall see shortly (Fig. 5.8), it still produces many puzzling surprises.

### 5. 5. Foreign-atom location

Another key question in any implantation study is "What kind of site does the implanted atom end up on?" In the semiconductor case, a group-III dopant such as boron behaves as an acceptor if located on a lattice site in silicon,

but would probably behave as a weak donor if located on some interstitial site. Hence, one could observe either n- or p-type doping behaviour, depending on the site of the implanted atom. Similarly, in the hyperfine-field experiments discussed in several contributions to this seminar, the strength of the magnetic or quadrupole field may depend markedly on where the foreign atom is located within the crystal lattice.

We do not yet have an adequate theoretical framework to predict the lattice-location behaviour of implanted ions in various crystal lattices. The problem is obviously a complex one, involving many solid-state parameters and it is also intimately connected to the lattice-disorder problem that we have just discussed.

As we have already seen (section 4), the channelling-effect technique provides us with a simple, direct method of pin-pointing the site of foreign atoms in a crystal lattice, and so is a useful probe for answering this particular question.

In the case of the simple semiconductors (silicon and germanium), about 25 different implanted species have been investigated, and it is therefore possible to establish a few empirical guidelines on foreign atom location in these two lattices:

(i) All group-V and group-VI dopants (i.e. the typical "donors") and also group-IVA (tin, lead) tend to exhibit a large substitutional component under implantation conditions where the lattice structure is maintained — i.e. at implant temperature above  $\sim 300^\circ\text{C}$ , or in low-temperature implants after annealing to  $\sim 600^\circ\text{C}$  (Fig. 5.5). They are never found in any of the well-defined interstitial sites of the lattice. When the concentration of implanted ions exceeds the equilibrium solubility level, a gradual fall-off in substitutional content may occur at high anneal temperatures (i.e.  $> 800^\circ\text{C}$ ), as seen for the Bi curve in Fig. 5.5. In this particular case, the Bi concentration exceeds the equilibrium solubility level by almost a factor of 100,

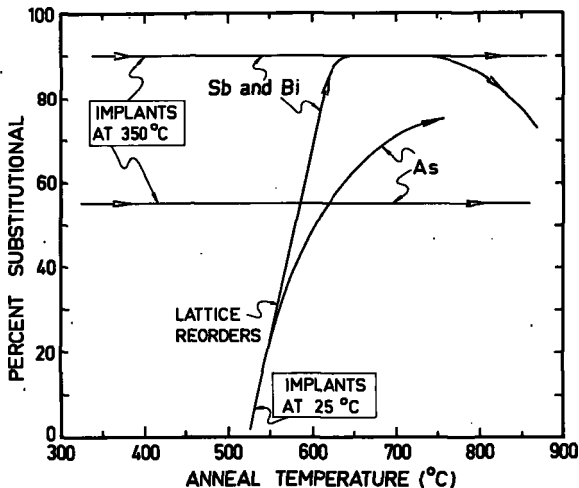


FIG. 5.5. Anneal behaviour of the substitutional component of various group V implants in silicon. In room-temperature implants, the substitutional component is not detectable until the lattice has largely reordered (i.e.  $\approx 600^\circ\text{C}$ ) Constructed from data in Refs [1] of section 4, [6].

Implant conditions:  $3 \times 10^{14}$  ions/cm<sup>2</sup> at 40 keV.

thus illustrating that ion implantation is not limited by solubility considerations until the anneal temperature enters the bulk-diffusion regime.

(ii) The group-II and group-III dopants (i.e. the "acceptors"), on the other hand, as well as group-IVB (zirconium, hafnium) and rare-earth elements such as ytterbium, exhibit a much more complicated behaviour. They tend to be located partly on substitutional sites and partly on the tetrahedral interstitial sites — with the ratio between substitutional and interstitial fractions depending strongly on the particular species and on the implantation and annealing conditions. The anneal behaviour of a typical group-III implant (thallium) is illustrated in Fig. 5.6.

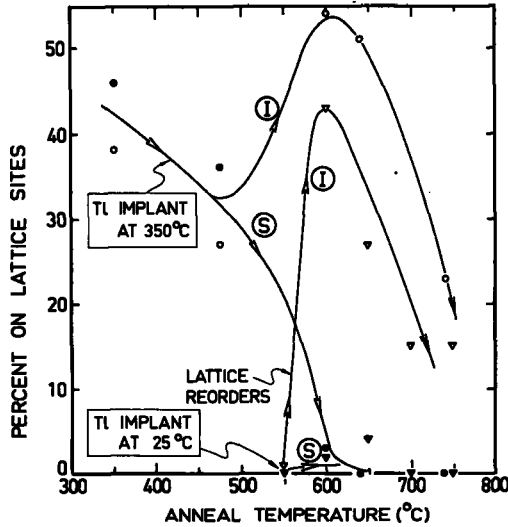


FIG. 5.6. Anneal behaviour of thallium implants in silicon. (S) denotes the substitutional component and (I) the tetrahedral interstitial component. Implant conditions:  $3 \times 10^{14}$  ions/cm<sup>2</sup> at 40 keV (constructed from data in Refs [1] of section 4, [6]).

(iii) If a double-implantation (involving a group-V and a group-III species) is carried out, then both dopants end up predominantly on substitutional sites, provided the group-V implant dose exceeds that of the group III. This suppression of the interstitial group-III component by an excess of a suitable donor is illustrated in Fig. 5.7; it suggests that electrical compensation effects can sometimes determine the site of an implanted atom.

(iv) In low-dose (i.e.  $\leq 10^{13}$  ions/cm<sup>2</sup>) unannealed room-temperature implants, all elements end up largely on substitutional sites. On subsequent annealing, however, groups-II and -III elements move at least partially to interstitial sites, whereas groups-V and -VI elements remain substitutional.

To illustrate the complexity that can occur, particularly with group-III implants, we might point out that in the case of a room-temperature boron implant in silicon [9, 10], the boron atoms end up largely on substitutional sites; on annealing to around 400°C (or, alternatively, by carrying out the implantation at 400°C), most of the boron atoms move to interstitial sites, but on further annealing to above 800°C, they move onto substitutional sites again.

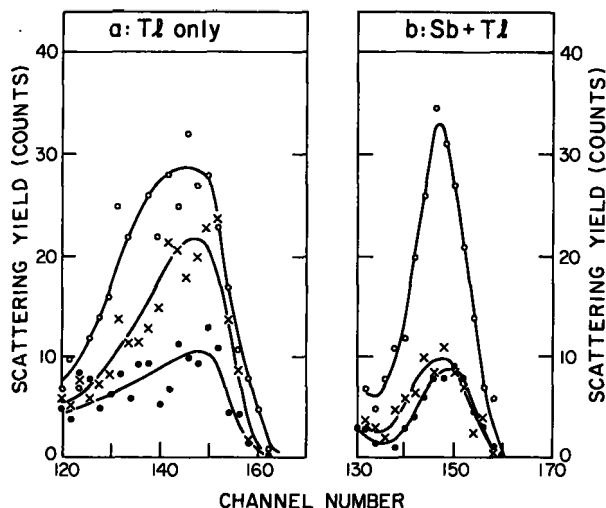


FIG. 5. 7. Backscattering energy spectra of 1.8 MeV  $^{12}\text{C}$  ions from a germanium crystal implanted at 30 keV and 350°C with  $2 \times 10^{14}$  Tl ions/cm<sup>2</sup> plus (on the right-hand part)  $4 \times 10^{14}$  Sb ions/cm<sup>2</sup>. In both cases, only the high-energy part of the scattering spectrum - i. e. that from the implanted atoms - is shown (constructed from data in Eriksson et al., Ref. [7]).

Obviously, therefore, the lattice location of implanted atoms depends markedly on implantation and annealing conditions; furthermore, it is not necessarily the same as for atoms introduced by thermal-equilibrium methods.

The last of the above 'rules' - i. e. that low-dose implants (where the individual tracks do not overlap one another) tend to be highly substitutional - may be a fairly general one. It has been tested not only for a variety of implanted ions (boron, antimony, bismuth, thallium, gold) in silicon, but also in other crystal lattices. Thus, Feldman [8] has recently observed that bismuth implanted into iron at room temperature is found on lattice sites before annealing; but, after annealing, it has moved almost entirely to some sort of precipitation site. This explains why the hyperfine-field effects for bismuth diffused into iron are quite different to those for an unannealed implant; it is only in the latter case that the foreign atoms are substitutionally located.

### 5.6. Electrical behaviour of implanted dopants

We should like to close this very brief sketch of ion-implantation problems in semiconductors by showing a comparison between substitutional content and electrical properties. Of course, the ultimate objective is to produce a region whose electrical characteristics are determined solely by dopant atoms located at well-defined positions in the semiconductor lattice. For example, if you implant  $10^{14}$  Sb ions/cm<sup>2</sup> and (after annealing the damage) find that they are all on substitutional sites, then you hope to find  $10^{14}$  electrically-active carriers (donors)/cm<sup>2</sup> also. Figure 5.8a shows that such an objective can indeed be accomplished; i. e. for room-temperature implants at sufficiently

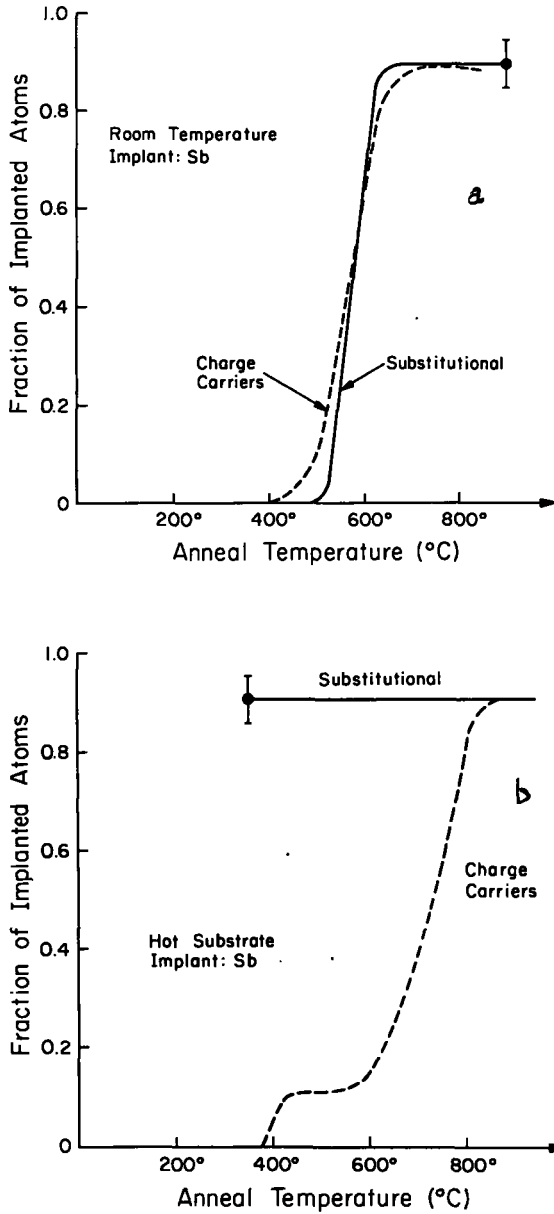


FIG. 5. 8. The anneal behaviour of the number of implanted antimony ions on lattice sites (channelling-effect measurements) and the number of carriers (Hall-effect measurements) for implantation conditions such that the concentration of implanted atoms does not greatly exceed the maximum solubility value: (a) Room-temperature implantations such that an amorphous layer is formed. The steep rise in the curve reflects the anneal of the amorphous layer. (b) Implantation at 350°C substrate temperatures. After implantation approximately 90% of the atoms are on substitutional lattice sites. Anneal temperatures of 800°C are required before the number of carriers approaches the number of implanted atoms.

high doses to form a completely amorphous layer, we observe a rather good correlation between the number of charge carriers and the number of substitutional antimony atoms.

This same correlation does not occur, however, if we carry out the implantation at 350°C. We know from channelling-effect studies that the disorder anneals continuously during such a hot-substrate implantation (Fig. 5.4), and that the antimony atoms end up on lattice sites without any further anneal treatment (Fig. 5.5). Yet, for some reason, these substitutional antimony atoms do not become electrically active until the crystal is annealed to 800°C or higher (Fig. 5.8 b); i. e. to an even higher temperature than that required to anneal the amorphous layer in Fig. 5.8a.

The explanation for this puzzling difference in behaviour is almost certainly associated with the radiation damage problem. Although most (i. e. ~95%) of the damage anneals away continuously in the hot implant, the residual disorder consists largely of a complex dislocation network, as revealed by electron microscopy. This dislocation network may indeed interfere with the electrical characteristics. Furthermore, it does not anneal significantly until the region 800-900°C, and so could account for the high-temperature anneal stage in Fig. 5.8b. In the room temperature implant, on the other hand, the implanted region is converted completely into an amorphous layer; during subsequent annealing at ~600°C, this layer regrows epitaxially on the undamaged underlying crystal to form a crystalline region that does not contain the above dislocation network, and so the high-temperature anneal stage is not required.

## SUMMARY

This is perhaps a good point at which to close. We have seen that, although ion implantation offers a lot of potential as a means of fabricating exotic types of solid state materials, we need a much better understanding of the intricacies of the lattice disorder problem before this potential can be fully exploited.

## REFERENCES TO SECTION 5

- [1] KINGSBURY, E.F., OHL, R.S., *Bell Syst. Tech. J.* **31** (1952) 802.
- [2] ERIKSSON, L., DAVIES, J.A., JESPERSGÅRD, P., *Phys. Rev.* **161** (1967) 219.
- [3] DEARNALEY, G., FREEMAN, J.H., GARD, G.A., WILKINS, M.A., *Can. J. Phys.* **46** (1968) 587.
- [4] LINDHARD, J., NIELSEN, V., SCHARFF, M., THOMSEN, P.V., *Kgl. Danske Videnskab. Selskab, Mat.-Fys. Medd.* **33** 10 (1963).
- [5] ERIKSSON, L., DAVIES, J.A., MAYER, J.W., *Science* **163** (1969) 627.
- [6] ERIKSSON, L., DAVIES, J.A., JOHANSSON, N.G.E., MAYER, J.W., *J. appl. Phys.* **40** (1969) 842.
- [7] ERIKSSON, L., FLADDA, G., BJÖRKQVIST, K., *Appl. Phys. Letts* **14** (1969) 195.
- [8] FELDMAN, L., private communication (1971).
- [9] FLADDA, G., BJÖRKQVIST, K., ERIKSSON, L., SIGURD, D., *Appl. Phys. Letts* **16** (1970) 313.
- [10] NORTH, J.C., GIBSON, W.M., *Appl. Phys. Letts* **16** (1970) 126.

## 6. NUCLEAR AND CRYSTALLOGRAPHIC APPLICATIONS OF CHANNELLING

### 6.1. Introduction

The most extensive applications of channelling, as we have seen in the previous two sections, have been in the solid-state field. In this final section, we should like to discuss some of the applications that are evolving in other fields - particularly in nuclear physics, where channelling provides a method of observing nuclear lifetimes in the  $10^{-14}$  to  $10^{-19}$  s. But, first we should like to describe what might be considered a crystallographic application, i.e. the use of channelling for determining accurately the alignment of a crystal. This is an important pre-requisite of all the channelling studies that we have discussed already; it also involves an experimental technique that has been especially useful in some of the nuclear life-time studies.

### 6.2. Crystal-alignment techniques

The channelling effect provides a simple method [1] for precise orientation of a single crystal. For this purpose, wide-angle Rutherford scattering is particularly useful, because it can be applied to any crystal provided a proton beam of  $E \gtrsim 50$  keV is available. With care, an accuracy of  $0.02^\circ$  can be achieved and an alignment to within  $0.1^\circ$  takes only 10-15 minutes. The crystal is mounted on a suitable goniometer allowing rotation of the crystal at a certain tilting angle  $\theta$  to the beam (Fig. 6.1) and is then rotated through a full  $360^\circ$  in the azimuthal angle  $\phi$ . This produces a yield curve such as the one in Fig. 6.2, in which sharp attenuations occur as the various close-packed planes are successively aligned with the incident beam. A stereogram (Fig. 6.3) can then be constructed by marking off on the circumference of a circle, the azimuthal angles at which these planar "dips" in yield occur. By properly connecting the pairs of points<sup>1</sup> that correspond to intersections of the same plane, we readily obtain the exact location P of a major crystal axis - in this case the  $\langle 100 \rangle$ . This whole operation can be performed in situ prior to the main channelling study. The beam can then be aligned exactly with the major axis by setting the goniometer at the azimuthal and tilt angles corresponding to the point P on the stereogram.

One interesting feature of the method is that, by measuring the energy spectrum of the scattered protons, we are able to study simultaneously the channelling behaviour of the beam at different depths beneath the crystal surface, as was discussed in section 3.9 (see Fig. 3.19). Hence, the method determines the crystal orientation as a function of depth, and thus provides information on the mosaic spread along the beam direction. Typical depth resolution with a solid state detector is about  $1000 \text{ \AA}$ ; however, Bøgh [2] has shown that this can be improved to  $50\text{-}100 \text{ \AA}$  by using an electromagnetic analyser (see, for example, Fig. Fig. 4.15).

An alternative, but closely related, technique for determining the orientation (or even the structure) of a single crystal is to utilize the "blocking" effect: i.e. the directional dependence of the emission of atomic particles originating from lattice sites. The rows and planes of atoms

<sup>1</sup> Strictly speaking, these interconnecting 'lines' in the stereogram of Fig. 6.3 are slightly curved 'arcs' - but the curvature of a  $5^\circ$  section of a spherical surface is far too small to be detected.

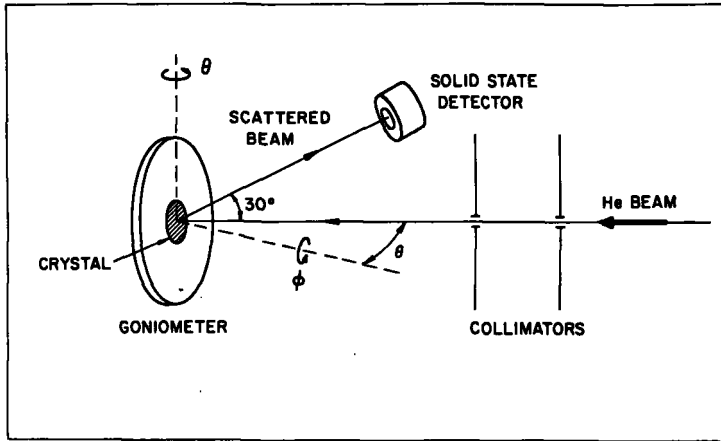


FIG. 6.1. Schematic diagram of a typical 2-axis goniometer assembly for channelling experiments, indicating the relationship between the tilt angle  $\theta$  and the azimuthal angle  $\phi$  in Figs 6.2 and 6.3.

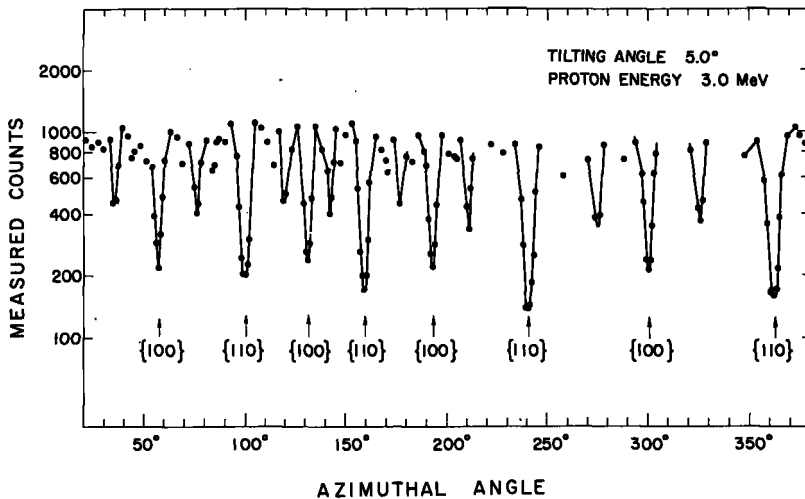


FIG. 6.2. Rutherford scattering yield obtained on rotation of a tungsten crystal around the  $\langle 100 \rangle$  axis with a tilt angle ( $\theta$ ) of  $5.0^\circ$  between the rotation axis and the incident proton beam (see Fig. 6.1). The incident proton energy was 3.0 MeV.

deflect (block) all particles that start out along low-index directions so that in an angular distribution outside the crystal there is a deficit of particles in directions parallel to atomic rows and planes. Wide-angle Rutherford scattering is again the most convenient process with which to observe blocking but now the beam is brought in along a "random" direction in order to avoid channelling (see Fig. 3.13). During the backscattering process, the proton or helium ion penetrates almost to the center of the lattice atom; it can therefore be considered as "originating" from a lattice site. A photographic film is placed 20-30 cm from the crystal (to provide

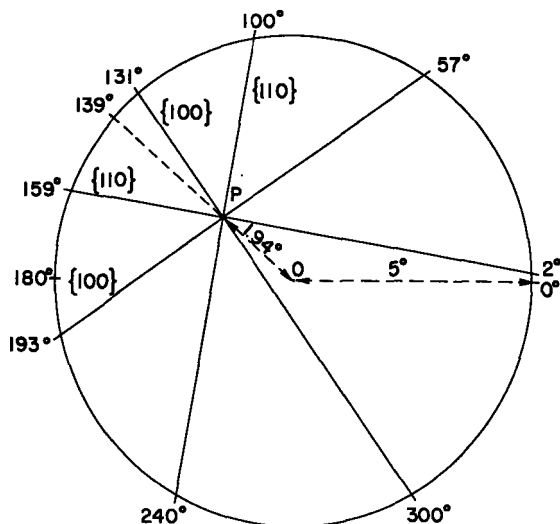


FIG. 6.3. Stereographic representation of the 360° rotation in Fig. 6.2. Azimuthal angles corresponding to the planar "dips" in Fig. 6.2 are marked off on the circumference, and points corresponding to the same plane are connected by a straight line. The intersection point, P, denotes the location of the  $\langle 100 \rangle$  axis. The radius of the stereogram corresponds to the tilting angle of 5.0°.

adequate angular resolution), and a "pattern" due to the orientation dependence of the emitted particles is observed: i. e. strong attenuations in emission rate occur along all the major axes and planes, thereby producing a crystallographic projection on the surface of the film, as is illustrated in Fig. 6.4.

It is of interest to note the large number of higher-index planes (and axes) that can be observed in these blocking patterns. It turns out that, with complex crystal structures such as SiC or BaTiO<sub>3</sub>, a considerable amount of structural information can be deduced by comparing the relative intensities of these various high-index planes. Thus, in the case of SiC for example, there are more than 50 possible polymorphic structures; yet, by means of a blocking pattern, Barrett et al. [4] were able to determine unambiguously which structure to assign to a particular specimen.

The most commonly used "detector" for observing blocking patterns is a piece of photographic film. The pattern in Fig. 6.4, however, was obtained by an even simpler method: viz. by using a sheet of cellulose nitrate and subsequently "developing" the sheet by etching away, with aqueous sodium hydroxide, the damaged plastic material around each helium-ion track. This is in fact one of the standard nuclear track detectors that are often used in nuclear physics. The grey areas in Fig. 6.4 contain  $\sim 10^3$  tracks/mm<sup>2</sup>, whereas the black (transparent) areas contain much fewer tracks - due to blocking. The use of cellulose nitrate has certain advantages over photographic film. It avoids the need for dark-room techniques, since the plastic is completely insensitive to light; it is even relatively insensitive to those energetic particles whose tracks have a fairly low ionization density along them - such as protons or electrons.



FIG. 6.4. Blocking pattern of helium ion "tracks" on a sheet of cellulose nitrate (after etching in 5N NaOH at 60°C for 2-3 min), produced by the backscattering of 1.0-MeV He<sup>+</sup> from a {111} surface of GaAs. The central black dot with the bright halo is the aperture through which the incident beam entered the scattering chamber; the apices of the prominent equilateral triangle correspond to the three  $\langle 110 \rangle$  axes at 34.4° from the central  $\langle 111 \rangle$  axis. A large number of higher-index axes and planes are clearly visible in the blocking pattern (from Marsden et al. Ref.[3]).

Another advantage is that, when necessary, the cellulose nitrate provides quantitative information on the exact number of particles emitted within a given solid angle, since each backscattered helium ion produces one etch pit. Hence, by placing the etched sheet under a microscope, and scanning stepwise through each of the axes or planes, it is possible to count the individual tracks and thus construct the orientation dependence of the emission yield: i. e. one can produce a series of "blocking" yield curves similar to those obtained with a solid state detector (Figs 3.12, 3.13) - except of course that the blocking pattern does not normally provide much energy (or depth) resolution. One might argue that quantitative information on the orientation dependence is available also with photographic

film by using densitometer techniques to measure the contrast between different areas. This is certainly true, but considerably greater accuracy may be achieved by counting directly the individual events or 'tracks'.

In the next sub-section, we shall see a practical example (Fig. 6.6) of how these 'track'-detectors may be used to provide quantitative information on the blocking phenomenon in studying various nuclear life-times.

### 6.3. Nuclear life-time studies

The most interesting application of channelling in the field of nuclear physics is almost certainly in the measurement of short nuclear life-times. This application is based on essentially the same principle as that for foreign-atom location: i. e. the ability, by means of channelling (or blocking) behaviour, to pinpoint within  $\sim 0.1 \text{ \AA}$  the location of a nucleus (relative to the crystal lattice) at the instant that it collides with or emits an energetic charged particle.

Suppose, for example, we excite a lattice nucleus by bombardment with an external beam of suitable energetic particles (fast neutrons, protons, etc). If this recoiling "compound nucleus" subsequently decays by emitting a positively charged particle (proton, alpha particle, fission fragment, etc.), then the blocking pattern resulting from this emission can be used to determine how far the nucleus has recoiled before decaying, as shown schematically in Fig. 6.5. Those nuclei decaying within  $\sim 0.1 \text{ \AA}$  of the lattice site

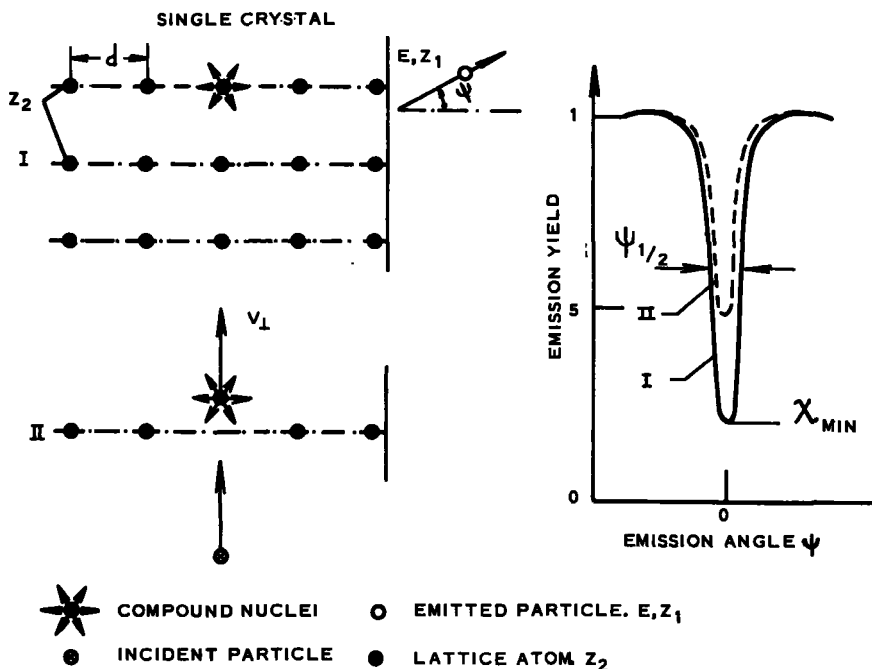


FIG. 6.5. A schematic representation of the angular distribution on emergence from a single crystal of charged particles emitted (I) from lattice positions and (II) from a recoiling compound nucleus formed by interaction of an incident particle with a lattice atom. The emission angle  $\psi = 0$  is parallel to a row of lattice atoms of spacing  $d$  and atomic number  $Z_2$  (from Ref. [5]).

exhibit the full blocking effect (curve I in Fig. 6.5); those decaying at a slightly greater distance (0.1 - 0.5 Å) exhibit partial blocking - i. e. a somewhat weaker and narrower dip such as that in curve II of Fig. 6.5 (see also Fig. 4.21); and those decaying at much greater recoil distances (i. e.  $\sim 0.7$  Å or greater) exhibit essentially an isotropic emission pattern. Since recoil velocities are usually in the range  $10^7 - 10^9$  cm/sec, the time taken to recoil 0.1 Å is only  $10^{-16} - 10^{-18}$  s. This time scale can be extended a factor of 2-3 by observing the blocking effect along an axis that is not perpendicular to the recoil direction, since it is only the velocity component  $v_{\perp}$  perpendicular to the blocking axis that is involved in reducing the intensity of the blocking pattern.

Thus, the principle involved in such a nuclear life-time measurement is a simple one. Quantitative evaluation of the life-time can be quite complex, however, as it requires a careful evaluation of the dependence of the blocking 'dip' (i) on recoil distance in the intermediate region (0.1 - 0.7 Å) where partial blocking occurs and (ii) on the depth beneath the crystal surface from which the emission originates. In certain cases, only a rough estimate of the life-time is required and then the problem can be greatly simplified by assuming that a sharp transition between full blocking and isotropic emission occurs at a critical distance  $r_c$ , where  $r_c$  is roughly 3-4 times greater than the Thomas-Fermi screening length,  $a$  (i. e.  $r_c \sim 0.4$  Å). The fraction of decays that occur before and after the nucleus has recoiled this cut-off distance  $r_c$  depends exponentially on the mean life-time  $\tau$  of the excited nucleus: i. e.

$$\text{the fraction decaying at } r < r_c = 1 - e^{-r_c/v_{\perp}\tau}$$

$$\text{and the fraction decaying at } r > r_c = e^{-r_c/v_{\perp}\tau}$$

Consequently, the observed minimum yield  $\chi_{\text{obs}}$  from the recoiling nucleus can be expressed as follows:

$$\chi_{\text{obs}} \approx \chi_{\text{min}}(1 - e^{-r_c/v_{\perp}\tau}) + e^{-r_c/v_{\perp}\tau} \quad (6.1)$$

where  $\chi_{\text{min}}$  is the minimum yield observed from a nucleus on a lattice site (curve I in Fig. 6.5). Rearranging Eq. (1) we obtain

$$e^{-r_c/v_{\perp}\tau} = \frac{\chi_{\text{obs}} - \chi_{\text{min}}}{(1 - \chi_{\text{min}})} \approx \chi_{\text{obs}} - \chi_{\text{min}} \quad (6.2)$$

Hence, the difference  $\chi_{\text{obs}} - \chi_{\text{min}}$  between the observed yield along an axis and that which would have occurred for perfect blocking provides a simple estimate of the mean life-time  $\tau$ .

#### 6.4. Fission life-times

The idea of using the blocking effect to measure short nuclear life-times has been generally recognized for quite some time. As early as 1965 it was proposed independently and almost simultaneously by Gemmell and Holland [6], by Lindhard [7], and by Tulinov [8]. Successful applications were not attempted until several years later, however, because of

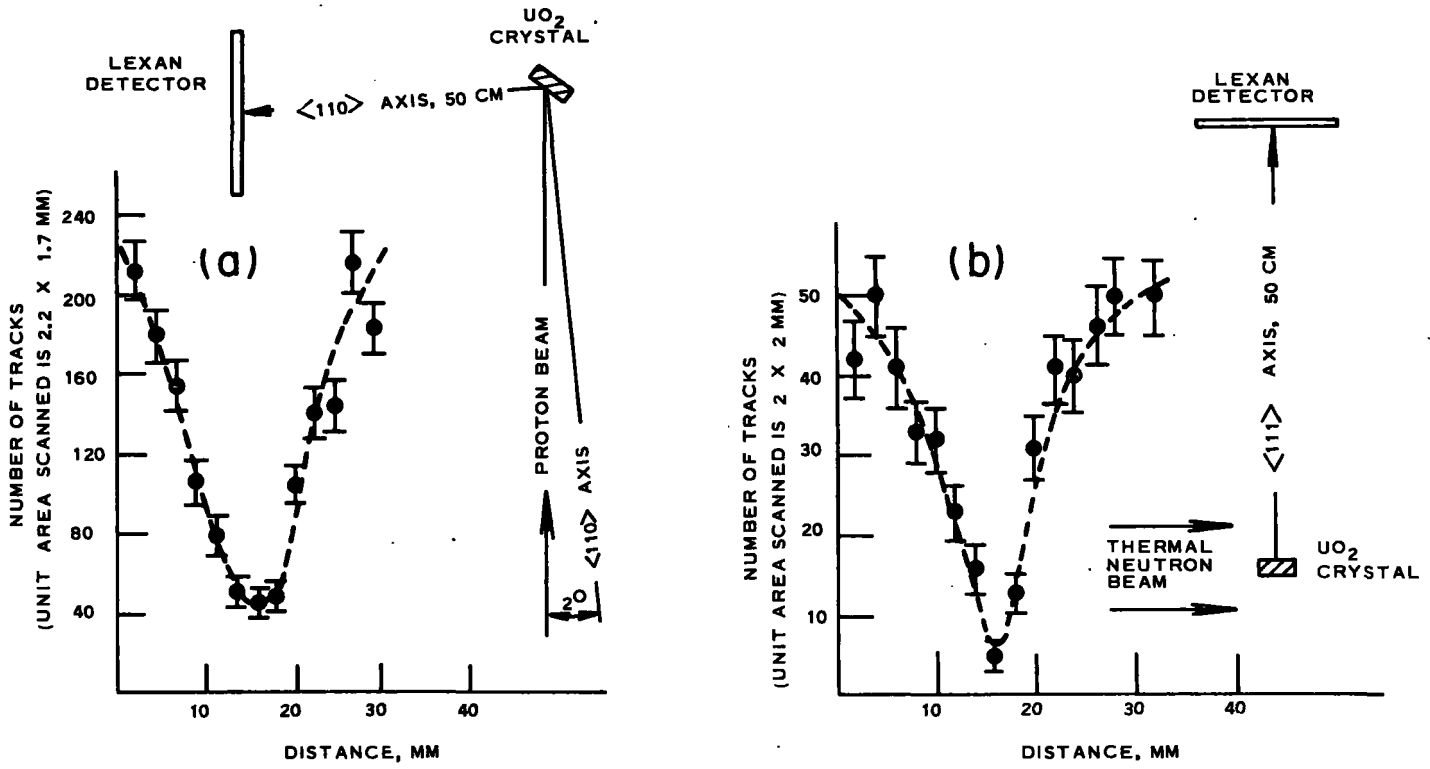


FIG. 6.6. Fission fragment angular distribution around the  $\langle 111 \rangle$  axis in a single crystal of  $UO_2$ : a) for 12-MeV proton-induced fission, and b) for thermal-neutron fission. A distance of 1 mm at the plastic (lexan) 'track detector' subtends an angle of  $0.1^\circ$  at the crystal (from Brown et al., Ref.[9]).

the difficulty in finding a suitable reaction that involved charged-particle emission, and that might have a life-time within the accessible range for the blocking technique.

The first useful application<sup>2</sup> was an investigation by F. Brown et al. [9] of the fission life-time of the excited nucleus  $^{239}\text{Np}$  (created by 12-MeV proton bombardment of  $^{238}\text{U}$ ) in a single crystal of  $\text{UO}_2$ . The resulting blocking pattern (Fig. 6.6a) was almost indistinguishable from that obtained for thermal-neutron-induced  $^{235}\text{U}$ -fission in the same crystal (Fig. 6.6b). In the latter case, the recoil velocity is negligible, and so this provides a useful standard for the full blocking effect ( $X_{\text{min}}$ ) averaged over the crystal depth from which fission fragments are being emitted. Using Eq. (2), one can thus conclude that the fission life-time  $\tau$  in the 12-MeV proton bombardment (which creates a  $^{239}\text{Np}$  recoil nucleus with a velocity of  $2 \times 10^7$  cm/s) must be shorter than  $\sim 4 \times 10^{-17}$  s, since the difference ( $X_{\text{obs}} - X_{\text{min}}$ ) in Fig. 6.6 is certainly no greater than  $\sim .03$ .

Subsequently, Gibson and Nielsen [5] investigated more carefully the proton-induced fission of  $^{238}\text{U}$  and in a narrow proton-energy region around 10 MeV they observed a small but detectable reduction in the blocking effect (Fig. 6.7), compared to the behaviour at lower (9 MeV) and higher

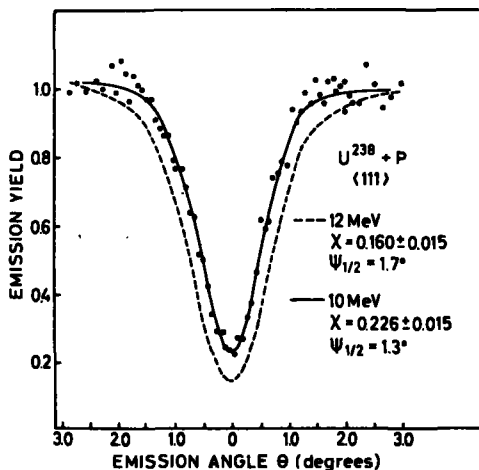


FIG. 6.7. Measured angular distributions, normalized at large emission angles, of fission fragments emitted parallel to a  $\langle 111 \rangle$  axis for bombardment of uranium oxide crystals with 10-MeV protons (solid line and closed circles) and with 12- and 9-MeV protons (dotted line). The values indicated for the minimum yield for the 12-MeV curve are the averages, weighted by their respective statistical uncertainty, of three runs at 12 MeV and one at 9 MeV. For the 10-MeV case, the minimum yield is the result of 2 runs at 10 MeV (from Gibson and Nielsen, Ref. [5]).

<sup>2</sup> Actually, the first attempt to study nuclear life-times by means of blocking is due to Treacy [10], who tried unsuccessfully 12 years ago to measure the  $^{12}\text{C}(\text{d}, \text{p})$  life-time in an organic crystal, using a 3-MeV deuteron beam. At that time, the concept of channelling had not been recognized, and so he only expected to observe some sort of two-atom shadowing effect, rather than the much stronger blocking that results from the sequence of collisions with an aligned row of atoms. It is interesting to speculate that, if Treacy had used SiC or UC (instead of an organic crystal) for his  $^{12}\text{C}$  life-time experiment, he would undoubtedly have been the discoverer of the channelling (and blocking) phenomenon. An organic crystal was unfortunately a rather unlucky choice, since such crystals are now known to exhibit rather poor channelling dips.

(12 MeV) energies. From the difference in  $\chi$ -values between the two curves, one concludes that in the 10-MeV case  $\sim 7\%$  of the nuclei must be recoiling beyond  $r_c$  before decaying - and so (from Eq. (2)) the mean life-time  $\tau$  is  $\sim 6 \times 10^{-17}$ s. The interpretation of this strange oscillatory dependence of life-time on proton energy is rather complicated, but is associated with the onset of so-called "second-chance" fission - i. e. emission of a fast neutron before fission occurs. At 9 MeV there is negligible neutron emission; fission, therefore, involves a highly excited nucleus and so the life-time is very short. At 10 MeV, there is enough energy available for neutron emission and a significant amount of second-chance fission occurs; in such cases the nucleus is apparently de-excited enough to have a measurable fission life-time. At 12 MeV and higher energies, however, even the second-chance fission nucleus still has sufficient excitation energy that an immeasurably short life-time is again involved.

Several other fission-life-time studies have also been attempted (e. g. fast neutrons and 25-MeV  $^4\text{He}$  ions on  $^{238}\text{U}$ , and 200-MeV neon ions on tungsten), but with results similar to those of Brown et al. [9]: i. e. no detectable deviation from perfect blocking, indicating that the life-times are too short to be observed.

### 6.5. Life-times of the (p, p') reaction

Recently, several groups [11-13] have also investigated life-times of various (p, p') reactions in silicon and germanium lattices - with considerably better success. Essentially the same blocking technique is involved, except that the plastic track detector is replaced by a solid-state position-sensitive detector, since for protons this can provide not only the angular distribution but also the energy spectrum of the emitted particles. Time is running short, so we will not discuss these experiments in detail. We shall merely summarize them by pointing out that in several cases life-times in the region  $10^{-16}$ -  $10^{-17}$  s have been observed and measured by means of the blocking effect.

### 6.6. Doppler-shift life-time studies

One of the most commonly used techniques of measuring nuclear life-times has been the Doppler shift method in which, from the observed energy shift of an emitted  $\gamma$ -ray, one deduces the velocity of the recoiling nucleus at the instant of emission. If the initial recoil velocity  $v_R$  and the rate of slowing down ( $-dE/dx$ ) are both known, it is possible to derive the mean life-time  $\tau$  of the recoiling nucleus. Typical recoil velocities and ranges are  $10^8$  cm/s and  $10^{-4}$  cm respectively, so that life-times in the region  $10^{-11}$ -  $10^{-13}$  secs are normally measurable by this technique.

The "blocking-effect" offers a rather simple way to extend such studies to much shorter life-times [14]. The  $\gamma$ -ray itself, of course, does not undergo channelling or blocking effects with the lattice structure - but the recoiling nucleus does! Hence, if this excited nucleus starts out almost parallel to an axial row (Fig.6.8), then a major change in its velocity and direction will occur when it passes the next lattice site: i. e. after a time  $t_1 = d/v_R \cos\theta$ . Since  $d$  is  $\sim 4 \times 10^{-8}$ cm, a typical value of  $t_1$  would be  $\sim 4 \times 10^{-16}$  s. Nuclei decaying at  $t < t_1$  exhibit a much smaller Doppler shift and in favourable cases (such as shown in Fig.6.8) perhaps none at all.

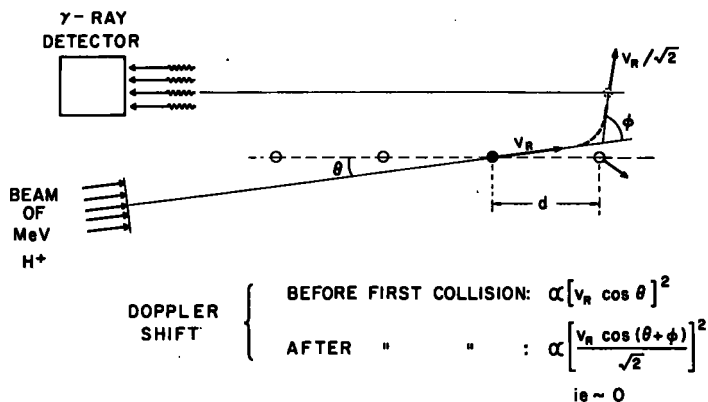


FIG. 6. 8. Schematic representation of the effect of blocking on the direction and magnitude of the recoil velocity  $v_R$ .

Thus, two  $\gamma$ -peaks should be observed, whose relative intensities give directly the mean life-time  $\tau$ . Note that the blocking effect not only extends Doppler-shift measurements to much shorter life-times (i.e. down to  $10^{-14}$ -  $10^{-16}$ s), but also it eliminates the need for  $(-dE/dx)$  data, since the recoil velocity  $v_R$  is essentially constant over the path length  $d$ .

However, as far as we know, no one has yet attempted such a measurement.

### 6.7. Polarized deuteron beams

As a final example of potential channelling applications in nuclear physics, we should like to cite an interesting but rather puzzling experiment by Kaminsky [ 15] on the use of channelling to produce highly polarized deuterium beams.

His experimental arrangement is illustrated in Fig.6.9. A well-collimated beam of 200-keV deuterons is allowed to pass through a thin magnetized nickel crystal parallel to its  $\langle 110 \rangle$  axis. On emerging from the crystal the un-neutralized deuterons are swept away by an electrostatic deflecting field; the neutralized deuterium atoms ( $D^0$ ) then drift a considerable distance (50-100 cm) in a weak magnetic field and eventually strike a tritium (in titanium) target. An array of three solid-state detectors is used to search for anisotropy in the emitted  $\alpha$ -particles from the  ${}^3\text{H}(d,\alpha)$  reaction, and this anisotropy in turn indicates the degree of tensor polarization present in the deuterium beam.

The idea behind the experiment is that the magnetized (nickel) crystal has an excess of, say, spin-up electrons and therefore there is an enhanced probability that the neutralized deuterium will emerge with a spin-up electron. During the subsequent transition from strong to weak magnetic fields, a hyperfine coupling between electron and nuclear spins may then induce some degree of nuclear polarization. The main reason for using a well-channelled deuteron beam is to prevent it from interacting with the innermost (K- and L-shell) electrons; this enhances the probability of

electron capture occurring from the 3d-shell, which of course is the shell that contains the polarized electrons. However, there are also other advantages, such as less multiple scattering (and therefore a much greater transmission to the tritium target) and less radiation damage to the nickel foil.

The result of Kaminsky's first experiment was a very striking one in that he observed the maximum possible degree of tensor polarization, indicating that 100% of the deuterium atoms emerging from the nickel crystal must have captured a spin-up electron. This is a very surprising result. There are 28 electrons in each Ni atom and, when fully magnetized, the number of extra spin-up (or spin-down) electrons is only 0.6 per atom - so that one would normally expect the electron polarization of the emerging deuterium to be no more than 2-3%. Even if channelling restricts electron capture to electrons in the outermost shells (3d and 4s), this still involves 10 electrons and so the maximum electron polarization (on a random-selection basis) would still only be ~6%.

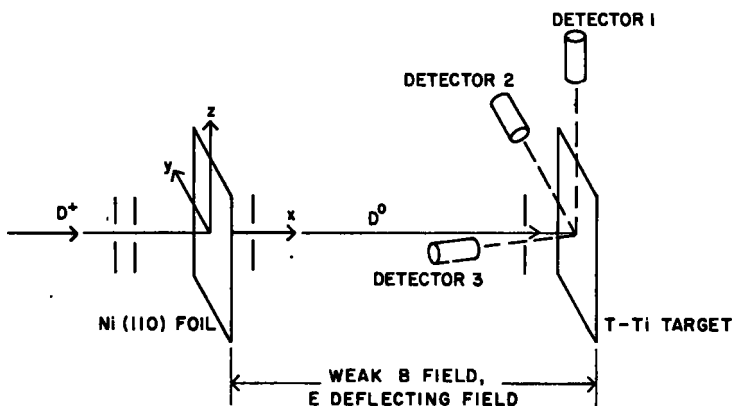


FIG. 6.9. Schematic diagram of Kaminsky's experimental arrangement for producing and analysing a beam of polarized deuterium (from Ref. [15]).

Feldman et al. [16] also has attempted to produce polarized deuterium beams in this manner. His result was somewhat less striking in that it only required ~50% of the emerging deuterium to have captured polarized electrons - but even this figure exceeds the above simple estimates by roughly a factor of ten.

From these unexpectedly large degrees of polarization, it is evident that some rather interesting atomic physics must be involved in the electron-exchange processes that occur within a magnetized crystal. Further investigations of this polarization effect may therefore be of value not only as a potential method of producing polarized nuclear particles, but also as a technique for studying the nature of atomic-collision processes in crystals.

## SUMMARY

This concludes a rather sketchy account of channelling applications in crystallography and nuclear physics. In these areas, channelling has not yet attracted such widespread attention as it has in the solid-state field (sections 4 and 5), and, indeed, many of the examples discussed here have not yet been fully exploited.

## REFERENCES TO SECTION 6

- [1] ANDERSEN, J.U., DAVIES, J.A., NIELSEN, K.O., ANDERSEN, S.L., Nucl. Instrum. Meth. 38 (1965) 210.
- [2] BØGH, E., Interaction of Radiation with Solids, (BISHAY, A., Ed.), Plenum Press, New York (1967) 361.
- [3] MARSDEN, D.A., JOHANSSON, N.G.E., BELLAVANCE, G.R., Nucl. Instrum. Meth. 70 (1969) 291.
- [4] BARRETT, C.S., BARRETT, M.A., MUELLER, R.M., WHITE, W., J. appl. Phys. 41 (1970) 2727.
- [5] GIBSON, W.M., NIELSEN, K.O., Physics and Chemistry of Fission (Proc. 2nd Int. Symp., Vienna), IAEA, Vienna (1969) 861.
- [6] GEMMELL, D.S., HOLLAND, R.E., Phys. Rev. Letts 14 (1965) 945.
- [7] LINDHARD, J., Kgl. Danske Videnskab Selskab, Mat. fys. Medd. 34 14 (1965).
- [8] TULINOV, A.F., Sov. Phys. Doklady 10 (1965) 463.
- [9] BROWN, F., MARSDEN, D.A., WERNER, R.D., Phys. Rev. Letts 20 (1968) 1449.
- [10] TREACY, P.B., Austr. J. of Sci. 22 (1960) 334.
- [11] MARUYAMA, M., TSUKADA, K., OZAWA, K., FUJIMOTO, F., KOMAKI, K., MANNAMI, M., SAKURAI, T., Nuclear Physics A145 (1970) 581.
- [12] CLARK, G.J., POATE, J.M., FUSCHINI, E., MARONI, C., MASSA, I.G., UGUZZONI, A., VERONDINI, E., AERE-R6756 (1971).
- [13] GIBSON, W.M., MARUYAMA, M., MINGAY, D.W., SELLSCHOP, J.P.F., TEMMER, G.M., VAN BREE, R., Bull. Am. Phys. Soc. 16 (1971) 557.
- [14] LITHERLAND, A.E., personal communication (1969).
- [15] KAMINSKY, M., Phys. Rev. Letts 23 (1969) 819.
- [16] FELDMAN, L.C., MINGAY, D.W., SELLSCHOP, J.P.F., personal communication (1970).



# STATIC MAGNETIC INTERACTION AND NUCLEAR MAGNETIC MOMENTS

S. OGAZA

Institute of Nuclear Physics,  
Cracow, Poland

## Abstract

STATIC MAGNETIC INTERACTION AND NUCLEAR MAGNETIC MOMENTS.

1. Introduction and definitions; 2. Nuclear magnetic dipole moments; 3. Hyperfine magnetic fields; 4. Conduction electron polarization; 5. Core polarization and localized moments; 6. Rare-earth solutes; 7. The  $d^{10}s^2p^n$  solutes.

## 1. INTRODUCTION AND DEFINITIONS

The subject of this paper is the present state of understanding of the static magnetic interactions and of nuclear magnetic moments. By "static magnetic interaction" we shall understand the interaction between a static magnetic field  $\vec{B}$  and a static magnetic dipole moment of nuclear state  $\vec{\mu}$ . Such an interaction is described by the Hamiltonian

$$\mathcal{H}(M_1) = -\vec{\mu} \cdot \vec{B} = -\mu_z B \quad (1)$$

when the z-axis is chosen to be parallel to  $B$ , and the vector  $\vec{B}$  has the components  $(0, 0, B)$ . Let us dwell for a while on this interaction and its general properties. This Hamiltonian is a special case of the general Hamiltonian describing the interaction between a static multipole moment  $\mathcal{M}(\pi L)$  and an external field  $V(L)$ , which can always be written in the form

$$\mathcal{H}(\pi L) = \sum_{\mu} (-1)^{\mu} \mathcal{M}(\pi L) V_{-\mu}(L) \quad (2)$$

where the  $V_{-\mu}(L)$  are appropriately chosen spherical tensor components used to describe the external field. If this field can be described classically, i. e. if it is produced by macroscopic charge and current distributions, such as currents in electromagnets or, under certain conditions, ions in a crystal lattice, then the matrix elements of the interaction Hamiltonian in the angular momentum representation are given by

$$\begin{aligned} \langle \text{Im}' | \mathcal{H}(\pi L) | \text{Im} \rangle &= \langle \text{Im} | \mathcal{M}_{\mu}(\pi L) | \text{Im}' \rangle V_{-\mu}(L) \\ &= (-1)^{I-m'} \begin{pmatrix} I & L & I \\ -m' & \mu & m \end{pmatrix} \langle I || \mathcal{M}(\pi L) || I \rangle V_{-\mu}(L) \quad (3) \end{aligned}$$

If the Hamiltonian describes an axially symmetric interaction, it is diagonal when the symmetry axis is chosen as the quantization axis.

The moment associated with a magnetic multipole quantum can be written in the general form

$$\mathcal{M}(ML, \mu) = \frac{-(2L+1)!}{e q^L (L+1)} \int \vec{j}(\vec{r}) (\vec{r} \times \nabla) [j_L(qr) Y_{L\mu}(\vec{r})] d\tau \quad (4)$$

where  $q$  is the momentum,  $\vec{j}(\vec{r})$  the nuclear current density, and the radial function  $j(qr)$  is a spherical Bessel function of order  $L$ , representing the radial wave-function for a freely propagating quantum. The wavelength of the proton is usually large compared to the nuclear radius and for  $qr \ll 1$  one can employ the Bessel function expansion; in most cases, retaining only the leading term is a good approximation. In this case, the magnetic multipole moment reduces to the simple form

$$\mathcal{M}(ML, \mu) = \frac{-1}{c(L+1)} \int \vec{j}(\vec{r}) (\vec{r} \times \nabla) r^L Y_{L\mu}(\vec{r}) d\tau \quad (5)$$

which is often used as a definition of the magnetic multipole moment.

The internal structure of a nucleon extends over a domain small compared to the size of the nucleus. To a first approximation, we may therefore regard the nucleons as point particles having a charge and a magnetic moment. Neglecting relativistic effects in the nucleon motion, the current density for such point particles is given by

$$\vec{j}(\vec{r}) = \underbrace{\sum_k e(\frac{1}{2} - t_z(k)) \frac{1}{2} (\vec{v}_k \delta(\vec{r} - \vec{r}_k) + \delta(\vec{r} - \vec{r}_k) \vec{v}_k)}_{\text{convection current}} + \underbrace{\frac{e\hbar}{2M} \sum_k g_s(k) \nabla \times \vec{s}_k \delta(\vec{r} - \vec{r}_k)}_{\text{contribution from magnetization}} \quad (6)$$

where  $t_z = +\frac{1}{2}$  for neutrons and  $-\frac{1}{2}$  for protons. The spin  $g$ -factor is

$$g_s = \frac{1}{2} (g_p + g_n) + t_z (g_n - g_p) \quad (7)$$

In Eq. (6) the only parameters are the magnetic moments  $\mu = \frac{1}{2} g_s$ , which are found to be  $\mu_p = 2.79$  n.m.,  $\mu_n = -1.91$  n.m. and differ considerably from the point-particle values satisfying the Dirac equation,  $\mu_p = 1$ ,  $\mu_n = 0$ . In the point-particle approximation, we obtain for the magnetic multipole moment

$$\mathcal{M}(ML, \mu) = \frac{e\hbar}{2Mc} \sum_k (g_s(k) \vec{s}_k + \frac{2}{2L+1} g_l(k) \vec{l}_k \cdot \nabla (r_k^L Y_{L\mu}(\vec{s}_k, \vec{q}_k))) \quad (8)$$

using the identities  $\nabla \times (\nabla \times \vec{r}) r^L Y_{L\mu} = (L+1) \nabla r^L Y_{L\mu}$  and  $\hbar \vec{l} = M(\vec{r} \times \vec{v})$ , where  $g_l = \frac{1}{2} - t_z$  is the orbital  $g$ -factor. Expression (8) still holds with the "true"  $g$ -factors as long as they are constant for individual nucleons.

The magnetic multipole moment is an irreducible tensor of rank  $l$ . Its parity  $\pi = (-1)^{L+1}$ , and, consequently, a nuclear state can have only odd static magnetic multipole moments, which are defined as the expectation values of the multipole operator for the state  $m = I$ :

$$\mu(L) = \sqrt{\frac{4\pi}{2L+1}} \langle II | \mathcal{M}(ML) | II \rangle \quad (9)$$

The most important static magnetic moment of nuclear states is the dipole moment, usually simply referred to as the nuclear magnetic moment. It is defined as

$$\vec{\mu} = \sqrt{\frac{4\pi}{3}} \langle II | \mathcal{M}_0(M1) | II \rangle = \sqrt{\frac{4\pi}{3}} \begin{pmatrix} I & 1 & I \\ -I & 0 & I \end{pmatrix} \langle I | \mathcal{M}(M1) | I \rangle \quad (10)$$

The operator of the static magnetic dipole moment is a vector operator and is often written as

$$\vec{\mu} = g\mu_n \vec{I} \quad (11)$$

The relation between the magnetic dipole moment operator and the vector  $\vec{\mu}$  has the form

$$\mathcal{M}(M1, \mu) = \sqrt{\frac{3}{4\pi}} \frac{e\hbar}{2Mc} \mu_\mu \quad (12)$$

where  $\mu_\mu$  denotes the spherical components of  $\vec{\mu}$ . Thus a definition equivalent to definition (10) is

$$\mu = \langle II | \mu_z | II \rangle \quad (13)$$

The matrix elements of the static magnetic interaction (3) can also be written as

$$\langle Im' | \mathcal{M}(M1) | Im \rangle = -\sqrt{\frac{4\pi}{3}} B(-1)^{I-m'} \begin{pmatrix} I & 1 & I \\ -m' & 0 & m \end{pmatrix} \langle I | \mathcal{M}(M1) | I \rangle \quad (14)$$

and we see that the interaction matrix is a diagonal one. Thus the energy eigenvalues are given by the well-known expression (in terms of the nuclear g-factor)

$$E(m) = \langle Im | \mathcal{M}(M1) | Im \rangle = -gB\mu_n m \quad (15)$$

A nuclear state of angular momentum  $I$  splits into  $2I+1$  equally spaced magnetic sub-levels under the influence of the discussed static magnetic interaction. A direct measurement of this energy splitting makes it possible to extract values of the static magnetic moment for known fields, or to study the fields acting on the nucleus with a known magnetic moment. As an illustration of the magnitude of the energy splitting, let us take a field of 20 kGauss and a nuclear  $g$ -factor of 1. For such a case we obtain

$$|\Delta E| = |E(m) - E(m-1)| \approx 6 \times 10^{-8} \text{ eV}$$

or, introducing the Larmor frequency,

$$\omega = \frac{E(m) - E(m-1)}{\hbar} = -gB\mu_n/\hbar$$

we obtain  $\omega$  of the order of  $10^8 \text{ s}^{-1}$ .

The static magnetic interaction, as a product of two factors, e. g. the nuclear magnetic dipole moment and the magnetic field acting on the nucleus, is a very large subject to review, so that I am forced to select certain problems. We shall limit our review to a discussion of the present understanding of the nuclear magnetism, e. g. the structure of the magnetic dipole operator and of the nuclear wave-functions, and to the problems of hyperfine fields acting on the nucleus and produced by its surroundings.

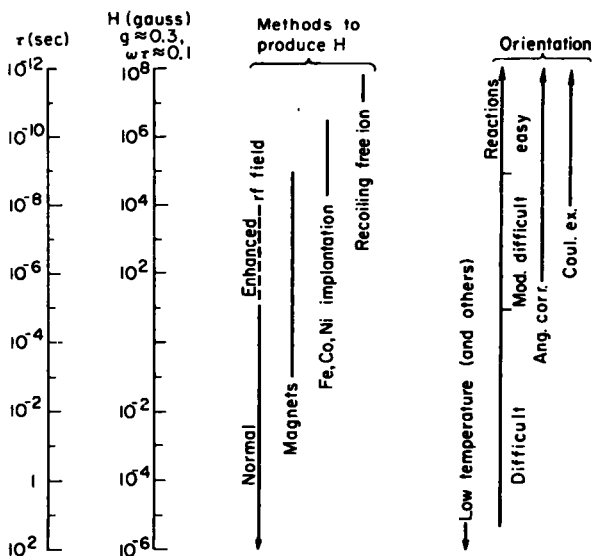


FIG. 1. Illustration of the applicability of different experimental techniques for magnetic-moment determinations.

This choice was guided by the fact that perturbed angular correlations or distributions, which are one of the main subjects of these Proceedings, turned out to be a very powerful method, with further perspectives for success, for the study of these problems. As an illustration of the limitations chosen Fig. 1 may serve, where the first two lines indicate the magnetic field necessary to cause an easily observable perturbation (that is for  $\omega\tau = 0, 1$ ) in nuclear states having a  $g$ -factor of 0.3 (an often observed value) and various mean life-times  $\tau$ . The second group of lines indicates the methods of producing the necessary fields. Radio-frequency fields (used in NMR measurements) are suitable for life-times of about  $10^{-5}$  s, and extend to about 10 ns when use is made of hyperfine enhancement of the fields in ferromagnetic materials. Conventional magnets can be used to perturb states down to about 1 ns, and for still shorter life-times two techniques are used: the static hyperfine fields in ferromagnetic materials, and transient magnetic fields present in highly excited free ions. The third group of lines contains information about producing oriented nuclei essential to angular correlation or distribution experiments. In nuclear reactions, the main problem is the preservation of orientation for times comparable to the nuclear life-time. This is easy only for life-times shorter than about 1 ns, and moderately difficult for times up to  $1 \mu\text{s}$ . Angular correlations with radioactive sources and Coulomb excitation are methods very similar to nuclear reactions for orienting nuclei, but random coincidences and vanishing excitation probabilities set the limits for these methods.

The most attractive region for angular correlation and distribution experiments is thus from about 10 psec to  $1 \mu\text{sec}$ , and the large number of nuclear states with lifetimes in this range, makes these methods so powerful and promising to study both the nuclear magnetism and the hyperfine fields.

## 2. NUCLEAR MAGNETIC DIPOLE MOMENTS

Most theories of magnetic moments start from the single-particle model, where

$$\vec{\mu} = g_l \vec{l} + g_s \vec{s} = g_l \vec{j} + (g_s - g_l) \vec{s}$$

with  $g_l = 1$  (0) and  $g_s = 5.58$  (-3.82) for proton (neutron), represents the dipole moment of a point nucleon moving in a static binding field. For a nucleon in a shell-model orbit the expectation value of this operator may be evaluated in the vector model. Using the general expression for the expectation values of vector operators

$$\langle jm | v_z | jm \rangle = \frac{m}{j(j+1)} \langle jm | \vec{v} \cdot \vec{j} | jm \rangle \quad (16)$$

we obtain the well-known Schmidt values

$$\begin{aligned} \mu_{sp} &= \frac{\langle \vec{\mu} \cdot \vec{j} \rangle}{j(j+1)} j = \frac{1}{j+1} \left\{ g_l j(j+1) + (g_s - g_l) \langle \vec{s} \cdot \vec{j} \rangle \right\} \\ &= j \left\{ g_l \pm (g_s - g_l) \frac{1}{2j+1} \right\} \text{ for } j = l \pm \frac{1}{2} \end{aligned} \quad (17)$$

where the quantity  $\langle \vec{s} \cdot \vec{j} \rangle$  has been evaluated by squaring the identity  $\vec{j} - \vec{s} = \vec{l}$ . This expression is valid for single-particle and for single-hole configurations, as the operators  $\vec{l}$  and  $\vec{s}$  are even under particle-hole conjugation.

Expressions (15) and (17) are expected, however, to be modified, owing to nucleonic interactions which influence the intrinsic structure of nucleons in nuclei, and their velocity dependence gives rise to additional terms in expression (15). The smallness of the kinetic energies of nucleons in nuclei compared with the excitation energy of nucleons may suggest, however, that the interaction terms in the magnetic moment may be treated as corrections to the predominant one-particle moment (for a more detailed discussion see Ref. [1]).

An estimate of additional terms in the nuclear-current operator (thus also modifications to the magnetic-moment operator) involves an analysis of the mesonic currents associated with the interactions in nuclei. An interesting specific effect, which was studied more or less tentatively by several authors [2], is a possibility of reducing the anomalous nucleonic moments caused by the presence of neighbouring nucleons, which inhibit certain meson emission and absorption processes. Recently, Chemtob [3] using the meson-theoretical approach in the one-meson exchange approximation, performed numerical calculations of the interaction moments for odd-mass nuclei with closed shells in the  $jj$ -coupling sense  $\pm$  one nucleon. A comparison of experimental magnetic moments for this group of nuclei with Chemtob's theoretical predictions is shown in Fig. 2. The absolute values

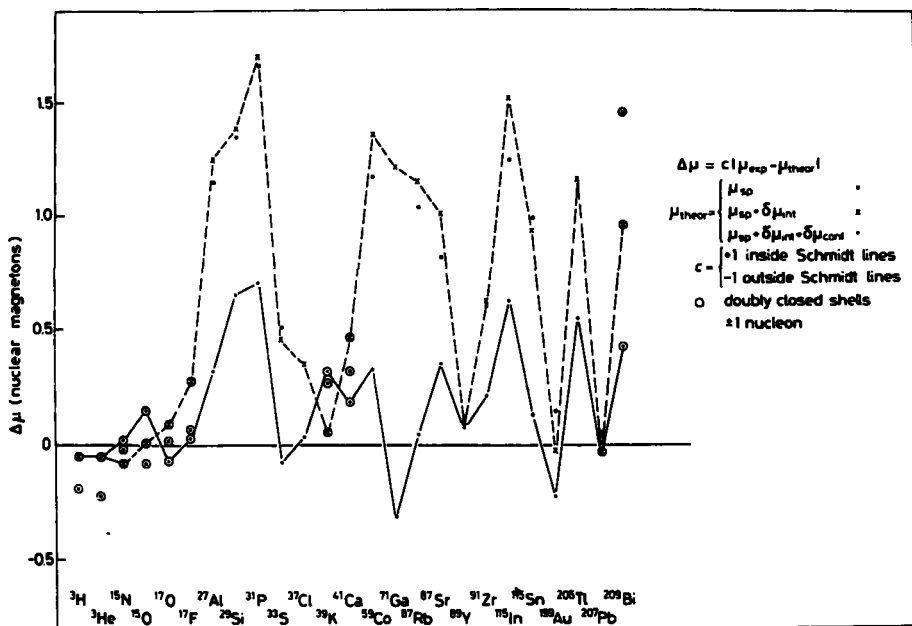


FIG. 2. Deviations of theoretical predictions on magnetic moments of odd-mass nuclei with  $jj$ -closed shells  $\pm$  one nucleon from experimental values. The sign of the deviations is chosen to be positive if experimental magnetic moments are between the Schmidt lines, negative for excess moments.

of the differences between the experimental and theoretical magnetic moments are shown in this figure, but they are given a positive sign for experimental moments lying between the Schmidt lines, and a negative sign for excess moments. It can immediately be seen that the interaction moments are not the predominant correction needed to explain the experimental data. This correction essentially causes a small shift of both Schmidt lines, upwards for odd-proton and downwards for odd-neutron nuclei. The satisfactory features are the explanation of the excess moments of  $^3\text{H}$  and  $^3\text{He}$  and the very small correction for  $^{207}\text{Pb}$  (-0.07 n. m.) compared with the much larger (although not sufficient) one for  $^{209}\text{Bi}$  (0.50 n. m.), both going in the right direction.

Although for the lightest nuclei ( $A \leq 17$ ) the agreement between experiment and theory is fairly good (the agreement for the  $^{16}\text{O}$  region may be fortuitous, as significant configuration mixings are suggested there), the large deviations for heavier nuclei must be explained by other effects. The large difference between the light and heavy nuclei makes it unlikely that we are dealing with a modification of the intrinsic properties of nucleons. The observed trend of the deviations finds, however, a simple explanation in terms of a polarization effect of the closed shells, due to forces exerted by the valence nucleon on the rest of the system. The polarization effect on magnetic moments depends decisively on the configuration of the closed shells since the main effect is associated with the presence of unsaturated spins in the closed shells, which can be partially aligned by interaction with the spin of the valence nucleon.

In the treatment of the spin polarization different equivalent methods can be used (see Ref. [4]). One can use an average spin-dependent field in which the particles in the closed shells move, a method similar to that applied in the treatment of the quadrupole polarizability of nuclei. One can calculate the spin polarization effect in terms of a coupling of the valence particle to the collective spin-mode characterized by the quantum numbers  $\lambda = 1$ ,  $\sigma = 1$ ,  $\tau = 1$ ,  $\pi = +$ , which might appear at about 5-7 MeV; this method is an extension of the treatment of electric-dipole polarization. Finally, one can use the more conventional language of configuration mixing, in which we speak of the admixture of configurations with particle-hole excitations coupled with the valence-nucleon mode characterized by the wavefunction

$$|j\rangle = |(\text{closed shell}) j\rangle + \sum_{i,k} c_{ik} |[(j_i^{-1} j_k) J, j] I = j\rangle \quad (18)$$

where the important restriction on the quantum numbers is that  $j_i$  and  $j_k$  are spin-orbit partners, e. g.  $j_i = \ell + \frac{1}{2}$ ,  $j_k = \ell - \frac{1}{2}$ .

The effect of the spin polarization on magnetic moments depends on the form of the residual interaction. The main effect is expected to come from a simple spin-exchange force of the type  $V_{\sigma\tau}(r_{12})(\vec{\sigma}_1 \cdot \vec{\sigma}_2)(\vec{\tau}_1 \cdot \vec{\tau}_2)$ , in which case the magnetic moment operator takes the simple form

$$\vec{\mu} = g_p \vec{j} + (g_s - g_p) \vec{s}(1 + \alpha) = g_p \vec{j} + (g_s^{\text{eff}} - g_p) \vec{s} \quad (19)$$

where  $\alpha$  is the spin polarizability ( $\alpha < 0$ ). A rough estimate of  $\alpha$  in first-order perturbation theory can easily be made:

$$\begin{aligned} \alpha^{(1)} &= 2 \sum_{i,k} c_{ik} \langle j_i^{-1} j_k | \sigma_z | 0 \rangle = - \frac{8V_{\sigma\tau}}{\Delta \epsilon_{\ell s}} \sum_{i,k} \langle j_i^{-1} j_k | s_z | 0 \rangle^2 \\ &= - \frac{8V_{\sigma\tau}}{6\Delta \epsilon_{\ell s}} \sum_k (2j_k + 1) \frac{2j_k - 1}{2j_k} \end{aligned} \quad (20)$$

For  $^{208}\text{Pb}$ , for example, the closed shells of the  $h_{11/2}$  protons and  $i_{13/2}$  neutrons can contribute to the effect, thus with  $V_{\sigma\tau} \approx 25/A$  MeV and  $\Delta \epsilon_{\ell s} \approx 5$  MeV we obtain

$$\alpha^{(1)} = \frac{-8 \cdot 25}{6 \cdot 208 \cdot 5} (12 + 14) \approx -0.8$$

This rough estimate indicates that  $g_s$  changes by the amount of its own value.

It is clear that in such a situation the first-order perturbation effect is not adequate and higher-order terms must be considered, e. g. the total polarizability is not only the effect of the last particle, but also of the particles in the closed shells acting back on the closed shells themselves. The total polarizability can, however, be expressed in terms of the first-order polarizability as (see Ref. [4]):

$$\alpha = \frac{\alpha^{(1)}}{1 - \alpha^{(1)}} \quad (21)$$

For the  $^{208}\text{Pb}$  core we obtain  $\alpha \approx -0.45$  and  $g_s^{\text{eff}} \approx 0.6 g_s$ .

Although the force considered produces the predominant part of the effect, the polarization effect, nevertheless, cannot be described simply in terms of a renormalized  $g_s$  factor, and the complete spin dependence of the actual interaction has to be considered in order to make quantitative estimates. Several attempts in this direction have been made with the use of realistic nucleon-nucleon interactions [5, 6]. Results of calculations with the Kallio-Kolltveit and the Hamada-Johnston interactions [6] are shown also in Fig. 2. With the exception of nuclei with the  $^{16}\text{O}$  and  $^{40}\text{Ca}$  cores (the only ones closed in the L-S sense), where only higher-order effects can contribute, the calculations are made in first-order perturbation theory. Second-order contributions for  $^{29}\text{Si}$  and  $^{209}\text{Bi}$  deteriorate the agreement between theory and experiment. This is not disturbing for  $^{29}\text{Si}$ , as it is a deformed nucleus and should be treated rather within the Hartree-Fock framework with a deformed basis, but  $^{209}\text{Bi}$  remains an unsolved problem. Although an overall improvement in the comparison of experimental and theoretical results on the magnetic moments is noted, an enormous amount of work has still to be done in order to test the ideas and reach a quantitative agreement.

Going away from closed shells, the problem of calculating magnetic moments of bound nuclear states becomes more complex and difficult, as we enter all the open problems of describing the state of a many-particle system with many degrees of freedom. Although the proper wave-function is the crucial point in calculating nuclear magnetic moments, the broad scope of the problem and the restricted space of this paper do not allow us to go into details. Instead of trying to make a very incomplete review of the open questions in nuclear-structure theory and of the recent attempts towards better understanding of nuclear structure and forces, let us draw some conclusions about the agreement of experimental data and theoretical predictions on nuclear moments.

We do not have "good" wave-functions for few particle configurations, and the various attempts to describe collective states in spherical and transition nuclei have met with moderate success in reproducing the experimental magnetic moments.

In the recent years, the most significant advances in experimental information on magnetic properties of nuclei have been made in determining the  $g$ -factors of  $2^+$  states throughout a wide range of nuclei ( $56 \leq A \leq 208$ ) which show a surprisingly narrow distribution of values between about 0.25 and 0.45, implying a common character of these states in deformed and nondeformed nuclei. Figure 3 shows, for example, experimental  $g$ -factors of the first  $2^+$  states in the region Ge-Te, together with some theoretical predictions. Calculations based on the description of these states in terms of harmonic quadrupole vibrations about the spherical equilibrium shape by means of random-phase approximation (Kisslinger

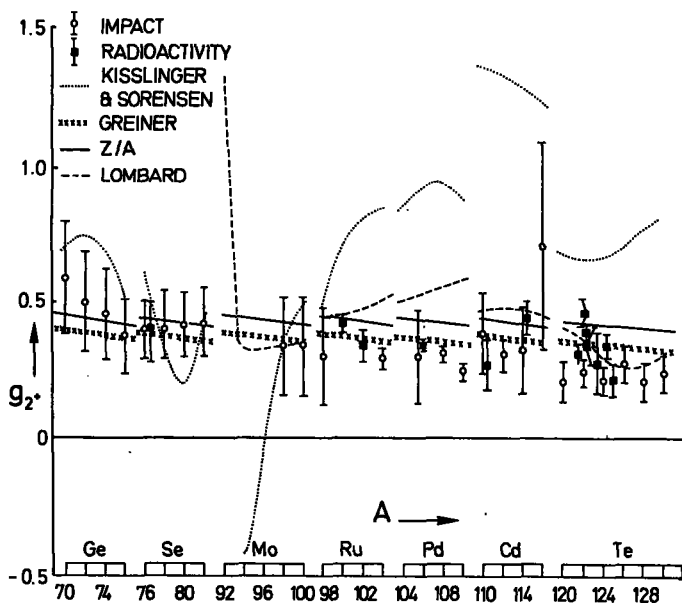


FIG. 3. Comparison of experimental and theoretical  $g$ -factors for the first  $2^+$  states for isotopes of Ge, Se, Mo, Ru, Pd, Cd, and Te.

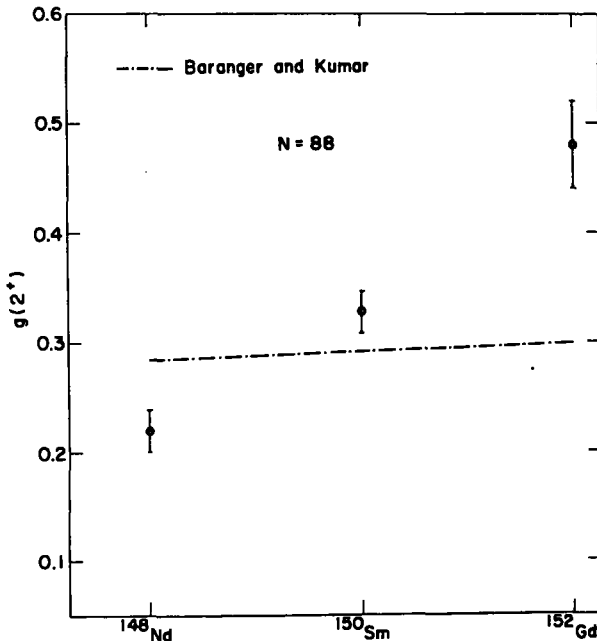


FIG. 4.  $g$ -factors of the first  $2^+$  states for the  $N = 88$  isotopes.

and Sorensen, Lombard) have yielded substantial fluctuations in  $g$ -factors because of large admixtures of two-particle configurations. The phenomenological model of Greiner [7] based on the assumption of a distribution of the protons more spherical than that of the neutrons because of the difference in the pairing interaction, gives, in the region shown, reasonable agreement with experiment. This is not so surprising as the inclusion of pairing results essentially only in a lowering of the collective  $g$ -factors compared to the classical hydrodynamical value  $Z/A$ . The low values of  $g(2^+)$  in the Te-isotopes and the high values for the Hg-isotopes are, however, beyond the scope of Greiner's model.

A different approach was made by Baranger and Kumar [8], who describe the nuclear motion as completely collective, but use a microscopic theory of the collective parameters utilizing pairing plus quadrupole forces in their calculations. Their unified model applied to nuclei from barium to lead predicts nearly constant values of the  $g$ -factors for the first  $2^+$  states in fair accord with experiment, a sharp decrease in  $g$ -values for the mercury isotopes when approaching the double magic  $^{208}\text{Pb}$ , and an increase of the  $g$ -values in Nd and Sm isotopes when approaching the  $N = 82$  closed shell. Experimentally, no drop in the  $g$ -values for the mercury isotopes was found, and in the Nd-Sm isotopes a sharp decrease is observed instead of the predicted rise. Another failure of the Baranger-Kumar predictions is found in the  $N = 88$  nuclei (Fig.4), where they predict a nearly constant value of the  $g$ -factor but experimentally we find a very marked variation.

A somewhat clearer and more satisfactory situation exists for the deformed nuclei, for which the wave-functions used describe rather well most of the observed features for low excited states. The magnetic moments for these nuclei have additional contributions arising from the collective rotations, and have the form

$$\mu = g_R I + (g_K - g_R) \frac{K^2}{I+1} [1 + (-1)^{I+\frac{1}{2}} (2I+1)b_0 \delta_{K, \frac{1}{2}}] \quad (22)$$

where  $g_R$  is the rotational  $g$ -factor and  $b_0$  (entering only for  $K = \frac{1}{2}$  states) is a decoupling parameter.

The rotational  $g$ -factors for the ground state rotational bands were calculated by Prior, Nilsson and Boehm [9], who started from the cranking formula and used Nilsson's wave-functions with inclusion of pairing correlations. The cranking-model expression for  $g_R$  is

$$g_R = \frac{\mathcal{F}_p}{\mathcal{F}_p + \mathcal{F}_n} + (g_S^p - 1) \frac{W_p}{\mathcal{F}_p + \mathcal{F}_n} + g_S^n \frac{W_n}{\mathcal{F}_p + \mathcal{F}_n} \quad (23)$$

where

$$\mathcal{F} = 2\hbar^2 \sum_{\mu, \nu} \frac{\langle \mu | j_x | \nu \rangle^2}{E_\mu + E_\nu} (U_\nu V_\mu - U_\mu V_\nu)^2 \quad (24)$$

$$W = 2\hbar^2 \sum_{\mu, \nu} \frac{\langle \mu | j_x | \nu \rangle \langle \nu | s_x | \mu \rangle}{E_\mu + E_\nu} (U_\nu V_\mu - U_\mu V_\nu)^2$$

for the even-even nuclei. These expressions are modified for the odd-A nuclei by excluding in the sums terms with  $\mu = \alpha$ , where  $\alpha$  is the state occupied by the odd nucleon, and by adding one-quasi-particle transition terms

$$2\hbar^2 \sum_{\nu \neq \alpha} \frac{\langle \nu | j_x | \alpha \rangle^2}{E_\nu - E_\alpha} (U_\nu U_\alpha + V_\nu V_\alpha)^2 \text{ to } \mathcal{F}, \text{ and}$$

$$2\hbar^2 \sum_{\nu \neq \alpha} \frac{\langle \nu | j_x | \alpha \rangle \langle \alpha | j_x | \nu \rangle}{E_\nu - E_\alpha} (U_\nu U_\alpha + V_\nu V_\alpha)^2 \text{ to } W$$

A comparison of experimental and theoretical results for  $g_R$  is shown in Figs 5 and 6, where the shown theoretical values correspond to the pairing parameters  $G_p = 23.5/A$  MeV and  $G_n = 18/A$  MeV, obtained from the best fit to the odd-even mass differences. As is easy to see, the general agreement is reasonably good, and one is even tempted to extract the pairing parameters from rotational  $g$ -factors instead from the odd-even mass difference. There are, however, still some experimental problems, as different methods yielded different results in the Sm, Gd, and Yb isotopes.

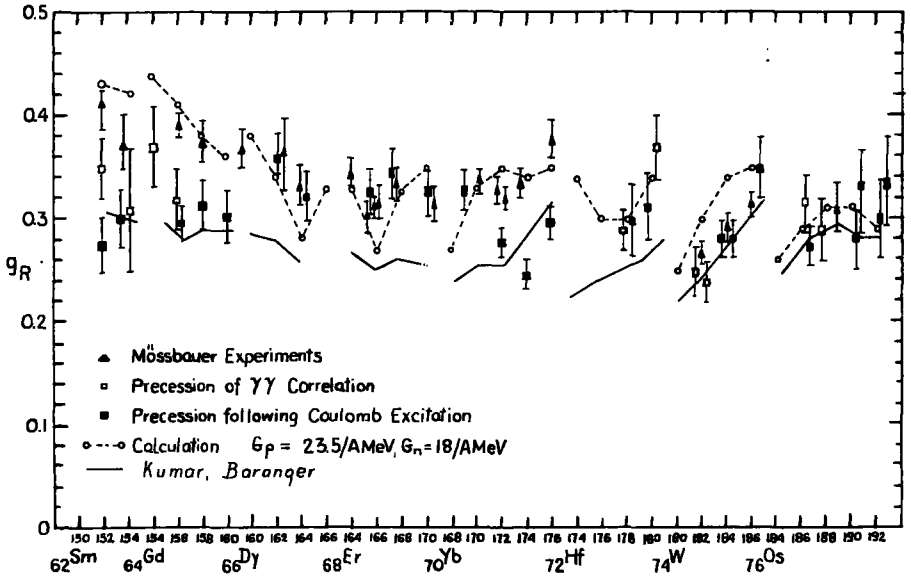


FIG. 5. Comparison of experimental and theoretical values of  $g_R$  for  $2^+$  states of deformed nuclei. Dashed lines are the theoretical predictions of Prior et al. [9] with the pairing parameters indicated. The solid lines are the predictions of Baranger and Kumar [8].

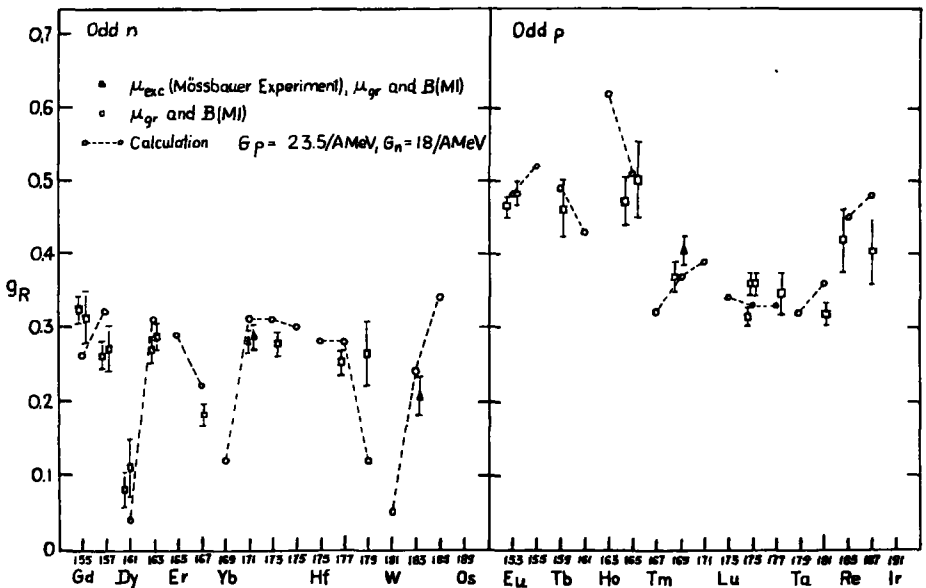


FIG. 6. The derived rotational  $g_R$ -factors for odd-mass deformed nuclei. The dashed lines are the predictions of Prior et al. [9].

The intrinsic gyromagnetic factors  $g_K$  are given by the formula

$$g_K K = g_l K + (g_s - g_l) \langle K | s_z | K \rangle \quad (25)$$

and can be calculated for the Nilsson wave-functions. A systematic deviation of the Nilsson estimates with  $g_s^{\text{free}}$  can, to a very large extent, be explained by a spin-polarization effect. A comparison of the experimental effective  $g_s$ -factors with theoretical estimates, derived with the simple spin-exchange interaction  $V_{\sigma} \vec{\sigma}_1 \cdot \vec{\sigma}_2 \vec{\tau}_1 \cdot \vec{\tau}_2$  [10] is shown in Fig.7. (It may be noted that the same interaction explains quite well the retardation of the Gamov-Teller beta transitions.) It has also been pointed out [11] that the expectation value of the transverse spin component  $\langle s_+ \rangle$  (entering into  $b_0$  and  $B(M1, K \rightarrow K \pm 1)$ ) may be more influenced by the spin polarization than the  $\langle s_0 \rangle$  value, thus in deformed nuclei a difference in the longitudinal and transverse polarization may occur. The presently obtained evidence of these two polarizations is shown in Table I.

A general conclusion that can be obtained from the comparison of experimental and theoretical values of magnetic moments is that we do not yet have a theory which could predict magnetic moments better than to a few tenths of the nuclear magneton. The "phenomenological" as well as the "microscopic" theories are only approximation schemes based on a number of parameters taken from observation. The different approaches result, of course, in a different ability of reproducing magnetic properties of nuclei, but, generally, the more internal parameters are taken

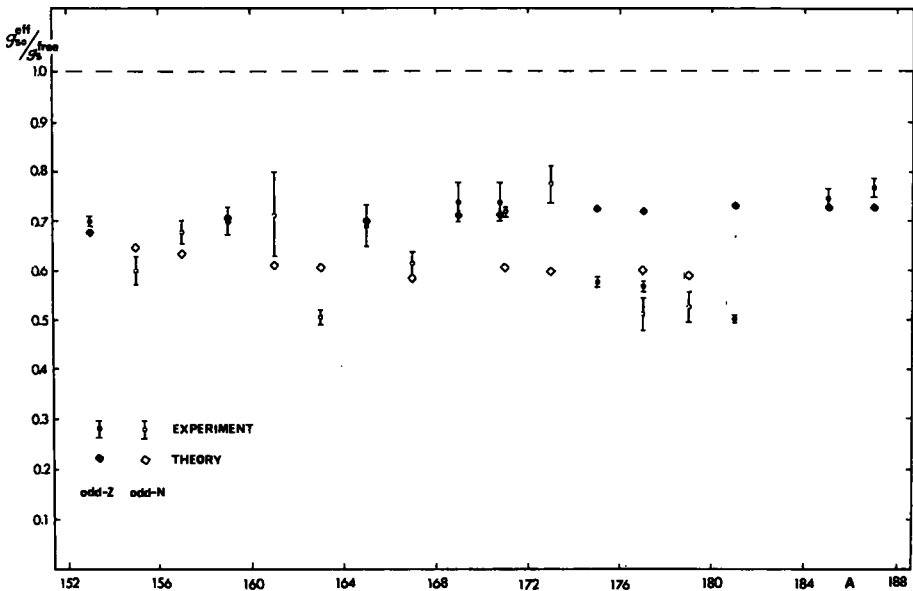


FIG. 7. The effective spin  $g$ -factors,  $g_s^{\text{eff}}$ , for odd-A deformed nuclei reproduced from Ref. [10].

TABLE I. EFFECT OF LONGITUDINAL AND TRANSVERSE SPIN POLARIZATION ON MAGNETIC PROPERTIES OF ODD-MASS DEFORMED NUCLEI

Nucleus	Experimental data	$g_{s_0}^{\text{eff}} / g_s^{\text{free}}$		$g_{s_1}^{\text{eff}} / g_s^{\text{free}}$	
		Experimental	Theoretical	Experimental	Theoretical
$^{153}\text{Eu}$	$g_K([413]5/2) = +0.654(3)$	0.70(1)	0.694	0.64(1)	0.627
	$B(M1, [411]3/2 \rightarrow [413]5/2) = 3.97 \times 10^{-3}$				
$^{169}\text{Tm}$	$g_K([411]1/2) = -1.57(13)$	0.74(4)	0.713	0.52(6)	0.572
	$(g_K - g_R)_{b_0} = +0.316(38)$				
$^{171}\text{Tm}$	$g_K([411]1/2) = -1.28(12)$	0.74(4)	0.710	0.55(9)	0.572
	$(g_K - g_R)_{b_0} = +0.337(71)$				
$^{171}\text{Yb}$	$g_K([521]1/2) = +1.45(2)$	0.72(1)	0.608	0.73(1)	0.546
	$(g_K - g_R)_{b_0} = -0.472(6)$				
$^{183}\text{W}$	$g_K([510]1/2) = -2.27(5)$	0.90(1)	0.651	0.41(1)	0.497
	$(g_K - g_R)_{b_0} = -1.25(3)$				

from observation the better is the agreement with experiment. Nevertheless, the magnetic moments still remain an important and sensitive tool for testing the nuclear coupling schemes and for pinning down the main components of the nuclear wave-function.

We have tried to point out some of the open problems in the theory of nuclear magnetism, the most important of which is the proper description of the structure of the nuclear states. Although the experimentalists are, at present, in the lead in investigating magnetic properties of nuclei, nevertheless, a further effort in obtaining accurate and reliable data is needed, particularly for states whose structure is understood, by now. New valuable information on magnetic moments can be expected and obtained for short-lived excited nuclear states; to determine them, high magnetic fields of the order of  $10^5 - 10^6$  G, e.g. hyperfine fields are needed.

### 3. HYPERFINE MAGNETIC FIELDS

The subject of hyperfine magnetic fields and the methods applied for their investigation are a very wide field, and we shall not give a complete review of this field. We shall therefore limit our presentation to hyperfine fields occurring in the case of nuclei embedded as solutes in ferromagnetic lattices. Such solutes are produced as alloys, by diffusion, and by implantation of radioactive nuclei by means of magnetic isotope separators, or by recoil implantation in nuclear reaction and Coulomb excitation processes. Solute fields are of considerable interest because they can be used to study the particular interactions that give rise to hyperfine fields, and they have also practical importance as they provide magnetic fields of about  $10^4$  to  $10^6$  G at solute nuclei.

Before entering the discussion of the different effects that contribute to the solute hyperfine fields, it is necessary to define the term "hyperfine field", as there is some confusion in the literature about hyperfine, internal, and effective fields.

In a ferromagnet a nucleus ranging over a certain domain may experience an effective field

$$H_{\text{eff}} = H_0 + H_{\text{hf}}^{\text{C}} + H_{\text{L}} - DM \quad (26)$$

where  $H_0$  is the applied external field,  $H_{\text{hf}}^{\text{C}}$  the corrected hyperfine field,  $D$  is the demagnetization factor and  $H_{\text{L}}$  is the Lorentz field,  $4/3\pi M$ , plus the field arising from dipoles in the Lorentz cavity. As  $H_{\text{hf}}^{\text{C}}$  and  $H_{\text{L}}$  are essentially co-linear, the sum  $H_{\text{hf}}^{\text{C}} + H_{\text{L}}$  is usually called the hyperfine or internal field. The name "hyperfine" implies that this field arises from the hyperfine structure of an atom. In fact, a hyperfine field can be observed only under a special set of conditions affecting the hyperfine structure, and, in general, these conditions have to be specified in order to make the name "hyperfine field" meaningful.

For a free atom, the spin Hamiltonian is

$$\mathcal{H} = \gamma_I \vec{H}_0 \cdot \vec{I} - \gamma_N \vec{H}_0 \cdot \vec{I} + A \vec{J} \cdot \vec{I} \quad (27)$$

where  $\gamma_J$  is the Landé  $g$ -factor times the Bohr magneton,  $\gamma_I$  the nuclear  $g$ -factors times the nuclear magneton, and  $A$  the hfs constant. For  $H_0 = 0$ , the spins  $I$ ,  $J$ , and  $F$  are good quantum numbers, but not  $M_I$ , and no hyperfine field exists. For large  $H_0$ ,  $M_I$  and  $M_J$  become good quantum numbers, and the effective spin Hamiltonian may be approximated by

$$\mathcal{H} = \gamma_J H_0 J_z - \gamma_I H_0 I_z + A J_z I_z \quad (28)$$

The system is then resolved into  $(2J + 1)$  manifolds of  $(2I + 1)$  states, and within each manifold,  $M_I$  is a good quantum number, the nuclear states have relative energies  $-\gamma_I H_{\text{eff}} M_I$ , and the hyperfine field may be defined as

$$H_{\text{hf}} = H_{\text{eff}} - H_0 = -\frac{A}{\gamma_I} M_J \quad (29)$$

This definition is only accurate to first order as terms of the order  $(A/\gamma_I H_0)^2$  are omitted. For the free atom case, the system is isotropic, for every  $M_J$  one has a unique  $H_{\text{hf}}$ , and  $H_0$ ,  $H_{\text{eff}}$ , and  $H_{\text{hf}}$  are collinear.

In the case of a weak crystal field, the free-ion approximation may sometimes be still valid, as, for example, in the case of rare earths, where the spin-orbit coupling is large compared to the crystal field, but this approximation is not applicable in general. For each crystal-field multiplet, however, we may use the anisotropic spin Hamiltonian

$$\mathcal{H} = -\sum \gamma_i H_i S_i^z - \gamma_I \vec{H}_0 \cdot \vec{I} + \sum A_i S_i^z I_i \quad (30)$$

with the effective spin  $\vec{S}^z$  of the electronic multiplet. In the high-field limit, each crystal-field level is resolved into  $(2S + 1)$  manifolds of  $(2I + 1)$  states and within each manifold

$$\vec{H}_{\text{eff}} = \vec{H}_0 + \vec{H}_{\text{hf}} \quad (31)$$

and

$$|\vec{H}_{\text{hf}}^z| = \frac{A_f}{\gamma_I} M_S \quad (32)$$

can be defined with the effective external field  $H_0$  and effective hfs constant  $A_f$ . The similarity of the definition for the two cases is superficial, and none of the three features of the free-ion case may be valid for the weak-crystal field. Therefore, if we speak of a hyperfine field, we have to specify carefully the conditions under which it is observed.

In a ferromagnet, the spin-spin exchange "field" takes the role of the external field. In the weak-crystal case, if the spin-orbit coupling is large compared to the exchange and crystal fields, and the exchange energy is

large (or small) compared to the crystal-field energy, then the spin Hamiltonian can be diagonalized in the  $J, M$  (or  $S', M_{S'}$ ) representation. Thus the exchange field orients  $\vec{S}$ , which in turn orients  $\vec{J}$  (or  $\vec{S}'$ ) through spin-orbit coupling, and  $J$  (or  $S'$ ) determines  $H_{hf}$ .

For a solute in a ferromagnetic material, the situation is even more difficult than in the two cases mentioned, for which the wave-functions for the atom or ion, and so the contributions to  $H_{hf}$ , can be worked out rather rigorously. The spin Hamiltonian for the solute may be written in a general form

$$\mathcal{H} = V_{cf} + 2\mu_B \vec{H}_{ex} \cdot \vec{S} + \lambda \vec{L} \cdot \vec{S} - \gamma_I \vec{H}_c \cdot \vec{I} + 2\mu_B \gamma_I \langle r^{-3} \rangle \left\{ \vec{L} \cdot \vec{I} + [\xi L(L+1) - \kappa] \vec{S} \cdot \vec{I} - \frac{3}{2} \xi [(\vec{L} \cdot \vec{S})(\vec{L} \cdot \vec{I}) + (\vec{L} \cdot \vec{I})(\vec{L} \cdot \vec{S})] \right\} \quad (33)$$

This Hamiltonian will only be used to follow the contributions to  $H_{hf}$  and not as a means for exact calculations. It is written in terms of the co-ordinates of the lattice (crystal field potential  $V_{cf}$ , exchange field  $\vec{H}_{ex}$ ) and of the solute ion core ( $\vec{L}$ ,  $\vec{S}$ , and  $\vec{I}$ ). The expectation value  $\langle r^{-3} \rangle$  is evaluated for the open electronic shell (if any) of the solute. Generally, the first three terms must be evaluated first, as they are large and determine the zeroth-order wave-functions for evaluating matrix elements of the other six terms, which are linear in  $\vec{I}$ . The fourth term describes conduction-electron polarization:  $H_c$  is essentially, but not exactly, proportional to the lattice magnetization. The five terms in curly brackets represent the familiar Fermi magnetic hfs interaction in operator notation. The  $\vec{L} \cdot \vec{I}$  term represents orbital magnetism, the  $\vec{S} \cdot \vec{I}$

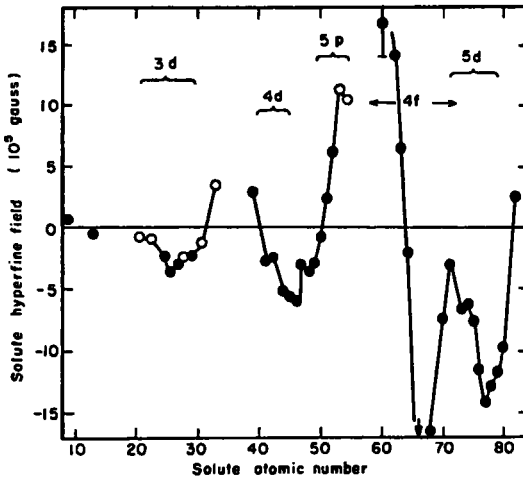


FIG. 8. Solute hyperfine fields in iron lattice, reproduced from the review of Shirley et al. [12].

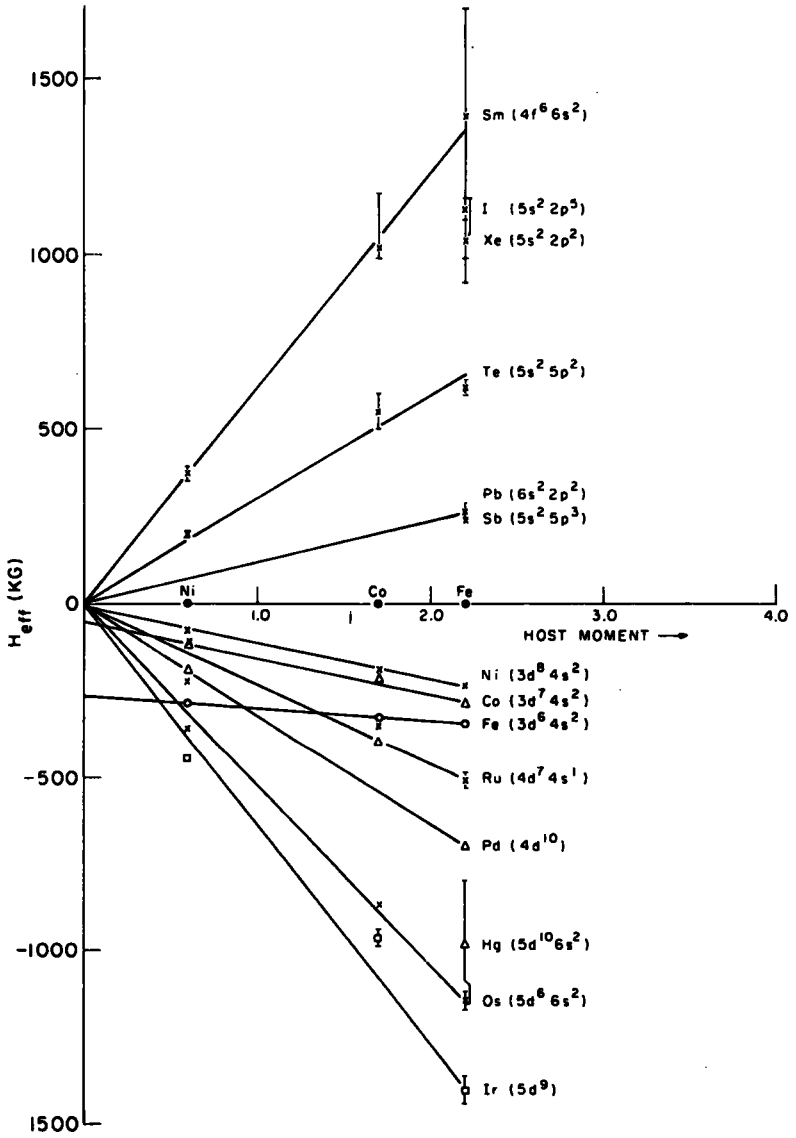


FIG. 9. Dependence of the solute hyperfine fields on the magnetic moment of the ferromagnetic host.

term core polarization, and the three terms in  $\xi$  spin-dipolar-nuclear-dipolar interaction. The complexity of the  $H_{\text{hf}}$  concept for rare earths in ferromagnets arises from the fact, that the spin-orbit term  $\vec{L} \cdot \vec{S}$  is not small compared to the first two terms in the Hamiltonian.

To study the mechanism producing hyperfine fields at the solutes in ferromagnets, it is useful to survey the fields reported in the Fe, Co, and Ni lattices. A review of these fields was made recently in a publication by Shirley, Rosenblum, and Matthias [12] on which we rely strongly in this part of this contribution. The data as collected up to now give strong evidence of the induced nature of the solute fields by several characteristic features:

- i) The solute fields vary rather smoothly with atomic number, as is shown in Fig.8 for the iron host.
- ii) For most of the solutes, the induced field is approximately proportional to the atomic moment of the host lattice as is seen in Fig.9.
- iii) The temperature dependence of the solute fields follows the Curie-Weiss dependence of the spontaneous magnetization of the host, to a first approximation.
- iv) The solute fields are independent of the solute concentration for concentrations less than about one atomic percent [13].

In the following, we shall discuss a few of the hyperfine field mechanisms that are suggested by the iron-host data, but most of the conclusions hold also for Co and Ni hosts, though fewer data for these hosts are available.

#### 4. CONDUCTION ELECTRON POLARIZATION (CEP)

The large negative fields found in the  $d^{10}s$  solutes: Cu(-213 kG), Ag (-282 kG), and Au (-1175 kG), and perhaps also those in the  $d^{10}s^2$  solutes, arise largely from the outer  $s$  electrons via CEP, and for those solutes the term  $-\gamma_1 \vec{H}_c \cdot \vec{I}$  in Eq.(33) dominates. Freeman and Watson [14], using the unrestricted Hartree-Fock method, deduced a negative spin density (relative to the 3d spin polarization) in the 4s orbital of iron in the outer portion of the iron atom. For a "non-magnetic" solute atom in an iron lattice the negative (CE) polarization at the cell boundary is expected to persist across the solute cell. Daniel and Friedel [15] proposed a simple model to relate this polarization to screening by conduction electrons, in which the difference between  $s$ -wave phase shifts at the solute in the "spin-up" and "spin-down" half-bands was found to produce a net negative spin polarization and a negative hyperfine field at the solute nucleus. The conduction-band  $s$ -wave states resemble atomic functions near the solute nucleus. The hyperfine field that they produce may therefore be derived from the field  $H_{\text{ns}}$  that can arise from a free-atom atomic  $ns$  state; thus the induced CEP field may be written as

$$H_{\text{CEP}} = p H_{\text{ns}} \quad (34)$$

where

$$H_{\text{ns}} = - \frac{a_{\text{ns}}}{2\gamma_1} \quad (35)$$

for the solute, and  $a_{ns}$  can be found in the paramagnetic resonance literature.

It should be noted that  $p$  is, essentially, defined by Eq.(35), and that it absorbs all the host- and solute-dependent factors, which modify  $H_{ns}$ , as the solute is in a host lattice, and not a free atom. In Ref.[12] the values of  $p$  were deduced from observed fields in the  $d^{10}s$  and  $d^{10}s^2$  solutes, and the results may be summarized by a simple and useful empirical relation

$$H_{hf} = 0.027 \mu H_{ns} \quad (36)$$

for solute fields, where  $\mu$  is the host moment in Bohr magnetons. The CEP model, and relation (36) are expected to apply to transition-metal solutes, but would, at best, describe only contributions of the  $s$ -band to  $H_{hf}$ . In fact, Shirley et al. [12] found for transition-series solutes to the left of Mn, Ru, and Os, respectively, a surprisingly good agreement between hyperfine fields estimated from Eq.(36) and the 17 measured values for 12 elements in Fe, Co, and Ni hosts. In the upper part of the  $d$ -groups, however, large deviations from the estimates of Eq.(36) are observed, indicating another contribution to  $H_{hf}$ . The inadequacy of the CEP estimates for these solutes is illustrated in Fig.10, where the estimated and observed fields for the 4d and 5d solutes are shown. This strong contribution to  $H_{hf}$  in those solutes can be explained by a core polarization from localized moments.

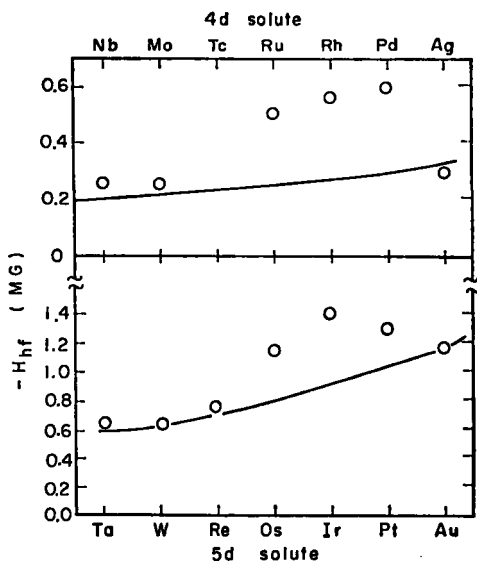


FIG.10. Variation of  $H_{hf}$  with atomic number for 4d and 5d solutes in iron. The solid lines are the CEP estimates of Ref. [12].

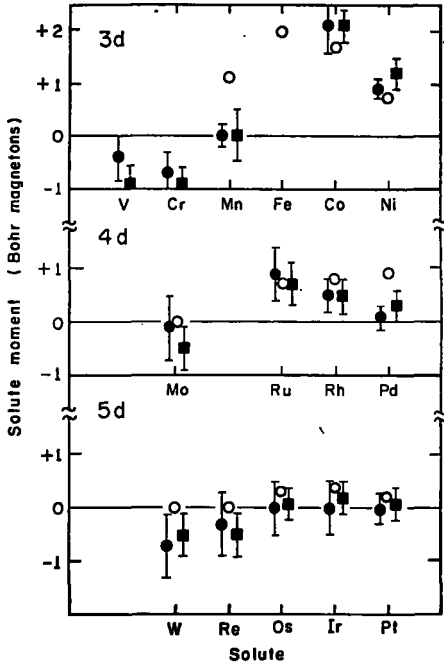


FIG. 11. Derived localized moments for solutes in iron. The open circles are obtained from  $H_{hf}$ , the filled ones from neutron-scattering data.

## 5. CORE POLARIZATION AND LOCALIZED MOMENTS

To describe this mechanism, let us assume that  $V_{cf}$  in Eq.(33) is strong enough to quench the orbital angular momentum of the solute d-shell. This leaves us, in lattices with cubic symmetry, with

$$\mathcal{H} = 2\mu_B \vec{H}_{ex} \cdot \vec{S} - \gamma_1 \vec{H}_c \cdot \vec{I} - 2\mu_B \gamma_1 \langle r^{-3} \rangle \kappa \vec{S} \cdot \vec{I} \quad (37)$$

The exchange field is by far the largest, and we may imagine that it is evaluated first to give  $\langle S_z \rangle$ . Then, we have

$$H_{hf} = p H_s + 2 \langle S_z \rangle H_d \quad (38)$$

where, by definition,  $H_d = \mu_B \kappa \langle r^{-3} \rangle$ , and it is the (core-polarization) hyperfine field arising from one unpaired d electron. For the 4d group, Freeman and Watson have calculated  $H_{4d} = -370$  kG, and from the Knight-shift in platinum  $H_{5d} = -1180$  kG was deduced. Using these values, and comparing observed values of  $H_{hf}$  with Eq.(38), one can derive  $\langle S_z \rangle$  or  $\mu$  — the magnitude of the d-electron spin moment on each solute (the

localized moment). The obtained localized moments are rather tentative, they can easily be corrected if more reliable values for  $H_{nd}$  become available. The obtained localized moments are shown in Fig.11, together with two other sets of values deduced from neutron-scattering data. The conclusion which one can draw from the analysis can be summarized as follows: i) the trends of the localized moments with solute atomic number are in qualitative agreement among the three sets of values and establish localized solute moments in the upper ends of the transition series; ii) the agreement within each of the three sets of values of  $\mu$  is reasonable, iii) a disturbing disagreement exists between neutron and  $H_{hf}$  values of  $\mu$  for Mn, and a different trend for the 4d solutes Ru, Pd is evident. Freeman emphasized this point at the Asilomar Conference on Hyperfine Interactions (1967), indicating that the two methods involved measure two rather different quantities, the spin density at the solute nucleus and a magnetic disturbance near the solute atom, thus the results do not have to be identical.

## 6. RARE-EARTH SOLUTES

A still different mechanism is responsible for the hyperfine fields at rare-earth solutes in ferromagnets. Their 4f shell is shielded from the crystal field by the external electrons, thus  $\lambda \vec{L} \cdot \vec{S} \gg V_{cf}$  and  $J$  is a good quantum number. All the terms in Eq.(33) must be considered with  $\xi = (2l+1-4s)/s(2l-1)(2l+3)(2l-1)$ , taking  $l=3$ . The  $\vec{L} \cdot \vec{I}$  term should lead to large values for  $H_{hf}$ , and indeed, large fields have been reported (see Fig.8):  $H_{hf}$  for rare earths in iron changes sign near the middle of the 4f shell. This happens because  $L$  gives the dominant contribution to  $H_{hf}$  for most rare earths, while  $S$  orients the solute moment by spin-exchange polarization, and  $L$  and  $S$  are parallel when the 4f shell is less than half-filled, but antiparallel when it is more than half-filled. The upper limit for  $H_{hf}$  expected at rare earths in ferromagnets is the free-atom field  $H_{4f} = 2\langle r^{-3} \rangle \mu_B NJ$  [16] (to within small corrections for CEP). The experimentally obtained rare-earth fields in iron were found substantially lower than the free-atom values [17] but later investigations [18] indicated a systematic error in earlier experiments caused by incomplete magnetization of the iron foil, and the reported values of  $H_{hf}$  for the rare earths in iron shall be increased by about 80%. But still the free-atom values are not reproduced, and this point remains unsolved. Two qualitatively distinct possibilities for an explanation exist. For  $V_{cf} \ll J \gamma_j H_{ex} \sim kT$ , the rare earth atom would be a truly localized moment, and the observed  $H_{hf}$  would be a thermal average over  $(2J+1)$  substates, and at absolute zero,  $H_{hf}$  would approach  $H_{4f}$ . If, on the other hand,  $J \gamma_j H_{ex} < V_{cf}$ , then the observed  $H_{hf}$  is an average over several cubic-crystal field representations (mixed by  $H_{ex}$ ) each of which gives  $H_{hf} < H_{4f}$ , and  $H_{hf}$  will remain smaller than  $H_{4f}$  even at absolute zero.

## 7. THE $d^{10}s^2p^n$ SOLUTES

The least clear situation prevails for solute elements with atomic configurations  $d^{10}s^2p^n$ , which tend to have  $H_{hf} > 0$ , as documented in the  $4d^{10}s^25p^n$  series, where  $H_{hf}$  increases rapidly with  $n$ . Different approaches

to explain these fields were tried, but it seems that the observed values of  $H_{\text{hf}}$  for Fe, I and Xe in iron can arise only from the 5s shell (as inner s shells) polarized positively to the host 3d spins. The solute d shell is filled, and core polarization by the p shell gives only  $H_p \approx 300$  kG/electron spin [19]. On the other hand, a single 5s electron in neutral iodine has  $H_s \approx 30$  MG, and only a 3% polarization of the 5s shell would explain the observed field.

The necessary polarization can be created by two known mechanisms, the Pauli distortion effect and the covalent bonding. Orthogonalization of the host-3d and solute-5s wave-functions leads to an admixture of 3d into 5s orbital with spin parallel to the 3d spins resulting in a solute hyperfine field  $H_{\text{hf}} \approx 5$  MG for xenon in iron. Similar calculations indicate that  $H_{\text{hf}}$  should be positive for all halogens, rare gases, and alkalis. For Cs in iron for example,  $\langle 3d|5s \rangle^2$  is about half of that of Xe in iron and so should be the hyperfine field if the explanation is appropriate. Experimental evidence, however, does not support this expectation as in iron  $H_{\text{hf}}(\text{Xe}) = 1.04$  MG, and  $H_{\text{hf}}(\text{Cs}) < 30$  kG and additional contributions have to be taken into account.

#### REFERENCES

- [1] BOHR, A., MOTTELSON, B.R., Nuclear Structure, 1, Benjamin (1969).
- [2] DRELL, S.D., WALECKA, J.D., Phys. Rev. 120 (1960) 1069; NYMAN, E.M., Nucl. Phys. B1 (1967) 535; ROSS, M., Phys. Rev. 88 (1957) 1111; MIYAZAWA, H., Progr. theor. Phys. 5 (1951) 801; HARA, Y., KUROBOSHI, E., Progr. theor. Phys. 21 (1959) 768; ICHIMURA, M., YAZAKI, K., Nucl. Physics 63 (1965) 402.
- [3] CHEMTOB, M., Nucl. Physics A123 (1969) 449.
- [4] MOTTELSON, B.R., Nordita Publ. 288 (1969).
- [5] BLOMQUIST, J., FREED, N., ZETTERSTRÖM, H.O., Physics Letts 18 (1965) 47.
- [6] MAVROMATIS, H.A., ZAMICK, L., BROWN, G.E., Nucl. Physics 80 (1966) 545; MAVROMATIS, H.A., ZAMICK, L., Physics Letts 20 (1966) 171; Nucl. Physics A104 (1967) 17.
- [7] GREINER, W., Nucl. Physics 80 (1966) 417.
- [8] BARANGER, M., KUMAR, K., Nucl. Physics A110 (1968) 490.
- [9] PRIOR, O., BOEHM, F., NILSSON, S.G., Nucl. Physics A110 (1968) 490.
- [10] BOCHNACKI, Z., OGAZA, S., Nucl. Physics 69 (1965) 186.
- [11] BOCHNACKI, Z., OGAZA, S., Nucl. Physics 83 (1966) 619.
- [12] SHIRLEY, D.A., ROSENBLUM, S.S., MATTHIAS, E., Phys. Rev. 170 (1968) 363.
- [13] KONTANI, M., ITOH, J., J. Phys. Soc. Japan 22 (1967) 345.
- [14] WATSON, R.E., FREEMAN, A.J., Phys. Rev. Letts 6 (1961) 277.
- [15] DANIEL, E., FRIEDEL, J., J. Phys. Chem. Solids 24 (1963) 1601.
- [16] ELLIOTT, R.J., Rev. mod. Phys. 36 (1964) 385.
- [17] BOEHM, F., HAGEMANN, G.B., WINTHER, A., Physics Letts 21 (1966) 217; GRODZINS, L., BORCHERS, R.R., HAGEMANN, G.B., Physics Letts 21 (1966) 214; GILAD, P., GOLDRING, G., KALISH, R., HERBER, Phys. Rev. 151 (1966) 281.
- [18] DEUTSCH, B.I., HAGEMANN, G.B., HAGEMANN, K.A., OGAZA, S., Hyperfine Interactions and Nuclear Radiations, North-Holland Publ. Co. (1968).
- [19] CLOGSTONE, A.M., JACCARINO, V., Phys. Rev. 121 (1961) 1357.



## FACULTY AND PARTICIPANTS

### DIRECTORS

L. Fonda	Istituto di Fisica, 158 Via F. Severo, 10125 Trieste, Italy	Italy
G. Ripka (also lectured)	CEN de Saclay, B.P. No. 2, 91 Gif-sur-Yvette, France	France

### LECTURERS AND SEMINAR LECTURERS

G. Alaga*	Institute "Ruđer Bošković", P.O. Box 1016, Zagreb, Yugoslavia	Yugoslavia
G. Alberi*	Istituto di Fisica, 158 Via F. Severo, 10125 Trieste, Italy	Italy
M. Bauer	Departamento de Física, Universidad Nacional Autónoma de Mexico, A.P. 20-364, Mexico 20, D.F. Mexico	Mexico
L. Bertocchi*	Istituto di Fisica, 158 Via F. Severo, 10125 Trieste, Italy	Italy
K. Bleuler*	Institut für Theoretische Kernphysik, Universität Bonn, Nussallee 14-16, 53 Bonn, Fed. Rep. of Germany	Switzerland
S. Boffi	Istituto di Fisica, 4 Viale Taramelli, 27100 Pavia, Italy	Italy

---

\* The contributions of lecturers whose names are assigned asterisks are not published in these Proceedings.

R. Bonifacio*	Istituto di Fisica, 16 Via Celoria, 20133 Milano, Italy	Italy
F. Calogero*	Istituto di Fisica, 5 Piazzale delle Scienze, 00185 Roma, Italy	Italy
C. Ciofi degli Atti	Istituto Superiore di Sanità, 293 Viale Regina Elena, 00161 Roma, Italy	Italy
J.A. Davies	Chalk River Nuclear Lab., Chalk River, Ontario, Canada	Canada
V. de Giorgio*	CISE, Casella Postale 3986, 20100 Milano, Italy	Italy
B. Deutch*	Institute of Physics, University of Aarhus, Aarhus C, Denmark	USA
K. Dietrich	Institut für Theoretische Physik, Universität Heidelberg, Im Neuenheimer Feld 5, 6900 Heidelberg 1, Fed. Rep. of Germany	Federal Republic of Germany
J. Gillespie	Physics Department, Boston University, 111 Cummington St., Boston, Massachusetts, 02215, USA	USA
L. Grodzins*	Massachusetts Institute of Technology, Cambridge, Massachusetts, 02139, USA	USA
M.E. Grypeos	Nuclear Research Centre "Democritos", Athens, Greece	Greece
R. Guardiola	Department of Physics, University of Valencia, Valencia, Spain	Spain
A. Kallio*	Department of Theoretical Physics, University of Oulu, Kirkkokatu 11, Oulu, Finland	Finland
M.W. Kirson	Department of Physics, The Weizmann Institute of Science, Rehovoth, Israel	Israel
M.-C. Lemaire (Miss)	CEN de Saclay, B.P. No.2, 91 Gif-sur-Yvette, France	France

## LIST OF PARTICIPANTS

591

J. Lindhard *	Institute of Physics, University of Aarhus, Aarhus C, Denmark	Denmark
M. V. Mihailović*	Institute "Josef Stefan", Jamova 39, Ljubljana, Yugoslavia	Yugoslavia
M. A. NagaraJan	Institut de Physique, Université de Liège, Sart-Tilman, Liège 1, Belgium	India
J. Németh	Roland Eötvös University, Puskin u. 5, Budapest, Hungary	Hungary
S. Ogaza	Department of Physics, University of Kraków, Cracow, Poland	Poland
F. Palumbo*	Lab. FNA, CNEN, Centro di Studi Nucleari della Casaccia, C.P. No. 2400, 00100 Roma, Italy	Italy
J. Raynal	CEN de Saclay, B.P. No. 2, 91 Gif-sur-Yvette, France	France
A. Rimini	Istituto di Fisica, 158 Via F. Severo, 10125 Trieste, Italy	Italy
J. D. Rogers*	Institute of Physics, Av. Luiz Englert, Porto Alegre, Brazil	USA
W. Rybarska (Miss)	Laboratory of Theoretical Physics, JINR, Head Post Office, P.O. Box 79, Moscow, USSR	Poland
L. Šips	Institute "Ruder Bošković", P.O. Box 1016, Zagreb, Yugoslavia	Yugoslavia
W. von Oertzen	Max-Planck-Institut für Kernphysik, Postfach 1248, 6900 Heidelberg, Fed. Rep. of Germany	Federal Republic of Germany
T. Weber	Istituto di Fisica, 158 Via F. Severo, 10125 Trieste, Italy	Italy
K. Wildermuth	Institut für Theoretische Physik, Universität Tübingen, Köstlinstrasse 6, 7400 Tübingen, Fed. Rep. of Germany	Federal Republic of Germany

B. N. Zakhariev	Laboratory of Theoretical Physics, JINR, Head Post Office P.O. Box 79, Moscow, USSR	USSR
M. Zielińska-Pfabé (Mrs.)	Institute for Nuclear Research, Hoża 69, Warsaw, Poland	Poland

## EDITOR

A. M. Hamende	International Centre for Theoretical Physics, Trieste, Italy	Italy
---------------	--	-------

## PARTICIPANTS

Y. K. Agarwal	Technische Hochschule Darmstadt, 61 Darmstadt, Fed. Rep. of Germany	India
Israr Ahmad	Department of Physics, Aligarh Muslim University, Aligarh (U.P.), India	India
S. S. Ahmad	Istituto di Fisica, Via Marzolo 8, 35100 Padova, Italy	Pakistan
K. Allaart	Natuurkundig Laboratorium der Vrije Universiteit, De Boelelaan 1081, Amsterdam, The Netherlands	The Netherlands
C. M. Amaral	Centro Brasileiro de Pesquisas Fisicas, Av. Wenceslau Braz 71 ZC-82, Rio de Janeiro, Brazil	Brazil
N. J. Azziz	Facultad de Ingeniería y Agrimensura, Instituto de Física, J. Herrera y Reissig 565, Montevideo, Uruguay	Uruguay
M. Baldo	Istituto di Fisica, 57 Corso Italia, 95129 Catania, Italy	Italy
D. Belchner	Institut für Theoretische Physik, Universität Tübingen, Köstlinstrasse 6, 7400 Tübingen, Fed. Rep. of Germany	Federal Republic of Germany
F. Bertrand (Miss)	Commissariat à l'énergie atomique, B.P. 27, Villeneuve, St. Georges, France	France

## LIST OF PARTICIPANTS

593

P. Beuzit	CEN de Saclay, B.P. No.2, 91 Gif-sur-Yvette, France	France
M.L. Bogdanović (Miss)	"Boris Kidrić" Institute of Nuclear Sciences, P.O. Box 522, Belgrade, Yugoslavia	Yugoslavia
S.U. Campisano	Istituto di Fisica, 57 Corso Italia, 95129 Catania, Italy	Italy
G. Carraro	EURATOM, BCMN, Steenweg near Retie, Geel (Antwerp), Belgium	Italy
F. Catara	Istituto di Fisica, 57 Corso Italia, 95129 Catania, Italy	Italy
A. Chaumeaux	CEN de Saclay, B.P. No.2, 91 Gif-sur-Yvette, France	France
I.-T. Cheon	Faculty of Liberal Arts, Kobe-Gakuin University, Tarumi, Kobe, Japan	Korea
D. Clement	Institut für Theoretische Physik, Universität Tübingen, Köstlinstrasse 6, 7400 Tübingen, Fed. Rep. of Germany	Federal Republic of Germany
E. Coffou	Institute "Ruder Bošković", P.O. Box 1016, Zagreb, Yugoslavia	Yugoslavia
J.M. Cohenca	Instituto de Física, Universidade de São Paulo, C.P. 8105, São Paulo, Brazil	Brazil
J. Dąbrowski	Institute for Nuclear Research, Hoża 69, Warsaw, Poland	Poland
P.K.A. David	Institut für Strahlen- und Kernphysik, Nussallee 14-16, 53 Bonn, Fed. Rep. of Germany	Federal Republic of Germany
S.M. de Barros Cuyabano (Mrs.)	Centro Brasileiro de Pesquisas Fisicas, Av. Wenceslau Braz 71 ZC-82, Rio de Janeiro, Brazil	Brazil
M. Dechargé	Commissariat à l'énergie atomique, B.P. 510, 75-Paris XV <sup>e</sup> , France	France

J.-M. Delbrouck (Mrs.)	Physique nucléaire, Université de Liège, 1A, Quai Roosevelt, 4000 Liège, Belgium	Belgium
D.R. de Oliveira.	Instituto de Física Teórica, Rua Pamplona 145, São Paulo, Brazil	Brazil
O. Dietzsch	Instituto de Física, Universidade de São Paulo, C.P. 8105, São Paulo, Brazil	Brazil
M. di Toro	Istituto di Fisica, 57 Corso Italia, 95129 Catania, Italy	Italy
L. Döhnert	Departamento de Física, Universidad Central de Venezuela, Caracas, Venezuela Mailing: Apartado 62468, Chacao, Caracas, Venezuela	Venezuela
C.G. Dussel	Comisión Nacional de Energía Atómica, Av. del Libertador 8250, Buenos Aires (S29), Argentina	Argentina
O.I. El Amin	Department of Physics, University of Khartoum, P.O. Box 846, Khartoum, Sudan	Sudan
K. Erkelenz	Institut für Theoretische Kernphysik, Universität Bonn, Nussallee 14-16, 53 Bonn, Fed. Rep. of Germany	Federal Republic of Germany
S.I. Fedotov	Laboratory of Theoretical Physics, JINR, Head Post Office, P.O. Box 79, Moscow, USSR	USSR
H.C. Flocard	Institut de physique nucléaire, B.P. No.1, 91-Orsay, France	France
J.E. Fuentes Betancourt	Departamento de Física, Universidad de la Habana, Habana, Cuba	Cuba
I. Gabrielli	Istituto di Fisica, 158 Via F. Severo, 10125 Trieste, Italy	Italy
F. Giga (Miss)	Department of Physics, University of Dar es Salaam, P.O. Box 35063, Dar es Salaam, Tanzania	Tanzania

## LIST OF PARTICIPANTS

595

A.C. Moura Gonçalves	Centro Brasileiro de Pesquisas Físicas, Av. Wenceslau Braz 71 ZC-82, Rio de Janeiro, Brazil	Brazil
J. Gosset	CEN de Saclay, B.P. No. 2, 91 Gif-sur-Yvette, France	France
J.A. Guillaumon Filho	Instituto de Física, Universidade de São Paulo, C.P. 8105, São Paulo, Brazil	Brazil
T. Gujadhur	Department of Theoretical Physics, Imperial College, Prince Consort Road, London SW 7, England	Mauritius
P.O. Haapakoski	Research Institute for Theoretical Physics, Siltavuorenpenger 20B, Helsinki 17, Finland	Finland
P. Haensel	Institute for Theoretical Physics, University of Warsaw, Warsaw, Poland	Poland
H.H. Hansen	EURATOM, BCMN, Steenweg near Retie, Geel (Antwerp), Belgium	Federal Republic of Germany
M.Y.M. Hassan	Department of Physics, Cairo University, Giza, Cairo, Egypt, Arab Rep. of	Egypt, Arab. Rep. of
J. Hendeković	Institute "Ruder Bošković", P.O. Box 1016, Zagreb, Yugoslavia	Yugoslavia
R.P. Hirsekorn	Technische Universität Braunschweig, Mendelssohnstrasse 1A, 33 Braunschweig, Fed. Rep. of Germany	Federal Republic of Germany
S. Islam	Theoretical Physics Laboratory, Dacca University, Dacca-2, Pakistan	Pakistan
C. Jacquemin	Institut de physique nucléaire, B.P. No. 1, 91-Orsay, France	France
J.M.F. Jeronymo	Departamento de Física, Pontificia Universidade Católica, Rua Marques S. Vicente 209, Rio de Janeiro ZC-20, Brazil	Brazil
K. Junker	Physics Division, Eidg. Institut für Reaktorforschung, CH-5303 Würenlingen, Switzerland	Austria

S. Khadkikar	Physical Research Laboratory, Navrangpura, Ahmedabad-9, India	India
A. M. Khan	Pakistan Institute of Nuclear Science and Technology, Post Office Nilore, Rawalpindi, Pakistan	Pakistan
K. M. Khanna	Department of Physics, Dibrugarh University, Assam, India	India
E. Koltay Gyarmati (Mrs.)	Institute of Nuclear Research, P.O. Box 51, Debrecen 1, Hungary	Hungary
M. Kozłowski	Institute of Experimental Physics, Hoża 69, Warsaw 1, Poland	Poland
R. J. Kulesa	Department of Physics, Jagellonian University, Reymonta 4, Cracow 16, Poland	Poland
P. Kulišić	Institute "Ruder Bošković", P.O. Box 1016, Zagreb, Yugoslavia	Yugoslavia
D. R. Kulkarni	Physical Research Laboratory, Navrangpura, Ahmedabad-9, India	India
N. Kumar	Indian Institute of Technology, IIT Post Office, Kanpur 16 (U.P.), India	India
J. Kuźmiński	Institute of Physics, Silesian University, Bankowa 12, Katowice, Poland	Poland
A. Lejeune	Institut de physique, Université de Liège, Sart-Tilman, Liège 1, Belgium	Belgium
E. Ley-Koo	Departamento de Física, Universidad Nacional Autónoma de México, A. P. 20-364, México 20, D.F., Mexico	Mexico
K. L. Lim	Department of Mathematics, University Malaya, Kuala Lumpur, Malaysia	Malaysia
N. Lisboa Mayer (Miss)	Centro Brasileiro de Pesquisas Físicas, Av. Wenceslau Braz 71 ZC-82, Rio de Janeiro, Brazil	Brazil

## LIST OF PARTICIPANTS

597

V. Lopac (Miss)	Institute "Ruder Bošković", P.O. Box 1016, Zagreb, Yugoslavia	Yugoslavia
D.C. Martin	Department of Physics, University of Surrey, Guildford, Surrey, UK	United Kingdom
M. Meinhart	Institut für Theoretische Physik, Rosenplatz, D-44 Münster, Fed. Rep. of Germany	Austria
D.J. Millener	Nuclear Physics Laboratory, University of Oxford, Oxford, United Kingdom	New Zealand
H. Mommsen	Institut für Strahlen- und Kernphysik, Nussallee 14-16, 53 Bonn, Fed. Rep. of Germany	Federal Republic of Germany
E.V. Moya (Miss)	Departamento de Física, Zaragoza University, Zaragoza, Spain	Spain
A. Mudnić	Institute "Ruder Bošković", P.O. Box 1016, Zagreb, Yugoslavia	Yugoslavia
J. Mwanje	Department of Physics, Makerere University, P.O. Box 7062, Kampala, Uganda	Uganda
L.O. Norlin	Fysiska Institutionen, Box 530, S 75121 Uppsala 1, Sweden	Sweden
P. Nunberg	Lab. FNA, CNEN, Centro di Studi Nucleari della Casaccia, C.P. No. 2400, 00100 Roma, Italy	Italy
R.W.F. Oakley	Department of Physics, University of Surrey, Guildford, Surrey, UK	United Kingdom
J.C. Palathingal	Madras Christian College, Tambaram, Madras-59, India	India
G. Pauli	Istituto di Fisica, 158 Via F. Severo, 10125 Trieste, Italy	Italy
T. Persi	People's University, Pula, Yugoslavia	Yugoslavia
G. Pisent	Istituto di Fisica, Via Marzolo 8, 35100 Padova, Italy	Italy

D. Rabenstein	Reaktorstation E 14, 8046 Garching, Fed. Rep. of Germany	Federal Republic of Germany
S. Radhakant	Tata Institute of Fundamental Research, Colaba, Bombay-5, India	India
A. A. Răduță	Laboratory of Theoretical Physics, JINR, Head Post Office P.O. Box 79, Moscow, USSR	Romania
J. F. Renuart	Centre de Physique Nucléaire, Université Catholique de Louvain, 3030 Héverlé, Belgium	Belgium
J. Řízek	Nuclear Research Institute, Řež near Prague, Czechoslovak Socialist Republic	Czechoslovak Socialist Republic
M. J. C. Rots	Instituut voor Kern- en Stralingsfysika, Katholieke Universiteit Leuven, Celestijnenlaan 200D, 3030 Héverlé, Belgium	Belgium
M. J. Saarela	Kirkkokatu 28, Oulu, Finland	Finland
D. Schütte	Institut für Theoretische Kernphysik, Universität Bonn, Nussallee 14-16, 53 Bonn, Fed. Rep. of Germany	Federal Republic of Germany
A. E-T. Sharaf El-Din	Department of Physics, University of Khartoum, Khartoum, Sudan	Sudan
M. A. Shaukat	Pakistan Institute of Nuclear Science and Technology, Post Office Nilore, Rawalpindi, Pakistan	Pakistan
A. K. M. Siddiq	Department of Physics, University of Dacca, Dacca-2, Pakistan	Pakistan
L. D. Skouras	Nuclear Research Centre "Democritos", Athens, Greece	Greece
A. Soenoto	Istituto di Fisica Teorica, Mostra d'Oltremare, Pad. 19, Napoli, Italy	Indonesia
F. Stancu (Mrs.)	Institut de physique, Université de Liège, Sart-Tilman, Liège 1, Belgium	Romania

## LIST OF PARTICIPANTS

599

M. P. Stojanović (Mrs.)	"Boris Kidrić" Institute of Nuclear Sciences, P.O. Box 522, Belgrade, Yugoslavia	Yugoslavia
G. Stratan	Laboratory of Theoretical Physics, JINR, Head Post Office P.O. Box 79, Moscow, USSR	Romania
M. Šunjić	Institute "Ruder Bošković", P.O. Box 1016, Zagreb, Yugoslavia	Yugoslavia
L. Tauhata	Centro Brasileiro de Pesquisas Físicas, Av. Wenceslau Braz 71 ZC-82, Rio de Janeiro, Brazil	Brazil
J. W. Tépél	Atomic Energy Board, Bag 256, Pretoria, Republic of South Africa	South Africa
G. A. Timmer	Fysisch Laboratorium, Bylhouwerstraat 6, Utrecht, The Netherlands	The Netherlands
C. H. Traore	Laboratoire d'énergie solaire, B.P. 134, Bamako, Mali	Mali
G. Vanden Berghe	Institute for Nuclear Science, Proeftuinstraat 40, 9000 Gent, Belgium	Belgium
L. Verdini	Istituto di Fisica, 158 Via F. Severo, 10125 Trieste, Italy	Italy
P. B. Vitta	Department of Physics, University of Dar es Salaam, P.O. Box 35063, Dar es Salaam, Tanzania	Tanzania
W. Wajntal	Laboratório de Acelerador Eletrostático, Universidade de São Paulo, C.P. 8105, São Paulo, Brazil	Brazil
M. E. L. Warquier	Institute for Nuclear Science, Proeftuinstraat 40, 9000 Gent, Belgium	Belgium
K. C. Wong	Department of Physics, University of Singapore, Singapore 10	Singapore
K. S. Wu	Institute of Nuclear Energy Research, P.O. Box No. 3, Lung-Tan, Taiwan, Republic of China	Republic of China
O. Zohni	Department of Physics, Cairo University, Giza, Cairo, Egypt, Arab. Rep. of	Egypt, Arab. Rep. of

# HOW TO ORDER IAEA PUBLICATIONS

Exclusive sales agents for IAEA publications, to whom all orders and inquiries should be addressed, have been appointed in the following countries:

UNITED KINGDOM Her Majesty's Stationery Office, P.O. Box 569, London S.E.1  
UNITED STATES OF AMERICA UNIPUB, Inc., P.O. Box 433, New York, N.Y. 10016

In the following countries IAEA publications may be purchased from the sales agents or booksellers listed or through your major local booksellers. Payment can be made in local currency or with UNESCO coupons.

ARGENTINA Comisión Nacional de Energía Atómica, Avenida del Libertador 8250, Buenos Aires  
AUSTRALIA Hunter Publications, 58 A Gipps Street, Collingwood, Victoria 3066  
BELGIUM Office International de Librairie, 30, avenue Marnix, Brussels 5  
CANADA Information Canada, Ottawa  
C.S.S.R. S.N.T.L., Spálená 51, Prague 1  
FRANCE Alfa, Publishers, Hurbanovo námestie 6, Bratislava  
Office International de Documentation et Librairie, 48, rue Gay-Lussac, F-75 Paris 5<sup>e</sup>  
HUNGARY Kultura, Hungarian Trading Company for Books and Newspapers, P.O.Box 149, Budapest 62  
INDIA Oxford Book and Stationery Comp., 17, Park Street, Calcutta 16  
Prakash Publishers, Film Colony, Chaura Rasta, Jaipur-3 (Raj.)  
ISRAEL Heiliger and Co., 3, Nathan Strauss Str., Jerusalem  
ITALY Agenzia Editoriale Commissionaria, A.E.I.O.U., Via Meravigli 16, I-20123 Milan  
JAPAN Maruzen Company, Ltd., P.O.Box 5050, 100-31 Tokyo International  
NETHERLANDS Martinus Nijhoff N.V., Lange Voorhout 9-11, P.O.Box 269, The Hague  
PAKISTAN Mirza Book Agency, 65, The Mall, P.O.Box 729, Lahore-3  
POLAND Ars Polona, Centrala Handlu Zagranicznego, Krakowskie Przedmiescie 7, Warsaw  
ROMANIA Cartimex, 3-5 13 Decembrie Street, P.O.Box 134-135, Bucarest  
SOUTH AFRICA Van Schaik's Bookstore, P.O.Box 724, Pretoria  
Universitas Books (Pty) Ltd., P.O.Box 1557, Pretoria  
SWEDEN C.E.Fritzes Kungl. Hovbokhandel, Fredsgatan 2, Stockholm 16  
U.S.S.R. Mezhdunarodnaya Kniga, Smolenskaya-Sennaya 32-34, Moscow G-200  
YUGOSLAVIA Jugoslovenska Knjiga, Terazije 27, Belgrade

Orders from countries where sales agents have not yet been appointed and requests for information should be addressed directly to:



Publishing Section,  
International Atomic Energy Agency,  
Kärntner Ring 11, P.O.Box 590, A-1011 Vienna, Austria



INTERNATIONAL  
ATOMIC ENERGY AGENCY  
VIENNA, 1972

PRICE: US \$18.00  
Austrian Schillings 420,-  
(£6.90; F.Fr. 90,-; DM 57,-)

SUBJECT GROUP: III  
Physics/Theoretical Physics